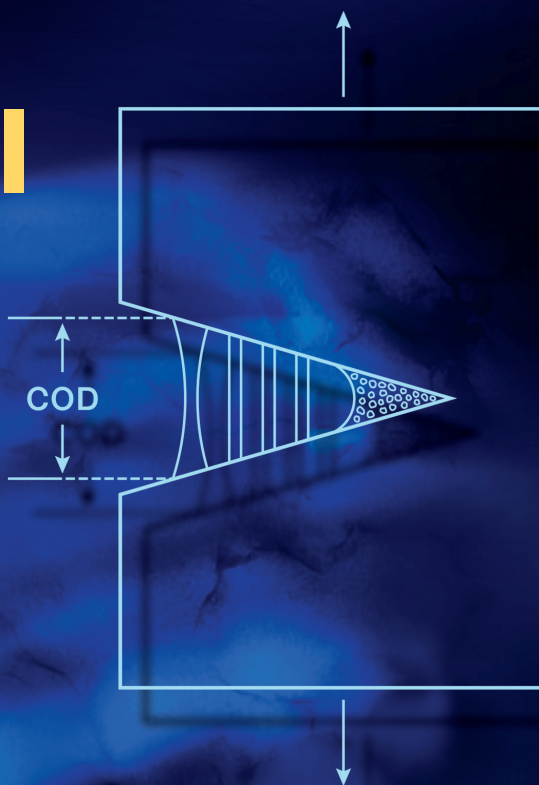I. M. Ward

J. Sweeney

Mechanical Properties of Solid Polymers

Third Edition

COD

Mechanical Properties of Solid Polymers

Mechanical Properties of Solid Polymers

Third Edition

I. M. WARD

School of Physics and Astronomy, Leeds University, Leeds, UK

J. SWEENEY

School of Engineering, Design and Technology,
University of Bradford, Bradford, UK

Contents

Preface

This book is the third edition of *Mechanical Properties of Solid Polymers* and follows the format of the first two editions in writing the chapters as separate units. Therefore, each chapter can be regarded as a self-contained introduction and review of progress in the different aspects of the mechanical behaviour.

Since the publication of the second edition in 1983, the subject has advanced considerably in many respects, especially with regard to non-linear viscoelasticity, yield and fracture. We have altered some chapters very little, notably those dealing with viscoelastic behaviour and the earlier research on anisotropic mechanical behaviour and rubber elasticity, only adding sections to deal with the latest developments.

On the other hand, it has been necessary to change substantially the chapters on non-linear viscoelasticity, yield and fracture and in some cases incorporate material from the second edition of *An Introduction to the Mechanical Properties of Solid Polymers*. A separate chapter is also added on polymer composites.

In all cases, the approach of the previous textbooks has been followed. This is to obtain a formal description of the behaviour using the mathematical techniques of solid mechanics, followed by an attempt to seek understanding in terms of the molecular structure and morphology.

Finally, we wish to thank Margaret Ward for undertaking a substantial part of the initial typing of the new text and Glenys Bowles for providing secretarial assistance.

<div align="right">

I. M. Ward
J. Sweeney

</div>

1

Structure of Polymers

The mechanical properties that form the subject of this book are a consequence of the chemical composition of the polymer and also of its structure at the molecular and supermolecular levels. We shall therefore introduce a few elementary ideas concerning these aspects.

1.1 Chemical Composition

1.1.1 Polymerisation

Linear polymers consist of long molecular chains of covalently bonded atoms, each chain being a repetition of much smaller chemical units. One of the simplest polymers is polyethylene, which is an addition polymer made by polymerising the monomer ethylene, $CH_2{=}CH_2$, to form the polymer.

$$\left[\!\!\left[-CH_2-CH_2- \right]\!\!\right]_n$$
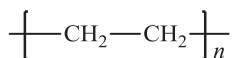
Note that the double bond is removed during the polymerisation (Figure 1.1). The well-known vinyl polymers are made by polymerising compounds of the form.

$$\underset{\displaystyle H_2C{=\!\!=}CH}{\overset{\displaystyle X}{\vert}}$$
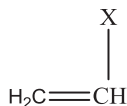
where X represents a chemical group; examples are as follows:

Polypropylene

$$\left[\!\!\left[-CH_2-\underset{}{\overset{\displaystyle CH_3}{\underset{\vert}{CH}}}- \right]\!\!\right]_n$$
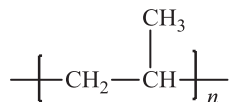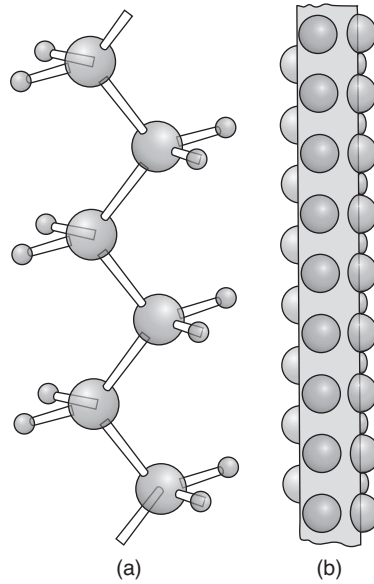
Figure 1.1   *(a) The polyethylene chain (CH₂)ₙ in schematic form (larger spheres, carbon; smaller spheres, hydrogen) and (b) sketch of a molecular model of a polyethylene chain.*

Polystyrene

$$\left[-CH_2-\underset{\underset{\displaystyle C_6H_5}{\shortmid}}{CH} \right]_n$$

and

poly(vinyl chloride)

$$\left[-CH_2-\underset{\underset{\displaystyle Cl}{\shortmid}}{CH} \right]_n$$
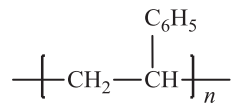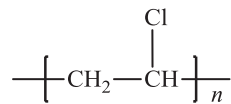
Natural rubber, polyisoprene, is a diene, and its repeat unit

$$\left[-CH_2-CH=\underset{\underset{\displaystyle CH_3}{\shortmid}}{C}-CH_2 \right]_n$$
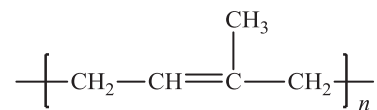
contains a double bond.

A condensation reaction is one in which two or more molecules combine into a larger molecule with or without the loss of a small molecule (such as water). One example is the formation of polyethylene terephthalate (the polyester used for Terylene and Dacron fibres and transparent films and bottles) from ethylene glycol and terephthalic acid:

$$n\left(\text{HO}-\text{CH}_2-\text{CH}_2-\text{OH}\right) + n\left(\text{HOOC}-\bigcirc-\text{COOH}\right)$$

$$\Longrightarrow \text{H}\left[\text{O}-\text{CH}_2-\text{CH}_2-\text{O}-\overset{\text{O}}{\underset{\text{O}}{\text{C}}}-\bigcirc-\overset{\text{O}}{\text{C}}-\text{OH}\right]_n + n\text{H}_2\text{O}$$
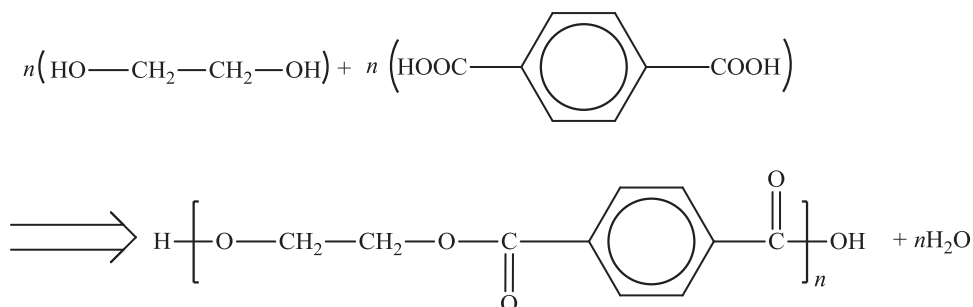
Another common condensation polymer is nylon 6,6.

$$\left[-\text{NH}-\left(\text{CH}_2\right)_6-\text{NH}-\overset{}{\underset{\text{O}}{\text{C}}}-\left(\text{CH}_2\right)_4-\overset{\text{O}}{\text{C}}-\right]_n$$
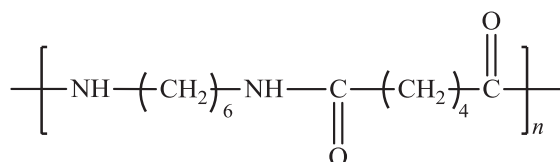
1.1.2   Cross-Linking and Chain-Branching

Linear polymers can be joined by other chains at points along their length to make a cross-linked structure (Figure 1.2). Chemical cross-linking produces a thermosetting polymer, so called because the cross-linking agent is normally activated by heating, after which the
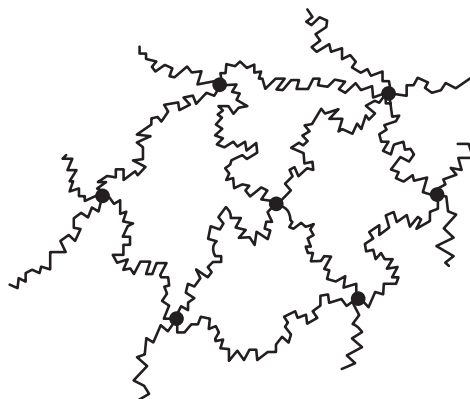
Figure 1.2   *Schematic diagram of a cross-linked polymer.*
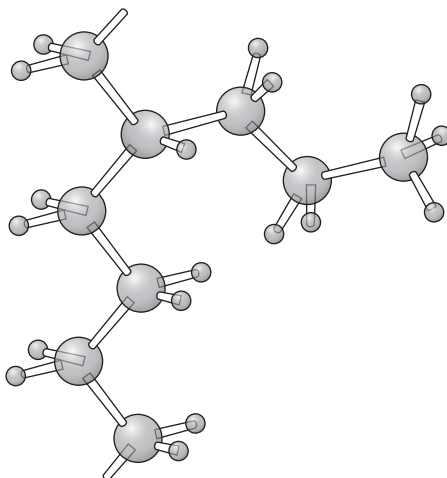
Figure 1.3   *A chain branch in polyethylene.*

material does not soften and melt when heated further, for example Bakelite and epoxy resins. A small amount of cross-linking through sulfur bonds is needed to give natural rubber its characteristic feature of rapid recovery from a large extension.

Very long molecules in linear polymers can entangle to form temporary physical cross-links, and we shall show later that a number of the characteristic properties of solid polymers are explicable in terms of the behaviour of a deformed network.

A less extreme complication is chain branching, where a secondary chain initiates from a point on the main chain, as is illustrated for polyethylene in Figure 1.3. Low-density polyethylene, as distinct from the high-density linear polyethylene shown in Figure 1.1, possesses on average one long branch per molecule and a larger number of small branches, mainly ethyl (—CH_2—CH_3) or butyl (—$(CH_2)_3$—CH_3) side groups. The presence of these branch points leads to considerable differences in mechanical behaviour compared with linear polyethylene.

1.1.3   Average Molecular Mass and Molecular Mass Distribution

Each sample of a polymer contains molecular chains of varying lengths, that is of varying molecular mass (Figure 1.4). The mass (length) distribution is of importance in determining the properties of the polymer, but until the advent of gel permeation chromatography [1,2] it could be determined only by tedious fractionation procedures. Most investigations therefore quoted different types of average molecular mass, the commonest being the number average $\bar{M}_n$ and the weight average $\bar{M}_n$, defined as

$$\bar{M}_n = \frac{\sum N_i M_i}{\sum N_i} \quad \bar{M}_w = \frac{\sum (N_i M_i) M_i}{\sum N_i M_i},$$

where N_i is the number of molecules of molecular mass M_i, and Σ denotes summation over all i molecular masses.
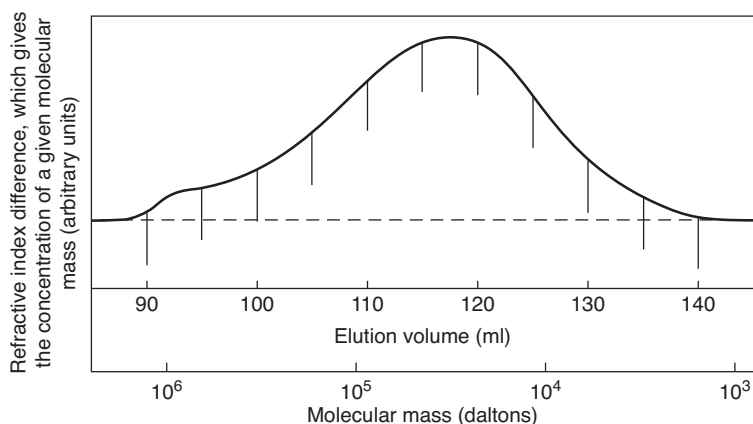
Figure 1.4   *The gel permeation chromatograph trace gives a direct indication of the molecular distribution. (Results obtained in Marlex 6009 by Dr. T. Williams.)*

The weight average molecular mass is always higher than the number average, as the former is strongly influenced by the relatively small number of very long (massive) molecules. The ratio of the two averages gives a general idea of the width of the molecular mass distribution.

Fundamental measurements of average molecular mass must be performed on solutions so dilute that intermolecular interactions can be ignored or compensated for. The commonest techniques are osmotic pressure for the number average and light scattering for the weight average. Both methods are rather lengthy, so in practice an average molecular mass was often deduced from viscosity measurements of either a dilute solution of the polymer (which relates to M_n) or a polymer melt (which relates to M_w). Each method yielded a different average value, which made it difficult to correlate specimens characterised by different groups of workers.

The molecular mass distribution is important in determining flow properties, and so may affect the mechanical properties of a solid polymer indirectly by influencing the final physical state. Direct correlations of molecular mass to viscoelastic behaviour and brittle strength have also been obtained.

1.1.4   Chemical and Steric Isomerism and Stereoregularity

A further complication of the chemical structure of polymers lies in the possibility of different chemical isomeric forms within a repeat unit or between a series of repeat units. Natural rubber and gutta percha are chemically both polyisoprene, but the former is the *cis* form and the latter is the *trans* form (see Figure 1.5). The characteristic properties of rubber are a consequence of the loose packing of molecules (i.e. large *free volume*) that arises from its structure.

Vinyl monomer units

$$\text{---CH}_2\text{---CH---}\ \ \overset{\displaystyle X}{\underset{\displaystyle |}{}}$$

cis-1,4 Polyisoprene

trans-1,4 Polyisoprene
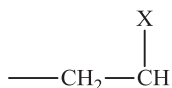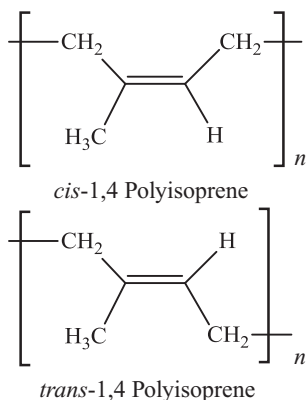
Figure 1.5   *cis-1,4-Polyisoprene and trans-1,4-polyisoprene.*

can be added to a growing chain either head-to-tail:
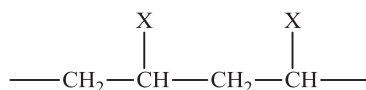
or head-to-head:
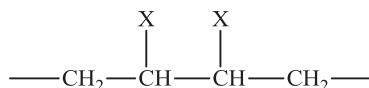
Head-to-tail substitution is usual, and only a small proportion of head-to-head linkages can produce a reduction in the tensile strength because of the loss of regularity.

Stereoregularity provides a more complex situation, which we will examine in terms of the simplest type of vinyl polymer (Figure 1.6) and for which we shall suppose that the polymer chain is a planar zigzag. Two very simple regular polymers can be constructed. In the first (Figure 1.6(a)) the substituent groups are all added in an identical manner to give an *isotactic* polymer. In the second regular polymer (Figure 1.6(b)) there is an inversion of the manner of substitution between consecutive units, giving a *syndiotactic* polymer for which the substituent groups alternate regularly on opposite sides of the chain. The regular sequence of units is called *stereoregularity*, and stereoregular polymers are crystalline and can possess high melting temperatures. The working range of a polymer is thereby extended compared with the amorphous atactic form, whose range is limited by the lower softening point. The final alternative structure is formed when the orientation of successive substituents takes place randomly (Figure 1.5(c)) to give an irregular *atactic* polymer that is incapable of crystallising. Polypropylene ($—CH_2CHCH_3—$)$_n$ was for many years
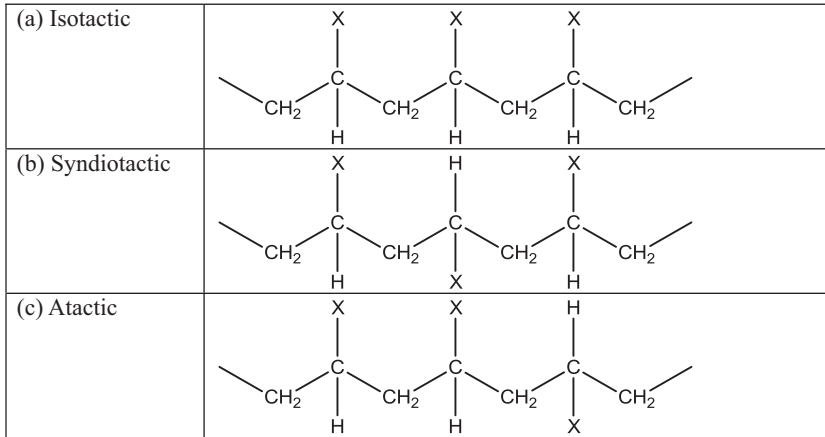
(a) Isotactic	

Figure 1.6   *A substituted α-olefin can take three stereosubstituted forms.*

obtainable only as an atactic polymer, and its widespread use began only when stereospecific catalysts were developed to produce the isotactic form. Even so, some faulty substitution occurs and atactic chains can be separated from the rest of the polymer by solvent extraction.

1.1.5   Liquid Crystalline Polymers

Liquid crystals (or plastic crystals as they are sometimes called) are materials that show molecular alignment in one direction but not three-dimensional crystalline order. During the last 20 years, liquid crystalline polymers have been developed where the polymer chains are so straight and rigid that small regions of almost uniform orientation (domains) separated by distinct boundaries are produced. In the case where these domains occur in solution, polymers are termed *lyotropic*. Where the domains occur in the melt, the polymers are termed *thermotropic*.

An important class of lyotropic liquid crystal polymers are the aramid polymers such as polyparabenzamide
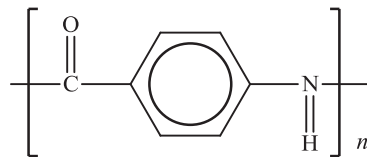
and polyparaphenylene terephthalamide
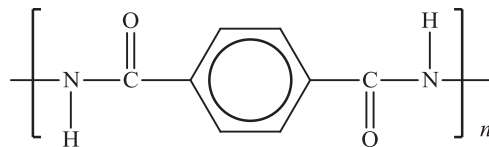
better known as Kevlar, which is a commercially produced high stiffness and high strength fibre. It is important to emphasise that although Kevlar fibres are prepared by spinning a lyotropic liquid crystalline phase, the final fibre shows clear evidence of three-dimensional order.

Important examples of thermotropic liquid crystalline polymers are copolyesters produced by condensation of hydroxybenzoic acid (HBA)
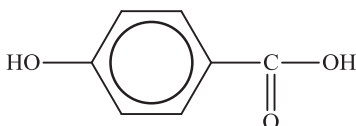
and 2,6-hydroxynaphthoic acid (HNA)
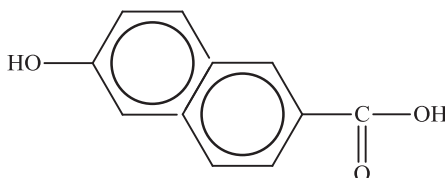
most usually in the proportions HBA:HNA = 73:27.

In addition to these main-chain liquid crystalline polymers, there are also side-chain liquid crystalline polymers, where the liquid crystalline nature arises from the presence of rigid straight side-chain units (called the mesogens) chemically linked to an existing polymer backbone either directly or via flexible spacer units.

The review by Noël and Navard [3] gives further information on liquid crystalline polymers, including methods of preparation.

1.1.6   Blends, Grafts and Copolymers

A *blend* is a physical mixture of two or more polymers. A *graft* is formed when long side chains of a second polymer are chemically attached to the base polymer. A *copolymer* is formed when chemical combination exists in the main chain between two or more polymers, $[A]_n$, $[B]_n$, and so on. The two principal forms are block copolymers ([AAAA. . .] [BBB. . .]) and *random* copolymers, the latter having no long sequences of A or B units.

All these processes are commonly used to enhance the ductility and toughness of brittle homopolymers or increase the stiffness of rubbery polymers. An example of a blend is acrylonitrile–butadiene–styrene copolymer (ABS), where the separate rubber phase gives much improved impact resistance.

The basic properties of polymers may be enhanced by physical as well as chemical means. An important example is the use of finely divided carbon black as a filler in rubber compounds. Polymers may be combined with stiffer filaments, such as glass and carbon

fibres, to form a composite. We shall show later that some semi-crystalline polymers may be treated as composites at a molecular level.

It must not be forgotten that all useful polymers contain small quantities of additives to aid processing and increase the resistance to degradation. The physical properties of the base polymer may be modified by the presence of such additives.

1.2   Physical Structure

The physical properties of a polymer of a given chemical composition are dependent on two distinct aspects of the arrangement of the molecular chains in space.

1. The arrangement of a single chain without regard to its neighbour: rotational isomerism.
2. The arrangement of chains with respect to each other: orientation and crystallinity.

1.2.1   Rotational Isomerism

Rotational isomerism arises because of the alternative conformations of a molecule that can result from the possibility of hindered rotation about the many single bonds in the structure. Spectroscopic techniques [4] developed in small molecules have been extended to polymers, and as an example we illustrate (Figure 1.7) the alternative trans and gauche conformations in the glycol residue of polyethylene terephthalate [5]: the former is a crystalline conformation, but the latter is present in amorphous regions.

To pass from one rotational isomeric form to another requires that an energy barrier be surmounted (Figure 1.8), so that the possibility of the chain molecules changing their
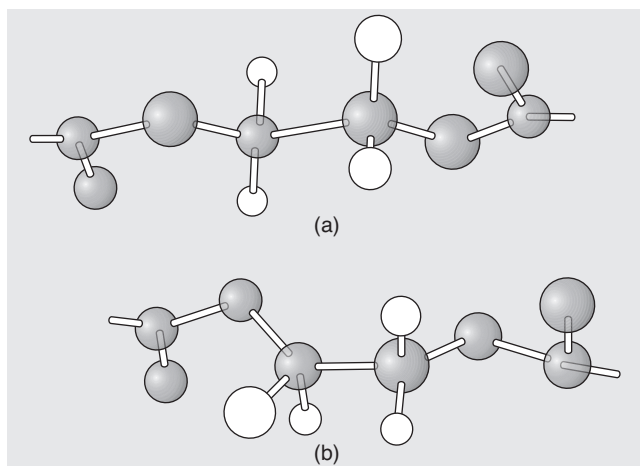
Figure 1.7   *Polyethylene terephthalate in the crystalline trans conformation (a) and in the gauche conformation present in 'amorphous' regions (b). (Adapted from Grime, D. and Ward, I.M. (1958) The assignment of infra-red absorptions and rotational isomerism in polyethylene terephthalate and related compounds. Trans. Faraday Soc., **54**, 959. Copyright (1958) Royal Society of Chemistry.)*
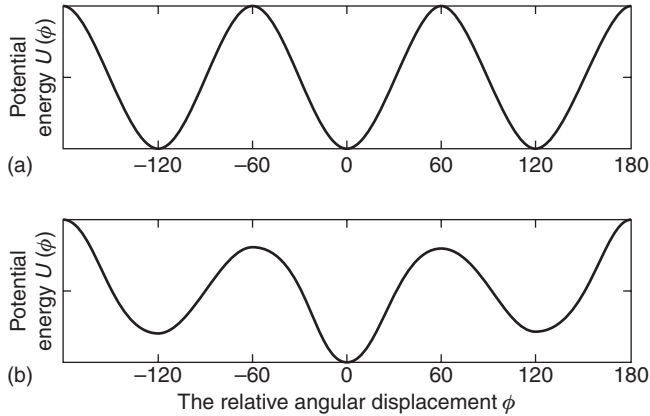
Figure 1.8   *Potential energy for rotation (a) around the C—C bond in ethane and (b) around the central C—C bond in n-butane. (Reprinted from McCrum, N.G., Read, B.E., Williams, G. (1991) Anelastic and Dielectric Effects in Polymeric Solids, Dover Publications, New York. Copyright (1991) Dover Publications.)*

conformations depends on the relative magnitude of the energy barrier compared with thermal energies and the perturbing effects of applied stress. Hence, arises the possibility of linking molecular flexibility to deformation mechanisms, a theme to which we will return on several occasions.

1.2.2   Orientation and Crystallinity

When we consider the arrangement of molecular chains with respect to each other, there are again two largely separate aspects, those of molecular orientation and crystallinity. In semi-crystalline polymers, this distinction may at times be an artificial one.

When cooled from the melt, many polymers form a disordered structure called the amorphous state. Some of these materials, such as polymethyl methacrylate, polystyrene and rapidly cooled (melt-quenched) polyethylene terephthalate, have a comparatively high modulus at room temperature, but others, such as natural rubber and atactic polypropylene, have a low modulus. These two types of polymer are often termed glassy and rubber-like, respectively, and we shall see that the form of behaviour exhibited depends on the temperature relative to a glass–rubber transition temperature (Tg) that is dependent on the material and the test method employed. Although an amorphous polymer may be modelled as a random tangle of molecules (Figure 1.9(a)), features such as the comparatively high density [6] show that the packing cannot be completely random. X-ray diffraction techniques indicate no distinct structure, rather a broad diffuse maximum (the amorphous halo) that indicates a preferred distance of separation between the molecular chains.

When an amorphous polymer is stretched, the molecules may be preferentially aligned along the stretch direction. In polymethyl methacrylate and polystyrene, such molecular orientation may be detected by optical methods, which measure the small difference between the refractive index in the stretch direction and that in the perpendicular direction.

(a)

(b)
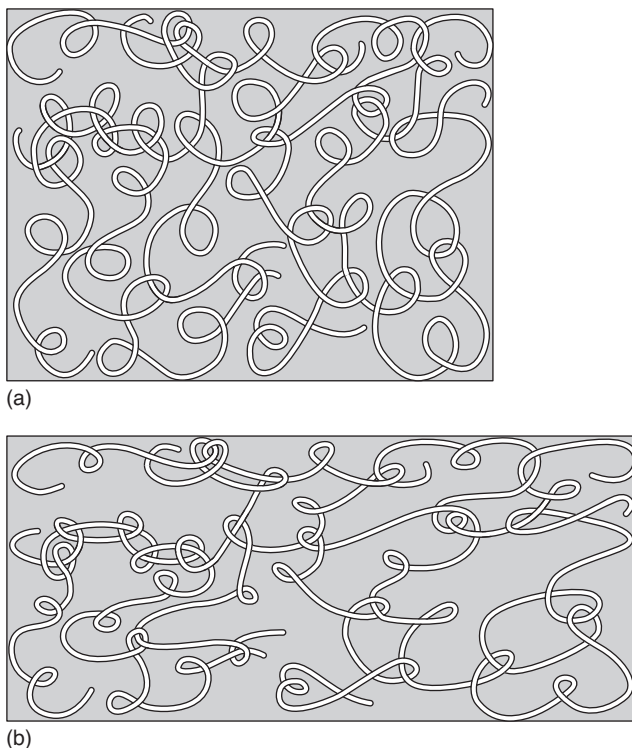
Figure 1.9   *Schematic diagrams of (a) unoriented amorphous polymer and (b) oriented amorphous polymer.*

X-ray diffraction methods for relaxed amorphous polymers still reveal no evidence of three-dimensional order, so the structure may be regarded as a somewhat oriented tangled skein (Figure 1.9(b)) that is oriented amorphous but not crystalline.

In polyethylene terephthalate, however, stretching produces both molecular orientation and small regions of three-dimensional order, termed crystallites, because the orientation processes have brought the molecules into adequate juxtaposition for regions of three-dimensional order to form.

Many polymers, including polyethylene terephthalate, also crystallise if they are cooled slowly from the melt. In this case, we may say that they are crystalline but unoriented. Although such specimens are unoriented in the macroscopic sense, that is, they possess isotropic bulk mechanical properties, they are not homogeneous in the microscopic sense and often show a spherulitic structure under a polarising microscope.

In summary, it may be said that for a polymer to crystallise the molecule must have a regular structure, the temperature must be below the crystal melting point and sufficient time must be available for the long molecules to become ordered in the solid state.

The structure of the crystalline regions of polymers can be deduced from wide-angle X-ray diffraction patterns of highly stretched specimens. When the stretching is uniaxial,
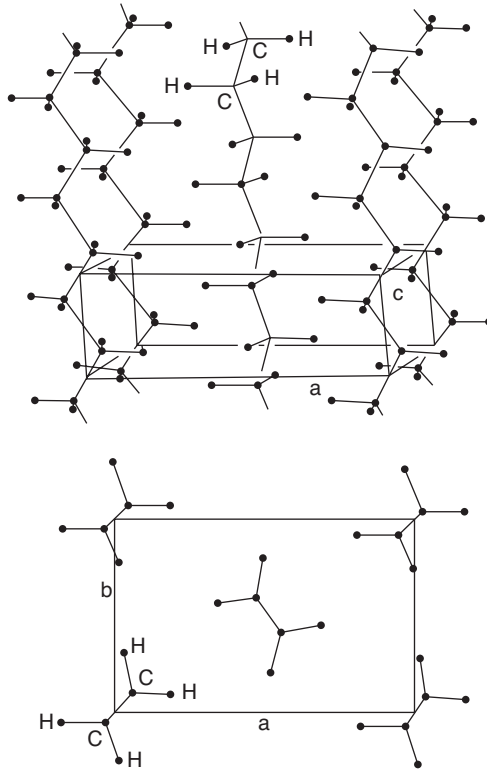
Figure 1.10   *Arrangement of molecules in polyethylene crystallites. (Reprinted with permission from Hill, R. (ed.) (1953) Fibres from Synthetic Polymers, Elsevier, Amsterdam. Copyright (1953) Elsevier Ltd.)*

the patterns are related to those obtained from fully oriented single crystals. The crystal structure of polyethylene was determined by Bunn [7] as long ago as 1939 (Figure 1.10).

In addition to the discrete reflections from the crystallites, the diffraction pattern of a polymer shows diffuse scattering attributed to amorphous regions. Such polymers are said to be semi-crystalline, with the crystalline fraction being controlled by molecular regularity. By comparing the relative amounts of crystalline and amorphous scattering of X-rays, the crystallinity has been found to vary from more than 90 per cent for linear polyethylene to about 30 per cent for oriented polyethylene terephthalate.

The first model to describe the structure of a semi-crystalline polymer was the so-called fringed micelle model (Figure 1.11), which is a natural development of the imagined situation in an amorphous polymer. The molecular chains alternate between regions of order (the crystallites) and disorder (the amorphous regions).

The fringed micelle model was called into question by the discovery of polymer single crystals grown from solution [8]. Linear polyethylene, for example, forms single crystal lamellae with lateral dimensions of the order of 10–20 μm and thickness of 10nm. Electron diffraction shows that the molecular chains are oriented approximately normal to the

Figure 1.11 *The fringed micelle representation of crystalline polymers. (Reprinted with permission from Hill, R. (ed.) (1953) Fibres from Synthetic Polymers, Elsevier, Amsterdam. Copyright (1953) Elsevier Ltd.)*

lamellar surface. As the molecules are typically about 1 μm in length, it follows that they must be folded back and forth within the crystals. The simplest geometric arrangement is that the folds are sharp and regular producing the adjacent re-entry model shown in Figure 1.12(a). This model provoked controversy and an alternative switchboard model shown schematically in Figure 1.12(b) was proposed [9].

The crystallisation of polymers from the melt has proved even more controversial, as a single molecule is unlikely to be laid down on a crystalline substrate without interference from its neighbours, and it might be expected that the highly entangled topology of the chains that exists in the melt would be substantially retained in the crystalline state. These
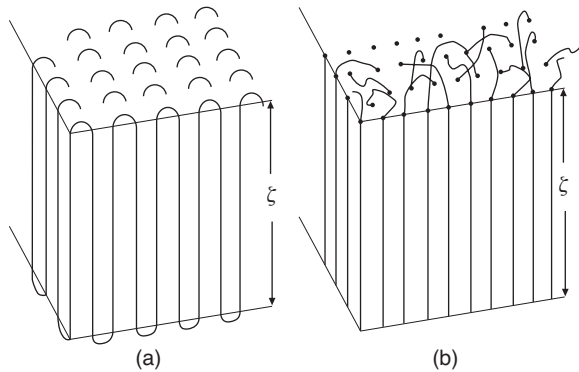
Figure 1.12 *Crystallites with folded lamellar crystals of thickness ζ in the direction of the c axis for (a) regular folding and (b) irregular folding of the chain molecules.*

(a)   (b)
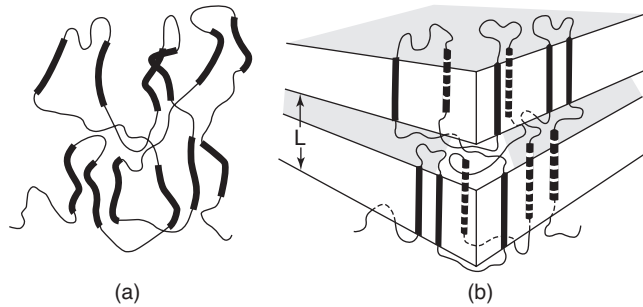
Figure 1.13   *Chain conformation (a) in the melt and (b) in the crystal according to the solidification model. (Adapted from Stamm, M., Fischer, E.W., Dettenmaier, M. and Convert, P. (1979) Chain conformation in the crystalline state by means of neutron scattering methods. Discuss. Chem. Soc. (London), **68**, 263. Copyright (1979) RSC.)*

issues were explored to great effect by neutron scattering measurements, notably by Fischer [10, 11] and also other researchers [12]. The neutron scattering measurements showed that the radii of gyration in the melt and in the semi-crystalline state for polyethylene quenched from the melt, for polyethylene oxide crystallised by slow cooling and for isotactic polypropylene, isothermally crystallised, were almost identical. On the basis of these results, Fischer proposed the solidification model shown in Figure 1.13 [10], where straight sequences of the original melt are incorporated into the growing lamellae without long-range diffusional motion.

Although it is accepted that kinetic factors determine the growth rate of crystallisation and the morphology, there is still debate in this area also. The theory proposed by Lauritzen and Hoffman [13] led the field and predicted the growth rate as the function of the degree of supercooling, the temperature difference between the crystallisation temperature and the melting point. It was assumed that the free energy barrier associated with nucleation of the crystallisation was energetic in origin. An alternative model for chain folding in polymer crystals has been proposed by Sadler and Gilmer [14], which assumes that the free energy barrier for nucleation is predominantly entropic. For a comprehensive review of these theories and related issues, the reader is referred to an excellent review in Reference [15] and also to Reference [16].

There is, of course, much evidence to support the existence of a lamellar morphology in crystalline polymers. Typically, spherulites l–10 μm in diameter are formed, which grow outwards until they impinge upon neighbouring spherulites (Figure 1.14). The spherulitic textures are formed by the growth of dominant lamellae from a central nucleus in all directions by a twisting of these lamellae along the fibrils, the intervening spaces being filled in by subsidiary lamellae, possibly due to low molecular weight material. This is shown schematically in Figure 1.15, where, for ease of illustration, regular chain folding is sketched. For a good review of polymer morphology, see the text by Bassett [17] and also more recent work directed by the same author.

Orientation through plastic deformation (drawing) destroys the spherulitic structure. What remains is determined to a large extent by the degree of crystallinity. Mechanical testing, described in the subsequent chapters, has helped to establish several models. At

Figure 1.14   *A photograph of typical spherulitic structure under a polarising microscope.*

one extreme, some highly oriented, highly crystalline specimens of linear polyethylene behave as blocks or lamellae of crystalline material, connected together by tie molecules or crystalline bridges and separated by the amorphous component. Such materials in some respects can be treated as microscopic composites. At the other extreme one has materials such as polyethylene terephthalate in which the crystalline and amorphous components are so intermixed that a single-phase model appears to be more appropriate.

Direction of growth
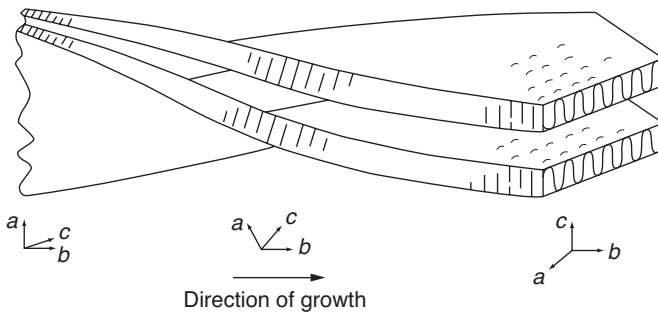
Figure 1.15   *A model of the lamellar arrangement in a polyethylene spherulite. The small diagrams of the a, b, c axes show the orientation of the unit cell at various points. (Adapted from Takayanagi, M. (1963) Viscoelastic properties of crystalline polymers. Memoirs of the Faculty of Engineering Kyushu Univ.,* **23***, 1. Copyright (1963) Kyushu University.)*
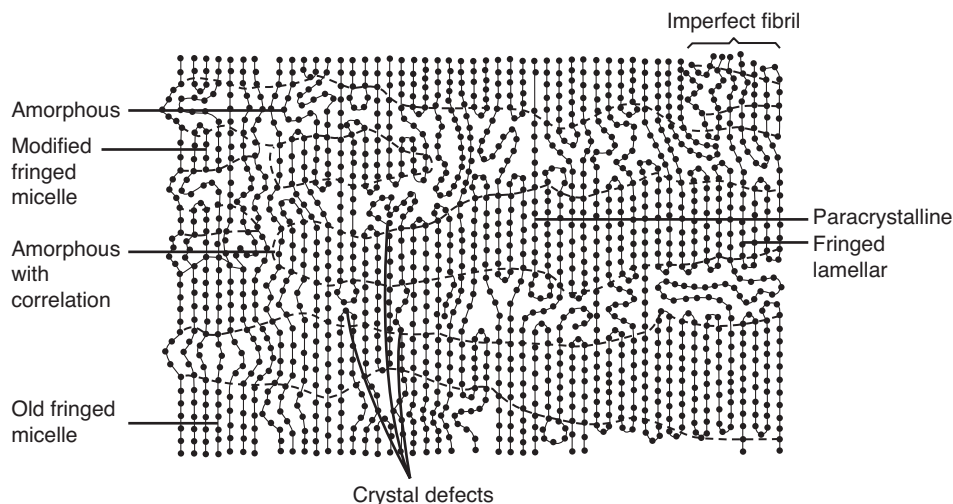
Figure 1.16   *Schematic composite diagram of different types of order and disorder in oriented polymers. (Reproduced from Hosemann, R. (1962) Crystallinity in high polymers, especially fibres. Polymer, 3, 393. Copyright (1962) Elsevier Ltd.)*

The current state of knowledge suggests that chain folding and the threading of molecules through the crystalline region both occur in typical polymers.

A schematic attempt to illustrate this situation, and other types of irregularity, is given in Figure 1.16.

References

1. Vaughan, M.F. (1960) Fractionation of polystyrene by gel filtration. *Nature*, **188**, 55.
2. Moore, J.C. (1964) Gel permeation chromatography. I. A new method for molecular weight distribution of high polymers. *J. Polym. Sci. A*, **2**, 835.
3. Noël, C. and Navard, P. (1991) Liquid crystal polymers. *Prog. Polym. Sci.*, **16**, 55.
4. Mizushima, S. I. (1954) *Structure of Molecules and Internal Rotation*, Academic Press, New York.
5. Grime, D. and Ward, I.M. (1958) The assignment of infra-red absorptions and rotational isomerism in polyethylene terephthalate and related compounds. *Trans. Faraday Soc.*, **54**, 959.
6. Robertson, R.E. (1965) Polymer order and polymer density. *J. Phys. Chem.*, **69**, 1575.
7. Bunn, C.W. (1939). The crystal structure of long-chain normal paraffin hydrocarbons: the "shape" of the >CH2 group. *Trans. Faraday Soc.*, **35**, 482.
8. Fischer, E.W. (1957) Stufen- und spiralförmiges Kristallwachstum bei Hochpolymeren, Naturforschung, **12a**, 753; Keller, A. (1957) A note on single crystals in polymers: evidence for a folded chain configuration. *Philos. Mag.*, **2**, 1171; Till, P.H. (1957) The growth of single crystals of linear polyethylene. *J. Polym. Sci.*, **24**, 301.

9. Flory, P.J. (1962) On the morphology of the crystalline state in polymers. *J. Amer. Chem. Soc.*, **84**, 2857.
10. Fischer, E.W. (1978) Studies of structure and dynamics of solid polymers by elastic and inelastic neutron scattering. *Pure and Appl. Chem.*, **50**, 1319.
11. Stamm, M., Fischer, E.W., Dettenmaier, M. and Convert, P. (1979) Chain conformation in the crystalline state by means of neutron scattering methods. *Discuss. Chem. Soc. (London)*, **68**, 263.
12. Stamm, M., Schelten, J. and Ballard, D.G.H. (1981) Determination of the chain conformation of polypropylene in the crystalline state by neutron scattering. *Coll. Pol. Sci.*, **259**, 286.
13. Lauritzen, J.I. and Hoffman, J.D. (1960) Theory of formation of polymer crystals with folded chains in dilute solution. *J. Res. Nat. Bur. Std.*, **64A**, 73.
14. Sadler, D.M. and Gilmer, G.H. (1984) A model for chain folding in polymer crystals: rough growth faces are consistent with the observed growth rates. *Polymer*, **25**,1446.
15. Gedde, U.W. (1995) *Polymer Physics*, Chapman and Hall, London.
16. Strobl, G. (1997) *The Physics of Polymers*, 2nd edn, Springer, Berlin.
17. Bassett, D.C. (1981) *Principles of Polymer Morphology*, Cambridge University Press, Cambridge.
18. McCrum, N.G., Read, B.E., Williams, G. (1991) *Anelastic and Dielectric Effects in Polymeric Solids*, Dover Publications, New York.
19. Hill, R. (ed.) (1953) *Fibres from Synthetic Polymers*, Elsevier, Amsterdam.
20. Takayanagi, M. (1963) Viscoelastic properties of crystalline polymers. *Mem. Fac. Eng. Kyushu Univ.*, **23**, 1.
21. Hosemann, R. (1962) Crystallinity in high polymers, especially fibres. *Polymer*, **3**, 393.

Further Reading

Billmeyer, F.W. (1984) *Textbook of Polymer Science*, 3rd edn, John Wiley & Sons, New York.
Bower, D.I. (2002) *An Introduction to Polymer Physics*, Cambridge University Press, Cambridge.
Cowie, J.M.G. and Arrighi, V. (2008) *Polymers: Chemistry and Physics of Modern Materials*, 3rd edn, Taylor & Francis Group, Boca Raton, Florida.
Hamley, I.W. (1998) *The Physics of Block Copolymers*, Oxford University Press, Oxford.
Mark, J., Ngai, K., Graessley, W. *et al.* (2004) *Physical Properties of Polymers*, 3rd edn, Cambridge University Press, Cambridge.
Odian, G.G. (2004) *Principles of Polymerization*, 4th edn, Wiley-Interscience, Hoboken, New Jersey.
Painter, P.C. and Coleman, M.M. (2008) *Essentials of Polymer Science and Engineering*, DEStech Publications, Lancaster Pennsylvania.
Rubinstein, M. and Colby, R.H. (2003) *Polymer Physics*, Oxford University Press, Oxford.
Sperling, L. (2006) *Introduction to Physical Polymer Science*, 4th edn, John Wiley & Sons, New York.
Tadokoro, H. (1979) *Structure of Crystalline Polymers*, John Wiley & Sons, Ltd, New York.

van Krevelen, D.W. and te Nijenhuis, K. (2009) *Properties of Polymers*, 4th edn, Elsevier, Oxford.

Wunderlich, B. *Macromolecular Physics, Vols 1 1973 Vol 2 1976, Vol 3 1980*, Academic Press, New York.

Young, R.J. and Lovell, P.A. (2011) *Introduction to Polymers*, 3rd edn, CRC Press/Taylor & Francis Group, Boca Raton, Florida.

2

The Mechanical Properties of Polymers: General Considerations

2.1 Objectives

Discussions of the mechanical properties of solid polymers often contain two inter-related objectives. The first of these is to obtain an adequate macroscopic description of the particular facet of polymer behaviour under consideration. The second objective is to seek an explanation of this behaviour in molecular terms, which may include details of the chemical composition and physical structure. In this book, we will endeavour, where possible, to separate these two objectives and, in particular, to establish a satisfactory macroscopic or phenomenological description before discussing molecular interpretations.

This should make it clear that many of the established relationships are purely descriptive, and do not necessarily have any implications with regard to an interpretation in structural terms. For engineering applications of polymers this is sufficient, because a description of the mechanical behaviour under conditions that simulate their end use is often all that is required, together with empirical information concerning their method of manufacture.

2.2 The Different Types of Mechanical Behaviour

It is difficult to classify polymers as particular types of materials such as a glassy solid or a viscous liquid, since their mechanical properties are so dependent on the conditions of testing, for example the rate of application of load, temperature and amount of strain.

A polymer can show all the features of a glassy, brittle solid or an elastic rubber or a viscous liquid depending on the temperature and time scale of measurement. Polymers are usually described as viscoelastic materials, a generic term which emphasises their intermediate position between viscous liquids and elastic solids. At low temperatures, or high frequencies of measurement, a polymer may be glass-like with a Young's modulus

of 1–10 GPa and will break or flow at strains greater than 5%. At high temperatures or low frequencies, the same polymer may be rubber-like with a modulus of 1–10 MPa, withstanding large extensions (~100%) without permanent deformation. At still higher temperatures, permanent deformation occurs under load, and the polymer behaves like a highly viscous liquid.

In an intermediate temperature or frequency range, commonly called the glass transition range, the polymer is neither glassy nor rubber-like. It shows an intermediate modulus, is viscoelastic and may dissipate a considerable amount of energy on being strained. The glass transition manifests itself in several ways, for example by a change in the volume coefficient of expansion, which can be used to define a glass transition temperature T_g. The glass transition is central to a great deal of the mechanical behaviour of polymers for two reasons. First there are the attempts to link the time–temperature equivalence of viscoelastic behaviour with the glass transition temperature T_g. Secondly, glass transitions can be studied at a molecular level by such techniques as nuclear magnetic resonance and dielectric relaxation. In this way, it is possible to gain an understanding of the molecular origins of the viscoelasticity.

The different features of polymer behaviour such as creep and recovery, brittle fracture, necking and cold drawing are usually considered separately, by comparative studies of different polymers. It is customary, for example, to compare the brittle fracture of poly-methyl methacrylate, polystyrene and other polymers, which show similar behaviour at room temperature. Similarly comparative studies have been made of the creep and recovery of polyethylene, polypropylene and other polyolefins. Such comparisons often obscure the very important point that the whole range of phenomena can be displayed by a single poly-mer as the temperature is changed. Figure 2.1 shows load–elongation curves for a polymer at four different temperatures. At temperatures well below the glass transition (curve A), where brittle fracture occurs, the load rises to the breaking point linearly with increasing elongation, and rupture occurs at low strains (−10%). At high temperatures (curve D), the
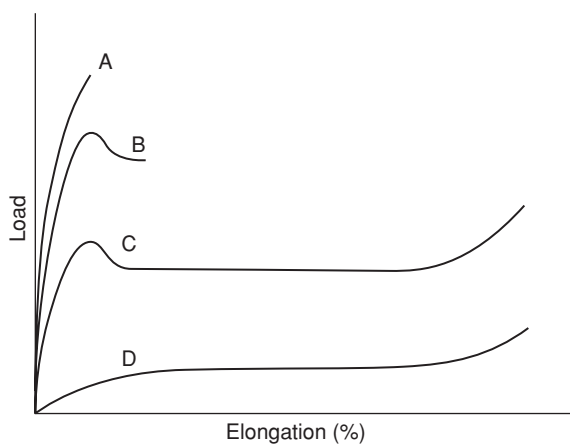
Figure 2.1   *Load–elongation curves for a polymer at different temperatures. Curve A, brittle fracture; curve B, ductile failure; curve C, cold drawing; curve D, rubber-like behaviour.*

polymer is rubber-like and the load rises to the breaking point with a sigmoidal relationship to the elongation, and rupture occurs at very high strains (∼30–1000%).

In an intermediate temperature range below the glass transition (curve B), the load–deformation relationship resembles that of a ductile metal, showing a load maximum, i.e. a yield point before rupture occurs. At slightly higher temperatures (curve C), still below the glass transition, the remarkable phenomenon of necking and cold drawing is observed. Here, the conventional load–elongation curve again shows a yield point and a subsequent decrease in conventional stress. However, with a further increase in the applied strain, the load falls to a constant level at which deformations of the order of 300–1000% are accomplished. At this stage, a neck has formed and the strain in the specimen is not uniform. (This is discussed in detail in Chapter 12.) Eventually, the load begins to rise again and finally fracture occurs.

It is usual to discuss the mechanical properties in the different temperature ranges separately, because different approaches and mathematical formalisms are adopted for the different features of mechanical behaviour. This conventional treatment will be followed here, although it is recognised that it somewhat arbitrarily isolates particular facets of the mechanical properties of polymers.

2.3   The Elastic Solid and the Behaviour of Polymers

Mechanical behaviour is, in most general terms, concerned with the deformations which occur under loading. In any specific case, the deformations depend on details such as the geometrical shape of the specimen or the way in which the load is applied. Such considerations are the province of the plastics engineer, who is concerned with predicting the performance of a polymer in a specified end use. In our discussion of the mechanical properties of polymers, we will ignore such questions as these, which relate to solving particular problems of behaviour in practice. We will concern ourselves only with the generalised equations termed *constitutive relations*, which relate stress and strain for a particular type of material. First it will be necessary to find constitutive relations that give an adequate description of the mechanical behaviour. Secondly, where possible, we will obtain a molecular understanding of this behaviour by a molecular model that predicts the constitutive relations.

One of the simplest constitutive relations is Hooke's law, which relates the stress σ to the strain e for the uniaxial deformation of an ideal elastic isotropic solid. Thus

$$\sigma = Ee,$$

where E is the Young's modulus.

There are five important ways in which the mechanical behaviour of a polymer may deviate from that of an ideal elastic solid obeying Hooke's law. First, in an elastic solid the deformations induced by loading are independent of the history or rate of application of the loads, whereas in a polymer the deformations can be drastically affected by such considerations. This means that the simplest constitutive relation for a polymer should in general contain time or frequency as a variable in addition to stress and strain. Secondly, in an elastic solid all the situations pertaining to stress and strain can be reversed. Thus, if a stress is applied, a certain deformation will occur. On removal of the stress, this

deformation will disappear exactly. This is not always true for polymers. Thirdly, in an elastic solid obeying Hooke's law, which in its more general implications is the basis of small-strain elasticity theory, the effects observed are *linearly* related to the influences applied. This is the essence of Hooke's law; stress is exactly proportional to strain. This is not generally true for polymers, but applies in many cases only as a good approximation for very small strains; in general, the constitutive relations are non-linear. It is important to note that *non-linearity* is not related to *recoverability*. In contrast to metals, polymers may recover from strains beyond the proportional limit without any permanent deformation.

Fourthly, the definitions of stress and strain in Hooke's law are only valid for small deformations. When we wish to consider larger deformations a new theory must be developed in which both stress and strain are defined more generally.

Finally, in many practical applications (such as films and synthetic fibres) polymers are used in an oriented or anisotropic form, which requires a considerable generalisation of Hooke's law.

It will be convenient to discuss these various aspects separately as follows: (1) behaviour at large strains in Chapters 3 and 4 (finite elasticity and rubber-like behaviour, respectively); (2) time-dependent behaviour in Chapters 5–7 and 10 (viscoelastic behaviour); (3) the behaviour of oriented polymers in Chapters 8 and 9 (mechanical anisotropy); (4) non-linearity in Chapter 11 (non-linear viscoelastic behaviour); (5) the non-recoverable behaviour in Chapter 12 (plasticity and yield) and (6) fracture in Chapter 13 (breaking phenomena). However, it should be recognised that we cannot hold to an exact separation and that there are many places where these aspects overlap and can be brought together by the physical mechanisms, which underlie the phenomenological description.

2.4   Stress and Strain

It is desirable at this juncture to outline very briefly the concepts of stress and strain. For a more comprehensive discussion, the reader is referred to standard textbooks on the theory of elasticity [1–6].

2.4.1   The State of Stress

The components of stress in a body can be defined by considering the forces acting on an infinitesimal cubical volume element (Figure 2.2) whose edges are parallel to the coordinate axes 1, 2 and 3. In equilibrium, the forces per unit area acting on the cube faces are:

P_x on the 23 plane,
P_y on the 31 plane,
P_z on the 12 plane.

These three forces are then resolved into their nine components in the 1, 2 and 3 directions as follows:

$$P_x: \sigma_{11}, \quad \sigma_{12}, \quad \sigma_{13};$$
$$P_y: \sigma_{21}, \quad \sigma_{22}, \quad \sigma_{23};$$
$$P_z: \sigma_{31}, \quad \sigma_{32}, \quad \sigma_{33}.$$
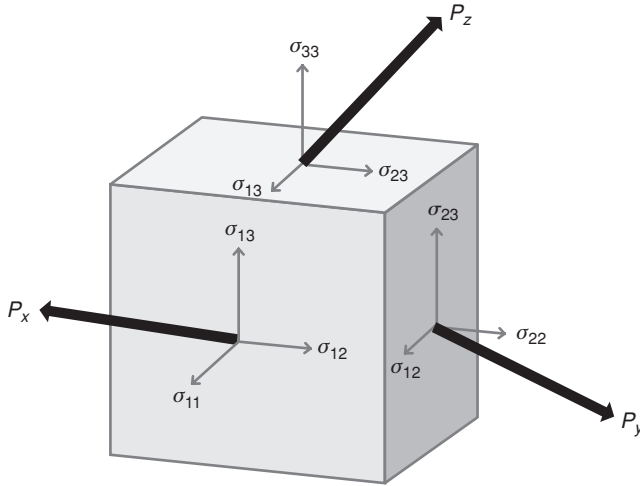
Figure 2.2 *The stress components.*

The first subscript refers to the direction of the normal to the plane on which the stress acts, and the second subscript to the direction of the stress. In the absence of body torques, the total torque acting on the cube must also be zero, and this implies three equalities:

$$\sigma_{12} = \sigma_{21}, \ \sigma_{13} = \sigma_{31}, \ \sigma_{23} = \sigma_{32}.$$

Therefore, the components of stress are defined by six independent quantities: σ_{11}, σ_{22} and σ_{33}, the normal stresses, and σ_{12}, σ_{23} and σ_{31}, the shear stresses.

These form the six independent components of the stress tensor Σ or σ_{ij}:

$$\Sigma = \sigma_{ij} = \begin{pmatrix} \sigma_{11} & \sigma_{12} & \sigma_{13} \\ \sigma_{12} & \sigma_{22} & \sigma_{23} \\ \sigma_{13} & \sigma_{23} & \sigma_{33} \end{pmatrix}.$$

The state of stress at a point in a body is determined when we can specify the normal components and the shear components of stress acting on a plane drawn in any direction through the point. If we know these six components of stress at a given point, the stresses acting on any plane through this point can be calculated. (See Reference [1], Section 67; and Reference [2], Section 47.)

2.4.2 The State of Strain – Engineering Components

The displacement of any point **X** (see Figure 2.3) in the body may be resolved into its components u_1, u_2 and u_3 parallel to 1, 2 and 3 (Cartesian coordinate axes chosen in the undeformed state) so that if the coordinates of the point in the undisplaced position were (X_1, X_2, X_3), they become $(X_1 + u_1, X_2 + u_2, X_3 + u_3)$ on deformation. In defining the strains, we are not interested in the *displacement* or rotation but in the *deformation*. The latter is the displacement of a point relative to adjacent points. Consider a point very close

$(X_1 + \mathrm{d}X_1 + u_1 + \mathrm{d}u_1, X_2 + \mathrm{d}X_2 + u_2 + \mathrm{d}u_2, X_3 + \mathrm{d}X_3 + u_3 + \mathrm{d}u_3)$

$(X_1 + u_1, X_2 + u_2, X_3 + u_3)$

$(X_1 + \mathrm{d}X_1, X_2 + \mathrm{d}X_2, X_3 + \mathrm{d}X_3)$
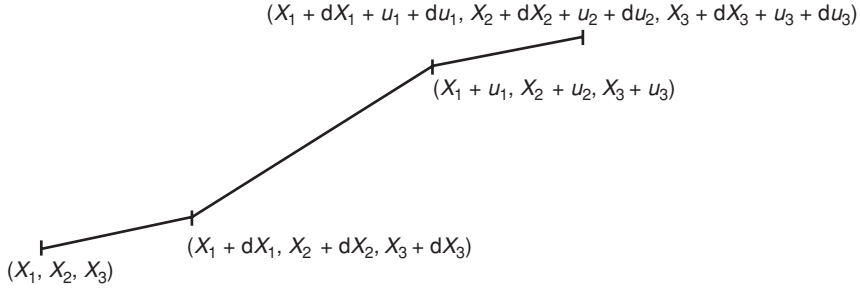
(X_1, X_2, X_3)

Figure 2.3   *The displacements produced by deformation.*

to **X**, which in the undisplaced position had coordinates $(X_1 + \mathrm{d}X_1, X_2 + \mathrm{d}X_2, X_3 + \mathrm{d}X_3)$ and let the displacement, which it has undergone, have components $(u_1 + \mathrm{d}u_1, u_2 + \mathrm{d}u_2, u_3 + \mathrm{d}u_3)$. The quantities required are then $\mathrm{d}u_1$, $\mathrm{d}u_2$ and $\mathrm{d}u_3$, the *relative* displacements.

If $\mathrm{d}X_1$, $\mathrm{d}X_2$ and $\mathrm{d}X_3$ are sufficiently small, that is infinitesimal:

$$\mathrm{d}u_1 = \frac{\partial u_1}{\partial X_1}\mathrm{d}X_1 + \frac{\partial u_1}{\partial X_2}\mathrm{d}X_2 + \frac{\partial u_1}{\partial X_3}\mathrm{d}X_3,$$

$$\mathrm{d}u_2 = \frac{\partial u_2}{\partial X_1}\mathrm{d}X_1 + \frac{\partial u_2}{\partial X_2}\mathrm{d}X_2 + \frac{\partial u_2}{\partial X_3}\mathrm{d}X_3,$$

$$\mathrm{d}u_3 = \frac{\partial u_3}{\partial X_1}\mathrm{d}X_1 + \frac{\partial u_3}{\partial X_2}\mathrm{d}X_2 + \frac{\partial u_3}{\partial X_3}\mathrm{d}X_3.$$

Thus, we require to define the nine quantities:

$$\frac{\partial u_1}{\partial X_1}, \quad \frac{\partial u_1}{\partial X_2}, \ldots, \quad \text{etc.}$$

For convenience, these nine quantities are regrouped and denoted as follows:

$$e_{11} = \frac{\partial u_1}{\partial X_1}, \quad e_{22} = \frac{\partial u_2}{\partial X_2}, \quad e_{33} = \frac{\partial u_3}{\partial X_3},$$

$$e_{23} = \frac{\partial u_3}{\partial X_2} + \frac{\partial u_2}{\partial X_3}, \quad e_{31} = \frac{\partial u_1}{\partial X_3} + \frac{\partial u_3}{\partial X_1}, \quad e_{12} = \frac{\partial u_2}{\partial X_1} + \frac{\partial u_1}{\partial X_2},$$

$$2\varpi_1 = \frac{\partial u_3}{\partial X_2} - \frac{\partial u_2}{\partial X_3}, \quad 2\varpi_2 = \frac{\partial u_1}{\partial X_3} - \frac{\partial u_3}{\partial X_1}, \quad 2\varpi_3 = \frac{\partial u_2}{\partial X_1} - \frac{\partial u_1}{\partial X_2}.$$

The first three quantities e_{11}, e_{22} and e_{33} correspond to the fractional expansions or contractions along the 1, 2 and 3 axes of an infinitesimal element at **X** – the normal strains. The second three quantities e_{23}, e_{31} and e_{12} correspond to the components of shear strain in the 23, 31 and 12 planes respectively. The last three quantities ϖ_1, ϖ_2 and ϖ_3 do not correspond to a deformation of the element at **X**, but are the components of its rotation as a rigid body.
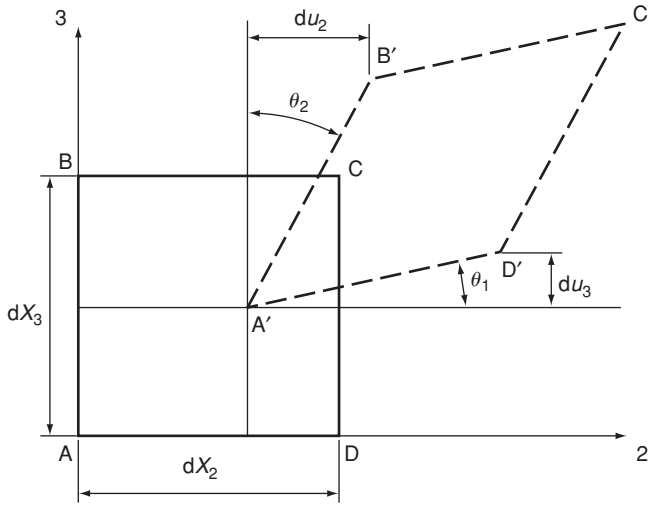
Figure 2.4 *Shear strains.*

The concept of shear strain can be conveniently illustrated by a diagram showing the two-dimensional situation of shear in the 23 plane (see Figure 2.4). ABCD is an infinitesimal square that has been displaced and deformed into the rhombus A′B′C′D′, θ_1 and θ_2 being the angles that A′D′ and A′B′ make with the 2 and 3 axes, respectively.

Now,

$$\tan \theta_1 \approx \theta_1 = \frac{du_3}{dX_2} \rightarrow \frac{\partial u_3}{\partial X_2},$$

$$\tan \theta_2 \approx \theta_2 = \frac{du_2}{dX_3} \rightarrow \frac{\partial u_2}{\partial X_3}.$$

The shear strain in the 23 plane is given by

$$e_{23} = \frac{\partial u_3}{\partial X_2} + \frac{\partial u_2}{\partial X_3} = \theta_1 + \theta_2.$$

$2\varpi_1 = \theta_1 - \theta_2$ does not correspond to a deformation of ABCD but to twice the angle through which AC has been rotated.

Therefore, the deformation is defined by the first six quantities $e_{11}, e_{22}, e_{33}, e_{23}, e_{31}, e_{12}$ that are called the components of strain. It is important to note that engineering strains have been defined. In Chapter 3, we take a more general approach and examine a number of strain-related tensor quantities in Section 3.1.5. For the purposes of this chapter, which concerns small strains, we define the strain tensor ε_{ij} as

$$\varepsilon_{ij} = \frac{1}{2} \left(\frac{\partial u_i}{\partial X_j} + \frac{\partial u_j}{\partial X_i} \right),$$

where i and j take values 1, 2 and 3, and we sum over all possible values. Then,

$$\varepsilon_{ij} = \begin{pmatrix} e_{11} & \frac{1}{2}e_{12} & \frac{1}{2}e_{13} \\ \frac{1}{2}e_{12} & e_{22} & \frac{1}{2}e_{23} \\ \frac{1}{2}e_{13} & \frac{1}{2}e_{23} & e_{33} \end{pmatrix}$$

in terms of the engineering components of strain.

2.5   The Generalised Hooke's Law

The most general *linear* relationship between stress and strain is obtained by assuming that each of the tensor components of stress is linearly related to all the tensor components of strain and vice versa. Thus

$$\sigma_{11} = a\varepsilon_{11} + b\varepsilon_{22} + c\varepsilon_{33} + d\varepsilon_{13} + \cdots \text{ etc.}$$

and

$$\varepsilon_{11} = a'\sigma_{11} + b'\sigma_{22} + c'\sigma_{33} + d'\sigma_{13} + \cdots \text{ etc.,}$$

where $a, b, \ldots, a', b', \ldots$ are constants. This is the generalised Hooke's law.

In tensor notation, we relate the second-rank tensor σ_{ij} to the second-rank strain tensor ε_{ij} by fourth-rank tensors $c_{ijk\ell}$ and $s_{ijk\ell}$. Thus,

$$\sigma_{ij} = c_{ijk\ell}\varepsilon_{k\ell}$$

or equivalently

$$\varepsilon_{ij} = s_{ijk\ell}\sigma_{k\ell},$$

where

$$\sigma_{ij} = \sigma_{11}, \sigma_{22}, \ldots \text{ etc.}$$

and

$$\varepsilon_{ij} = \varepsilon_{11}, \varepsilon_{22}, \ldots \text{ etc.}$$

The fourth-rank tensors $s_{ijk\ell}$ and $c_{ijk\ell}$ contain the compliance and stiffness constants respectively, with i, j, k, ℓ taking values 1, 2 and 3.

It is customary to adopt an abbreviated nomenclature in which the generalised Hooke's law relates the six independent components of stress to the six independent components of the engineering strains.

We have

$$\sigma_p = c_{pq}e_q \quad \text{and} \quad \varepsilon_p = s_{pq}\sigma_q,$$

where σ_p represents $\sigma_{11}, \sigma_{22}, \sigma_{33}, \sigma_{13}, \sigma_{23}$ or σ_{12} and ε_q represents $e_{11}, e_{22}, e_{33}, e_{13}, e_{23}$ or e_{12}. We form matrices c_{pq} and s_{pq} in which p and q take the values 1, 2, $\ldots$, 6. In the case of the stiffness constants, the values of p and q are obtained in terms of i, j, k, ℓ by

substituting 1 for 11, 2 for 22, 3 for 33, 4 for 23, 5 for 13 and 6 for 12. For the compliance constants, rather more complicated rules apply owing to the occurrence of the factor-2 difference between the definition of the tensor shear strain components and the definition of engineering shear strains. Thus

$s_{ijk\ell} = s_{pq}$, when p and q are 1, 2 or 3,
$2s_{ijk\ell} = s_{pq}$, when either p or q are 4, 5 or 6,
$4s_{ijk\ell} = s_{pq}$, when both p and q are 4, 5 or 6.

A typical relationship between stress and strain is now written as

$$\sigma_1 = c_{11}e_1 + c_{12}e_2 + c_{13}e_3 + c_{14}e_4 + c_{15}e_5 + c_{16}e_6.$$

The existence of a strain–energy function (see Reference [2], p. 149; Reference [3], p. 267) provides the relationships

$$c_{pq} = c_{qp}, \quad S_{pq} = s_{qp}$$

and reduces the number of independent constants from 36 to 21. We then have

$$c_{pq} = \begin{pmatrix}
c_{11} & c_{12} & c_{13} & c_{14} & c_{15} & c_{16} \\
c_{12} & c_{22} & c_{23} & c_{24} & c_{25} & c_{26} \\
c_{13} & c_{23} & c_{33} & c_{34} & c_{35} & c_{36} \\
c_{14} & c_{24} & c_{34} & c_{44} & c_{36} & c_{46} \\
c_{15} & c_{25} & c_{35} & c_{36} & c_{55} & c_{56} \\
c_{16} & c_{26} & c_{36} & c_{46} & c_{56} & c_{66}
\end{pmatrix}$$

and similarly

$$s_{pq} = \begin{pmatrix}
s_{11} & s_{12} & s_{13} & s_{14} & s_{15} & s_{16} \\
s_{12} & s_{22} & s_{23} & s_{24} & s_{25} & s_{26} \\
s_{13} & s_{23} & s_{33} & s_{34} & s_{35} & s_{36} \\
s_{14} & s_{24} & s_{34} & s_{44} & s_{45} & s_{46} \\
s_{15} & s_{25} & s_{35} & s_{45} & s_{55} & s_{56} \\
s_{16} & s_{26} & s_{36} & s_{46} & s_{56} & s_{66}
\end{pmatrix}.$$

These matrices define the relationships between stress and strain in a general elastic solid, whose properties vary with direction, that is an anisotropic elastic solid. In most of this book, we will be concerned with isotropic polymers; all discussion of anisotropic mechanical properties will be reserved for Chapter 8.

It is then most straightforward to use the compliance constants matrix, and note that measured quantities, such as the Young's modulus E, Poisson's ratio ν and the torsional or shear modulus G, relate directly to the compliance constants.

For an isotropic solid, the matrix s_{pq} reduces to

$$
s_{pq} = \begin{pmatrix}
s_{11} & s_{12} & s_{12} & 0 & 0 & 0 \\
s_{12} & s_{11} & s_{12} & 0 & 0 & 0 \\
s_{12} & s_{12} & s_{11} & 0 & 0 & 0 \\
0 & 0 & 0 & 2(s_{11} - s_{12}) & 0 & 0 \\
0 & 0 & 0 & 0 & 2(s_{11} - s_{12}) & 0 \\
0 & 0 & 0 & 0 & 0 & 2(s_{11} - s_{12})
\end{pmatrix}.
$$

It can be shown that the Young's modulus is given by

$$
E = 1/s_{11},
$$

the Poisson's ratio by

$$
\nu = -s_{12}/s_{11}
$$

and the torsional modulus by

$$
G = 1/2(s_{11} - s_{12}).
$$

Thus, we obtain the stress–strain relationships, which are the starting point in many elementary textbooks of elasticity (see Reference [1], pp. 7–9):

$$
e_{11} = \frac{1}{E}\left(\sigma_{11} - \nu(\sigma_{22} + \sigma_{33})\right),
$$

$$
e_{22} = \frac{1}{E}\left(\sigma_{22} - \nu(\sigma_{11} + \sigma_{33})\right),
$$

$$
e_{33} = \frac{1}{E}\left(\sigma_{33} - \nu(\sigma_{11} + \sigma_{22})\right),
$$

$$
e_{13} = \frac{1}{G}\sigma_{13},
$$

$$
e_{23} = \frac{1}{G}\sigma_{23},
$$

$$
e_{12} = \frac{1}{G}\sigma_{12},
$$

where

$$
G = \frac{E}{2(1 + \nu)}.
$$

Another basic quantity is the bulk modulus K, which determines the dilatation $\Delta = e_{11} + e_{22} + e_{33}$, produced by a uniform hydrostatic pressure. Using the stress–strain relationships above, it can be shown that the strains produced by a uniform hydrostatic pressure p are given by

$$
e_{11} = e_{22} = e_{33} = (s_{11} + 2s_{12})p.
$$

Then,

$$
K = \frac{p}{\Delta} = \frac{1}{3(s_{11} + 2s_{12})} = \frac{E}{3(1 - 2\nu)}.
$$

This completes our introduction to linear elastic behaviour at small strains. The extension to large strains will be considered in the next chapter on finite elasticity.

References

1. Timoshenko, S. and Goodier, J.N. (2008) *Theory of Elasticity*, 3rd edn, McGraw-Hill Higher Education, International Editions, New York.
2. Love, A.E.H. (1944) *A Treatise on the Mathematical Theory of Elasticity*, 4th edn, Macmillan, New York.
3. Solecki, R. and Conant, R.J. (2003) *Advanced Mechanics of Materials*, Oxford University Press, New York.
4. Bedford, A. and Liechti, K.M. (2000) *Mechanics of Materials*, Prentice Hall, Upper Saddle River, New Jersey.
5. Hibbeler, R.C. (2004) *Mechanics of Materials*, 6th edn, Prentice Hall, Upper Saddle River, New Jersey.
6. Richards, R. (2001) *Principles of Solid Mechanics*, CRC Press LLC, Boca Raton, Florida.

3

The Behaviour in the Rubber-Like State: Finite Strain Elasticity

In the rubber-like state, a polymer may be subjected to large deformations and still show complete recovery. The behaviour of a rubber band stretching to two or three times its original length and, when released, recovering essentially instantaneously to its original shape is a matter of common experience. To a good approximation, this is elastic behaviour at large strains. The first stage in developing an understanding of this behaviour is to seek a generalised definition of strain, which will not suffer the restriction of that derived in Chapter 2, i.e. that the strains are small. This is followed by a rigorous definition of stress for the situation where the deformations are not small. These considerations are the basis of finite elasticity theory. This subject has been considered in several notable texts [1–3], and it is not intended to duplicate the elegant treatments presented elsewhere. For the most part, the development of finite strain elasticity theory has been made using tensor calculus. In this book, the treatment is at a relatively elementary level, and it is hoped that in this way the exposition will be clear to those who only require an outline of the subject in order to understand the relevant mechanical properties of polymers.

3.1 The Generalised Definition of Strain

Figure 3.1 represents a deformed and an undeformed body. Points in a small area on the undeformed body are assigned co-ordinates $\mathbf{X} = (X_1, X_2, X_3)$. On deformation, this area is transformed so that in general both its shape and state of rotation are changed; the point $\mathbf{X} = (X_1, X_2, X_3)$ moves to the point $\mathbf{x} = (x_1, x_2, x_3)$. Locally this can be expressed as a linear transformation, so that the new co-ordinates are given in terms of the old co-ordinates as

$$
\begin{aligned}
x_1 &= f_{11}X_1 + f_{12}X_2 + f_{13}X_3 \\
x_2 &= f_{21}X_1 + f_{22}X_2 + f_{23}X_3 \, . \\
x_3 &= f_{31}X_1 + f_{32}X_2 + f_{33}X_3
\end{aligned}
\tag{3.1}
$$
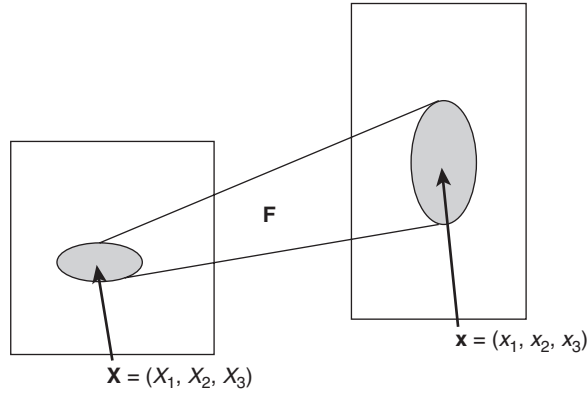
Figure 3.1   *Undeformed and deformed material elements.*

This leaves one point, the origin, unchanged, and thus rigid-body translations have been automatically eliminated by this approach. We adopt the Lagrangian approach to strain, in which the reference state is the undeformed state of the material, in contrast to the alternative Eulerian model, in which reference is made to the deformed state. We can rewrite Equation (3.1) in matrix form as

$$\mathbf{x} = \mathbf{FX},\tag{3.2}$$

where

$$\mathbf{F} = \begin{bmatrix} f_{11} & f_{12} & f_{13} \\ f_{21} & f_{22} & f_{23} \\ f_{31} & f_{32} & f_{33} \end{bmatrix}.$$

As a matter mainly of notation, Equation (3.1) can be differentiated to give

$$\frac{\partial x_i}{\partial X_j} = f_{ij} \quad (i, j = 1, 2, 3),$$

which we may express as

$$\mathbf{F} = \frac{\partial \mathbf{x}}{\partial \mathbf{X}}.$$

The matrix $\mathbf{F}$ and its components are referred to as *deformation gradients*; $\mathbf{F}$ is also termed the *deformation gradient tensor*. It defines a transformation of the undeformed state onto the deformed state.

3.1.1   The Cauchy–Green Strain Measure

The deformation gradient $\mathbf{F}$ contains geometrical information that is not related to strain (i.e. dimensional or shape change); namely, it includes rigid-body rotations. The matrix associated with rotation is familiar from its use in changing the representation of a vector when the axis set is rotated. It also defines the rigid-body rotation of an element of material,

and so is in itself a deformation gradient. Suppose an element of material is specified within a 1–2–3 Cartesian axis system and is rotated so that lines of material points originally along the 1, 2 and 3 axes become aligned with new axes labelled 1′, 2′, 3′. Then the positions of the new axes can be defined in terms of their direction cosines within the old axis set. Let the 1′-axis have direction cosines $(\ell_{11}, \ell_{12}, \ell_{13})$ with respect to the 1–2–3 axes, the 2′-axis direction cosines $(\ell_{21}, \ell_{22}, \ell_{23})$ with respect to the 1–2–3 axes and the new 3-axis direction cosines $(\ell_{31}, \ell_{32}, \ell_{33})$ with respect to the 1–2–3 axes. Then the matrix of rotation **R** is given by

$$R = \begin{bmatrix} \ell_{11} & \ell_{12} & \ell_{13} \\ \ell_{21} & \ell_{22} & \ell_{23} \\ \ell_{31} & \ell_{32} & \ell_{33} \end{bmatrix}. \tag{3.3}$$

This gives the new co-ordinate vector $(\mathbf{x}_1, \mathbf{x}_2, \mathbf{x}_3)$ when operating on the old co-ordinates (X_1, X_2, X_3). Note that in two dimensions, it reduces to

$$\mathbf{R} = \begin{bmatrix} \cos\theta & \sin\theta \\ -\sin\theta & \cos\theta \end{bmatrix}, \tag{3.4}$$

where θ is the anticlockwise angle through which the new axis set has been rotated in the 1–2 plane.

Having defined the rotation matrix, the question we now address is how to remove rigid-body rotations from the deformation gradient **F**. In the following arguments, use will be made of the concept of the *transpose* $\mathbf{M}^\mathbf{T}$ of the matrix **M**, in which the rows of elements of **M** are written as columns, such that an element a_{ij} of $\mathbf{M}^\mathbf{T}$ is given by $a_{ij} = b_{ji}$, where b_{ji} is an element of **M**. In the case of a matrix of rotation **R**, $\mathbf{R}^\mathbf{T} = \mathbf{R}^{-1}$, where $\mathbf{R}^{-1}$ is the inverse of **R**, corresponding to a rotation back to the original state, with $\mathbf{R}\mathbf{R}^{-1} = \mathbf{R}^{-1}\mathbf{R} = \mathbf{I}$, the identity matrix. We will also make use of the identity

$$(\mathbf{AB})^\mathrm{T} = \mathbf{B}^\mathrm{T}\mathbf{A}^\mathrm{T}. \tag{3.5}$$

Suppose that the deformation gradient **F** consists of a 'pure' deformation **V**, ('pure' in the sense that it does not include any rigid-body rotation), and a rotation **R**, then according to the *polar decomposition theorem* we may write

$$\mathbf{F} = \mathbf{RV}. \tag{3.6}$$

RV is known as the *polar decomposition* of **F**. Now let us form the matrix

$$\mathbf{C} = \mathbf{F}^\mathrm{T}\mathbf{F}. \tag{3.7}$$

Using Equation (3.6), **F** becomes

$$\mathbf{C} = (\mathbf{RV})^\mathrm{T}\mathbf{RV}$$

and using the identity (3.5)

$$\mathbf{C} = \mathbf{V}^\mathrm{T}\mathbf{R}^\mathrm{T}\mathbf{RV}.$$

As noted above, $\mathbf{R}^\mathbf{T} = \mathbf{R}^{-1}$, so that $\mathbf{R}^\mathbf{T}\mathbf{R} = \mathbf{I}$. Therefore,

$$\mathbf{C} = \mathbf{V}^\mathrm{T}\mathbf{V}. \tag{3.8}$$

Notice now that the quantity $\mathbf{C}$ is not dependent on the rotation $\mathbf{R}$; by performing the operation (Equation (3.7)), we have effectively stripped the rigid-body rotations off $\mathbf{F}$, leaving a quantity that depends only on the pure deformation $\mathbf{V}$. The diagonal entries of $\mathbf{V}$ are associated with changes in length, or normal strains; and the off-diagonal entries with angle changes or shear strains. $\mathbf{C}$ is therefore a useful measure of strain, and is known as the *right Cauchy–Green strain measure* (The *left* Cauchy–Green strain measure is simply $\mathbf{FF^T}$). Note that, if instead of Equation (3.6) it had been assumed that

$$\mathbf{F} = \mathbf{VR},$$

then the use of the left Cauchy–Green strain measure would have had the same effect of removing the rigid-body rotation.

$\mathbf{C}$, unlike $\mathbf{F}$, is always symmetric ($f_{ij} = f_{ji}$, i = 1, 2, 3). When a deformation gradient $\mathbf{F}$ is itself symmetric, it already corresponds to a deformation with no rigid-body motions, a pure deformation $\mathbf{V}$. It is possible to derive such a quantity from the Cauchy–Green measure $\mathbf{C}$. This requires knowledge of how to obtain principal values of $\mathbf{C}$ or $\mathbf{V}$, and of how to transform $\mathbf{C}$ and $\mathbf{V}$ between different axis sets.

3.1.2   Principal Strains

Suppose we have a deformation gradient $\mathbf{V}$ that is symmetric and so does not include rigid-body rotations. As we have seen, $\mathbf{V}$ operates on a vector $\mathbf{X}$ corresponding to a point in space and moves it to $\mathbf{x}$. By implication, $\mathbf{V}$ transforms a line of points to another line of points, with a straight line transformed to another straight line. For example, the line joining the origin to $\mathbf{X}$ will be transformed to the line joining the origin to $\mathbf{x}$. The principal directions of the deformation $\mathbf{V}$ correspond to lines that are transformed parallel to themselves, so that perpendicular lines remain perpendicular and there is no angle change that would be identified with shear strain. In mathematical terms, the eigenvectors of $\mathbf{V}$ are the principal directions, and the corresponding eigenvalues are the stretch ratios along the principal directions, known as the *principal extension ratios*.

The condition for the transformed line being parallel to the initial line is

$$\mathbf{VX} = \lambda\mathbf{X},$$

where λ is a constant. As we will show, this defines a cubic equation in λ, with the three solutions of the principal extension ratios. In components, this equation becomes

$$\begin{aligned}
v_{11}X_1 + v_{12}X_2 + v_{13}X_3 &= \lambda X_1 \\
v_{12}X_1 + v_{22}X_2 + v_{23}X_3 &= \lambda X_2 \\
v_{13}X_1 + v_{23}X_2 + v_{33}X_3 &= \lambda X_3
\end{aligned} \tag{3.9}$$

and it follows that

$$\begin{aligned}
(v_{11} - \lambda)X_1 + v_{12}X_2 + v_{13}X_3 &= 0 \\
v_{12}X_1 + (v_{22} - \lambda)X_2 + v_{23}X_3 &= 0 \\
v_{13}X_1 + v_{23}X_2 + (v_{33} - \lambda)X_3 &= 0
\end{aligned} \tag{3.10}$$

or in matrix form

$$\begin{pmatrix} v_{11} - \lambda & v_{12} & v_{13} \\ v_{12} & v_{22} - \lambda & v_{23} \\ v_{13} & v_{23} & v_{33} - \lambda \end{pmatrix} \mathbf{X} = 0. \tag{3.11}$$

For solutions other than the trivial $\mathbf{X} = 0$, the matrix must be singular. This is true provided the determinant is zero:

$$\begin{vmatrix} v_{11} - \lambda & v_{12} & v_{13} \\ v_{12} & v_{22} - \lambda & v_{23} \\ v_{13} & v_{23} & v_{33} - \lambda \end{vmatrix} = 0. \tag{3.12}$$

This defines the cubic equation in λ. The three solutions for λ – the eigenvalues of $\mathbf{V}$ – are the principal extension ratios λ_I, λ_{II} and λ_{III}. We shall see that these quantities provide a simple way to the model of a molecular network, which is one of the key concepts in understanding the mechanical behaviour of polymers. The corresponding directions – the eigenvectors and principal directions – are obtained by substituting the λ values back into Equation (3.11) and solving for X_1, X_2 and X_3, subject to the condition that $\mathbf{X}$ is a unit vector, $X_1^2 + X_2^2 + X_3^2 = 1$, ensuring that its components are direction cosines.

Suppose $\mathbf{V}$ is represented by $\mathbf{V}'$ in principal axes, then, for principal extension ratios λ_I, λ_{II} and λ_{III},

$$\mathbf{V}' = \begin{pmatrix} \lambda_I & 0 & 0 \\ 0 & \lambda_{II} & 0 \\ 0 & 0 & \lambda_{III} \end{pmatrix}, \tag{3.13}$$

where the directions of the I, II, and III principal axes in the original 1–2–3 axes set are given by the direction cosines of the principal stretches λ_I, λ_{II} and λ_{III}.

Exactly the same technique can be used to analyse the Cauchy–Green tensor $\mathbf{C}$. When a deformation gradient $\mathbf{F}$ includes rigid-body rotation, it is necessary to first form the Cauchy–Green measure $\mathbf{C}$ and then find its principal components and directions using the methods outlined above for $\mathbf{V}$. The principal directions of $\mathbf{C}$ are the same as those of the pure deformation $\mathbf{V}$ that underlies $\mathbf{F}$ ($\mathbf{F} = \mathbf{VR}$). Writing the analogue of Equation (3.12) for $\mathbf{C}$

$$\begin{vmatrix} c_{11} - \mu & c_{12} & c_{13} \\ c_{12} & c_{22} - \mu & c_{23} \\ c_{13} & c_{23} & c_{33} - \mu \end{vmatrix} = 0 \tag{3.14}$$

gives three roots for μ; μ_I, μ_{II} and μ_{III}. The corresponding principal directions are obtained by substituting the values of μ into the analogue of Equation (3.11)

$$\begin{pmatrix} c_{11} - \mu & c_{12} & c_{13} \\ c_{12} & c_{22} - \mu & c_{23} \\ c_{13} & c_{23} & c_{33} - \mu \end{pmatrix} \mathbf{X} = 0 \tag{3.15}$$

and solving for the three sets of direction cosines $\mathbf{X}$. In principal axes, the Cauchy–Green strain is

$$\mathbf{C}' = \begin{pmatrix} \mu_{\text{I}} & 0 & 0 \\ 0 & \mu_{\text{II}} & 0 \\ 0 & 0 & \mu_{\text{III}} \end{pmatrix}. \tag{3.16}$$

Making use of Equation (3.8) in principal axes

$$\mathbf{C}' = \mathbf{V}'^{\text{T}}\mathbf{V}'$$

and using Equations (3.13) and (3.16) gives the relationship between the principal values of $\mathbf{C}$ and the principal extension ratios:

$$\lambda_{\text{I}} = \sqrt{\mu_{\text{I}}}; \quad \lambda_{\text{II}} = \sqrt{\mu_{\text{II}}}; \quad \lambda_{\text{III}} = \sqrt{\mu_{\text{III}}}. \tag{3.17}$$

To now find the deformation $\mathbf{V}$ in the original 1–2–3 axes, it is necessary to transform the deformation $\mathbf{V}'$ given by Equation (3.13) using the appropriate rotation $\mathbf{R}$, discussed below.

In Figure 3.2, we illustrate deformations both in arbitrary or global 1–2–3 axes and in principal I–II–III axes.

When viewed in principal directions, the deformation gradient has a simple physical interpretation. Consider a spherical surface of undeformed material of unit radius centred on the origin. A point on this surface is $(\ell_1, \ell_2, \ell_3,)$ where

$$\ell_1^2 + \ell_2^2 + \ell_3^2 = 1 \tag{3.18}$$

and ℓ_1, ℓ_2 and ℓ_3 are in fact direction cosines. This point is transformed to a point (x_1, x_2, x_3) via the action of a deformation gradient in principal axes:

$$\begin{pmatrix} x_1 \\ x_2 \\ x_3 \end{pmatrix} = \begin{pmatrix} \lambda_{\text{I}} & 0 & 0 \\ 0 & \lambda_{\text{II}} & 0 \\ 0 & 0 & \lambda_{\text{III}} \end{pmatrix} \begin{pmatrix} \ell_1 \\ \ell_2 \\ \ell_3 \end{pmatrix}.$$

The three equations defined above can be used to substitute for the original co-ordinates $(\ell_1, \ell_2, \ell_3,)$ in Equation (3.18). The result is

$$\frac{x_1^2}{\lambda_{\text{I}}^2} + \frac{x_2^2}{\lambda_{\text{II}}^2} + \frac{x_3^2}{\lambda_{\text{III}}^2} = 1.$$

This equation represents an ellipsoid with axes along the principal directions. The lengths of its semi-axes are λ_{I}, λ_{II}, λ_{III} along I, II and III principal directions, respectively, as shown in Figure 3.3.

3.1.3   Transformation of Strain

To obtain the components of strain in a rotated axis set, we start with the deformation gradient $\mathbf{G}$ and rewrite (3.3):

$$\mathbf{x} = \mathbf{F}\mathbf{X}.$$
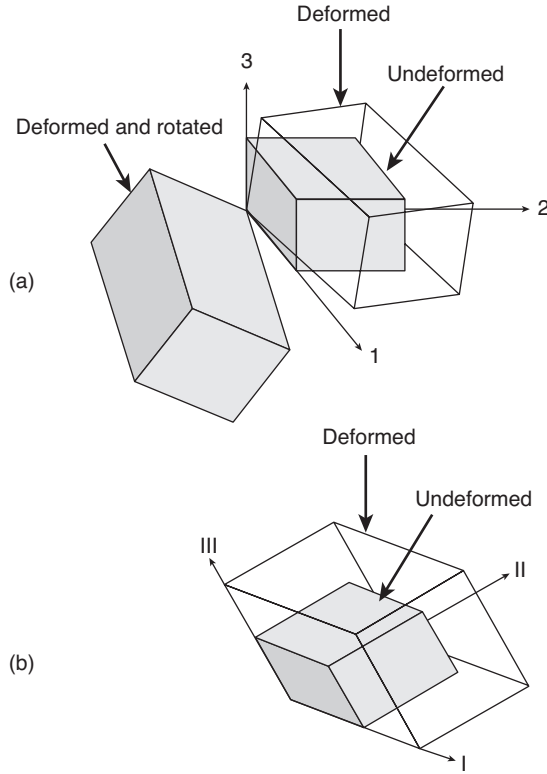
Figure 3.2 *Material element initially cubic in shape. (a) Deformed in arbitrary global axes (1–2–3), by normal and shear strains both with and without rigid-body rotation. (b) Deformed in principal axes (I–II–III), in which there is no rotation or shear.*
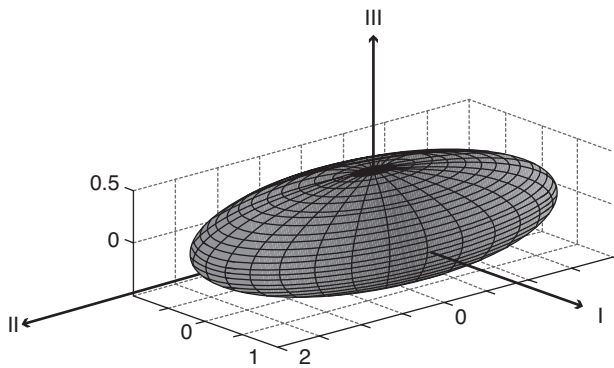
Figure 3.3 *Strain ellipsoid for $\lambda_I = 1$, $\lambda_{II} = 2$ and $\lambda_{III} = 0.5$.*

In an axis set rotated according to the matrix $\mathbf{R}$ with respect to the original set, the new co-ordinates of points in the deformed body are given by

$$\mathbf{x}' = \mathbf{Rx} = \mathbf{RFX}. \tag{3.19}$$

In the rotated axes, the co-ordinates of the undeformed body are given by

$$\mathbf{X}' = \mathbf{RX}$$

so that

$$\mathbf{X} = \mathbf{R}^{-1}\mathbf{X}' = \mathbf{R}^{\mathrm{T}}\mathbf{X}'$$

Substituting for $\mathbf{X}$ in Equation (3.19) now gives

$$\mathbf{x} = \mathbf{RFR}^{\mathrm{T}}\mathbf{X}'. \tag{3.20}$$

This resembles Equation (3.2). We may write

$$\mathbf{F}' = \mathbf{RFR}^{\mathrm{T}} \tag{3.21}$$

to give Equation (3.20) as $\mathbf{x}' = \mathbf{F}'\mathbf{X}'$, and conclude that Equation (3.21) defines the deformation gradient in the rotated axis set.

It can be easily shown that the Cauchy–Green strain tensor also transforms like this.

$$\mathbf{C}' = \mathbf{RCR}^{\mathrm{T}} \tag{3.22}$$

$\mathbf{C}$ and $\mathbf{F}$ are both second-order tensors and so must transform in the same way.

3.1.4   Examples of Elementary Strain Fields

All uniform strain fields can, as we have seen, be expressed in terms of principal extension ratios. Some commonplace strain fields are naturally expressed in this way, such as the uniaxial field, which for incompressible stretching along the I axis is of the form $\lambda_{\mathrm{I}} = \lambda$, $\lambda_{\mathrm{II}} = \lambda_{\mathrm{III}} = \lambda^{-1/2}$. Other strain states are customarily expressed in non-principal axes.

One such is that of *pure shear*. In the 1–2 plane, this can be expressed as the deformation gradient

$$F = \begin{pmatrix} 1 & \gamma \\ \gamma & 1 \end{pmatrix}.$$

Here $\mathbf{F}$ is symmetric and so no rigid-body rotation is included in the deformation. The effect of this deformation on a unit square of material is illustrated in Figure 3.4. Using the methods of Section 3.1.2, the principal extension ratios are the solutions of

$$\begin{vmatrix} 1-\lambda & \gamma \\ \gamma & 1-\lambda \end{vmatrix} = 0.$$

The principal values can be easily shown to be $\lambda_{\mathrm{I}} = 1+\gamma$, $\lambda_{\mathrm{II}} = 1-\gamma$. Using Equation (3.11), we can find the direction cosines (ℓ_1, ℓ_2) associated with λ_{I} as

$$\begin{pmatrix} 1-(1+\gamma) & \gamma \\ \gamma & 1-(1+\gamma) \end{pmatrix} \begin{pmatrix} \ell_1 \\ \ell_2 \end{pmatrix} = \begin{pmatrix} 0 \\ 0 \end{pmatrix}.$$

This gives $\ell_1 = \ell_2$. Hence, the principal I direction is at $45°$ to the 1 direction.
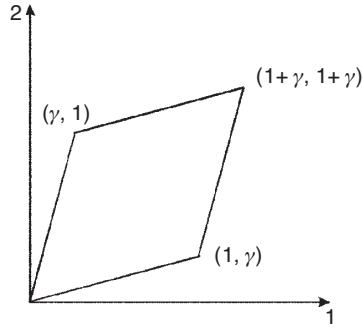
Figure 3.4   *A pure shear deformation of a unit square.*

Simple shear is actually a more complex state than pure shear, in that it includes a rigid-body deformation. We shall see that it is a combination of tensile and compressive perpendicular principal strains of a rotated solid. Consider the deformation gradient

$$\mathbf{F} = \begin{pmatrix} 1 & \gamma \\ 0 & 1 \end{pmatrix}.$$

Its effect on a unit square of material is illustrated in Figure 3.5. The horizontal sides of the original square remain horizontal and the same length, whereas the initially vertical sides undergo an increase in length. Stress must be applied vertically to the horizontal sides to ensure this. The asymmetry of $\mathbf{F}$ indicates that it includes some rigid-body rotation. To find the principal extension ratios, we first eliminate this by finding the Cauchy–Green strain measure $\mathbf{C}$:

$$\mathbf{C} = \mathbf{F}^{\mathrm{T}}\mathbf{F} = \begin{pmatrix} 1 & 0 \\ \gamma & 1 \end{pmatrix} \begin{pmatrix} 1 & \gamma \\ 0 & 1 \end{pmatrix} = \begin{pmatrix} 1 & \gamma \\ \gamma & \gamma^2 + 1 \end{pmatrix}.$$

Principal values of $\mathbf{C}$ are given by the method of Equation (3.14). The principal extension ratios are given by the square roots of these quantities as specified in Equation (3.17). After
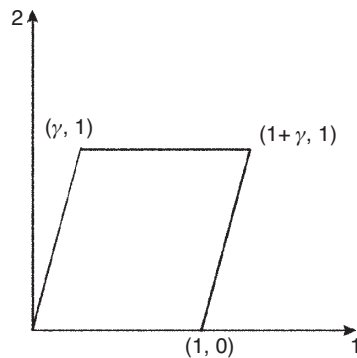
Figure 3.5   *A simple shear deformation of a unit square.*

some algebra these are found to be

$$\lambda_{\mathrm{I}} = \sqrt{1 + \gamma^2/2 + \sqrt{(1 + \gamma^2/2)^2 - 1}}$$

$$\lambda_{\mathrm{II}} = \sqrt{1 + \gamma^2/2 - \sqrt{(1 + \gamma^2/2)^2 - 1}}.$$

The deformation gradient in principal directions is thus given by

$$\mathbf{V}' = \begin{pmatrix} \lambda_{\mathrm{I}} & 0 \\ 0 & \lambda_{\mathrm{II}} \end{pmatrix}.$$

The eigenvectors of $\mathbf{C}$ define the direction cosines of the I and II directions with respect to the original 1– 2 axes. They give the angle of transformation θ and the associated rotation matrix $\mathbf{R}_\theta$ required to transform $\mathbf{V}'$ back to the 1–2 axes set to give the deformation gradient $\mathbf{V}$:

$$\mathbf{V} = \mathbf{R}_\theta^{\mathrm{T}} \mathbf{V}' \mathbf{R}_\theta.$$

Here, we have adapted Equation (3.21). $\mathbf{V}$, unlike $\mathbf{F}$, contains no rigid-body rotation, and the two are related (see Equation (3.6)) by

$$\mathbf{F} = \mathbf{R}_\phi \mathbf{V},$$

where $\mathbf{R}_\phi$ represents the rigid-body rotation inherent in $\mathbf{F}$ about the angle ϕ. This angle can be evaluated using the relation

$$\mathbf{R}_\phi = \mathbf{F} \mathbf{V}^{-1}.$$

The application of the deformation $\mathbf{F} = \mathbf{R}_\phi \mathbf{V}$ is illustrated in Figure 3.6. A unit square in Figure 3.6(a) is operated on first by $\mathbf{V}$, a combination of tension and shear, to give the shape in Figure 3.6(b). Then the shape is operated on further by $\mathbf{R}_\phi$ to give the simple shear of 3.6(c). The Figure 3.6 corresponds to a value $\gamma = 0.9$.

The algebraic expressions for $\mathbf{V}$ and ϕ are lengthy and will not be reproduced here. They can be readily evaluated numerically and the principal extension ratios and the rigid-body rotation are plotted as a function of shear strain in Figure 3.7.
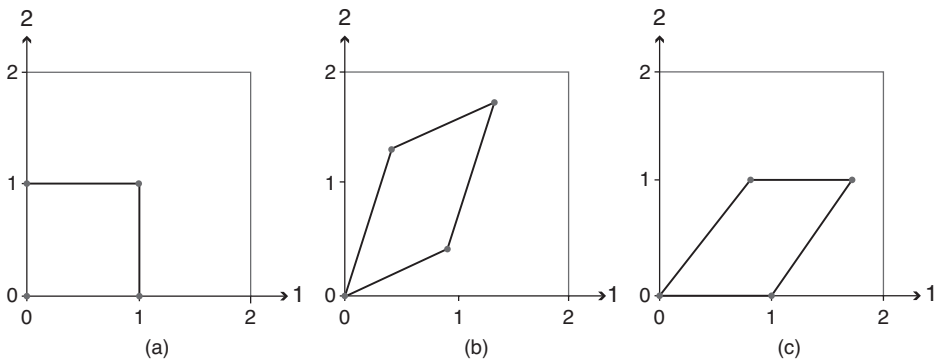
Figure 3.6   (a) The unit square, (b) the unit square operated on by **V** and (c) the unit square operated on by $R_\phi V$.
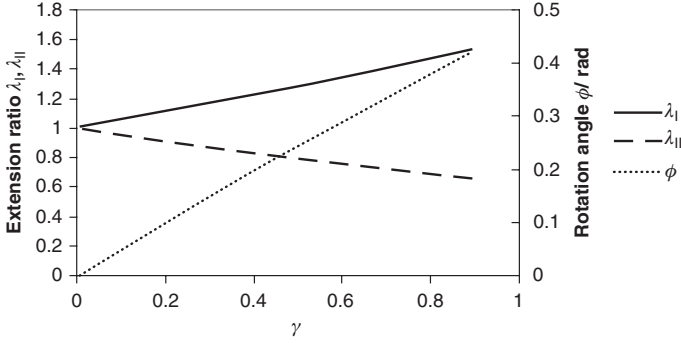
Figure 3.7 *Development of principal stretches and clockwise rigid-body rotation angle in simple shear.*

3.1.5 Relationship of Engineering Strains to General Strains

Recall that, in developing small strain theory, we made use of displacements u_1, u_2 and u_3 in the x_1, x_2 and x_3 directions The displacements are related to the initial and deformed positions X_i and x_i respectively by

$$u_1 = x_1 - X_1$$
$$u_2 = x_2 - X_2 \,.$$
$$u_3 = x_3 - X_3$$

(3.23)

Now introduce a deformation $\mathbf{V}$ that does not include rigid-body rotations. Then, $\mathbf{x} = \mathbf{VX}$ becomes

$$x_1 = v_{11}X_1 + v_{12}X_2 + v_{13}X_3$$
$$x_2 = v_{12}X_1 + v_{22}X_2 + v_{23}X_3$$
$$x_3 = v_{13}X_1 + v_{23}X_2 + v_{33}X_3$$

(3.24)

and we can now make use of Equation (3.23) to rewrite Equation (3.24) in terms of displacements:

$$u_1 = (v_{11} - 1)X_1 + v_{12}X_2 + v_{13}X_3$$
$$u_2 = v_{12}X_1 + (v_{22} - 1)X_2 + v_{23}X_3 \,.$$
$$u_3 = v_{13}X_1 + v_{23}X_2 + (v_{33} - 1)X_3$$

(3.25)

We can now use the strain-displacement equations (Chapter 2) to derive the normal engineering strains e_{11}, e_{22} and e_{33}:

$$e_{11} = \frac{\partial u_1}{\partial X_1} = v_{11} - 1$$
$$e_{22} = \frac{\partial u_2}{\partial X_2} = v_{22} - 1 \,.$$
$$e_{33} = \frac{\partial u_3}{\partial X_3} = v_{33} - 1$$

(3.26)

and the shear strains:

$$e_{12} = \frac{\partial u_1}{\partial X_2} + \frac{\partial u_2}{\partial X_1} = v_{12} + v_{12} = 2v_{12}$$

$$e_{23} = \frac{\partial u_2}{\partial X_3} + \frac{\partial u_3}{\partial X_2} = v_{23} + v_{23} = 2v_{23} .$$

(3.27)

$$e_{13} = \frac{\partial u_3}{\partial X_1} + \frac{\partial u_1}{\partial X_3} = v_{13} + v_{13} = 2v_{13}$$

Putting the values of the v_{ij} derived from Equations (3.26) and (3.27) into the matrix $\mathbf{V}$ then gives

$$\mathbf{V} = \begin{pmatrix} 1 + e_{11} & \frac{1}{2}e_{12} & \frac{1}{2}e_{13} \\[2mm] \frac{1}{2}e_{12} & 1 + e_{22} & \frac{1}{2}e_{23} \\[2mm] \frac{1}{2}e_{13} & \frac{1}{2}e_{23} & 1 + e_{33} \end{pmatrix} .$$

(3.28)

Transformations as defined by Equation (3.1) and rotation operations such as axis transformations (3.21) can be performed on small strains provided that the components are first used to form the matrix $\mathbf{V}$.

3.1.6   Logarithmic Strain

Principal true or logarithmic strains ε_{I}, $\varepsilon_{\mathrm{II}}$ and $\varepsilon_{\mathrm{III}}$ are defined in terms of the principal extension ratios by

$$\varepsilon_i = \ln(\lambda_i) \quad (i = \mathrm{I, II, III})$$

(3.29)

These strains are exactly additive, in contrast with engineering strains that are only approximately so. To illustrate this, consider two pure deformations $\mathbf{V}^a$ and $\mathbf{V}^b$ that are applied successively to give a total deformation $\mathbf{V}$, so that

$$\mathbf{V} = \mathbf{V}^a \mathbf{V}^b .$$

$\mathbf{V}$ is said to be *multiplicatively decomposed* into $\mathbf{V}^a$ and $\mathbf{V}^b$. When operating with finite strains, deformation gradients must be used that, being tensors, are combined multiplicatively. Suppose that both $\mathbf{V}^a$ and $\mathbf{V}^b$ have the same principal directions and are expressed in diagonal form, with principal extension ratios respectively λ_i^a and λ_i^b ($i = \mathrm{I, II, III}$), then $\mathbf{V}$ is diagonal with entries λ_i ($i = \mathrm{I, II, III}$) such that

$$\lambda_i = \lambda_i^a \lambda_i^b \quad (i = \mathrm{I, II, III}).$$

It now follows that

$$\varepsilon_i = \ln(\lambda_i) = \ln(\lambda_i^a \lambda_i^b) = \ln(\lambda_i^a) + \ln(\lambda_i^b) = \varepsilon_i^a + \varepsilon_i^b \ (i = \mathrm{I, II, III}),$$

where the ε_i^a and ε_i^b are the logarithmic strains associated respectively with $\mathbf{V}^a$ and $\mathbf{V}^b$.

Note also that the incompressibility (constant volume) condition

$$\lambda_{\mathrm{I}} \lambda_{\mathrm{II}} \lambda_{\mathrm{III}} = 1$$

(3.30)

is exactly equivalent to

$$\varepsilon_{\mathrm{I}} + \varepsilon_{\mathrm{II}} + \varepsilon_{\mathrm{III}} = 0 \tag{3.31}$$

in contrast to the analogous sum for small strains, which is only approximately zero.

Physical justification for the logarithmic strain can be obtained by considering it as similar to the definition of small strain as extension/(original length), but taking account of the increasing length of the body upon which the increments in extension are applied as the deformation progresses. For stretching of a body from length L_1 to length L_2, the true strain ε is then given by the integral

$$\varepsilon = \int_{L_1}^{L_2} \frac{\mathrm{d}l}{l} = \ln\left(\frac{L_2}{L_1}\right) = \ln\lambda.$$

The logarithmic strain has also been termed the *natural strain* by Nadai [4], and is discussed by other authors, for example Rees [5]. In terms of the engineering strain e,

$$\varepsilon = \ln\lambda = \ln(1 + e) = e - \frac{1}{2}e^2 + \frac{1}{3}e^3 - \cdots$$

so it is clear that e approximates to ε at small values.

3.2 The Stress Tensor

The stress tensor has been introduced in Chapter 2. In small strain elasticity theory, the components of stress are defined by considering the equilibrium of an elemental cube within the body. When the strains are small, the dimensions of the body, and therefore the areas of the cube faces, are to a first approximation unaffected by the strain. It is then of no consequence whether the components of stress are defined with respect to the cube before deformation or the cube after deformation. For finite strains, however, this is not true and there are alternative definitions of stress depending on whether the deformed or undeformed state is chosen as a reference. We will choose to adopt the stress associated with the *deformed state* – the *true stress* or *Cauchy stress* – throughout this work. In our present axis notation, we can express this stress tensor Σ as

$$\sum = \begin{pmatrix} \sigma_{11} & \sigma_{12} & \sigma_{13} \\ \sigma_{12} & \sigma_{22} & \sigma_{23} \\ \sigma_{13} & \sigma_{23} & \sigma_{33} \end{pmatrix}. \tag{3.32}$$

To transform between different axis sets, we use the same method as for deformation gradients as given by Equation (3.21). Note that, unlike the deformation gradient, the stress tensor is always symmetric. This is the consequence of the equilibrium of torques applied to a material element, as pointed out in Chapter 2. As a second-order tensor, the stress is subject to the same axis transformation operations as the deformation gradient and Cauchy–Green measure (Equations (3.21) and (3.22)). The principal stresses are the eigenvalues

of $\mathbf{\Sigma}$ and the associated principal directions are the eigenvectors, obtained in exactly the same way as for the deformation $\mathbf{V}$ and Cauchy–Green measure $\mathbf{C}$ as specified in Equations (3.12)–(3.16). Thus, in principal directions, the stress tensor is

$$\mathbf{\Sigma}' = \begin{pmatrix} \sigma_{\mathrm{I}} & 0 & 0 \\ 0 & \sigma_{\mathrm{II}} & 0 \\ 0 & 0 & \sigma_{\mathrm{III}} \end{pmatrix}, \tag{3.33}$$

where the principal directions are the eigenvectors of $\mathbf{\Sigma}$.

3.3   The Stress–Strain Relationships

Using the above definitions of finite strain and stress, we wish to construct stress–strain relationships for finite strains that are analogous to the generalised Hooke's law for small strain elasticity. Each component of stress can be a function of every component of strain, and vice versa. For a linear relation, we would expect equations such as

$$\sigma_{11} = a\varepsilon_{11} + b\varepsilon_{22} + c\varepsilon_{33} + d\varepsilon_{12} + e\varepsilon_{23} + f\varepsilon_{31}.$$

We could use this as a starting point for finite elasticity. It would be desirable to reduce the number of elastic constants a, b, and so on, by considerations such as material symmetry. Rather than developing a general theory of finite elasticity, however, we will introduce appropriate restrictions at an early stage, as appropriate for a representation of the behaviour of rubbers. The principal restrictions are driven by the simplifications that:

1. Rubber is isotropic in its undeformed state.
2. Volume changes associated with deformation are very small and may be neglected, i.e. a rubber is incompressible.

First consider the impact of these assumptions on small strain elasticity.
For an isotropic material, Hooke's law may be written as

$$\begin{aligned} e_{11} &= \frac{1}{E}\left(\sigma_{11} - \nu(\sigma_{22} + \sigma_{33})\right) \\ e_{22} &= \frac{1}{E}\left(\sigma_{22} - \nu(\sigma_{33} + \sigma_{11})\right) \\ e_{33} &= \frac{1}{E}\left(\sigma_{33} - \nu(\sigma_{11} + \sigma_{22})\right) \\ e_{12} &= \frac{2}{E}(1 + \nu)\sigma_{12} \\ e_{23} &= \frac{2}{E}(1 + \nu)\sigma_{23} \\ e_{31} &= \frac{2}{E}(1 + \nu)\sigma_{31} \end{aligned} \tag{3.34}$$

Rewrite the expressions for the normal strains as

$$e_{11} = \frac{1+v}{E}\left(\sigma_{11} - \frac{v}{1+v}(\sigma_{11} + \sigma_{22} + \sigma_{33})\right)$$
$$e_{22} = \frac{1+v}{E}\left(\sigma_{22} - \frac{v}{1+v}(\sigma_{11} + \sigma_{22} + \sigma_{33})\right). \qquad (3.35)$$
$$e_{33} = \frac{1+v}{E}\left(\sigma_{33} - \frac{v}{1+v}(\sigma_{11} + \sigma_{22} + \sigma_{33})\right)$$

Now we put

$$p = \frac{v}{1+v}(\sigma_{11} + \sigma_{22} + \sigma_{33}). \qquad (3.36)$$

p is proportional to the hydrostatic pressure $(\sigma_{11} + \sigma_{22} + \sigma_{33})/3$, and equal to it when Poisson's ratio $v = \frac{1}{2}$. Now Equation (3.35) becomes

$$e_{11} = \frac{1+v}{E}(\sigma_{11} - p)$$
$$e_{22} = \frac{1+v}{E}(\sigma_{22} - p). \qquad (3.37)$$
$$e_{33} = \frac{1+v}{E}(\sigma_{33} - p)$$

We now apply the incompressibility $e_{11} + e_{22} + e_{33} = 0$. Adding the above equations then gives

$$0 = \frac{1+v}{E}(\sigma_{11} + \sigma_{22} + \sigma_{33} - 3p).$$

Applying the definition for p from Equation (3.36), it is clear that the right-hand side is zero only when Poisson's ratio $v = \frac{1}{2}$; this condition corresponds to incompressibility. Putting this condition into Equation (3.37) and appending the shear terms then gives

$$e_{11} = \frac{3}{2E}(\sigma_{11} - p)$$
$$e_{22} = \frac{3}{2E}(\sigma_{22} - p)$$
$$e_{33} = \frac{3}{2E}(\sigma_{33} - p)$$
$$e_{12} = \frac{3}{E}\sigma_{12} \qquad \qquad \qquad . \qquad (3.38)$$
$$e_{23} = \frac{3}{E}\sigma_{23}$$
$$e_{31} = \frac{3}{E}\sigma_{31}$$

If the stresses are known, then p is known and the strains can be obtained from the above equations. If, however, the strains are known, then the normal stresses are only accessible via the quantities $\sigma_{11} - p$, and so on, and are indeterminate to the extent of what is now an

arbitrary constant p. This reflects the fact that, when an incompressible material is subject to hydrostatic stress, it suffers no change in strain, so that for a general strain field the stress is uncertain within a hydrostatic pressure and in this sense indeterminate.

We will now propose a theory of finite deformations by generalising the Equation (3.38). Defining the behaviour in principal directions is sufficient to define the material behaviour, as the behaviour for arbitrary directions is obtainable by transformation. Rewriting Equation (3.38) in principal directions gives

$$2e_{\mathrm{I}} = \frac{3}{E}(\sigma_{\mathrm{I}} - p)$$
$$2e_{\mathrm{II}} = \frac{3}{E}(\sigma_{\mathrm{II}} - p) \ . \qquad (3.39)$$
$$2e_{\mathrm{III}} = \frac{3}{E}(\sigma_{\mathrm{III}} - p)$$

We now create the theory of finite strain by replacing the engineering strains on the left-hand side of Equation (3.39) by measures of finite strain. We choose as a measure of finite strain the Cauchy–Green measure, which (see Equations (3.16) and (3.17)) has principal values λ_{I}^2, λ_{II}^2 and λ_{III}^2. Then,

$$\lambda_{\mathrm{I}}^2 = \frac{3}{E}(\sigma_{\mathrm{I}} - p)$$
$$\lambda_{\mathrm{II}}^2 = \frac{3}{E}(\sigma_{\mathrm{II}} - p) \ . \qquad (3.40)$$
$$\lambda_{\mathrm{III}}^2 = \frac{3}{E}(\sigma_{\mathrm{III}} - p)$$

This is essentially the scheme proposed by Rivlin [6]. Note that, unlike the Equation (3.37), the sum of the left-hand sides of Equation (3.40) does not equal zero. Therefore, in these equations, the quantity p is no longer the prevailing hydrostatic pressure, but must be reinterpreted as an arbitrary pressure that is evaluated with reference to the conditions that apply in any particular case.

Take as an example the simple case of uniaxial stretching along the I direction with an applied stress $\sigma_{\mathrm{I}} = \sigma$, $\sigma_{\mathrm{II}} = \sigma_{\mathrm{III}} = 0$. The extension ratio along I is $\lambda_{\mathrm{I}} = \lambda$, with the symmetry so that the extension ratios in the other two principal directions are equal. Then, the incompressibility condition (3.30) becomes

$$\lambda \lambda_{\mathrm{II}}^2 = 1 \Rightarrow \lambda_{\mathrm{II}} = \lambda_{\mathrm{III}} = \lambda^{-1/2}.$$

Using the second or third of Equations (3.40), the values of stress and extension ratio yield

$$\lambda^{-1} = -\frac{3p}{E} \Rightarrow p = -\frac{E}{3\lambda}.$$

The first of Equation (3.40), when rearranged, gives for the stress

$$\sigma = \frac{E}{3}\lambda^2 + p,$$

which using the above value for p gives

$$\sigma = \frac{E}{3}\left(\lambda^2 - \frac{1}{\lambda}\right). \tag{3.41}$$

The value of p can easily be evaluated when one of the stresses is zero, such as in-plane stress problems. For small strains, the use of $\lambda = 1 + e$ returns Hooke's law in one dimension:

$$\sigma = Ee.$$

provided third-order terms in e are neglected. It is a requirement that all finite strain theories reduce to Hooke's law at small strains.

In the above development, the stresses are understood to be *true* stresses, that is, the force per unit area of the deformed body. It is also of interest to find the nominal stress, that is, the stress obtained by dividing the force by the cross-sectional area of material before deformation. For a normal stress acting along the I direction, an original unit area is changed on deformation to the area $\lambda_{\mathrm{II}}\lambda_{\mathrm{III}}$. To regain the nominal stress σ^{nom}, we need to multiply the true stress by this area:

$$\sigma^{\mathrm{nom}} = \lambda_{\mathrm{II}}\lambda_{\mathrm{III}}\sigma. \tag{3.42}$$

Using the incompressibility condition (3.30) this becomes

$$\sigma^{\mathrm{nom}} = \frac{\sigma}{\lambda_{\mathrm{I}}} = \frac{\sigma}{\lambda}$$

and (3.41) becomes

$$\sigma^{\mathrm{nom}} = \frac{E}{3}\left(\lambda - \frac{1}{\lambda^2}\right). \tag{3.43}$$

An expression of this form is often associated with the stretching of rubber elastic networks, having been derived on physical grounds (see Chapter 4). However, we can see here that it arises on purely phenomenological grounds once the assumptions of isotropy and incompressibility have been made, and does not imply that the material is rubber-like. These materials are sometimes referred to as neo-Hookean.

The finite deformation theory developed here is the result of a simple generalisation of linear elasticity. There are much more sophisticated theories available, some of which are motivated by physical arguments. A more secure basis for the development of finite strain theories is the stored energy or strain energy function, which will now be considered.

3.4   The Use of a Strain Energy Function

3.4.1   Thermodynamic Considerations

The simplest (and 'weakest') definition of an elastic material is one for which the stress depends only on the current strain; these materials are termed *Cauchy elastic*. A subset of these materials is occupied by those for which the strain energy depends only on the current strain. These are termed *Green elastic* or *hyperelastic* and for these the strain energy is a function of the current strain only, and fully defines the material behaviour. For Cauchy

elastic material, it is possible for the strain energy to depend on the strain path – the route or history via which the current strain level is attained – and thermodynamically non-physical behaviour may be permitted. Hyperelastic materials are not subject to this hazard, and have become the standard way to define finite strain elasticity. The different definitions of elasticity have been discussed by Ogden [3].

3.4.1.1 Development of Strain Energy Functions

We shall develop the concept of strain energy using a small strain approach. Because we will wish to follow the phenomenological treatment by one based on statistical mechanics, it is important at the outset to examine the different types of strain energy function that can be defined, depending on experimental conditions. This introduces thermodynamic considerations.

Suppose we have a cylinder of material of axial length L and cross-sectional area A. A force f is acting along the axis such as to stretch the body. The body extends by a small length δx as this force f acts (the smallness of δx allows us to assume that f remains constant). The associated increment in energy is then $f\,\delta x$. We are generally more concerned with the energy per unit volume W. Dividing by the body's volume, the increment in this quantity is given by

$$\delta W = \frac{f\,\delta x}{AL},$$

which can be re-expressed in terms of nominal stress and strain as

$$\delta W = \frac{f}{A} \times \frac{\delta x}{L} = \sigma^{\mathrm{nom}}\delta e.$$

The stress is nominal as the area A relates to the undeformed material. For small strains, the nominal and true stresses can be assumed equal. Then, when all six components of stress are acting, the energy is additive and, expressing the result in differential form, we have

$$dW = \sigma_{11}de_{11} + \sigma_{22}de_{22} + \sigma_{33}de_{33} + \sigma_{12}de_{12} + \sigma_{23}de_{23} + \sigma_{31}de_{31}. \qquad (3.44)$$

Now consider a small strain deformation of unit volume of an elastic solid occurring under adiabatic conditions. The first law of thermodynamics gives

$$dW = dU - dQ$$

relating the work done on the solid dW to the increase in internal energy dU and the mechanical value of the heat supplied dQ. For an adiabatic change of state, $dQ = 0$ and $dW = dU$. We can imagine that the deformation is produced by independent changes in each of the components of strain, i.e.

$$dW = dU = \frac{\partial U}{\partial e_{11}}de_{11} + \frac{\partial U}{\partial e_{22}}de_{22} + \frac{\partial U}{\partial e_{33}}de_{33}\frac{\partial U}{\partial e_{12}}de_{12} + \frac{\partial U}{\partial e_{23}}de_{23} + \frac{\partial U}{\partial e_{31}}de_{31}. \quad (3.45)$$

Comparison of this equation with Equation (3.44) leads us to make the identifications

$$\sigma_{11} = \frac{\partial U}{\partial e_{11}}, \sigma_{22} = \frac{\partial U}{\partial e_{22}}, \sigma_{33} = \frac{\partial U}{\partial e_{33}}, \sigma_{12} = \frac{\partial U}{\partial e_{12}}, \sigma_{23} = \frac{\partial U}{\partial e_{23}}, \sigma_{31} = \frac{\partial U}{\partial e_{31}}. \quad (3.46)$$

We can therefore define a strain energy function or stored energy function that defines the energy stored in the body as a result of the strain. Here we have performed an analysis involving energy per unit volume under the simplifying assumption that the conditions are adiabatic. For other conditions, other forms of energy are appropriate, as discussed by Baker [7] and Houlsby and Puzrin [8].

In the case of fluids, it is appropriate to define the enthalpy H as

$$H = U + pV, \tag{3.47}$$

where p is pressure and V is the volumetric strain. However, for solids an alternative formulation is used in which pV is replaced by another energy-like term, which involves the products of corresponding stress and strain components, in the form which we now define in compact notation:

$$\sigma_{ij}e_{ij} = \sigma_{11}e_{11} + \sigma_{22}e_{22} + \sigma_{33}e_{33} + \sigma_{12}e_{12} + \sigma_{23}e_{23} + \sigma_{31}e_{31}$$

Enthalpy is now defined as

$$H = U - \sigma_{ij}e_{ij}, \tag{3.48}$$

where the sign of the second term has changed since p denotes a negative stress. This form reduces to the more traditional form (Equation (3.47)) for gases or liquids with low viscosities, which can sustain only hydrostatic pressures. Given that U is a function of strain only, differentiation with respect to each stress component yields

$$e_{ij} = -\frac{\partial H}{\partial \sigma_{ij}} \quad (i,j = 1, 2, 3). \tag{3.49}$$

This gives an alternative set of stress–strain relationships parallel with Equation (3.46) but for the strain in terms of the stress.

To analyse non-adiabatic cases, it is useful to introduce free energies, which are essentially internal energies minus the heat exchanged. The Helmholtz free energy A is defined as

$$A = U - TS, \tag{3.50}$$

where S is the entropy. This can be used to analyse isothermal conditions. In this case the first law, with $dQ \neq 0$, gives

$$dW = dU - dQ = dU - T\,dS = dA$$

and we can introduce a third strain energy function that is identical to A and reproduces the Equation (3.46) with A replacing U. The Helmholtz free energy is associated with constant volume conditions.

Finally, we introduce a second free energy, the Gibbs free energy G defined as

$$G = U - \sigma_{ij}e_{ij} - TS. \tag{3.51}$$

Differentiating with respect to the stress gives

$$e_{ij} = -\frac{\partial G}{\partial \sigma_{ij}} \quad (i,j = 1, 2, 3)$$
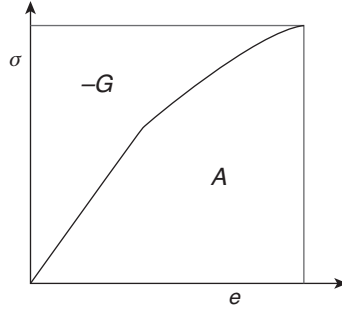
Figure 3.8   *Areas defined by a stress–strain curve corresponding to Helmholtz free energy (A) and Gibbs free energy (G).*

another set of stress–strain relationships resembling Equation (3.49). The Gibbs free energy is associated with constant pressure conditions.

Examining Equations (3.50) and (3.51), it is clear that

$$A - G = \sigma_{ij}e_{ij}.$$

A and –*G* can be regarded as *complementary*. This can be interpreted for the one-dimensional case, with the areas under or to the right of a stress–strain curve being associated with *A* and –*G* respectively (see Figure 3.8). Thus, *A* is the strain energy, and –*G* the complementary energy.

3.4.1.2   Finite Strains

For finite strains, we can adapt Equation (3.44) by recognising that the stresses are nominal stresses. In this case, it is most effective to operate in principal directions. Choosing the principal extension ratios as strain measures, and noting that

$$\lambda_i = 1 + e_i \Rightarrow d\lambda_i = de_i \ (i = \text{I, II, III})$$

Equation (3.44) becomes

$$dW = dU = \sigma_{\text{I}}^{\text{nom}}d\lambda_{\text{I}} + \sigma_{\text{II}}^{\text{nom}}d\lambda_{\text{II}} + \sigma_{\text{III}}^{\text{nom}}d\lambda_{\text{III}}.$$

Introducing true stresses by correcting for the cross-sectional areas as in Equation (3.42), we have

$$dW = dU = \lambda_{\text{II}}\lambda_{\text{III}}\sigma_{\text{I}}d\lambda_{\text{I}} + \lambda_{\text{III}}\lambda_{\text{I}}\sigma_{\text{II}}d\lambda_{\text{II}} + \lambda_{\text{I}}\lambda_{\text{II}}\sigma_{\text{III}}d\lambda_{\text{III}}. \tag{3.52}$$

Similarly, in principal directions Equation (3.45) becomes

$$dW = dU = \frac{\partial U}{\partial \lambda_{\text{I}}}d\lambda_{\text{I}} + \frac{\partial U}{\partial \lambda_{\text{II}}}d\lambda_{\text{II}} + \frac{\partial U}{\partial \lambda_{\text{III}}}d\lambda_{\text{III}}. \tag{3.53}$$

Comparison of Equations (3.52) and (3.53) leads to the relations for finite deformation

$$\sigma_{\text{I}} = \frac{1}{\lambda_{\text{II}}\lambda_{\text{III}}} \frac{\partial U}{\partial \lambda_{\text{I}}}, \quad \sigma_{\text{II}} = \frac{1}{\lambda_{\text{III}}\lambda_{\text{I}}} \frac{\partial U}{\partial \lambda_{\text{II}}}, \quad \sigma_{\text{III}} = \frac{1}{\lambda_{\text{I}}\lambda_{\text{II}}} \frac{\partial U}{\partial \lambda_{\text{III}}}. \tag{3.54}$$

For incompressible material, the expressions are slightly simpler, but involve the un-known hydrostatic term p as discussed in Section 3.3. Using the incompressibility relation (3.30) and incorporating the hydrostatic term, results in

$$\sigma_{\mathrm{I}} = \lambda_{\mathrm{I}}\frac{\partial U}{\partial \lambda_{\mathrm{I}}} - p, \quad \sigma_{\mathrm{II}} = \lambda_{\mathrm{II}}\frac{\partial U}{\partial \lambda_{\mathrm{II}}} - p, \quad \sigma_{\mathrm{III}} = \lambda_{\mathrm{III}}\frac{\partial U}{\partial \lambda_{\mathrm{III}}} - p. \tag{3.55}$$

3.4.2 The Form of the Strain Energy Function

The strain energy function U is a function of the components of some measure of strain, such as the stretch $\mathbf{V}$ or the Cauchy–Green measure $\mathbf{C}$. U is a physical quantity with a numerical value upon which all observers will agree – it is independent of the axis set. On the other hand, the components of $\mathbf{V}$ and $\mathbf{C}$ are entirely dependent on the axis set. Unless a function of these components is chosen with care, it will itself be dependent on the axis set and so will be inadmissible as a strain energy function. This places restrictions on the form of U, which can be approached in two ways:

1. There are certain combinations of the strain components that are themselves independent of the axis set, known as *strain invariants*. Any function of these quantities is itself independent of the axis set, and in this sense will be a permissible form of U.
2. Alternatively, principal values of strain components are used, such as the extension ratios λ_{I}, λ_{II} and λ_{III}. While the three values of these quantities will be agreed by all observers, the assignation of the labels I, II and III is arbitrary. The value of U defined in this way must be unchanged under the interchange of any pair of these labels; in other words, U must be a *symmetric function* of the principal strain values.

Both these approaches are discussed below.

3.4.3 The Strain Invariants

Any second-order tensor has a number of invariants associated with it. One such is the *trace* of the tensor, equal to the sum of its diagonal terms, applicable to any strain tensor. We define the *first invariant* I_1 as the trace of the Cauchy–Green strain measure tr($\mathbf{C}$):

$$I_1 = \mathrm{tr}(\mathbf{C}) = c_{11} + c_{22} + c_{33}.$$

Adopting principal directions, this can be expressed in terms of the extension ratios via Equation (3.17):

$$I_1 = \lambda_{\mathrm{I}}^2 + \lambda_{\mathrm{II}}^2 + \lambda_{\mathrm{III}}^2. \tag{3.56}$$

The second invariant I_2 can also defined in terms of the trace function and $\mathbf{C}$:

$$I_2 = \frac{1}{2}\left[(\mathrm{tr}(\mathbf{C}))^2 - \mathrm{tr}(\mathbf{C}^2)\right],$$

which clearly as a function of invariants is also invariant, and can be readily re-expressed in terms of principal extension ratios as

$$I_2 = \lambda_{\mathrm{I}}^2\lambda_{\mathrm{II}}^2 + \lambda_{\mathrm{II}}^2\lambda_{\mathrm{III}}^2 + \lambda_{\mathrm{III}}^2\lambda_{\mathrm{I}}^2. \tag{3.57}$$

The third invariant is related to the volume of the material, which, like energy, is the same for all axis sets. A volume of material that is initially a unit cube is deformed to a

volume equal to the product of the three principal extension ratios. The third invariant I_3 is defined directly as the square of this volume:

$$I_3 = \lambda_I^2 \lambda_{II}^2 \lambda_{III}^2 \qquad (3.58)$$

and is also equal to the determinant of $\mathbf{C}$, $\det(\mathbf{C})$. For incompressible material $I_3 = 1$.

These three invariants are all that is necessary for our purposes in defining strain energy functions.

3.4.4   Application of the Invariant Approach

In this section, we give examples of applications using the approach to the strain energy function listed as (1) in Section 3.4.2. We shall restrict the discussion to incompressible materials, so that only the invariants I_1 and I_2 will be of concern.

The most elementary form is a function of I_1 only:

$$U = C(I_1 - 3).$$

Here C is a material constant and the 3 ensures that the strain energy is zero at zero strain. This form is known as the neo-Hookean or Gaussian model. It can be derived for rubbers using a physical argument based on thermodynamics [9], and will be discussed further in Chapter 4. In many cases, a more complex approach is required.

In a classic work of Rivlin and Saunders [10] on vulcanised rubber, a strain energy function of the form $U(I_1, I_2)$ was introduced. Experiments were performed on sheets of material in plane stress with the III direction normal to the plane. Homogeneous deformations were applied using a biaxial stretching machine so that the principal extension ratios λ_I and λ_{II} were under experimental control. Incompressibility applies and Equations (3.55) give the principal stresses

$$\sigma_i = \lambda_i \frac{\partial U}{\partial \lambda_i} - p = \lambda_i \left(\frac{\partial U}{\partial I_1} \frac{\partial I_1}{\partial \lambda_i} + \frac{\partial U}{\partial I_2} \frac{\partial I_2}{\partial \lambda_i} \right) - p \quad (i = \text{I, II, III}). \qquad (3.59)$$

The incompressibility condition (3.30) leads to a simplified expression for I_2 derived from Equation (3.57):

$$I_2 = \frac{1}{\lambda_I^2} + \frac{1}{\lambda_{II}^2} + \frac{1}{\lambda_{III}^2}.$$

From this equation and Equation (3.56), expressions for the derivatives are obtained:

$$\frac{\partial I_1}{\partial \lambda_i} = 2\lambda_i; \quad \frac{\partial I_2}{\partial \lambda_i} = -\frac{2}{\lambda_i^3} \quad (i = \text{I, II, III}).$$

Substitution of these expressions into Equations (3.59) now yields the stresses

$$\sigma_I = 2 \left(\lambda_I^2 \frac{\partial U}{\partial I_1} - \frac{1}{\lambda_I^2} \frac{\partial U}{\partial I_2} \right) - p$$

$$\sigma_{II} = 2 \left(\lambda_{II}^2 \frac{\partial U}{\partial I_1} - \frac{1}{\lambda_{II}^2} \frac{\partial U}{\partial I_2} \right) - p \qquad .$$

$$\sigma_{III} = 2 \left(\lambda_{III}^2 \frac{\partial U}{\partial I_1} - \frac{1}{\lambda_{III}^2} \frac{\partial U}{\partial I_2} \right) - p = 0$$

The last component is equated to zero according to the plane stress condition, giving an expression for p. On substituting p back into the first two equations and making use of the incompressibility condition (3.30) to eliminate λ_{III}, the in-plane stresses are

$$\sigma_{\mathrm{I}} = 2\left(\lambda_{\mathrm{I}}^2 - \frac{1}{\lambda_{\mathrm{I}}^2\lambda_{\mathrm{II}}^2}\right)\left(\frac{\partial U}{\partial I_1} + \lambda_{\mathrm{II}}^2\frac{\partial U}{\partial I_2}\right)$$

$$\sigma_{\mathrm{II}} = 2\left(\lambda_{\mathrm{II}}^2 - \frac{1}{\lambda_{\mathrm{I}}^2\lambda_{\mathrm{II}}^2}\right)\left(\frac{\partial U}{\partial I_1} + \lambda_{\mathrm{I}}^2\frac{\partial U}{\partial I_2}\right)$$

Both the stresses and the extension ratios are available from experimental data, so the above equations provide sufficient information to evaluate the derivatives $\dfrac{\partial U}{\partial I_1}$ and $\dfrac{\partial U}{\partial I_2}$. They can be rearranged to give

$$\frac{\partial U}{\partial I_1} = \left(\frac{\lambda_{\mathrm{I}}^2\sigma_{\mathrm{I}}}{\lambda_{\mathrm{I}}^2 - 1/\lambda_{\mathrm{I}}^2\lambda_{\mathrm{II}}^2} - \frac{\lambda_{\mathrm{II}}^2\sigma_{\mathrm{II}}}{\lambda_{\mathrm{II}}^2 - 1/\lambda_{\mathrm{I}}^2\lambda_{\mathrm{II}}^2}\right)\Big/2\left(\lambda_{\mathrm{I}}^2 - \lambda_{\mathrm{II}}^2\right)$$

$$\frac{\partial U}{\partial I_2} = \left(\frac{\sigma_{\mathrm{I}}}{\lambda_{\mathrm{I}}^2 - 1/\lambda_{\mathrm{I}}^2\lambda_{\mathrm{II}}^2} - \frac{\sigma_{\mathrm{II}}}{\lambda_{\mathrm{II}}^2 - 1/\lambda_{\mathrm{I}}^2\lambda_{\mathrm{II}}^2}\right)\Big/2\left(\lambda_{\mathrm{I}}^2 - \lambda_{\mathrm{II}}^2\right)$$

(3.60)

Rivlin and Saunders used these equations to plot the graphs shown in Figure 3.9. Pairs of values of principal extension ratio were chosen such as to provide a range of values of I_1 for a constant I_2, and a range of values of I_1 for a constant I_2. It can be seen from the figure that $\dfrac{\partial U}{\partial I_1}$ is approximately constant and independent of both invariants. $\dfrac{\partial U}{\partial I_2}$, however, is independent of I_1 but decreases with increasing I_2. This is suggestive of a form of strain energy function

$$U = C_1(I_1 - 3) + f(I_2 - 3) \tag{3.61}$$

a generalisation of the neo-Hookean model discussed above, where f is a function with $f(0) = 0$. The second term is generally smaller than the first, and decreases as I_2 increases. In this case,

$$\frac{\partial U}{\partial I_1} \sim 170 \text{ kPa,}$$

whereas

$$\frac{\partial U}{\partial I_2} \sim 15 \text{ kPa.}$$

This suggests that the use of a constant in place of the function f could be a useful model. This form is then

$$U = C_1(I_1 - 3) + C_2(I_2 - 3). \tag{3.62}$$

This is known as the Mooney–Rivlin model [11].

Rivlin and Saunders carried out experiments in simple tension, torsion, pure shear and pure shear superposed on simple extension to extend the range of combinations of principal extension ratio. This showed behaviour generally consistent with Equation (3.61). Their work illustrates the importance of exploring a wide range of combinations of extension ratio to establish the function U. The traditional form of materials test – the uniaxial stretch – involves a very specific mode of deformation. Finding materials parameters by least squares
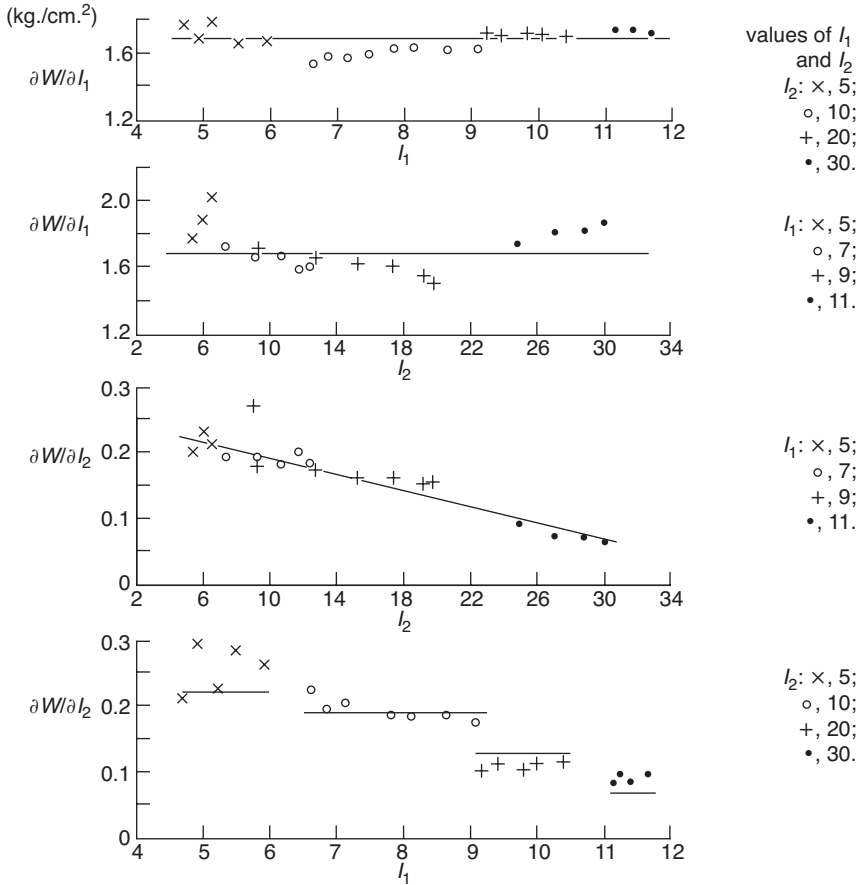
Figure 3.9   *Derivatives of strain energy plotted against invariants. (Reproduced from Rivlin, R.S. and Saunders, D.W. (1951) Large elastic deformations of isotropic materials. VII. Experiments on the deformation of rubber. Phil. Trans. R. Soc. A, **243**, 251. Copyright (1951) Royal Society Publishing.)*

fitting to data generated in this way, or in any other way involving a single combination of extension ratios, is likely to produce suspect results that give rise to poor predictions in general.

More recently, Kawabata *et al*. [12] applied a similar approach to an isoprene rubber vulcanisation. They showed that the strain energy function of Equation (3.61) was applicable to this material. They modelled temperature dependence satisfactorily by modifying the first term to be proportional to the absolute temperature.

3.4.5   Application of the Principal Stretch Approach

Rivlin adopted a formulation for the strain energy function U that involved the squares of the extension ratios because he envisaged that negative values of these quantities were

possible, while U must be always positive. However, as demonstrated in Section 3.1.2, any strain field can be expressed in terms of principal extension ratios λ_I, λ_{II}, λ_{III} that are essentially positive quantities, and can be interpreted as the dimensions of the principal axes of the strain ellipsoid.

The use of the invariant approach, which is closely linked to Rivlin's use of strain in the form of even powers of the extension ratios as exemplified in Equation (3.40), now appears to be unnecessarily restrictive. In this section, we give examples of applications using the approach to the strain energy function listed as (2) in Section 3.4.2. We shall again restrict the discussion to incompressible materials.

Valanis and Landel [13] have introduced a strain energy function of the form

$$U = u(\lambda_I) + u(\lambda_{II}) + u(\lambda_{III}). \tag{3.63}$$

This form has the essential property specified in (2) in Section 3.4.2, that U is a symmetric function of the principal extension ratios. Stresses are derived using Equation (3.55) that gives

$$\sigma_i = \lambda_i u'(\lambda_i) - p \quad (i = \text{I, II, III}).$$

Valanis and Landel used the expression for the stress difference in the I–II plane

$$\sigma_I - \sigma_{II} = \lambda_I u'(\lambda_I) - \lambda_{II} u'(\lambda_{II}) \tag{3.64}$$

to analyse the validity of their approach. They chose, for the range $1 < \lambda < 2.5$, the function

$$u'(\lambda) = 2\mu \ln(\lambda)$$

so that Equation (3.64) becomes

$$\sigma_I - \sigma_{II} = 2\mu \left(\lambda_I \ln(\lambda_I) - \lambda_{II} \ln(\lambda_{II}) \right).$$

In the small strain limit, the logarithmic strain approaches the engineering strain (see Section 3.1.6) and comparison of this expression with Hooke's law then reveals that μ is the shear modulus. In order to validate the model over a range of material data, a plot was made of

$$\frac{\sigma_I - \sigma_{II}}{2\mu} \text{ versus } \left\{ \lambda_I u'(\lambda_I) - \lambda_{II} u'(\lambda_{II}) \right\} / 2\mu$$

to give a common plot of slope unity. This is shown in Figure 3.10, which combines data on natural rubber from three sources. The analysis gives excellent support to the Valanis–Landel proposal.

The form (3.63) of U has also been used by Ogden [14], who proposed an n-term energy function

$$U = \sum_n \frac{\mu_n}{\alpha_n} \left(\lambda_I^{\alpha_n} + \lambda_{II}^{\alpha_n} + \lambda_{III}^{\alpha_n} - 3 \right). \tag{3.65}$$

For $n = 1$, u in Equation (3.63) is a power law function

$$u(\lambda) = \frac{\mu_1}{\alpha_1} \lambda^{\alpha_1} - 1$$
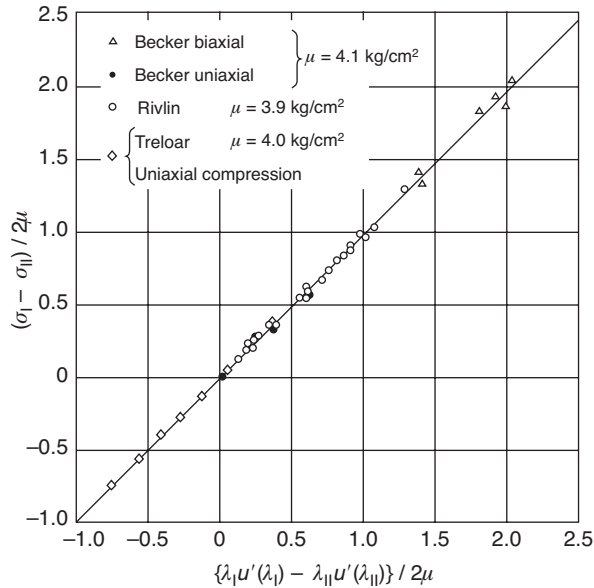
Figure 3.10 *Various data sets plotted according to the proposal of Valanis and Landel. (Adapted from Valanis, K.C. and Landel, R.F. (1967) The strain-energy function of a hyperelastic material in terms of the extension ratios. J. Appl. Phys., **38**, 2997. Copyright (1967) American Institute of Physics.)*

and for higher values of n, u is a summation. Principal stress components are given via Equation (3.55) as

$$\sigma_i = \sum_n \mu_n \lambda_i^{\alpha_n} - p \quad (i = \text{I, II, III}).$$

Ogden showed that the data of Treloar [15] for the stretching modes simple tension, equibiaxial tension and pure shear could be fitted well with a four-term model, in contrast to the poor fits obtained for the neo-Hookean model and the single-term Ogden model with exponent $\alpha = 1$. The results, in Figure 3.11, show a highly effective representation. There have been numerous applications of the Ogden model both to rubbers and in polymers in general, owing to its effectiveness and ease of use.

Other forms of the Landel–Valanis functions u are of course possible. Recently, Darijani, Naghdabadi and Kargarnovin [16] explored a number of possibilities, involving polynomial, logarithmic and exponential functions. In this scheme, strain energy functions are constructed using a set of basic functions of the principal stretches. These are:

- Power law $(\lambda^m - 1)$
- Polynomial $(\lambda - 1)^m$
- Logarithmic $(\ln \lambda)^m$
- Exponential $\exp(m(\lambda - 1)) - 1$
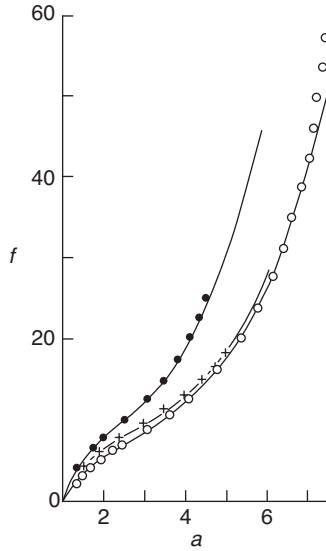
Figure 3.11 *Ogden's four-term model applied to Treloar's results, plotted as nominal stress against extension ratio. ○ − simple tension; + − pure shear; ● equibiaxial tension. (Reproduced from Ogden, R.W. (1972) Large deformation isotropic elasticity—on the correlation of theory and experiment for incompressible rubber-like. Solids Proc. R. Soc. A, **326**, 565. Copyright (1972) Royal Society Publishing.)*

The strain energy functions are combinations of these basic forms, set up to ensure physically realistic values of stress at zero, infinitely large or infinitely small strain. Darijani, Naghdabadi and Kargarnovin list eight possible forms of strain energy function. For instance, the 'exponential–exponential' form is

$$u(\lambda) = \sum_{k=1}^{M} A_k \left(\exp(m_k(\lambda - 1)) - 1\right) + \sum_{k=1}^{N} B_k \left(\exp(n_k(\lambda^{-1} - 1)) - 1\right) \quad (3.66)$$

and the 'power law-logarithmic' form is

$$u(\lambda) = \sum_{k=1}^{M} A_k \left(\lambda^{m_k} - 1\right) + \sum_{k=1}^{N} B_k (\ln \lambda)^k.$$

The strain energy U is created from these functions using Equation (3.63). Darjini, Naghdabadi and Kargarnovin applied these methods to a number of published results on rubbers, including those of Treloar that are the subject of Figure 3.11. The performance of the exponential–exponential (3.66) with this set of data is examined in Figure 3.12, for two versions of the model; three-term ($M = 2, N = 1$) and two-term ($M = N = 1$). The three-term model gives an excellent fit to the data. Other published data, due to Kawabata *et al*. [12], Lambert-Diani and Rey [17] and Alexander [18] were also subject to analysis using a range of the available strain energy functions. It was concluded that strain energy functions involving exponential terms gave the best performance.
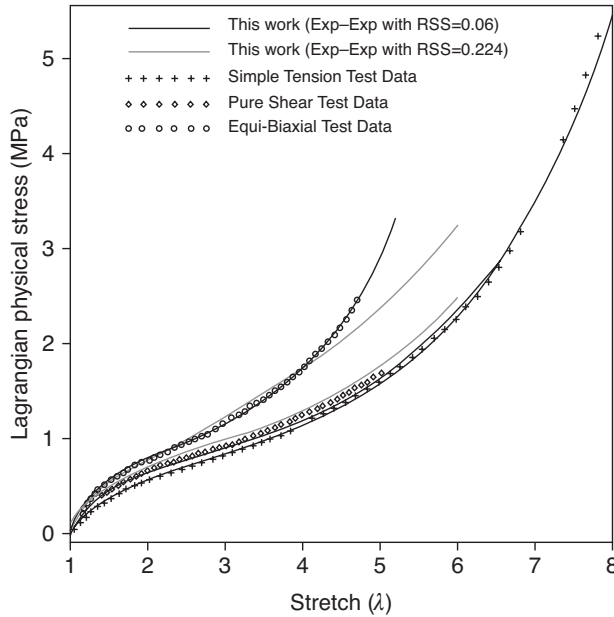
Figure 3.12 *Predictions of Treloar's data using Equations (3.66) and (3.63). The RSS (residual sum of square error) = 0.06 corresponds to a three-term model, and the RSS = 0.224 to a two-term model. (Reproduced from Darijani, H., Naghdabadi, R. and Kargarnovin, M.H. (2010) Constitutive modeling of rubber-like materials based on consistent strain energy density functions. Polym Eng Sci, **50**, 1058. Copyright (2010) John Wiley & Sons, Ltd.)*

A major conclusion of this work is that a programme of multiaxial strain experiments at a range of combinations of principal stretches is essential for the evaluation of the strain energy function. It is additionally clear that the principal stretch approach has produced a greater number of advances in recent years than the invariant approach. It also seems more amenable to being adapted for physically based models, as it is more obviously related to the stretching of molecular chains. As pointed out by Hopkins [19], the use of extension ratios seems wholly natural in any physical theory, and this is especially true when we are translating the extension ratios to changes in the molecular conformation, i.e. directly to events at a microscopic level. These ideas will be pursued further in the next chapter.

References

1. Green, A.E. and Zerna, W. (2002) *Theoretical Elasticity*, Courier Dover Publications, Mineola, New York.
2. Green, A.E. and Adkins, J.E. (1970) *Large Elastic Deformations and Non-Linear Continuum Mechanics*, Clarendon Press, Oxford.
3. Ogden, R.W. (1997) *Non-linear Elastic Deformations*, Courier Dover Publications, Mineola, New York.

4. Nadai, A. (1950) *Theory of Flow and Fracture of Solids*, Vol. 1, 2nd edn, McGraw-Hill, New York.

5. Rees, D.W.A. (2006) *Basic Engineering Plasticity*, Butterworth-Heinemann, Oxford.

6. Rivlin, R.S. (1949) Large elastic deformations of isotropic materials. I. Fundamental concepts. *Phil. Trans. R. Soc. A*, **240**, 459.

7. Baker, G. (2005) Thermodynamics in solid mechanics: a commentary. *Phil. Trans. R. Soc. A*, **363**, 2465.

8. Houlsby, G.T. and Puzrin, A.M. (2006) *Principles of Hyperplasticity*, Springer, London.

9. Rivlin, R.S. and Saunders, D.W. (1951) Large elastic deformations of isotropic materials. VII. Experiments on the deformation of rubber. *Phil. Trans. R. Soc. A*, **243**, 251.

10. Treloar, L.R.G. (1943) The elasticity of a network of long-chain molecules. II. *Trans. Faraday Soc.*, **39**, 241.

11. Mooney, M. (1940) A theory of large elastic deformation. *J. Appl. Phys.*, **2**, 582.

12. Kawabata, S., Matsuda, M., Tei, K. and Kawai, H. (1981) Experimental survey of the strain energy density function of isoprene rubber vulcanizate. *Macromolecules*, **14**, 154.

13. Valanis, K.C. and Landel, R.F. (1967) The strain-energy function of a hyperelastic material in terms of the extension ratios. *J. Appl. Phys.*, **38**, 2997.

14. Ogden, R.W. (1972) Large deformation isotropic elasticity—on the correlation of theory and experiment for incompressible rubber-like solids. *Proc. R. Soc. A*, **326**, 565.

15. Treloar, L.R.G. (1944) Stress-strain data for vulcanised rubber under various types of deformation. *Trans. Faraday Soc.*, **40**, 59.

16. Darijani, H., Naghdabadi, R. and Kargarnovin, M.H. (2010) Constitutive modeling of rubber-like materials based on consistent strain energy density functions. *Polym. Eng. Sci.*, **50**, 1058.

17. Lambert-Diani, J. and Rey, C. (1999) New phenomenological behavior laws for rubbers and thermoplastic elastomers. *Eur. J. Mech. A Solids*, **18**, 1027.

18. Alexander, H. (1968) A constitutive relation for rubber-like materials. *Int. J. Eng. Sci.*, **6**, 549.

19. Hopkins, H.G. (1976) The mechanics of rubber elasticity [and discussions]. *Proc. R. Soc. A*, **351**, 322.

4

Rubber-Like Elasticity

4.1 General Features of Rubber-Like Behaviour

The most noticeable feature of natural rubber and other elastomers is the ability to undergo large and reversible elastic deformation. It is not unexpected that stress can cause polymeric molecules to adopt an extended configuration, but at first sight it may seem surprising that on removal of the stress the molecules retract, on average, to their initial coiled form. Simple theories of rubber-like elasticity assume, as an approximation, that both extension and retraction occur instantaneously, and neglect any permanent deformation. Natural rubber (*cis*-polyisoprene) in its native state does not satisfy this last criterion, as molecules in extended configurations tend to slide past one another and do not recover completely. Molecules need to be chemically cross-linked by sulfur bonds (vulcanisation) to prevent any permanent flow, and we shall show that the degree of cross-linking determines the extensibility of the rubber for a given stress.

The application of stress is considered to cause molecules to change from a coiled to an extended configuration instantaneously. For this reason, it is possible to apply equilibrium thermodynamics to determine how the stress is related to changes in both internal energy and entropy. The general nature of thermodynamics implies that this type of approach can give no direct information on molecular rearrangements but, when augmented by molecular theories of a statistical nature, it is possible to derive an equation of state that relates the force causing extension to molecular parameters. We will show that this equation of state is identical to the neo-Hookean form of Section 3.4.4, which was derived as the equivalent of Hooke's law for finite deformations. It will be shown that the reason for this direct link between the behaviour at a molecular level and the mechanics of finite elasticity arises because of the applicability of the so-called affine deformation assumption. Affine deformation in the molecular theory of rubber elasticity means that we can assume that the changes in the length and orientation of lines joining adjacent cross-links in the molecular network are identical to the changes in lines marked on the macroscopic rubber. It is also assumed that there is no change in volume on deformation. This assumption can be justified
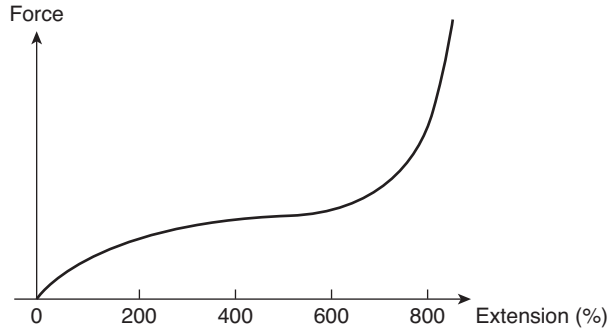
Figure 4.1   *The force developed in uniaxial extension of a typical lightly cross-linked rubber.*

as a good approximation because the bulk modulus (K) is some 10^4 times greater than the shear modulus (G): typical values are 10^{10} Pa and 10^6 Pa. As a consequence, at low strains, Poisson's ratio, given by

$$\nu = \frac{3K - 2G}{2(3K + 2G)}$$

is effectively $1/2$ and deformation occurs essentially at constant volume.

A schematic force–extension curve for a typical rubber is shown in Figure 4.1, with the maximum extensibility varying between 500 and 1000 per cent, depending on the extent of cross-linking. The behaviour is Hookean, with a linear relationship between stress and strain only at strains of the order of 1 per cent of so. At larger strains the force–extension relation is non-linear, and we will show that its form is determined essentially by changes in configurational entropy rather than internal energy.

High extension results in a greatly reduced entropy, so that retraction is a consequence of the necessity for entropy to be maximised. A fully extended chain is a state of zero entropy because there is only one possible conformation of bonds through which it can occur. In contrast, there are a very large number of ways of obtaining a given end-to-end distance for a contracted configuration of the chain. As all configurations have approximately the same internal energy, in the absence of external stress an extended chain will return to a more probable state. For this reason, rubber is sometimes referred to as a 'probability spring' or 'entropy spring', in contrast to the 'energy spring' characteristics of the elasticity of materials of low molecular mass, where extension causes an increase in internal energy. For a fuller discussion, see Treloar [1].

4.2   The Thermodynamics of Deformation

The change in internal energy during deformation dU is given by

$$\mathrm{d}U = \mathrm{d}Q + \mathrm{d}W, \tag{4.1}$$

where dQ and dW are the heat absorbed and the work due to external forces respectively. For a reversible process dQ relates to the entropy change dS by the relationship

$$dQ = T\,dS. \tag{4.2}$$

Hence, for a reversible process we have

$$dU = T\,dS + dW. \tag{4.3}$$

When an elastic solid of initial length L is extended uniaxially under a tensile force f, the work done on the solid in an infinitesimal displacement is

$$dW = f\,dL. \tag{4.4}$$

By combining Equations (4.3) and (4.4) we have

$$dU = f\,dL + T\,dS. \tag{4.5}$$

It is convenient to introduce the Helmholtz free energy A, which relates to changes that occur at constant volume (see Section 3.4.1)

$$A = U - TS. \tag{4.6}$$

Thus, for a change that occurs at constant temperature and constant volume we have

$$dA = dU - T\,dS. \tag{4.7}$$

By combining Equations (4.3) and (4.7) we see that dA = dW for isothermal changes at constant volume. Hence the tension f is given by

$$f = \left(\frac{\partial W}{\partial L}\right)_{T,V} = \left(\frac{\partial A}{\partial L}\right)_T = \left(\frac{\partial U}{\partial L}\right)_T - T\left(\frac{\partial S}{\partial L}\right)_T. \tag{4.8}$$

For any change in the Helmholtz free energy A (not necessarily an isothermal change)

$$dA = dU - T\,dS - S\,dT. \tag{4.9}$$

But d$U = f\,dL + T\,dS$ from Equation (4.3), hence

$$dA = f\,dL - S\,dT. \tag{4.10}$$

Then

$$\left(\frac{\partial A}{\partial L}\right)_T = f \quad \text{and} \quad \left(\frac{\partial A}{\partial T}\right)_L = -S \tag{4.11}$$

But

$$\frac{\partial}{\partial l}\left(\frac{\partial A}{\partial T}\right)_L = \frac{\partial}{\partial T}\left(\frac{\partial A}{\partial L}\right)_T.$$

Substituting

$$\left(\frac{\partial S}{\partial L}\right)_T = -\left(\frac{\partial f}{\partial T}\right)_L. \tag{4.12}$$

Hence, Equation (4.8) becomes

$$\left(\frac{\partial U}{\partial L}\right)_T = f - T\left(\frac{\partial f}{\partial T}\right)_L. \tag{4.13}$$

As long ago as 1935 Meyer and Ferri [2] showed that the tensile force at constant length was very nearly proportional to the absolute temperature, that is, $f = \alpha T$. Differentiating this relationship we obtain

$$\left(\frac{\partial f}{\partial T}\right)_L = \alpha, \text{ a constant.}$$

By substitution Equation (4.13) gives

$$\left(\frac{\partial U}{\partial L}\right)_T = 0,$$

which when applied to Equation (4.8) demonstrates that elasticity arises entirely from changes in entropy to this good first approximation.

4.2.1 The Thermoelastic Inversion Effect

A typical set of results for the tensile force at constant length as a function of temperature is shown in Figure 4.2. The curves are linear at all elongations, but it is to be noted that above
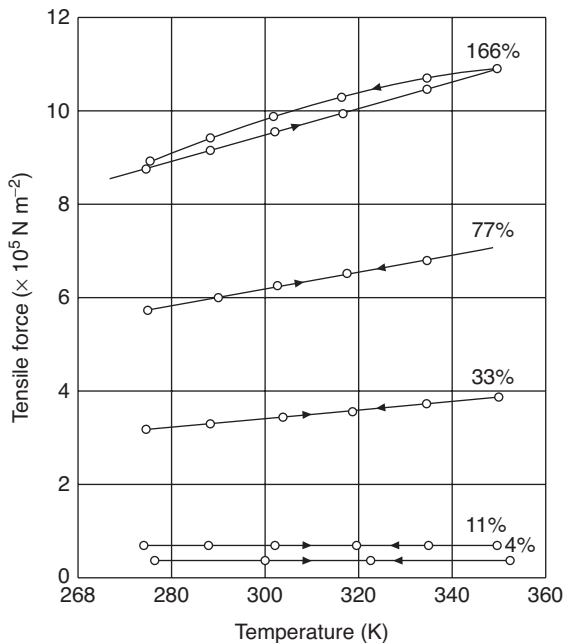
Figure 4.2 *Force at constant length as a function of absolute temperature. Elongations as indicated (Meyer and Ferri [2]). (Adapted from Treloar, L.R.G. (2005) The Physics of Rubber Elasticity, Oxford University Press, Oxford. Copyright (2005) Oxford University Press.)*

about 10% elongation the tensile force increases with increasing temperature, below this elongation it decreases slightly. This is called the thermoelastic inversion effect. In physical terms, it is caused by the thermal expansion of the rubber with increasing temperature. This increases the length in the unstrained state, and hence reduces the effective elongation. It was therefore considered by Gee [3] and others that the more appropriate experiment is to measure the tensile force as a function of temperature at constant extension ratio where the expansion is corrected for. The experimental results obtained in this way by Gee [3] showed that the stress was directly proportional to absolute temperature, and hence suggested that there was no internal energy change (Equation (4.3)). The conclusion is based on certain approximations relating to the difference between constant volume conditions and constant pressure conditions that have subsequently been reconsidered (for a discussion of this, see Section 4.5).

4.3 The Statistical Theory

The kinetic or statistical theory of rubber elasticity, originally proposed by Meyer, Von Susich and Valko [4], assumes that the very long molecular chains are each capable of assuming a wide variety of configurations in response to the thermal vibrations of their constituent atoms. Although the molecular chains are interlinked to form a coherent network, the number of cross-links is assumed to be small enough not to interfere markedly with the motion of the chains. In the absence of external forces, the chain molecules will adopt configurations corresponding to a state of maximum entropy. When forces are applied, the chains will tend to extend in the direction of the force, thus reducing the entropy and producing a state of strain.

Quantitative evaluation of the stress–strain characteristics of the rubber network then involves calculation of the configurational entropy of the whole assembly of chains as a function of the state of strain. This calculation is considered in two stages: calculation of the entropy of a single chain and calculation of the change in entropy of a network of chains as a function of strain.

4.3.1 Simplifying Assumptions

In reality, atoms are tightly packed along the length of a molecular chain. It is, however, convenient to represent molecular chains in terms of 'ball and stick' models, such as that shown for polyethylene in Figure 4.3. Here, we show the fully extended molecule, which takes the form of a planar zigzag. If essentially free rotation from one conformation to another occurs, subject only to the limitation that the valence bond angle between carbon atoms must remain at $109.5°$, the local situation $C_1C_2C_3C_4$ can change from the planar zigzag to a variety of conformations. In principle, it is possible to calculate the number of molecular configurations that correspond to any chosen end-to-end length of the molecule: there will be only one fully extended configuration, but for a molecule containing possibly hundreds of backbone atoms, the number of alternative contracted configurations will be very large. In practice, it is more convenient to consider the 'freely jointed' chain, a mathematical abstraction in which the atoms are reduced to mere points, joined by one-dimensional equal links, with no restriction on the angle between adjacent links. It is
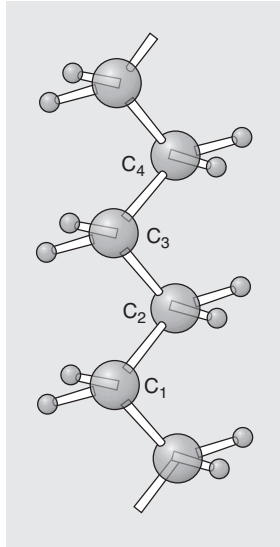
Figure 4.3   *The polyethylene chain.*

assumed in this simple model that there is no difference in internal energy between the different molecular conformations along the chain.[1]

4.3.2   Average Length of a Molecule between Cross-Links

Consider a freely jointed chain with n links, each of vector length ℓ_i. The vector end-to-end length of a single chain is then given by

$$\mathbf{r} = \sum_{i=1}^{n} \ell_i. \tag{4.14}$$

For a large number of chains (q), or one chain considered at many different times, the mean length

$$\bar{\mathbf{r}}(q) = \frac{1}{q} \sum_{i=1}^{q} \mathbf{r}_i = 0 \tag{4.15}$$

as the vector length is equally likely to be positive or negative.

We follow the procedure used, for example, with sinusoidally varying quantities such as alternating current and voltage, where the mean value is zero, and calculate the mean square chain length

$$\overline{r^2} = \frac{1}{q} \sum_{j=1}^{q} \mathbf{r}_j^2 = \frac{1}{q} \sum_{j=1}^{q} \left(\sum_{i=1}^{n} \ell_i \right)_j^2. \tag{4.16}$$

---

[1] Conformation is used to denote differences in the immediate situation of a bond, for example, *trans* or *gauche* conformations. Configuration is retained to refer to the arrangement of the whole molecular chain.

Expand, giving

$$\overline{r^2} = \frac{1}{q} \sum_1^q \left(\ell_1^2 + \ell_2^2 + \cdots \ell_n^2 + \underline{\ell}_1 \bullet \underline{\ell}_2 + \underline{\ell}_1 \bullet \underline{\ell}_3 + \cdots \underline{\ell}_{n-1} \bullet \underline{\ell}_n \right)$$

but $\ell_1^2 = \ell_2^2 = \cdots \ell_n^2$ and $\underline{\ell}_m \bullet \underline{\ell}_n = \ell_m \ell_n \cos\theta$. In a freely jointed chain, θ can have any value with equal probability; hence $\sum \underline{\ell}_m \bullet \underline{\ell}_n = 0$, $m \neq n$. Therefore

$$\overline{r^2} = \frac{1}{q} \sum_1^q n\ell^2 = n\ell^2.$$

The root mean square chain length is then

$$\sqrt{\overline{r^2}} = \ell\sqrt{n} = r_{\text{rms}} \tag{4.17}$$

compared with the fully extended chain length of *ln*; that is, for a chain of 100 bonds between cross-links the maximum extensibility is 10.

4.3.3   The Entropy of a Single Chain

The expression just derived indicates the reason for the high extensibility of lightly cross-linked rubbers and serves to introduce the important concept of a mean square length, but yields no information on the probability of a chain having a particular end-to-end length. This latter problem was first analysed mathematically by Kuhn [5] and by Guth and Mark [6].

Consider a chain of *n* links each of length *l*, which has a configuration such that one end P is at the origin (Figure 4.4). The probability distribution for the position of the end Q is derived using approximations that are valid provided that the distance between the chain
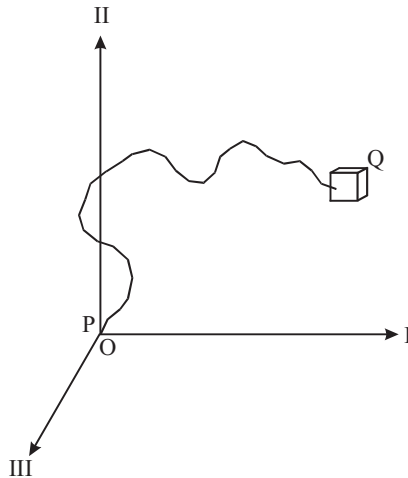
Figure 4.4   *The freely jointed chain.*
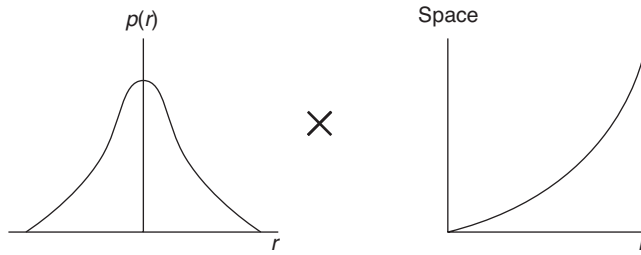
Figure 4.5   *The Gaussian probability distribution for the free end of a chain must be multiplied by the volume in which that end can reside: $P(r) = p(r) \times 4\pi r^2 \mathrm{d}r$.*

ends P and Q is much less than the extended chain length nl. The probability that Q lies within the elemental volume $\mathrm{d}X_1\,\mathrm{d}X_2\,\mathrm{d}X_3$ at the point (X_1, X_2, X_3) can be shown to be

$$p(X_1, X_2, X_3)\mathrm{d}X_1\mathrm{d}X_2\mathrm{d}X_3 = \frac{b^3}{\pi^{3/2}} \exp\left(-b^2 r^2\right) \mathrm{d}X_1\mathrm{d}X_2\mathrm{d}X_3, \qquad (4.18)$$

where $b^2 = 3/2nl^2$.

This distribution has the form of the Gaussian error function and is spherically symmetrical about the origin, where the value is a maximum (Figure 4.5). The most probable end-to-end length is not, however, zero, as the probability that Q falls within an elemental volume situated between r and $(r + \mathrm{d}r)$ from the origin, irrespective of direction, is the product of the probability distribution $p(r)$ and the volume of the concentric shell, $4\pi r^2 \mathrm{d}r$. The overall probability is then

$$\begin{aligned} P(r)\mathrm{d}r &= p(r)4\pi r^2\mathrm{d}r = \left(b^3/\pi^{3/2}\right) \exp\left(-b^2 r^2\right) 4\pi r^2\mathrm{d}r \\ &= \left(4b^3/\pi^{1/2}\right) r^2 \exp\left(-b^2 r^2\right) \mathrm{d}r, \end{aligned} \qquad (4.19)$$

which is illustrated in Figure 4.6.
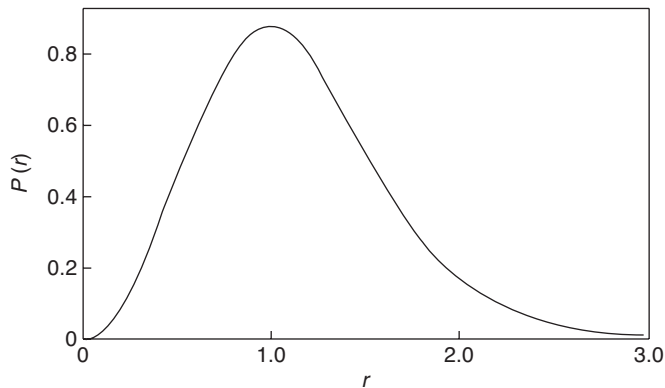
Figure 4.6   *The distribution function $P(r) = constant \times r^2 \exp\left(-b^2 r^2\right)$.*

It is seen that the most probable end-to-end distance, irrespective of direction, is not zero, but it is a function of b, that is, of the length l of the links and the number n of links in the chain, as shown in Section 4.3.2.

Another important quantity is the root mean square chain length $(\overline{r^2})^{1/2}$

$$\overline{r^2} = \int_0^\infty r^2 P(r)\mathrm{d}r.$$

Substitution of the above expression for $P(r)$ gives

$$\overline{r^2} = 3/2b^2 = n\ell^2, \tag{4.20}$$

so that the root mean square length $(\overline{r^2})^{1/2} = \ell\sqrt{n}$, that is, it is proportional to the square root of the number of links in the chain, as shown in Section 4.3.2.

The entropy of the freely jointed chain s is proportional to the logarithm of the number of configurations Q so that

$$s = k \ln \Omega,$$

where k is Boltzmann's constant. If $\mathrm{d}x_1\,\mathrm{d}x_2\,\mathrm{d}x_3$ is constant, the number of configurations available to the chain is proportional to the probability per unit volume $p(x_1, x_2, x_3.)$. The entropy of the chain is thus, according to Equation (4.18), given by

$$s = c - kb^2 r^2 = c - kb^2 \left(x_1^2 + x_2^2 + x_3^2 \right), \tag{4.21}$$

where c is an arbitrary constant.

4.3.4 The Elasticity of a Molecular Network

We wish to calculate the strain energy function for a molecular network, assuming that this is given by the change in entropy of a network of chains as a function of strain.

The actual network is replaced by an ideal network in which each segment of a molecule between successive points of cross-linkage is considered to be a Gaussian chain.

Three additional assumptions are introduced:

1. In either the strained or unstrained state, each junction point may be regarded as fixed at its mean position.
2. The effect of the deformation is to change the components of the vector length of each chain in the same ratio as the corresponding dimensions of the bulk material (the 'affine' deformation assumption).
3. The mean square end-to-end distance for the whole assembly of chains in the unstrained state is the same as for a corresponding set of free chains and is therefore given by Equation (4.20).

In effect, it is necessary to calculate the difference in probability between a spherical distribution of chain end-to-end vectors in the unstrained state and an ellipsoidal distribution for uniaxial extension (Figure 4.7). This difference is related to changes in entropy, and so to tensile force.

As discussed in Section 2.2, we can restrict our discussion to the case of normal strain without loss of generality. We choose principal extension ratios λ_I, λ_II and λ_III, parallel to

Unstrained sample   Stretched sample
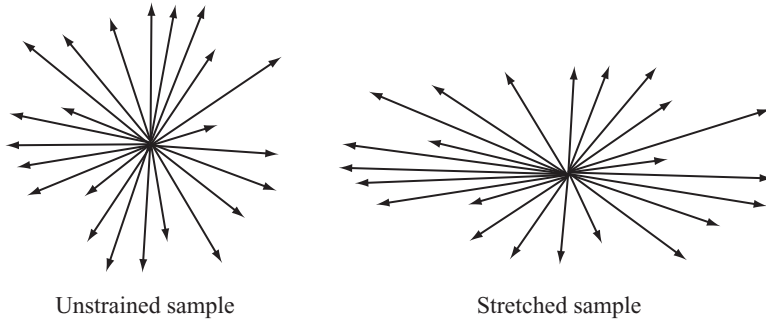
Figure 4.7   *Schematic representation of chain end-to-end vectors in the initial and final states.*

the three principal coordinate axes I, II and III. The affine deformation assumption implies that the relative displacement of the chain ends is defined by the macroscopic deformation. Thus, in Figure 4.8 we take a system of coordinates I, II and III in the undeformed body.

   In this coordinate system, a representative chain PQ has one end P at the origin. We refer any point in the deformed body to this system of coordinates. Thus, the origin, i.e., the end of the chain P, could be moved bodily during the deformation. The other end $Q(X_I, X_{II}, X_{III})$ is displaced to the point $Q'(x_I, x_{II}, x_{III})$, and from the affine deformation assumption we have (see Section 3.1.2)

$$x_I = \lambda_I X_I, \; x_{II} = \lambda_{II} X_{II}, \; x_{III} = \lambda_{III} X_{III}.$$

The entropy of the chain in the undeformed state is given by

$$s = c - kb^2 \left(X_I^2 + X_{II}^2 + X_{III}^2 \right).$$
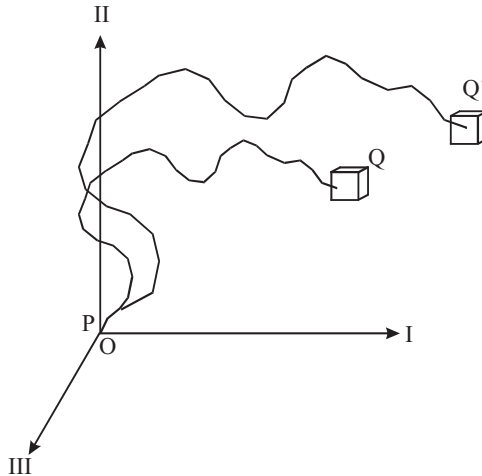
Figure 4.8   *The end of the chain $Q(X_I, X_{II}, X_{III})$ is displaced to the point $Q'(x_I, x_{II}, x_{III})$.*

After deformation the entropy becomes

$$s' = c - kb^2 \left(\lambda_{\mathrm{I}}^2 X_{\mathrm{I}}^2 + \lambda_{\mathrm{II}}^2 X_{\mathrm{II}}^2 + \lambda_{\mathrm{III}}^2 X_{\mathrm{III}}^2 \right), \tag{4.22}$$

giving the change in entropy

$$\Delta s = s' - s = -kb^2 \left\{ \left(\lambda_{\mathrm{I}}^2 - 1 \right) X_{\mathrm{I}}^2 + \left(\lambda_{\mathrm{II}}^2 - 1 \right) X_{\mathrm{II}}^2 + \left(\lambda_{\mathrm{III}}^2 - 1 \right) X_{\mathrm{III}}^2 \right\}. \tag{4.23}$$

Let there be N chains per unit volume in the network, with m of these having a given value of b (say b_p). The total entropy change for this particular group of chains is

$$\Delta s_b = \sum_1^m \Delta s = kb_p^2 \left\{ \left(\lambda_{\mathrm{I}}^2 - 1 \right) \sum_1^m X_{\mathrm{I}}^2 + \left(\lambda_{\mathrm{II}}^2 - 1 \right) \sum_1^m X_{\mathrm{II}}^2 + \left(\lambda_{\mathrm{III}}^2 - 1 \right) \sum_1^m X_{\mathrm{III}}^2 \right\}, \tag{4.24}$$

where $\sum_1^m X_I^2$ is the sum of the squares of the I components for these m chains in the undeformed network. As there is no preferred direction for the chain vectors in the undeformed (isotropic) state, there is no preference for the I, II or III directions, so that

$$\sum_1^m X_{\mathrm{I}}^2 = \sum_1^m X_{\mathrm{II}}^2 = \sum_1^m X_{\mathrm{III}}^2,$$

but

$$\sum_1^m X_{\mathrm{I}}^2 + \sum_1^m X_{\mathrm{II}}^2 + \sum_1^m X_{\mathrm{III}}^2 = \frac{1}{3} \sum_1^m r^2,$$

giving

$$\sum_1^m X_{\mathrm{I}}^2 = \sum_1^m X_{\mathrm{II}}^2 = \sum_1^m X_{\mathrm{III}}^2 = \frac{1}{3} \sum_1^m r^2. \tag{4.25}$$

From Equation (4.20)

$$\sum_1^m r^2 = mr^2 = m \left(\frac{3}{2b_p^2} \right). \tag{4.26}$$

Combining Equations (4.25), (4.26) and (4.24)

$$\Delta s_b = -\frac{1}{2} mk \left\{ \lambda_{\mathrm{I}}^2 + \lambda_{\mathrm{II}}^2 + \lambda_{\mathrm{III}}^2 - 3 \right\}. \tag{4.27}$$

We can now add the contribution of all the chains in the network (N per unit volume) and obtain the entropy change of the network ΔS where

$$\Delta S = \sum_1^N \Delta s = -\frac{1}{2} Nk \left(\lambda_{\mathrm{I}}^2 + \lambda_{\mathrm{II}}^2 + \lambda_{\mathrm{III}}^2 - 3 \right). \tag{4.28}$$

Assuming no change in internal energy on deformation, this gives the change in the Helmholtz free energy

$$\Delta A = -T\Delta S = \frac{1}{2} NkT \left(\lambda_{\mathrm{I}}^2 + \lambda_{\mathrm{II}}^2 + \lambda_{\mathrm{III}}^2 - 3 \right).$$

If we assume that the strain energy function U is zero in the undeformed state, this gives

$$U = \Delta A = \frac{1}{2}NkT\left(\lambda_{\text{I}}^2 + \lambda_{\text{II}}^2 + \lambda_{\text{III}}^2 - 3\right). \tag{4.29}$$

The above equation reproduces the neo-Hookean strain energy form of Section 3.4.4. Consider a simple uniaxial elongation $\lambda_{\text{I}} = \lambda$. The incompressibility condition gives $\lambda_{\text{I}}\lambda_{\text{II}}\lambda_{\text{III}} = 1$. Hence, by symmetry $\lambda_{\text{II}} = \lambda_{\text{III}} = \lambda^{-1/2}$ and

$$U = \frac{1}{2}NkT\left(\lambda^2 + \frac{2}{\lambda} - 3\right). \tag{4.30}$$

From Equation (3.43), the nominal stress along I denoted here denoted by f is

$$f = \frac{\partial U}{\partial \lambda} = NkT\left(\lambda - \frac{1}{\lambda^2}\right). \tag{4.31}$$

Comparison Equation (4.31) with Equation (3.43) shows that $NkT = E/3$, where E is Young's modulus. For small strain, we can put $\lambda = 1 + e_{\text{I}}$ and it follows from Equation (4.31) that

$$f = 3NkTe_{\text{I}} = Ee_{\text{I}}.$$

Since for an incompressible material $E \equiv 3G$, we see that the quantity NkT in Equation (4.31) is equivalent to the shear modulus of rubber, G. This term is sometimes written in terms of the mean molecular mass M_c of the chains, that is, between successive points of cross-linkage. Then

$$G = NkT = \rho RT/M_c,$$

where ρ is the density of the rubber and R is the gas constant.

4.4   Modifications of Simple Molecular Theory

The theory of the deformation of a molecular network described above formed the starting point for substantial research activity in polymer science. It does, however, rest on many simplifying assumptions, most notably freely jointed chains that can deform independently with a Gaussian distribution of end-to-end lengths that give rise to no changes in internal energy on deformation. There have been a considerable number of different approaches to developing a better theoretical basis, and because these often address different issues it is convenient to consider them in turn. At this stage, it is important to recognise that in the discussion of this chapter, molecular theories are being considered to refine and modify the theory of rubber elasticity as distinct from phenomenological equations based on solid mechanics that have been described in Chapter 3. Because both approaches often address similar issues relating to the deviation of experimental results from the simple equation of state (4.30), some authors [7] have combined the two approaches in an ad hoc manner to achieve satisfactory empirical fits to experimental data. Boyce and Arruda [8] have reviewed both approaches.

4.4.1 The Phantom Network Model

A key assumption of the single molecular theory is that the junction points in the network move affinely with the macroscopic deformation; that is, they remain fixed in the macroscopic body. It was soon proposed by James and Guth [9] that this assumption is unnecessarily restrictive. It was considered adequate to assume that the network junction points fluctuate around their most probable positions [9, 10] and the chains are portrayed as being able to transect each other. This has been termed the phantom network model. The vector **r** joining the two junction points is considered as the sum of a time average mean $\bar{\mathbf{r}}$ and the instantaneous fluctuation $\Delta\mathbf{r}$ from the mean so that

$$\mathbf{r} = \bar{\mathbf{r}} + \Delta\mathbf{r},$$

where the fluctuations $\Delta\mathbf{r}$ are independent of deformation and the mean vectors $\bar{\mathbf{r}}$ deform affinely following the macroscopic strain. This changes the $\frac{1}{2}NkT$ term in Equation (4.29) by a factor $\xi = 1 - 2/\phi$, where φ is the number of chains emanating from a network junction point, so that $G = \frac{1}{2}(1 - 2/\phi)NkT$.

4.4.2 The Constrained Junction Model

More recent network models of rubber elasticity by Ronca and Allegra [11] and Flory and Erman [12] are based on the phantom network model but assume that the junction point fluctuations are restricted due to the presence of entanglements. The strength of the constraints is defined by a parameter

$$\kappa = \frac{<(\Delta R)^2>}{<(\Delta s)^2>},$$

where $<(\Delta R)^2>^{1/2}$ is the radius of the average region in which the junction points would fluctuate in the absence of constraints, and $<(\Delta s)^2>$ is the average radius of the region in which the junction points would fluctuate under the action of constraints only. The total Helmholtz free energy is then

$$A = \frac{1}{2}\xi kT \left(\lambda_{\mathrm{I}}^2 + \lambda_{\mathrm{II}}^2 + \lambda_{\mathrm{III}}^2 - 3\right) + \frac{1}{2}NkT \sum_{i=\mathrm{I}}^{\mathrm{III}} [B_i + D_i - \ln(B_i + 1) - \ln(D_i + 1)],$$

(4.32)

where $B_i = \kappa^2(\lambda_i^2 - 1)(\lambda_i^2 + \kappa)^{-2}$ and $D_i = \lambda_i^2\kappa^{-1}B_i$ for principal directions $i = \mathrm{I}$, II, and III.

Later refinements of the constrained junction model place the effects of the constraints on the centres of mass of the network chains [13] or consider distributing the constraints continuously along the chains [14].

4.4.3 The Slip Link Model

Edwards and co-workers have proposed a different molecular model that subsumes the considerations discussed above, which are based on phantom, affine and constraint junctions to describe the deformation of a molecular network. Edwards and his colleagues have
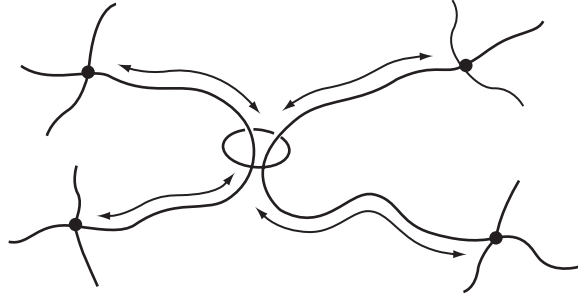
Figure 4.9 *Slip-link model. (Reproduced from Ball, R.C., Doi, M., Edwards, S.F. et al. (1981) Elasticity of entangled networks. Polymer, **22**, 1010. Copyright (1981) Elsevier Ltd.)*

advanced purely geometrical ideas to explain both the strain softening at low strains and the rapid strain hardening at high strains. Ball *et al*. [15] considered that in a rubber network there will be two types of junction points: the permanent cross-links where the chains are joined by chemical bonds and entanglements that are temporary junction points caused by chains becoming entangled. In an ingenious intuitive step, these temporary junction points are replaced by slip links (Figure 4.9), which allow the chains to slide over one another. The change in free energy associated with the slip links that results from the deformation is given by

$$\frac{F_s}{kT} = \frac{1}{2} N_s \sum_{i=I}^{III} \left[\frac{(1+\eta)\,\lambda_i^2}{1+\eta\lambda_i^2} + \log\left(1 + \eta\lambda_i^2\right) \right], \tag{4.33}$$

where N_s is the number of slip links per unit volume, the λ_i are the principal extension ratios and η is the slipperiness factor that in principle can vary between infinity for perfect sliding and zero for no sliding, i.e., a cross-link.

The total free energy change is then

$$F = F_c + F_s, \tag{4.34}$$

where

$$\frac{F_c}{kT} = \frac{1}{2} N_c \sum_{i=I}^{III} \lambda_i^2 \tag{4.35}$$

and N_c is the number of permanent cross-links per unit volume.

It can be seen that the first term in Equation (4.34) is the free energy of a phantom network, equivalent to the first term in Equation (4.32) of the constrained junction model. The second term can be thought of as equivalent to the second term in Equation (4.32), but because there is no fixed limit to the ratio of slip links N_s to permanent cross-links N_c, the maximum value of the free energy can be greater than that of the affine network that would replace $\frac{1}{2} N_c$ in the first term by N_c.

Edwards and Vilgis [16] subsequently extended this theory to include the limitation of finite extensibility for the network that they regarded as arising when the network chains
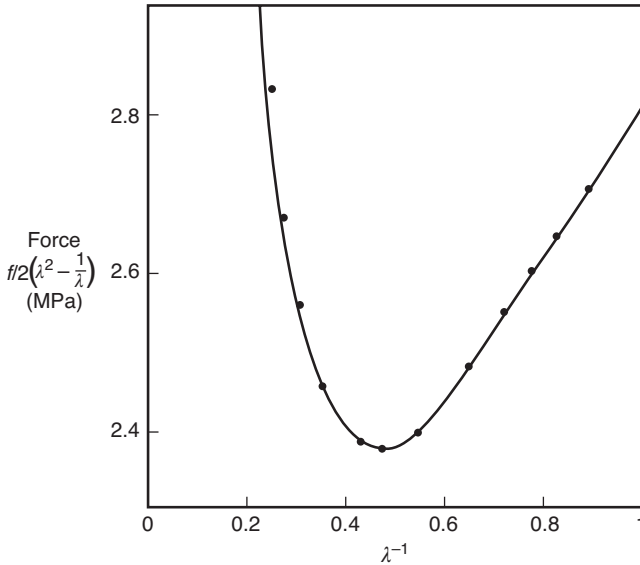
Figure 4.10 *Stress–strain data for natural rubber according to Mullins. The solid line is calculated by the Edwards and Vilgis theory using the parameters $N_ckT = 1.2$ MPa, $NskT = 2.1$ MPa, $\eta = 0.2$, $\alpha^{-1} = \lambda_{max} = 7.5$. (Reproduced from Edwards, S.F. and Vilgis, Th. (1986) The effect of entanglements in rubber elasticity. Polymer, **27**, 483. Copyright (1986) Elsevier Ltd.)*

are fully extended, that is, $\lambda_{max} \propto n^{1/2}$, where n is the number of links in the polymer chain between junction points (see Equation (4.17)).

This introduces another constant $\alpha = [(\lambda_1^2 + \lambda_2^2 + \lambda_3^3)^{-1/2}]_{max}$ into Equations (4.33) and (4.35). For example,

$$\frac{F_s}{kT} = \frac{1}{2}N_c\left[\frac{\sum_{i=I}^{III}\lambda_i^2(1-\alpha^2)}{1-\alpha^2\sum_{i=I}^{III}\lambda_i^2} - \log\left(1-\alpha^2\sum_{i=I}^{III}\lambda_i^2\right)\right].$$

Edwards and Vilgis showed that their theory could produce an excellent fit to data for natural rubber by assuming reasonable values of N_c, N_s, η and α (Figure 4.10).

Following the ideas of Edwards and co-workers, Heinrich and Kaliske proposed a tube model [17], and later a constrained tube model [18]. The Gaussian distribution of the Edwards papers is replaced by the non-Gaussian Langevin distribution (see Section 4.4.4), and an inextensibility parameter identical to that of Edwards and Vilgis is introduced. Marckmann and Verron [19] have reviewed these models and a recent attempt by Miehe, Goktepe and Lulei [20] to incorporate these ingredients into a comprehensive model.

4.4.4 The Inverse Langevin Approximation

An early development of the simple molecular network theory is the so-called 'inverse Langevin approximation' for the probability distribution. The Gaussian approximation is

only valid for end-to-end distances that are much less than the extended chain length. It was shown by Kuhn and Grün [21] and James and Guth [9] that removing this restriction (but still maintaining the other assumptions of freely jointed chains) gives a probability distribution $p(r)$ as

$$\ln p(r) = c - n \left[\frac{r}{n\ell} \beta + \ln \frac{\beta}{\sinh \beta} \right]. \tag{4.36}$$

In this equation β is defined by

$$\frac{r}{n\ell} = \coth \beta - \frac{1}{\beta} = \mathscr{L}(\beta),$$

where $\mathscr{L}$ is the Langevin function and $\beta = \mathscr{L}^{-1}(r/n\ell)$ is the inverse Langevin function. This expression may be expanded to give

$$\ln p(r) = c - n \left[\frac{3}{2} \left(\frac{r}{n\ell} \right)^2 + \frac{9}{20} \left(\frac{r}{n\ell} \right)^4 + \frac{99}{350} \left(\frac{r}{n\ell} \right)^6 + \cdots \right], \tag{4.37}$$

from which it can be seen that the Gaussian distribution is the first term of the series, an adequate approximation for $r \ll nl$.

The distribution functions for 25- and 100-link random chains obtained from the Gaussian and inverse Langevin approximations respectively are compared in Figure 4.11.
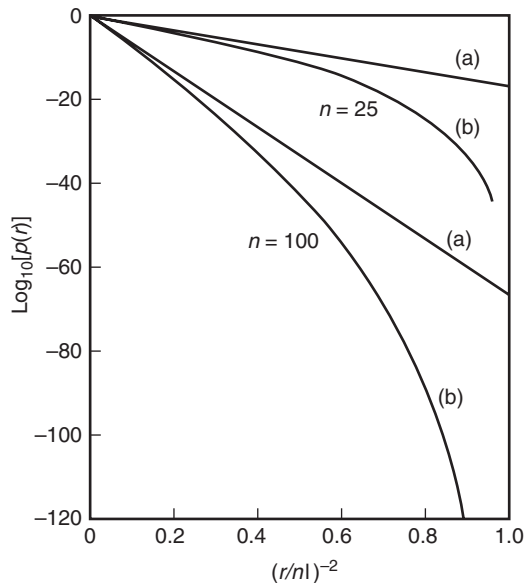
Figure 4.11   *Distribution functions for 25- and 100-link random chains: (a) Gaussian approximation and (b) inverse Langevin approximation. (Reproduced from Treloar, L.R.G. (1975) The Physics of Rubber Elasticity, 3rd edn, Oxford University Press, Oxford. Copyright (1975) Oxford University Press.)*

For the inverse Langevin approximation, we have from Equation (4.36)

$$S = k \ln p(r) = c - kn \left(\frac{r}{n\ell} \beta + \ln \frac{\beta}{\sinh \beta} \right),$$ (4.38)

and the tension in the chain

$$f = T \frac{\partial S}{\partial r} = \frac{kT}{\ell} \mathscr{L}^{-1} \left(\frac{r}{n\ell} \right),$$ (4.39)

which, following an expansion similar to Equation (4.37), gives

$$f = \frac{kT}{l} \left\{ 3 \left(\frac{r}{n\ell} \right) + \frac{9}{5} \left(\frac{r}{n\ell} \right)^3 + \frac{297}{175} \left(\frac{r}{n\ell} \right)^5 + \frac{1539}{875} \left(\frac{r}{n\ell} \right)^7 + \cdots \right\}.$$ (4.40)

The final part of the exercise is to reconsider the stress–strain relations using the inverse Langevin distribution function. This was done by James and Guth using an analogous development to that for the Gaussian distribution function.

The tensile force per unit unstrained area is

$$f = \frac{NkT}{3} n^{1/2} \left\{ \mathscr{L}^{-1} \left(\frac{\lambda}{n^{1/2}} \right) - \lambda^{-3/2} \mathscr{L}^{-1} \left(\frac{1}{\lambda^{1/2} n^{1/2}} \right) \right\}.$$ (4.41)

Figure 4.12 shows Treloar's fit to the experimental data for natural rubber, using this relationship and a suitable choice of the parameters N and n. The maximum extension of
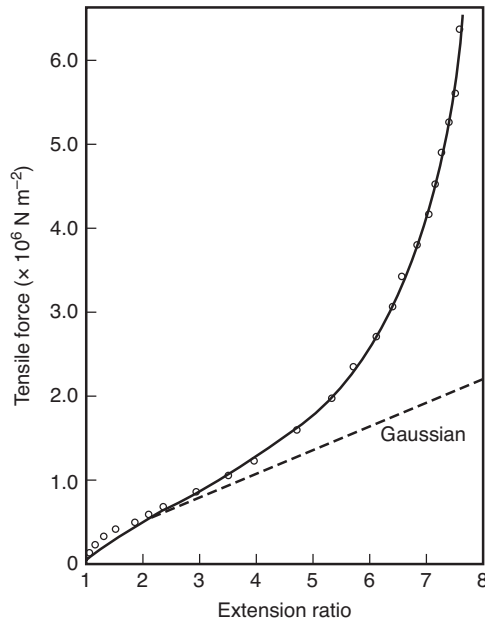
Figure 4.12 *Theoretical non-Gaussian force–extension curve obtained by fitting experimental data to the James and Guth theory, with NkT = 0.273 MPa, n = 75. (Reproduced from Treloar, L.R.G. (1975) The Physics of Rubber Elasticity, 3rd edn, Oxford University Press, Oxford. Copyright (1975) Oxford University Press.)*

the network is primarily determined by the number of random links n. This result is relevant to the cold-drawing and crazing behaviour of polymers (Sections 12.6 and 13.5.1), where the basic deformation also involves the extension of a molecular network.

It can be seen from Figure 4.12 that there is broad agreement between the form of the force–extension curve predicted by the inverse Langevin approximation and that observed in practice.

A more recent approach along similar lines, pioneered by Arruda and Boyce [22], involves further development of the non-Gaussian model of James and Guth [9]. The James and Guth model was essentially one of three mutually perpendicular molecular chains, and this is generalised by increasing the number of chains. Thus, Arruda and Boyce introduced the eight-chain model, in which the chains are envisaged as being attached at one end to the to the corners of a cube of material, and at the other end to the cube centre. The cube is aligned with the principal strain directions. On deformation of the cube into a rectangular element with extension ratios along its sides λ_I, λ_{II} and λ_{III}, each of the eight chains develops the same extension ratio λ_{chain} defined by

$$\lambda_{chain} = \frac{1}{\sqrt{3}} \left(\lambda_I^2 + \lambda_{II}^2 + \lambda_{III}^2 \right)^{1/2}.$$

The analogue of the three-chain Equation (4.41) for uniaxial stretching becomes

$$f = \frac{NkT}{3} n^{1/2} \mathscr{L}^{-1} \left[\frac{\lambda_{chain}}{n^{1/2}} \right] \frac{\lambda - 1/\lambda^2}{\lambda_{chain}}. \tag{4.42}$$

Arruda and Boyce [22] showed that the eight-chain model performed much better than three- and four-chain models in predicting the behaviour of vulcanised rubber in uniaxial and biaxial tension and shear, and also performed excellently in modelling uniaxial and plane strain compression of gum and neoprene rubber.

Wu and van der Giessen [23] produced a further generalisation to an infinitely large number of chains – the full network model. Their expression for force is more complex than Equations (4.41) or (4.42), but they showed that it could be approximated very well with a linear combination of the three- and eight-chain expressions. Contrary to expectations, the full network model performed less well than the eight-chain model for uniaxial and biaxial testing of natural gum-rubber and silicone rubber. Wu and van der Giessen pointed out that both models were approximations, in that entanglement (slip link) effects and other intermolecular interactions are ignored, as is the existence of non-affine deformation. They raised the possibility that the eight-chain model was fortuitously compensating for these effects.

Sweeney [24] has compared the eight-chain, full network and Edwards–Vilgis models and shown that the first two can be approximated very well by the Edwards–Vilgis model, provided the chain extensibility limit is not approached too closely. This latter proviso is a result of the different forms of the singularity in strain energy that controls the approach to the extensibility limit. The additional feature of slip links in the Edwards–Vilgis model means that is the most general of the three, and this is reflected in the greater number of fitting parameters.

4.4.5 The Conformational Exhaustion Model

Another approach to rubber elasticity has been developed by Stepto and Taylor [25, 26], which also accounts for the Mooney–Rivlin softening. Their approach is not phenomenological, but is based on structural considerations that give an accurate description of the molecular conformational states of the units in the polymer chains as the network is stretched. They have proposed a method for calculating the free energy of a stretched molecular network based on the rotational isomeric state of the network chains with conformational energies determined from observations of conformational properties.

Using a series of Monte Carlo calculations, the elastic properties of the network are derived from the network chain end-to-end distance distribution, and are assumed to arise solely as a result of allowed conformational changes in individual network chains. Figure 4.13 shows the calculation for the probability density functions $p(r)$ calculated from the simulated radial end-to-end distance distribution functions $P(r)$, where

$$p(r) = \frac{P(r)}{4\pi r^2}$$

as explained in Section 4.3.3.

Comparison of the Monte Carlo $p(r)$ with those predicted on the basis of the Gaussian distribution function (Equation (4.18)) and the Langevin function (Equation (4.36)) shows clear differences. In particular, the molecular structure-based Monte Carlo $p(r)$ reflects clearly the limited extensibility of chains in the true network.
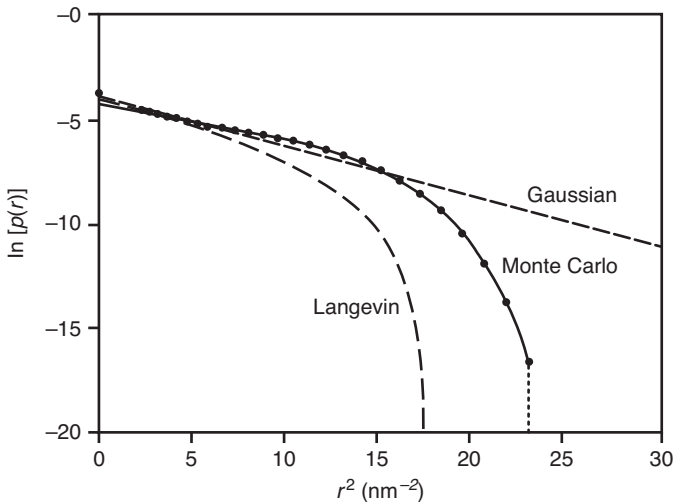
Figure 4.13 *Plot of ln[p(r)] vs r^2 at 298 K for polydimethyl siloxane chains of 40 bonds compared with Gaussian and Langevin treatments of the freely jointed chain. (Reproduced from Stepto, R.F.T. and Taylor, D.J.R. (1995) Molecular modeling of the elastic behavior of polymer-chains in networks – comparison of polymethylene and poly(dimethylsiloxane). J. Chem. Soc. Faraday Trans., 91, 2639. Copyright (1995) Royal Society of Chemistry.)*

In the Stepto theory, the free energy of the network is given by

$$F = \frac{RT\rho}{M_c} s \left(\lambda^2 + \frac{2}{\lambda} - 3 \right),$$

where R, T, ρ and M_c have the same meaning as in Section 4.3.4 but there is a new factor s that is a function of λ and quantitatively accounts for the Mooney–Rivlin softening. In this theory, softening arises because some chains in the deformed network reach their full extensibility so that on further deformation these chains do not give a contribution to the reduction in entropy and hence to the network stress, which is correspondingly reduced. Stepto and Taylor have shown that their theory gives an exact quantitative fit to the stress–strain behaviour of polydimethyl siloxane networks [25, 26], based only on the values for the rotational isomeric states obtained from the Flory–Crescenzi–Mark rotation isomeric state model for polydimethyl siloxane [27]. In addition, the optical birefringence, that is, the stress-optical coefficient, for cross-linked polyethylenes, was also quantitatively predicted [28, 29].

4.4.6   The Effect of Strain-Induced Crystallisation

Although we have seen how the extension to non-Gaussian statistics gives rise to a very large increase in tensile stress at large extensions, in the case of natural rubber it has been proposed that the observed increase in tensile stress occurs primarily because of strain-induced crystallisation [30]. The basic physical idea is that the melting point T_c of the rubber is increased due to extension. $T_c = \Delta H / \Delta S$, where ΔH and ΔS are the enthalpy and entropy of fusion respectively. Because the entropy of the extended rubber is low, the change in entropy on crystallisation is reduced and T_c correspondingly increased. A higher degree of supercooling then gives rise to crystallisation and the crystallites act to increase the modulus by forming additional physical cross-links.

The precise effect of crystallisation is, however, difficult to determine. Experiments on butadiene rubbers [31], which do not crystallise on extension, when directly compared with natural rubber, suggested that the influence of crystallisation was relatively unimportant.

4.5   The Internal Energy Contribution to Rubber Elasticity

The simple treatment of rubber elasticity given above makes two assumptions, which require further consideration. First, it has been assumed that the internal energy contribution is negligible, which implies that different molecular conformations of the chains have identical internal energies. Secondly, the thermodynamic formulae that have been derived are, strictly, only applicable to measurements at constant volume, whereas most experimental results are obtained at a known pressure. These two assumptions are interrelated in the sense that the experimental work of Gee (see Section 4.2.1) based on the approximation

$$\left(\frac{\partial f}{\partial T} \right)_{P,\lambda} = \left(\frac{\partial f}{\partial T} \right)_{V,L} \tag{4.43}$$

(where λ is the extension ratio relative to natural length) leads to the conclusion that the internal energy contribution was zero. Here a specimen is stretched uniaxially with a

nominal tensile stress f, in the presence of a superposed hydrostatic pressure P – hence the hydrostatic pressure of the system is $P - f/3$. Although Gee's approximation is much better than the assumption that

$$\left(\frac{\partial f}{\partial T}\right)_{P,L} = \left(\frac{\partial f}{\partial T}\right)_{V,L}, \tag{4.44}$$

it is based on the premise that the material is isotropically compressible under hydrostatic pressure even when strained, that is,

$$\frac{\mathrm{d}V}{V} = 3\frac{\mathrm{d}L}{L} \quad \text{or} \quad \left(\frac{\partial(\ln L)}{\partial(\ln V)}\right)_{f,T} = \frac{1}{3}.$$

More rigorous consideration suggests that this is not correct and that there is an anisotropic compressibility in the strained state. Gee's experimental result that the internal energy contribution is negligible, based on measurements of the change in stress with temperature at constant length, is therefore capable of another interpretation, which leads to the conclusion that the internal energy contribution may not be zero.

The internal energy component of the tensile force f is given by

$$f_e = \left(\frac{\partial U}{\partial L}\right)_{T,V} \tag{4.45}$$

(see Equation (4.8)). Volkenltein and Ptitsyn [32] showed that, if the unperturbed dimensions of an isolated chain are temperature dependent, f_e is given by

$$\frac{f_e}{f} = T\frac{\partial\left(\ln \overline{r_0^2}\right)}{\partial T}, \tag{4.46}$$

where $\overline{r_0^2}$ is the root mean square length (where the subscript 0 indicates a free chain unconstrained by cross-linkages).

Experimental data on dilute solutions of polymers using light scattering and viscosity measurements show that $\overline{r_0^2}$ depends in general on temperature. This implies that the energy of a chain depends on its conformation and that for a rubber, f_e will in general differ from zero. Flory and his collaborators [33] were particularly prominent in performing stress–temperature measurements on polymer networks, together with physicochemical measurements to confirm these points and to obtain the energy difference between different conformations, for example, the *trans* and *gauche* conformations of the polyethylene chain.

The value f_e can be expressed in terms of the tensile force–temperature relationship by the equation

$$\frac{f_e}{f} = -T\left[\frac{\partial\left\{\ln(f/T)\right\}}{\partial T}\right]_{V,L}, \tag{4.47}$$

which follows by manipulating Equation (4.13) while acknowledging the validity of Equation (4.45). However, this expression for constant volume is not easily related to the interpretation of most laboratory experiments, where an equation at constant pressure P is more appropriate.

In addressing this problem, Flory, Ciferri and Hoeve [34] adopted a procedure based on the theory of the Gaussian network. They showed that if the rubber network obeys Gaussian statistics, the expression for measurement of simple extension at constant pressure is

$$\left[\frac{\partial \{\ln f/T\}}{\partial T}\right]_{P,L} + \frac{\alpha}{\lambda^3 - 1} = -\frac{d\left(\ln \overline{r_0^2}\right)}{dT}, \tag{4.48}$$

where α is the coefficient of volume expansion of the rubber at constant pressure, that is,

$$\alpha = \frac{1}{V}\left(\frac{\partial V}{\partial T}\right)_P. \tag{4.49}$$

Using Equations (4.46) and (4.48), they then went on to derive an expression for f_e/f

$$\frac{f_e}{f} = -T\left[\frac{\partial \{\ln(f/T)\}}{\partial T}\right]_{P,L} - \frac{\alpha T}{(\lambda^3 - 1)}. \tag{4.50}$$

Equating Equations (4.47) and (4.50) shows that the derivatives involving f are unequal, and that Equation (4.44) is false. A correction factor can be derived that enables the constant pressure derivative to be derived from the constant volume derivative. Graessley and Fetters [35] introduced such a factor $\Delta_{P,L}$ equivalent to

$$\Delta_{P,L} = \left[\frac{\partial(f/T)}{\partial(1/T)}\right]_{V,L} - \left[\frac{\partial(f/T)}{\partial(1/T)}\right]_{P,L},$$

which can itself be shown to be equivalent to

$$\Delta_{P,L} = fT\left(\left[\frac{\partial \{\ln(f/T)\}}{\partial T}\right]_{P,L} - \left[\frac{\partial \{\ln(f/T)\}}{\partial T}\right]_{V,L}\right). \tag{4.51}$$

By equating Equations (4.47) and (4.50) we can derive an expression for the right-hand side of (4.51), showing that for this analysis

$$\Delta_{P,L} = \frac{\alpha fT}{\lambda^3 - 1}. \tag{4.52}$$

Treloar [36, 37] considered the behaviour in torsion and showed that the relationship corresponding to (4.48) is

$$\left[\frac{\partial \{\ln(M/T)\}}{\partial T}\right]_{P,L,\psi} = \frac{-d\left(\ln \overline{r_0^2}\right)}{dT} + \alpha,$$

where M is the torsional moment and ψ is the twist (expressed as radians per unit length of the strained axis). M_e, the internal energy contribution to the couple at constant volume, is given by an equation similar to (4.47):

$$\frac{M_e}{M} = -T\left[\frac{\partial \{\ln(M/T)\}}{\partial T}\right]_{V,L,\psi}.$$

Allen, Bianchi and Price [38, 39] adopted the alternative approach of constructing apparatus to undertake measurements at constant volume, so that Equation (4.47) could be used directly. They were also able to compare $\left[\frac{\partial f}{\partial T}\right]_{V,L}$, $\left[\frac{\partial f}{\partial T}\right]_{P,L}$, and $\left[\frac{\partial f}{\partial P}\right]_{T,L}$.

Although it was shown that the Flory equation was not correct, the errors involved tended to compensate so the values of f_e/f obtained by both sets of workers were similar.

In a review of this research, Price [40] concluded that the Gaussian theory is able to account satisfactorily for the temperature dependence of the force, but it does not give an adequate representation of the pressure dependence of the force and the strain-induced dilatation. In a later review, Graessley and Fetters [35] followed the approximation and the Gaussian network model to deduce their improved correction factor $\Delta_{P,L}$ that was in much better agreement with the dilation data:

$$\Delta_{P,L} = \frac{\alpha f T}{3} \frac{\lambda^3 + 2}{\lambda^3 - 1}.$$

This correction will clearly begin to deviate from that of Equation (4.52) at sufficiently high λ.

For a comprehensive account of early work in this area, the reader is referred to Chapter 13 in Treloar [1].

4.6   Conclusions

The phenomenological theories following the approach of Rivlin and others were based on empirically developed strain energy functions. These have been overtaken by molecular network models notably by Edwards and colleagues, Boyce and colleagues and Stepto and colleagues.

It can be concluded that these latest developments offer the way forward, and that it is less rewarding to attempt to ascribe physical significance to higher order terms in invariant-based strain energy functions; rather we should accept more complex formulations in terms of the principal extension ratios directly. An important issue is to incorporate the internal energy contribution into the purely geometrical considerations concerned with the deformation of the molecular network.

References

1. Treloar, L.R.G. (2005) *The Physics of Rubber Elasticity*, Oxford University Press, Oxford.
2. Meyer, K.H. and Ferri, C. (1935) On elasticity of rubber. *Helv. Chim. Acta*, **18**, 570.
3. Gee, G. (1946) The interaction between rubber and liquids. 9. The elastic behaviour of dry and swollen rubbers. *Trans. Faraday Soc.*, **42**, 585.
4. Meyer, K.H, Von Susich, G. and Valko, E. (1932) The elastic properties of organic high polymers and their kinetic explanation. *Kolloidzeitschrift*, **59**, 208.
5. Kuhn, W. (1934) Concerning the shape of thread shapes molecules in solution. *Kolloidzeitschrift*, **68**, 2; (1936) Relationship between molecular size, static molecular shape and elastic characteristics of high polymer materials. *Kolloidzeitschrift*, **76**, 258.
6. Guth, E. and Mark, H. (1934) Zur Innermolekularen, Statistik, Insbesondere Bei Kettenmolekiilen I. *Monatshefte für Chemie.*, **65**, 93.

7. Meissner, B. (2000) Tensile stress-strain behaviour of rubberlike networks up to break. Theory and experimental comparison. *Polymer*, **41**, 7827.
8. Boyce, M.C. and Arruda, E.M. (2000) Constitutive models of rubber elasticity: a review. *Rubber Chem. Technol.*, **73**, 504.
9. James, H.M. and Guth, E. (1947) Theory of the increase in rigidity of rubber during cure. *J. Chem. Phys.*, **15**, 669.
10. Mark, J.E. and Erman, B. (1988) *Rubberlike Elasticity. A Molecular Primer*, John Wiley & Sons, Chichester.
11. Ronca, G. and Allegra, G.J. (1975) Approach to rubber elasticity with internal constraints. *Chem. Phys.*, **63**, 4990.
12. Flory, P.J. and Erman, B. (1982) Theory of elasticity of polymer networks, 3. *Macromolecules*, **15**, 800.
13. Erman, B. and Monnerie, L. (1989) Theory of elasticity of amorphous networks – effect of constraints along chains. *Macromolecules*, **22**, 3342.
14. Kloczkowski, A., Mark, J.E. and Erman, B. (1995) A diffused-constraint theory for the elasticity of amorphous polymer networks. 1. Fundamentals and stress-strain isotherms in elongation. *Macromolecules*, **28**, 5089.
15. Ball, R.C., Doi, M., Edwards, S.F. *et al*. (1981) Elasticity of entangled networks. *Polymer*, **22**, 1010.
16. Edwards, S.F. and Vilgis, Th. (1986) The effect of entanglements in rubber elasticity. *Polymer*, **27**, 483.
17. Heinrich, G. and Kaliske, M. (1997) Theoretical and numerical formulation of a molecular based constitutive tube-model of rubber elasticity. *Comput. Theo. Polym. Sci.*, **7**, 227.
18. Kaliske, M. and Heinrich, G. (1999) An extended tube-model for rubber elasticity: statistical-mechanical theory and finite element implementation. *Rubber Chem. Technol.*, **72**, 602.
19. Marckmann, G. and Verron, E. (2006) Comparison of hyperelastic models for rubberlike materials. *Rubber Chem. Technol.*, **79**, 835.
20. Miehe, C., Goktepe, S. and Lulei, F. (2004) A micro-macro approach to rubber-like materials – part 1: the non-affine micro-sphere model of rubber elasticity. *J. Mech. Phys. Solids*, **52**, 2617.
21. Kuhn, W. and Grün, F. (1942) Relations between elastic constants and the strain birefringence of high-elastic substances. *Kolloidzitschrift*, **101**, 248.
22. Arruda, E.M. and Boyce, M.C. (1993) A 3-dimensional constitutive model for the large stretch behavior of rubber elastic-materials. *J. Mech. Phys. Solids*, **41**, 389.
23. Wu, P.D. and van der Giessen, E. (1993) On improved network models for rubber elasticity and their applications to orientation hardening in glassy-polymers. *Mech. Phys. Solids*, **41**, 427.
24. Sweeney, J. (1999) A comparison of three polymer network models in current use. *Comput. Theo. Polym. Sci.*, **9**, 27.
25. Stepto, R.F.T. and Taylor, D.J.R. (1995) Modeling the elastic behavior of real chains in polymer networks. *Macromol. Symp.*, **93**, 261.
26. Stepto, R.F.T. and Taylor, D.J.R. (1995) Molecular modeling of the elastic behavior of polymer-chains in networks – comparison of polymethylene and poly (dimethylsiloxane). *J. Chem. Soc. Faraday Trans.*, **91**, 2639.

27. Flory, P.J., Crescenzi, V. and Mark, J.E. (1964) Configuration of poly-(dimethylsiloxane) chain. 3. Correlation of theory and experiment. *J. Am. Chem. Soc.*, **86**, 146.
28. Taylor, D.J.R., Stepto, R.F.T. and Jones, R.A. (1999) Computer simulation studies of molecular orientation and the stress-optical properties of polyethylene networks. *Macromolecules*, **32**, 1978.
29. Cail, J.I., Taylor, D.J.R. and Stepto, R.F.T. (2000) Computer simulation studies of molecular orientation in polyethylene networks: orientation functions and the legendre addition theorem. *Macromolecules*, **33**, 4966.
30. Mark, J.E. (1979) Effect of strain-induced crystallization on the ultimate properties of an elastomeric polymer network. *Polymer Eng. Sci.*, **19**, 6, 409.
31. Doherty, W.O.S., Lee, K.L. and Treloar, L.G.R. (1980) Non-Gaussian effects in styrene-butadiene rubber. *Br. Polym. J.*, **12**, 19.
32. Volkenshtein, M.V. and Ptitsyn, O.B. (1953) O Rastyazhenii Polimernykh Tsepochek. *Dokl Akad SSR*, **91**, 1313; (1955) Vnutrennee Vrashchenie V Polimernykh Tsepyakh I Ikh Fizicheskie Svoistva. 2. Rastyazhenie Polimernoi Tsepi. *Zhur Tech Fiz*, **25**, 649, 662.
33. Ciferri, A., Hoeve, C.A.J. and Flory, P.J. (1961) Stress-temperature coefficients of polymer networks and conformational energy of polymer chains. *J. Am. Chem. Soc.*, **83**, 1015.
34. Flory, P.J., Ciferri, A. and Hoeve, C.A.J. (1960) The thermodynamic analysis of thermoelastic measurements on high elastic materials. *J. Polym. Sci.*, **45**, 235.
35. Graessley, W.W. and Fetters, L.J. (2001) Thermoelasticity of polymer networks. *Macromolecules* **34**, 7147.
36. Treloar, L.R.G. (1969) Volume changes and mechanical anisotropy of strained rubbers. *Polymer*, **10**, 279.
37. Treloar, L.R.G. (1969) Theoretical stress/temperature relations for rubber in torsion. *Polymer*, **10**, 291.
38. Allen, G., Bianchi, U. and Price, C. (1963) Thermodynamics of elasticity of natural rubber. *Trans. Faraday Soc.*, **59**, 2493.
39. Allen, G., Kirkham, M.C., Padget, J. *et al.* (1971) Thermodynamics of rubber elasticity at constant volume. *Trans. Faraday Soc.*, **67**, 1278.
40. Price, C. (1976) Thermodynamics of rubber elasticity. *Proc., Roy. Soc. Lond.*, **A 351**, 331.

Further Reading

Gent, A.N. (2001) *Engineering with Rubber: How to Design Rubber Components*, 2nd edn, Carl Hanser Verlag, Munich.

Mark, J.E. and Erman, B. (2007) *Rubberlike Elasticity: A Molecular Primer*, 2nd edn, Cambridge University Press, Cambridge.

Mark, J.E., Erman, B. and Frederick, F.R. (eds) (2005) *The Science and Technology of Rubber*, Elsevier Academic Press, Burlington, MA.

5

Linear Viscoelastic Behaviour

In this chapter, we describe the common forms of viscoelastic behaviour and discuss the phenomena in terms of the deformation characteristics of elastic solids and viscous fluids. The discussion is confined to linear viscoelasticity, for which the Boltzmann superposition principle enables the response to multistep loading processes to be determined from simpler creep and relaxation experiments. Phenomenological mechanical models are considered and used to derive retardation and relaxation spectra, which describe the timescale of the response to an applied deformation. Finally, we show that in alternating strain experiments the presence of the viscous component leads to a phase difference between stress and strain.

5.1 Viscoelasticity as a Phenomenon

The behaviour of materials of low relative molecular mass is usually discussed in terms of two particular types of ideal material: the elastic solid and the viscous liquid. The former has a definite shape and is deformed by external forces into a new equilibrium shape; on removal of these forces it reverts instantaneously to its original form. The solid stores all the energy that it obtains from the external forces during the deformation, and this energy is available to restore the original shape when the forces are removed. By contrast, a viscous liquid has no definite shape and flows irreversibly under the action of external forces.

One of the most interesting features of polymers is that a given polymer can display all the intermediate range of properties between an elastic solid and a viscous liquid depending on the temperature and the experimentally chosen timescale. Bouncing putty, a silicone product, flows over a period of hours, fractures like a ductile solid when deformed rapidly and bounces like an elastomer when dropped. Of greater commercial importance are the rubber-like, and in extreme cases brittle, characteristics exhibited by molten polymers at high processing rates. This form of response, which combines both liquid-like and solid-like features, is termed viscoelasticity.

5.1.1   Linear Viscoelastic Behaviour

Newton's law of viscosity defines viscosity η by stating that stress σ is proportional to the velocity gradient in the liquid:

$$\sigma = \eta \frac{\partial V}{\partial y},$$

where V is the velocity, and y is the direction of the velocity gradient, For a velocity gradient in the 12 plane,

$$\sigma_{12} = \eta \left(\frac{\partial V_1}{\partial X_2} + \frac{\partial V_2}{\partial X_1} \right),$$

where $\dfrac{\partial V_1}{\partial X_2}$ and $\dfrac{\partial V_2}{\partial X_1}$ are the velocity gradients in the 2 and 1 directions respectively (see Figure 5.1 for the case where the velocity gradient is in the 2 direction).

Since $V_1 = \partial u_1 / \partial t$ and $V_2 = \partial u_2 / \partial t$, where u_1 and u_2 are the displacements in the 1 and 2 directions respectively, we have

$$
\begin{aligned}
\sigma_{12} &= \eta \left[\frac{\partial}{\partial X_2} \left(\frac{\partial u_1}{\partial t} \right) + \frac{\partial}{\partial X_1} \left(\frac{\partial u_2}{\partial t} \right) \right] \\
&= \eta \frac{\partial}{\partial t} \left(\frac{\partial u_1}{\partial X_2} + \frac{\partial u_2}{\partial X_1} \right) \\
&= \frac{\partial e_{12}}{\partial t}
\end{aligned}
$$

It can be seen that the shear stress σ_{12} is directly proportional to the rate of change of shear strain with time. This formulation brings out the analogy between Hooke's law for elastic solids and Newton's law for viscous liquids. In the former, the stress is linearly related to the strain, in the latter the stress is linearly related to the *rate of change of strain* or *strain rate*.
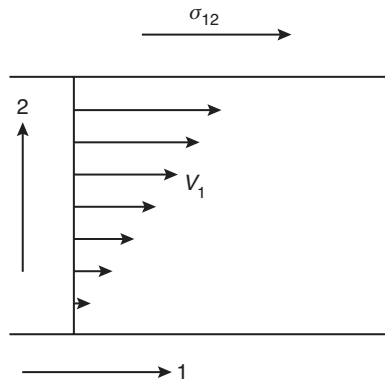
Figure 5.1   *The velocity gradient.*

Hooke's law describes the behaviour of a linear *elastic* solid and Newton's law that of a linear *viscous* liquid. A simple constitutive relation for the behaviour of a linear viscoelastic solid is obtained by combining these two laws.

For elastic behaviour $(\sigma_{12})_E = Ge_{12}$, where G is the shear modulus.

For viscous behaviour $(\sigma_{12})_V = \eta\,(\partial e_{12}/\partial t)$.

A possible formulation of linear viscoelastic behaviour combines these equations, thus

$$\sigma_{12} = (\sigma_{12})_E + (\sigma_{12})_V = Ge_{12} + \eta\frac{\partial e_{12}}{\partial t}$$

This makes the simplest possible assumption that the shear stresses related to strain and strain rate are additive. The equation represents one of the simple models for linear viscoelastic behaviour (the Voigt or Kelvin model) and will be discussed in detail in Section 5.2.5.

Most of the experimental work on linear viscoelastic behaviour is confined to a single mode of deformation, usually corresponding to a measurement of the Young's modulus or the shear modulus. Our initial discussion of linear viscoelasticity will therefore be confined to the one-dimensional situation, recognising that greater complexity will be required to describe the viscoelastic behaviour fully. For the simplest case of an isotropic polymer at least two of the modes of deformation defining two of the quantities E, G and K for an elastic solid must be examined, if the behaviour is to be completely specified.

In defining the constitutive relations for an elastic solid, we have assumed that the strains are small and that there are linear relationships between stress and strain. We now ask how the principle of linearity can be extended to materials where the deformations are time dependent. The basis of the discussion is the Boltzmann superposition principle. This states that in linear viscoelasticity effects are simply additive, as in classical elasticity, the difference being that in linear viscoelasticity it matters at which instant an effect is created. Although the application of stress may now cause a time-dependent deformation, it can still be assumed that each increment of stress makes an independent contribution. From the present discussion, it can be seen that the linear viscoelastic theory must also contain the additional assumption that the strains are small. In Chapter 11, we will deal with attempts to extend linear viscoelastic theory either to take into account non-linear effects at small strains or to deal with the situation at large strains.

5.1.2 Creep

It is convenient to introduce the discussion of linear viscoelastic behaviour with the one-dimensional situation of creep under a fixed load. For an elastic solid, the following is observed at the two levels of stress σ_0 and $2\sigma_0$ (Figure 5.2(a)).

The strain follows the pattern of the loading programme exactly and in exact proportionality to the magnitude of the loads applied.

The effect of applying a similar loading programme to a linear viscoelastic solid has several similarities (Figure 5.2(b)). In the most general case, the total strain e is the sum of three separate parts e_1, e_2 and e_3. e_1 and e_2 are often termed the *immediate* elastic deformation and the *delayed* elastic deformation respectively. e_3 is the Newtonian flow, that is that part of the deformation, which is identical with the deformation of a viscous liquid obeying Newton's law of viscosity.
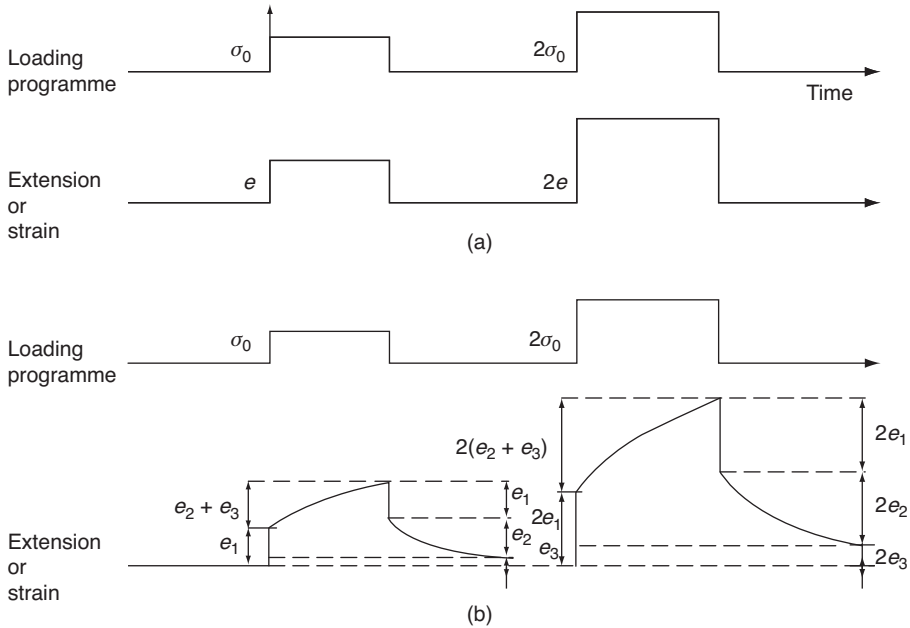
Figure 5.2   *(a) Deformation of an elastic solid and viscoelastic solid, and (b) deformation of a linear viscoelastic solid.*

Because the material shows linear behaviour, the magnitude of the strains e_1, e_2 and e_3 are exactly proportional to the magnitude of the applied stress. Thus the simple loading experiment defines a creep compliance $J(t)$ that is only a function of time:

$$\frac{e(t)}{\sigma} = J(t) = J_1 + J_2 + J_3,$$

where J_1, J_2 and J_3 correspond to e_1, e_2 and e_3 respectively.

The term J_3, which defines the Newtonian flow, can be neglected for rigid polymers at ordinary temperatures, because their flow viscosities are very large. Linear amorphous polymers do show a finite J_3 at temperatures above their glass transitions, but at lower temperatures their behaviour is dominated by J_1 and J_2. Cross-linked polymers do not show a J_3 term, and this is true to a very good approximation for highly crystalline polymers as well.

This leaves J_1 and J_2. At any given temperature, the separation of the compliance into terms J_1 and J_2 may involve an arbitrary division, which expresses the fact that at the shortest experimentally accessible times we will observe a limiting compliance J_1. We will assume, however, that there is a real distinction between the elastic and delayed responses. In some texts, the immediate elastic response in a creep experiment is called the 'unrelaxed' response to distinguish it from the 'relaxed' response that is observed at times sufficiently long for the various relaxation mechanisms to have occurred. To emphasise that the values of such terms as J_1 are sometimes arbitrary, we will enclose them in brackets.

We have already discussed in the introductory chapter how polymers can behave as glassy solids, viscoelastic solids, rubbers or viscous liquids depending on the timescale or on the
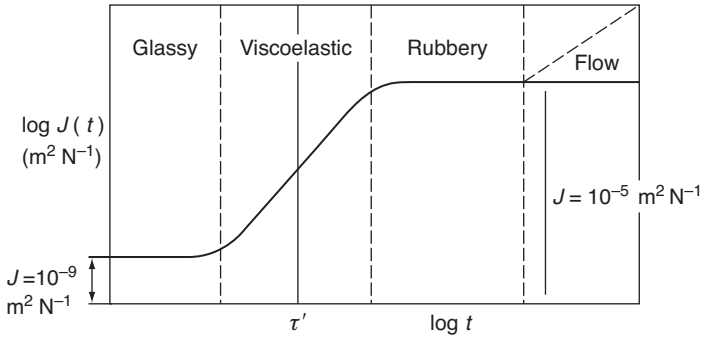
Figure 5.3   *The creep compliance J(t) as a function of time t. τ′ is the characteristic time (the retardation time).*

temperature of the experiment. How does this fit in with our present discussion? Figure 5.3 shows the variation in compliance with time at constant temperature over a very wide timescale for an idealised amorphous polymer with only one relaxation transition. This diagram shows that for short-time experiments the observed compliance is 1 GPa^{-1}, that for a glassy solid. It is also time independent. At very long times the observed compliance is 10 MPa^{-1}, that for a rubbery solid, and it is again time independent. At intermediate times, the compliance lies between these values and is time dependent; this is the general situation of viscoelastic behaviour.

These considerations suggest that the observed behaviour will depend on the timescale of the experiment relative to some basic time parameter of the polymer. For creep, this parameter is called the retardation time τ' and falls in the middle range of our timescale as shown in the diagram. The distinction between a rubber and a glassy plastic can then be seen as somewhat artificial in that it depends only on the value of τ' at room temperature for each polymer. Thus, for a rubber, τ' is very small at room temperature compared with normal experimental times that are greater than say 1 s, whereas the opposite is true for a glassy plastic. The value of this parameter τ' for a given polymer relates to its molecular constitution, as will be discussed later.

These considerations lead immediately to a qualitative understanding of the influence of temperature on polymer properties. With increasing temperature, the frequency of molecular rearrangements is increased, reducing the value of τ'. Thus, at very low temperatures, a rubber will behave like a glassy solid, as is well known, and equally a glassy plastic will soften at high temperatures to become rubber-like.

In the diagram illustrating creep under constant load recovery curves are also displayed. We will presently show that the recovery behaviour is basically similar to the creep behaviour if we neglect the quantity e_3, the Newtonian flow. This is a direct consequence of linear viscoelastic behaviour.

5.1.3   Stress Relaxation

The counterpart of creep is stress relaxation, where the sample is subjected to constant strain e, and the decay of stress $\sigma(t)$ is observed. This is illustrated in Figure 5.4.
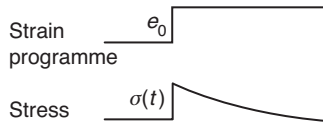
Figure 5.4   *Stress relaxation.*

The assumption of linear behaviour enables us to define the stress relaxation modulus $G(t) = \sigma(t)/e$. In the case of stress relaxation, the presence of viscous flow will affect the limiting value of the stress. Where viscous flow occurs, the stress can decay to zero at sufficiently long times, but where there is no viscous flow the stress decays to a finite value, and we obtain an equilibrium or relaxed modulus G_r, at infinite time. Figure 5.5 is a schematic graph of the stress relaxation modulus as a function of time. This is to be compared with the corresponding graph for creep (Figure 5.3).

The same regions of behaviour, viz. glassy, viscoelastic, rubbery and flow, can be identified, and a transition time τ is defined that characterises the timescale of the viscoelastic behaviour. We will shortly discuss stress relaxation and creep in detail and show that as customarily defined, the characteristic times τ and τ', although of the same order of magnitude, are not identical. Similar considerations to those discussed for creep apply to the effect of changing temperature on stress relaxation; i.e., changing temperature is equivalent to changing the timescale. Time–temperature equivalence is applicable to all linear viscoelastic behaviour in polymers and is considered fully in Chapter 7. The measurement of G_r may present difficulties as in the case of the elastic response. We will assume that there is a relaxed response to which it relates, but encloses the term involving it in brackets as for those involving the elastic response.

5.2   Mathematical Representation of Linear Viscoelasticity

The models discussed here, which are phenomenological and have no direct relation with chemical composition or molecular structure, in principle enable the response to a complicated loading pattern to be deduced from a single creep (or stress–relaxation) plot extending
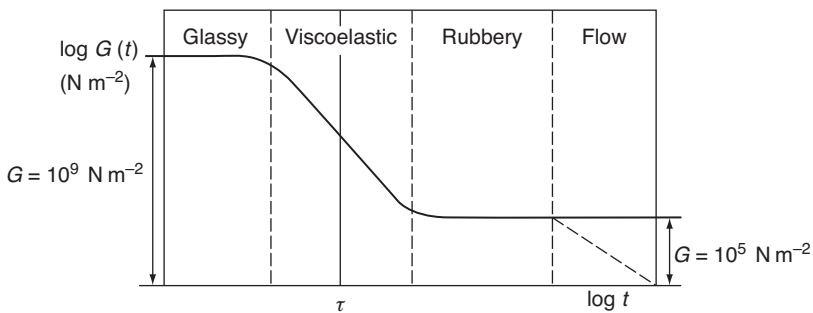
Figure 5.5   *The stress relaxation characteristic modulus G(t) as a function of time. τ is the characteristic time (the retardation time).*

over a long time interval. Interpretation depends on the assumption in linear viscoelasticity that the total deformation can be considered as the sum of independent elastic (Hookean) and viscous (Newtonian) components. In essence, the simple behaviour is modelled by a set of either integral or differential equations, which are then applicable in other situations.

5.2.1 The Boltzmann Superposition Principle

Boltzmann proposed, as long ago as 1876 [1], that

1. The creep is a function of the entire past loading history of the specimen.
2. Each loading step makes an independent contribution to the final deformation, so that the total deformation can be obtained by the addition of all the contributions.

Figure 5.6 illustrates the creep response to a multistep loading programme, in which incremental stresses $\Delta\sigma_1$, $\Delta\sigma_2, \ldots$, are added at times τ_1, $\tau_2, \ldots$, respectively. The total creep at time t is then given by

$$e(t) = \Delta\sigma_1 J(t - \tau_1) + \Delta\sigma_2 J(t - \tau_2) + \Delta\sigma_3 J(t - \tau_3) + \cdots, \qquad (5.1)$$

where $J(t - \tau)$ is the creep compliance function. For a particular loading step the relevant form of the function is that for the time interval between the present instant and that at which the load increment was applied.

The summation of Equation (5.1) can be generalised in integral form as

$$e(t) = \int_{-\infty}^{t} J(t - \tau)\mathrm{d}\sigma(\tau). \qquad (5.2)$$

It is usual to separate out the instantaneous elastic response in terms of the unrelaxed modulus G_u, giving

$$e(t) = \frac{\sigma}{G_u} + \int_{-\infty}^{t} J(t - \tau)\frac{\mathrm{d}\sigma(\tau)}{\mathrm{d}\tau}\mathrm{d}\tau, \qquad (5.3)$$

where σ represents the total stress at the end of the experiment. Note that the integral extends from $-\infty$ to t, which implies that all previous elements of loading history must be taken into account and, in principle, the user must know the history of each specimen
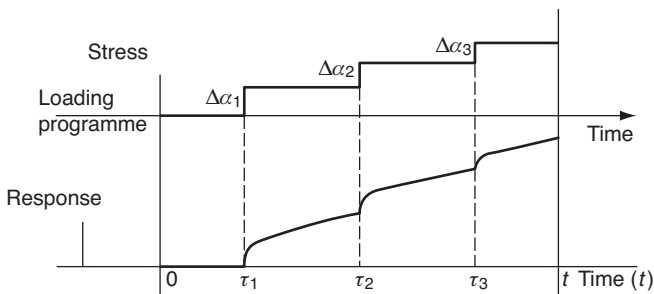
Figure 5.6   *The creep behaviour of a linear viscoelastic solid.*
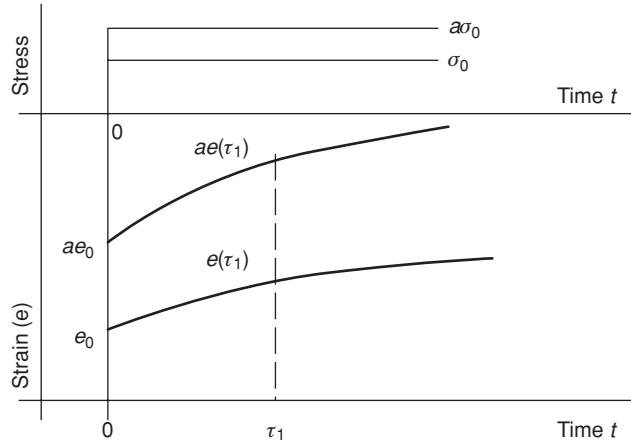
Figure 5.7   *Creep for single step loading. For stress a σ_0 the strain at any time ($\tau \geq 0$) is a times greater than that for stress σ_0.*

since its manufacture. In fact, when creep levels are low enough for linearity to apply, the deformation effectively levels off at sufficiently long times, so that only comparatively recent history is relevant, and this can be standardised by a conditioning treatment (see Section 6.1.1). For this reason, viscoelastic solids are sometimes said to be materials with 'fading memory'.

The integral in Equation (5.3) is called a Duhamel integral, and it is a useful illustration of the consequences of the Boltzmann superposition principle to evaluate the response for a number of simple loading programmes. Recalling the development that leads to Equation (5.2), it can be seen that the Duhamel integral is most simply evaluated by treating it as the summation of a number of response terms. Consider two specific cases:

1. *Single-step loading of a stress σ_0 at time $\tau = 0$ (Figure 5.7). For this case*

$$J(t - \tau) = J(t) \quad \text{and} \quad e(t) = \sigma_0 J(t)$$

2. *Two-step loading of a stress σ_0 at time $\tau = 0$ followed by an additional stress σ_0 at time $\tau = t_1$ (Figure 5.8). For this case the creep deformation produced by the two loading steps are*

$$e_1 = \sigma_0 J(t) \quad \text{and} \quad e_2 = \sigma_0 J(t - t_1)$$

so that

$$e(t) = e_1 + e_2 = \sigma_0 J(t) + \sigma_0 J(t - t_1)$$

The 'additional creep' $e'_c(t - t_1)$ produced by the second loading step is given by

$$e'_c(t - t_1) = \sigma_0 J(t) + \sigma_0 J(t - t_1) - \sigma_0 J(t) = \sigma_0 J(t - t_1)$$

The above illustrates one consequence of the Boltzmann principle, viz. that the additional creep $e'_c(t - t_1)$ produced by adding the stress σ_0 is identical with the creep that would
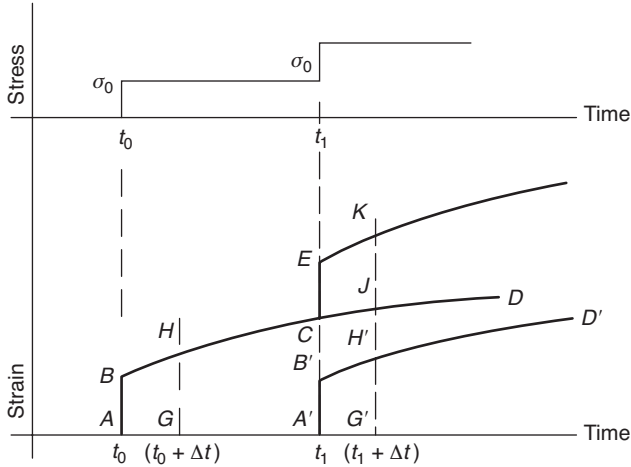
Figure 5.8   *Creep for two equal loading steps. Additional instantaneous strain CE = AB. Additional total strain at* $(t_1 + \Delta t)$: *JK = GH.*

have occurred had this stress σ_0 been applied without any previous loading at the same instant in time t_1.

The principle is illustrated in Figure 5.8, where ABD represents creep under σ_0 alone. The response to an additional stress σ_0 at t_1 is found by sliding ABD along the time axis by t_1 to give curve $A'B'D'$, and at any time adding together the individual strains due to ABD and $A'B'D'$; e.g., at Δt after the initial loading step the deformation is GH; at Δt after t_1 the deformation due to the initial σ_0 is $G'J$. The total deformation at $(t_1 + \Delta t)$ is found by adding to $G'J$ the strain $JK = G'H' = GH$.

If the second load had been $a\sigma_0$, where a is a constant, then $CE = A'B' = aAB$; $JK = aG'H' = aGH$ etc.

3. *Creep and recovery.* In this case (Figure 5.9), the stress σ_0 is applied at time $\tau = 0$ and removed at time $\tau = t_1$. The deformation $e(t)$ at a time $t > t_1$ is given by the addition of two terms $e_1 = \sigma_0 J(t)$ and $e_2 = -\sigma_0 J(t - t_1)$, which express the application and removal of the stress σ_0 respectively. Thus, $e(t) = \sigma_0 J(t) - \sigma_0 J(t - t_1)$.

The recovery $e_r(t - t_1)$ will be defined as the difference between the anticipated creep under the initial stress and the actual measured response.

Thus

$$e_r(t - t_1) = \sigma_0 J(t) - [\sigma_0 J(t) - \sigma_0 J(t - t_1)] = \sigma_0 J(t - t_1),$$

which is identical to the creep response to a stress σ_0 applied at a time t_1. This procedure demonstrates a second consequence of the Boltzmann superposition principle, that the creep and recovery responses are identical in magnitude.

The initial creep curve, ABD in Figure 5.9, is again moved along the time axis by t_1 to give $A'B'D'$. At any subsequent time, the overall deformation is given by the difference between the two curves (CFG). It is important to realise that at a time $t_2 > t_1$, the residual deformation is obtained by subtracting $A'B'D'$ from the deformation that would have occurred had
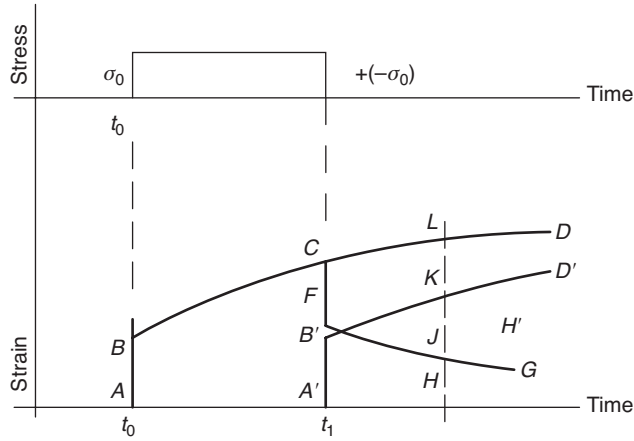
Figure 5.9 *Recovery considered as the addition of a negative stress increment, that is subtract B'D' from CD.*

unloading not taken place; for example, residual deformation $HJ = HL - HK$, and not $A'C - HK$, where $A'C$ is the maximum strain attained before unloading.

5.2.2   The Stress Relaxation Modulus

Stress relaxation behaviour can be represented in an exactly complementary fashion using the Boltzmann superposition principle. Consider a stress relaxation programme in which incremental strains $\Delta e_1, \Delta e_2, \Delta e_3$ and so on are added at times τ_1, τ_2, τ_3 etc., respectively. The total stress at time t is then given by

$$\sigma(t) = \Delta e_1 G(t - \tau_1) + \Delta e_2 G(t - \tau_2) + \Delta e_3 G(t - \tau_3) + \cdots, \tag{5.4}$$

where $G(t - \tau)$ is the stress relaxation modulus. Equation (5.4) may be generalised in an identical manner in which Equation (5.1) leads to Equations (5.2) and (5.3) to give

$$\sigma(t) = [G_r e] + \int_{-\infty}^{t} G(t - \tau) \frac{de(\tau)}{d\tau} d\tau, \tag{5.5}$$

where G_r is the equilibrium or relaxed modulus.

5.2.3   The Formal Relationship between Creep and Stress Relaxation

We have already seen that stress relaxation is the converse of creep in a general sense. It is therefore to be expected that they will be formally related through a simple mathematical relationship.

For simplicity consider only the time-dependent terms in Equation (5.3). Then

$$e(t) = \int_{-\infty}^{t} J(t-\tau) \frac{d\sigma(\tau)}{d\tau} d\tau.$$

Consider a stress programme starting at time $\tau = 0$ in which the stress decreases exactly as the relaxation function $G(t)$. In this case, the corresponding strain must remain constant as in a typical stress relaxation experiment. Thus, if

$$\frac{\mathrm{d}\sigma(\tau)}{\mathrm{d}\tau} = \frac{\mathrm{d}G(\tau)}{\mathrm{d}\tau}$$

then

$$\int_0^t \frac{\mathrm{d}G(\tau)}{\mathrm{d}\tau} J(t - \tau)\mathrm{d}\tau = \text{constant}. \tag{5.6}$$

For simplicity we can normalise the definitions of $G(\tau)$ and $J(\tau)$ so that the constant is unity. We then have

$$\int_0^t \frac{\mathrm{d}G(\tau)}{\mathrm{d}\tau} J(t - \tau)\mathrm{d}\tau = 1. \tag{5.7}$$

This expression is sometimes integrated to give

$$\int_0^t G(\tau)J(t - \tau) = t. \tag{5.8}$$

These equations provide a formal connection between the creep and stress relaxation functions. However, this approach is of greatest interest from a purely theoretical standpoint. In practice, the problem of interchangeability of creep and stress relaxation data is usually dealt with via relaxation or retardation spectra, and by approximate methods.

5.2.4 Mechanical Models, Relaxation and Retardation Time Spectra

The Boltzmann superposition principle is one starting point for a theory of linear viscoelastic behaviour, and is sometimes called the *'integral representation* of linear viscoelasticity', because it defines an integral equation. An equally valid starting point is to relate the stress to the strain by a linear differential equation, which leads to a differential representation of linear viscoelasticity. In its most general form, the equation is expressed as

$$P\sigma = Q\mathrm{e},$$

where P and Q are linear differential operators with respect to time. This representation has been found of particular value in obtaining solutions to specific problems in the deformation of viscoelastic solids [2, 3].

Most generally the differential equation is

$$a_0\sigma + a_1\frac{\mathrm{d}\sigma}{\mathrm{d}t} + a_2\frac{\mathrm{d}^2\sigma}{\mathrm{d}t^2} + \cdots = \mathrm{b}_0\sigma + \mathrm{b}_1\frac{\mathrm{d}\mathrm{e}}{\mathrm{d}t} + b_2\frac{\mathrm{d}^2\mathrm{e}}{\mathrm{d}t^2} + \cdots . \tag{5.9}$$

It is often adequate to represent the experimental data obtained over a limited timescale by including only one or two terms on each side of this equation. We will now show that this is equivalent to describing the viscoelastic behaviour by mechanical models constructed

of elastic springs that obey Hooke's law and viscous dashpots that obey Newton's law of viscosity.

The simplest models consist of a single spring and a single dashpot either in series or in parallel and these are known as the Maxwell model and the Kelvin or Voigt models respectively.

5.2.5   The Kelvin or Voigt Model

This model (Figure 5.10(a)) consists of a spring of modulus E_K, in parallel with a dashpot of viscosity η_K. If a constant stress σ is applied at time $t = 0$, there can be no instantaneous extension of the spring, as it is retarded by the dashpot. Deformation then occurs at a varying rate, with the stress shared between the two components until, after a time dependent on the dashpot viscosity, the spring approaches a finite maximum extension. When the stress is removed the reverse process occurs: there is no instantaneous retraction, but the initial unstretched length is eventually recovered (Figure 5.10(b)). The model does represent the time-dependent component of creep to a first approximation.

The stress–strain relations are, for the spring, $\sigma_1 = E_K e_1$ and for the dashpot

$$\sigma_2 = \eta_K \frac{de_2}{dt}$$

The total stress σ is shared between spring and dashpot: $\sigma = \sigma_1 + \sigma_2$; but the strain in each component is the total strain: $e = e_1 = e_2$.

$$\therefore \sigma = E_K e + \eta_K \frac{de}{dt}. \tag{5.10}$$

Solving for $0 < t < t_1$, when the stress is σ

$$\frac{E_K}{\eta_K} \int_0^t dt = \int_0^e \frac{de}{\sigma/E_K - 1},$$

where η_K/E_K has the dimensions of time, and represents the rate at which the deformation occurs: it is the retardation time τ'. Hence by integration

$$\frac{t}{\tau'} = \ln \left(\frac{\sigma/E_K}{\sigma/E_K - e} \right)$$

(a) σ (b)

$\sigma_1, e_1\ E_K$ $\sigma_2, e_2\ \eta_K$

Strain

Time
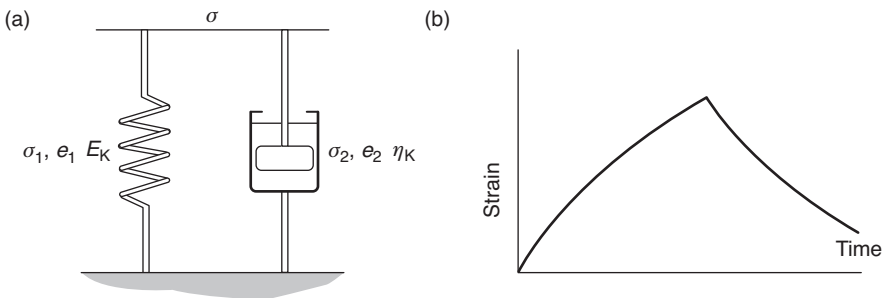
Figure 5.10   *(a) The Kelvin, or Voigt, unit; (b) creep and recovery behaviour.*

giving

$$\frac{\sigma}{E_K} = \left(\frac{\sigma}{E_K} - e\right) \exp\left(t/\tau'\right)$$

Rearranging, we obtain

$$e = \frac{\sigma}{E_K}\left[1 - \exp\left(-t/\tau'\right)\right]. \tag{5.11}$$

It is convenient in creep experiments to replace E_K by $1/J$, where J is the spring compliance, to give

$$e = J\sigma\left[1 - \exp\left(-t/\tau'\right)\right]. \tag{5.12}$$

For $t > t_1$ after unloading, the solution becomes

$$e = e_{t_1} \exp\left(\frac{t_1 - t}{\tau'}\right), \text{ where } e_{t_1} = J\sigma\left[1 - \exp\left(-t_1/\tau'\right)\right]. \tag{5.13}$$

The retardation time τ' is the time after loading for the strain to reach

$$\left(1 - \frac{1}{\exp(1)}\right)$$

of its equilibrium value; after stress removal the strain decays to $(1/\exp(0))$ of its maximum value in time τ'.

The Kelvin model is unable to describe stress relaxation, as at constant strain the dashpot cannot relax. In mathematical terms $(de/dt) = 0$, giving $\sigma = E_K e$.

5.2.6 The Maxwell Model

The Maxwell model consists of a spring and dashpot in series as shown in Figure 5.11(a).
The equations for the stress–strain relations are

$$\sigma_1 = E_m e_1, \tag{5.14a}$$

relating the stress σ_1 and the strain e_1 in the spring, and

$$\sigma_2 = \eta_m \frac{de_2}{dt} \tag{5.14b}$$
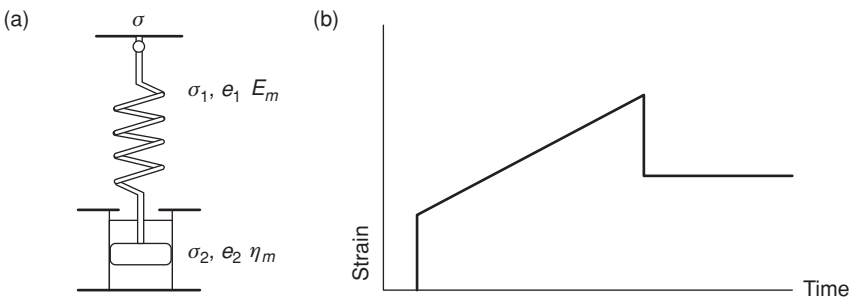
Figure 5.11 (a) The Maxwell unit and (b) creep and recovery behaviour.

relating the stress σ_2 and the strain e_2 in the dashpot. Because the stress is identical for the spring and the dashpot, the total stress $\sigma = \sigma_1 = \sigma_2$. The total strain e is the sum of the strain in the spring and the dashpot, that is $e = e_1 + e_2$.

To find the relationship between total stress and total strain, Equation (5.14a) can be written as

$$\frac{d\sigma_1}{dt} = E_m \frac{de_1}{dt}$$

and added to Equation (5.14b), giving

$$\frac{de}{dt} = \frac{1}{E_m} \frac{d\sigma}{dt} + \frac{\sigma}{\eta_m}. \tag{5.15}$$

The Maxwell model is of particular value in considering a stress relaxation experiment. In this case,

$$\frac{de}{dt} = 0 \quad \text{and} \quad \frac{1}{E_m} \frac{d\sigma}{dt} + \frac{\sigma}{\eta_m} = 0.$$

Thus,

$$\frac{d\sigma}{\sigma} = -\frac{E_m}{\eta_m} dt.$$

At time $t = 0$, $\sigma = \sigma_0$, the initial stress, and integrating we have

$$\sigma = \sigma_0 \exp\left(\frac{-E_m}{\eta_m}\right) t. \tag{5.16}$$

This equation shows that the stress decays exponentially with a characteristic time constant $\tau = \eta_m / E_m$:

$$\sigma = \sigma_0 \exp\left(\frac{-t}{\tau}\right),$$

where τ is called the 'relaxation time'. There are two inadequacies of this simple model that can be understood immediately.

First, under conditions of constant stress, i.e.

$$\frac{d\sigma}{dt} = 0, \quad \frac{de}{dt} = \frac{\sigma}{\eta_m}$$

and Newtonian flow is observed. This is clearly not generally true for viscoelastic materials, where the creep behaviour is more complex.

Secondly, the stress relaxation behaviour cannot usually be represented by a single exponential decay term, nor does it necessarily decay to zero at infinite time.

5.2.7   The Standard Linear Solid

We have seen that the Maxwell model describes the stress relaxation of a viscoelastic solid to a first approximation, and the Kelvin model describes the creep behaviour, but that neither model is adequate for the general behaviour of a viscoelastic solid where it is necessary to describe both stress relaxation and creep.
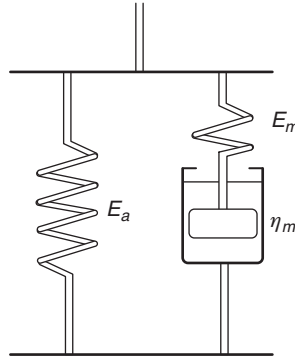
Figure 5.12   *The standard linear solid.*

Consider again the general linear differential equation, which represents linear viscoelastic behaviour. From the present discussion, it follows that to obtain even an approximate description of both stress relaxation and creep, at least the first two terms on each side of Equation (5.9) must be retained, that is the simplest equation will be of the form

$$a_0 \sigma + a_1 \frac{d\sigma}{dt} = b_0 + b_1 \frac{de}{dt}. \tag{5.17}$$

This will be adequate to a first approximation for creep (when $d\sigma/dt = 0$) and for stress relaxation (when $de/dt = 0$), giving an exponential response in both cases.

It is very easy to show that the model shown in Figure 5.12 has this form. The stress–strain relationship is

$$\sigma + \tau \frac{d\sigma}{dt} = E_a e + (E_m + E_a) \tau \frac{de}{dt}, \quad \text{where } \tau = \frac{\eta_m}{E_m}. \tag{5.18}$$

This model is known as the 'standard linear solid' and is usually attributed to Zener [4]. It provides an approximate representation to the observed behaviour of polymers in their main viscoelastic range. As has been discussed, it predicts an exponential response only. To describe the observed viscoelastic behaviour quantitatively would require the inclusion of many terms in the linear differential Equation (5.9). These more complicated equations are equivalent to either a large number of Maxwell elements in parallel or a large number of Voigt elements in series (Figures 5.13(a) and (b)).

5.2.8   Relaxation Time Spectra and Retardation Time Spectra

It is next required to obtain a quantitative description of stress relaxation and creep that will help to form a link with the original mathematical description in terms of the Boltzmann integrals. It is simple and instructive to do this by development of the Maxwell and Kelvin models.

Consider first stress relaxation, described by

$$\sigma(t) = [G_r e] + \int_{-\infty}^{t} G(t - \tau) \frac{de(\tau)}{d\tau} d\tau, \tag{5.5}$$
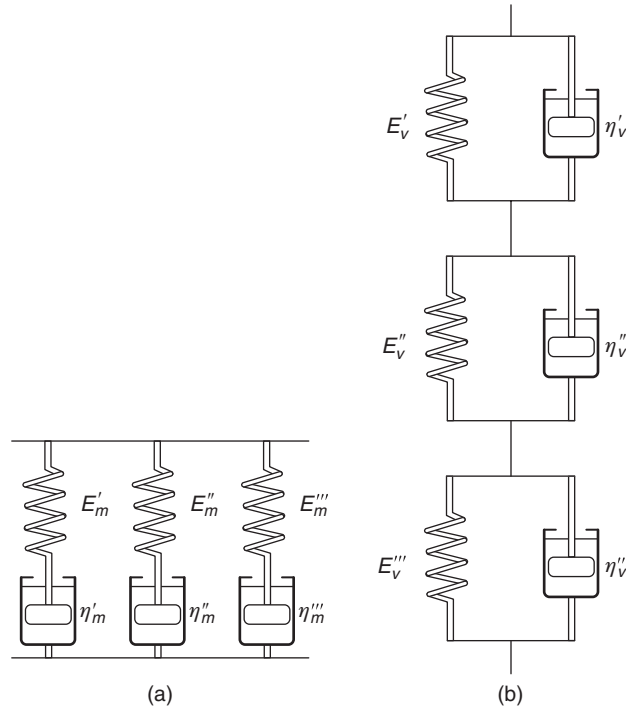
Figure 5.13   *(a) Maxwell elements in parallel and (b) Voigt elements in series.*

where $G(t)$ is the stress relaxation modulus. For stress relaxation at constant strain e, Equation (5.16) shows that the Maxwell model gives

$$\sigma(t) = E_m e \exp \frac{-t}{\tau}$$

and the stress relaxation modulus $G(t) = E_m \exp(-t/\tau)$. For a series of Maxwell elements joined in parallel, again at constant strain e, the stress is given by

$$\sigma(t) = e \sum_n E_n \exp \frac{-t}{\tau_n},$$

where E_n, τ_n are the spring constant and relaxation time respectively of the nth Maxwell element.

The summation can be written as an integral, giving

$$\sigma(t) = [G_r e] + e \int_0^\infty f(\tau) \exp \frac{-t}{\tau} \mathrm{d}\tau, \tag{5.19}$$

where the spring constant E_n is replaced by the weighting function $f(\tau)\,\mathrm{d}\tau$ that defines the concentration of Maxwell elements with relaxation times between τ and $\tau + \mathrm{d}\tau$.

The stress relaxation modulus is given by

$$G(t) = [G_r] + \int_0^\infty f(\tau) \exp \frac{-t}{\tau} d\tau. \tag{5.20}$$

The term $f(\tau)$ is called the 'relaxation time spectrum'. In practice, it has been found more convenient to use a logarithmic timescale. A new relaxation time spectrum $H(\tau)$ is now defined, where $H(\tau) \, d (\ln \tau)$ gives the contributions to the stress relaxation associated with relaxation times between $\ln \tau$ and $\ln \tau + d (\ln \tau)$. The stress relaxation modulus is then given by

$$G(t) = [G_r] + \int_{-\infty}^\infty H(\tau) \exp \frac{-t}{\tau} d(\ln \tau). \tag{5.21}$$

An exactly analogous treatment, using a series of the Kelvin models, leads to a similar expression for the creep compliance $J(t)$.

Thus

$$J(t) = [J_u] + \int_{-\infty}^\infty L(\tau) \left(1 - \exp \frac{-t}{\tau} \right) d(\ln \tau), \tag{5.22}$$

where J_u is the instantaneous elastic compliance and $L(\tau)$ is the *retardation time spectrum*, $L(\tau) \, d (\ln \tau)$ defining the contributions to the creep compliance associated with retardation times between $\ln \tau$ and $\ln \tau + d (\ln \tau)$.

The relaxation time spectrum can be calculated exactly from the measured stress relaxation modulus using Fourier or Laplace transform methods, and similar considerations apply to the retardation time spectrum and the creep compliance. It is more convenient to consider these transformations at a later stage, when the final representation of linear viscoelasticity, that of the complex modulus and complex compliance, has been discussed.

It is important to recognise that the relaxation time spectrum and the retardation time spectrum are only mathematical descriptions of the macroscopic behaviour and do not necessarily have a simple interpretation in molecular terms. It is a quite separate exercise to correlate observed patterns in the relaxation behaviour, such as a predominant relaxation time, with a specific molecular process. It should also be emphasised, as will be apparent from the further detailed discussion, that qualitative interpretations in general molecular terms can often be obtained from the experimental data directly, without recourse to calculation of the relaxation time spectrum or the retardation time spectrum.

5.3 Dynamical Mechanical Measurements: The Complex Modulus and Complex Compliance

An alternative experimental procedure to creep and stress relaxation is to subject the specimen to an alternating strain and simultaneously measure the stress. For linear viscoelastic

behaviour, when equilibrium is reached, the stress and strain will both vary sinusoidally, but the strain lags behind the stress. Thus, we write

$$\text{strain } e = e_0 \sin \omega t$$
$$\text{stress } \sigma = \sigma_0 \sin(\omega t + \delta),$$

where ω is the angular frequency and δ is the phase lag.

Expanding $\sigma = \sigma_0 \sin \omega t \cos \delta + \sigma_0 \cos \omega t \sin \delta$, we see that the stress can be considered to consist of two components: (1) of magnitude $(\sigma_0 \cos \delta)$ in phase with the strain and (2) of magnitude $(\sigma_0 \sin \delta)$ 90° out of phase with the strain.

The stress–strain relationship can therefore be defined by a quantity G_1 in phase with the strain and by a quantity G_2 90° out of phase with the strain, i.e.

$$\sigma = e_0 G_1 \sin \omega t + e_0 G_2 \cos \omega t, \tag{5.23}$$

where

$$G_1 = \frac{\sigma_0}{e_0} \cos \delta \quad \text{and} \quad G_2 = \frac{\sigma_0}{e_0} \sin \delta.$$

A phasor diagram (Figure 5.14) then indicates that G_1 and G_2 define a complex modulus G^*. If $e = e_0 \exp(i\omega t)$, $\sigma = \sigma_0 \exp[i(\omega t + \delta)]$, so that

$$\begin{aligned} G^* = \frac{\sigma}{e} &= \frac{\sigma_0}{e_0} \exp(i\delta) \\ &= \frac{\sigma_0}{e_0}(\cos \delta + i \sin \delta) \\ &= G_1 + G_2, \end{aligned} \tag{5.24}$$

where G_1, which is in phase with the strain, is called the storage modulus because it defines the energy stored in the specimen due to the applied strain, and G_2, which is $\pi/2$ out of phase with the strain, defines the dissipation of energy and is called the loss modulus, for a reason that becomes evident through calculating the energy (ΔE) dissipated per cycle:

$$\Delta E = \oint \sigma \, de = \int_0^{2\pi/\omega} \sigma \frac{de}{dt} dt.$$
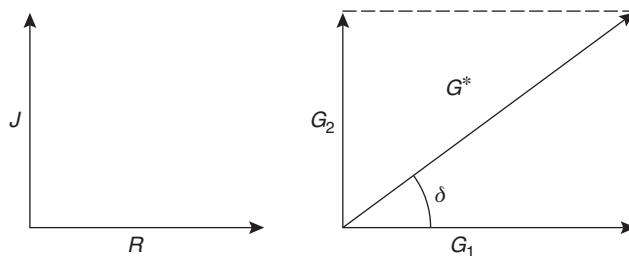
Figure 5.14 *Phasor diagram for complex modulus $G^* = G_1 + iG_2$ and phase lag $\tan \delta = G_2/G_1$.*

Substituting for σ and e,

$$\Delta E = \omega e_0^2 \int_0^{2\pi/\omega} \left(G_1 \sin \omega t \cos \omega t + G_2 \cos^2 \omega t \right) \mathrm{d}t. \tag{5.25}$$

The integral is solved by using $\sin \omega t \cos \omega t = \frac{1}{2} \sin 2\omega t$ and $\cos^2 \omega t = \frac{1}{2}(1 + \cos 2\omega t)$, to give

$$\Delta E = \pi G_2 e_0^2. \tag{5.26}$$

If the integral for ΔE is evaluated over a quarter-cycle rather than over the complete period, the first term

$$G_1 \omega e_0^2 \int_0^{\pi/2\omega} \sin \omega t \cos \omega t \, \mathrm{d}t \tag{5.27}$$

gives the maximum stored elastic energy (E).

Evaluating as before, we obtain

$$E = \frac{1}{2} G_1 e_0^2, \tag{5.28}$$

which, as expected, is independent of frequency. Equations (5.26) and (5.28) can be rewritten as

$$G_1 = \frac{2E}{e_0^2} G_2 = \frac{\Delta E}{\pi e_0^2}.$$

Hence

$$\frac{G_2}{G_1} = \tan \delta = \frac{\Delta E}{2\pi E}. \tag{5.29}$$

The ratio $\Delta E/E$ is called the specific loss

$$\frac{\Delta E}{E} = 2\pi \tan \delta. \tag{5.30}$$

Typical values of G_1, G_2 and $\tan \delta$ for a polymer are 1 GPa, 10 MPa and 0.01 respectively. In such cases, $|G^*|$ is approximately equal to G_1, and it is customary to define the dynamic mechanical behaviour in terms of the 'modulus' $G \approx G_1$ and the phase angle δ or $\tan \delta = G_2/G_1$.

A complementary treatment can be developed to define a complex compliance $J^* = J_1 - iJ_2$, which is directly related to the complex modulus, as $G^* = 1/J^*$.

5.3.1   Experimental Patterns for G_1, G_2 and so on as a Function of Frequency

Now consider the complex moduli and compliances as a function of frequency for a typical viscoelastic solid, in a similar manner to the creep and stress relaxation as a function of time.

Figure 5.15 shows the variation in G_1, G_2 and $\tan \delta$ with frequency for a polymer that shows no flow. At low frequencies, the polymer is rubber-like and has a low modulus G_1 of
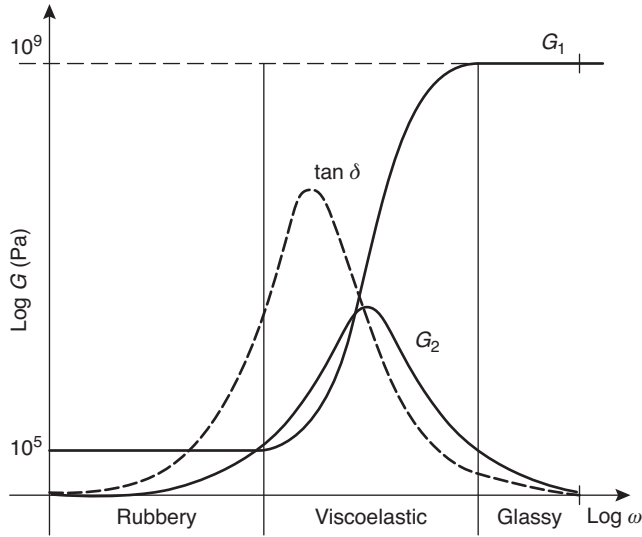
Figure 5.15   *The complex modulus $G_1 + iG_2$ as a function of frequency ω.*

~0.1 MPa, which is independent of frequency. At high frequencies, the polymer is glassy with a modulus of ~1 GPa, which is again independent of frequency. At intermediate frequencies, the polymer behaves as a viscoelastic solid, and its modulus G_1 increases with increasing frequency.

The complementary pattern of behaviour is shown by the loss modulus G_2. At low and high frequencies G_2 is zero, the stress and strain being exactly in phase for the rubbery and glassy states. At intermediate frequencies, where the polymer is viscoelastic, G_2 rises to a maximum value, this occurring at a frequency close to that for which the storage modulus is changing most rapidly with frequency. The viscoelastic region is also characterised by a maximum in the loss factor tan δ, but this occurs at a slightly lower frequency than that in G_2, since tan $\delta = G_2/G_1$ and G_1 is also changing rapidly in this frequency range.

An analogous diagram (Figure 5.16) shows the variation in the compliances J_1 and J_2 with frequency.

The next development is to obtain a mathematical representation for the dynamic mechanical behaviour as a function of frequency. As in the case of stress relaxation and creep, a very easy starting point for the argument is based on the Maxwell and Voigt models.

Using Equation (5.11) for the Maxwell model,

$$\frac{\mathrm{d}e}{\mathrm{d}t} = \frac{1}{E_m}\frac{\mathrm{d}\sigma}{\mathrm{d}t} + \frac{\sigma}{\eta_m}\eta$$

and the definition of the relaxation time as $\tau = \eta_m/E_m$, we can write

$$\sigma + \tau\frac{\mathrm{d}\sigma}{\mathrm{d}t} = E_m\tau\frac{\mathrm{d}e}{\mathrm{d}t}.$$
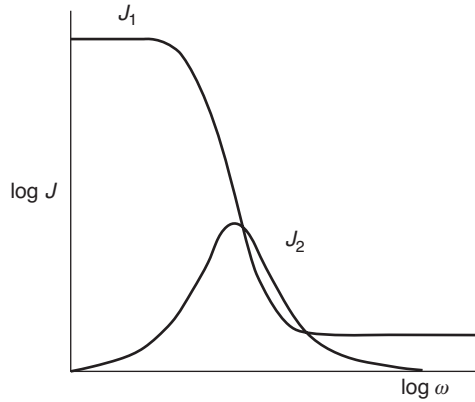
Figure 5.16 *The complex compliance J* = J₁ − iJ₂ as a function of frequency.*

Put

$$\sigma = \sigma_0 e^{i\omega t} = (G_1 + G_2)e.$$

This gives

$$\sigma_0 e^{i\omega t} + i\omega\tau\sigma_0 e^{i\omega t} = \frac{E_m \tau i\omega\sigma_0 e^{i\omega t}}{G_1 + iG_2}$$

from which it follows that

$$G_1 + iG_2 = \frac{E_m i\omega\tau}{1 + i\omega\tau},$$

i.e.

$$G_1 = \frac{E_m \omega^2 \tau^2}{1 + \omega^2 \tau^2}, \quad G_2 = \frac{E_m \omega\tau}{1 + \omega^2 \tau^2}, \quad \text{and} \quad \tan\delta = \frac{1}{\omega t}. \tag{5.31}$$

This result gives the pattern shown in Figure 5.17 for G_1, G_2 and $\tan\delta$ as a function of frequency (or $\omega\tau$, which is more convenient). It is seen that the qualitative features are correct in the case of G_1, G_2, but not for $\tan\delta$.

A similar manipulation of the equation representing the Voigt model, introducing the complex compliances, leads to a comparable qualitative picture of J_1, J_2 and $\tan\delta$ as a function of frequency. Again the qualitative features are correct for J_1 and J_2 but not for $\tan\delta$, which in this case is equal to $\omega\tau'$.

The Maxwell and Voigt models are therefore inadequate to describe the dynamic mechanical behaviour of a polymer, as they do not provide an adequate representation of both the creep and stress relaxation behaviour. A good measure of qualitative improvement could be gained, as in the previous discussion of creep and stress relaxation, by using a three-parameter model, e.g. the standard linear solid, and it is an interesting exercise to show that this model gives a more realistic variation in G_1, G_2, and $\tan\delta$ with frequency.

It is, however, desirable to move directly to the general representation, using the relaxation time spectrum.
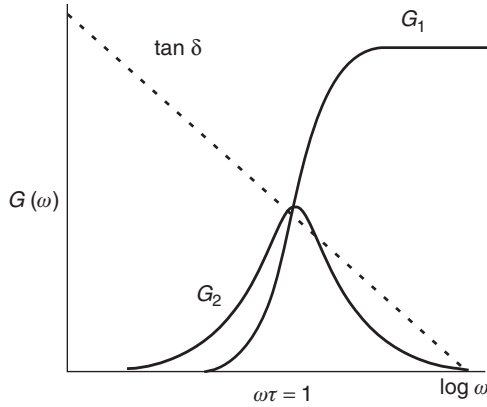
Figure 5.17   *The complex modulus $G^* = G_1 + iG_2$ as a function of frequency ω.*

The general representation for the stress relaxation modulus (Equation 5.21),

$$G(t) = \frac{\sigma(t)}{e} = [G_r] + \int_{-\infty}^{\infty} H(\tau) \exp \frac{-t}{\tau} d(\ln \tau),$$

follows by generalising the stress relaxation response from a single Maxwell element, where $G(t) = E_m \exp(-t/\tau)$.

The response of a Maxwell element to an alternating strain is defined by the relationships

$$G_1 = \frac{E_m \omega^2 \tau^2}{1 + \omega^2 \tau^2} \quad \text{and} \quad G_2 = \frac{E_m \omega \tau}{1 + \omega^2 \tau^2}.$$

An identical generalisation to the previous one then gives

$$G_1(\omega) = [G_r] + \int_{-\infty}^{\infty} \frac{H(\tau) \omega^2 \tau^2}{1 + \omega^2 \tau^2} d(\ln \tau) \tag{5.32}$$

and

$$G_2(\omega) = \int_{-\infty}^{\infty} \frac{H(\tau) \omega \tau}{1 + \omega^2 \tau^2} d(\ln \tau). \tag{5.33}$$

As previously, the spring constant E_m is replaced by the weighting function $H(\tau)d(\ln\tau)$ that defines the contribution to the response of elements whose relaxation time is between $\ln\tau$ and $\ln\tau + d(\ln\tau)$. It is seen that the stress relaxation modulus $G(t)$ and the real and imaginary parts of the complex compliance G_1 and G_2 can all be directly related to the same relaxation time spectrum $H(\tau)$.

Similar relationships hold between the creep compliance $J(t)$, the real and imaginary parts of the complex compliance J_1 and J_2 and the retardation time spectrum $L(t)$. These

relationships can be readily derived by consideration of the response of a Voigt element to an alternating stress. They will not be derived here, but the results are quoted for completeness:

$$J_1(\omega) = [J_u] + \int_{-\infty}^{\infty} \frac{L(\tau)}{1 + \omega^2\tau^2} d(\ln \tau) \tag{5.34}$$

$$J_2(\omega) = \int_{-\infty}^{\infty} \frac{J(\tau)\omega\tau}{1 + \omega^2\tau^2} d(\ln \tau). \tag{5.35}$$

5.4 The Relationships between the Complex Moduli and the Stress Relaxation Modulus

The exact formal relationships between the various viscoelastic functions are conveniently expressed using Fourier or Laplace transform methods (cf. Section 5.4.2). However, it is often adequate to use simple approximations due to Alfrey in which the exponential term for a single Kelvin or Maxwell unit is replaced by a step function, as shown schematically in Figure 5.18.

Consider

$$G(t) = [G_r] + \int_{-\infty}^{\infty} H(\tau) \exp \frac{-t}{\tau} d(\ln\tau). \tag{5.36}$$

If we assume that $e^{-t/\tau} = 0$ up to the time $\tau = t$, and $e^{-t/\tau} = 1$ for $\tau > t$, we can write

$$G(t) = [G_r] + \int_{\ln t}^{\infty} H(\tau) d(\ln \tau).$$
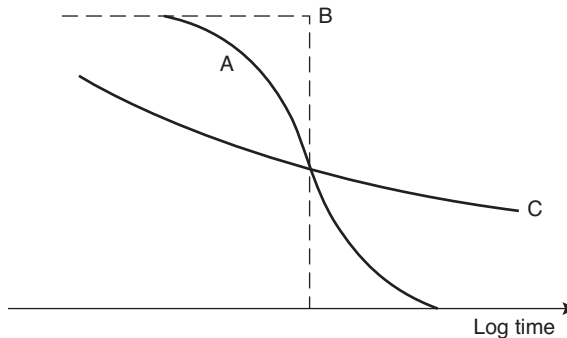
Figure 5.18   *The Alfrey approximation: the stress relaxation of a Maxwell unit A is replaced by a step function B. The curve C represents relaxation of a typical viscoelastic polymer.*

This gives the relaxation time spectrum

$$H(\tau) = - \left[\frac{dG(t)}{d \ln t} \right]_{t=\tau} , \qquad (5.37)$$

which is known as the 'Alfrey approximation' [5, 6].

The relaxation time spectrum can be expressed to a similar degree of approximation in terms of the real and imaginary parts of the complex modulus:

$$H(\tau) = \left[\frac{dG_1(\omega)}{d \ln \omega} \right]_{1/\omega=\tau} = \frac{2}{\pi} [G_2(\omega)]_{1/\omega=\tau} . \qquad (5.38)$$

These relationships are illustrated diagrammatically for the case of a single relaxation transition in Figure 5.19. To obtain the complete relaxation time spectrum, the longer time part of $H(\tau)$ will be found from the stress relaxation modulus data of Figure 5.19(a) and the shorter time part from the dynamic mechanical data of Figure 5.19(b).
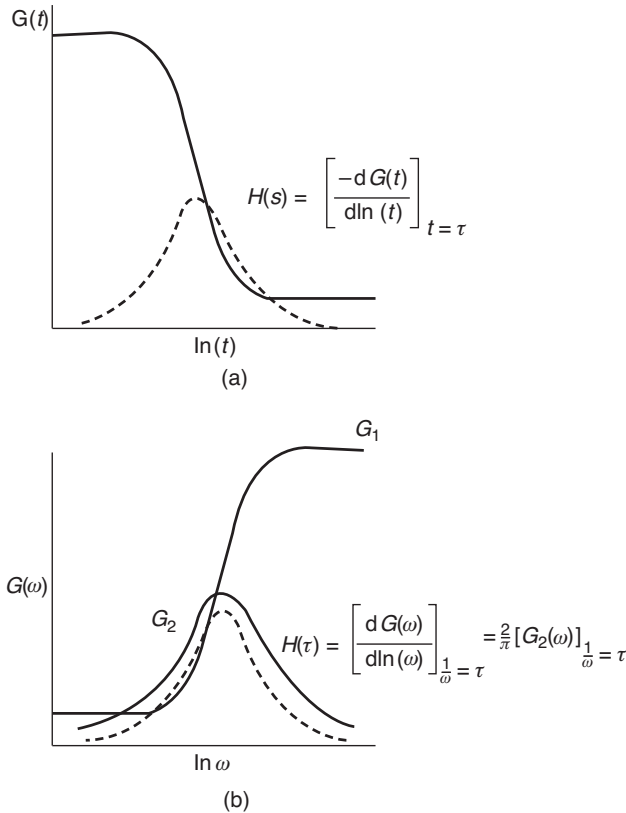
Figure 5.19   *The Alfrey approximations for the relaxation time spectrum $H(\tau)$: (a) from the stress relaxation modulus $G(t)$ and (b) from the real and imaginary parts G_1 and G_2 respectively of the complex modulus $G(\omega)$.*

Figure 5.19 shows that the relaxation time spectrum can be determined directly from the gradient of plots of the relaxation modulus or the dynamic modulus G_1 versus logarithm of time, or from G_2 even more directly.

Complementary relationships can be used to obtain the retardation time spectrum in terms of the complex compliances and the creep compliance.

5.4.1 Formal Representations of the Stress Relaxation Modulus and the Complex Modulus

A complete exposition of the mathematical structure of linear viscoelasticity has been given by Gross [7]. Here we will only summarise certain parts of his argument to illustrate the use of Laplace and Fourier transforms in establishing the formal connections between various viscoelastic functions:

1. *The stress relaxation modulus.* This modulus is a continuous, decreasing function that goes to zero at infinite time. In Gross' nomenclature, it is represented in integral form as

$$G(t) = [G_r] + \int_0^\infty \overline{\beta}\,\overline{F}(\tau)\exp\frac{-t}{\tau}\,\mathrm{d}\tau, \tag{5.39}$$

where $\overline{F}(\tau)\mathrm{d}\tau$ is the relaxation spectrum, and $\overline{\beta}$ is a normalisation factor such that

$$\int_0^\infty \overline{F}(\tau)\mathrm{d}\tau = 1, \overline{\beta} = G(0).$$

This equation, in terms of our models, represents an infinite series of Maxwell elements and it is formally identical to Equation (5.20).

It can be transformed into a Laplace integral or Laplace transform by putting $1/\tau = s$, the relaxation frequency, and introducing a frequency function $\overline{N}(s)\mathrm{d}s$ defined as

$$\overline{N}(s) = \frac{\overline{\beta}\,\overline{F}(1/s)}{s^2}.$$

Thus

$$G(t) = [G_r] + \int_0^\infty \overline{N}(s)e^{-ts}\mathrm{d}s. \tag{5.40}$$

The importance of this representation is that when $G(t)$ has been determined, the relaxation time spectrum can be found, in principle, by standard methods for the inversion of the Laplace integral. In practice this requires computation methods, as it is not usually possible to find an analytical expression to fit the stress relaxation modulus.

The Alfrey approximation is now given by putting

$$e^{-ts} = 1 \quad \text{for} \quad s \le 1/t$$

and

$$e^{-ts} = 0 \quad \text{for} \quad s > 1/t$$

and

$$G(t) = [G_r] + \int_0^{1/t} \overline{N}(s)\mathrm{d}s. \tag{5.41}$$

2. *The complex modulus.* The Boltzmann Superposition Principle gives us

$$\sigma(t) = [G_r e(t)] + \int_{-\infty}^{\infty} G(t - \tau)\frac{\mathrm{d}e(\tau)}{\mathrm{d}\tau}\mathrm{d}\tau.$$

Put $e(\tau) = e_0 e^{i\omega t}$. Then

$$\sigma(t) = [G_r e(t)] + i\omega \int_{-\infty}^{t} G(t - \tau)e_0 e^{i\omega \tau}\mathrm{d}\tau. \tag{5.42}$$

Put $t - \tau = T$. Then

$$\sigma(t) = [G_r e(t)] + i\omega \int_0^{\infty} G(T)e^{-i\omega t}\mathrm{d}T\,e_0 e^{i\omega t}. \tag{5.43}$$

Now $e(t) = e_0 e^{i\omega t}$. Thus

$$\frac{\sigma(t)}{e(t)} = [G_r] + i\omega \int_0^{\infty} G(\tau)e^{-i\omega \tau}\mathrm{d}\tau = G^*(\omega),$$

the complex modulus, where we have changed the dummy variable from T back to τ. Therefore

$$G_1(\omega) = \omega \int_0^{\infty} G(\tau)\sin \omega\tau\,\mathrm{d}\tau \tag{5.44}$$

and

$$G_2(\omega) = \omega \int_0^{\infty} G(\tau)\cos \omega\tau\,\mathrm{d}\tau, \tag{5.45}$$

where $G^*(\omega) = (G_r + G_1) + iG_2$. Equations (5.44) and (5.45) are one-sided Fourier transforms.

Inversion gives the stress relaxation modulus

$$G(t) = \frac{2}{\pi}\int_0^{\infty} \frac{G_1(\omega)}{\omega}\sin \omega t\,\mathrm{d}\omega \tag{5.46}$$

and

$$G(t) = \frac{2}{\pi} \int_0^\infty \frac{G_2(\omega)}{\omega} \cos \omega t \, d\omega. \tag{5.47}$$

These equations imply a relationship between $G_1(\omega)$ and $G_2(\omega)$, the dispersion or compatibility relations, which are the viscoelastic analogue of the Kramers–Krönig relations for optical dispersion and magnetic relaxation.

5.4.2   Formal Representations of the Creep Compliance and the Complex Compliance

Similar relationships hold for the creep compliance and complex compliance to those derived for the stress relaxation modulus and the complex modulus. The details of the derivations will not be given, but the results are quoted for completeness.

1. *Creep compliance*. In this case the *rate of change* of creep compliance is expressed as a Laplace integral. Thus

$$\frac{dJ(t)}{dt} = \int_0^\infty s N(s) e^{-ts} \, ds, \tag{5.48}$$

   where

$$N(s) = \frac{F(1/s)}{s^2}, \quad s = \frac{1}{\tau}$$

   and $F(\tau)d\tau$ is the distribution of retardation times. Note that $N(s) \neq \overline{N}(s)$, and that $F(\tau) \neq \overline{F}(\tau)$, i.e. the retardation time spectrum is not identical to the relaxation time spectrum.

2. *Complex compliance*. Here it is found that

$$J_1(\omega) = \int_0^\infty \frac{dJ(\tau)}{d\tau} \cos \omega \tau \, d\tau \tag{5.49}$$

   and

$$J_2(\omega) = - \int_0^\infty \frac{dJ(\tau)}{d\tau} \sin \omega \tau \, d\tau. \tag{5.50}$$

Again both $J_1(\omega)$ and $J_2(\omega)$ are Fourier transforms, which may be inverted to give the creep compliance in terms of the components of the complex compliance. The inversion formulae both give the creep compliance, implying a relationship between the real and imaginary parts of the complex compliance, as in the case of the complex modulus.

5.4.3   The Formal Structure of Linear Viscoelasticity

Gross [7] has discussed the formal structure of the theory of linear viscoelasticity. A summary of his treatment will be presented here, as a suitable conclusion to our discussion.

There are two groups of experiments:

Group 1: Experiments that take place under a given stress, either fixed or alternating. These define the creep compliance or the complex compliance.

Group 2: Experiments that take place under a given strain, either fixed or alternating. These define the stress relaxation modulus or the complex modulus.

Within each group, the viscoelastic functions exist in three levels:

(a) Top level	Complex compliance	(Group 1)
	Complex modulus	(Group 2)
(b) Medium level	Creep function	(Group 1)
	Relaxation function	(Group 2)
(c) Bottom level	Retardation spectrum	(Group 1)
	Relaxation spectrum	(Group 2)

To go *up* a level, one applies either a Laplace transform or a one-sided complex Fourier transform.

To go *down* a level, one applies either an inverse Laplace transform or an inverse Fourier transform.

The relationships between the groups vary in complexity. At the top level, the complex compliance is merely the inverse of the complex modulus. The relationships between the creep function and the relaxation function and between the retardation spectrum and the relaxation spectrum involve integral equations and integral transforms respectively.

5.5   The Relaxation Strength

A concept that is of value in considering the relationship of viscoelastic behaviour to physical and chemical structure is that of 'relaxation strength'. In a stress relaxation experiment, the modulus relaxes from a value G_u at very short times to G_r, at very long times (Figure 5.20(b)). Similarly in a dynamic mechanical experiment, the modulus changes from G_r, at low frequencies to G_u at very high frequencies. G_u is the unrelaxed modulus and G_r is the relaxed modulus (Figure 5.20(c)).

This behaviour is shown by the standard linear solid of Figure 5.20(a). Consider in turn the behaviour in the initial unrelaxed state, and in the final relaxed state.

1. A total applied stress σ is given in terms of the initial unrelaxed strain e_1 by adding the stresses in both springs. Thus

$$\sigma = G_r e_1 + (G_u - G_r)e_1 = G_u e_1$$

and the initial unrelaxed strain

$$e_1 = \frac{\sigma}{G_u} = \frac{\sigma}{\text{Unrelaxed modulus}}$$
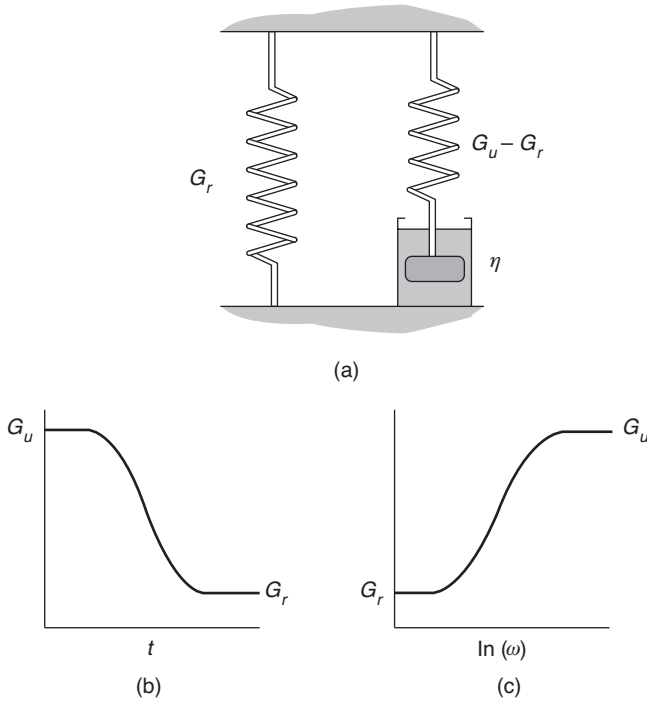
Figure 5.20 *The standard linear solid (a) gives a response in a stress relaxation test shown in (b) and in a dynamic mechanical test in (c). G_u is the unrelaxed modulus and G_r, the relaxed modulus.*

2. The final relaxed strain e_2 is given in terms of an applied stress σ by

$$e_2 = \frac{\sigma}{G_r} = \frac{\sigma}{\text{Relaxed modulus}}$$

because the spring $(G_u - G_r)$ is now ineffective. The relaxation strength is conventionally defined as

$$\frac{\text{Final strain} - \text{Initial strain}}{\text{Initial strain}}.$$

This is

$$\frac{e_2 - e_1}{e_1} = \left\{ \frac{1}{G_r} - \frac{1}{G_u} \right\} G_u = \frac{G_u - G_r}{G_r} \tag{5.51}$$

The equation for the standard linear solid in Figure 5.20(a) is

$$\sigma + \tau_1 \frac{\mathrm{d}\sigma}{\mathrm{d}t} = G_r \left\{ e + \tau_2 \frac{\mathrm{d}e}{\mathrm{d}t} \right\}, \tag{5.52}$$

where

$$\tau_1 = \frac{\eta}{G_u - G_r} \quad \text{and} \quad \tau_2 = \frac{\tau_1}{G_r}.$$

Then for dynamic mechanical measurements it may be shown that

$$G_1(\omega) = \frac{G_r\left(1 + \omega^2\tau_1\tau_2\right)}{1 + \omega^2\tau_1^2} = \frac{G_r + \omega^2\tau^2 G_u}{1 + \omega^2\tau^2} \tag{5.53}$$

$$G_2(\omega) = \frac{G_r(\tau_2 - \tau_1)\omega}{1 + \omega^2\tau_1^2} = \frac{(G_u - G_r)\omega\tau}{1 + \omega^2\tau^2} \tag{5.54}$$

and

$$\tan\delta = \frac{(\tau_2 - \tau_1)\omega}{1 + \omega^2\tau_1\tau_2} = \frac{(G_u - G_r)\omega\tau}{G_r + \omega^2\tau^2 G_u}, \tag{5.55}$$

where we have put

$$\tau = \tau_1 = \frac{\eta}{G_u - G_r}.$$

The following relationships then hold:

$$\tan\delta_{max}(\omega^2\tau^2 = G_r/G_u) = \frac{G_u - G_r}{2\sqrt{G_u G_r}} \tag{5.56}$$

$$G_{2_{max}}(\omega^2\tau^2 = 1) = \frac{G_u - G_r}{2} \tag{5.57}$$

$$\int_{-\infty}^{\infty} G_2(\omega)\mathrm{d}(\ln\omega) = \frac{\pi}{2}(G_u - G_r) \tag{5.58}$$

$$\int_{-\infty}^{\infty} \tan\,\mathrm{d}(\ln\omega) = \frac{\pi}{2}\frac{(G_u - G_r)}{\sqrt{G_u G_r}}. \tag{5.59}$$

All the relationships defined above are proportional to $G_u - G_r$, and hence to the relaxation strength. $\tan\delta_{max}$ and $\int_{-\infty}^{\infty}\tan\delta\mathrm{d}(\ln\omega)$ are closest to our original definition in being normalised to a dimensionless quantity. This provides some formal justification for the use of $\tan\delta$ rather than G_2 for estimating the relaxation strength to correlate with structural parameters [8].

References

1. Boltzmann, L. (1876) Zur Theorie der elastischen Nachwirkung. *Pogg. Ann. Phys. Chem.*, **7**, 624.
2. Lee, E.H. (1960) Viscoelastic stress analysis in *Proceedings of the First Symposium on Naval Structural Mechanics*, (eds J.N. Goodier and J.F. Hoff), Pergamon Press, Oxford, p. 456.
3. Christensen, R.M. (2003) *Theory of Viscoelasticity*, 2nd edn, Dover Publications, Inc., Mineola, NY.

4. Zener, C. (1948) *Elasticity and Anelasticity of Metals*, Chicago University Press, Chicago.
5. Alfrey, T. and Doty, P. (1945) The methods of specifying the properties of viscoelastic materials. *J. Appl. Phys.*, **16**, 700.
6. Alfrey, T. (1948) *Mechanical Behaviour of High Polymers*, John Wiley & Sons, New York.
7. Gross, B. (1953) *Mathematical Structure of the Theories of Viscoelasticity*, Hermann, Paris.
8. Gray, R.W. and McCrum, N.G. (1968) On the γ relaxations in linear polyethylene and polytetrafluoroethylene. *J. Polymer Sci. B. Polym. Lett.*, **6**, 691.

Further Reading

Drozdov, A.D. (1998) *Mechanics of viscoelastic solids*, John Wiley & Sons, Chichester.
Ferry, J.D. (1980) *Viscoelastic Properties of Polymers*, John Wiley & Sons, New York.
Shaw, M.T. and MacKnight, W.J. (2005) *Introduction to Polymer Viscoelasticity*, 3rd edn, John Wiley & Sons, Hoboken.
Wineman, A.S. and Rajagopal, K.R. (2000) *Mechanical Response of Polymers*, Cambridge University Press, New York.

6

The Measurement of Viscoelastic Behaviour

For a satisfactory understanding of the viscoelastic behaviour of polymers, data are required over a wide range of frequency (or time) and temperature. The number of experiments required can sometimes be reduced by using either the equivalence of creep, stress relaxation and dynamic mechanical data (described in Chapter 5) or the equivalence of time and temperature as variables (to be discussed in Chapter 7). Nevertheless a variety of techniques need to be combined to cover a wide range of both time and temperature.

There are five main classes of experiment, which will be discussed in turn:

1. Transient measurements: creep and stress relaxation
2. Low-frequency vibrations: free oscillation methods
3. High-frequency vibrations: resonance methods
4. Forced vibration non-resonance methods
5. Wave propagation methods.

The approximate frequency scale for each technique is indicated in Figure 6.1.

6.1 Creep and Stress Relaxation

Reliable creep and stress relaxation data are obtainable only if the specimens are well defined and strictly comparable. As deformations and deformation rates are usually quite small, if linearity is to hold then precision measurements are required: conditions that may be difficult to attain throughout the highly significant short-time regime.

6.1.1 Creep Conditioning

Leaderman [1] was the first worker to emphasise that specimens must be cyclically conditioned at the highest temperature of measurement in order to obtain reproducible
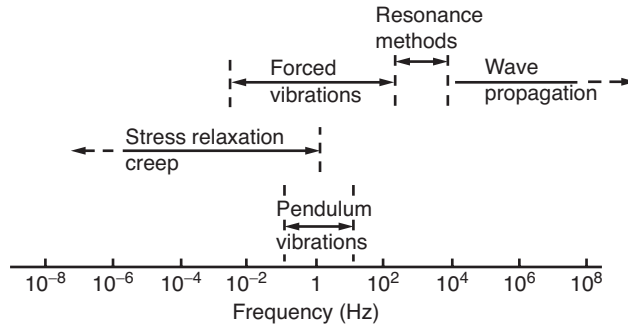
Figure 6.1   *Approximate frequency scales for different experimental techniques. (Reproduced from Becker (1969) Mater. Plast. Elast., **35**, 1387. Copyright (1969).)*

measurements in creep and recovery. Each cycle consists of application of the maximum load for the maximum period of loading, followed by a recovery period after unloading of about 10 times the loading period; cycling must be continued until reproducibility is obtained.

The conditioning procedure has two major effects on the creep and recovery behaviour. First, subsequent creep and recovery responses under a given load are identical; i.e., the sample has lost its 'long-term' memory and now only remembers loads applied in its immediate past history. Secondly, after the conditioning procedure, the deformation produced by any loading programme is almost completely recoverable provided that the recovery period is about 10 times the period during which loads are applied. For tensile creep measurements over a wide range of temperature, greater elaboration is required.

6.1.2   Specimen Characterisation

Many early experiments on the viscoelastic behaviour of polymers were unsatisfactory because the specimens were inadequately characterised, so that 'like' was not compared with 'like'.

Average molecular mass and its distribution are both critical parameters, and all polymers contain processing and stabilising additives, which can sometimes have a significant effect on the response to stress and strain, particularly at temperatures well above that of the laboratory.

The physical structure of the polymer, in terms of morphology, crystallinity and molecular orientation, will also be important and should be well characterised.

6.1.3   Experimental Precautions

Measurements made in the vicinity of a major relaxation region, for instance creep tests on isotactic polypropylene close to room temperature, are sensitive to small changes in temperature, so that a controlled temperature environment is essential. For some polymers, such as nylon, it is also essential to control the humidity, because the presence of moisture in the polymer has a dramatic effect on the mechanical behaviour [2] (in nylon by reducing the effect of interchain hydrogen bonding). Whenever possible, several nominally identical
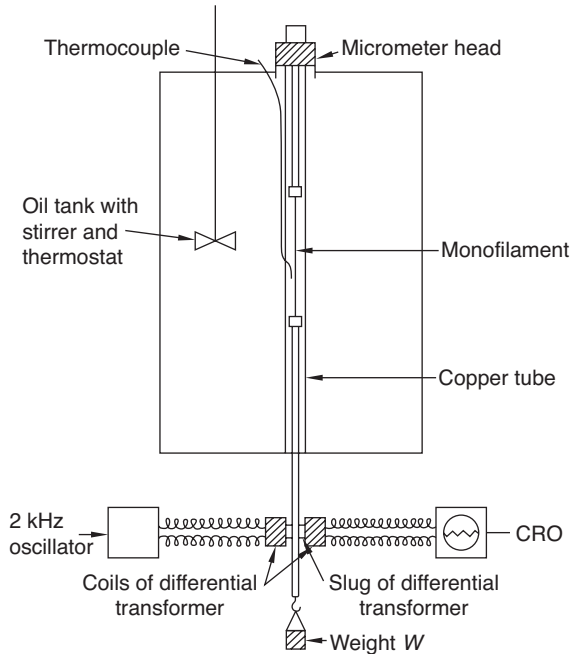
Figure 6.2   *High-temperature tensile creep testing apparatus. (Reproduced from Leaderman, H. (1962) Large longitudinal retarded elastic deformation of rubberlike network polymers. Trans. Soc. Rheol., 6, 361. Copyright (1962) Society of Rheology.)*

specimens should be examined, to confirm that inter-specimen variability is small compared with the effects under examination.

For creep testing, gravitational loading is usually used to provide the constant force, with specimen extension monitored by linear displacement transducers. An example is shown in Figure 6.2.

In the linear viscoelastic region, strains are unlikely to exceed 1 per cent, so that the change of cross section, and hence stress, with strain will be small. At larger strains, the effective load should be reduced in a manner proportional to the decrease in cross-sectional area, to maintain a constant stress. Leaderman [3] used the device illustrated in Figure 6.3, in which a flexible tape (B) attached to the specimen (A) is wound round the periphery of a cylindrical drum C. A similar tape F, attached to a profiled cam D, supports a fixed mass E. As the specimen extends under load, the moment of E decreases according to the cam profile.

The creep and relaxation plots in Figures 5.2 and 5.4 are idealised because, as already mentioned, the immediate response is no more than that occurring before the first measurement after loading, and it is evident that the relevant time interval should be no longer than necessary. For instance, if the load is applied very slowly during a stress relaxation experiment, a low value of maximum stress will be obtained (Figure 6.4). Conversely, too rapid a stress application will result in the complications of dynamic loading (Figure 6.5). This point is of particular importance, because some attempts to relate viscoelasticity to molecular parameters are particularly dependent on the short-time response. As explained in Section 6.2, some of the difficulties concerned with the early stages of deformation can be removed by employing time–temperature equivalence.
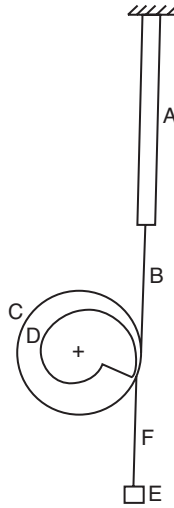
Figure 6.3   *Cam arrangement for creep under constant stress. (Reproduced from Leaderman, H. (1962) Large longitudinal retarded elastic deformation of rubberlike network polymers. Trans. Soc. Rheol., **6**, 361. Copyright (1962) Society of Rheology.)*
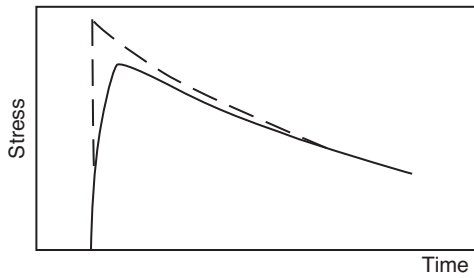
Figure 6.4   *Effect on stress relaxation of the strain being applied slowly: (- - -) ideal; (—) actual.*
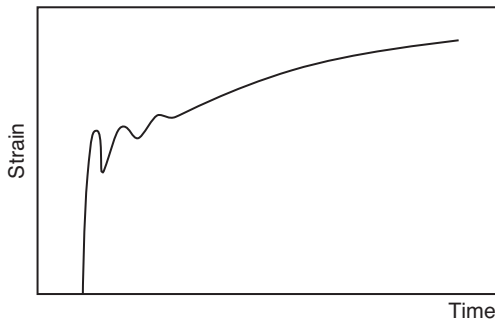
Figure 6.5   *Damped vibrations resulting from rapid loading in a creep experiment.*
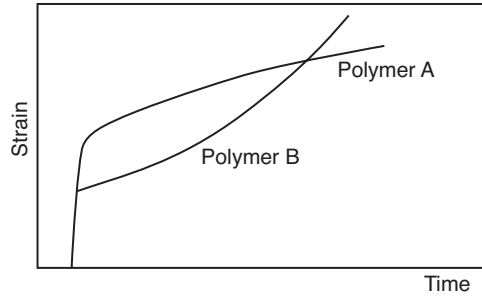
Figure 6.6 *Short-term creep behaviour at a single temperature implies nothing about the eventual deformation.*

Specimens in extensional and torsional tests must be firmly clamped at their ends. However, the stresses in the clamp region will differ greatly from those in the bulk of the specimen and, if the complete length of the specimen is measured, end effects can be ignored only where the length is at least 10 times the diameter. For oriented samples, end effects are even more important. As an approximate guide, it is reasonable to consider that the ratio of length to diameter should be greater than $10 \sqrt{E/G}$, where E and G are the Young's modulus (in the fibre direction) and the torsional modulus respectively. A more satisfactory technique for high accuracy with robust specimens is to use an extensometer attached to the specimen away from its ends, strain being converted into an electrical signal by a displacement transducer [4]. For less robust specimens, non-contacting laser methods are available [5].

In stress relaxation measurements, as in standard mechanical testing devices, changing stress may be monitored using a strain gauge load cell. Since these devices rely on changes in strain, it must be confirmed that they are very stiff in comparison with the specimen so that the specimen strain is held effectively constant.

A range of measurement equipment is described and illustrated in the books by Turner and Godwin [6] and Ward [7].

Where materials are being examined for their suitability for specific applications it is essential that creep measurements are performed over an extended timescale. It is possible that a material that shows good short-term creep shows accelerated creep at longer times (Figure 6.6). As discussed later, comparable problems may occur for materials that are viscoelastically non-linear, so that the recovery response is very different from that during the early stages of creep.

6.2   Dynamic Mechanical Measurements

A variety of techniques are required capable of covering wide ranges of both time and temperature (Figure 6.1). Free oscillation pendulum methods, which have the advantage of simplicity, are confined to the frequency range 10^{-1}–10 Hz. Forced vibration techniques, although more complicated, may yield higher reproducibility and can extend the frequency range by a further decade on either side, linking up with creep and stress relaxation at the

lowest frequencies and resonance methods at the higher end. The latter, which are very sensitive to inter-specimen variability, are important above 10 kHz.

6.2.1   The Torsion Pendulum

The simplest device consists of a specimen of circular cross section suspended vertically with its upper end rigidly clamped [8]. Its lower end supports a disc, or preferably a bar, fitted with adjustable weights (Figure 6.7), whose distance from the axis can be altered thus changing the moment of inertia (I) and the period of oscillation. When the bar is twisted and released, the oscillations gradually decrease in amplitude, and the logarithmic decrement Λ, the natural logarithm of the ratio of amplitude of successive oscillations, is recorded.

   Because the specimen is loaded by the inertia bar, the specimen is subjected to tensile as well as torsional stresses, which perturb the nominally free vibrations. For more precise work, the specimen can be mounted as in Figure 6.8, with the inertia bar clamped at its upper end. The assembly is then suspended by an elastic wire or ribbon, which has a negligible effect on damping.

   For an *elastic* rod, the equation of motion is $I\ddot{\theta} + \tau\theta = 0$, where τ is the torsional rigidity of the rod, which is related to the shear modulus G through

$$\tau = \frac{\pi r^4 G}{2l},$$

where l is the length and r is the radius of the rod. The elastic system executes simple harmonic motion with an angular frequency

$$\omega = \sqrt{\frac{\tau}{I}} = \sqrt{\frac{\pi r^4 G}{2lI}}. \tag{6.1}$$

   The high sensitivity to sample dimensions implies that inter-specimen comparisons can be subject to large uncertainties.
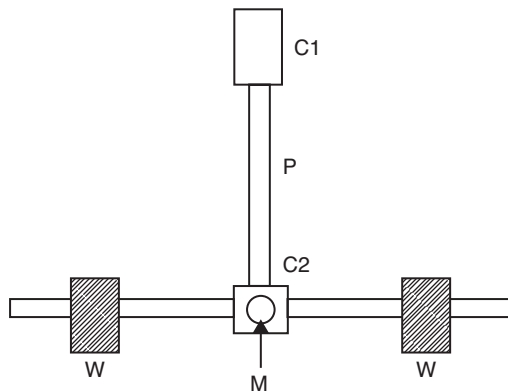
Figure 6.7   *Free vibration torsion pendulum: P, polymer specimen; C1, fixed upper clamp; C2, lower clamp fixed to inertia bar; W, sliding masses to change moment of inertia; M, mirror to reflect light beam.*
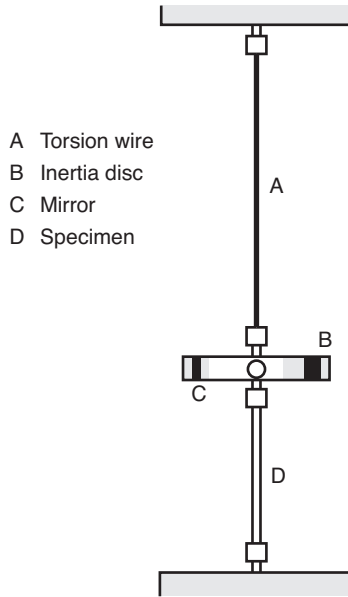
Figure 6.8 *Apparatus for measuring torsional rigidity at low frequencies.*

When the vibrations are damped the amplitude decreases with time, but with light damping there is only a small effect on the period

$$\left(\frac{2\pi}{\omega} \right).$$

For linear viscoelastic solids, the torsional modulus is complex, and may be written as $G^* = G_1 + iG_2$. When the damping is small, it is justified to replace G_1 for G in Equation (6.1), hence

$$\omega^2 = \frac{\pi r^4 G_1}{2lI}. \tag{6.2}$$

The logarithmic decrement can then be related to the specific loss (Equation (5.30)) and hence $\tan \delta$.

$$\Lambda = \ln \left(\frac{A_n}{A_{n+1}} \right),$$

where A_n denotes the amplitude of the nth oscillation. For small damping

$$\Lambda = \ln \left(1 + \frac{\Delta A}{A_n} \right) = \frac{\Delta A}{A_n} - \frac{1}{2} \frac{\Delta A^2}{A_n^2}.$$

Hence

$$\Lambda = \frac{1}{2} \left(\frac{A_n^2 - A_{n+1}^2}{A_n^2} \right).$$

But A^2 is proportional to stored energy, giving

$$\Lambda = \frac{1}{2}\frac{\Delta E}{E} = \pi \tan \delta \tag{6.3}$$

from which $G_2 = G_1 \tan \delta$ can be obtained.

6.2.2   Forced Vibration Methods

Free vibration methods suffer from the disadvantage that the frequency of vibration depends on the stiffness of the specimen, which varies with temperature, so that forced vibration methods are to be preferred when the frequency and temperature dependence of viscoelastic behaviour are to be investigated.

   As indicated in Section 5.3 above, when a sinusoidal strain is imposed on a linear viscoelastic body, the strain lags behind the stress by the phase angle δ, which determines the degree of damping. The strains must be low enough for linearity to apply, and the strain must at all times remain positive. In practice, the strain amplitude is typically ± 0.5 per cent, superposed on an initial extension slightly in excess of 0.5 per cent, to allow for some degree of stretch during the experiment. The specimen must be short enough for there to be no appreciable variation in stress along its length, that is the length must be short compared with the wavelength of the stress waves. Assuming that the lowest value of the modulus is 10^7 Pa for a specimen of density 10^3 kg/m^3, the longitudinal wave velocity is 10^2 m/s. At 100 Hz, the wavelength of the stress waves is 1 m, which suggests that at that frequency the upper limit on specimen length is about 0.1 m. As the stress must never vanish, a lower limit to frequency is set by the stress relaxation time.

   Typically strain and stress are measured by unbonded strain-gauge transducers, the signals from which are then fed to a phase meter, which provides a direct reading of the relative amplitudes and the phase difference, hence giving values of the modulus and $\tan \delta$ [9].

6.2.3   Dynamic Mechanical Thermal Analysis (DMTA)

There are a number of commercial machines available for dynamic testing under varying temperature conditions. An actuator imposes an oscillatory (linear or angular) displacement, and typically a strain-gauge load cell measures force. Testing is frequently in bending mode, producing results that may be difficult to interpret in terms of viscoelasticity owing to the non-uniform nature of the stress field. However, such testing is useful in locating the temperatures of relaxation transitions (see Chapter 10). Temperature ranges are typically -150 to $600°$C, and frequency ranges are 10^{-6} to 200 Hz. In some cases, a single machine can operate in a range of testing modes—bend, tension, compression, shear and torsion— by the use of different loading fixtures. Modulus and $\tan \delta$ data (see Chapter 5) are routinely derived using the manufacturer's proprietary software. Recent examples are due to Damman and Buijs [10], investigating liquid-crystal polymer in tension; Beaudoir, Bergeret and Quantin [11], examining the properties of a polybutylene terephthalate composite in compression–tension; and Zhou and Chudnovsky [12], comparing drawn and undrawn polycarbonate in torsion. A commercial DMTA set-up is shown in Figure 6.9.

Figure 6.9 *DMTA testing heads for various modes: (a) dual cantilever, (b) three-point bend, (c) tension, (d) compression and (e) shear sandwich (showing two specimens). Photographs by TA Instruments, Delaware USA. (Reproduced from Hillier, K.W. and Kolsky, H. (1949) An investigation of the dynamic elastic properties of some high polymers.* Proc. Phys. Soc. B, **62**, 111. *Copyright (1949) Institute of Physics.)*

6.3   Wave-Propagation Methods

Wave-propagation methods are in three broad categories:

1. In the kilohertz frequency range.
2. In the megahertz frequency range: ultrasonic methods.
3. In the gigahertz frequency range: Brillouin spectroscopy.

6.3.1   The Kilohertz Frequency Range

At frequencies in the kilohertz range, the wavelength of the stress waves is of the order of the length of a viscoelastic specimen. Typically [13], a thin monofilament is stretched longitudinally, with one end attached to a stiff massive diaphragm, such as a loudspeaker. A piezoelectric crystal pickup then detects the changes in signal amplitude and phase along the length of the specimen. As shown in Figure 6.10 for low-density polyethylene, a plot of the phase (θ) against distance (l) takes the form of damped oscillations about the line $\theta = kl$, where k is the propagation constant.

Where the attenuation coefficient α is small, it has been shown [14] that $V_{max}/V_{min} = (\alpha l + \beta)$, where V is the signal amplitude. A plot of

$$\tanh^{-1}\left(\frac{V_{max}}{V_{min}}\right)$$

against l then gives a line of slope α.

It is possible to relate α and k to the storage and loss moduli E_1 and E_2, and to $\tan\delta$. For a filament of density ρ, in which c is the longitudinal wave velocity

$$E_1 = \frac{\omega^2}{k^2}\rho, \quad E_2 = \frac{2\alpha c^3 \rho}{\omega}$$
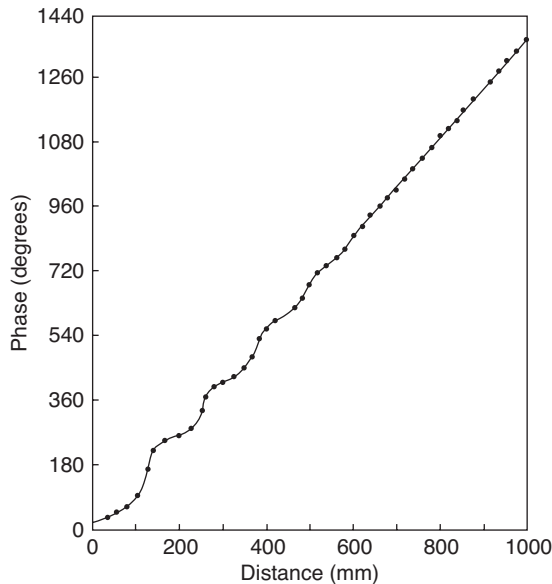
Figure 6.10   *The variation in phase angle with distance along a polyethylene monofilament for transmission of sound waves at 3000 Hz. (Reproduced from Chan, O.K., Chen, F.C., Choy, C.L., et al. (1978) The elastic constants of extruded polypropylene and polyethylene terephthalate J. Phys. D,* **11***, 617. Copyright (1978) Institute of Physics.)*

and

$$\tan \delta = \frac{2\alpha c}{\omega}.$$

For further information the reader is referred to review articles by Kolsky [15].

6.3.2 The Megahertz Frequency Range: Ultrasonic Methods

Measurements of the velocity and attenuation of elastic waves at ultrasonic frequencies are important, especially for oriented polymers and composites. Compact solid specimens with dimensions of the order of 10 mm are required.

In a typical application of this technique, Chan, Chen and Choy [16] measured the elastic constants of a uniaxially oriented rod 12 mm in diameter, by cutting discs of thickness 4–8 mm parallel, perpendicular and at 45° to the axis of the rod (Figure 6.11). Quartz transducers were bonded to the discs, so that longitudinal and transverse waves were propagated along the geometrical axes of each disc. In principle, nine different velocities v_{ab} can be measured, where a refers to the direction of polarisation and b to the direction of wave propagation. For a specimen of density ρ, we can then define $Q_{ab} = \rho v_{ab}^2$, where Q_{ab} is either an elastic stiffness constant or a linear combination of such constants. Velocities were measured using the pulse echo-overlap technique [17], and tan δ was obtained by making attenuation measurements [18].
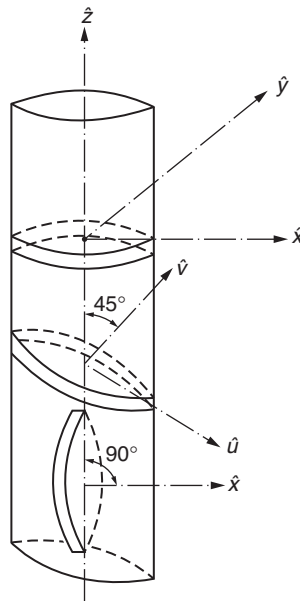
Figure 6.11 *Schematic diagram illustrating the sample discs employed in ultrasonic measurements. (Reproduced from Dyer, S.R.A., Lord, D., Hutchinson, I.J. et al. (1992) Elastic anisotropy in unidirectional fiber reinforced composites. J. Phys. D, **25**, 66. Institute of Physics.)*
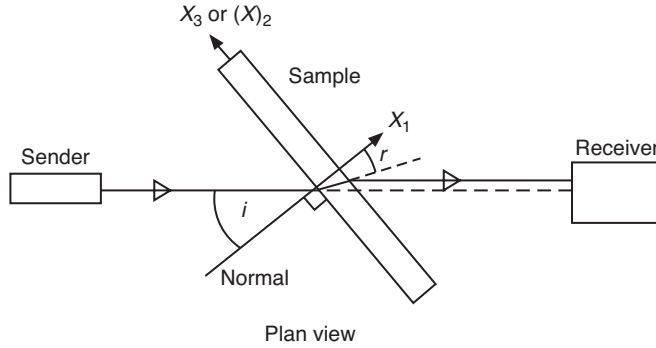
Figure 6.12   *Schematic diagram showing layout of ultrasonic apparatus used for measurement of elastic constants.*

An alternative approach [19, 20] is to immerse a specimen, thickness d, in a water-filled tank fitted with both a transmitter and a receiver of ultrasonic waves, and measure the change (τ) in transit time with and without the specimen in the beam. If V is the velocity in the polymer and V_w that in the water, we have

$$\frac{1}{V} = \frac{1}{V_w} - \frac{\tau}{d}. \tag{6.4}$$

The various wave velocities, which can be derived from measurements made over a range of incident angles, are related to the elastic stiffness constants.

In a variation in the above-mentioned method, Wright, Faraday and White [21] detected the component of the incident beam that was reflected from the immersed specimen and hence measured the critical angle of incidence.

More recently, this technique has been developed to measure the anisotropy of uniaxial composites [22]. A specimen of uniform thickness, placed between the transmitting and receiving heads in a water-filled container, could be rotated about a vertical axis to change the angle of incidence and hence the direction of the beam in the sample (Figure 6.12). The velocity V and angle of refraction r of the wave are then calculated following the method of Markham [19]. Let X_1 and X_2 axes define the isotropic plane perpendicular to the fibre axis. It can then be shown [23] that for quasi-tensile waves propagating in the X_1–X_3 plane at an angle r to the X_1 axis, with the specimen axis X_2 vertical,

$$V_t^2 = \frac{B_{11} + B_{33} + \left[(B_{33} - B_{11})^2 + 4B_{13}^2\right]^{1/2}}{2\rho}$$

and for quasi-shear waves

$$V_s^2 = \frac{B_{11} + B_{33} - \left[(B_{33} + B_{11})^2 + 4B_{13}^2\right]^{1/2}}{2\rho}.$$

where ρ is the specific gravity of the specimen.

The elastic stiffness constants C_{ij} are obtained from

$$B_{11} = C_{11} \cos^2 r + C_{44} \sin^2 r$$
$$B_{33} = C_{33} \sin^2 r + C_{44} \cos^2 r.$$
$$B_{13} = (C_{44} + C_{13}) \sin r \cos r$$

6.3.3   The Hypersonic Frequency Range: Brillouin Spectroscopy

Brillouin spectroscopy enables the elastic constants of polymers to be determined at frequencies of several gigahertz, i.e. three orders of magnitude higher than those pertaining to ultrasonic measurements, which are known as hypersonic frequencies.

The principle of the method is to use Fabry-Perot spectroscopy to measure the frequency shift in laser light scattered through 90° after passage through a parallel polymer sheet.

The hypersonic velocity V_s is obtained from the equation

$$V_s = \frac{f_B \lambda_i}{\sqrt{2}},$$

where λ_i is the laser wavelength and f_B is the measured Brillouin shift.

For an isotropic polymer, the hypersonic sound velocity is determined as a function of direction, and the elastic constants are obtained by fitting the data to a set of equations known as the Christoffel equations, which essentially relate the values of V_s to the stiffness constants C_s through $C_s = \rho V_s^2$, where ρ is the density [24]. For a detailed discussion of this technique, the reader is referred to papers by Kruger, Pietralla and co-workers. [25–27]. More recently, the development of non-scanning Fabry—Perot interferometry has made possible faster acquisition of data to enable study of liquid–glass transitions [28].

References

1. Leaderman, H. (1943) *Elastic and Creep Properties of Filamentous Materials and Other High Polymers*, Textile Foundation, Washington, DC.
2. Hadley, D.W., Pinnock, P.R. and Ward, I.M. (1969) Anisotropy in oriented fibres from synthetic polymers. *J. Mater. Sci.*, **4**, 152.
3. Leaderman, H. (1962) Large longitudinal retarded elastic deformation of rubberlike network polymers. *Trans. Soc. Rheol.*, **6**, 361.
4. Ward, I.M. (1964) The temperature dependence of extensional creep in polyethylene terephthalate. *Polymer*, **5**, 59.
5. Spathis, G. and Kontou, E. (1999) An experimental and analytical study of the large strain response of glassy polymers with a noncontact laser extensometer. *J. Appl. Polym. Sci.*, **71**, 2007.
6. Turner, S., and Godwin, G. (1983) *Mechanical Testing of Plastics*, 2nd edn, Plastics and Rubber Institute, London.
7. Ward, I.M. (1983) *Mechanical Properties of Solid Polymers*, 2nd edn, John Wiley & Sons, Chichester.

8. Schmieder, K. and Wolf, K. (1952) Uber die Temperaturabhangigkeit und Frequenzabhangigkeit des mechanischen Verhaltens einiger hochpolymerer Stoffe. *Kolloidzeitschrift*, **127**, 65.

9. Pinnock, P.R. and Ward, I.M. (1963) Dynamic mechanical measurements on polyethylene terephthalate. *Proc. Phys. Soc.*, **81**, 261; Takayanagi, M. (1965) in *Proceedings of Fourth International Congress on Rheology*, Part 1, Interscience, New York, p. 161; Becker, G.W. (1969) *Mat. Plast. Elast.*, **35**, 1387.

10. Damman, S.B. and Buijs,J.A.H.M. (1994) Liquid-crystalline main-chain polymers with a poly(*p*-phenylene terephthalate) backbone. 5. Dynamic-mechanical behavior of the polyester with dodecyloxy side-chains. *Polymer*, **35**, 2359.

11. Beaudoin, O., Bergeret, A., Quantin, J.C. *et al*. (1998) Viscoelastic behaviour of glass beads reinforced poly(butylene terephthalate): experimental and theoretical approaches. *Compos. Interfaces*, **5**, 543.

12. Zhou, Z., Chudnovsky, A. and Bodnyak C.P. (1995) Cold-drawing (necking) behavior of polycarbonate as a double glass-transition. *Polym. Eng. Sci.*, **35**, 304.

13. Hillier, K.W. and Kolsky, H. (1949) An investigation of the dynamic elastic properties of some high polymers. *Proc. Phys. Soc. B*, **62**, 111; Kolsky, H. (1960) *Structural Mechanics*, Pergamon Press, Oxford.

14. Hillier, K.W. (1961) Measurement of dynamic elastic properties, in *Progress in Solid Mechanics* (eds I.N. Sneddon and R. Hill), North-Holland, Amsterdam, pp. 199–243.

15. Kolsky, H. (1958) The propagation of stress waves in viscoelastic solids. *Appl. Mech. Rev.*, **11**, 9; (1960) *Structural Mechanics*, Pergamon Press, Oxford.

16. Chan, O.K., Chen, F.C., Choy, C.L. *et al*. (1978) The elastic constants of extruded polypropylene and polyethylene terephthalate. *J. Phys. D*, **11**, 617.

17. Papadakis, E.P. (1964) Ultrasonic attenuation and velocity in 3 transformation products in steel. *J. Appl. Phys.*, **35**, 1474; Kwan, S.F., Chen, F.C. and Choy, C.L. (1975) Ultrasonic studies of 3 fluoropolymers. *Polymer*, **16**, 481.

18. Roderick, R.L. and Truell, R. (1952) The measurement of ultrasonic attenuation in solids by the pulse technique and some results in steel. *J. Appl. Phys.*, **23**, 267.

19. Markham, M.F. (1970) Measurement of the elastic constants of fibre composites by ultrasonics. *Composites*, **1**, 145.

20. Rawson, F.F. and Rider, J.G. (1974) Elastic constants of oriented polyvinyl-chloride. *J. Phys. D*, **7**, 41.

21. Wright, H., Faraday, C.S.N., White, E.F.T. *et al*. (1971) Elastic constants of oriented glassy polymers. *J. Phys. D*, **4**, 2002.

22. Dyer, S.R.A., Lord, D., Hutchinson, I.J. *et al*. (1992) Elastic anisotropy in unidirectional fiber reinforced composites. *J. Phys. D*, **25**, 66.

23. Musgrave, M.J.P. (1954) On the propagation of elastic waves in aeolotropic media. I. General principles. *Proc. R. Soc.*, **A226**, 339.

24. Auld, B.A. (1973) *Acoustic Fields and Waves in Solids*. John Wiley & Sons, New York, p. 211.

25. Kruger, J.K., Marx, A., Peetz, L. *et al*. (1986) Simultaneous determination of elastic and optical-properties of polymers by high-performance Brillouin spectroscopy using different scattering geometries. *Colloid Polym. Sci.*, **264**, 403.

26. Krbecek, H., Kruger, J.K. and Pietralla, M. (1993) Poisson ratios and upper bounds of intrinsic birefringence from brillouin scattering of oriented polymers. *J. Polym. Sci. Phys. Ed.*, **31**, 1477.

27. Krbecek,H.H., Kupisch,W. and Pietralla,M. (1996) A new Brillouin scattering analysis of high frequency relaxations in liquids demonstrated at the hypersound relaxation of PPG. *Polymer*, **37**, 3483–3491.
28. Ike, Y. and Kojima, S. (2006) Brillouin scattering study of polymer dynamics. *Mater. Sci. Eng.*, **A442**, 383–386.

Further Reading

Kolsky, H. (2003) *Stress Waves in Solids*, Courier Dover Publications, Mineola, New York.

7

Experimental Studies of Linear Viscoelastic Behaviour as a Function of Frequency and Temperature: Time–Temperature Equivalence

7.1 General Introduction

An introduction to the extensive experimental studies of linear viscoelastic behaviour in polymers falls conveniently into three parts, in which amorphous polymers, crystalline polymers and temperature dependence are discussed in turn.

7.1.1 Amorphous Polymers

Many of the earlier investigations of linear viscoelastic behaviour in polymers were confined to amorphous polymers. During the early 1950s R.S. Marvin [1,2] of the National Bureau of Standards, Washington, DC, coordinated the assembly of data from many laboratories who had measured the complex shear modulus and complex shear compliance of a specimen of polyisobutylene $(CH_2—CCH_3CH_3)_n$ of high relative molecular mass over a wide range of frequencies. The results, redrawn in Figure 7.1, show clearly the four regions, that is the glassy, the viscoelastic, rubbery and flow regions that are characteristic for amorphous high polymers. At high frequencies, the complex modulus has a value around 10^9 Pa. For material of high molecular mass, a plateau in modulus occurs, and appreciable molecular flow occurs only at frequencies below 10^{-5} Hz (i.e. period > 1 day).

The reader may use the *Alfrey* approximation (see Section 5.4) to derive relaxation and retardation time spectra from the data of Figure 7.1. These spectra can be approximated by a 'wedge and box' distribution (3), shown by the dotted lines in Figure 7.2.
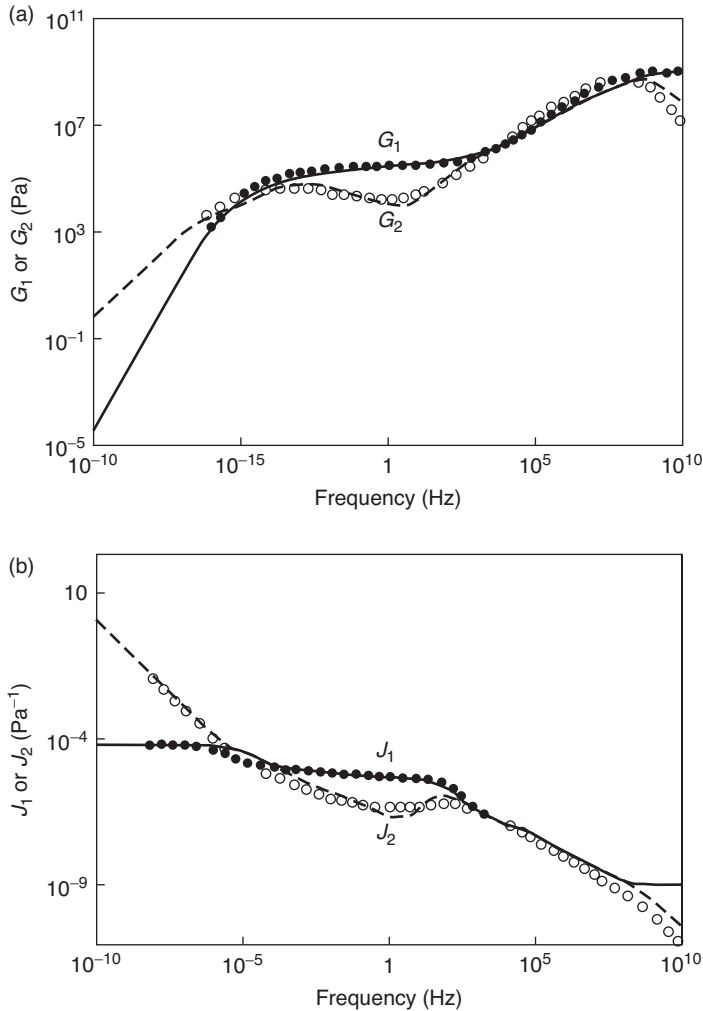
Figure 7.1   *Complex shear modulus (a) and complex shear compliance (b) for 'standard' polyisobutylene reduced to 25°C. Points from averaged experimental measurements; curves from a theoretical model for viscoelastic behaviour. (Reproduced from Marvin, R.S. and Oser, H. (1962) Model for the viscoelastic behavior of rubberlike polymers including entanglement effects. J. Res. Natl Bur. Stand. B,* **66**, *171. Copyright (1962).)*

The observed plateau in the rubbery region is a consequence of high molecular mass, as the long molecules tend to entangle, with the formation of physical cross-links that restrict molecular flow through the formation of temporary networks. At long times such physical entanglements are usually labile and lead to some irreversible flow, in contrast with the situation for permanent chemical cross-links, such as those introduced when rubber is vulcanised. It follows directly from the theory of rubber elasticity (Chapter 4) that the value
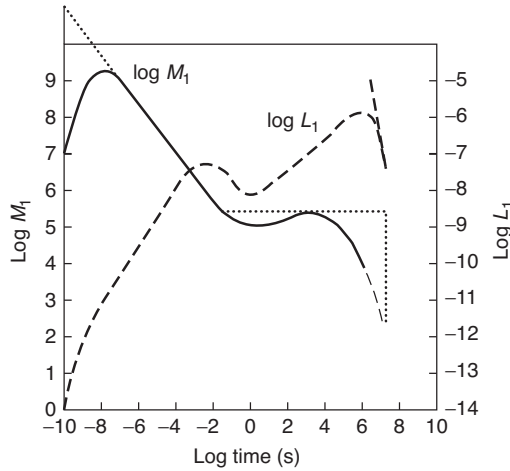
Figure 7.2 *Approximate distribution functions of relaxation (M_1) and retardation (L_1) times for polyisobutylene. (Reproduced from Marvin, R.S. (1954) The dynamic mechanical properties of polyisobutylene, in Proceedings of the Second International Congress of Rheology (ed. V.G.W. Harrison), Butterworths, London, pp. 156–164. Copyright (1954) Elsevier Ltd.)*

of the modulus in the rubber-like plateau region is directly related to the number of effective cross-links per unit volume.

The influence of molecular entanglements is illustrated by Figure 7.3, which shows the stress relaxation behaviour for two samples of polymethyl methacrylate. It is seen that the lower molecular mass sample does not show a rubbery plateau region of modulus but passes directly from the viscoelastic region to the region of permanent flow.
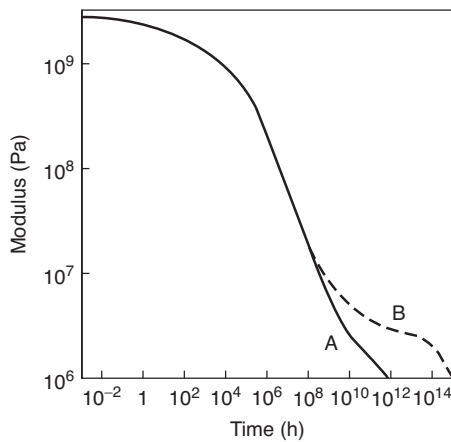
Figure 7.3 *Master stress-relaxation curves for low molecular mass (molecular mass 1.5 × 10^5 daltons, curve A) and high molecular mass (molecular mass 3.6 × 10^6 daltons, curve B) polymethyl methacrylate. (Reproduced with permission from McLoughlin and Tobolsky, J. Colloid Sci., **7**, 555. Copyright (1952) Elsevier Ltd.)*

7.1.2   Temperature Dependence of Viscoelastic Behaviour

Previously we have referred only indirectly to the effect of temperature on viscoelastic behaviour. From a practical viewpoint, however, the temperature dependence of polymer properties is of paramount importance because plastics and rubbers show very large changes in properties with changing temperature.

In purely scientific terms, the temperature dependence has two primary points of interest. In the first place, as we have seen in Chapter 6, it is not possible to obtain from a single experimental technique a complete range of measuring frequencies to evaluate the relaxation spectrum at a single temperature. It is therefore a matter of considerable experimental convenience to change the temperature of the experiment, and so bring the relaxation processes of interest within a timescale that is readily available. This procedure, of course, assumes that a simple interrelation exists between timescale and temperature, and we will discuss shortly the extent to which this assumption is justified.

Secondly, there is the question of obtaining a molecular interpretation of the viscoelastic behaviour. In most general terms, polymers change from glass-like to rubber-like behaviour as either the temperature is raised or the timescale of the experiment is increased. In the glassy state at low temperatures, we would expect the stiffness to relate to changes in the stored elastic energy on deformation that are associated with small displacements of the molecules from their equilibrium positions. In the rubbery state at high temperatures, on the other hand, the molecular chains have considerable flexibility, so that in the undeformed state they can adopt conformations that lead to maximum entropy (or, more strictly, minimum free energy). The rubber-like elastic deformations are then associated with changes in the molecular conformations.

The molecular physicist is interested in understanding how this conformational freedom is achieved in terms of molecular motions, for example to establish which bonds in the structure become able to rotate as the temperature is raised. One approach, which has proved successful to some degree, has been to compare the viscoelastic behaviour with dielectric relaxation behaviour and more particularly with nuclear magnetic resonance behaviour.

We have tacitly assumed that there is only one viscoelastic transition, corresponding to the change from the glassy low-temperature state to the rubbery state. In practice there are several relaxation transitions. For a typical amorphous polymer, the situation is summarised in Figure 7.4. At low temperatures, there are usually several secondary transitions involving comparatively small changes in modulus. These transitions are attributable to such features as side-group motions, for example methyl ($-CH_3$) groups in polypropylene
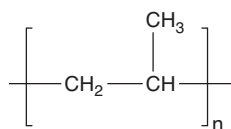
In addition, there is one primary transition, usually called the 'glass transition', that involves a large change in modulus. The temperature at which it occurs is commonly denoted by T_g.

7.1.3   Crystallinity and Inclusions

Although the viscoelastic behaviour of semi-crystalline polymers gives some indication of the four characteristic regions that can be identified for amorphous polymers, they are much less clearly defined, as is illustrated in Figure 7.5, which shows data for
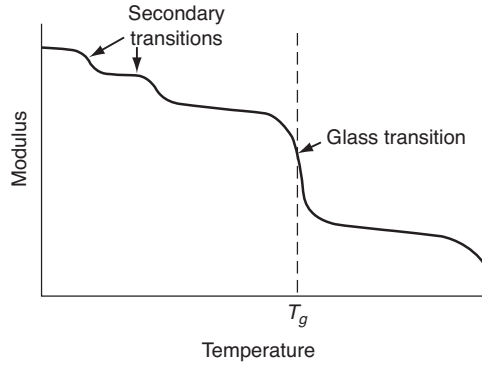
Figure 7.4   *Temperature dependence of modulus in a typical polymer.*

polychlorotrifluoroethylene $(CClF—CF_2)_n$ and polyvinyl fluoride $(CH_2CHF)_n$ obtained by Schmieder and Wolf [4]. The fall in modulus over the glass transition region for semi-crystalline materials is, at between one and two orders of magnitude, much less than for amorphous polymers, and the change in modulus or loss factor with temperature or frequency is much more gradual, indicating a broader relaxation time spectrum. At high temperatures (or low frequencies), molecular mobility is severely curtailed by the
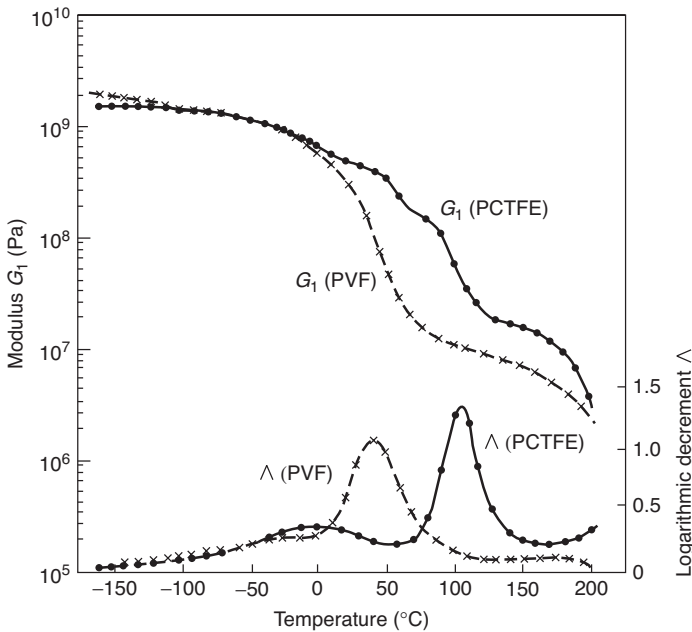
Figure 7.5   *Shear modulus G_1 and logarithmic decrement Λ of polychlorotrifluoroethylene (PCTFE) and polyvinyl fluoride (PVF) as a function of temperature at ~3 Hz. (Reproduced from Schmieder, K. and Wolf, K. (1953) Mechanische Relaxationsercheinungen an Hochpolymeren – Beziehungen Zur Struktur. Kolloidzeitschrift, **134**, 149. Copyright (1953) Springer Science + Business Media.)*

crystalline regions, so it is no longer correct to regard the polymer as rubber-like. These differences are clearly illustrated by the data of Thompson and Woods [5] for polyethylene terephthalate
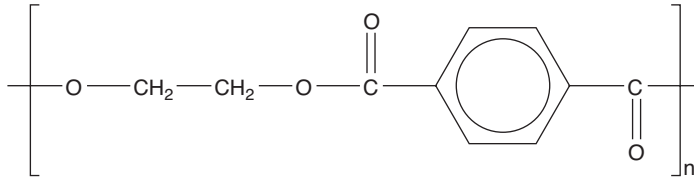
a material that is amorphous when quenched rapidly from the melt (Figure 7.6(a)), but semi-crystalline when slowly cooled or subsequently heat treated (Figure 7.6(b)).

Molecular mobility may be restricted by other factors, such as the addition of nanometre-scale inclusions. This and other factors have been reviewed recently by Aharoni [6], with particular reference to changes in the glass transition temperature T_g.

7.2   Time–Temperature Equivalence and Superposition

Time–temperature equivalence in its simplest form implies that the viscoelastic behaviour at one temperature can be related to that at another temperature by a change in the timescale only. Consider the idealised double logarithmic plots of creep compliance versus time shown in Figure 7.7(a). The compliances at temperatures T_1 and T_2 can be superimposed exactly by a horizontal displacement log a_t, where a_t is called the shift factor. Similarly (Figure 7.7(b)), in dynamic mechanical experiments, double logarithmic plots of tan δ versus frequency show an equivalent shift with temperature.

The experimental procedure is illustrated in Figures 7.8 and 7.9. A series of creep compliance curves each typically extending over 2 h, so that individual tests can be performed on successive days, is plotted using a specimen that has been mechanically conditioned at the highest temperature used. The individual plots are then transposed along the logarithmic time axis until they coincide, using any required temperature within the experimental range as the reference value. The variation in shift factor with temperature should also be recorded, for comparison with the predictions of theoretical interpretations to be discussed shortly.

Ferry and co-workers [7], on the basis of the molecular theory of viscoelasticity, proposed that superposition should incorporate a small vertical shift factor $T_0\rho_0/T\rho$, where ρ is the density at the experimental temperature T and ρ_0 relates to the reference temperature T_0. Further corrections have been suggested by McCrum and Morris [8] to deal with the changes in unrelaxed and relaxed compliances with temperature.

The situation is illustrated schematically in Figure 7.10. When we compare the creep compliance curves at the two temperatures T_1 and T_2, we see that the relaxed and unrelaxed compliances are both changing with temperature. McCrum and Morris [8] propose a scaling procedure for obtaining a modified or 'reduced' compliance curve at the temperature T_1, to give the dashed curve $J_\rho^T(t)$ in Figure 7.10. The shift factor is now obtained by a horizontal shift of $J_\rho^{T_1}(t)$ to superimpose $J^{T_2}(t)$.
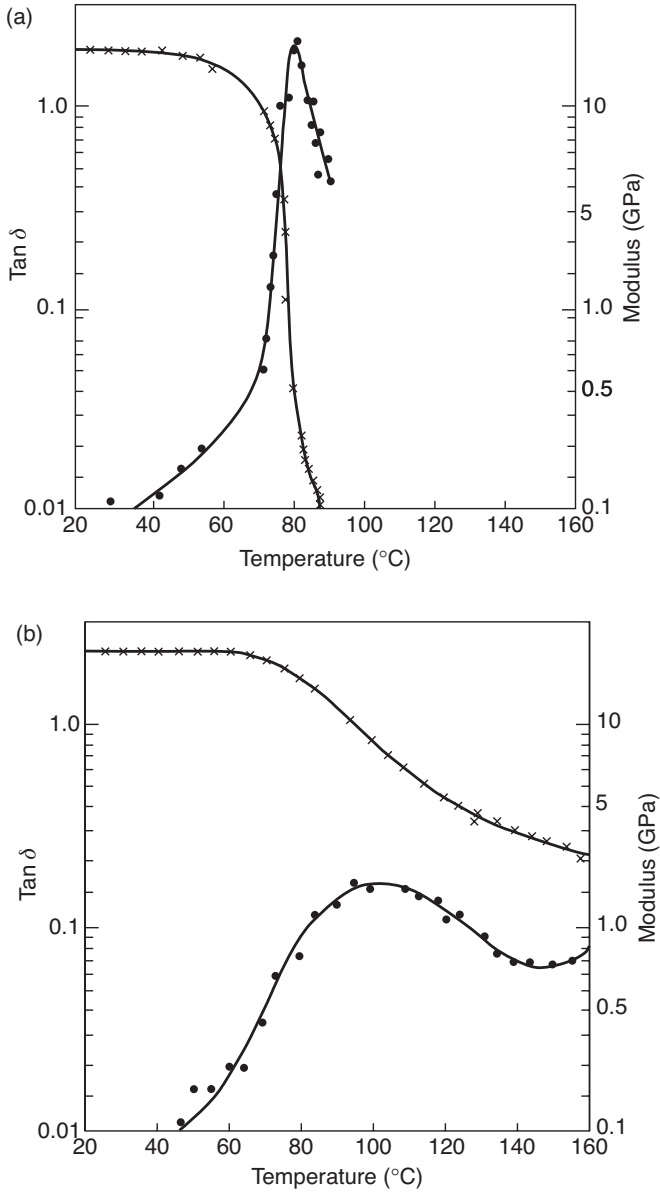
Figure 7.6   *Tensile modulus and loss factor tan δ for unoriented amorphous polyethylene terephthalate (a) and unoriented crystalline polyethylene terephthalate (b) as a function of temperature at ~1.2 Hz: (x) modulus; (●) tan δ. (Reproduced from Thompson, A.B. and Woods, D.W. (1956) The transitions of polyethylene terephthalate. Trans. Faraday Soc., 52, 1383. Copyright (1956) Royal Society of Chemistry.)*
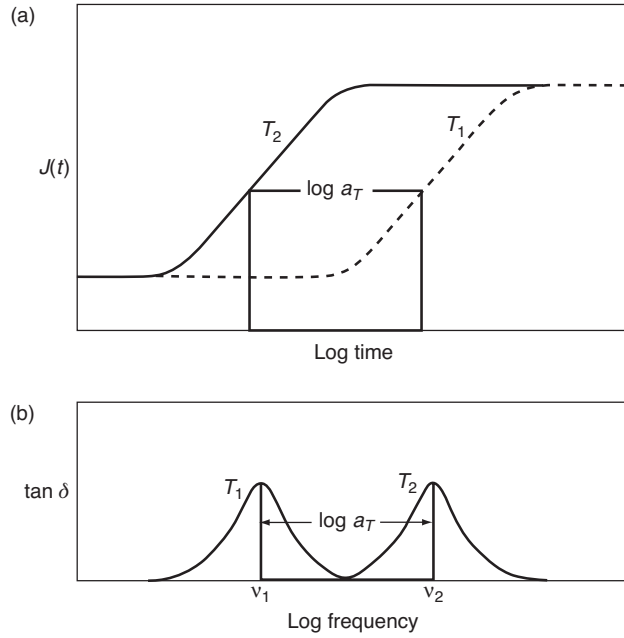
Figure 7.7   *Schematic diagrams illustrating the simplest form of time–temperature equivalence for (a) compliance, J(t) and (b) loss factor, tan δ.*
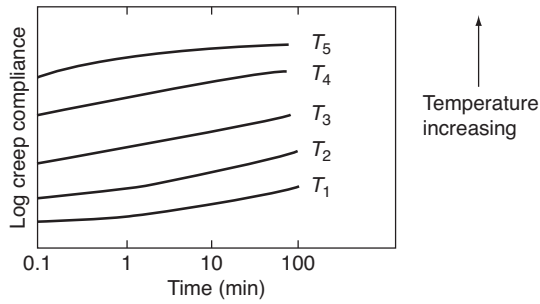
Figure 7.8   *Creep plots at different temperatures (schematic).*
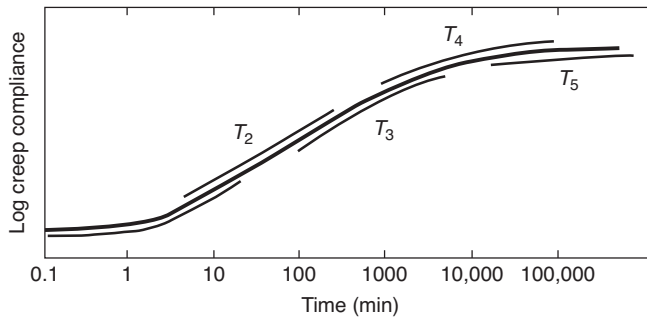
Figure 7.9   *Master curve of creep from superposing plots of Figure 7.8.*
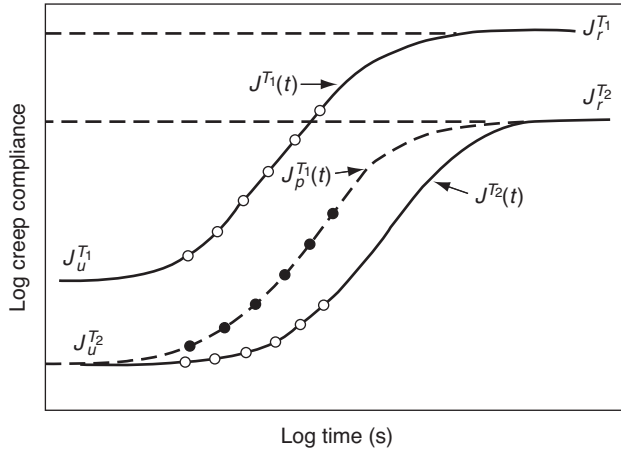
Figure 7.10   *Schematic diagram illustrating McCrum's reduction procedure for superposition of creep data: $J_r^{T_1}$ and $J_u^{T_1}$ are the relaxed and unrelaxed compliances respectively, at the temperature T_1; $J_r^{T_2}$ and $J_u^{T_2}$ are the corresponding quantities at the temperature T_2.*

7.3   Transition State Theories

The simplest theories that attempt to deal with the temperature dependence of viscoelastic behaviour are the transition state or barrier theories. The transition state theory of time-dependent processes stems from the theory of chemical reactions and is associated with the names of Eyring, Glasstone and others [9]. The basic idea is that for two molecules to react they must first form an *activated complex* or *transition state*, which then decomposes to give the final products of the reaction.

The potential energy diagram for two reacting molecules is closely analogous to that for the internal rotation of molecules discussed in Section 1.2.1. Figure 7.11 shows the change
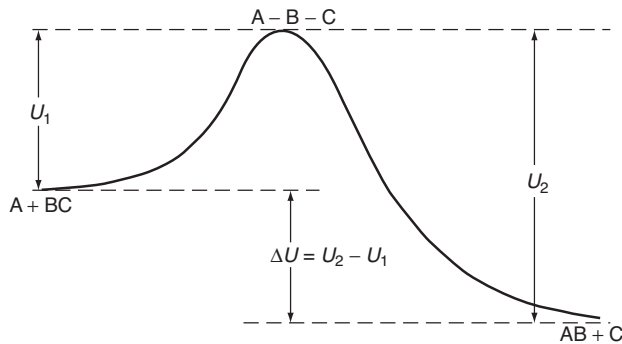
Figure 7.11   *Change of potential energy in a chemical reaction. (Adapted from Glasstone (1953), Textbook of Physical Chemistry, 2nd edn, Macmillan, London. Copyright (1953) Macmillan Publishing.)*

in potential energy for the reaction between an atom A and a diatomic molecule BC that results in the formation of a diatomic molecule AB and an atom C. The intermediate step is the formation of the activated complex A–B–C.

The theory of absolute reaction rates now argues as follows. The activated complex can be treated by statistical methods as a normal molecule, except that in addition to having three translational degrees of freedom, it has a fourth degree of freedom of movement along what is termed the reaction coordinate. The reaction coordinate is the direction leading to the lower potential energy of the final reactants. The theory shows that the rate of reaction is the product of two quantities, the probability of forming the activated complex and the effective rate of crossing the energy barrier by the activated complexes. It can be shown that the effective rate of crossing the energy barrier, which is the low-frequency vibration of the activated complex in the direction of the reaction coordinate, is equal to kT/h. This is a universal frequency whose value is dependent only on the temperature and is independent of the nature of the reactants and the type of reaction (k is Boltzmann's constant and h is Planck's constant). Because there is equilibrium between the initial reacting species and the transition state, the probability of forming the activated complex is determined in absolute terms by the Boltzmann factor $e^{-\Delta G/RT}$, where ΔG is the free energy difference per mole between the system when the reactants are relatively far from each other and when they form the activated complex. For reactions occurring under constant pressure conditions, ΔG is the Gibbs free energy difference per mole.

We now argue that, by analogy, the frequency of molecular jumps between two rotational isomeric states of a molecule (Section 1.2.1) is given by

$$\nu = \frac{kT}{h} e^{-\Delta G/RT}, \tag{7.1}$$

where ΔG is the Gibbs free energy barrier height per mole.

This equation states that the frequency of molecular conformational changes depends on the *barrier height* and not on the free energy difference between the equilibrium sites. Equation (7.1) may be written as

$$\nu = \frac{kT}{h} e^{\Delta S/R} e^{-\Delta H/RT} = \nu_0 e^{-\Delta H/RT}. \tag{7.2}$$

This form of Equation (7.1) emphasises the way in which temperature affects ν primarily through the activation energy ΔH. To a good approximation the activation energy for the process (actually an enthalpy) is thus given by

$$\Delta H = -R \left[\frac{\partial (\ln \nu)}{\partial (1/T)} \right]_P \tag{7.3}$$

Equation (7.2) is known as the 'Arrhenius equation', because it was first shown by Arrhenius [10] that it describes the influence of temperature on the velocity of chemical reactions.

We now take the intuitive step (to be justified below by the site model theory) that the viscoelastic behaviour can be directly related to a controlling molecular rate process with a constant activation energy.

Consider the tan δ curves of Figure 7.7(b). At the temperatures T_1 and T_2 the peak value of tan δ occurs at frequencies ν_1 and ν_2 respectively. The assumption is that ν_1 and ν_2 are related by the equation

$$\frac{\nu_1}{\nu_2} = \frac{e^{-\Delta H/RT_1}}{e^{-\Delta H/RT_2}},$$

that is

$$\log \frac{\nu_1}{\nu_2} = \log a_T = \frac{\Delta H}{R} \left\{ \frac{1}{T_2} - \frac{1}{T_1} \right\}. \tag{7.4}$$

The activation energy for the process can therefore be obtained from a plot of log a_T against the reciprocal of the absolute temperature. For large values of ΔH, changes in temperature give very large changes in frequency. Dynamic mechanical data on polymers are often dealt with in terms of the Arrhenius equation and a constant activation energy. In some cases, this can be regarded as only an approximate treatment due to the limited range of experimental frequencies available. In general, it has been found that the temperature dependence of the glass transition relaxation behaviour of amorphous and crystalline polymers does not fit a constant activation energy, in contrast to more localised molecular relaxations.

7.3.1   The Site Model Theory

The site model theory is based on transition state theory, and although first developed to explain the dielectric behaviour of crystalline solids [11, 12] has also been applied to mechanical relaxations in polymers [13].

In its simplest form there are two sites, separated by an equilibrium free energy difference $\Delta G_1 - \Delta G_2$, the barrier heights being ΔG_1 and ΔG_2 per mole respectively (Figure 7.12).

The transition probability for a jump from site 1 to site 2 is given by

$$\omega_{12}^0 = A'e^{-\Delta G_1/RT} \tag{7.5}$$

and for a jump from site 2 to site 1 by

$$\omega_{21}^0 = A'e^{-\Delta G_2/RT}, \tag{7.6}$$

where A' is a constant.
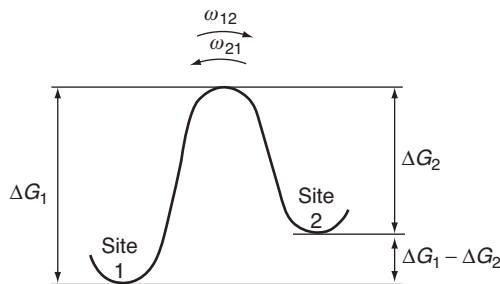
Figure 7.12   *The two-site model.*

(In some treatments, the change in molecular conformation is imagined to be a simple rotation of $180°$ around one bond. It is then considered that the transition probability is $2\omega_{12}^0$, where ω_{12}^0 is the probability for a jump in either a clockwise or anticlockwise direction.)

To give rise to a mechanical relaxation process, the energy difference between the two sites must be changed by the application of the applied stress. There is then a change in the populations of site 1 and site 2, and it is assumed that this relates directly to the strain. It is not difficult to imagine how this might arise at a molecular level if, for example the uncoiling of a molecular chain involved internal rotations. Locally, the chain conformations could be changing from crumpled *gauche* conformations to extended *trans* conformations (see Section 1.2.1).

Assume that the applied stress σ causes a small linear shift in the free energies of the sites such that

$$\delta G_1' = \lambda_1 \sigma \tag{7.7}$$

and

$$\delta G_2' = \lambda_2 \sigma \tag{7.8}$$

for sites 1 and 2 respectively, where λ_1 and λ_2 are constants with the dimensions of volume. The transition probabilities ω_{12} and ω_{21} in the presence of the applied stress are then given by

$$\omega_{12} \simeq \omega_{12}^0 \left[1 - \frac{\delta G_1'}{RT} \right] = \omega_{12}^0 \left[1 - \frac{\lambda_1 \sigma}{RT} \right], \tag{7.9}$$

where ω_{12}^0 is the transition probability in the absence of the stress. Similarly

$$\omega_{21} \simeq \omega_{21}^0 \left[1 - \frac{\lambda_2 \sigma}{RT} \right]. \tag{7.10}$$

The rate equations for sites 1 and 2 are then

$$\frac{dN_1}{dt} = -N_1 \omega_{12} + N_2 \omega_{21}, \tag{7.11}$$

$$\frac{dN_2}{dt} = -N_2 \omega_{21} + N_1 \omega_{12}, \tag{7.12}$$

where we can write the occupation number N_1 of state 1 as $N_1 = N_1^0 + n$ and similarly $N_2 = N_2^0 - n$, where N_1^0 and N_2^0 are the occupation numbers at zero stress, $N_1^0 + N_2^0 = N_1 + N_2 = N$.

Combining these equations and making suitable approximations gives a rate equation

$$\frac{dn}{dt} + n \left(\omega_{12}^0 + \omega_{21}^0 \right) = N_1^0 \omega_{12}^0 \left[\frac{\lambda_1 - \lambda_2}{RT} \right] \sigma, \tag{7.13}$$

which describes the change in the site population n as a function of time. Assuming that this change in site population is directly related to the observed strain e, e is given by

$$e = e_u + n\bar{e}. \tag{7.14}$$

In this equation e_u is the instantaneous or unrelaxed elastic deformation and it is considered that each change in site population produces a proportionate change in strain by an amount $\bar{e}$.

Equation (7.13) can then be seen to have the form

$$\frac{de}{dt} + Be = C,$$

where B and C are constants. This is formally identical to the equation of a Voigt element, with a characteristic retardation time given by $\tau' = 1/B$ which is

$$\tau' = \frac{1}{\left(\omega_{12}^0 + \omega_{21}^0\right)} = \frac{e^{\Delta G_2/RT}}{A'[\exp\{-(\Delta G_1 - \Delta G_2)/RT\} + 1]}. \tag{7.15}$$

Since RT is usually small compared with the equilibrium free energy difference we may approximate to

$$\tau' = \frac{1}{A'}e^{\Delta G_2/RT}. \tag{7.16}$$

Equation (7.16) is formally equivalent to Equation (7.1).

It follows that the time–temperature behaviour of the relaxation process is governed by the unperturbed transition probabilities, and to a good approximation by ΔG_2, a free energy of activation. The *magnitude* of the relaxation [13, 14], on the other hand, is proportional to

$$p\left[\frac{\exp[-(\Delta G_1 - \Delta G_2)/RT]}{(1 + \exp[-(\Delta G_1 - \Delta G_2)/RT])^2}\right]\frac{(\lambda_1 - \lambda_2)^2}{RT},$$

where p is the number of species per unit volume. Thus, the intensity of the relaxation on this model is low at both high and low temperatures and passes through a maximum when the free energy difference $(\Delta G_1 - \Delta G_2)$ and RT are of the same order of magnitude.

It must be emphasised that the site model is applicable only to relaxation processes showing a constant activation energy, examples being those associated with localised motions in the crystalline regions of semi-crystalline polymers. The temperature dependence of the glass transition relaxation behaviour of polymers does not fit a constant activation energy model, and where this has appeared to be true it is probably a consequence of the limited range of experimental frequencies that were available.

7.4 The Time–Temperature Equivalence of the Glass Transition Viscoelastic Behaviour in Amorphous Polymers and the Williams, Landel and Ferry (WLF) Equation

In considering time–temperature equivalence of the glass transition behaviour in amorphous polymers, we will follow a treatment very close to that given by Ferry [15]. To fix our ideas, consider the storage compliance J_1 of an amorphous polymer (poly-*n*-octyl methacrylate) as a function of temperature and frequency (Figure 7.13). It can be seen that there is an overall change in the shape of the compliance-frequency curve as the temperature changes. At high temperatures, there is an approximately constant high compliance, the rubbery compliance. At low temperatures, the compliance is again approximately constant but at a low value,
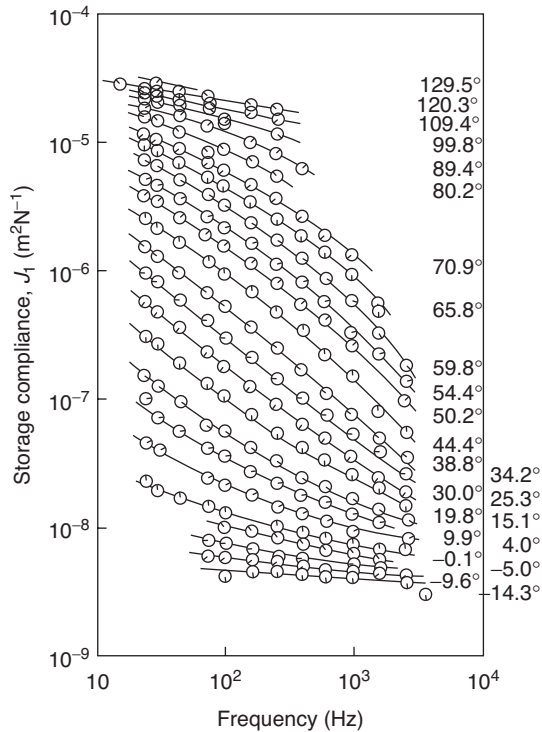
Figure 7.13   *Storage compliance of poly-n-octyl methacrylate in the glass transition region plotted against frequency at 24 temperatures as indicated. (Adapted from Ferry, J.D. (1980) Viscoelastic Properties of Polymers, 3rd edn, John Wiley & Sons, New York, Ch. 11. Copyright (1960) John Wiley & Sons, Inc.)*

the glassy compliance. At intermediate temperatures, there is the frequency-dependent viscoelastic compliance.

The simplest way of applying time–temperature equivalence is to produce a 'master compliance curve' by choosing one particular temperature and applying only a horizontal shift on a logarithmic timescale to make the compliance curves for other temperatures join as smoothly as possible to the curve at this particular temperature. This simple procedure is very nearly, but not quite, the procedure adopted by Ferry and his co-workers. The molecular theories of viscoelasticity suggest that there should be an additional small vertical shift factor $T_0\rho_0/T\rho$ in changing from the actual temperature T in kelvins (at a density ρ) to the reference temperature T_0 in kelvins (at a density ρ_0). The physical meaning of this vertical correction factor is that the molecular theories suggest that the equilibrium modulus changes with temperature in the transition range in a manner according to the theory of rubber elasticity (see Chapter 4). This is quite distinct from changes in the molecular relaxation times, which affect the measured modulus at a given time or frequency due to affecting the viscoelastic behaviour. In practice, the correction factor has a very small effect in the viscoelastic range of temperatures compared with the large changes in the viscoelastic behaviour. Thus, it is usually adequate to apply a simple horizontal shift on the timescale only (see Figure 7.14).
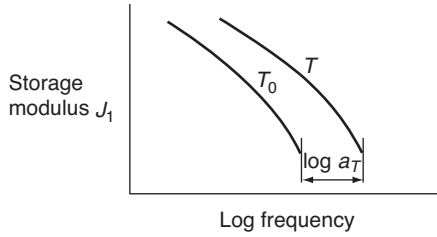
Figure 7.14 *Diagram illustrating shift factor log a_T for change in temperature T to T_0.*

This procedure gives the storage compliance as a function of frequency over a very wide range of frequencies, as shown in Figure 7.15 Thus, it is now possible to calculate the retardation time spectrum, and compare this with any theoretical models that may be proposed.

We may also consider the significance of the horizontal shift on the logarithmic timescale, as shown in Figure 7.16.

The remarkable observation, which was established largely by the work of Williams, Landel and Ferry, is that for all amorphous polymers this shift factor–temperature relationship is *approximately* identical.

It was found that the relationship

$$\log a_T = \frac{C_1(T - T_s)}{C_2 + (T - T_s)},$$
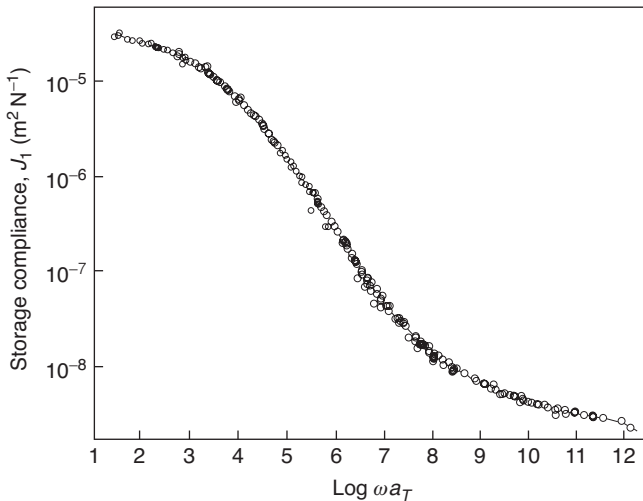
Figure 7.15 *Composite curve obtained by plotting the data of Figure 7.13 with suitable shift factors, giving the behaviours over an extended frequency scale at temperature T_0. (Adapted from Ferry, J.D. (1980) Viscoelastic Properties of Polymers, 3rd edn, John Wiley & Sons, New York, Ch. 11. Copyright (1960) John Wiley & Sons, Inc.)*
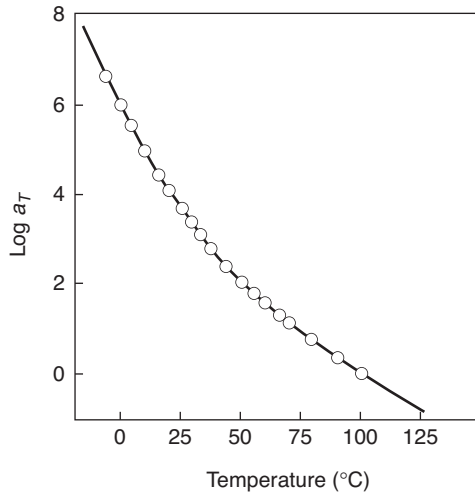
Figure 7.16   *Temperature dependence of the shift factor a_T used in plotting Figure 7.15 Points, chosen empirically; curve is WLF equations with a suitable choice of T_g (or T_s). (Adapted from Ferry, J.D. (1980) Viscoelastic Properties of Polymers, 3rd edn, John Wiley & Sons, New York, Ch. 11. Copyright (1960) John Wiley & Sons, Inc.)*

where C_1 and C_2 are constants, and T_s is a reference temperature peculiar to a particular polymer, holds extremely well over the temperature range $T = T_s \pm 50°$C for all amorphous polymers. This equation, known as the 'WLF equation' [7] (we shall see that there are other forms for the WLF equation), was originally considered to be only an empirical equation and the constants C_1 and C_2 were originally determined by arbitrarily choosing $T_s = 243$ K for polyisobutylene.

Following this empirical discovery, there was naturally some speculation as to whether the WLF equation has a more fundamental interpretation. This brings us to considerations of the dilatometric glass transition and to discussion of the use of the concept of free volume.

The glass transition can be defined on the basis of dilatometric measurements. As shown in Figure 7.17 if the specific volume of the polymer is measured against temperature, a change of slope is observed at a characteristic temperature, which we may call T_g. In the first place, this change in slope may be somewhat less sharp than this diagram suggests. Secondly, it is known that if dilatometric measurements are carried out at very slow rates of temperature change, one approaches a roughly constant value for the glass transition temperature T_g. The value of T_g will vary by only 2–3 K when the heating rate is decreased from 1 K/min to 1 K per day. Thus, it appears possible to define a rate-independent value of T_g to at least a very good approximation.

It has subsequently been shown that the original WLF equation can be rewritten in terms of this dilatometric transition temperature such that

$$\log a_T = \frac{C_1^g(T - T_g)}{C_2^g + (T - T_g)},$$

where C_1^g and C_2^g are new constants and $T_g = T_s - 50°$C.
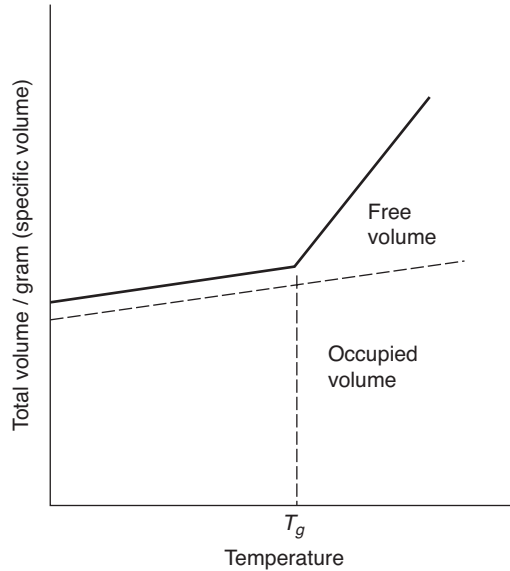
Figure 7.17   *The volume–temperature relationship for a typical amorphous polymer.*

Moreover, it is now possible to give a plausible theoretical basis to the WLF equation in terms of the concept of free volume [7].

In liquids, the concept of free volume has proved useful in discussing transport properties such as viscosity and diffusion. These properties are considered to relate to the difference $v_f = v - v_0$, where v is the total macroscopic volume, v_0 is the actual molecular volume of the liquid molecules, the 'occupied volume', and v_f is the proportion of holes or voids, the 'free volume'. Figure 7.17 shows the schematic division of the total volume of the polymer into both occupied and free volumes. It is argued that the occupied volume increases uniformly with temperature. The discontinuity in the expansion coefficient at T_g then corresponds to a sudden onset of expansion in the free volume. This suggests that certain molecular processes that control the viscoelastic behaviour commence at T_g, and not merely that T_g is the temperature when their timescale becomes comparable with that of the measuring timescale. This would seem to imply that T_g is a genuine thermodynamic temperature. This point is not, however, completely resolved, and it has been shown by Kovacs [16] that the T_g measured dilatometrically is still sensibly dependent on the timescale, that is the rate of heating. However, as already mentioned, this time dependence is small. Thus, to a good approximation it can be assumed that the free volume is constant up to T_g and then increases linearly with increasing temperature.

The fractional free volume $f = v_f/v$ can therefore be written as

$$f = f_g + \alpha_f(T - T_g), \qquad (7.17)$$

where f_g is the fractional free volume at the glass transition T_g and α_f is the coefficient of expansion of the free volume.

The WLF equation can now be obtained in a simple manner. The model representations of linear viscoelastic behaviour all show that the relaxation times are given by expressions of the form $\tau = \eta/E$ (see the Maxwell model in Section 5.2.6), where η is the viscosity of a dashpot and E the modulus of a spring.

If we ignore the changes in the modulus E with temperature compared with changes in the viscosity η, this suggests that the shift factor a_T for changing temperature from T_g to T will be given by

$$a_T = \frac{\eta_T}{\eta_{T_g}}. \tag{7.18}$$

At this juncture, we introduce Doolittle's viscosity equation [17], which relates the viscosity to the free volume. This equation is based on experimental data for monomeric liquids and gives

$$\eta = a \exp(b\upsilon/\upsilon_f), \tag{7.19}$$

where a and b are constants. Using (7.18) and (7.19), it can be shown that the Doolittle equation becomes

$$\ln a_T = b \left\{ \frac{1}{f} - \frac{1}{f_g} \right\}. \tag{7.20}$$

Substituting $f = f_g + \alpha_f(T - T_g)$, we have

$$\log a_T = -\frac{(b/2.303 f_g)(T - T_g)}{f_g/\alpha_f + T - T_g}, \tag{7.21}$$

which is the WLF equation.

Ferry and his co-workers have given further consideration to the exact form of the WLF equation. It can be shown that a better fit to data for different polymers can be obtained by changing the constants C_1^g and C_2^g; and that the actual values obtained for C_1^g and C_2^g yield values for f_g and α_f, which are plausible on physical grounds. The reader is referred to Ferry's book [15] for detailed discussion of these points. We will, however, note here that the fractional free volume at the glass transition temperature f_g is 0.025 ± 0.003 for most amorphous polymers. The thermal coefficient of expansion of free volume α_f is a more variable quantity, but has the physically reasonable 'universal' average value of $4.8 \times 10^{-4} \text{ K}^{-1}$.

It is of some interest to complete our discussion of the WLF equation by indicating the lines of its derivation by Bueche [18] using a transition state model.

It is possible to develop the transition state theory on the basis of free volume by expressing the frequency ν of the controlling molecular process by the equation

$$\nu = A \int_{f_c}^{\infty} \phi(f) \mathrm{d}f.$$

It is assumed that the required unit of structure can move when the local fractional free volume f exceeds some critical value f_c.

Bueche evaluated $\phi(f)$, and showed that with some approximations

$$\nu = \nu_g \exp \left\{ -N f_c \left[\frac{1}{f} - \frac{1}{f_g} \right] \right\}, \tag{7.22}$$

where ν_g is the frequency at T_g. If $f = f_g + \alpha_f(T - T_g)$ it may be shown that

$$\ln \frac{\nu}{\nu_g} = \frac{(Nf_c/f_g)(T - T_g)}{T - T_g + f_g/f}. \tag{7.23}$$

Assuming that there is a direct link between the shift factor a_T and the ratio of the frequencies of the controlling molecular process, Equation (7.23) is identical in form to Equation (7.21). Note also that Equation (7.22) is Bueche's analogy to the Doolittle equation (7.20).

In conclusion, we observe that for time–temperature equivalence to be exact, a necessary simplicity is implied. At a molecular level, the individual relaxation times for molecular processes must shift uniformly with temperature. In phenomenological terms, the spectrum of relaxation times must shift as a unit on a logarithmic timescale to shorter times with increasing temperature.

Staverman and Schwarzl [19] call these materials thermorheologically simple, and Lee and his collaborators [20] have worked out the theoretical consequences of this assumption, so that complex problems concerning the deformation of viscoelastic solids in variable temperature situations can be solved.

7.4.1 The Williams, Landel and Ferry Equation, the Free Volume Theory and Other Related Theories

The WLF equation gives the shift factor for time–temperature superposition as

$$\log a_T = \frac{C_1^g(T - T_g)}{C_2^g + (T - T_g)}.$$

We have seen that this relationship can be regarded as describing the change in the internal viscosity of the polymer as we change the temperature from the glass transition temperature T_g to the test temperature T (Equation (7.18)).

We may therefore write the WLF equation as

$$\log \eta_T = \log \eta_{T_g} + \frac{C_1^g(T - T_g)}{C_2^g + (T - T_g)},$$

where η_T, η_{T_g} is the viscosity of the polymer at temperatures T, T_g, respectively. In this form, the equation implies that at a temperature $T = T_g - C_2^g$ (i.e. $T = T_g - 51.6$ for the WLF equation in its universal form) the viscosity of the polymer is infinite.

This has led to the view that the WLF equation should be related at molecular level to the temperature $T = T_g - 51.6$, which we will call T_2, rather than to the dilatometric glass transition T_g.

There have been two basic approaches along these lines:

1. The free volume theory is modified so that the changes in free volume with temperature relate to a discontinuity that occurs at T_2 rather than T_g. This is discussed in Section 7.4.2.
2. It is considered that T_2 represents a true thermodynamic transition temperature. A modified transition state theory is developed in which the frequency of molecular jumps relates to the cooperative movement of a group of segments of the chain. The number of segments acting cooperatively is then calculated from statistical thermodynamic considerations. This is the theory of Adam and Gibbs [21], which is described in Section 7.4.3.

7.4.2   The Free Volume Theory of Cohen and Turnbull

Cohen and Turnbull [22] have proposed that the free volume v_f corresponds to that part of the excess volume $v - v_0$ (v = total measured specific volume, v_0 = occupied volume as in Section 7.4), which can be redistributed without a change in energy. It is then assumed on the basis of arguments concerning the nature of the 'cage' formed round a molecule by its neighbours that the redistribution can take place without a change in energy at temperatures above a critical temperature, which is to be identified with T_2, where the cage reaches a critical size.

Thus

$$v_f = 0 \quad \text{for } T < T_2$$

and

$$v_f = \alpha \bar{v}_m (T - T_2) \quad \text{for } T \geq T_2,$$

where α is the average expansion coefficient and $\bar{v}_m$ the average value of the molecular volume v_0 in the temperature range T_2 to T.

For a viscosity equation of the form

$$\eta = a \exp(bv/v_f) \tag{7.19}$$

this gives

$$\eta = a \exp \frac{B'}{T - T_2},$$

where B' is a constant, and correspondingly for the average relaxation time

$$\tau = \tau_0 \exp \frac{B'}{T - T_2}.$$

There is much experimental evidence from dielectric relaxation for the validity of this equation for amorphous polymers. As we have discussed, putting $T_2 = T_g - 51.6$ gives us the WLF equation and the relaxation time will become infinitely long as we approach T_2 due to the disappearance of free volume.

7.4.3   The Statistical Thermodynamic Theory of Adam and Gibbs

Gibbs and Di Marzio [23, 24] proposed that the dilatometric T_g is a manifestation of a true equilibrium second-order transition at the temperature T_2. In a further development, Adams and Gibbs [21] have shown how the WLF equation can then be derived. On their theory, the frequency of molecular jumps is given by

$$v_c = A \exp -\frac{n \Delta G*}{kT}, \tag{7.24}$$

where A is a constant ($A = kT/h$ on the transition state theory), ΔG^* is the free energy difference hindering rearrangement *per segment* (the barrier height) and n is the number of segments acting cooperatively as a unit to make a configurational rearrangement.

The essence of the Adam and Gibbs theory is that n can be calculated on thermodynamic equilibrium grounds as follows:

If S is the configurational entropy of the system, that is the entropy for a mole of segments,

$$S = \frac{N_A}{n} s_n,$$ (7.25)

where N_A is Avogadro's number and s_n is the entropy of a unit of n segments. Thus

$$n = \frac{N_A s_n}{S} \quad \text{and} \quad \upsilon_c = A \exp \frac{-N_A s_n \Delta G^*}{SkT}.$$ (7.26)

It is assumed that s_n is independent of temperature and that S, the configurational entropy of the system, can be calculated directly for any temperature from the specific heat at constant pressure.

A further assumption is that $S = 0$ at the thermodynamic transition temperature T_2. In molecular terms, n becomes infinite and there are no configurations available into which the system may rearrange. We may note that although the entropy S is assumed to be zero at T_2, this is not necessarily (or ever, in practice) a state of complete order.

This gives the entropy $S(T)$ at a temperature T as

$$S(T) = \Delta C_p \ln \frac{T}{T_2},$$ (7.27)

where ΔC_p is the difference in specific heat between the supercooled liquid and the glass at T_g and is assumed to be constant over the temperature range considered.

Substituting for $S(T)$ and approximating somewhat we find that

$$\upsilon_c = A \exp -\frac{N_A \Delta G^* s_n}{k \Delta C_p (T - T_2)}.$$ (7.28)

This gives a relaxation time equation of the form

$$\tau = \tau_0 \exp\{B/(T - T_2)\},$$

which as we have seen reduces to the WLF equation if we put

$$T_2 = T_g - 51.6.$$

7.4.4   An Objection to Free Volume Theories

Hoffman, Williams and Passaglia [13] have raised a serious objection to the free volume ideas. Williams [25] showed that the β-relaxations of polymethyl acrylate and polypropylene oxide behave somewhat similarly under constant pressure and constant volume conditions. It would be expected, however, on the free volume concept, that because the occupied volume υ_0 would increase with temperature, the results for these two conditions would be very different. Williams concluded that the dielectric relaxation time was not a unique function of volume. He suggested that this implied that the free volume did not remain constant for constant *total* volume, whilst temperature and pressure are varied. An alternative view is that relationships of the form

$$\eta = \eta_0 \exp U_\eta / R(T - T_2) \quad \text{and} \quad \tau = C \exp U_\tau / R(T - T_2)$$

should indeed be based on concepts that are more fundamental than those of free volume.

7.5 Normal Mode Theories Based on Motion of Isolated Flexible Chains

We have so far discussed two types of theories, those based on the site model, and those based on the WLF equation and its ramifications, which deal with time–temperature equivalence. The site model theories predict constant activation energies and are more applicable to relaxation transitions originating from localised chain motions, whereas the WLF equation theories deal with the glass transition behaviour in amorphous polymers.

In the introductory section on amorphous polymers (Section 7.1.1), we considered the relaxation spectrum of amorphous polymers and noted that it was quite complex. The normal mode theories, now to be discussed, attempt to predict the relaxation spectrum for amorphous polymers, as well as the time–temperature equivalence.

These theories are associated with the names of Rouse, Bueche and Zimm [26–28] and are based on the idea of representing the motion of polymer chains in a viscous liquid by a series of linear differential equations. They are essentially *dilute solution* theories, but we shall see that, rather unexpectedly perhaps, they can be extended to predict the behaviour of the pure polymer. Because of its simplicity, we will give an account of the theory due to Rouse [26].

Each polymer chain is considered to consist of a number of submolecules. This is similar to the composition of a rubber network where molecular chains join the cross-link points (see Figure 7.18(a)). We can then represent the polymer molecules as a system of beads connected by springs whose behaviour is that of a freely jointed chain on the Gaussian theory of rubber elasticity (Figure 7.18(b)). The molecular chains between the beads are all of equal length, this portion of the polymer chain being long enough for the separation of its ends to approximate to a Gaussian probability distribution. It is assumed that only the beads interact directly with the solvent molecules. If a bead is displaced from its equilibrium position, there are two types of forces acting on it; first, the forces due to this viscous interaction with the solvent molecules and secondly, the forces due to the tendency of the molecular chains to return to a state of maximum entropy by Brownian diffusional movements.
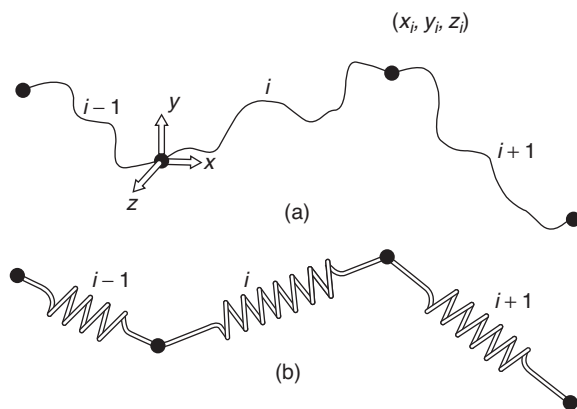

Figure 7.18 *The Rouse model: (a) the network of chains and (b) the representation of the network as a combination of springs and beads.*

Consider the motion of the bead situated at the point $(x_i y_i z_i)$ between the ith and $(i + 1)$th submolecules. The origin of coordinates is the bead between the $(i - 1)$th and ith submolecules, that is at the other end of the ith submolecule.

For a Gaussian distribution of links in the submolecule, the probability that this bead will lie at the point $x_i y_i z_i$ in the volume element $dx_i\ dy_i,\ dz_i$ is

$$p_i(x_i\,y_i\,z_i)dx_i\ dy_i\ dz_i = \frac{b^3}{\pi^{3/2}} \exp\left\{-b^2\left(x_i^2 + y_i^2 + z_i^2\right)\right\} dx_i\ dy_i\ dz_i,$$

where

$$b^2 = 3/2zl^2$$

with l the length of each link, n the total number of links in the molecular chain, m the number of submolecules, giving $z = n/m = $ number of links in a submolecule.

The conformational probability of the entire chain can be represented by a point in $3m$-dimensional space. The probability that this point lies at the point $x_1 y_1 \ldots z_m$ in the volume element $dx_1\ dy_1 \ldots dz_m$ is given by

$$P_m dx_1 \ldots dz_m = \prod_{i=1}^{m} p_i(x_i\ y_i\ z_i)dx_i\ dy_i\ dz_i$$

$$= \left(\frac{b^3}{\pi^{3/2}}\right)^m \exp\left\{-b^2\left[\sum_{i=1}^{m} x_i^2 + y_i^2 + z_i^2\right]\right\} dx_1 \ldots dz_m.$$

At equilibrium, the most probable values of the x_i, y_i and z_i coordinates are zero, that is each submolecule is in a coiled-up configuration. Any change from the equilibrium position will result in a decrease in entropy ΔS, or an increase in Helmholtz free energy $\Delta A = -T \Delta S$. (All conformations are assumed to have the same internal energy.)

Consider the change of x_i due to displacements of the ith submolecule from the equilibrium situation $(0, 0, 0)$, that is the change of x_i is referred to a private coordinate system with its origin at the bead between the $(i - 1)$th and ith submolecules.

There will be a restoring force

$$T\left(\frac{\partial S_m}{\partial x_i} - \frac{\partial S_m}{\partial x_{i-1}}\right)$$

due to displacements of the bead between the submolecules $i - 1$ and i and a restoring force

$$T\left(\frac{\partial S_m}{\partial x_{i+1}} - \frac{\partial S_m}{\partial x_i}\right)$$

due to displacements of the bead between the submolecules i and $i + 1$.

The total equation of motion is

$$\eta \dot{x}_i = T\left(2\frac{\partial S_m}{\partial x_i} - \frac{\partial S_m}{\partial x_{i-1}} - \frac{\partial S_m}{\partial x_{i+1}}\right) \tag{7.29}$$

η is the coefficient of friction defining the viscous interaction between the beads and the solvent. S_m is the entropy of a molecule of conformation $x_1 y_1 \ldots z_m$ and is given by

$$S_m = k \ln P_m. \tag{7.30}$$

Combining Equations (7.29) and (7.30) we have

$$\eta \dot{x}_i + \frac{3kT}{zl^2}(2x_i - x_{i-1} - x_{i+1}) = 0, \tag{7.31}$$

with $3m$ equations for coordinates $x_1 y_1 \ldots z_m$. If we make the intuitive connection between displacement and strain, we can see that these equations of motion for the chain molecules are directly equivalent to the equation of a Voigt element that has the form $\eta \dot{e} + Ee = 0$.

It therefore follows that these equations can be regarded as defining a set of creep compliances and stress relaxation moduli, or complex compliances and moduli.

The mathematical problem is to uncouple the $3m$ equations using a normal coordinate transformation. This involves obtaining the eigenfunctions that are linear combinations of the positions of the submolecules. Each eigenfunction then describes a configuration that decays with a time constant given by an associated eigenvalue, that is a single viscoelastic element with characteristic time-dependent properties.

For stress relaxation and dynamic mechanical experiments respectively, it can be shown that the stress relaxation modulus $G(t)$ and the real part of the complex modulus $G_1(\omega)$ are given by

$$G(t) = NkT \sum_{p=1}^{m} e^{-t/\tau_p} \tag{7.32}$$

and

$$G_1(\omega) = NkT \sum_{p=1}^{m} \frac{\omega^2 \tau_p^2}{1 + \omega^2 \tau_p^2}, \tag{7.33}$$

where N is the number of molecules per cubic centimetre and τ_p, the relaxation time of the pth mode, is given by

$$\tau_p = zl^2 \eta [24kT \sin^2\{p\pi/2(m+1)\}]^{-1}, \quad p = 1, 2, \ldots, m. \tag{7.34}$$

These equations predict that $G(t)$ and $G_1(\omega)$ are determined by a discrete spectrum of relaxation times, each of which characterises a given normal mode of motion. These normal modes are shown schematically in Figure 7.19. In the first mode, corresponding to $p = 1$, the ends of the molecule move whilst the centre of the molecule remains stationary. In the second mode, there are two nodes in the molecule. The general case of the pth mode has p nodes, with motion of the molecule occurring in $p + 1$ segments.

On this model the submolecule is the shortest length of chain that can undergo relaxation and the motion of segments *within* the submolecules are ignored. But such motions contribute to the relaxation spectrum for values of $m \gtrsim 5$. Thus, we would only expect the Rouse theory to be applicable for $m \gg 1$ where the equation for τ_p reduces to

$$\tau_p = \frac{m^2 zl^2 \eta}{6\pi^2 p^2 kT} = \frac{n^2 l^2 \eta_0}{6\pi^2 p^2 kT}, \tag{7.35}$$

where $\eta_0 = \eta/z$ is the friction coefficient per random link. The relaxation times depend on temperature directly through the factor $1/T$, through the quantity nl^2 that defines the equilibrium mean square separation of the chain ends and may change due to differences in the energy of different chain conformations, and through changes in the friction coefficient
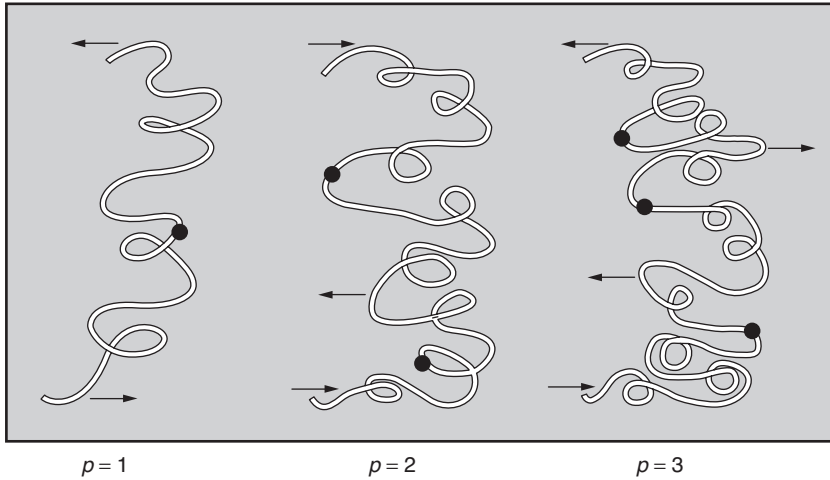
Figure 7.19   *Illustration of the first three normal modes of a chain molecule.*

η_0. η_0 changes rapidly with temperature and is primarily responsible for changes in τ_p. The fact that each τ_p has the same temperature dependence on this molecular theory shows that it satisfies the requirements of thermorheological simplicity and gives theoretical justification for time–temperature equivalence.

Rouse's theory is the simplest molecular theory of polymer relaxation. A later theory of Zimm [28] does not assume that the velocity of the liquid solvent is unaffected by the movement of the polymer molecules (the 'free draining approximation'). The hydrodynamic interaction between the moving submolecules is taken into account and this gives a modified relaxation spectrum.

The Rouse, Zimm and Bueche theories are satisfactory for the longer relaxation times, which involve movement of submolecules. This has been confirmed for dilute polymer solutions, where the theory would be expected to be most appropriate [29, 30]. More remarkably, it also holds for solid amorphous polymers (Reference 11, Chapter 13), provided that the friction coefficient is suitably modified.

Ferry has shown that if the three longest relaxation times are ignored, the distribution of relaxation times $H(\ln \tau)$ is given by

$$H(\ln \tau)\mathrm{d}(\ln \tau) == NkT \left(\frac{\mathrm{d}p}{\mathrm{d}\tau} \right) \mathrm{d}\tau \tag{7.36}$$

and from Equation (7.35)

$$H(\ln \tau) = \left(\frac{Nnl}{2\pi} \right) \left(\frac{kT\eta_0}{6} \right)^{1/2} \tau^{-1/2}. \tag{7.37}$$

This equation predicts that the plot of log $H(\ln \tau)$ against log τ should have a slope of $-\frac{1}{2}$. The results for five methacrylate polymers summarised in Figure 7.20 confirm this prediction for long relaxation times. The Zimm theory predicts a slope of $-\frac{2}{3}$ and is perhaps a better fit at shorter relaxation times. At very short relaxation times, the theory fails
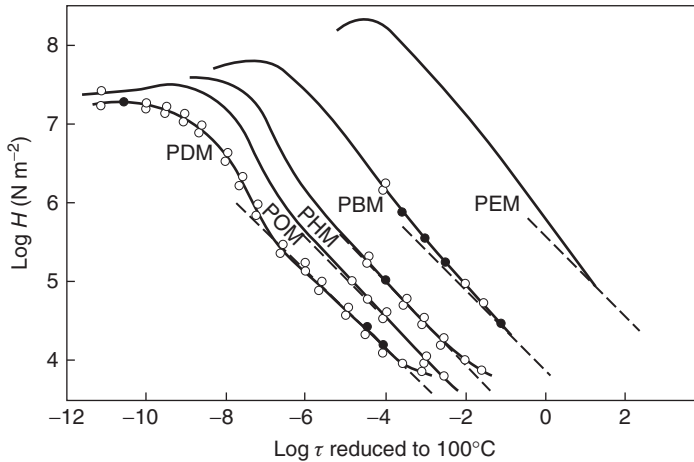
Figure 7.20   *Relaxation time spectra H(ln τ) for poly-n-dodecyl methacrylate (PDM), poly-n-octyl methacrylate (POM), poly-n-hexyl methacrylate (PHM), poly-n-butyl methacrylate (PBM), polyethyl methacrylate (PEM). Dashed lines are a slope of $-\frac{1}{2}$ predicted by the Rouse theory. (Adapted from Ferry, J.D. (1980) Viscoelastic Properties of Polymers, 3rd edn, John Wiley & Sons, New York, Ch. 11. Copyright (1960) John Wiley & Sons, Inc.)*

completely, as we have anticipated, because the movement of short segments is involved. Another way of looking at this, suggested by Williams [31], is that a theory based essentially on the Gaussian statistics of polymer chains can only hold for low values of the 'modulus', that is for values less than 10 MPa.

7.6   The Dynamics of Highly Entangled Polymers

In a concentrated polymer solution, a melt or a solid polymer, the molecular chains cannot pass through one another, a constraint that effectively confines each chain within a tube [32]. The centre line of this tube defines the overall path of the chain in space, and has been called by Edwards the primitive chain (Figure 7.21). Each chain 'sees' its environment as a tube because, although all the other chains are moving, there are so many entanglements that at any one time the tube is well defined. de Gennes [33] has described the possible motions of a polymer chain confined to a tube as snake-like, and has called the phenomenon 'reptation'. He considered two distinct forms of motion. Firstly, the comparatively short-term wriggling motions that correspond to the migration of a molecular kink along the chain, for which the longest relaxation time is proportional to the square of the molecular mass. Secondly, there is the much longer time associated with the movement of the chain as a whole through the polymer. This motion corresponds to an overall movement of the centre of gravity of the chain, and has a characteristic time proportional to the cube of the molecular mass.

   Doi and Edwards [32] have extended the work of de Gennes, and have derived mathematical expressions for features such as the stress relaxation that occurs after a large
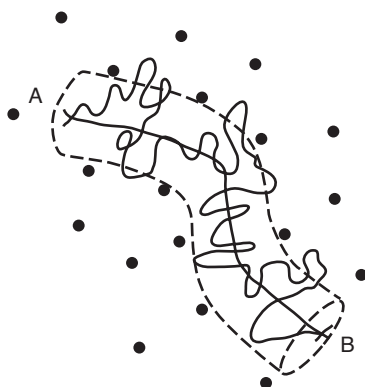
Figure 7.21   *Chain segment AB in dense rubber. The points A and B denote the cross-linked points and the dots represent other chains that, in this drawing, are assumed to be perpendicular to the paper. Due to entanglements the chain is confined to the tube-like region denoted by the broken line. The bold line shows the primitive path. (Reproduced from Doi, M. and Edwards, S.F. (1978) J. Chem. Soc. Faraday Trans.,* **74***, 1802. Copyright (1978) Royal Society of Chemistry.)*

strain. Their explanation for the physical situation is illustrated in Figure 7.22, in which the hatched area indicates the deformed part of the tube. Here (a) represents the tube before deformation, when the conformation of the primitive chain is in equilibrium. The deformation is considered to be affine, so that each molecule deforms to the same extent as the macroscopic body. In (b), the situation immediately after the step deformation is given, with the primitive chain in the affinely deformed conformation. In (c), the situation after a characteristic time τ_R is given, with the primitive chain recovering to its equilibrium
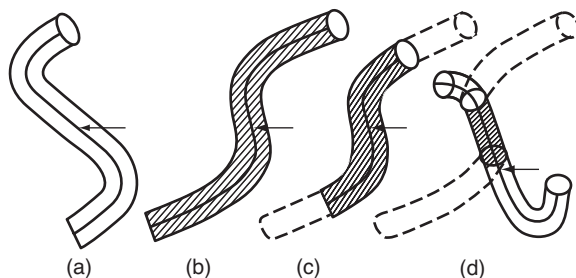
Figure 7.22   *Explanation of the stress relaxation after a large step strain. (a) Before deformation the conformation of the primitive chain is in equilibrium (t = −0). (b) Immediately after deformation, the primitive chain is in the affinely deformed conformation (t = +0). (c) After time τ_R, the primitive chain contracts along the tube and recovers the equilibrium contour length (t ≈ τ_R). (d) After the time τ_d, the primitive chain leaves the deformed tube by reptation (t ≈ τ_d). The oblique lines indicate the deformed part of the tube. (Reproduced from Doi, M. and Edwards, S.F. (1986) The Theory of Polymer Dynamics, Oxford University Press, New York. Copyright (1986) Oxford University Press.)*

contour length by contracting along the tube. For these very short-term motions, the constraints of the tube are not felt, so the motions are the same as those for the Rouse chain without constraints. The relaxation time τ_R is therefore the longest Rouse relaxation time. After a longer characteristic time τ_d (Figure 7.22(d)), the primitive chain leaves the deformed tube by reptation. Hence, τ_d is called the disengagement or reptation time and is the terminal relaxation time. If N is the number of segments in the chain, τ_d is proportional to N^3 (i.e. to the cube of the molecular mass), whereas τ_R is proportional to N^2. For a fuller discussion, refer to the advanced text by Doi and Edwards [32].

Recent research has addressed the shortcomings of the original Doi–Edwards exposition of reptation theory: first for low shear rate linear behaviour and secondly for non-linear behaviour at large shear rates. Doi–Edwards linear reptation theory predicts that τ_d scales with N as N^3, whereas there is a large body of experimental evidence that viscosity scales with molecular mass M as $M^{3,4}$. Secondly, linear theory predicts that the dynamic loss modulus $G_2(\omega)$ is proportional to $\omega^{-1/2}$ in the intermediate frequency range, whereas experiment gives a much weaker frequency dependence, with a power law between 0 and $-1/4$ depending on chain length.

The physical origin of the 3.4 scaling was recognised to be due to the relaxation of a part of the stress by a faster process than reptation, this process becoming less important as N becomes large, so that the viscosity increases faster than the asymptotic N^3 relationship: hence the apparent 3.4 relationship with molecular weight. Doi [34] identified this faster process with what he called contour-length fluctuations. These fluctuations involve the chain contracting within the tube and then stretching out again, so that orientation of the ends of the tube is forgotten and part of the stress is relaxed. Milner and McLeish [35] propose a quantitative theory for the stress relaxation in monodisperse linear polymer melts that incorporates reptation and contour-length fluctuations. The basis for the theory is that linear chains can be regarded as two-armed stars. In star polymers, reptation cannot occur because the arms do not have a single tube. The stress relaxes by arm retraction, where the star contracts by fluctuations down its tube towards the branch point, i.e. similar to the contour-length fluctuations of Doi.

The stress relaxation modulus $G(t)$ then has three components:

1. High-frequency modes due to contour-length fluctuations at the ends of the tubes.
2. Lower frequency modes associated with reptation.
3. Very high-frequency (short-time) Rouse modes where the tube constraints are not felt.

It was shown that the Milner–McLeish theory predicted the loss modulus $G_2(\omega)$ for monodisperse polystyrene melts, in addition to achieving the 3.4 molecular weight relationship for the viscosity that converges to 3 for high molecular weight. More recently, Likhtman and McLeish [36] have produced a more satisfactory expression for the stress relaxation modulus, which incorporates contour-length fluctuations, longitudinal stress relaxation along the tube and constraint release, where the effect of tube breakdown is taken into account in a less *ad hoc* fashion. The previous predictions of Milner and McLeish are modified to some extent, but the main advance is that the Likhtman–McLeish theory is more self-consistent and avoids many of the approximations in the original theory.

The Doi–Edwards model also has some shortcomings for describing non-linear behaviour at high shear rates where the viscosity is not linearly proportional to the shear rate. The Doi–Edwards theory predicts that the viscosity $\eta(\dot{\gamma})$ reduces with $\dot{\gamma}$ (shear thinning) as

$\dot{\gamma}^{-3/2}$, which would imply that there is a maximum in the shear stress as a function of $\dot{\gamma}$, which is not observed. Shear thinning is due to the orientation of the entangled chain network under flow. Marrucci [37] proposed that the severity of the orientation is reduced due to what he termed convective constraint release, which relates to the relaxation (i.e. contraction) of chains extended affinely by the flow, by retraction to their equilibrium length in their tubes. Marrucci and others have developed theories for the non-linear behaviour based on this idea [38, 39].

An alternative approach is that convective constraint release can be regarded as due to a hopping motion of the tube, most simply following Rouse dynamics [40]. This has been developed analytically by Milner, McLeish and Likhtman [41], whose theory predicts a monotonically increasing shear stress with increasing shear strain rate, with no stress maximum for polymer melts.

For an account of the application of Doi–Edwards theory to the prediction of dynamic moduli G_1 and G_2 as functions of frequency, the reader is referred to papers by Janeschitz-Kriegl and co-workers on polystyrenes [42, 43, 44].

The application of tube-theory to the dynamics of entangled flexible polymers in the melt has been comprehensively reviewed by McLeish [45]. This review addresses the current understanding of reptation, contour-length fluctuations and constraint release and gives attention to polymers of complex topology including long-chain branching.

References

1. Marvin, R.S. (1954) The dynamic mechanical properties of polyisobutylene, in *Proceedings of the Second International Congress of Rheology* (ed. V.G.W. Harrison), Butterworths, London, pp. 156–164.
2. Marvin, R.S. and Oser, H. (1962) Model for the viscoelastic behavior of rubberlike polymers including entanglement effects. *J. Res. Natl Bur. Stand. B*, **66**, 171.
3. Marvin, R.S. and Bergen, J.T. (1960) *Viscoelasticity: Phenomenological Aspects*, Academic Press, New York, p. 27.
4. Schmieder, K. and Wolf, K. (1953) Mechanische Relaxationsercheinungen an Hochpolymeren – Beziehungen Zur Struktur. *Kolloidzeitschrift*, **134**, 149.
5. Thompson, A.B. and Woods, D.W. (1956) The transitions of polyethylene terephthalate. *Trans. Faraday Soc.*, **52**, 1383.
6. Aharoni, S.M. (1998) Increased glass transition temperature in motionally constrained semicrystalline polymers. *Polym. Adv. Technol.*, **9**, 169.
7. Williams, M.L., Landel, R.F. and Ferry, J.D. (1955) Mechanical properties of substances of high molecular weight. 19. The temperature dependence of relaxation mechanisms in amorphous polymers and other glass-forming liquids. *J. Am. Chem. Soc.*, **77**, 3701.
8. McCrum, N.G. and Morris, E.L. (1964) On measurement of activation energies for creep and stress relaxation. *Proc. R. Soc.*, **A281**, 258.
9. Glasstone, S., Laidler, K.J. and Eyring, H. (1941) *The Theory of Rate Processes*, McGraw-Hill, New York.
10. Arrhenius, Z. (1889) Über die Reaktionsgeschwindigkeit bei der Inversion von Rohrzucker durch Säuren. *J. Physik. Chem.*, **4**, 226.
11. Debye, P. (1945) *Polar Molecules*, Dover, New York.

12. Fröhlich, H. (1968) *Theory of Dielectrics*, 2nd edn, Oxford University Press, Oxford.

13. Hoffman, J.D., Williams, G. and Passaglia, E. (1966) Analysis of alpha beta and gamma relaxations in polychlorotrifluoroethylene and polyethylene – dielectric and mechanical properties. *J. Polym. Sci., C*, **14**, 173.

14. Wachtman, J.B. (1963) Mechanical and electrical relaxation in ThO_2 containing CaO. *Phys. Rev.*, **131**, 517.

15. Ferry, J.D. (1980) *Viscoelastic Properties of Polymers*, 3rd edn, John Wiley & Sons, New York, Ch. 11.

16. Kovacs, A. (1958) La Contraction Isotherme Du Volume Des Polymeres Amorphes. *J. Poym. Sci.*, **30**, 131.

17. Doolittle, A.K. (1951) Studies in Newtonian flow. 2. The dependence of the viscosity of liquids on free-space. *J. Appl. Phys.*, **22**, 1471.

18. Bueche, F. (1953) Segmental mobility of polymers near their glass temperature. *J. Chem. Phys.*, **21**, 1850.

19. Staverman, A.J. and Schwarzl, F. (1956) *Die Physik der Hochpolymeren*, Springer-Verlag, Berlin, Chap. 1.

20. Lee, E.H. (1960) Viscoelastic stress analysis, in *Proceedings of the First Symposium on Naval Structural Mechanics* (London), (eds J.N. Goodier and J.F. Hoff), Pergamon Press, Oxford, p. 456.

21. Adam, G. and Gibbs, J.H. (1965) On temperature dependence of cooperative relaxation properties in glass-forming liquids. *J. Chem. Phys.*, **43**, 139.

22. Cohen, M.H. and Turnbull, D. (1959) Molecular transport in liquids and glasses. *J. Chem. Phys.*, **3l**, 1164.

23. Gibbs, J.H. and di Marzio, E.A. (1958) Nature of the glass transition and the glassy state. *J. Chem. Phys.*, **28**, 373.

24. Gibbs, J.H. and di Marzio, E.A. (1958) Chain stiffness and the lattice theory of polymer phases. *J. Chem, Phys.*, **28**, 807.

25. Williams, G. (1964) Complex dielectric constant of dipolar compounds as function of temperature, pressure and frequency. 1. Alpha-relaxation of polymethylacrylate. *Trans. Faraday Soc.*, **60**, 1548.

26. Rouse, P.E. (1953) A theory of the linear viscoelastic properties of dilute solutions of coiling polymers. *J. Chem. Phys.*, **21**, 1272.

27. Bueche, F. (1954) The viscoelastic properties of plastics. *J. Chem. Phys.*, **22**, 603.

28. Zimm, B.H. (1956) Dynamics of polymer molecules in dilute solution – viscoelasticity, flow birefringence and dielectric loss. *J. Chem. Phys.*, **24**, 269.

29. Tschoegl, N.W. and Ferry, J.D. (1963) Viskoelastische Eigenschaften von Poly-isobutylenen in Verdunnten Losungen. *Kolloidzeitschrift*, **189**, 37.

30. Lamb, J. and Matheson, A.J. (1964) Viscoelastic properties of polystyrene solutions. *Proc. Roy. Soc. A*, **281**, 207.

31. Williams, G. (1962) Upper limit of the shear modulus calculated from the Rouse theory. *J. Polymer Sci.*, **62**, 87.

32. Doi, M. and Edwards, S.F. (1986) *The Theory of Polymer Dynamics*, Oxford University Press, New York.

33. de Gennes, P.G. (1971) Reptation of a polymer chain in presence of fixed obstacles. *J. Chem. Phys.*, **55**, 572.

34. Doi, M. (1983) Explanation for the 3.4-power law for viscosity of polymeric liquids on the basis of the tube model. *J. Polym. Sci. Polym. Phys. Ed.*, **21**, 667.
35. Milner, S.T. and McLeish, T.C.B. (1998) Reptation and contour-length fluctuations in melts of linear polymers. *Phys. Rev. Lett.*, **81**, 725.
36. Likhtman, A.E. and McLeish, T.C.B. (2002) Quantitative theory for linear dynamics of linear entangled polymers. *Macromolecules*, **35**, 6332.
37. Marrucci, G. (1996) Dynamics of entanglements: a nonlinear model consistent with the Cox-Merz rule. *J. Non-Newtonian Fluid Mech.*, **62**, 279.
38. Ianniruberto, G. and Marrucci, G. (1996) On compatibility of the Cox-Merz rule with the model of Doi and Edwards. *J. Non-Newtonian Fluid Mech.*, **65**, 241.
39. Mead, D.W., Larson, R.G. and Doi, M. (1998) A molecular theory for fast flows of entangled polymers. *Macromolecules*, **31**, 7895.
40. Viovy, J.L., Rubinstein, M. and Colby, R.H. (1991) Constraint release in polymer melts – tube reorganization versus tube dilation. *Macromolecules*, **24**, 3587.
41. Milner, S.T., McLeish, T.C.B. and Likhtman, A.E. (2001) Microscopic theory of convective constraint release. *J. Rheol*, **45**, 539.
42. Janeschitz-Kriegl, H. (1982) Some pending problems in polymer melt rheology, as seen from the point of view of Doi slip-link model. *Rheol. Acta.*, **21**, 388.
43. Schausberger, A., Schinlauer, G. and Janeschitz-Kriegl, H. (1985) Linear elastico-viscous properties of molten standard polystyrenes. 1. Presentation of complex moduli-role of short-range structural parameters. *Rheol. Acta.*, **24**, 220.
44. Schindlauer, G., Schausberger, A. and Janeschitz-Kriegl, H. (1985) Linear elastico-viscous properties of molten standard polystyrenes. 2. Improvement of conventional characterization on molar mass-distribution. *Rheol. Acta.*, **24**, 228.
45. McLeish, T.C.B. (2002) Tube theory of entangled polymer dynamics. *Adv. Phys.*, **51**(6), 1379.

8

Anisotropic Mechanical Behaviour

8.1 The Description of Anisotropic Mechanical Behaviour

An oriented polymer is in the strictest terms an anisotropic non-linearly viscoelastic material. A comprehensive understanding of anisotropic mechanical behaviour is therefore a very considerable task. In this chapter, we will restrict the discussion to cases where the strains are small.

The mechanical properties of an anisotropic elastic solid for small strains are defined by the generalised Hooke's law:

$$e_{ij} = s_{ijk\ell}\sigma_{k\ell} \quad \sigma_{ij} = c_{ijk\ell}e_{k\ell},$$

where the $s_{ijk\ell}$ are the compliance constants and the $c_{ijk\ell}$ are the stiffness constants. This has been discussed in Chapter 2. The use of this representation does not necessarily restrict the discussion to time-independent behaviour. The compliance and stiffness constants could be time dependent, defining creep compliances and relaxation stiffnesses in step function loading experiments, or complex compliances and complex stiffnesses in dynamic mechanical measurements. For simplicity, the methods of measurement are usually carefully standardised, for example by measuring each creep compliance after the same loading programme and the same time interval. It will be assumed that for such measurements, there is an exact equivalence between elastic and linear viscoelastic behaviour, as proposed by Biot [1].

In an elastic material, the presence of symmetry elements leads to a reduction in the number of independent elastic constants and corresponding reductions will be assumed for anisotropic linear viscoelastic behaviour, although there is not enough experimental evidence to confirm that exactly the same rules hold in every case [2].

There are two important points to emphasise regarding the description of data:

1. In practice an abbreviated notation is often used in which

$$e_p = s_{pq}\sigma_q \quad \sigma_p = c_{pq}e_q.$$

As explained in Section 2.5, σ_p represents $\sigma_{11}, \sigma_{22}, \ldots, \sigma_{12}$, etc., and e_p represents $e_{11}, e_{22}, \ldots, e_{12}$, etc., and in the compliance and stiffness matrices s_{pq} and c_{pq}, p, q take the values $1, 2, \ldots, 6$.

The conversion rules from the $s_{ijk\ell}$ and $c_{ijk\ell}$ notation to the abbreviated notation are given in Section 2.5. It is important to remember that the engineering strains e_p are not the components of a tensor. Similarly, the 6×6 compliance matrix s_{pq} does not represent a tensor, and therefore tensor manipulation rules do not apply. As will be demonstrated, for working out problems involving transformation of coordinates from one system of axes to another, it is always desirable to use the original tensor notation in terms of e_{ij}, $\sigma_{k\ell}$ and $s_{ijk\ell}$ or $c_{ijk\ell}$.

2. It is usually more convenient to work in terms of compliance constants than stiffness constants. This is because in the experimental procedures it is easier to apply a simple stress of a given type, e.g. a tensile stress or a shear stress, and measure the corresponding strains, e.g.

$$e_1 = s_{11}\sigma_1 + s_{12}\sigma_2 + s_{13}\sigma_3 + s_{14}\sigma_4 + s_{15}\sigma_5 + s_{16}\sigma_6.$$

The compliance constants s_{11}, s_{12}, s_{13}, etc., can be found by applying stresses σ_1, σ_2, σ_3, etc., and measuring e_1 in each case. The procedures will become clearer as the various experimental methods are discussed.

8.2   Mechanical Anisotropy in Polymers

8.2.1   The Elastic Constants for Specimens Possessing Fibre Symmetry

Studies of mechanical anisotropy in polymers have for the most part been restricted to drawn fibres and uniaxially drawn films, both of which show isotropy in a plane perpendicular to the direction of drawing. The number of independent elastic constants is reduced to five [3, p. 138]. Choosing the 3 direction as the axis of symmetry, the compliance matrix s_{ij} reduces to

$$\begin{pmatrix} s_{11} & s_{12} & s_{13} & 0 & 0 & 0 \\ s_{12} & s_{11} & s_{13} & 0 & 0 & 0 \\ s_{13} & s_{13} & s_{33} & 0 & 0 & 0 \\ 0 & 0 & 0 & s_{44} & 0 & 0 \\ 0 & 0 & 0 & 0 & s_{44} & 0 \\ 0 & 0 & 0 & 0 & 0 & 2(s_{11} - s_{12}) \end{pmatrix}.$$

The various compliance constants are illustrated diagrammatically in Figure 8.1. The situation is most easily appreciated for a fibre specimen, but a uniaxially oriented sheet possesses identical symmetry.
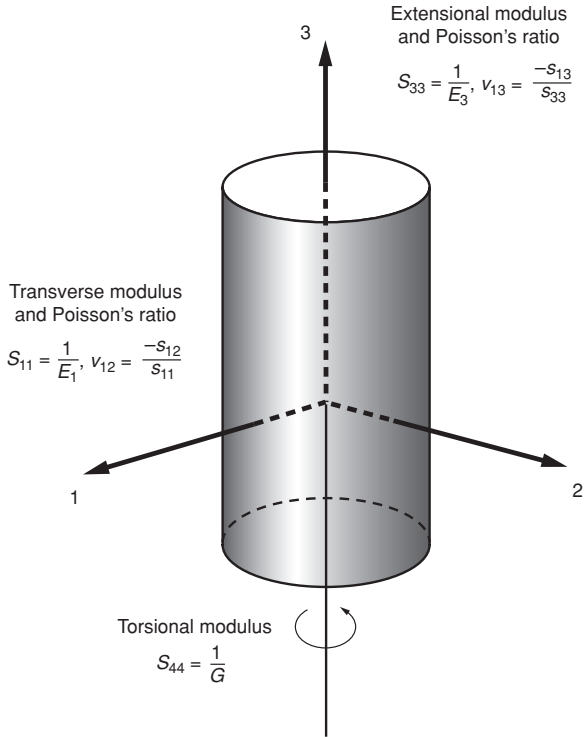
Figure 8.1   *The fibre compliance constants.*

The relationships of these compliance constants to the better-known Young's moduli and Poisson's ratios are as follows:

1. Consider application of a stress along the 3 direction, that is along the fibre axis, or the draw direction for the polymer film. Then $e_{33} = s_{33}\sigma_{33}$ and

$$\text{Young's modulus: } E_3 = \frac{\sigma_{33}}{e_{33}} = \frac{1}{s_{33}}, \text{ giving } s_{33} = \frac{1}{E_3}.$$

2. Similarly the strain in the plane transverse to the fibre axis for a stress σ_{33} along the fibre axis is given by $e_{11} = e_{22} = s_{13}\sigma_{33}$ and

$$\text{Poisson's ratio: } \nu_{13} = -\frac{e_{11}}{e_{33}} = -\frac{s_{13}}{s_{33}}.$$

(The negative sign ensures that Poisson's ratio is the conventionally positive quantity since e_{11} is negative, i.e. a contraction.)

3. In a similar manner, s_{11}, s_{12} and s_{13} are related to the modulus E_1 (the transverse modulus) and the corresponding Poisson's ratios $\nu_{21} = \nu_{12}, \nu_{31}$ and ν_{13} for application of a stress in a plane perpendicular to the fibre axis, i.e.

$$s_{11} = \frac{1}{E_1} \quad \text{and} \quad \nu_{21} = -\frac{s_{12}}{s_{11}} = -\frac{s_{12}}{s_{22}}, \quad \nu_{31} = -\frac{s_{13}}{s_{11}}, \quad \nu_{13} = -\frac{s_{13}}{s_{33}}.$$
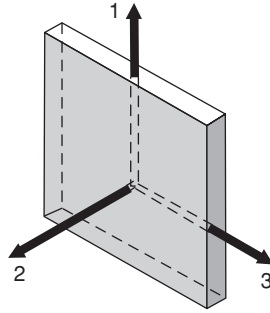
Figure 8.2   *Choice of axes for a polymer sheet possessing orthorhombic symmetry.*

The remaining Poisson's ratios v_{23} and v_{32} are not independent quantities, since

$$v_{23} = -\frac{s_{23}}{s_{33}} = -\frac{s_{13}}{s_{33}} = v_{13} \quad \text{and} \quad v_{32} = -\frac{s_{23}}{s_{22}} = -\frac{s_{13}}{s_{11}} = v_{31}.$$

4. The shear compliance is the reciprocal of the shear or torsional modulus G. There are two equivalent shear compliances $s_{44} = s_{55} = 1/G$. These relate to torsion about the symmetry axis 3, i.e. shear in the 23 or 13 planes.

The shear compliance s_{66} relates to shear in the 12 plane and is related to the compliance constants s_{11} and s_{12}, such that $s_{66} = 2(s_{11} - s_{12})$. This relationship expresses the fact that these specimens are isotropic in a plane perpendicular to the symmetry axis, i.e. that the elastic behaviour in this plane is specified by only two elastic constants as for an isotropic material. It will be seen that this property is very important in determining the elastic constants for fibres.

8.2.2   The Elastic Constants for Specimens Possessing Orthorhombic Symmetry

Oriented polymer films that are prepared by either rolling, rolling and annealing, or some commercial one-way draw processes, may possess orthorhombic rather than transversely isotropic symmetry. For such films, the elastic behaviour is specified by nine independent elastic constants. Choose the initial drawing or rolling direction as the 3 axis for a system of rectangular Cartesian coordinates; the 1 axis to lie in the plane of the film and the 2 axis normal to the plane of the film (Figure 8.2). The compliance matrix is

$$\begin{pmatrix} s_{11} & s_{12} & s_{13} & 0 & 0 & 0 \\ s_{12} & s_{22} & s_{23} & 0 & 0 & 0 \\ s_{13} & s_{23} & s_{33} & 0 & 0 & 0 \\ 0 & 0 & 0 & s_{44} & 0 & 0 \\ 0 & 0 & 0 & 0 & s_{55} & 0 \\ 0 & 0 & 0 & 0 & 0 & s_{66} \end{pmatrix}.$$

There are three Young's moduli,

$$E_1 = \frac{1}{s_{11}}, \quad E_2 = \frac{1}{s_{22}} \quad \text{and} \quad E_3 = \frac{1}{s_{33}},$$

and six Poisson's ratios,

$$v_{21} = -\frac{s_{21}}{s_{11}}, \quad v_{31} = -\frac{s_{31}}{s_{11}}, \quad v_{32} = -\frac{s_{32}}{s_{22}}$$

$$v_{12} = -\frac{s_{21}}{s_{22}}, \quad v_{13} = -\frac{s_{31}}{s_{33}}, \quad v_{23} = -\frac{s_{32}}{s_{33}}.$$

There are three independent shear moduli $G_1 = 1/s_{44}$, $G_2 = 1/s_{55}$ and $G_3 = 1/s_{66}$ corresponding to shear in the 23, 13 and 12 planes respectively. For a sheet of general dimensions, torsion experiments where the sheet is twisted about the 1, 2 or 3 axis will involve a combination of shear compliances. This will be discussed in greater detail later, when methods of obtaining the elastic constants are described.

8.3   Measurement of Elastic Constants

The measurement of elastic constants is a very different undertaking for the two situations of a sheet and a fibre. The experimental methods employed for these two cases will therefore be discussed separately.

8.3.1   Measurements on Films or Sheets

8.3.1.1   Extensional Moduli

The simplest measurement on a polymer film is to determine the Young's modulus in various directions in the film by cutting long thin strips in the selected directions.

For anisotropic materials, it is important to recognise that it is generally necessary to measure samples of very high aspect ratio[1] to minimise 'end effects'. These end effects arise from non-uniform stress conditions near the clamps that are much more severe than would be anticipated on the basis of St Venant's principle. The situation has been discussed in detail by Horgan [4, 5] and by Folkes and Arridge [6].

We will consider a film of orthorhombic symmetry, the 1 and 3 axes lying in the plane of the film and the 2 axis normal to the film as in Section 8.2.2 above.

Consider a long strip cut in a direction making an angle θ with the 3 direction (Figure 8.3(a)).

The Young's modulus for this strip $E_\theta = 1/s_\theta$, where s_θ is the compliance in a direction making an angle θ with the 3 direction.

To calculate s_θ in terms of the compliance constants, we will use the full tensor notation.

The compliance constants s_{ijkl} referred to one system of Cartesian axes are related to those s'_{pqmn} referred to a second system of Cartesian axes by the tensor transformation rule:

$$s'_{pqmn} = a_{pi}a_{qj}a_{mk}a_{nl}s_{ijkl},$$

where a_{pi}, a_{qj}, ... define the cosines of the angles between the p axis in the second system and the i axis in the first, the q axis in the second system and the j axis in the first, ... and p, q, m, n take the values 1, 2, 3 in the second system of axes and $i, j, k, \ell,$ take the values $1', 2', 3'$ in the first system of axes.

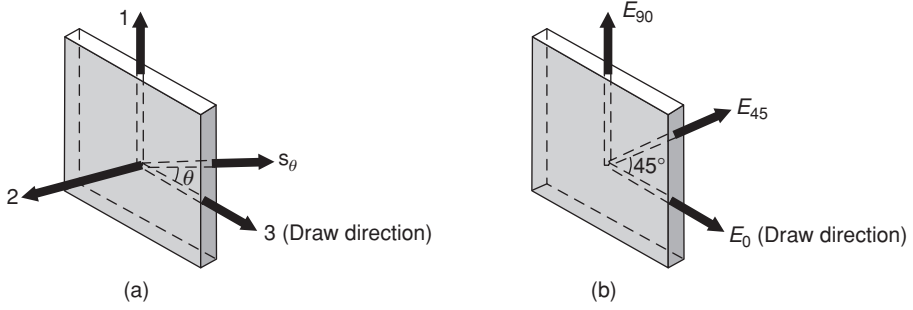---

[1] Aspect ratio is the ratio of length to width or thickness.

Figure 8.3   (a) The compliance s_θ is at an angle θ to the initial draw direction in the plane of the sheet. (b) The E_0, E_{45} and E_{90} moduli.

We will take the direction of the strip to be the $3'$ direction in a second system of Cartesian axes. Then $s_\theta = s_{3'3'3'3'}$ is given by

$$s_{3'3'3'3'} = a_{3'1}a_{3'1}a_{3'1}a_{3'1}s_{1111} + a_{3'3}a_{3'3}a_{3'3}a_{3'3}s_{3333}$$
$$+ a_{3'1}a_{3'1}a_{3'3}a_{3'3}s_{1133} + a_{3'3}a_{3'3}a_{3'1}a_{3'1}s_{3311}$$
$$+ a_{3'1}a_{3'3}a_{3'3}a_{3'1}s_{1331} + a_{3'3}a_{3'1}a_{3'1}a_{3'3}s_{3113}$$
$$+ a_{3'3}a_{3'1}a_{3'3}a_{3'1}s_{3131} + a_{3'1}a_{3'3}a_{3'3}a_{3'1}s_{1313}.$$

Note that all compliance terms containing the subscript 2 will vanish, because $a_{3'2} = 0$.

The change in coordinate systems corresponds to a rotation of the coordinate axes through an angle θ about the 2 direction as axis.

We therefore put $a_{3'1} = \sin\theta$ and $a_{3'3} = \cos\theta$ and

$$s_{3'3'3'3'} = \sin^4\theta s_{1111} + \cos^4\theta s_{3333} + 2\sin^2\theta\cos^2\theta s_{1133} + 4\sin^2\theta\cos^2\theta s_{1313}.$$

In the abbreviated notation,

$$s_\theta = s_{3'3'} = \sin^4\theta s_{11} + \cos^4\theta s_{33} + \sin^2\theta\cos^2\theta(2s_{13} + s_{55}). \tag{8.1}$$

(Note factor 4 in converting from $s_{ijk\ell}$ to s_{pq}, when p and q = 4, 5, 6, i.e. 23, 13, 12.)

It is thus possible to undertake three independent measurements on these sheets. For convenience, choose these to be the Young's modulus on strips at $0°$, $45°$ and $90°$ to the initial draw direction and denote these by E_0, E_{45} and E_{90} respectively (see Figure 8.3(b)). From Equation (8.1)

$$E_0 = \frac{1}{s_{33}}, \quad E_{90} = \frac{1}{s_{11}} \quad \text{and} \quad \frac{1}{E_{45}} = \frac{1}{4}[s_{11} + s_{33} + (2s_{13} + s_{55})]. \tag{8.2}$$

Such measurements yield immediately two of the nine independent elastic constants, s_{11} and s_{33}, and give the combination $(2s_{13} + s_{55})$ but do not involve s_{12}.

For a transversely isotropic sheet where 3 is the symmetry axis, there are only five independent elastic constants, and $s_{55} = s_{44}$.
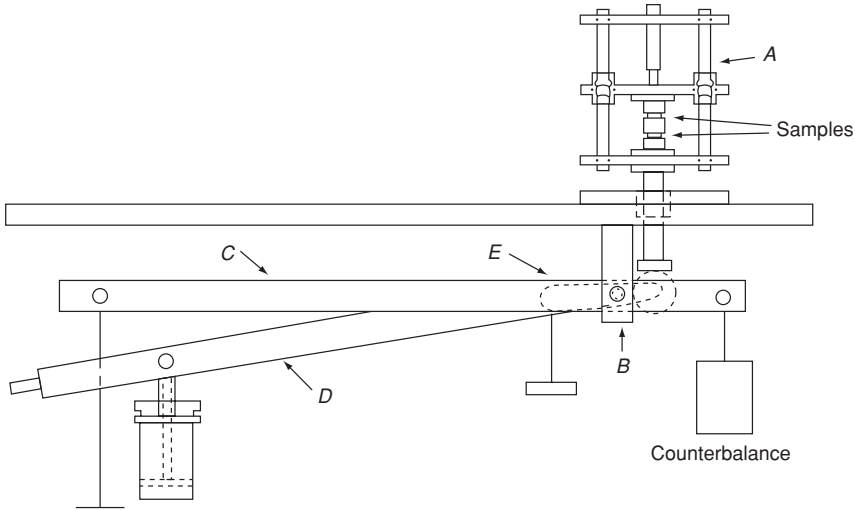
Figure 8.4 *Schematic diagram of compression apparatus. (Reproduced from Wilson, I., Cunningham, A., Duckett, R.A. et al. (1976) The determination of the extensional compliance perpendicular to the plane of sheet for thin polyethylene terephthalate sheets. J. Mater. Sci., **11**, 2189. Copyright (1976).)*

8.3.1.2 The Transverse Stiffness

The stiffness normal to the plane of the sheet c_{22} has been determined by measuring the compressional strain of narrow strips under load in a compressional creep apparatus [7]. The load is applied to the compression cage A (Figure 8.4) via two level arms pivoted about a common fulcrum B. The load is placed on the weight pan at the end of the larger arm C, and supported by the rod D. This rod is held in position by an electromagnet E, and until released, prevents the load from being applied to the samples.

Because the apparatus was originally designed for compression of much thicker samples, an intermediate steel spacer was inserted in the compression cage. To improve the accuracy of the measurements, two identical samples were compressed in each experiment as indicated in the diagram.

Experiments comparing narrow strips cut in the 1 and 3 directions (Figure 8.3), together with a theoretical analysis of the frictional effects, indicated that for polyethylene terephthalate sheets the frictional constraints prevented any strains developing in either the 1 or the 3 directions. In this case $e_1 = e_3 = 0$ and $\sigma_2 = c_{22}e_2$ or

$$e_2 = \left[s_{22} + \frac{s_{12}(s_{23}s_{13} - s_{12}s_{33}) + s_{23}(s_{13}s_{12} - s_{23}s_{11})}{s_{11}s_{33} - s_{13}^2} \right] \sigma_2.$$

8.3.1.3 Lateral Compliances and Poisson's Ratios

For a polymer film possessing orthorhombic symmetry, there are three lateral compliances s_{12}, s_{13} and s_{23}, which relate to the six Poisson's ratios defined in Section 8.2.2.
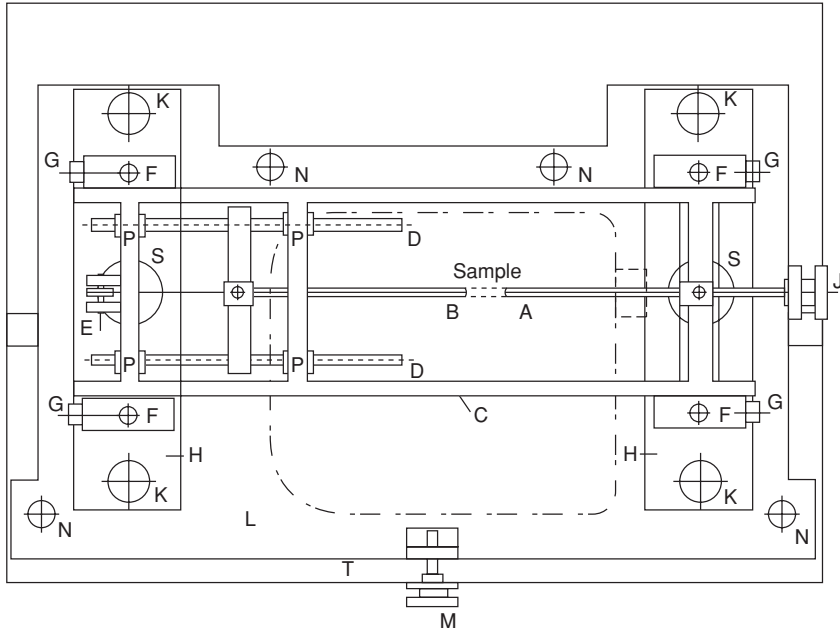
Figure 8.5   *Overhead projection of Poisson's ratio apparatus. A is a sample grip fixed to frame C. B is sample grip attached to sliding rods D, which move through linear bearing C. E is pulley for loading weights. G, J, M and S are positioning screws. (Reproduced from Ladizesky, N.H. and Ward, I.M. (1971) Determination of Poisson's ratio and Young's modulus of low-density polyethylene. J. Macromol. Sci. B,* **5**, *661. Copyright (1971).)*

The lateral compliance s_{13} defines the contraction in the 1 direction for a stress applied along the 3 direction (Figure 8.2). This has been determined by measuring the change in shape of a grid of perpendicular lines printed on the surface of oriented polymer film, one set of lines being parallel to the draw direction [8]. The procedure was to align accurately an electron microscope grid on the surface of the sheet by viewing the sheet between crossed polars in a polarising microscope. A thin coat of aluminium was then deposited by placing the sheet in a vacuum coating unit. The sample, in the form of a long narrow strip, was cut parallel to the set of lines of the grid containing the draw direction using a special cutting device. The sample was extended in a robust but friction-free extensometer, by holding it between two clamps, one of which is fixed to the frame and the other is attached to sliding rods that move through four linear bearings (Figure 8.5).

The grid was photographed under a comparatively small 'zero load', sufficient to straighten the sample, and at a fixed time after application of further loads. The change in shape of the grid gave the extension and contraction parallel and normal to the draw direction and hence s_{33} and s_{13} respectively.

The lateral compliances s_{12} and s_{23} correspond to the contraction in the 2 direction (the thickness direction) for stresses applied along the 1 and 3 directions respectively (Figure 8.2). Several techniques have been developed for this measurement, the earliest being due to Saunders and co-workers who developed an apparatus to measure both
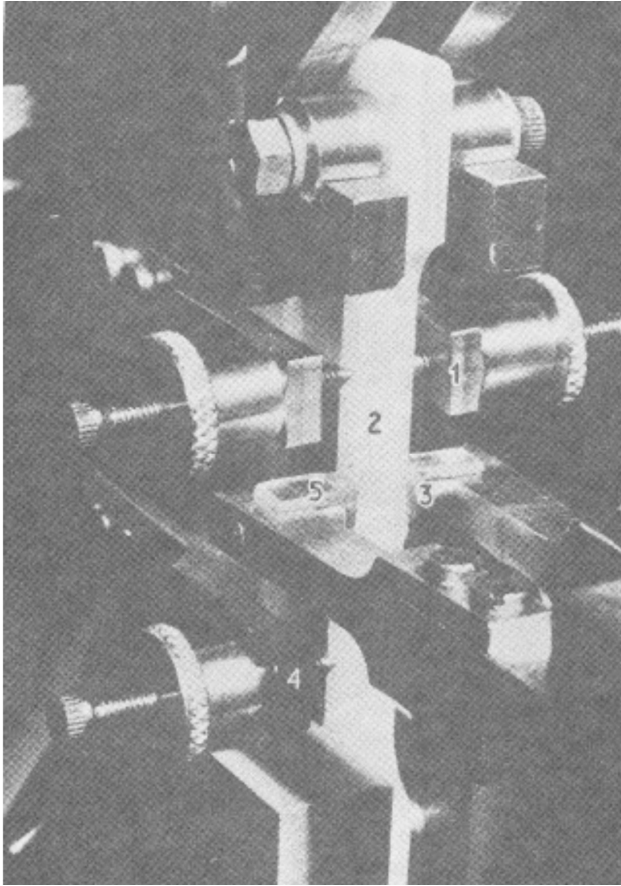
Figure 8.6 *Photograph of the extensometry system of Clayton, Darlington and Hall: (1) upper arm of tensile extensometer; (2) specimen; (3) brass contact pieces on lateral extensometer arms; (4) lower arm of tensile extensometer and (5) glass plates with 'shoulders' resting on ends of lateral extensometer arms. (Redrawn from Clayton, D., Darlington, M.W. and Hall, M.M. (1973) Tensile creep modulus, creep lateral contraction ratio, and torsional creep measurements on small nonrigid specimens. J. Phys. E., **6**, 218. Copyright (1973).)*

extensional strains on a wide range of polymers, including the relatively compliant low-density polyethylene at one extreme to highly rigid fibre-reinforced thermoplastics at the other. As their work is described in detail elsewhere [9, 10], only a summary will be presented here. The samples are loaded by a lever loading arm arrangement similar to that developed by Turner *et al*. [11]. The extensional and lateral strains are measured by extensometers, whose weight is supported by the main frame of the machine so that they do not affect the loading of the sample to any significant degree. The mode of operation of the extensometers can be understood by reference to Figure 8.6. The tensile extensometer consists of two arms (1) rotating freely in a vertical plane. The arms are supported on five bearings at their mid-points, and are attached to the specimen at one end by screw pins (2).
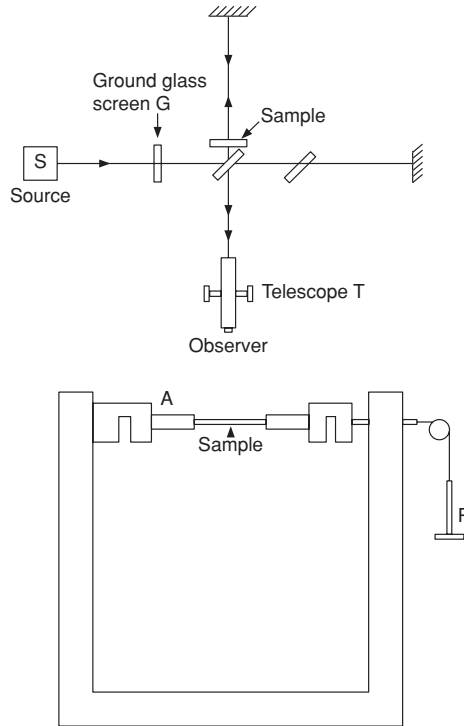
Figure 8.7 *Arrangement of Michelson interferometer apparatus for measuring Poisson's ratio. (Redrawn from Wilson, I., Cunningham, A. and Ward, I.M. (1976) Determination of Poissons ratio compliances for polyethylene terephthalate sheets using a Michelson interferometer. J. Mater. Sci., **11**, 2181. Copyright (1976).)*

At the other end, their displacement is monitored by a displacement capacitance transducer. The lateral extensometer (to measure change in thickness s_{12} or s_{23}) operates in a horizontal plane in an identical manner. The rotating arms (4) contact the specimen via brass domes (5). Thin glass cover slides are inserted between these domes and the specimen faces to prevent indentation of the specimen.

Movements of <0.25 μm can be readily detected that gives accurate tensile strain measurements in the range 0.1–7.5%. The lateral extensometers can be used to measure changes in width as well as thickness.

A second method for determination of the lateral compliances s_{12} and s_{23} uses a Michelson interferometer [12], and is particularly suitable for thin samples, with the obvious proviso that the films must possess a fairly high degree of optical clarity. A schematic diagram of the apparatus is shown in Figure 8.7. Consider that a sample of thickness t is inserted into one arm of the interferometer, which operates in a vertical fringe mode, with air only in both parts, to produce fringe shifts. When the sample extends under load, the resultant fringe shift Δm is given by

$$\Delta m = \frac{2}{\lambda} \left[(n_i - 1)\Delta t + t\,\Delta n_i \right],$$
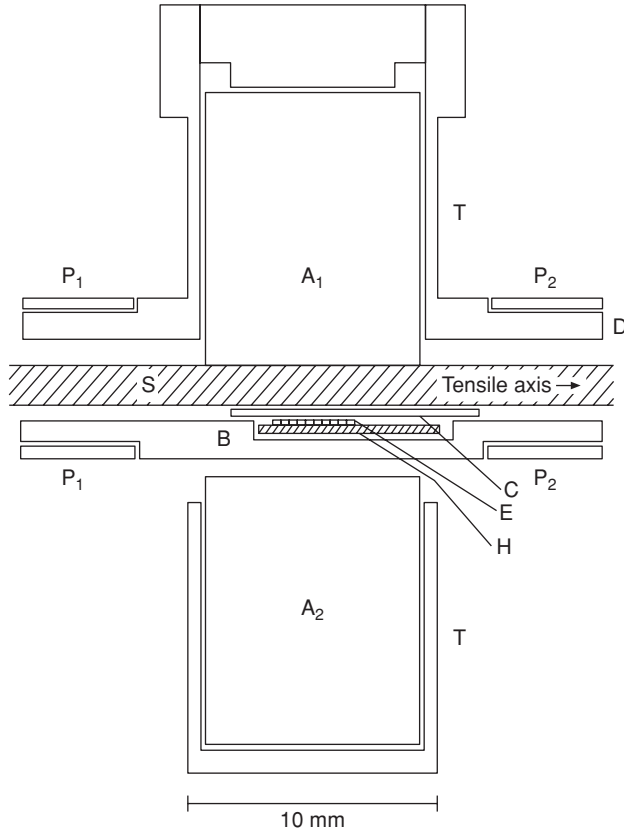
Figure 8.8 *Scale diagram of the Hall effect lateral extensometer. (Redrawn from Richardson, I.D. and Ward, I.M. (1978) Temperature-dependence of Poisson ratios in low-density polyethylene with parallel lamellas morphology. J. Polym. Sci. Polym. Phys.,* **16***, 667. Copyright (1978).)*

where Δt and Δn_i are the changes in thickness and refractive index respectively. For a stress σ applied along the 2 direction, $\Delta t_3 = s_{23} t \sigma_3$. Similarly $\Delta t_1 = s_{21} t \sigma_1$ for stress σ applied along the 1 direction. The change in refractive index is $\Delta n_i = \pi'_{ij} \sigma_j$, where π_{ij} is a photoelastic constant. Because the fringe shift depends on both Δt and Δn_i, it is necessary to make measurements in both air and water, or in two liquids, so that the lateral compliances and the stress-optical coefficients can be determined.

The lateral compliances of polymer sheets have also been determined using a specially constructed Hall effect lateral extensometer [13]. A thin polymer strip of polymer S, seen in cross section in Figure 8.8, is extended between two Alnico permanent magnets A_1 and A_2 mounted in a brass tube T. The like poles of the magnets are adjacent, so that the magnetic field between the magnets has a null point, and the field gradient is twice that of a single magnet. The polymer strip is held in contact with the magnet A_1 by a stainless steel plate B, containing the Hall effect device H, covered by a thin stainless steel plate C. The Hall plate is positioned so that the magnetic field sensing element E is on the axis of the magnets. Continuous contact between the plate containing the Hall effect device and the specimen
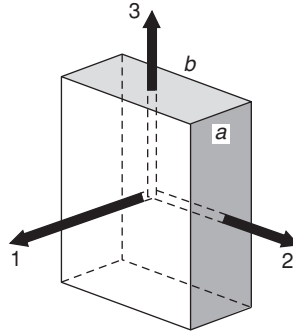
Figure 8.9   *The orthorhombic sheet.*

is ensured by exerting a small lateral compressive force by means of two pairs of phosphor bronze springs P_1 and P_2. Lateral strains down to 10^{-3} could be measured in sheets $\sim$0.5 mm thickness.

8.3.1.4   Torsion of Oriented Polymer Sheets

Torsion of oriented polymer sheets was undertaken by Raumann [14] to determine the shear compliances s_{44} and s_{66} for uniaxially oriented (transversely isotropic) low-density polyethylene. Torsion of oriented sheets can also be used to determine the shear compliances s_{44}, s_{55} and s_{66} for sheets possessing orthorhombic symmetry. As this situation is more general than that of transverse isotropy, it will be considered first.

For the orthorhombic sheets, a solution can only be found to the elastic torsion problem when the sheets are cut as rectangular prisms with their surfaces normal to the three axes of orthorhombic symmetry, and where the torsion axis coincides with one of these three axes.

A typical situation is illustrated in Figure 8.9. Torsion about the 3 axis involves the shear compliances in the 23 and 13 planes, which are s_{44} and s_{55} respectively.

The St Venant theory (see Reference 15, p. 283) gives the torque Q_z required to produce the twist T in a specimen of length ℓ, thickness a and width b:

$$Q_z = \frac{ab^3 T}{s_{55}\ell}\beta(c_z) = \frac{ba^3 T}{s_{44}\ell}\beta(c_z^+)$$

i.e. Q_z/T = torsional rigidity of the specimen, where

$$c_z = \frac{1}{c_z^+} = \frac{a}{b}\left(\frac{s_{55}}{s_{44}}\right)^{1/2}$$

and $\beta(c_z)$ is a rapidly converging function of c_z that for $c_z > 3$ can be approximated to

$$\beta(c_z) = \frac{1}{3}\left\{1 - \frac{0.630}{c_z}\right\}.$$

For a transversely isotropic sheet (with 3 direction as axis of symmetry), a similar expression describes torsion about an axis perpendicular to the symmetry axis. In this case, $s_{44} = s_{55}$ and the torque Q_z is given by

$$Q_z = \frac{bc^3 T}{s_{66}\ell}\beta(c^*) = \frac{cb^3 T}{s_{44}\ell}\beta(c^+),$$

where

$$c^+ = \frac{1}{c^*} = \frac{c}{b}\left(\frac{s_{44}}{s_{66}}\right)^{1/2}$$

where b is the thickness, c is the width and ℓ is the length of the specimen.

These formulae show that the relative contribution of the various shear compliances to the torque depends on their relative magnitude and the aspect ratios a/b or b/c. In principle, therefore, both compliances can be obtained from measurements on sheets of different aspect ratios, and this has been done for several polymers [16–18].

For transversely isotropic sheets, a much simpler formula applies for torsion around the symmetry axis 3, where the torque Q_z is given by

$$Q_z = (ab^3/s_{44}\ell)\beta(c),$$

where $c = a/b$. $\beta(c)$ is now the same function of $c = a/b$ only.

In practice, the torsion of oriented polymer sheets is complicated by several effects that cause an apparent increase in the stiffness of the sample [18].

First, there is the extension of lines parallel to the twist axis at the sample edge with respect to similar lines near the centre. This is analogous to the bifilar or multifilar effect in suspensions. When the twist axis is parallel to the symmetry axis in transversely isotropic sheets, the effect of such small axial stresses can be dealt with by the theoretical treatment of Biot [19]. In general, however, it is necessary to carry out experiments over a range of axial stresses, and extrapolate to zero axial stress.

Secondly, planes normal to the twist axes warp into characteristic patterns, but the grips at each end prevent such warping locally. Although Timoshenko and Goodier [20] have given a theoretical treatment for the effective increase in stiffness, it is again satisfactory to adopt a more empirical procedure. Following Folkes and Arridge [6], it is considered that such end effects are confined to a block with sample compliance s' and length p at each end of the sample of total length ℓ, the central region of homogeneous stress having the true sample compliance s^0. This gives a linear variation in measured overall sample compliance s with reciprocal length

$$s = s^0 + (2p/\ell)(s' - s^0).$$

s^0 can be found by taking measurements on samples of different length and extrapolating to zero reciprocal length [18].

8.3.1.5   *Simple Shear of Oriented Polymer Sheets*

In view of the complications arising in the torsion of oriented polymer sheets due to the effects of axial stress and end effects associated with the grips, there is considerable incentive to determine the shear compliances s_{44} and s_{66} by simple shear. Figure 8.10 shows a diagram of an apparatus designed by Lewis, Richardson and Ward [21]. Identical
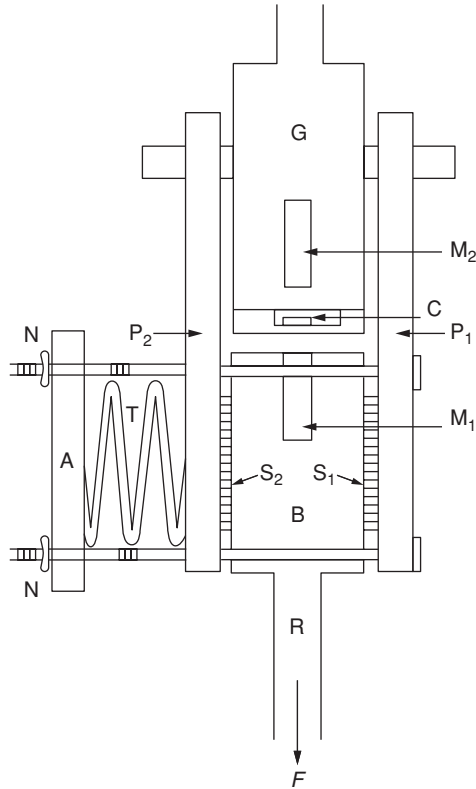
Figure 8.10 *Diagram of the Hall effect simple shear apparatus. C is the Hall plate between magnets M_1 and M_2. Samples S_1 and S_2 are mounted between plates P_1 and P_2 and the moveable block B pulled by force F. (Redrawn from Lewis, E.L.V., Richardson, I.D. and Ward, I.M. (1979) Hall-effect apparatus for the measurement of simple shear in polymers. J. Phys. E, **12**, 189 Copyright (1979).)*

samples S_1, and S_2 are mounted between outer brass plates P_1 and P_2, and an inner movable block B. The samples are held in place by a calibrated spring T, adjusted by four wing nuts N acting on a plate A. The shear stress is applied to the samples by a downward force *F* acting through shaft R on block B. Conveniently the force *F* may be applied by means of weights, running the shaft through linear bearings to minimise friction. The shear displacement is sensed by a Hall plate C mounted between the like poles of two magnets M_1 and M_2 of approximately equal magnetic moment. The principle of use of the Hall plate is therefore identical to that described for the lateral extensometer described above. The Hall voltage is measured by an incremental gaussmeter, the apparatus being calibrated by placing non-ferrous spacers of known thickness between the block B and G.

The measured values for the shear compliance of polymers are found to depend on the magnitude of the lateral compressive stress. Results are therefore obtained for a range of lateral stresses, and the true shear compliance found by extrapolation to zero lateral stress.

It has been shown that the values of shear compliance obtained in this way agree with those obtained from torsion of sheets [18].

8.3.2 Measurements on Fibres and Monofilaments

8.3.2.1 Extensional Modulus $E_3 = 1/s_{33}$

Dynamic mechanical measurements have been used to study the influence of molecular orientation on the extensional moduli of fibres drawn to different draw ratios* and also to compare the extensional moduli for a wide range of textile fibres produced by conventional manufacturing processes. The most extensive studies of this type are those of Wakelin *et al*. [22] and Meredith [23].

Detailed measurements of the extensional modulus of monofilaments have been made by longitudinal wave-propagation methods, where the relationship of the extensional modulus to molecular orientation and crystallinity has been examined. Early investigations using this technique were made by Hillier and Kolsky [24], Ballou and Smith [25], Nolle [26] and Hamburger [27].

The measurement of the extensional modulus was re-examined as a possible method for the measurement of molecular orientation in textile yarns by Charch and Moseley [28], Moseley [29] and Morgan [30]. Morgan has developed Hamburger's pulse-propagation method.

8.3.2.2 The Torsional Modulus $G = 1/s_{44}$

A convenient dynamic method for measuring the torsional modulus of synthetic fibre filaments was developed by Wakelin *et al*. [22].

A simpler method is that adopted by Meredith [23], where the fibre undertakes free torsional vibrations supporting known inertia bars at its free end.

8.3.2.3 The Extensional Poisson's Ratio $\nu_{13} = -s_{13}/s_{33}$

Measurements of the extensional Poisson's ratio ν_{13} have been attempted using optical diffraction and mercury-displacement techniques by Davis [31] and Frank and Ruoff [32] respectively. Satisfactory data were only obtained for nylon because this fibre is a particularly favourable case, showing no permanent deformation up to 5% extension.

More recently, measurements have been made by observing in a microscope the radial contraction, together with the corresponding lateral extension of a fibre monofilament [33]. The monofilament was extended between two moveable grips, which were part of a specially constructed microscope stage. Two ink marks were placed on the monofilament to act as reference points for the measurement of length and changes in length. An immersion liquid was used to reduce diffraction effects at the edges of the monofilament. The method was of limited accuracy, and errors of at least 10% were reported for 95% confidence limits on the mean value.

---

* The draw ratio is the ratio of the length of a line parallel to the draw direction in the drawn material to its length before drawing. For synthetic fibres it is often determined by measuring the ratio of the initial diameter D_i to final diameter D_f assuming that volume is conserved, i.e. draw ratio $= D_i/D_f$.
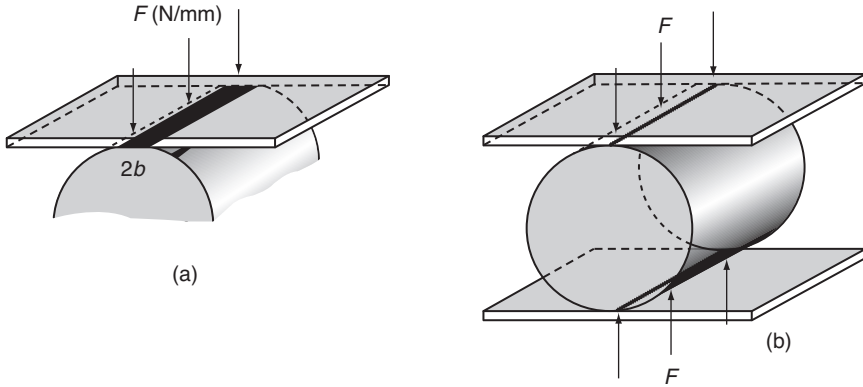
Figure 8.11   *The contact zone in the compression of a fibre monofilament (a) and for consideration of deformation in the central zone of the compressed monofilament it is sufficient to assume line contacts (b).*

8.3.2.4   The Transverse Modulus $E_1 = 1/s_{11}$

The two remaining elastic constants for fibres, the compliances s_{11} and s_{12}, have to be determined by more sophisticated methods. Both can be obtained from the compression of fibre monofilaments between parallel plates under conditions of plane strain. The transverse modulus is involved in the contact width $2b$ [33, 34] (Figure 8.11(a)).

The monofilament is a transversely isotropic solid; thus, it is isotropic in a plane perpendicular to the fibre axis. This implies that under compressive loading normal to the fibre axis the stresses in the transverse plane will be identical in form to those for the compression of an isotropic cylinder. As the length of monofilament under compression is comparatively long, friction ensures that the compression occurs under plane strain conditions. There is, therefore, no change in dimension along the fibre axis ($e_{33} = 0$) and only a normal stress acts along the fibre axis σ_{33} that can be found in terms of the normal stresses σ_{11} and σ_{22} in the plane perpendicular to the fibre axis. We have

$$\sigma_{33} = -\frac{s_{13}}{s_{33}}(\sigma_{11} + \sigma_{22}).$$

All the stresses can therefore be obtained from the solution to the problem of compression of an isotropic cylinder. The corresponding strains can then be obtained using the constitutive equations $e_p = s_{pq}\sigma_q$.

The contact zone is arranged to be small compared with the radius of the monofilament. It is therefore adequate to assume that we are dealing with the contact between two semi-infinite solids and follow Hertz's classic solution for the compression of an isotropic cylinder [35]. In this solution, the displacement of the cylinder within the contact zone is assumed to be parabolic and the boundary conditions are satisfied along the boundary plane only. For purely algebraic reasons, it is most convenient to use the complex variable method of McEwen [36] to obtain an analytical solution for b. It was shown by Ward *et al.* [33] that

$$b^2 = \frac{4FR}{\pi}\left(s_{11} - \frac{s_{13}^2}{s_{33}}\right),$$

where F is the load per unit length of monofilament in Newtons per metre, and R is the radius of the monofilament. This expression may be written as

$$b^2 = \frac{4FR}{\pi}(s_{11} - v_{13}^2 s_{33}).$$

Highly oriented polymers are usually much stiffer along their axis than transverse to it. The quantity s_{33} is therefore usually very small compared with s_{11}. Since the Poisson's ratio v_{13} is typically near to 0.5, it follows that the term $v_{13}^2 s_{33}$ is only a small correction factor and that the contact width depends primarily on s_{11}. Thus, the contact problem provides a good method in principle for determining s_{11}.

After pioneering work by Ward *et al.* [33], further experimental developments by Kotani, Sweeney and Ward [37] resulted in the apparatus shown schematically in Figure 8.12. The monofilament is compressed between two parallel glass plates on a microscope stage. Illumination is axial through the microscope normal to the visual field, resulting in the contact zone appearing as a dark rectangle. Displacement transducers were added to measure diametral compression.
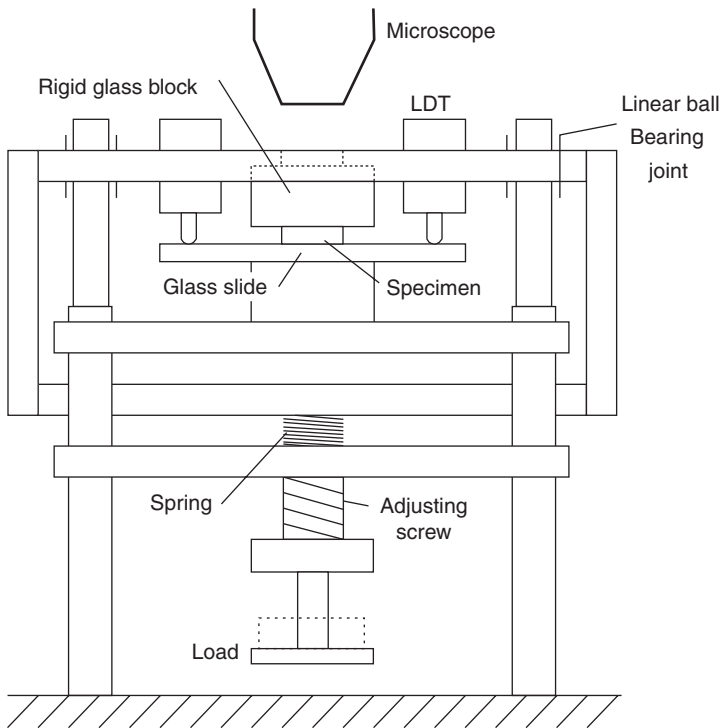

Figure 8.12 *Transverse fibre compression apparatus. (Reproduced from Kotani, T., Sweeney, J. and Ward, I.M. (1994) The measurement of transverse mechanical properties of polymer fibres. J. Mater. Sci., 29, 5551. Copyright (1994) Springer Science and Business Media.)*

Figure 8.13   *Measurement of contact width as a function of the applied force for polyethylene fibres. (Reproduced from Kotani, T., Sweeney, J. and Ward, I.M. (1994) The measurement of transverse mechanical properties of polymer fibres. J. Mater. Sci.,* **29**, *5551. Copyright (1994) Springer Science and Business Media.)*
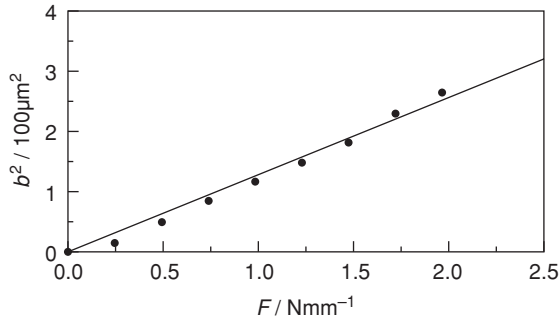
It can be shown [38] that the total diametral compression in the direction u_1 (i.e. parallel to the direction of the applied load) is

$$u_1 = -\frac{4F}{\pi}\left(s_{11} - \frac{s_{13}^2}{s_{33}}\right)\left(0.19 + \sinh^{-1}(R/b)\right). \tag{8.3}$$

Measurements of this type were undertaken simultaneously with the contact zone observations [37], and produced consistent values of $(s_{11} - s_{13}^2/s_{33})$ for a range of polymer fibres, namely polyethylene terephthalate, polyethylene and a thermotropic liquid crystalline polymer based on hydroxybenzoic and hydroxynaphthoic acid in the ratio 73:27 (Vectra). Values for E_1 were in the range 1.94–2.34 GPa for polyethylene terephthalate, 0.63–1.50 GPa for polyethylene and 0.96–1.01 GP for Vectra. Typical contact zone observations are shown in Figure 8.13.

Measurements of diametral compression only have been made by Kawabata [39] who devised an apparatus that used a linear differential transformer to measure diametral changes of 0.05 μm in single fibres of diameter 5 μm. Equation (8.3) was then used to calculate the transverse modulus E_1. Results were obtained for poly(p-phenylene terephthalamide) (Kevlar) and high modulus polyethylene (Tekmilon) fibres. Values of E_1 were in the range 2.31–2.59 GPa for Kevlar and a value of 1–2 GPa was found for Tekmilon.

8.3.2.5   The Transverse Poisson's Ratio $v_{12} = s_{12}/s_{11}$

The transverse Poisson's ratio can be determined by measuring u_2 the change in diameter parallel to the plane of contact in the compression of the monofilament under conditions of plane strain as described in the section on the transverse modulus above.

A simple analysis of this problem follows from the condition that the contact zone can be arranged to be small compared with the radius of the monofilament. To calculate the deformations in the diametral plane, it is then adequate to consider the problem as the compression of a cylinder under concentrated loads (Figure 8.11(b)). For an isotropic cylinder, this is a well-known problem to be found in textbooks on elasticity (see Reference 20, p. 122). It is necessary to satisfy the boundary conditions on the surface of the cylinder, and this is done by addition of an isotropic tension in the plane perpendicular to the fibre axis.
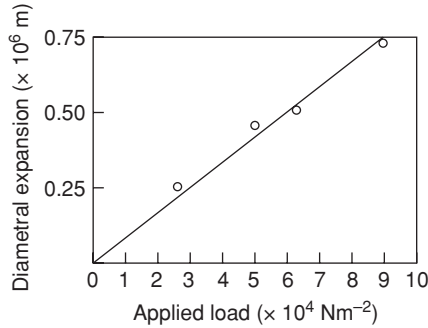
Figure 8.14 *Compression of polyethylene terephthalate monofilament (diameter 0.282 mm): measurement of diametral expansion as a function of applied load.*

The stresses for the transversely isotropic monofilament correspond exactly to those for the isotropic case. It is therefore very straightforward to calculate the strains and hence evaluate the diametral expansion u_2.

It is found that

$$u_2 = F \left\{ \left(\frac{4}{\pi} - 1 \right) \left(s_{11} - \frac{s_{13}^2}{s_{33}} \right) - \left(s_{12} - \frac{s_{13}^2}{s_{33}} \right) \right\}.$$

For most oriented monofilaments, s_{13}^2/s_{33} is small compared with s_{11}, as discussed previously. Hence, u_2 will depend primarily on s_{12} with a substantial term in s_{11}, which is about $s_{11}/4$. Thus, the measurement of the diametral expansion provides a method for determining s_{12} provided that s_{11} is determined from a measurement of the contact width b, as described in 8.3.2.4 above.

Measurements of u_2 have been carried out with the monofilament surrounded by an immersion liquid [33], and the diameter is measured directly with a calibrated eyepiece. The immersion liquid was chosen to have refractive index approximately equal to that of the monofilament, hence reducing diffraction effects without making the monofilament invisible. Very careful focusing of the microscope was necessary in these experiments. Inaccuracy in focusing can cause errors in the diameter measurements of the order of u_2 itself.

A typical set of results for polyethylene terephthalate is shown in Figure 8.14. It can be seen that the change in diameter is proportional to the applied load, as predicted theoretically.

8.4 Experimental Studies of Mechanical Anisotropy in Oriented Polymers

The review of experimental studies has two principal aims. First, we will describe early studies on low-density polyethylene and oriented monofilaments because these highlighted several unexpected features of the anisotropy, indicated the differences between individual polymers and provided the basis for the aggregate model against which many subsequent measurements have been tested. Secondly, we will provide very brief summaries of further work in this area, and indicate its relevance to our present understanding.
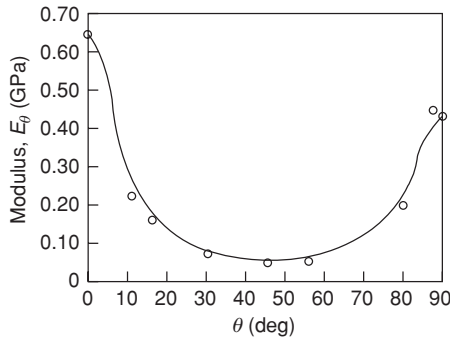
Figure 8.15 *Comparison of the observed variation in modulus E_0 with angle θ to draw direction and the theoretical relation (i.e. full curve) calculated from E_0, E_{45} and E_{90} for low-density polyethylene sheet drawn to a draw ratio of 4.65. (Reproduced from Raumann, G. and Saunders, D.W. (1961) The anisotropy of Young's modulus in drawn polyethylene. Proc. Phys. Soc., 77, 1028. Copyright (1961).)*

8.4.1   Sheets of Low-Density Polyethylene

Raumann and Saunders [40] uniaxially stretched isotropic sheets of low-density (i.e. branched) polyethylene to varying final extensions, and measured the tensile modulus in directions over a range of angles to the initial draw direction. For a highly oriented sample, the plot of Young's modulus ($1/s_\theta$) against angle with the draw direction (Figure 8.15) shows the lowest stiffness at an angle close to 45° to that direction.

The general compliance equation for transverse isotropy is

$$s_\theta = s_{11} \sin^4 \theta + s_{33} \cos^4 \theta + (2s_{13} + s_{44}) \sin^2 \theta \cos^2 \theta.$$

The experimental result implies that $(2s_{13} + s_{44})$ is much greater than either s_{11} or s_{33}, because when $\theta = 45°$ the terms will be equally weighted.

Replotting to obtain the modulus at a given angle as a function of draw ratio (Figure 8.16), the results are again somewhat unexpected: E_0 initially falls with increasing draw ratio, so that at low draw ratios $E_{90} > E_0$. Subsequently, Gupta and Ward [41] showed that this unusual behaviour was specific to room temperature measurements, and at a sufficiently low temperature, the behaviour resembled that of most other polymers (Figure 8.17).

8.4.2   Filaments Tested at Room Temperature

In a comprehensive study at room temperature, Hadley, Pinnock and Ward [42] determined the five independent elastic constants for oriented filaments of polyethylene terephthalate, nylon 6:6, low- and high-density polyethylene and polypropylene. The orientation was determined in terms of draw ratio and optical birefringence. Subsequent studies indicated that it would have been appropriate to record not only the overall orientation, as derived from birefringence, but also the crystal orientation, obtainable from X-ray measurements. The results are summarised in Table 8.1 and Figures 8.18–8.22 (see Section 8.6.2 for discussion of the aggregate theory predictions).

Although the detailed development of mechanical anisotropy in these particular filaments must depend on their exact chemical composition and subsequent processing, several
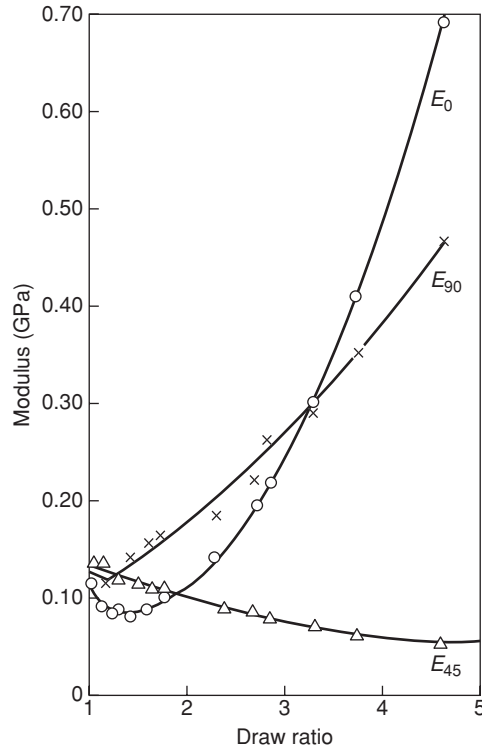
Figure 8.16   The variation in E_0, E_{45} and E_{90} with draw ratio in cold-drawn sheets of low-density polyethylene. Modulus measurements taken at room temperature. (Reproduced from Raumann, G. and Saunders, D.W. (1961) The anisotropy of Young's modulus in drawn polyethylene. Proc. Phys. Soc., **77**, 1028. Copyright (1961).)
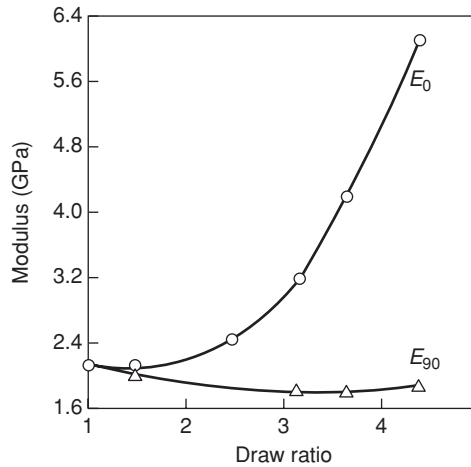

Figure 8.17   The variation in E_0 and E_{90} with draw ratio in cold-drawn sheets of low-density polyethylene. Modulus measurements taken at $-125°C$.

Table 8.1 *Elastic compliances of oriented fibres (units of compliance are 10^{-10} Pa^{-1}, errors quoted are 95% confidence limits) [42].*

| Material	Birefringence (Δn)	s_{11}	s_{12}	s_{33}	s_{13}	s_{44}	$v_{13} = -s_{13}/s_{33}$	$v_{12} = -s_{12}/s_{11}$
Low-density polyethylene film [14]		22	−15	14	−7	680	0.50	0.68
Low-density polyethylene 1	0.0361	40 ± 4	−25 ± 4	20 ± 2	−11 ± 2	878 ± 56	0.55 ± 0.08	0.61 ± 0.20
Low-density polyethylene 2	0.0438	30 ± 3	−22 ± 3	12 ± 1	−7 ± 1	917 ± 150	0.58 ± 0.08	0.73 ± 0.20
High-density polyethylene 1	0.0464	24 ± 2	−12 ± 1	11 ± 1	−5.1 ± 0.7	34 ± 1	0.46 ± 0.15	0.52 ± 0.08
High-density polyethylene 2	0.0594	15 ± 1	−16 ± 2	2.3 ± 0.3	−0.77 ± 0.3	17 ± 2	0.33 ± 0.12	1.1 ± 0.14
Polypropylene I	0.0220	19 ± 1	−13 ± 2	6.7 ± 0.3	−2.8 ± 1.0	18 ± 1.5	0.42 ± 0.16	0.68 ± 0.18
Polypropylene 2	0.0352	12 ± 2	−17 ± 2	1.6 ± 0.04	−0.73 ± 0.3	10 ± 2	0.47 ± 0.17	1.5 ± 0.3
Polyethylene terephthalate 1	0.153	8.9 ± 0.8	−3.9 ± 0.7	1.1 ± 0.1	−0.47 ± 0.05	14 ± 0.5	0.43 ± 0.07	0.44 ± 0.09
Polyethylene terephthalate 2	0.187	16 ± 2	−5.8 ± 0.7	0.71 ± 0.04	−0.31 ± 0.03	14 ± 0.2	0.44 ± 0.07	0.37 ± 0.06
Nylon 6:6	0.057	7.3 ± 0.7	−1.9 ± 0.4	2.4 ± 0.3	−1.1 ± 0.15	15 ± 1	0.48 ± 0.05	0.26 ± 0.08
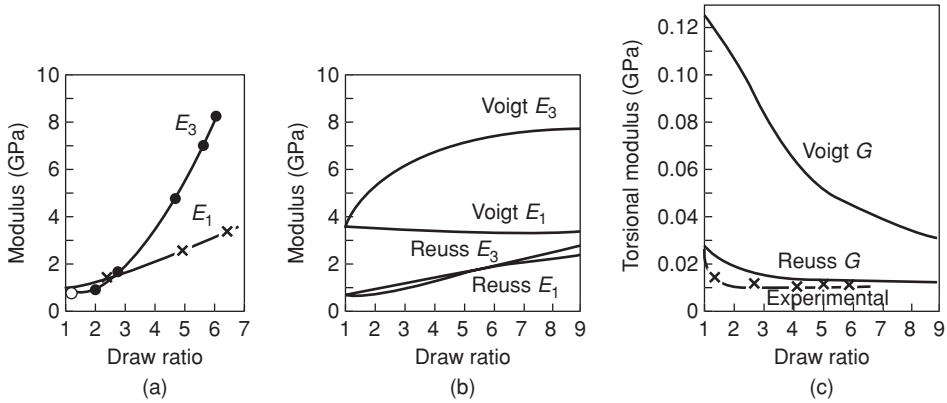
Figure 8.18   *Low-density polyethylene filaments: extensional (E_3), transverse (E_1) and torsional moduli (G); comparison between experimental results and simple aggregate theory for E_3 and E_1 ((a) and (b)) and for G (c).*

general features can be distinguished. The principal effect of drawing (i.e. increasing molecular orientation) is to increase the Young's modulus E_3 measured along the filament axis. In nylon 6:6 and polyethylene terephthalate, there is a corresponding but small decrease in the transverse modulus E_1. For polypropylene and high-density polyethylene E_1 is almost independent of draw ratio and for low-density polyethylene E_1 increases significantly, in agreement with the results of Raumann and Saunders. Note here, too, the anomalous behaviour of this polymer at low draw ratios. Overall, E_3 for highly oriented filaments is greater than E_1, with the anisotropy being greatest for polyethylene terephthalate:

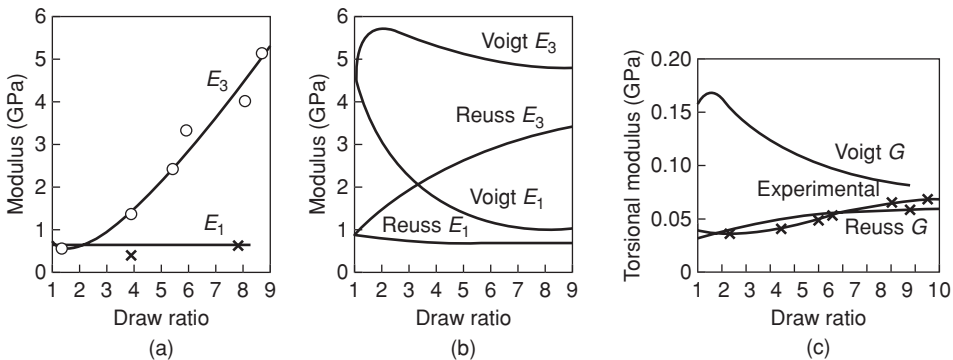$$\frac{E_3}{E_1} = \frac{s_{11}}{s_{33}} \approx 27.$$

Figure 8.19   *High-density polyethylene filaments: extensional (E_3), transverse (E_1) and torsional moduli (G); comparison between experimental results and simple aggregate theory for E_3 and E_1 ((a) and (b)) and for G (c).*

Figure 8.20 *Polypropylene filaments; extensional (E3), transverse (E1) and torsional moduli (G); comparison between experimental results and simple aggregate theory for E3 and E1 ((a) and (b)) and for G (c).*
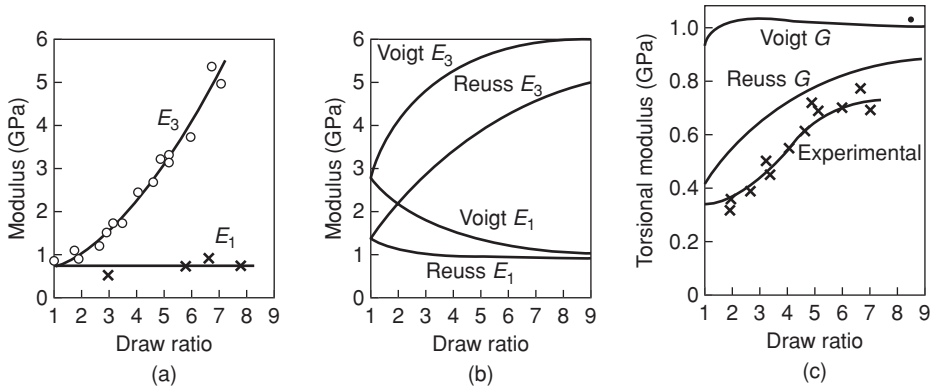
The shear modulus G of low-density polyethylene, and its change with orientation, provides another striking contrast with the other materials examined. A decrease in G by more than a factor of 3 over the range of orientation used compares with only small changes for the other filaments. In polyethylene terephthalate, high-density polyethylene and polypropylene $s_{44} \sim s_{11}$; in nylon $s_{44} \sim 2s_{11}$. By contrast, low-density polyethylene, at least as regards room-temperature behaviour, is exceptional, with the extensional compliance s_{33} having the same order of magnitude as the transverse compliance s_{11}, and with the shear compliance s_{44} being more than an order of magnitude greater than either s_{11} or s_{33}. Such measurements provide the basis for the discussion of relaxation transitions in Chapter 10.

In all cases, the compliance s_{13} is low and appears to decrease fairly rapidly with increasing draw ratio, in a manner comparable with s_{33}. Hence, the extensional Poisson's
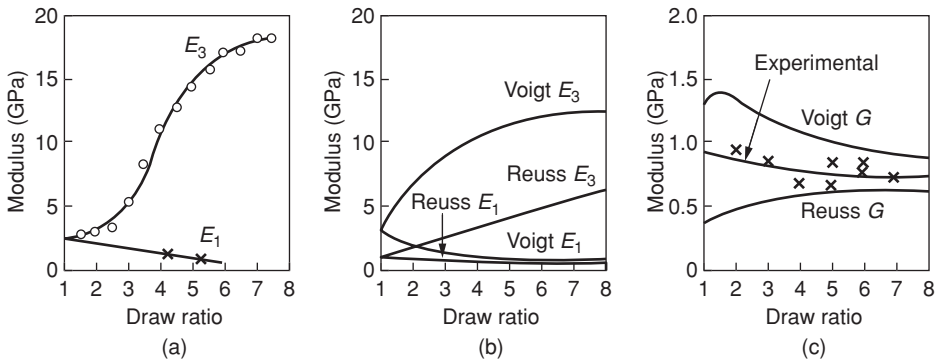

Figure 8.21 *Polyethylene terephthalate filaments: extensional (E_3), transverse (E_1) and torsional moduli (G); comparison between experimental results and simple aggregate theory for E_3 and E_1 ((a) and (b)) and for G (c).*

Figure 8.22 *Nylon filaments: extensional (E_3), transverse (E_1) and torsional moduli (G); comparison between experimental results and simple aggregate theory for E_3 and E_1 ((a) and (b)) and for G (c).*
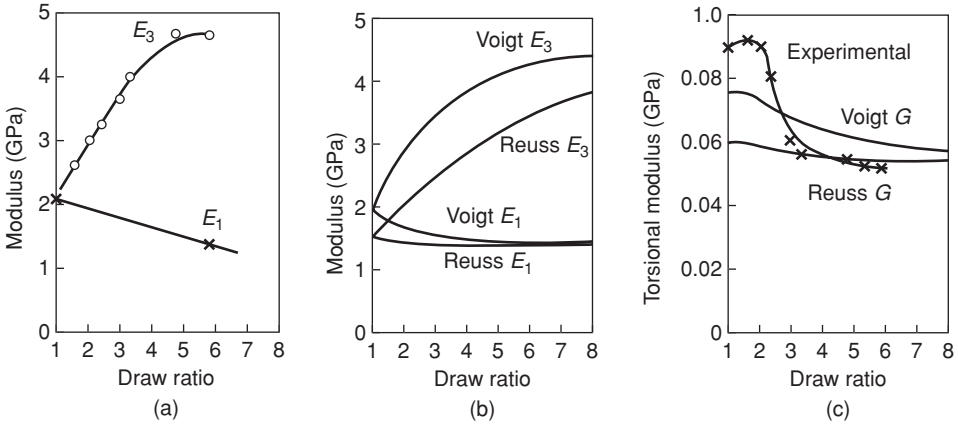
ratio $\nu_{13} = -s_{13}/s_{33}$ is rather insensitive to draw ratio and, with the exception of high-density polyethylene, does not differ significantly from 0.5. It is thus generally a valid approximation to assume that the filaments are incompressible. Note that for anisotropic bodies ν_{13} is not confined to a maximum value of 0.5, but is limited solely by the inequalities necessary for a positive strain energy [3]

$$s_{12}^2 < s_{11}^2; \quad s_{13}^2 < \frac{1}{2}s_{33}(s_{11} + s_{12}).$$

Hine and Ward [43] have used the ultrasonic immersion method (Section 6.3.2) to determine a full set of elastic constants for a range of fibres, by making uniaxially oriented fibre composites. In the first method, the oriented composites were produced by the Leeds hot compaction process. Here fibres are compacted under suitable conditions of temperature and pressure to form an homogenous oriented material in which only a small fraction of the original fibre is melted and re-crystallised to form the matrix of the fibre composite. This matrix fraction can be removed and results extrapolated to 100% fibre fraction. The measured elastic properties for a range of fibres are shown in Table 8.2. The overall patterns

Table 8.2 *The elastic properties of the plates of compacted fibres.*

Fibre type	E_{33} (GPa)	E_{11} (GPa)	ν_{13}	ν_{12}	G_{13} (GPa)
Tenfor polyethylene	57.7	4.68	0.45	0.55	1.63
Dyneema polyethylene	74.3	4.31	0.47	0.57	1.36
Polyethylene terephthalate	14.9	3.70	0.39	0.65	1.62
Polypropylene	11.0	2.41	0.39	0.58	1.52
Liquid crystal polymer	97.2	3.24	0.48	0.73	1.3

Standard deviation: E_{33} ±3%; all others, ± 2%.

of anisotropy determined by these ultrasonic measurements are similar to those found earlier by Hadley, Pinnock and Ward. It is particularly notable that ν_{12} is greater than 0.5, which is consistent with the view that in highly oriented fibres the high axial stiffness means that transverse compression becomes close to pure shear in the transverse plane.

More recently, Wilczynski, Ward and Hine [44] have proposed an 'inverse calculation' method where the elastic constants of a fibre can be estimated from fibre resin composite and the elastic constants of the resin. The method was confirmed by measurements on polyethylene/epoxy and carbon fibre/epoxy resin composites. It has been applied [45] to the determination of the elastic constants of an organic fibre, poly{2,6-dimidazo [4,5-6′. 4′5′-e] pyridinylene – 1,4(2,5 dihydroxy)phenylene} (PIPD). This fibre is a lyotropic liquid crystalline fibre with very high Young's modulus of 285 GPa and a much higher tensile strength (5.21 GPa) and compressive strength (500 MPa) than other polyaramid fibres such as Kevlar.

The technique of Brillouin spectroscopy (Section 6.3.3) has been applied to determine the elastic constants of oriented polymer fibres. Early studies of this nature were undertaken by Krüger *et al*. [46, 47] on oriented polycarbonate films, also determining the third-order constants, which define the elastic non-linear behaviour. Wang, Liu and Li [48, 49] have described measurements on oriented polyvinylidene fluoride and polychlorotrifluoroethylene films. In the latter case the results were interpreted using an aggregate model differing in detail from that of Ward discussed in Section 8.6.2.

Recent Brillouin spectroscopy measurements include those of Kumar, Renisch and Grimsditch [50] on uniaxially and biaxially stretched polypropylene films. Using the Ward aggregate model with a modified definition of molecular alignment, enabled elastic anisotropy and refractive index data to be quantitatively related to molecular orientation.

Choy, Leung and his colleagues, initially in collaboration with Ward, have undertaken very extensive measurements of the elastic constants of oriented polymers using the ultrasonic techniques described in Section 6.3.2. Results have been obtained for hydrostatically extruded polypropylene and polyethylene terephthalate [51], die-drawn polyethylene [52], hot-rolled nylon 66 [53] and polyoxymethylene [54], high modulus polyethylene [55] and polypropylene [56] produced by tensile drawing. The results have been analysed in terms of the aggregate model, which has proved a fair approximation for the low temperature data, and the Takayanagi model with tie molecules or crystalline bridges that is more satisfactory for high temperature data.

8.5   Interpretation of Mechanical Anisotropy: General Considerations

The mechanical anisotropy of oriented polymers is determined by the following factors, which will be discussed in turn: (1) the structure of the molecular chain and, where the polymer crystallises, the crystal structure; (2) the molecular orientation and, in a crystalline polymer, the morphology; (3) thermally activated relaxation processes in both crystalline and non-crystalline regions.

8.5.1   Theoretical Calculation of Elastic Constants

Major developments in fibre technology have led to ultra-high modulus fibres such as poly-paraphenylene terephthalamide (PPTA) (Kevlar and Twaron) and polyethylene (Dyneema,

Spectra and Certran). There has therefore been an increased interest in theoretical calculations of the elastic constants, of oriented polymers. This has been given added impetus by the development of more sophisticated computational techniques, some of which are available as commercial software packages (e.g. Accelrys, [57]).

Historically, this area developed in three stages:

1. Calculation of the elastic modulus of a single polymer chain. This method has provided useful estimates of the Young's modulus of an ideal perfectly oriented polymer. Only the intramolecular interactions within the polymer chain are taken into account, and only the stiffness in the chain direction can be estimated, none of the other elastic constants.

   In the simplest case, consider a planar zigzag chain of identical bonds, of which the classic example is polyethylene. There are two modes of deformation: bond stretching and valence angle opening.

   If these are defined by force constants k_s and k_v that can be estimated from infrared and Raman spectroscopy, it can be shown that the chain modulus $E_3 = \dfrac{1}{s_{33}}$ is proportional to $\left[\dfrac{\cos^2 \theta}{k_s} + \dfrac{\ell^2 \sin^2 \theta}{4k_v} \right]^{-1}$, where ℓ is the calculated bond length and θ is the inclination of the bond to the chain axis.

   Following the treatment presented by Treloar [58], consider an idealised polyethylene chain with n bonds of length ℓ, each bond inclined at an angle θ to the chain axis, along which the force F is applied.

   The change in length due to the force F is given by

$$\delta L = n\delta(\ell \cos \theta) = n(\delta \ell \cos \theta - \ell \sin \theta \delta \theta) \tag{8.4}$$

$$\delta \ell = F \cos \theta / k_s. \tag{8.5}$$

   The force F also applies a torque $\frac{1}{2} F \ell \sin \theta$ that causes valence angle deformation

$$\delta \alpha = F \ell \sin \theta / 2k_v. \tag{8.6}$$

   Since $\theta = 90^0 - \alpha/2$,

$$\delta \theta = -\delta \alpha/2 = -F \ell \sin \theta / 4k_v. \tag{8.7}$$

   Substituting Equations (8.5) and (8.7) into (8.4),

$$\text{we have } \delta L = nF \left[\dfrac{\cos^2 \theta}{k_s} + \dfrac{\ell^2 \sin^2 \theta}{4k_v} \right]. \tag{8.8}$$

   The longitudinal modulus E_3 is given by

$$E_3 = (F/A)/(\delta L/L), \tag{8.9}$$

where A is the cross-sectional area of the chain and the initial chain length $L = n\ell \cos \theta$. This gives

$$E_3 = \dfrac{\ell \cos \theta}{A} \left[\dfrac{\cos^2 \theta}{k_s} + \dfrac{\ell^2 \sin^2 \theta}{4k_v} \right]^{-1}. \tag{8.10}$$

   Treloar found that spectroscopic data for k_s and k_v indicated that bond stretching and bond bending make rather similar contributions to the deformation, bond bending

about 60% and bond stretching 40%. The chain modulus was estimated as 182 GPa i.e. of a similar order to that determined experimentally by X-ray diffraction or neutron diffraction.

2. The lattice dynamical method, which was originally proposed by Born and Huang [59], to calculate the velocity of sound waves in elastic solids and hence their elastic constants. The equation of motion of an atom is given by

$$m\frac{\partial^2 u}{\partial t^2} + fu = 0, \tag{8.11}$$

where u is the displacement from the equilibrium position and f is the force constant and is given by the second derivative of the interatomic potential energy, i.e.

$$f = \frac{\partial^2 U}{\partial x^2}.$$

The solution to Equation (8.11) is a sound wave

$$u = u_0 \exp\left[i(kx - \omega t)\right],$$

where $k = 2\pi/\lambda$ is the wave vector and $\omega = 2\pi\nu$ is the angular frequency. Note the similarity of Equation (8.11) to the macroscopic equation for the propagation of a plane elastic wave. In the simplest terms this is

$$\rho\frac{\partial^2 u}{\partial t^2} = \frac{\partial \sigma}{\partial x} = c\frac{\partial^2 \varepsilon}{\partial x^2}.$$

The solution to this equation is also given by a wave equation with longitudinal wave of velocity w

$$w = \nu\lambda = \left(\frac{c}{\rho}\right)^{1/2},$$

where c is the appropriate stiffness constant (c_{11}, c_{22}, c_{33}, etc.)

This method is the subject of a classic textbook by Born and Huang [59], and has been followed extensively by Japanese researchers [60] (for a review see reference [61]) to calculate full sets of elastic constants for polymer crystals.

We will describe the principles of this method by considering the calculation of the chain modulus E_c. For an external strain ε_i applied along the chain axis, the displacement Δx_i of each atom in the chain can be written as

$$\Delta x_i = \rho_i + W\varepsilon_i. \tag{8.12}$$

The total displacement Δx_i is the sum of two terms, one of which (the second term on the right-hand side of Equation (8.12)) is proportional to the external strain ε_i and the term ρ_i that is an internal strain. This additional displacement ρ_i occurs because the atoms in the chain can change their position when the elastic deformation energy V is minimised for a given macroscopic deformation, expressed formally in Equation (8.12) by the strain ε_i.

V is calculated on the basis of interval displacement vectors $\Delta\mathbf{R}$ given formally by

$$\Delta\mathbf{R} = \mathbf{B}_\rho\rho + \mathbf{B}_\varepsilon\varepsilon, \tag{8.13}$$

where $\mathbf{B}_\rho$ and $\mathbf{B}_\varepsilon$ are appropriate geometrical matrices. The elastic deformation energy V is minimised with respect to the internal strain ρ using an appropriate force constant matrix, to give the relationships between $\Delta\mathbf{R}$ and the macroscopic strain ε. Hence, we have V in terms of an equation, which for the one-dimensional calculation of the chain modulus E_c can also be written as

$$V = \frac{1}{2} v E_c \varepsilon^2,$$

where v is an effective volume.

3. The energy minimisation method

Most recent estimates of the crystal elastic constants for polymers follow the method of calculating the second derivatives of the Helmholtz Free Energy A with respect to deformation of a small volume element v_0 [62, 63]. The stiffness constants $c_{\ell mnk}$ are defined as

$$\frac{\partial^2 A}{\partial \varepsilon_{\ell m} \partial \varepsilon_{nk}} = v_0 c_{\ell mnk}, \tag{8.14}$$

where

$$\varepsilon_{\ell m} = \frac{1}{2} \left\{ \frac{\partial u_\ell}{\partial x_m} + \frac{\partial u_m}{\partial x_\ell} \right\} + \text{second-order terms}.$$

The Helmholtz Free Energy includes both intermolecular forces and intramolecular forces and also entropic contributions. The intramolecular contributions are the same as those required for the single-chain calculation, but there is more difficulty in producing force fields that include intermolecular contributions. The intermolecular contributions are typically Lennard–Jones type interactions and to obtain plausible values that are satisfactory for a range of different chemical compositions is often debatable. It is, however, possible to obtain some confirmation of their validity in a particular instance by verifying that the calculations predict the correct crystal structure and this must be regarded as a the first step to calculating the elastic constants.

Rutledge and Suter [62] have shown that for Kevlar the intermolecular contributions contribute significantly to the free energy, changing the minimum energy conformation of the chain and leading to significantly higher values for the tensile modulus. They also showed that entropy contributions to the free energy amounted to about 20% of the total free energy. It was concluded that for Kevlar, the tensile modulus E_3, calculated on the basis of internal energy contributions alone was about 20% higher than the true value, and ignoring the intermolecular interactions gave a value too low by a similar amount. This explained why the simple single-chain calculations produced results that were rather close to experimental values obtained by X-ray diffraction, for example.

8.5.1.1 Theoretical Values for Elastic Constants

The lattice dynamical theory and the energy minimisation method are very similar because in both cases the elastic constants are determined by imposing appropriate deformations to the unit cell and reminimising the energy, permitting the components of the structure to deform individually in a non-affine manner. In both cases, the energy involves intramolecular and intermolecular terms. The intramolecular terms involve bond stretching and bond angle bending as described above for the single-chain calculation for the linear zigzag chain of

polyethylene. For a more general chain conformation such as a helix, there will also be the possibility of bond torsion. The forms chosen for these terms can differ but the numerical values for the parameters are always optimised on the basis of infrared and Raman spectra (see, for example, References [64–66]).

For the intermolecular terms, the Lennard–Jones 6–12 potential

$$V(r) = -Dr^{-6} + Er^{-12}$$

is often chosen, but the 6- exponential Buckingham potential

$$V(r) = -Ar^{-6} + B\exp(-cr)$$

can also be used.

The optimisation of the intermolecular terms is less straightforward because these depend on the details of the crystal structure and especially the intermolecular distances. A customary procedure is therefore to use the computation modelling first to give predictions for the crystal structure based on assumptions of the structure from structure information (X-ray diffraction, infrared and Raman spectroscopy, nuclear magnetic resonance). This is then followed by the estimation of the elastic constants assuming that entropic considerations can be ignored. Essentially these give predictions for 0 K that should be corrected for thermal motion to give predictions for ambient temperature.

It is instructive to compare the results obtained by different researchers and some of these are shown in Table 8.3 for polyethylene.

It can be seen that a rather wide range of predicted values is obtained that is partly due to choice of different force constants. The results are also sensitive to the details of the assumed crystal unit cell structure, especially the angle made by the plane of the planar zigzag polyethylene chain with the *b*-axis of the orthorhombic unit cell. The overall pattern of elastic anisotropy is however clear. The stiffness in the chain axis direction c_{33} is by far the greatest value, and the shear stiffnesses c_{44}, c_{55} and c_{66} are the lowest values. This reflects the major differences between the intramolecular bond stretching and valence bond bending forces and the intermolecular dispersion forces, which determine the shear stiffnesses. The lateral stiffnesses also relate primarily to dispersion forces and are correspondingly low.

Table 8.3   *Elastic stiffness constants for crystalline polyethylene (GPa).*

c_{ij}	Odajima and Maeda [60]	Karasawa, Dasgupta and Goddard [67]	Sorenson, Liau and Kesner [68]	Tashiro, Kobayashi and Tadokoro [69]	Wobser and Blasenbrey [70]
c_{11}	9.27	14.0	14.3	7.99	13.8
c_{12}	3.68	7.9	7.2	3.28	7.34
c_{13}	3.36	2.1	1.92	1.13	2.46
c_{23}	6.67	4.8	3.3	2.14	3.96
c_{22}	10.93	13.5	12.2	9.92	12.5
c_{33}	257.4	338.9	341	316	325
c_{44}	3.46	5.3	3.64	3.19	3.19
c_{55}	1.27	3.0	2.27	1.62	1.98
c_{66}	4.99	5.9	7.3	3.62	6.24

Table 8.4 *Comparison of hot compacted sheet stiffness constants (in GPa) with theoretical predictions for polyethylene.*

	c_{33}	c_{11}	c_{13}	c_{12}	c_{44}
Theoretical values for uniaxially oriented sheet	290	9.15	5.15	3.95	2.86
Hot compacted sheet (Tenfor)	62.3	7.16	5.09	4.15	1.63

Finally, it is of interest to compare the theoretical values for a uniaxially oriented sheet (calculated by averaging the stiffness values using the Voigt averaging scheme) with those obtained for a die-drawn rod and a sheet made by hot compaction of high modulus polyethylene fibres (Table 8.4). It can be seen that although, as expected, these materials have not reached full axial orientation so that the experimental values of c_{33} are much less than the theoretical value, the patterns of anisotropy are very similar, and some of the values for the other elastic constants are surprisingly close.

8.5.2 Orientation and Morphology

The degree of mechanical anisotropy is usually much less than considerations of the molecular chain would imply; and, in particular, the very high intrinsic modulus along the axial direction is not achieved. This is demonstrated in Table 8.5, where measured values of elastic constants for ultra-high-modulus polyethylene are compared with theoretical values. Crystalline polymers are essentially composite materials with alternating crystalline and amorphous regions. The former regions can be highly aligned during processing, but the latter are less well oriented. Even when the overall orientation of the chain segments appears to be quite high, measured, for instance by birefringence, there are still very few chains where long lengths of a molecule are axially aligned. It is such molecules that are critical in increasing the stiffness, because there is such a large difference between the stresses involved in bond bending and stretching and in other modes of deformation. Peterlin [71] has proposed that the Young's modulus of an oriented filament is essentially determined by the proportion of extended chain tie molecules that produce links in the axial direction between crystalline blocks. An alternative proposal of crystalline bridges linking the crystalline blocks is discussed in Chapter 9.

Polymers that do not crystallise, such as polymethyl methacrylate, show a good correlation between the (low) degree of mechanical anisotropy and molecular orientation determined from birefringence. There is so much disorder that it seems unlikely that a significant proportion of the chains can achieve the high alignment of a crystalline polymer such as polyethylene. Other polymers such as polyethylene terephthalate, which have a

Table 8.5 *Elastic constants of ultra-high-modulus polyethylene.*

	20°C	−196°C	Theoretical
Axial modulus (GPa)	70	160	316
Transverse modulus (GPa)	1.3	–	8–10
Shear modulus (GPa)	1.3	1.95	1.6–3.6
Poisson's ratio	0.4	–	0.5

comparatively low overall crystallinity ($\sim$30% is typical), may occupy an intermediate position. The mechanical anisotropy produced by drawing correlates well with overall molecular orientation, but this result may arise because tie molecules play a vital role, and their number increases with overall molecular orientation.

In conclusion, it must be emphasised that although it is convenient for the purpose of constructing models to assume a composite that comprises distinct crystalline and non-crystalline components, on the molecular level a gradual transition must occur, extending over a number of monomer units, between the well-orientated and ordered crystallites and the bulk of the remaining material.

8.6   Experimental Studies of Anisotropic Mechanical Behaviour and Their Interpretation

In general, it is to be expected that mechanical anisotropy will depend both on the crystalline morphology and the molecular orientation. Two extreme models form the basis for present understanding: a single-phase aggregate model proposed by Ward in which anisotropy arises through the orientation of anisotropic units of structure; and a microscopic model, proposed by Takayanagi in which the crystalline and amorphous regions are considered as two distinct phases. It is appropriate to discuss the mechanical anisotropy of polymers in terms of one or other of these models. In this chapter, those polymers whose behaviour best approximates to the Ward aggregate model will be discussed. In the following chapter, those polymers that are best considered as composite solids will be discussed, following an introductory presentation to the theoretical understanding of the mechanical behaviour of composite materials.

8.6.1   The Aggregate Model and Mechanical Anisotropy

In this model, it is proposed that the polymer can be considered as an aggregate of identical units, which in the unstretched state are oriented randomly. As orientation develops, the units rotate and become completely aligned at the maximum achievable orientation. The elastic properties of the units are those of the mostly highly aligned structure, that could be a fibre with transverse isotropy or a film with orthorhombic symmetry [72]. In this chapter, the theory will be developed for a fibre, in the first instance for the case where both the fibre and the structural units possess transverse isotropy.

It is instructive to test the appropriateness of the model in two stages:

1. Can the elastic constants of the isotropic polymer be deduced from measurements on the most highly oriented sample?
2. Does the mechanical anisotropy develop with orientation in the predicted manner?

We shall consider each stage in turn.

8.6.2   Correlation of the Elastic Constants of an Oriented Polymer with Those of an Isotropic Polymer: The Aggregate Model

It is to be expected that the mechanical properties of polymers will depend on the exact details of the molecular arrangements, i.e. both the crystalline morphology and the molecular orientation, these being intimately related so that any attempt to separate their

Table 8.6 *Physical properties of polyethylene terephthalate fibres at room temperature [73].*

Birefringence	X-ray crystallinity (%)	Extensional modulus (GPa)	Torsional modulus (GPa)
0	0	2.0	0.77
0	33	2.2	0.89
0.142	31	9.8	0.81
0.159	30	11.4	0.62
0.190	29	15.7	0.79

influence must be an artificial one to a greater or lesser degree. In the case of polyethylene terephthalate, it was found that the degree of molecular orientation (as measured from birefringence, for example) was the primary factor in determining the mechanical anisotropy. Table 8.6 shows some extensional and torsional modulus results for a number of polyethylene terephthalate fibres measured at room temperature. It can be seen that the influence of crystallinity on these moduli is small compared with the effect of molecular orientation on the extensional modulus. It has therefore been proposed that to a first approximation the unoriented fibre or polymer can be regarded as an aggregate of anisotropic elastic units whose elastic properties are those of the highly oriented fibre or polymer [72, 74]. The average elastic constants for the aggregate can be obtained in two ways: either by assuming uniform stress throughout the aggregate (which will imply a summation of compliance constants) or uniform strain (which will imply a summation of stiffness constants). Because in general the principal axes of stress and strain do not coincide for an anisotropic solid, these two approaches both involve an approximation. With the first assumption of uniform stress, the strains throughout the aggregate are not uniform; with the alternative assumption of uniform strain, non-uniformity of stress occurs. It was shown by Bishop and Hill [75] that for a random aggregate the correct value lies between the two extreme values predicted by these alternative schemes.

Consider the case of uniform stress. This can be imagined as a system of N elemental cubes arranged end-to-end forming a 'series' model (Figure 8.23). Assume that each elemental cube is a transversely isotropic elastic solid, the direction of elastic symmetry being defined by the angle θ, which its axis makes with the direction of applied external stress σ. The strain in each cube e_1 is then given by the compliance formula

$$e_1 = \left[s_{11} \sin^4 \theta + s_{33} \cos^4 \theta + (2s_{13} + s_{44}) \sin^2 \theta \cos^2 \theta \right] \sigma,$$

where s_{11}, s_{33} etc. are the compliance constants of the cube. We ignore the fact that the cubes in general distort under the applied stress and do not satisfy compatibility of strain throughout the aggregate. Then, the average strain e is

$$e = \frac{\Sigma e_1}{N} = \left[s_{11} \overline{\sin^4 \theta} + s_{33} \overline{\cos^4 \theta} + (2s_{13} + s_{44}) \overline{\sin^2 \theta \cos^2 \theta} \right] \sigma,$$

where $\overline{\sin^4 \theta}$ etc. now define the average values of $\sin^4 \theta$, etc. for the aggregate of units. For a random aggregate, it is found that

$e/\sigma =$ average extensional compliance

$$= \overline{s'_{33}} = \frac{8}{15} s_{11} + \frac{1}{5} s_{33} + \frac{2}{15} (2s_{13} + s_{44}). \tag{8.15}$$
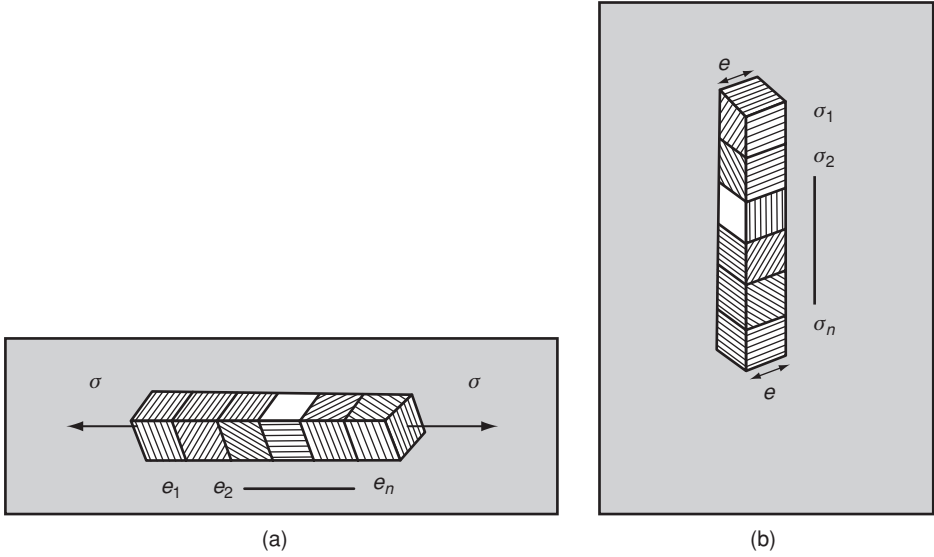
Figure 8.23   *The aggregate model (a) for uniform stress and (b) for uniform strain.*

In a similar manner, the case of uniform strain can be imagined as a system of N elemental cubes stacked in a 'parallel' model (Figure 8.23(b)). For this case, the stress in each cube σ_1 is given by the stiffness formula:

$$\sigma_1 = \left[c_{11} \sin^4 \theta + c_{33} \cos^4 \theta + 2(c_{13} + 2c_{44}) \sin^2 \theta \cos^2 \theta \right] e,$$

where c_{11}, c_{33} etc. are the stiffness constants of the cube. The average stress σ is then

$$\sigma = \frac{\Sigma \sigma_1}{N} = \left[c_{11} \overline{\sin^4 \theta} + c_{33} \overline{\cos^4 \theta} + 2(c_{13} + 2c_{44}) \overline{\sin^2 \theta \cos^2 \theta} \right] e,$$

where $\overline{\sin^4 \theta}$ etc. are the average values of $\sin^4 \theta$. For a random aggregate

$$\frac{\sigma}{e} = \overline{c'_{33}} = \frac{8}{15} c_{11} + \frac{1}{5} c_{33} + \frac{4}{15} (c_{13} + 2c_{44}). \qquad (8.16)$$

Equations (8.15) and (8.16) define one compliance constant and one stiffness constant for the isotropic polymer. For an isotropic polymer, there are two independent elastic constants, and these two schemes predict a value for the isotropic shear compliance $\overline{s'_{44}}$ and the isotropic shear stiffness $\overline{c'_{44}}$ respectively. These are

$$\overline{s'_{44}} = \frac{14}{15} s_{11} - \frac{2}{3} s_{12} - \frac{8}{15} s_{13} + \frac{4}{15} s_{33} + \frac{2}{5} s_{44} \qquad (8.17)$$

$$\overline{c'_{44}} = \frac{7}{30} c_{11} - \frac{1}{6} c_{12} - \frac{2}{15} c_{13} + \frac{1}{15} c_{33} + \frac{2}{5} c_{44}. \qquad (8.18)$$

Averaging the compliance constants defines the elastic properties of the isotropic aggregate in terms of $\overline{s'_{33}}$ and $\overline{s'_{44}}$. This is called the 'Reuss average' [76]. Averaging the stiffness constants defines the elastic properties of the aggregate in terms of $\overline{c'_{33}}$ and $\overline{c'_{44}}$. This is

Table 8.7 *Comparison of calculated and measured extensional and torsional compliances (in units of 0.1 $(GPa)^{-1}$) for unoriented fibres.*

	Extensional compliance			Torsional compliance		
	$\overline{s'_{11}} = \overline{s'_{33}}$ Calculated			$\overline{s'_{44}}$ Calculated		
	Reuss average	Voigt average	Measured	Reuss average	Voigt average	Measured
Low-density polyethylene	139	26	81	416	80	238
High-density polyethylene	10	2.1	17	30	6	26
Polypropylene	7.7	3.8	14	23	11	2.7
Polyethylene terephthalate	10.4	3.0	4.4	25	7.6	11
Nylon	6.6	5.2	4.8	17	13	12

called the 'Voigt average' [77]. In the latter case, it is desirable to invert the matrix and obtain the $\overline{s'_{33}}$ and $\overline{s'_{44}}$ corresponding to these values of $\overline{c'_{33}}$ and $\overline{c'_{44}}$ in order to compare directly the values obtained by the two averaging procedures.

The results of such a comparison are summarised in Table 8.7 for five polymers. For polyethylene terephthalate and low-density polyethylene, the measured isotropic compliances lie between the calculated bounds, suggesting that in these polymers the molecular orientation is indeed the primary factor determining the mechanical anisotropy. In nylon, the measured compliances lie just outside the bounds, suggesting that although molecular orientation is important in determining the mechanical anisotropy, other structural factors play an important part. Finally, in high-density polyethylene and polypropylene, measured values for the isotropic compliances $s'_{11} = s'_{33}$ lie well outside the calculated bounds, suggesting that factors other than orientation play a major role in the mechanical anisotropy. In polypropylene, Pinnock and Ward [78] suggested that simultaneous changes occur in morphology and molecular mobility, both of which affect the mechanical properties.

8.6.3   The Development of Mechanical Anisotropy with Molecular Orientation

Fibres and films of intermediate molecular orientation are often produced by a two-stage process in which the first stage consists of making an approximately isotropic specimen, which is then uniaxially stretched or drawn. The aggregate model can be extended to determine the mechanical anisotropy as a function of the draw ratio.

The starting point for such a theory was the observation that in general terms the birefringence–draw ratio curves for several crystalline polymers take a similar form, as noted previously by several workers (Crawford and Kolsky for low-density polyethylene [79] and Cannon and Chappel for nylon [80]), with the birefringence increasing rapidly at low draw ratios, but approaching the maximum value asymptotically at draw ratios greater than about five. Results for low-density polyethylene are shown in Figure 8.24(a).
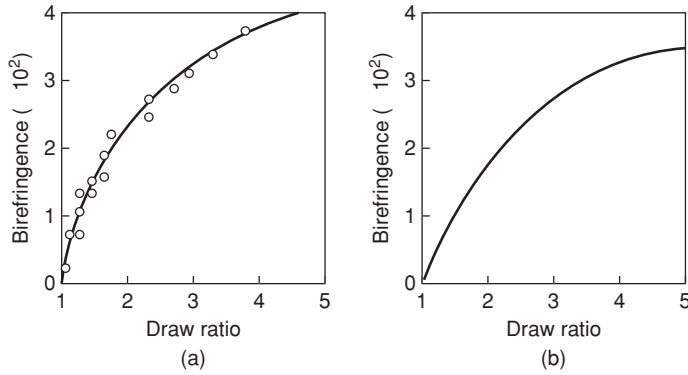
Figure 8.24   *Experimental (a) and theoretical (b) curves for the birefringence of low-density polyethylene as a function of draw ratio.*

Crawford and Kolsky concluded that the birefringence was directly related to the permanent strain, and they proposed a model of rod-like units rotating towards the draw direction on drawing. The essential mathematical step in the theory is illustrated in Figure 8.25. Each unit is considered to be transversely isotropic. The orientation of a single unit is therefore defined by the angle θ between its symmetry axis and the draw direction, and the angle ϕ which is the angle between the projection of the symmetry axis on a plane perpendicular to the draw direction and any direction in this plane. It is assumed that the symmetry axes of the anisotropic units rotate in the same manner as lines joining pairs of points in the macroscopic body, which deforms uniaxially at constant volume. This assumption is similar to the 'affine' deformation scheme of Kuhn and Grün for the optical anisotropy of rubbers [81] (see Section 4.3.4 for a definition of 'affine'), but ignores the required change in length of the units on deformation. We will therefore call it the 'pseudo-affine' deformation scheme. Kuhn and Grün did in fact consider this scheme and reject it in their discussion of rubber-like behaviour. The angle θ in Figure 8.25 thus changes to θ', $\phi = \phi'$, and it can be shown that

$$\tan \theta' = \frac{\tan \theta}{\lambda^{3/2}},$$

where λ is the draw ratio. This relationship can be used to calculate the orientation distribution function for the units in terms of the draw ratio.

On this model, the birefringence Δn of a uniaxially oriented polymer is given by

$$\Delta n = \Delta n_{\max} \left(1 - \frac{3}{2} \overline{\sin^2 \theta} \right),$$

Figure 8.25   *The pseudo-affine deformation scheme.*

where $\overline{\sin^2\theta}$ is the average value of $\sin^2\theta$ for the aggregate of units and $\Delta n_{\max}$ is the maximum birefringence observed for full orientation.

This pseudo-affine deformation scheme gives a reasonable first-order fit to the birefringence data for low-density polyethylene [79], nylon [80], polyethylene terephthalate [82] and polypropylene [78]. Figure 8.24(b) shows the first case. It is to be noted that this formulation of the birefringence equation ignores the distinction between different structural elements in the polymer (e.g. crystalline regions and disordered regions). With this reservation in mind, the aggregate model is now extended to predict the mechanical anisotropy in the manner outlined in Section 8.6.2. This gives the following equations for the compliance constants s'_{11}, s'_{12}, s'_{13}, s'_{33} and s'_{44} and the stiffness constants c'_{11}, c'_{12}, c'_{13}, c'_{33}, and c'_{44} of the partially oriented polymer:

$$s'_{11} = \frac{1}{8}(3I_2 + 2I_5 + 3)s_{11} + \frac{1}{4}(3I_3 + I_4)s_{13} + \frac{3}{8}I_1 s_{33} + \frac{1}{8}(3I_3 + I_4)s_{44}$$

$$c'_{11} = \frac{1}{8}(3I_2 + 2I_5 + 3)c_{11} + \frac{1}{4}(3I_3 + I_4)c_{13} + \frac{3}{8}I_1 c_{33} + \frac{1}{2}(3I_3 + I_4)c_{44}$$

$$s'_{12} = \frac{1}{8}(I_2 - 2I_5 + 1)s_{11} + I_5 s_{12} + \frac{1}{4}(I_3 + 3I_4)s_{13} + \frac{1}{8}I_1 s_{33} + \frac{1}{8}(I_3 - I_4)s_{44}$$

$$c'_{12} = \frac{1}{8}(I_2 - 2I_5 + 1)c_{11} + I_5 c_{12} + \frac{1}{4}(I_3 + 3I_4)c_{13} + \frac{1}{8}I_1 c_{33} + \frac{1}{2}(I_3 - I_4)c_{44}$$

$$s'_{13} = \frac{1}{2}I_3 s_{11} + \frac{1}{2}I_4 s_{12} + \frac{1}{2}(I_1 + I_2 + I_5)s_{13} + \frac{1}{2}I_3 s_{33} - \frac{1}{2}I_3 s_{44} \qquad (8.19)$$

$$c'_{13} = \frac{1}{2}I_3 c_{11} + \frac{1}{2}I_4 c_{12} + \frac{1}{2}(I_1 + I_2 + I_5)c_{13} + \frac{1}{2}I_3 c_{33} - 2I_3 c_{44}$$

$$s'_{33} = I_1 s_{11} + I_2 s_{33} + I_3(2s_{13} + s_{44})$$

$$c'_{33} = I_1 c_{11} + I_2 c_{33} + 2I_3(c_{13} + 2c_{44})$$

$$s'_{44} = (2I_3 + I_4)s_{11} - I_4 s_{12} - 4I_3 s_{13} + 2I_3 s_{33} + \frac{1}{2}(I_1 + I_2 - 2I_3 + I_5)s_{44}$$

$$c'_{44} = \frac{1}{4}(2I_3 + I_4)c_{11} - \frac{1}{4}I_4 c_{12} - I_3 c_{13} + \frac{1}{2}I_3 c_{33} + \frac{1}{2}(I_1 + I_2 - 2I_3 + I_5)c_{44}.$$

In these equations, s_{11}, s_{12} etc. are the compliance constants and c_{11}, c_{12} etc. are the stiffness constants for the anisotropic elastic unit, which in practice means those of the most highly oriented specimen obtained. The terms I_1, I_2, I_3, I_4 and I_5, are the orientation functions, defining the average values of

$$\sin^4\theta(I_1), \ \cos^4\theta(I_2), \ \cos^2\theta\sin^2\theta(I_3), \ \sin^2\theta(I_4), \ \cos^2\theta(I_5)$$

for the aggregate. Note that only two of these orientation functions are independent parameters (e.g. $I_4 = I_1 + I_3$, $I_5 = I_2 + I_3$, $I_4 + I_5 = 1$).

The orientation functions can be calculated on the pseudo-affine deformation scheme, and Figures 8.18–8.22 show that the aggregate model then predicts the general form of the mechanical anisotropy. It is particularly interesting that the predicted Reuss average curves for low-density polyethylene show the correct overall pattern, including the minimum in

the extensional modulus. This arises as follows. On the pseudo-affine deformation scheme, $\overline{\sin^4 \theta}$ and $\overline{\cos^4 \theta}$ decrease and increase monotonically respectively with increasing draw ratio, whereas $\overline{\sin^2 \theta \cos^2 \theta}$ shows a maximum value at a draw ratio of about 1.2. Thus, s'_{33} can pass through a maximum with increasing draw ratio (giving a minimum in the Young's modulus E_0) provided that $(2s_{13} + s_{44})$ is sufficiently large compared with s_{11} and s_{33}, which should be approximately equal. The theory assumes elastic constants for the units that are identical with those measured for the highly oriented polymer. In low-density polyethylene, s_{44} is much larger than s_{11} and s_{33}, which are fairly close in value; hence these conditions are fulfilled and the anomalous mechanical anisotropy is predicted.

At low temperatures, as discussed above (see Figure 8.17), a more conventional pattern of mechanical anisotropy is observed for low-density polyethylene. At the same time, the polar diagram of the modulus changes ([41], Figure 8.26) and s_{44} is no longer very much greater than the other elastic constants. These results are thus consistent with the aggregate model.

The theoretical curves of Figures 8.18–8.22 differ from those obtained experimentally in two ways. Firstly, there are features of detail (a small minimum in the transverse modulus
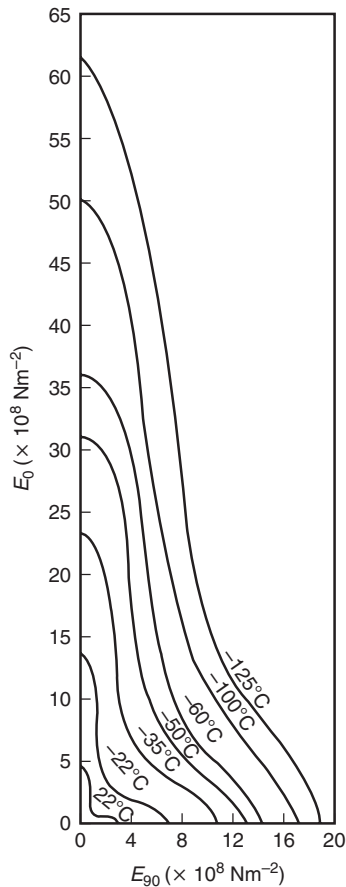
Figure 8.26   *Polar representation of the mechanical anisotropy in a highly oriented low-density polyethylene sheet at different temperatures.*
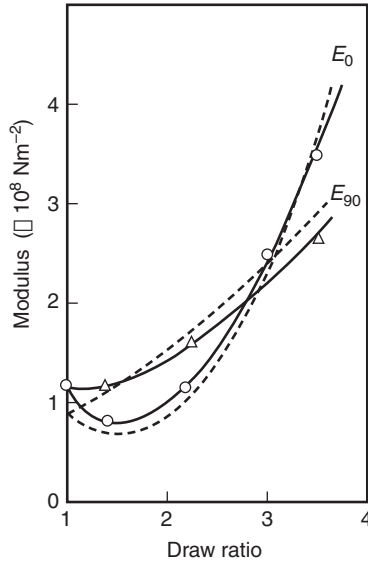
Figure 8.27   *Comparison of experimental ($-$) variation in E_0 and E_{90} for cold-drawn low-density polyethylene with those predicted by the aggregate model using orientation functions from nuclear magnetic resonance (- - -).*

of low-density polyethylene; a small minimum in the extensional modulus of high-density polyethylene), which are not predicted at all. It has been shown elsewhere [83] that such effects may be associated with mechanical twinning. Secondly, the predicted development of mechanical anisotropy with increasing draw ratio is much less rapid than is observed in practice. Deficiencies in the pseudo-affine deformation scheme are not unexpected due to the simplifying nature of the assumptions made. The quantities $\overline{\sin^4 \theta}$, $\overline{\cos^4 \theta}$ and $\overline{\sin^2 \theta \cos^2 \theta}$ can also be determined experimentally by wide-angle X-ray diffraction and nuclear magnetic resonance [84–86]. In low-density polyethylene, a considerably improved fit was obtained in this manner (Figure 8.27). The conclusion from these results is that the mechanical anisotropy of low-density polyethylene relates to the orientation of the crystalline regions and that it is predicted to a very good degree of approximation by the Reuss averaging scheme.

The aggregate model predicts only that the elastic constants should lie between the Reuss and Voigt average values. In polyethylene terephthalate, it is clear that the experimental compliances lie approximately midway between the two bounds. For cold-drawn fibres, it has been shown that this median condition applies almost exactly [87].

For low-density polyethylene, the Voigt averaging scheme does not predict the anomalous behaviour. However, the Reuss average does, and therefore appears to describe the physical situation more closely. A similar conclusion was reached by Odajima and Maeda [60] who compared theoretical estimates of the Reuss and Voigt averages of single crystals of polyethylene with experimental values.

In nylon, the Voigt average is closest to the experimentally observed data. It is interesting to note that both averaging schemes predict a maximum in the torsional modulus as a function of draw ratio.

The aggregate model would not appear to be generally applicable to high-density polyethylene and polypropylene. It appears that for polypropylene the aggregate model is applicable only at low draw ratios [78]. As discussed above, there are simultaneous changes in morphology and molecular mobility at higher draw ratios.

It is interesting that in different polymers the Reuss or Voigt averages or a mean of these is closest to the measured values. It is likely that these conclusions will relate to the detailed nature of the stress and strain distributions at a molecular level in the polymers and should in turn be related to the structure.

Kausch, who has applied the aggregate model to a range of both crystalline and amorphous polymers [88], also noted that for some materials the experimental increase in extensional modulus with stiffness was significantly greater than predicted, and has suggested that the effect may be due to an additional orientation of segments within each unit of the aggregate. Another possibility is that the increase in stiffness of crystalline polymers may be enhanced at the higher draw ratios through the competing process of pulling out more intercrystalline tie molecules. Subsequently [89], Kausch emphasised the value of reformulating the model in terms of a molecular network rather than orienting rods, which would allow the representation of high strain properties.In summary, it is evident that despite the highly simplistic nature of the assumptions made the aggregate model provides an appropriate model for a number of important polymers. For such materials, details of the crystal structure can play no more than a subsidiary role in the development of mechanical anisotropy, and the deformation is essentially that expected for a single-phase texture or a distorted network.

8.6.4   The Sonic Velocity

It has been suggested by Morgan [30] and others [28] that the sonic modulus (i.e. the extensional modulus measured at high frequencies by a wave-propagation technique) can be used to obtain a direct measure of molecular orientation in a manner analogous to the derivation of the so-called optical orientation function $f_0 = (1 - \frac{3}{2}\overline{\sin^2\theta})$ from the birefringence.

Consider the equations for the extensional modulus of the aggregate

$$s'_{33} = \overline{\sin^4\theta}s_{11} + \overline{\cos^4\theta}s_{33} + \overline{\sin^2\theta\cos^2\theta}(2s_{13} + s_{44}).$$

Table 8.1 summarises the measured values of s_{11}, s_{33} and s_{44} for a number of polymers, as obtained from the monofilament data of Hadley, Pinnock and Ward [42]. It can be seen that in all cases except that of low-density polyethylene, s_{11} and s_{44} are of approximately the same value, and that s_{33} is comparatively small. Remembering that Poisson's ratio is usually close to 0.5, this implies that s_{13} will also be comparatively small.

This suggests that, except for high degrees of orientation, both the terms $\overline{\cos^4\theta}s_{33}$ and $\overline{\sin^2\theta\cos^2\theta}s_{13}$ will be small and we can approximate to

$$s'_{11} = \overline{\sin^4\theta}s_{11} + \overline{\sin^2\theta\cos^2\theta}s_{44} \tag{8.20}$$

$$= \overline{(\sin^4\theta + \sin^2\theta\cos^2\theta)}s_{11}$$

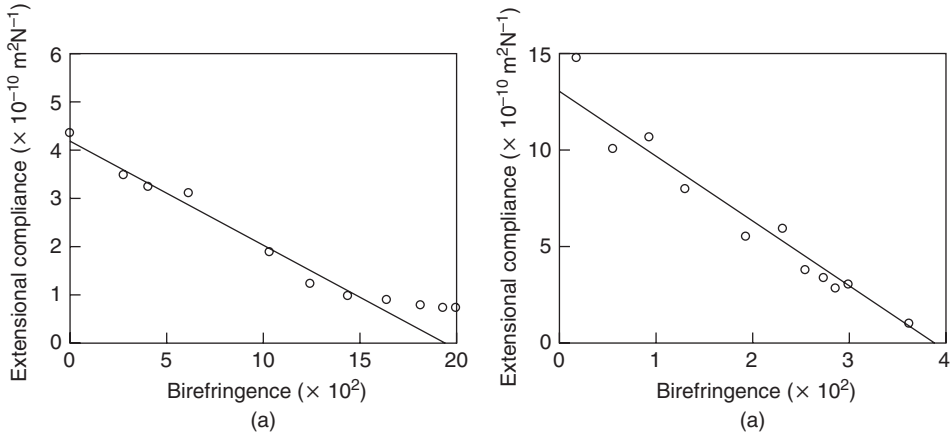$$= \overline{\sin^2\theta}s_{11}. \tag{8.21}$$

Figure 8.28 *Experimental curves showing the relationship between the extensional compliance and birefringence for fibres of (a) polyethylene terephthalate and (b) polypropylene.*

Remembering that the birefringence is given by $\Delta n = \Delta n_{\max}(1 - \frac{3}{2}\overline{\sin^2\theta})$, it can be seen that the extensional compliance, the reciprocal of the extensional modulus, should be directly related to the birefringence through $\overline{\sin^2\theta}$ independent of the mechanism of molecular orientation [90]. To this degree of approximation, it then follows that

$$s'_{33} = \frac{2}{3}s_{11}(\Delta n_{\max} - \Delta n). \tag{8.22}$$

We would therefore predict a linear relationship between the extensional compliance s'_{33} and the birefringence Δn, which extrapolates to zero extensional compliance at the maximum birefringence value.

Figure 8.28 shows results for polyethylene terephthalate and polypropylene, which suggest that this is a reasonable approximation. But the values of s_{11} obtained from these plots do not agree with that measured experimentally for the most highly oriented fibre monofilament, suggesting that this approximate treatment is not very soundly based.

Samuels [91] has carried the sonic velocity analysis one stage further by recognising the two-phase nature of a crystalline polymer. The natural extension of Equation (8.21) would then be

$$\frac{1}{E} = s'_{33} = \frac{\beta}{E^0_{t,c}}\overline{\sin^2\theta_c} + \frac{1-\beta}{E^0_{t,am}}\overline{\sin^2\theta_{am}}, \tag{8.23}$$

where E is the sonic modulus of the sample; $E^0_{t,c}$, $E^0_{t,am}$ are the lateral moduli of the crystalline and amorphous regions respectively; $\overline{\sin^2\theta_c}$, $\overline{\sin^2\theta_{am}}$ are orientation functions for the crystalline and amorphous regions respectively and β is the fraction of crystalline material.

For an isotropic sample $\overline{\sin^2 \theta_c} = \overline{\sin^2 \theta_{am}} = \frac{2}{3}$ and the isotropic sonic modulus E_u is given by

$$\frac{3}{2E_u} = \frac{\beta}{E_{t,c}^0} + \frac{1-\beta}{E_{t,am}^0}. \tag{8.24}$$

If we define orientation averages

$$f_c = \frac{1}{2}\left(3\overline{\cos^2 \theta_c} - 1\right), \quad f_{am} = \frac{1}{2}\left(3\overline{\cos^2 \theta_{am}} - 1\right)$$

for the crystalline and amorphous regions respectively, we can combine Equations (8.23) and (8.24) to give

$$\frac{3}{2}\left\{\frac{1}{E_u} - \frac{1}{E}\right\} = \frac{\beta f_c}{E_{t,c}^0} + \frac{(1-\beta)f_{am}}{E_{t,am}^0}. \tag{8.25}$$

Measurement of the dependence of the sonic modulus on crystallinity in isotropic samples gives through Equation (8.24) a method of determining $E_{t,c}^0$ and $E_{t,am}^0$. Measurements of the sonic modulus on oriented samples then give through Equation (8.25), a method of determining the orientation function of the amorphous regions f_{am}, providing that f_c can be obtained from another technique, i.e. wide-angle X-ray diffraction.

Samuels [91] obtained justification for this argument by combining such sonic modulus and X-ray diffraction measurements with the measurement of birefringence. Now the birefringence of a polymer on the two-phase model (ignoring form birefringence) is given by

$$\Delta n = \Delta n_c^0 f_c + (1-\beta)\Delta n_{am}^0 \left(\frac{1-\beta}{\beta}\right) \frac{f_{am}}{f_c}. \tag{8.26}$$

Samuels [91] showed that plots of $\Delta n / \beta f_c$ as a function of

$$\left(\frac{1-\beta}{\beta}\right) \frac{f_{am}}{f_c}$$

gave good straight line fits for a range of polypropylene samples. This provided support for his analysis and enabled values to be deduced for Δn_c^0, Δn_{am}^0, the maximum birefringence (i.e. for a completely oriented phase) of the crystalline and amorphous regions respectively. However, it should be noted that this treatment involves several approximations, as well as the basic assumption of homogeneous stress.

8.6.5   Amorphous Polymers

There are relatively few measurements on amorphous polymers, where the degree of mechanical anisotropy is much less than in crystalline polymers. Early studies include those of Hennig [92] on polyvinyl chloride, polymethylmethacrylate and polystyrene and Robertson and Buenker [93] on bisphenol A polycarbonate. The results are summarised in Table 8.8. Hennig's measurements on s_{33} and s_{11} were obtained from dynamic testing at

Table 8.8   *Elastic compliances of oriented amorphous polymers (units of compliance are GPa^{-1}).*

Material	Draw ratio	s_{33}	s_{11}	s_{44}
Polyvinyl chloride	1	0.313	0.313	0.820
	1.5	0.276	0.319	0.794
	2.0	0.255	0.328	0.781
	2.5	0.243	0.337	0.769
	2.8	0.238	0.341	0.763
	∞	0.204	0.379	0.730
Polymethyl methacrylate	1	0.214	0.214	0.532
	1.5	0.208	0.215	0.524
	2.0	0.204	0.215	0.518
	2.5	0.200	0.216	0.510
	3.0	0.196	0.217	0.505
Polystyrene	1	0.303	0.303	0.769
	2.0	0.296	0.304	0.769
	3.0	0.289	0.305	0.769
Polycarbonate	1	0.376	0.376	1.05
	1.3	0.314	0.408	0.980
	1.6	0.268	0.431	0.926

320 Hz, and the s_{44} measurements at 1 Hz. Robertson and Buenker used the vibrating reed technique to obtain values in the range 100–400 Hz.

A more comprehensive investigation on uniaxially oriented sheets of polymethyl-methacrylate and polystyrene was undertaken by Wright *et al*. [94] using ultrasonic measurements. The results are summarised in Figure 8.29 (a) and (b), where the stiffness constants are shown as a function of the birefringence. Rawson and Rider [95] have also reported ultrasonic data for oriented polyvinyl chloride and observed a similar degree of anisotropy to that seen in Table 8.8 from Hennig's work.

For amorphous polymers, Ward *et al*. [96] and Kausch [88] and later Rawson and Rider [95] are in agreement that the mechanical anisotropy can be discussed very satisfactorily by the aggregate model. Moreover, the development of anisotropy with draw ratio can often be described by the pseudo-affine deformation scheme [94].

8.6.6   Oriented Polyethylene Terephthalate Sheet with Orthorhombic Symmetry

All nine independent elastic constants have been determined for one-way drawn oriented polyethylene terephthalate sheet. The sheet was prepared by drawing isotropic sheet at constant width. It has been shown that there is then both a high degree of chain orientation in the draw direction and that the (100) crystal planes (which mainly reflect preferential orientation of the terephthalate residues in the chain) are preferentially oriented in the plane of the sheet. This type of orientation has been termed uniplanar axial. From the viewpoint of elastic anisotropy, the sheet possesses three orthogonal planes of symmetry and can be described as possessing orthorhombic symmetry.
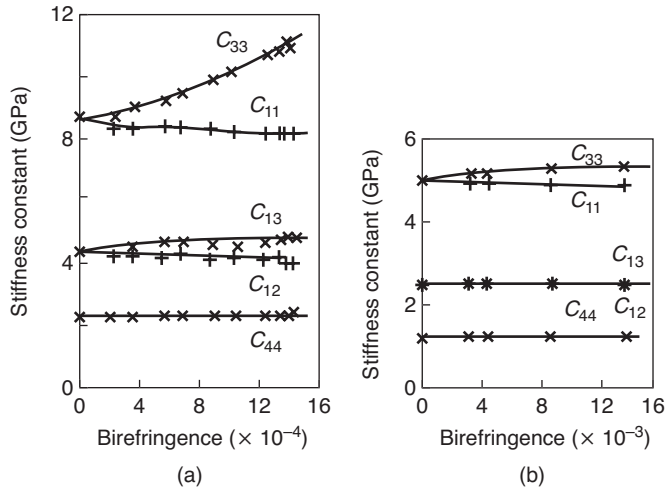
Figure 8.29   *Stiffness constants of uniaxially drawn amorphous polymers, measured at room temperatures, as a function of birefringence: (a) polymethylmethacrylate, (b) polystyrene. (Redrawn from Wright, H., Faraday, C.S.N., White, E.F.T. et al. (1971) The elastic constants of oriented glassy polymers. J. Phys. D, 4, 2002. Copyright (1971) Institute of Physics.)*

Collected results for the nine compliance constants are shown in Table 8.9. The 3 axis is the initial draw direction and the 1 axis lies in the plane of the sheet, following the convention indicated in Figure 8.2. s_{11} and s_{33} were obtained from measurements of extensional creep in a dead loading creep machine and refer to the 10s response at 0.1% strain. s_{13} was obtained from the deformation of an electron microscope grid printed on the surface of the sample [97], and s_{12} and s_{23} by the Michelson interferometer method [12]. s_{22} was determined by increasing the compressive strain of strips under load in a compressional creep apparatus [7]. s_{55} was determined by the torsion of rectangular samples cut with their long axes parallel to 3 and 1 respectively [18]. s_{44} and s_{66} were also determined in this way

Table 8.9   *Full set of compliances for the oriented polyethylene terephthalate sheet with orthorhombic symmetry [18].*

Compliance	Value (GPa^{-1})
s_{11}	0.361 ± 0.012
s_{22}	0.9 ± 0.16
s_{33}	0.066 ± 0.001
s_{12}	-0.38 ± 0.04
s_{13}	-0.018 ± 0.001
s_{23}	-0.037 ± 0.005
s_{44}	9.7 ± 0.3
s_{55}	0.564 ± 0.025
s_{66}	14.1 ± 0.8

by making measurements on samples of different aspect ratio [18]. In addition, s_{44} and s_{66} were determined by the simple shear technique [18, 21] and the values quoted in Table 8.9 are weighted means for the two methods.

It can be seen from Table 8.9 that the sheet shows a very high degree of mechanical anisotropy, and it is interesting to consider how this relates to the two major structural features: the high-chain axis orientation and the preferential orientation of the terephthalate residues. Infrared measurements have shown that the high degree of orientation in the crystalline regions is accompanied by a high proportion of glycol residues in the extended chain *trans* conformation and that these are also highly oriented along the draw direction [98]. The low value of the extensional compliance s_{33} can then be explained by supposing that the deformation involves bond stretching and bending in these extended chain molecules. These molecules could be the taut tie molecules proposed by Peterlin [71]. The transverse compliances s_{33} and s_{33} are approximately an order of magnitude greater, which is consistent with these relating primarily to dispersion forces. It also follows from such considerations that if the polymer is stressed in a direction perpendicular to the draw direction, the major contraction is likely to take place in the direction perpendicular to the draw direction (the 2 direction) rather than parallel to it (the 3 direction). Thus, the magnitude of s_{12} would be expected to be much greater than that of s_{23}, as is observed. The value of s_{13} is similar to that of s_{23}, which is consistent with this line of argument, namely the comparative difficulty of deformation in the 3 direction compared with the 1 and 2 directions. The Poisson's ratios reflect the same argument and in particular ν_{13} has the very small value of 0.05.

The anisotropy of the shear compliances is also very remarkable. Both s_{44} and s_{66} are large compared with s_{55} and reflect easy shear in the 23 and 12 planes respectively, presumably where the planar terephthalate chains are sliding over each other constrained only by weak dispersion forces. The compliance s_{55}, which geometrically involves distortion of the plane of the polyester molecule, is of a similar order of magnitude to s_{11} and s_{22}.

It is interesting to apply the aggregate model to these data, calculating bounds for the elastic constants of an 'equivalent fibre' by averaging the sheet constants in the plane normal to the sheet draw direction. This requires an extension of the mathematical treatment of Section 8.6.2 to deal with the case of a transversely isotropic aggregate of orthorhombic units. The basic equations have been given in detail elsewhere [99] so only the key results will be summarised here. If the orthorhombic unit constants are s_{11}, s_{13}, ..., s_{66} (Section 8.2.2), the Reuss average fibre constants s'_{33}, s'_{13}, ..., s'_{44} obtained by averaging in the 12 plane are given by

$$s'_{33} = s_{33}$$

$$s'_{11} = \frac{3}{8}s_{11} + \frac{1}{4}s_{12} + \frac{3}{8}s_{22} + \frac{1}{8}s_{66}$$

$$s'_{12} = \frac{1}{8}s_{11} + \frac{3}{4}s_{12} + \frac{1}{8}s_{22} - \frac{1}{8}s_{66}$$

$$s'_{13} = \frac{1}{2}(s_{13} + s_{23})$$

$$s'_{44} = \frac{1}{2}(s_{44} + s_{55})$$

Table 8.10   *Comparison of calculated and measured compliance constants (GPa⁻¹) for polyethylene terephthalate fibres based on the sheet compliances.*

Compliance constant	Calculated bonds		Experimental value
	Reuss	Voigt	
Highly-oriented fibres			
s_{11}	2.1	0.73	1.61
s_{12}	−1.9	−0.55	−0.58
s_{13}	−0.028	−0.025	−0.031
s_{33}	0.066	0.066	0.071
s_{44}	5.1	1.07	1.36
Isotropic fibres			
s_{33}	1.8	0.24	0.44
s_{44}	5.3	0.64	1.1

and the Voigt average fibre constants in similar terms are $c'_{33}, \ c'_{13}, \ldots, c'_{44}$, where

$$c'_{33} = c_{33}$$

$$c'_{11} = \frac{3}{8}c_{11} + \frac{1}{4}c_{12} + \frac{3}{8}c_{22} + \frac{1}{2}c_{66}$$

$$c'_{12} = \frac{1}{8}c_{11} + \frac{3}{4}c_{12} + \frac{1}{8}c_{22} - \frac{1}{2}c_{66}$$

$$c'_{13} = \frac{1}{2}(c_{13} + c_{23})$$

$$c'_{44} = \frac{1}{2}(c_{44} + c_{55}).$$

The results of this calculation are shown in Table 8.10 together with the experimental value obtained for a highly oriented fibre monofilament. Although the experimental values do not always lie exactly within the predicted bounds, they are always in the correct range. In Table 8.10, a comparison is given between the calculated and measured compliance constants for isotropic polyethylene terephthalate based on the sheet data. Again the measured values lie between the Reuss and Voigt bounds. Taking into account the very large degree of anisotropy and the very simplistic nature of these calculations, it is considered that these results afford good support for the contention that to a first approximation the mechanical anisotropy can be considered in terms of the single-phase aggregate model.

8.7   The Aggregate Model for Chain-Extended Polyethylene and Liquid Crystalline Polymers

Annealing polyethylene at high temperatures (∼230–240°C) and high pressures (∼200 MPa) produces a chain-extended structure consisting of small domains where the crystal thicknesses are ∼2 μm, i.e. an aggregate of small, highly aligned units. This material can

be aligned by hydrostatic extrusion, where a billet is extruded in the solid phase through a conical die to give a product with moderately high orientation and Young's moduli of ~40 GPa in the alignment direction. Not surprisingly, the aggregate model can be applied to the development of orientation, which follows the pseudo-affine deformation scheme, leading to an understanding of the mechanical anisotropy [100].

On the compliance averaging scheme, the tensile modulus of the oriented polymer E_3 is given by

$$\frac{1}{E_3} = s'_{33} = s_{11}\overline{\sin^4\theta} + s_{33}\overline{\cos^4\theta} + (2s_{13} + s_{44})\overline{\sin^2\theta\cos^2\theta}. \tag{8.27}$$

As before, θ represents the angle between the unit of the aggregate and the axis representing total alignment, and $\overline{\sin^4\theta}$ and so on represent average values.

For the very high degree of molecular orientation found in these polymers $\overline{\sin^4\theta} \ll 1$ and $\overline{\cos^4\theta} \approx \overline{\cos^2\theta} \approx 1$. We can then rewrite Equation (8.27) as

$$\frac{1}{E_3} = s'_{33} = \frac{1}{E_c} + s_{44}\overline{\sin^2\theta}, \tag{8.28}$$

where E_c is the tensile modulus of the aggregate unit. To a similar degree of approximation, it can be shown that

$$s'_{44} = s_{44} = \frac{1}{G}, \tag{8.29}$$

where G is the shear modulus of the polymer.

Combining Equations (8.28) and (8.29)

$$\frac{1}{E_3} = \frac{1}{E_c} + \frac{\overline{\sin^2\theta}}{G}. \tag{8.30}$$

Figure 8.30 show results for a plot of $1/E_3$ versus $1/G$ for hydrostatic extrusion of pressure-annealed polyethylene taken to a series of extrusion ratios (equivalent to draw ratios). It can be seen that the gradients of the fitted lines decrease with increasing extrusion ratio as the orientation parameter $\overline{\sin^2\theta}$ decreases, and that the lines converge to a value of E_c ~250 GPa, in the correct range for the chain modulus of polyethylene.

The aggregate model also has been used with success to describe the mechanical anisotropy of several liquid crystalline polymers. Ward and co-workers [101] examined the dynamic mechanical behaviour of several thermotropic polyesters in tension and shear over a wide temperature range, and used the single-phase aggregate model to relate quantitatively the fall in tensile modulus with temperature to the corresponding fall in shear modulus.

Figure 8.31 shows data for the temperature dependence for the tensile modulus and the shear modulus for a highly oriented thermotropic copolyester, on a plot of $1/E_3$ versus $1/G$. The results lie on a reasonable straight line extrapolating to a value of 173 GPa for the tensile modulus of a unit of aggregate. This value compares favourably with theoretical estimates based on bond stretching and bond bending modes of deformation.

In a second version of the aggregate model, Ward and co-workers assumed, on the basis of observation of the X-ray diffraction pattern, that the aggregate unit averages the deformation over a length of 8–10 monomer units. The chain modulus in this case can be determined experimentally by measuring the change in the X-ray diffraction pattern under
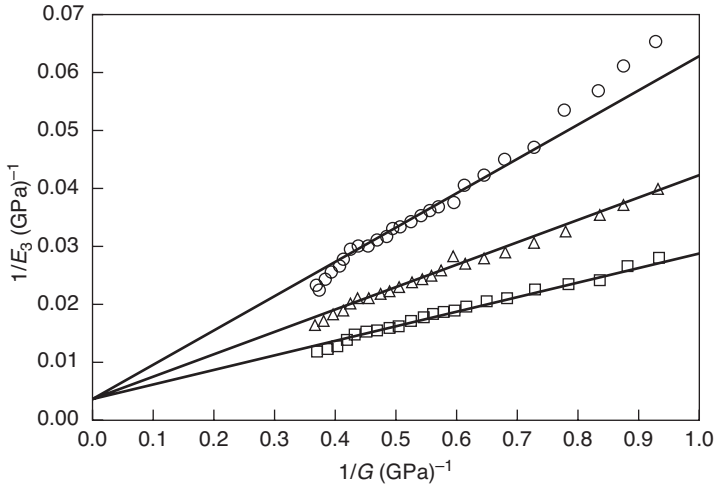
Figure 8.30   *A plot of $1/E_3$ against $1/G$ showing the validity of the aggregate model analysis for a range of R006-60 extrudates previously pressure annealed at 238°C for 15 min at 450 MPa pressure: (□)10:1; (△) 7:1; (○) 5:1. (Reproduced from Powell, A.K., Craggs, G., Ward, I.M. (1990) The structure and properties of oriented chain-extended polyethylene J. Mater. Sci., 25, 3990. Copyright (1990) Springer Science and Business Media.)*
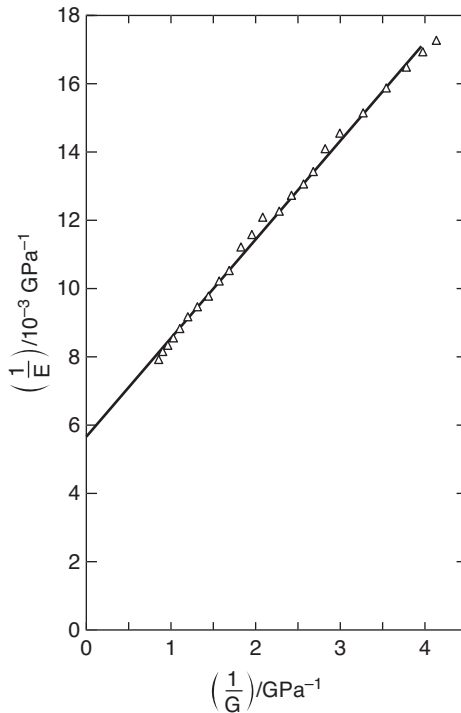
Figure 8.31   *Plot of $1/E_3$ versus $1/G$ for a highly oriented thermotropic copolyester.*
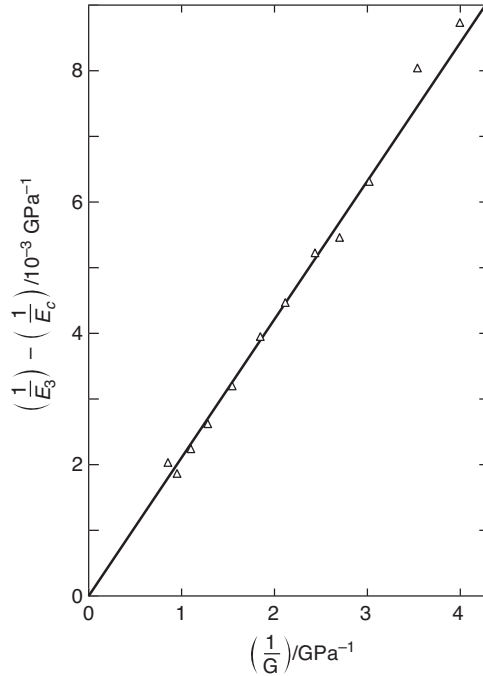
Figure 8.32 *Plot of (1/E₃ − 1/E_c) versus 1/G for a highly oriented thermotropic copolyester.*

stress, and a temperature-dependent E_c was observed. By rearrangement of Equation (8.30) a further plot of

$$\left(\frac{1}{E_3} - \frac{1}{E_c} \right) \text{ versus } \frac{1}{G}$$

was obtained (Figure 8.32) and this gave a good straight line through the origin.

The value of $\overline{\sin^2 \theta}$ obtained from the slope of this line is less than that found from the fitting procedure of Figure 8.31, which reflects the misalignment along the length of the liquid crystalline polymer chain. Because of the sinuous nature of the polymer chains, the authors have called the effect the 'sinuosity'.

Northolt and Van Aartsen [102] used the aggregate model to interpret the rapid increase in Young's modulus with increasing crystalline orientation for PPTA fibres. PPTA is a lytropic liquid crystalline polyester whose X-ray diffraction pattern suggests a crystallite size of about 70 nm in the axial direction and 5 nm transverse.

The sonic modulus E_{sonic} and the X-ray data for $\overline{\sin^2 \theta}$ were fitted on the assumption that PPTA fibres can be considered an aggregate of small crystals (similar to chain-extended polyethylene discussed above). We have

$$\frac{1}{E_{\text{sonic}}} = \frac{1}{E_c} + A \overline{\sin^2 \theta}. \tag{8.31}$$
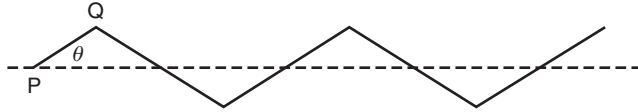
Figure 8.33   *Deformation of a rigid chain on the Northolt/Van Aartsen model.*

It was shown that the measured value for E_c and A agreed well with those calculated theoretically. For high orientation $A = 1/G$, so that Equation (8.31) is exactly equivalent to Equation (8.30).

In more recent research, Northolt and van der Hout [103] have proposed explicit theoretical models for the elastic modulus of a fibre consisting of fibrils containing rigid-rod chains. These models take as their starting point a planar zigzag chain. Deformation can occur by extensional strain along the axes of the rigid chain segments (e.g. PQ in Figure 8.33) and by shear. The extensional compliance of the fibre s_{33} is given by

$$s_{33} = \frac{1}{E_c} + \frac{\langle \sin^2 \theta \rangle}{2G},$$

where E_c is the axial Young's modulus of each segment, G is the shear modulus of the fibre and

$$\langle \sin^2 \theta \rangle = \frac{\int_0^{\pi/2} R'(\theta) \sin^2 \theta \cos \theta \mathrm{d}\theta}{\int_0^{\pi/2} R(\theta_0) \cos \theta_0 \mathrm{d}\theta_0}.$$

Note that this equation differs from the classical aggregate model equation in two respects:

1. The denominator of the second term as the left-hand side is $2G$ and not G.
2. The definition of $<\sin^2 \theta>$ differs from that for $\overline{\sin^2 \theta}$ in that the average is carried out in the plane of the chains and is not a three-dimensional average; $R(\theta_0)$ refers to the initial chain distribution and $R'(\theta)$ the final distribution under stress.

8.8   Auxetic Materials: Negative Poisson's Ratio

Although the possibility of materials with a negative Poisson's ratio had been recognised theoretically, it is only comparatively recently, since the mid-1980s, that examples of such materials have become available. These materials expand laterally when stretched and contract laterally when compressed, and are called auxetic from the classical Greek word auxetos meaning increase.

A simple example of a negative Poisson's ratio material is a cellular foam based on a re-entrant honeycomb, shown in Figure 8.34. On stretching, the axial fibrils straighten to produce lateral expansion. Other theoretical auxetic structures have since been studied, including rotating rhombi [104], rotating rigid parallelograms [105], rigid rectangles of differing sizes [106], deformable squares [107] and interlocking hexagons [108]. Fozdar *et al.* [109] used a form of three-dimensional printing to produce regular structural geometries, both single- and multilayer, and investigate their auxetic properties experimentally.
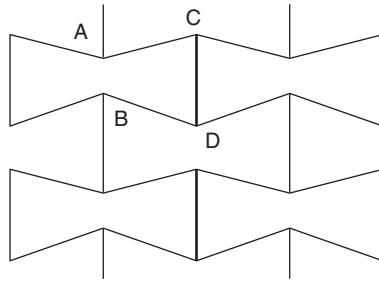
Figure 8.34 *Re-entrant honeycomb with negative Poisson's ratio made of bendable ligaments. A similar structure can be made with rigid ligaments if a spring is placed between points of type A and B. (Reproduced from Lakes, R. Deformation mechanisms in negative Poisson's ratio materials: structural aspects. J. Mater. Sci.,* **26***, 2287. Copyright (1991) Springer Science and Business Media.)*

The subject of geometrical structures and models in relation to auxetic polymers has been reviewed by Liu and Hu [110].

Since the pioneering work of Lakes [111], there have been a number of instances of auxetic polymer foams, recent examples mentioned in references [112], [113] and [114]. Evans and his collaborators [115] have shown how an anisotropic microstructure consisting of nodules and fibrils can be produced in polytetrafluoroethylene (PTFE), and give rise to a very large negative Poisson's ratio. Figure 8.35 is a schematic representation of the deformation of microporous PTFE.

Initially, there is expansion in both the axial and lateral directions as the fibrils are stretched, similar to the deformation of the re-entrant structure of Figure 8.34. This is followed by rotation of the nodules with a particular handedness as shown in the figure, to give further lateral expansion. Evans and Caddock [116] showed how two theoretical models, a translational model for stages (a) to (b) of Figure 8.35, and a rotational model for stages (b), (c) and (d), could provide a good confirmation of the observed changes in Poisson's ratio with strain. Their results are illustrated in Figure 8.36, from which it can be seen that experimental values of Poisson's ratio approaching -12 can be observed.

In a further study, Evans and Alderson [117–119] showed that in both PTFE and ultra-high molecular weight polyethylene (UHMPE) an isotropic microstructure of nodules and fibrils shown schematically on Figure 8.37 can give rise to a negative Poisson's ratio. Essentially this arises because when the materials are stretched, the extension of the fibrils causes the nodules to move apart.

The work on auxetic polymers arising from microporous structure has continued. Alderson *et al.* [120], in an attempt to produce auxetic material in a more easily usable form, have used melt-spinning to produce auxetic polypropylene fibres. This work was developed further, by way of a study of the processing parameters for melt-spinning of auxetic polypropylene, polyester and nylon fibres [121]. Ravirala *et al.* [122] have produced auxetic polypropylene film using melt extrusion. Less conventionally, Alderson *et al.* [123] have produced auxetic polyethylene by a combination of powder compaction and sintering, without an extrusion step.

As a practical means of creating material with negative Poisson's ratio, it has been proposed to use auxetic networks of polymer fibres within a conventional matrix to produce composites that are themselves auxetic. Here the individual fibres are not in general auxetic,
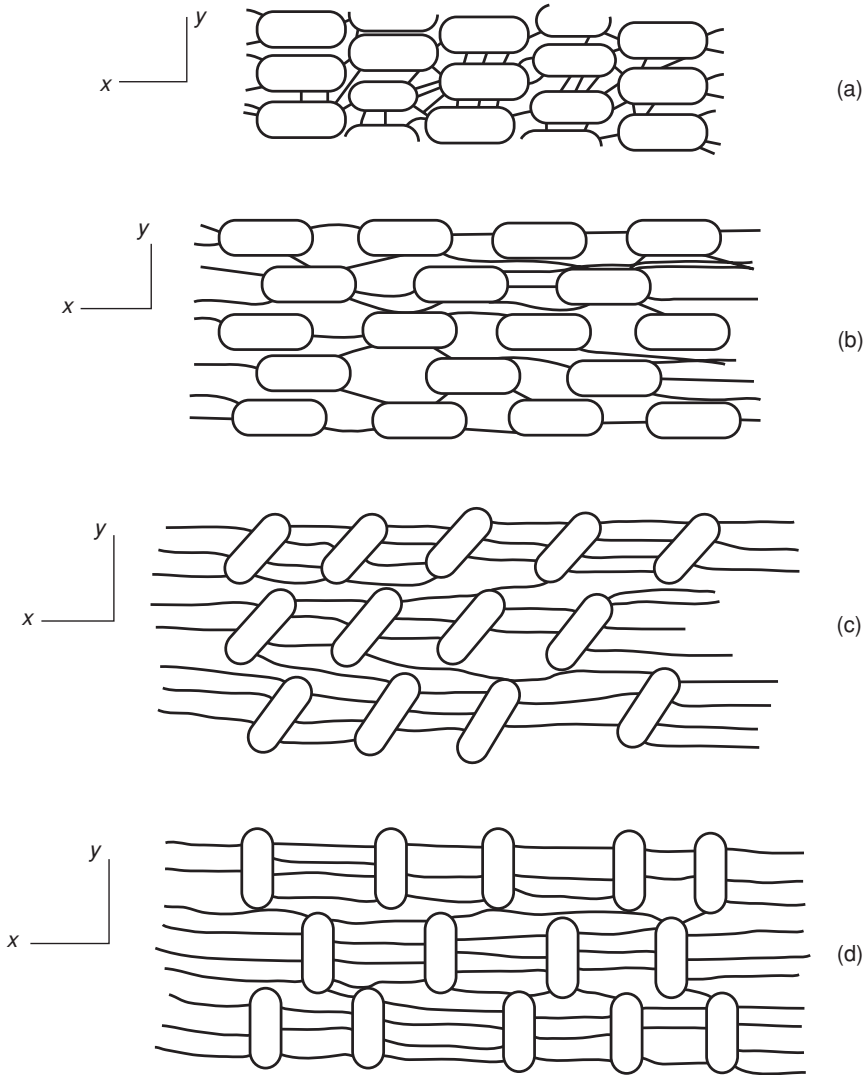
Figure 8.35 *A schematic representation of the structural changes observed in microporous polytetrafluoroethylene undergoing tensile loading in the x direction: (a) initial dense microstructure, (b) tension in fibrils causing transverse displacement of anisotropic nodal particles with lateral expansion, (c) rotation of nodes producing further lateral expansion and (d) fully expanded structure prior to further, plastic deformation due to node break-up. (Reproduced from Evans, K.E. and Caddock, B.D. (1989) Microporous materials with negative Poisson's ratios. II. Mechanisms and interpretation. J. Phys. D. Appl. Phys., **22**, 1883. Copyright (1989).)*
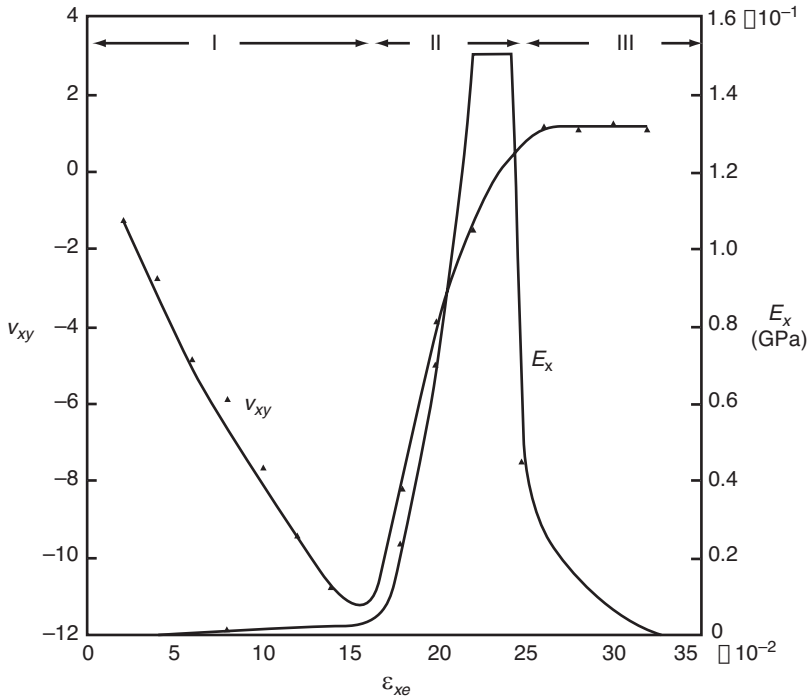
Figure 8.36 *Plot of Poisson's ratio v_{xy} ($= v_{12}$) and Young's modulus E_x ($= E_1$) against engineering strain ε_{xe} showing the three regions of behaviour: I, low modulus; II, increasing modulus; and III plastic [114]. (Reproduced from Caddock, B.D. and Evans, K.E. (1989) Microporous materials with negative Poisson's ratios. I. Microstructure and mechanical properties. J. Phys. D. Appl. Phys., 22, 1877. Copyright (1989) Institute of Physics.)*
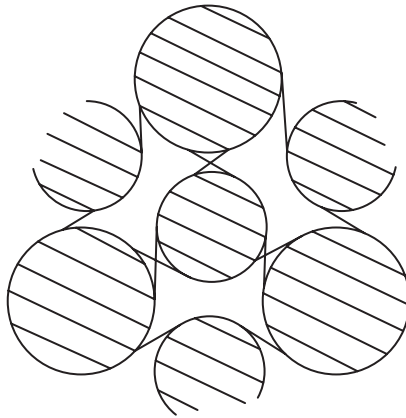
Figure 8.37 *Schematic diagram of an isotropic microstructure consisting of nodules and fibrils that causes a negative Poisson's ratio when pulled in any direction. (Reproduced from Evans, K.E. and Alderson, K.L. (1992) The static and dynamic moduli of auxetic microporous polyethylene. J. Mater. Sci. Lett., 11, 1721. Copyright (1992) Springer Science and Business Media.)*

but the overall network structure is. Material in sheet form, consisting of fibres compressed together, has been shown by experiment to possess negative out-of plane Poisson's ratios, an example being paper. Tatlier and Berhan [124] used finite element modelling of three-dimensional compressed fibre systems, and found that negative Poisson's ratios were predicted. The physical basis of the effect is that, during the compressive forming process, initially straight fibres become bent over other non-parallel fibres at contact points; then, on the application of tension, the fibres are deformed back to their initial straight configurations, producing a lateral expansion. Following the modelling work, Jayanty, Crowe and Berhan [125] infused auxetic sintered metal fibre networks with polymer, and successfully produced an auxetic composite. Also, they produced polymer composites using carbon nanofibres that also proved to be auxetic, even though the fibres were not originally in a fused network. This was attributed to the fibres forming an effective network as a result of proximity rather than true contact.

References

1. Biot, M.A. (1955) *International Union of Theoretical and Applied Mechanics Colloquium (Madrid)*, Springer-Verlag, Berlin, p. 251.
2. Rogers, T.G. and Pipkin, A.C. (1963) Asymmetric relaxation and compliance matrices in linear viscoelasticity. *J. Appl. Maths Phvs.*, **14**, 334.
3. Nye, J.F. (1957) *Physical Properties of Crystals*, Clarendon Press, Oxford, p. 138.
4. Horgan, C.O. (1972) On Saint-Venant's principle in plane anisotropic elasticity. *J. Elast.*, **2**(169), 335.
5. Horgan, C.O. (1974) The axisymmetric end problem for transversely isotropic circular cylinders. *Int. J. Solids Structure*, **10**, 837.
6. Folkes, M.J. and Arridge, R.G.C. (1975) The measurement of shear modulus in highly anisotropic materials: the validity of St. Venant's principle. *J. Phys. D*, **8**, 1053.
7. Wilson, I., Cunningham, A., Duckett, R.A. *et al.* (1976) The determination of the extensional compliance perpendicular to the plane of sheet for thin polyethylene terephthalate sheets. *J. Mater. Sci.*, **11**, 2189.
8. Ladizesky, N.H. and Ward, I.M. (1971) Determination of Poisson's ratio and Young's modulus of low-density polyethylene. *J. Macromol. Sci. B*, **5**, 661.
9. Clayton, D., Darlington, M.W. and Hall, M.M. (1973) Tensile creep modulus, creep lateral contraction ratio, and torsional creep measurements on small nonrigid specimens. *J. Phys. E.*, **6**, 218.
10. Darlington, M.W. and Saunders, D.W. (1975) Anisotropic creep behaviour in *Structure and Properties of Oriented Polymers* (ed. I.M. Ward), Applied Science Publishers, London, Chap. 10.
11. Dunn, C.M.R., Mills, W.H. and Turner, S. (1964) Creep in thermoplastics. *Br. Plastics*, **37**, 386.
12. Wilson, I., Cunningham, A. and Ward, I.M. (1976) Determination of Poissons ratio compliances for polyethylene terephthalate sheets using a Michelson interferometer. *J. Mater. Sci.*, **11**, 2181.
13. Richardson, I.D. and Ward, I.M. (1978) Temperature-dependence of Poisson ratios in low-density polyethylene with parallel lamellas morphology. *J. Polym. Sci. Polym. Phys.*, **16**, 667.

14. Raumann, G. (1962) The Anisotropy of the Shear Moduli of Drawn Polyethylene. *Proc. Phys. Soc.*, **79**, 1221.
15. Lekhnitskii, S.G. (1981) *Theory of Elasticity of an Anisotropic Elastic Body*, Mir, Moscow.
16. Ladizesky, N.H. and Ward, I.M. (1971) Measurement of shear moduli of oriented low-density polyethylene. *J. Macromol. Sci. B*, **5**, 745.
17. Ladizesky, N.H. and Ward, I.M. (1974) Deformation mechanisms of low density polyethylene with parallel lamellar morphology. *J. Macromol. Sci. B*, **9**, 565.
18. Lewis, E.L.V. and Ward, I.M. (1980) The measurement of shear compliances for oriented polyethylene terephthalate sheet. *J. Mater. Sci.*, **15**, 2354.
19. Biot, M.A. (1939) Increase of Torsional Stiffness of a Prismatical Bar Due to Axial Tension. *J. Appl. Phys.*, **10**, 860.
20. Timoshenko, S.P. and Goodier, J.N. (1970) *Theory of Elasticity*, 3rd edn, McGraw-Hill, New York, Chap. 10.
21. Lewis, E.L.V., Richardson, I.D. and Ward, I.M. (1979) Hall-effect apparatus for the measurement of simple shear in polymers. *J. Phys. E*, **12**, 189.
22. Wakelin, J.H., Voong, E.T.L., Montgomery, D.J. *et al.* (1955) Vibroscope measurements of the elastic moduli of nylon 66 and dacron filaments of various draw ratios. *J. Appl. Phys.*, **26**, 786.
23. Meredith, R. (1954) The torsional rigidity of textile fibers. *J. Text. Inst.*, **45**, 489.
24. Hillier, K.W. and Kolsky, H. (1949) An investigation of the dynamic mechanical properties of some high polymers. *Proc. Phys. Soc. B*, **62**, 111.
25. Ballou, J.W. and Smith, J.C. (1949) Dynamic measurements of polymer physical properties. *J. Appl. Phys.*, **20**, 493.
26. Nolle, A.W. (1950) Dynamic mechanical properties of rubberlike material. *J. Polym. Sci.*, **5**, 1.
27. Hamburger, W.J. (1948) Mechanics of elastic performance of textile materials: II. The application of sonic techniques to the investigation of the effect of visco-elastic behavior upon stress-strain relationships in certain high polymers. *Text. Res. J.*, **18**, 705.
28. Charch, W.H. and Moseley, W.W. (1959) Structure-property relationships in synthetic fibers: Part I: structure as revealed by sonic observations. *Text. Res. J.*, **29**, 525.
29. Moseley, W.W. (1960) The measurement of molecular orientation in fibers by acoustic methods. *J. Appl. Polym. Sci.*, **3**, 266.
30. Morgan, H.M. (1962) Correlation of molecular orientation measurements in fibers by optical birefringence and pulse velocity methods. *Text. Res. J.*, **32**, 866.
31. Davis, V.V. (1959) A diffraction method for the measurement of diameter changes in strained fibres. *J Text. Inst.*, **50**, 688.
32. Frank, F.I. and Ruoff, A.L. (1958) A method of measuring Poisson's ratio of fibers 1. *Text. Res. J.*, **28**, 213.
33. Hadley, D.W., Ward, I.M. and Ward, J. (1965) Transverse compression of anisotropic fibre monofilaments. *Proc. Roy. Soc. A*, **285**, 275.
34. Pinnock, P.R., Ward, I.M. and Wolfe, J.M. (1966) Compression of anisotropic fibre monofilaments. 2. *Proc. Roy. Soc. A*, **291**, 267.
35. Hertz, H. (1896) Miscellaneous Papers, Macmillan, London, p. 146.
36. McEwen, E. (1949) Stresses in elastic cylinders in contact along a generatrix (including the effect of tangential friction). *Phil. Mag.*, **40**, 454.

37. Kotani, T., Sweeney, J. and Ward, I.M. (1994) The measurement of transverse mechanical properties of polymer fibres. *J. Mater. Sci.*, **29**, 5551.
38. Abdul Jawad, S. and Ward, I.M. (1978) Transverse compression or oriented nylon and polyethylene extrudates. *J. Mater. Sci.*, **13**, 1381.
39. Kawabata, S. (1990) Measurement of the transverse mechanical properties of high-performance fibres. *J. Text. Inst.*, **81**, 432.
40. Raumann, G. and Saunders, D.W. (1961) The anisotropy of Young's modulus in drawn polyethylene. *Proc. Phys. Soc.*, **77**, 1028.
41. Gupta, V.B. and Ward, I.M. (1967) Mechanical and optical anisotropy in low-density polyethylene. *J. Macromol. Sci. B*, **1**, 373.
42. Hadley, D.W., Pinnock, P.R. and Ward, I.M. (1969) Anisotropy in oriented fibres from synthetic polymers. *J. Mater. Sci.*, **4**, 152.
43. Hine, P.J. and Ward, I.M. (1996) Measuring the elastic properties of high-modulus fibres. *J. Mater. Sci.*, **31**, 371.
44. Wilczynski, A.P., Ward, I.M. and Hine, P.J. (1995) Bounds for the elastic constants of reinforcing fibres in polymeric composites. *J. Mater. Sci.*, **30**, 5879.
45. Brew, B., Hine, P.J. and Ward, I.M. (1999) The properties of pipd-fibre/epoxy composites. *Comp. Sci. Tech.*, **59**, 1109.
46. Krüger, J.K., Marx, A., Peetz, L. *et al.* (1986) Simultaneous determination of elastic and optical properties of polymers by high performance Brillouin spectroscopy using different scattering geometries. *Colloid. Polym. Sci.*, **264**, 403.
47. Krüger, J.K., Grammes, C., Stockem, K. *et al.* (1991) Nonlinear elastic properties of solid polymers as revealed by Brillouin spectroscopy. *Colloid. Polym. Sci.*, **269**, 764.
48. Wang, C.H., Liu, Q.-L. and Li, B.Y. (1987) Brillouin scattering of oriented films of poly(vinylidene fluoride) and poly(vinylidene fluoride)-poly(methyl methacrylate) blends. *Polym. Phys.*, **25**, 485.
49. Cavanagh, D.B. and Wang, C.H. (1982) Studies of the effect of orientation on the elastic constants of stretched and hydrostatically extruded polychlorotrifluoroethylene: a reorientational model in semicrystalline polymers. *J. Polym. Sci. Polym. Phys. Edn.*, **20**, 1647.
50. Kumar, S.R., Rennesch, D.P. and Grimsditch, M. (2000) Effect of molecular orientation on the elastic constants of polypropylene. *Macromolecules*, **33**, 1819.
51. Chan, O.K., Chen, F.C., Choy, C.L. *et al.* (1978) Elastic constants of extruded polypropylene and polyethylene terephthalate. *J. Phys D: Appl. Phys.*, **11**, 617.
52. Leung, W.P., Chen, F.C., Choy, C.L. *et al.* (1984) Ultrasonic measurements of the mechanical relaxations and complex stiffnesses in oriented linear polyethylene. *Polymer*, **25**, 447.
53. Choy, C.L., Leung, W.P., Ong, E.L. *et al.* (1988) Mechanical anisotropy in rolled nylon 66. *Polym. Sci. B, Polym. Phys. Ed.*, **26**, 1569.
54. Choy, C.L., Leung, W.P. and Huang, C.E. (1983) Elastic moduli of highly oriented polyoxymethylene. *Polym. Eng. Sci.*, **23**, 910.
55. Choy, C.L. and Leung, W.P. (1985) Elastic moduli of ultradrawn polyethylene. *J. Polym. Sci. Polym. Phys. Ed.*, **23**, 1759.
56. Leung, W.P. and Choy, C.L. (1983) The elastic constants of ultradrawn polypropylene. *J. Polym. Sci. Polym. Phys. Ed.*, **21**, 725.

57. *Materials Studio 5*. Accelrys Inc., San Diego, CA, USA.

58. Treloar, L.R.G. (1960) Calculations of elastic moduli of polymer crystals: I. Polyethylene and nylon 66. *Polymer*, **1**, 95.

59. Born, M. and Huang, K. (1954) *Dynamical Theory of Crystal Lattices*, Clarendon Press, Oxford.

60. Odajima, A. and Maeda, T. (1967) Calculation of the elastic constants and the lattice energy of the polyethylene crystal. *J. Polym. Sci. Part C*, **15**, 55.

61. Tashiro, K. (1993) Molecular theory of mechanical properties of crystalline polymers. *Prog. Polym. Sci.*, **18**, 377.

62. Rutledge, G.C. and Suter, U.W. (1991) Calculation of mechanical properties of poly(p-phenylene terephthalamide) by atomistic modeling. *Polymer*, **32**, 2179.

63. Nicholson, T.M., Davies, G.R. and Ward, I.M. (1994) Conformations in poly(ethylene terephthalate): a molecular modelling study. *Polymer*, **35**, 4259.

64. Shachtschneider, J.H. and Snyder, R.G. (1963) Vibrational analysis of the n-paraffins—II: Normal co-ordinate calculations. *Spectrochem. Acta*, **19**, 117.

65. Snyder, R.G. and Shachtschneider, J.H. (1965) A valence force field for saturated hydrocarbons. *Spectrochem. Acta*, **21**, 169.

66. Snyder, R.G. and Zerbi, G. (1967) Vibrational analysis of ten simple aliphatic ethers: spectra, assignments, valence force field and molecular conformations. *Spectrochem. Acta*, **A 23**, 391.

67. Karasawa, N., Dasgupta, S. and Goddard, W.A. (1991) Mechanical properties and force field parameters for polyethylene crystal. *J. Phys. Chem.*, **95**, 2260.

68. Sorenson, R.A., Liau, W.B., Kesner, L. *et al.* (1988) Prediction of polymer crystal structures and properties: polyethylene and poly(oxymethylene). *Macromolecules*, **21**, 200.

69. Tashiro, K., Kobayashi, M. and Tadokoro, H. (1978) Calculation of three-dimensional elastic constants of polymer crystals. 2. Application to orthorhombic polyethylene and poly(vinyl alcohol). *Macromolecules*, **11**, 914.

70. Wobser, G., Blasenbrey, S. (1970) Structural and conformational calculation in polymers. 2. Ideal crystal and defective state (bundle model) in polyethylene. *Kolloidzeitschrift*, **241**, 985.

71. Peterlin, A. (1979) Mechanical properties of fibrous structure, in *Ultra-High Modulus Polymers* (eds A. Ciferri and I.M. Ward), Applied Science Publishers, London, Chap. 10.

72. Ward, I.M. (1962) Optical and mechanical anisotropy in crystalline polymers. *Proc. Phys. Soc.*, **80**, 1176.

73. Pinnock, P.R. and Ward, I.M. (1963) Dynamic mechanical measurements on polyethylene terephthalate. *Proc. Phys. Soc.*, **81**, 260.

74. Kausch, H.H. (1970) Über die Zusammenhänge von makroskopischer und molekularer Anisotropie in Hochpolymeren. *Kolloidzeitschrift*, **237**, 251.

75. Bishop, J. and Hill, R. (1951) A theory of the plastic distortion of a polycrystalline aggregate under combined stresses. *Phil. Mag.*, **42**, (414), 1248.

76. Reuss, A. (1929) Berechnung der Fließgrenze von Mischkristallen auf Grund der Plastizitätsbedingung für Einkristalle. *Zeit. Angew. Math. Mech.*, **9**, 49.

77. Voigt, W. (1928) *Lehrbuch der Kristallphysik*, Teubuer, Leipzig, p. 410.

78. Pinnock, P.R. and Ward, I.M. (1966) Mechanical and optical anisotropy in polypropylene fibres. *Br. J. Appl. Phys.*, **17**, 575.

79. Crawford, S.M. and Kolsky, H. (1951) Stress birefringence in polyethylene. *Proc. Phys. Soc. B*, **64**, 119.

80. Cannon, C.G. and Chappel, F.C. (1959) Effect of temperature and moisture content on the orientation produced by the drawing of nylon 66. *Br. J. Appl. Phys.*, **10**, 68.

81. Kuhn, W. and Grün, F. (1942) Relations between elastic constants and the strain birefringence of high-elastic substances. *Kolloid-zeitschrift*, **101**, 248.

82. Pinnock P.R. and Ward I.M. (1964) Mechanical and optical anisotropy in polyethylene terephthalate fibres. *Br. J. Appl. Phys.*, **15**, 1559.

83. Frank, F.C., Gupta, V.B. and Ward, I.M. (1970) Effect of mechanical twinning on tensile modulus of polyethylene. *Phil. Mag.*, **21**, 1127.

84. Gupta, V.B., Keller, A. and Ward, I.M. (1968) The effect of crystallite orientation on mechanical anisotropy in low-density polyethylene. *J. Macromol. Sci. B*, **2**, 139.

85. Gupta, V.B. and Ward, I.M. (1970) Crystallite orientation in low-density polyethylene and its effect on mechanical anisotropy. *J. Macromol. Sci. B*, **4**, 453.

86. McBrierty, V.J. and Ward, I.M. (1968) Investigation of the orientation distribution functions in drawn polyethylene by broad line nuclear magnetic resonance. *J Phys D: Appl. Phys.*, **1**, 1529.

87. Allison, S.W. and Ward, I.M. (1967) The cold drawing of polyethylene terephthalate. *Br. J. Appl. Phys.*, **18**, 1151.

88. Kausch, H.H. (1967) Elastic properties of anisotropic heterogeneous materials. *J. Appl. Phys.*, **38**, 4213; (1969) *Kolloidzeitschrift*, **234**, 1148; (1970) 237, 251; (1978) *Polymer Fracture*, Springer, Berlin, p. 33.

89. Kausch, H.H. (1971) Elastic and ultimate behavior of amorphous polymer networks. *J. Macromol. Sci. B.*, **5**, 269.

90. Ward, I.M. (1964) The correlation of molecular orientation parameters derived from optical birefringence and sonic velocity methods. *Text. Res. J.*, **34**, 806.

91. Samuels, R.J. (1974) *Structured Polymer Composites*, John Wiley & Sons, New York.

92. Hennig, J. (1964) Anisotropie des dynamischen Elastizitätsmodulus in einachsig verstreckten amorphen Hochpolymeren. *Kolloidzeitschrift*, **200**, 46.

93. Robertson, R.E. and Buenker, R.J. (1964) Some elastic moduli of bisphenol A polycarbonate. *J. Polym. Sci.*, **A2**(2), 4889.

94. Wright, H., Faraday, C.S.N., White, E.F.T. *et al.* (1971) The elastic constants of oriented glassy polymers. *J Phys. D*, **4**, 2002.

95. Rawson, F.F. and Rider, J.G. (1974) The elastic constants of oriented polyvinyl chloride. *J. Phys. D*, **7**, 41.

96. Kashiwagi, M., Folkes, M.J. and Ward, I.M. (1971) The measurement of molecular orientation in drawn poly(methyl methacrylate) by broad line nuclear magnetic resonance. *Polymer*, **12**, 691–697.

97. Wilson, I., Ladizesky, N.H. and Ward, I.M. (1976) Determination of Poissons ratio and extensional modulus for polyethylene terephthalate sheets by an optical technique. *J. Mater. Sci.*, **11**, 2177.

98. Cunningham, A., Ward, I.M., Willis, H.A. *et al.* (1974) An infra-red spectroscopic study of molecular orientation and conformational changes in poly(ethylene terephthalate). *Polymer*, **15**, 749.

99. Cunningham, A. (1974) The structure and properties of oriented polyethylene tereph-thalate. Ph.D. thesis. Leeds University.

100. Maxwell, A.S., Unwin, A.P. and Ward, I.M. (1996) The mechanical behaviour of oriented high-pressure annealed polyethylene. *Polymer*, **37**, 3283.

101. Davies, G.R. and Ward, I.M. (1988) Structure and properties of oriented thermotropic liquid crystal polymers in the solid state, in *High Modulus Polymers* (eds A.E. Zachariades and R.S. Porter), Marcel Dekker, New York, Chap. 2; Troughton, M.J., Davies, G.R. and Ward, I.M. (1989) Dynamic mechanical properties of random copolyesters of 4-hydroxybenzoic acid and 2-hydroxy 6-naphthoic acid. *Polymer*, **30**, 58; Green, D.I., Unwin, A.P., Davies, G.R. and Ward, I.M. (1990) An aggregate model for random liquid crystalline copolyesters. *Polymer*, **31**, 579.

102. Northolt, M.G. and Van Aartsen, J.J. (1977) Chain orientation distribution and elastic properties of poly (p-phenylene terephthalamide), a "rigid rod" polymer. *J. Polym. Sci. Polym. Symp.*, **58**, 283.

103. Northolt, M.G. and van der Hout, R. (1985) Elastic extension of an oriented crystalline fibre. *Polymer*, **26**, 310.

104. Attard, D. and Grima, J.N. (2008) Auxetic behaviour from rotating rhombi. *Phys. Status Solidi B*, **245**(Special Issue S1), 2395–2404.

105. Attard, D., Manicaro, E. and Grima, J.N. (2009) On rotating rigid parallelograms and their potential for exhibiting auxetic behaviour. *Phys. Status Solidi B*, **246**, 2033–2044.

106. Grima, J.N., Manicaro, E. and Attard, D. (2011) Auxetic behaviour from connected different-sized squares and rectangles. *Proc. R. Soc. A*, **467**, 439–458.

107. Grima, J.N., Farrugia, P.S., Caruana, C. *et al.* (2008) Auxetic behaviour from stretching connected squares. *J. Mater. Sci.*, **43**, 5962–5971.

108. Ravirala, N., Alderson, A. and Alderson, K.L. (2007) Interlocking hexagons model for auxetic behaviour. *J. Mater. Sci.*, **42**, 7433–7445.

109. Fozdar, D.Y., Soman, P., Lee, J.W. *et al.* (2011) Three-dimensional polymer constructs exhibiting a tunable negative Poisson's ratio. *Adv. Funct. Mater.*, **21**, 2712–2720.

110. Liu, Y. and Hu, H. (2010) A review on auxetic structures and polymeric materials. *Sci. Res. Essays*, **5**, 1052–1063.

111. Lakes, R.S. (1987) Foam structures with a negative Poisson's ratio. *Science*, **235**, 1038.

112. Bianchi, M., Scarpa, F.L. and Smith, C.W. (2008) Stiffness and energy dissipation in polyurethane auxetic foams. *J. Mater. Sci.*, **43**, 5851–5860.

113. Bianchi, M., Scarpa, F.L. and Smith, C.W. (2010) Shape memory behaviour in auxetic foams: Mechanical properties. *Acta Materiala*, **58**, 858–865.

114. Xu, T. and Li, G.Q. (2011) A shape memory polymer based syntactic foam with negative Poisson's ratio. *Mater. Sci. Eng. A – Struct. Mater.: Properties, Microstructure and Processing*, **528**, 6804–6811.

115. Caddock, B.D. and Evans, K.E. (1989) Microporous materials with negative Poisson's ratios. I. Microstructure and mechanical properties. *J. Phys. D. Appl. Phys.*, **22**, 1877.

116. Evans, K.E. and Caddock, B.D. (1989) Microporous materials with negative Poisson's ratios. II. Mechanisms and interpretation. *J. Phys. D. Appl. Phys.*, **22**, 1883.

117. Alderson, K.L. and Evans, K.E. (1992) The fabrication of microporous polyethylene having a negative Poisson's ratio. *Polymer*, **33**, 4435.

118. Evans, K.E. and Alderson, K.L. (1992) The static and dynamic moduli of auxetic microporous polyethylene. *J. Mater. Sci. Lett.*, **11**, 1721.
119. Neale, P.J., Pickles, A.P., Alderson, K.L. *et al.* (1995) The effect of the processing parameters on the fabrication of auxetic polyethylene. *J. Mater. Sci.*, **30**, 4087.
120. Alderson, K.L., Alderson, A., Smart, G. *et al.* (2002) Auxetic polypropylene fibres: part 1 - manufacture and characterization. *Plast. Rubber Compos.*, **31**(8), 344–349.
121. Alderson, K.L., Alderson, A., Davies, P.J. *et al.* (2007) The effect of processing parameters on the mechanical properties of auxetic polymeric fibers. *J. Mater. Sci.*, **42**, 7991.
122. Ravirala, N., Alderson, A., Alderson, K.L. *et al.* (2005) Auxetic polypropylene films. *Polym. Eng. Sci.*, **45**, 517–528.
123. Alderson, K.L., Webber, R.S., Kettle, A.P. *et al.* (2005) Novel fabrication route for auxetic polyethylene. Part 1. Processing and microstructure. *Polym. Eng. Sci.*, **45**, 568–578.
124. Tatlier, M. and Berhan, L. (2009) Modelling the negative Poisson's ratio of compressed fused fibre networks. *Phys. Status Solidi B*, **246**, 2018–2024.
125. Jayanty, S., Crowe, J. and Berhan, L. (2011) Auxetic fibre networks and their composites. *Phys. Status Solidi B*, **248**, 73–81.

9

Polymer Composites: Macroscale and Microscale

In this chapter, we first give a brief survey of the advantages to be gained by using a composite material whose components often have contrasting but complementary properties, for example ductile fibres reinforcing a brittle matrix. We then discuss two distinct applications of these general principles: macroscopic composites, composed of a polymeric matrix in which a second component is embedded, and microscale composites, used to model the morphology of partially crystalline polymers.

9.1 Composites: A General Introduction

Many useful engineering materials have a heterogeneous composition. Metals, for instance, are often used in the form of alloys. The addition of a small percentage of another metal, such as copper, magnesium and manganese, is necessary to prevent plastic deformation occurring in aluminium at very low stresses. An increase in carbon content from 0.1% to 3% is a primary determinant in whether a ferrous alloy becomes a mild steel or a cast iron. Concrete, which, like cast iron has good compressive but poor tensile properties, consists of a hard aggregate embedded in a metal silicate network.

Both animal and vegetable life are dependent on natural composites. Bones must be stiff and yet able to absorb significant amounts of energy without fracturing; they also provide anchor points for muscles, which are composite. The skeletal material of plants, and in particular wood, provides a splendid example of the desirable properties of a composite. As a gross simplification, its structure can be considered in terms of an array of relatively stiff fibres embedded in a more compliant matrix. The matrix permits stresses to be redistributed among the fibres, so retarding the onset of fracture at stress concentrations. Wood fails in compression when its fibres buckle. The fracture stress is higher in tension, as a large amount of work must be done in pulling the fibres out of the matrix.

Reinforced concrete has practically a century of use as a building material. Continuous steel rods, prestressed under tension, pass completely through each structural element and enable the material to withstand tensile as well as compressive stresses, to give a combination that combines the desirable features of each component.

A further form of composite is one where the second component acts as a filler. Carbon black in vehicle tyres is an example of a filler needed to provide the required properties. Each carbon particle provides an anchorage for many rubber molecules, and so assists in the redistribution of stress; and the carbon is also essential to obtain the desired hysteresis behaviour and abrasion resistance. A much simpler application of a filler is the use of sawdust or other cheap powder in mouldings made from a thermosetting plastic. Although the mechanical properties of the base material are degraded (except possibly for impact resistance), they are still adequate for the proposed application, and the product cost is reduced. We shall not consider fillers in the discussion that follows.

Another desirable property of a composite that will not be considered further is the protection that a compliant matrix affords to a brittle reinforcing fibre. Glass and other brittle materials fracture in tension due to the deepening of pre-existing cracks. Because of the absence of plastic flow (unlike the situation for polymers discussed in Chapter 13), blunting of the crack tip cannot occur, and so the stress rapidly approaches that required for fracture. If glass fibres are encapsulated in a soft plastic matrix, the possibility of surface scratches is reduced and the fracture stress is thereby increased. Good adhesion between fibre and matrix will assist in reducing stress concentrations, and transverse cracks will grow only with difficulty across a fibrous composite.

9.2   Mechanical Anisotropy of Polymer Composites

9.2.1   Mechanical Anisotropy of Lamellar Structures

It is instructive to start the discussion of polymer composites by modelling an idealised lamellar composite that consists of a high modulus layer and a more compliant matrix layer. Provided that the bonding between the layers remains intact, the volume fraction of each component and not the thickness of the individual layers is the important factor. As with the aggregate model discussed in Section 8.6, different values of overall stiffness are obtained depending on whether the components are in parallel or in series, yielding the Voigt or Reuss average modulus respectively.

The maximum stiffness is obtained when a uniaxial stress is applied parallel with the layers, as indicated in Figure 9.1. It is assumed that the strain is the same in all the composite layers, a form of loading known as the isostrain (or homogeneous strain) condition.

The force acting on the composite (F_c) is equal to the sum of the forces acting on the fibre and matrix layers

$$F_c = F_f + F_m. \tag{9.1}$$

Force is equal to stress multiplied by area. Hence

$$\sigma_c A_c = \sigma_f A_f + \sigma_m A_m,$$
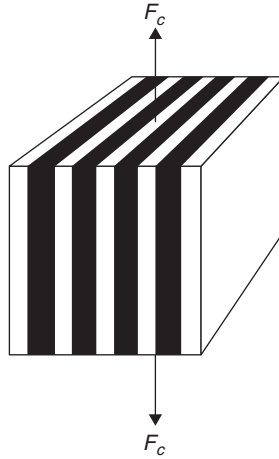
Figure 9.1 *Isostrain conditions for layered composite.*

where A_f and A_m represent the areas of the end faces occupied by each component. As both components are of length l, areas can be represented by volumes, or rather by volume fractions V_f and V_m. The volume fraction of the composite (V_c) is unity. Hence

$$\sigma_c V_c = \sigma_f V_f + \sigma_m V_m. \tag{9.2}$$

Under isostrain conditions, this expression can be rewritten in terms of Young's modulus (E) as

$$E_c = E_f V_f + E_m V_m, \tag{9.3}$$

which is a Voigt average modulus (see Section 8.6.1).

The modulus is, however, much lower in the direction transverse to the layered structure (Figure 9.2). In this case, each layer is subjected to the same force, and hence to the same stress, because the area remains constant through the stack. Loading of this form is known as the isostress (or homogeneous stress) condition.

The total deformation $\delta\ell_c$ is equal to the sum of the deformations in each component:

$$\delta\ell_c = \delta\ell_f + \delta\ell_m.$$

Length changes can be converted to strains using $\varepsilon = \delta\ell/\ell$:

$$\varepsilon_c \ell_c = \varepsilon_f \ell_f + \varepsilon_m \ell_m. \tag{9.4}$$

Substituting modulus E as the ratio of (uniform) stress to strain, we obtain

$$\frac{\sigma\ell_c}{E_c} = \frac{\sigma\ell_f}{E_f} + \frac{\sigma\ell_m}{E_m}.$$

As the cross section of the composite is assumed to be uniform, the length of a component is proportional to its volume fraction. Again, take V_c as unity to give

$$\frac{1}{E_c} = \frac{V_f}{E_f} + \frac{V_m}{E_m}. \tag{9.5}$$
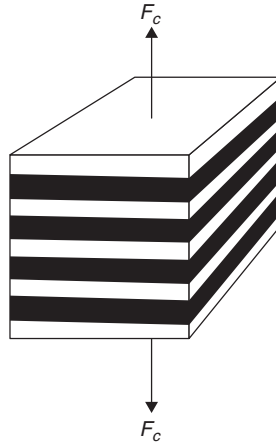
Figure 9.2   *Isostress conditions for layered composite.*

This expression can be rewritten as

$$E_c = \frac{E_f E_m}{E_m V_f + E_f V_m} \tag{9.6}$$

and is a Reuss average modulus (see Section 8.6.1).

9.2.2   Elastic Constants of Highly Aligned Fibre Composites

Although the lamellar composites are of particular interest with regard to semi-crystalline polymers, fibre composites, where a polymer matrix phase is reinforced with stiff and strong fibres, are of very great commercial importance and therefore have been the subject of extensive theoretical modelling. Because there is an analogy between aligned fibre composites and highly oriented crystalline polymers, it is valuable to precede discussion of the latter with an introductory account of the mechanical properties of fibre composites.

We take up the discussion following Section 9.2.1. In a conventional fibre composite, a matrix of moderate stiffness (∼1 GPa) is reinforced with a stiff and strong fibre (of modulus ∼100 GPa). Most usually this is glass or carbon fibre, but high-strength fibres such as aramid and polyethylene fibres are also used.

It is instructive to consider the calculation of the elastic constants for a undirectional fibre composite consisting of perfectly aligned fibres of infinite length. It is assumed that there is excellent adhesion between the fibres and the matrix.

The simplest approach is to extend the assumptions of Equations (9.3) and (9.5). Choosing the fibre direction as the 3 axis, the assumptions of homogeneous strain in the 3 direction and homogeneous stress in the 1 direction imply, in terms of the nomenclature proposed in Section 8.2.2, that the five independent elastic constants for the composite (E_1^c, E_1^c, ν_{13}^c, ν_{12}^c and G_4^c) are given by

$$\frac{1}{E_1^c} = \frac{V_f}{E_1^f} + \frac{V_m}{E^m} \tag{9.7a}$$

$$E_3^c = V_f E_3^f + V_m E^m \tag{9.7b}$$

$$v_{12}^c = \frac{V_f v_{12}^f E^m + V_m v^m E_1^f}{V_f E^m + V_m E_1^f} \tag{9.7c}$$

$$v_{13}^c = V_f v_{13}^f + V_m v^m \tag{9.7d}$$

and

$$\frac{1}{G_4^c} = \frac{V_f}{G_4^f} + \frac{V_m}{G^m}, \tag{9.7e}$$

where V_f and V_m are the fibre and matrix volume fractions respectively, E_1^f, E_3^f, v_{13}^f, v_{12}^f, and G_4^f are the fibre elastic constants and E^m, G^m and G_4^f are the elastic constants of the isotropic matrix. Equations (9.7b) and (9.7d) give good predictions for the axial Young's modulus E_3^c and the axial Poisson's ratio v_{13}^c, but the simple isostress equations for the lateral elastic constants E_1^c and v_{12}^c and the longitudinal shear modulus are not satisfactory because they do not take into account any constraints due to the very high axial stiffness of the fibres. This can be appreciated readily by undertaking the calculation of E_1^c on the assumption that, if the fibre Young's modulus E_3^f is much greater than that of the matrix E^m, when a stress is applied perpendicular to the fibre direction there is no strain in the fibre direction.

Consider a perfectly aligned fibre composite reinforced with isotropic fibres of infinite stiffness in an isotropic matrix of modulus E^m and Poisson's ratio v^m. In the matrix we have

$$e_1 = V_m \left\{ \frac{\sigma_1}{E^m} - \frac{v^m \sigma_2}{E^m} - \frac{v^m \sigma_3}{E^m} \right\}$$

$$e_2 = V_m \left\{ -\frac{v^m \sigma_1}{E^m} + \frac{\sigma_1}{E^m} - \frac{v^m \sigma_3}{E^m} \right\}$$

$$e_3 = V_m \left\{ -\frac{v^m \sigma_1}{E^m} - \frac{v^m \sigma_2}{E^m} + \frac{\sigma_3}{E^m} \right\}.$$

In this situation of plane strain,

$$e_3 = 0 \quad \text{and} \quad \sigma_3 = v^m (\sigma_1 + \sigma_2).$$

For stress σ_1 applied in the 1 direction, with $\sigma_2 = 0$, $\sigma_3 = v^m \sigma_1$ and

$$\sigma_3 = v^m \left\{ \frac{\sigma_1}{E^m} - \frac{(v^m)^2 \sigma_1}{E^m} \right\}$$

i.e. Young's modulus in the 1 direction, E_1^c is given by

$$E_1^c = \frac{E^m}{V_m \left(1 - (v^m)^2 \right)}. \tag{9.8}$$

This result differs significantly from Equation (9.7a) but still shows that the modulus in the transverse direction is very much less than that in the fibre direction.

Exact analytical expressions of all the elastic constants of a fibre composite with perfectly aligned fibres of infinite length have been obtained recently by Wilczynski [1–3] and confirmed by finite element calculations [4, 5]. It is, however, common practice to use the equations proposed by Halpin and Kardos [6] based on a generalised self-consistent model

developed by Hermans [7] for a composite with continuous aligned fibres. The Halpin–Tsai equations, as they are called, for E_3^c v_{13}^c are identical to Equations (9.7b) and (9.7d) but differ significantly for the transverse modulus E_1^c and the longitudinal shear modulus G_4^c. These are given by

$$\frac{E_1^c}{E^m} = \frac{1 + 2\eta_1 V_f}{1 - \eta_1 V_f}$$

$$\frac{G_4^c}{G^m} = \frac{1 + 2\eta_2 V_f}{1 - \eta_2 V_f},$$

where

$$\eta_1 = \frac{E_1^f / E^m - 1}{E_1^f / E^m + 1}$$

$$\eta_2 = \frac{G_4^f / G^m - 1}{G_4^f / G^m + 1}.$$

For glass fibres where E_1^f and G_4^f are made much greater than E^m and G^m, these equations reduce to

$$\frac{E_1^c}{E^m} = \frac{1 + 2V_f}{1 - V_f} \tag{9.9a}$$

$$\frac{G_4^c}{G^m} = \frac{1 + V_f}{1 - V_f}. \tag{9.9b}$$

It is important to note that Equations (9.9a) and (9.9b) show that the values of E_1^c and G_4^c are greater than those for a calculation based on a simplistic homogeneous stress approach, which would give

$$E_1^c = E^m / (1 - V_f)$$

$$G_4^c = G^m / (1 - V_f)$$

assuming that $E_1^f \gg E^m$ and $G_4^f \gg E^m$.

There is an extensive literature on composite materials stemming from the seminal papers of Eshelby [8], who considered the elastic field in and around an elliptic inclusion in an infinite matrix. His theory assumed a single particle in an infinite matrix and therefore was valid only for low-volume fractions ($\sim 1\%$). The extension to more concentrated systems was undertaken by Mori and Tanaka [9], whose method was used by Tandon and Weng [10] to derive the elastic constants of an aligned fibre composite. The composite moduli for this model are given by

$$\frac{E_1^c}{E^m} = \frac{2A}{2A + V_f\left(-2v^m A_3 + (1 - v^m)A_4 + (1 + v^m)A_5 A\right)} \tag{9.10a}$$

$$\frac{E_3^c}{E^m} = \frac{A}{A + V_f\left(A_1 + 2v^m A_2\right)}, \tag{9.10b}$$

where A, A_1, A_2, A_3, A_4 and A_5 are functions of Eshelby's tensor, the mechanical properties of the matrix and reinforcement, the filler concentration and the aspect ratio of the filler particles.

The Halpin–Tsai equations give excellent predictions to a good approximation in most circumstances. However, the Mori–Tanaka approach is more accurate for high aspect ratio inclusions. The reader is referred to a recent paper by Tucker and Liang [11] for a comprehensive review.

9.2.3 Mechanical Anisotropy and Strength of Uniaxially Aligned Fibre Composites

The theoretical considerations outlined above show that a uniaxially aligned fibre composite will show a high degree of mechanical anisotropy, i.e. $E_3^c > E_1^c \sim G_4^c$. Consider, for example, a glass-fibre/resin composite containing a 0.6 volume fraction of glass filaments with a tensile modulus of 70 GPa. For a matrix of modulus 5 GPa and a Poisson's ratio of 0.35, Equation (9.7a) gives the predicted axial Young's modulus E_3^c of 44 Gpa, and Equation (9.8) gives a transverse Young's modulus E_1^c of 14.2 GPa. The composite has a highly anisotropic stiffness, which decreases very rapidly at quite small angles to the direction of the reinforcing fibres. For this reason, parts made from preimpregnated sheets of uniaxially oriented fibres (called 'prepregs') are generally produced by 0/90 cross-ply laminates or even more sophisticated lay-ups.

The importance of these calculations in this textbook lies in the analogy between a highly aligned fibre composite and a highly oriented polymer where the highly oriented molecules with a very high chain modulus (~280 GPa in the case of polyethylene) can act in the role of the glass or carbon fibres, and the analogy will be pursued in later sections.

9.3 Short Fibre Composites

Although continuous filament composites are of considerable commercial importance, their fabrication is a rather complex process and a cheaper, though mechanically inferior product is obtained by mixing short lengths of fibre with a thermoplastic polymer.

A prime requirement is good adhesion between fibre and matrix, a condition that will be dependent on features such as chemical bonding and surface cleanliness, as well as mechanical factors. The ratio of surface area to fibre volume should be as high as possible. Considering cylinders of length ℓ and radius r:

Area $A = 2\pi r^2 + 2\pi r\ell$ and volume $V = \pi r^2 \ell$

$$\therefore \frac{A}{V} = \frac{2}{\ell} + \frac{2}{r}. \tag{9.11}$$

Expressed in terms of the aspect ratio $a = \ell/2r$ the above expression becomes

$$\frac{A}{V} = \left(\frac{2\pi}{V}\right)^{1/3} \left(a^{-2/3} + 2a^{1/3}\right). \tag{9.12}$$

It can be seen, therefore, that for optimum adhesion the aspect ratio should be either very small, where $a^{-2/3}$ becomes very large, corresponding to flat platelets (minerals such as talc

and mica, and at the nanoscale clay platelets – see Section 9.4), or very high, where $a^{1/3}$ is very large, corresponding to fibres. The latter case will now be examined in more detail.

9.3.1   The Influence of Fibre Length: Shear Lag Theory

Consider a short length of fibre aligned with the tensile stress direction. The stiff fibre will tend to restrain the deformation of the matrix, and so a shear stress will be set up in the matrix at its interface with the fibre, which will be a maximum at the ends of the fibre and a minimum in the middle (Figure 9.3(a)). This shear stress then transmits a tensile stress to the fibre, but as the fibre–matrix bond ceases at the fibre ends there can be no load transmitted from the matrix at each fibre extremity. The tensile stress is thus zero at each end of the fibre and rises to an intermediate maximum or plateau over a critical length $\ell_0/2$ (Figure 9.3(b)). For effective reinforcement, the fibre length must be greater than the critical value ℓ_0, otherwise the stress will be less than the maximum possible.

The reduction in tensile stress towards the ends of each fibre inevitably leads to a decrease in the tensile modulus compared with the continuous filament case. Consider a plane drawn perpendicular to the stress direction in an aligned discontinuous fibre composite (Figure 9.4), which must intercept individual filaments at random positions along their length. Hence, the stress carried by the composite must be lower than that for the continuous filament case, and is dependent on the length of each fibre. Cox [12] predicted a correction factor η_1 for the tensile modulus in the axial direction that takes into account the finite length of the fibres so that Equation (9.3) is modified to

$$E = \eta_1 E^f V_f + E^m V_m, \tag{9.13}$$

where

$$\eta_1 = 1 - \frac{\tan hax}{ax}, \tag{9.14}$$
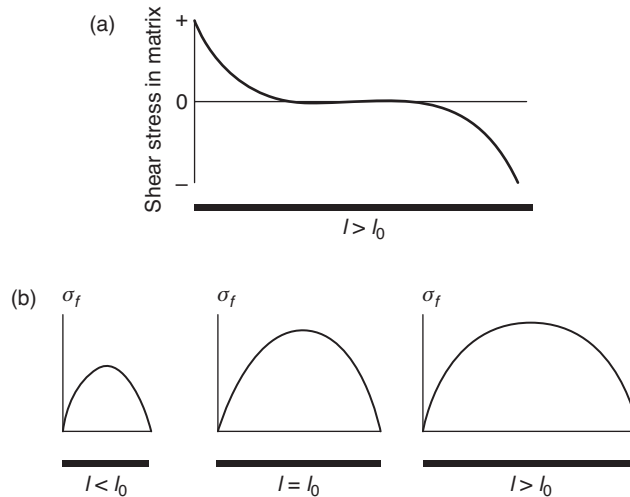
Figure 9.3   *Interfacial shear stress (a) and fibre tensile stress (b) as a function of fibre length (schematic).*
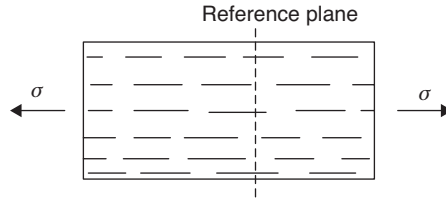
Figure 9.4 *Schematic section through a discontinuous fibre composite (fibre fraction shown very low for clarity).*

where a is the aspect ratio $\ell/2r$ and x is a dimensionless factor

$$x = \left[\frac{2G^m}{E^f \ln(R/r)} \right],\tag{9.15}$$

where G^m is the shear modulus of the matrix and R is half the separation between the nearest fibres. The basis of this expression is the assumption that the deformation of the complete composite can be modelled by considering a fibre to be embedded in a cylinder of matrix of radius R.

The factor x (Equation 9.15) depends on two key ratios: G^m/E^f, which is typically 0.01–0.02, and R/r, which is not much greater than unity. Figure 9.5 indicates that the length correction factor becomes significant for values of ax less than 10. In practice, the corresponding aspect ratio for effective reinforcement is usually greater than 100.

It has been pointed out by Tucker and Liang [11] that to give a result consistent with the self-consistent models, Equation (9.13) should be modified to

$$E^c = \eta_1 E^f V_f + (1 - \eta_1 V_f) E^m.$$

For a further discussion, the reader is referred to the texts by Kelly [13] and Hull and Clyne [14].
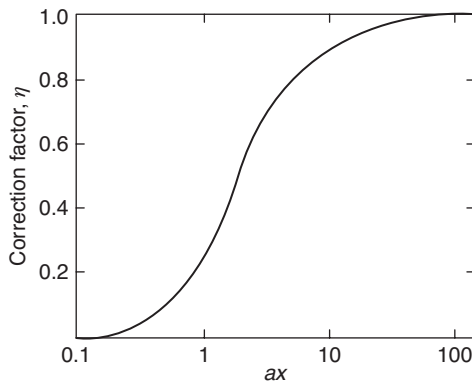
Figure 9.5 *Correction factor for the tensile modulus of short fibres as a function of aspect ratio.*
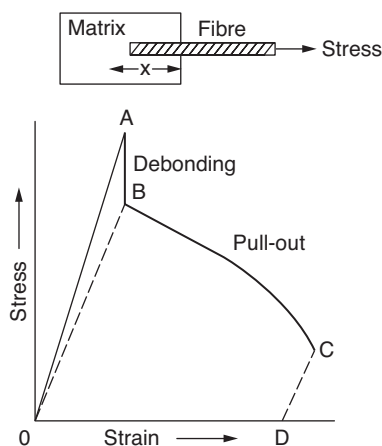
Figure 9.6 *Pull-out test and the resulting stress–strain curve showing the difference in magnitude of the energies of debonding (area OAB) and pull-out (area OBCD). (Reproduced from Anderson J.C. et al. (1990) Materials Science, 4th edn, Chapman and Hall, London. Copyright (1990) Taylor and Francis.)*

9.3.2   Debonding and Pull-Out

A composite frequently fails as a result of debonding between fibre and matrix. New interfaces are created, which involve the expenditure of energy, as is discussed in Chapter 13. The basic process can be modelled by considering a single fibre embedded in a block of matrix to a depth x, and it can be shown that the debonding energy is a maximum when x is equal to half the critical length. If the embedded length is less than $\ell_0/2$, the fibre will be pulled out of the matrix rather than fracturing, so involving the expenditure of further energy.

A stress–strain plot can be derived from a tensile load–extension experiment, as depicted schematically in Figure 9.6. The energy of debonding is obtained from the area OAB, and the usually larger pull-out energy is associated with the area OBCD. A strong fibre, which has not fractured after some debonding has occurred, will bridge the newly formed surfaces in the wake of a propagating crack, and thereby hinder crack opening. This toughening process has a microscopic analogy in the role of extended-chain bridging filaments in semi-crystalline polymers.

9.3.3   Partially Oriented Fibre Composites

The theoretical estimation of the elastic constants of a partially oriented short fibre reinforced composite is most simply undertaken by considering that it consists of an aggregate of units of structure, each of which consists of a perfectly aligned short fibre composite. This approach is analogous to the aggregate model for oriented polymers described in Section 8.6.1. It was first proposed by Brody and Ward [15] and subsequently by Advani and Tucker [16], all these workers setting out the tensor equations for the elastic constants, as described in Section 8.6.3.

Recent studies by Ward, Hine, Lusti and Gusev confirmed that this approach is viable, so that it is appropriate to summarise their conclusions.

The first step in these calculations is to obtain an estimate of the elastic constants of a fully aligned short fibre composite. Alternative approaches to these have been reviewed by Hine, Lusti and Gusev [5]. Following Tucker and Liang [11], they concluded that it was very satisfactory to use the method of Tandon and Weng [10] to obtain analytical expressions for all the elastic constants of the unit of structure. An alternative approach is to use the Cox shear lag theory (Section 9.3.1) to determine E_c^1 and a continuous fibre model to determine the other four elastic constants, of which the Wilczynski model [1] is considered to be the best. Again the Halpin–Tsai equations give a set of elastic constants to a good approximation, provided that the axial Young's modulus E_3^c is modified to

$$\frac{E_3^c}{E_m} = \frac{1 + \xi \eta V_f}{1 - \eta V_f},$$

(9.16)

where

$$\eta = \frac{E_f/E_m - 1}{E_f/E_m + \xi}$$

and

$$\xi = \ell/r = 2a.$$

Values for E_3^c obtained in this way are very similar to these calculated on the basis of shear lag theory. A limitation, as pointed out by Hine, Lusti and Gusev [5], relates to the estimates of E_{11}^c and V_{12}^c using the Halpin–Tsai equation.

It is found that the equation

$$\frac{E_{11}^c}{E_m} = \frac{1 + \xi \eta V_f}{1 - \eta V_f},$$

with $\xi = 2$ gives a good prediction for E_{11}^c but overestimates V_{12}^c, whereas with $\xi = 1$, there is a better prediction of V_{12}^c but an underestimate of E_{11}^c.

In their 1971 paper, Brody and Ward fitted published experimental data for short fibre composites incorporating glass or carbon fibres using Equations ((9.7a)–(9.7e)) to obtain the elastic constants of the unit of structure and orientation averages based on effective draw ratios and the pseudo-affine deformation scheme. In their systems rather low-fibre volume fractions were considered, and in many cases the experimental moduli appeared to lie closer to the Reuss than the Voigt bound. It was concluded that for efficient utilisation of high modulus fibres, they should be highly aligned and the polymer modulus should not be low.

With the advent of direct finite element calculations and the development of optical image analysing techniques for measuring fibre orientation, it has been possible to address the theoretical estimation of the elastic constants of a short fibre composite with much greater insight and accuracy.

Recent research has included studies of short glass fibre reinforced polypropylene samples made either by conventional injection moulding or shear controlled injection moulding (SCORIM) [17, 18], using image analysis to determine fibre orientation. The aggregate model was combined with Wilczynski [1], Tandon and Weng [10] or a finite element

numerical method of Gusev [19] to show that accurate predictions can be obtained for the elastic constants based on the Voigt upper bound. Similar results were obtained for a unidirectional glass fibre/epoxy composite [20]. In a more ambitious study, the elastic anisotropy and thermal expansion behaviour of short fibre composites were studied, where both the fibres (carbon fibres) and the polymer matrix (liquid crystalline polymer) possessed anisotropic material properties [21]. The model adopted for the unit properties was Tandon and Weng as modified by Qui and Weng [22] for discontinuous fibre reinforcement. In all cases, the experimental results were closest to the Voigt constant strain prediction. It is interesting to note that in these systems the best measure of fibre length was the number average fibre length [5].

9.4   Nanocomposites

Polymer nanocomposites consist of a polymer matrix with embedded filler particles with at least one dimension at the nanometre level, (i.e. 1–100 nm), much smaller than for the conventional polymer composites described above. The inclusion of nanoparticles can effect significant improvements in mechanical properties such as modulus, yield stress and fracture toughness for filler levels as low as a few per cent by weight. This is much lower than in conventional polymer composites, as illustrated in Figure 9.7, where the effect of talc reinforcement and clay nanoparticle reinforcement in a polypropylene matrix are compared. Talc filler is regarded as a conventional reinforcement, with particle diameters in the range 1–10 μm and thickness around 20 times less, whereas the clay particles are of length around 100 nm and thickness as low as 1 nm. Clay occurs in the form of platelets and has been
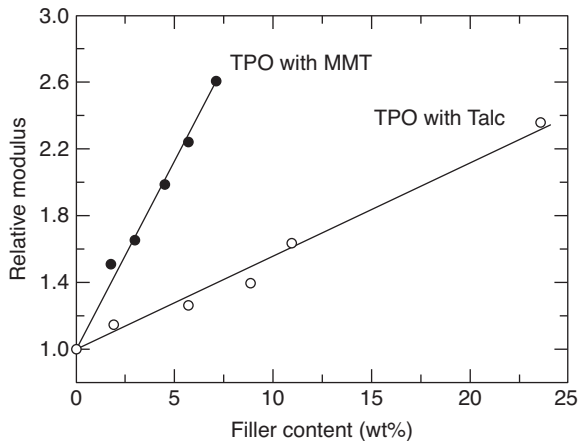
Figure 9.7   *Comparison of talc reinforcement with nanoclay (montmorillonite) reinforcement, in terms of the ratio of composite modulus to matrix modulus. The matrix material is a blend of polypropylene and thermoplastic elastomer (TPO). (Reproduced from Lee H-s. et al. (2005) TPO based nanocomposites. Part 1. Morphology and mechanical properties Polymer,* **46***, 11673–11689. Copyright (2005) Elsevier Ltd.)*

widely adopted as a nanofiller. Initial success was achieved using it in a Nylon 6 system [23], and further advances have been reported using other polymer matrices, examples being polyolefins [24], epoxy [25] and polyesters [26]. There is a range of nanoinclusions currently used in polymers, one of the most important recent developments being carbon nanotubes (CNTs), which hold promise of greater enhancements than do clays. Hussain, Jojjati and Okamoto [27] have reviewed the science and technology of a number of current polymer nanocomposite systems.

The dramatic difference in levels of reinforcement that are observed between conventional composites and nanocomposites, as illustrated in Figure 9.7, makes it clear that the elementary composite theories of Equations (9.3) and (9.6) cannot function for both types of composite. Since according to these models the composite modulus depends only on the moduli of the constituent parts and the filler loading, the predictions for the gradients of the two systems of Figure 9.7 would be essentially the same, given the similarity of the modulus values for the filler particles. A more sophisticated approach is needed that reflects important details of the nature of the reinforcement. One such detail that can be very different for conventional and nanoreinforced systems is the particle aspect ratio, which we have already seen to be a feature of both the Cox model described above and of the Halpin–Tsai Equation (9.16) for partially oriented fibre composites, and is also present in the Mori–Tanaka theory of Equations (9.10). In the example of Figure 9.7, for instance the nanoclay particles have aspect ratios in excess of 100, whereas for the talc particles the ratio is ∼20. On this basis, there appears to be the potential for composite theories to describe the level of property enhancements seen in nanocomposites, via the effect in the equations of the very high aspect ratios of the filler particles.

Alternatively, some workers have concluded that the observed improvements cannot be explained by composite theory, and that some additional phenomenon is required; this phenomenon has been termed the 'nano effect' [28]. The most frequently cited candidate for its physical origin is the confinement that nanoparticles impose on adjacent molecular chains. This would have the effect of lowering the glass transition temperature of the polymer matrix local to the particles, thus creating a zone of stiffer material – an 'interphase' – around the particle, of size greater than that of the particle's smaller dimension. Thermally measurable effects of molecular immobilisation created by particles have been observed, for example by Rittigstein and Torkelson on polystyrene/silica nanocomposite [29] and Sargsyan, Tonoyan and Davtyan [30] for the PMMA/silica system. Fertig and Garnich [31] presumed the existence of a stiff interphase, and included it within idealised finite element models of structure to produce realistic predictions of macroscopic elastic modulus.

The first approach – the use of detailed but conventional micromechanical modelling – has, however, also proved successful. Sheng, Boyce and Parks [32] have used the Halpin–Tsai equations, the Mori–Tanaka model and finite element modelling to simulate polymer/clay systems with both amorphous and semi-crystalline matrices. By taking account of the detailed geometry of the reinforcement, and in the semi-crystalline case anisotropic crystal layers around the clay particles, they were able to produce realistic predictions of the composite stiffness without recourse to arguments involving molecular confinement. Fornes and Paul [33], working on the Nylon 6/clay system, showed that the increased effectiveness of reinforcement could be explained using composite theory, provided the modelling took account of sufficient detail. They concluded that a necessary feature of

effective modelling of clay nanocomposites is the inclusion of three-dimensional effects, so that the ability of a platelet to reinforce in two dimensions – i.e. along two perpendicular axes in the plane of the platelet, as opposed to the single long axis apparent in a plane stress analysis – can be represented. A similar conclusion as to the ineffectiveness of two-dimensional modelling has been reached by Hbaieb, Wang and Chia [34].

While the physical origins of the effect remain to some extent open to question, technological progress in obtaining more effective nanocomposites continues to be made. In polymer/clay systems, much emphasis has been on methods of exposing the maximum surface area of the clay platelets, which occur in stacks several platelets thick as illustrated in Figure 9.8(a). Ideally the stack structure should be completely disrupted, resulting in what is known as a fully exfoliated system as shown in Figure 9.8(c). An intermediate arrangement is one in which the stack structure is essentially preserved, but the material between the platelets is that of the polymer matrix – an intercalated system, shown in Figure 9.8(b). In practice, it is generally recognised that complete exfoliation is difficult to achieve, but that intercalated systems give worthwhile results. The effect of the stack size on the composite stiffness has been analysed by finite element modelling of stochastically generated structures [35]. A quantitative understanding of this effect is an aid to processors in deciding whether the extra efforts involved in achieving higher levels of exfoliation are worthwhile.

Another crucial issue is the degree of bonding between the matrix and filler. The pioneering work with the Nylon 6/montmorillonite clay system took advantage of the favourable chemistry that prevails between polar polymers and hydrophilic clays. With non-polar polymers such as polyolefins, agents known as compatibilisers, such as polar functional oligomers [36], need to be added to the system to produce satisfactory bonding [37], and development may be required to determine the optimum levels. For example, an enhancement of 35% in elastic modulus at a 5 wt% clay loading can be achieved in a compatibilised polypropylene/clay system [38].
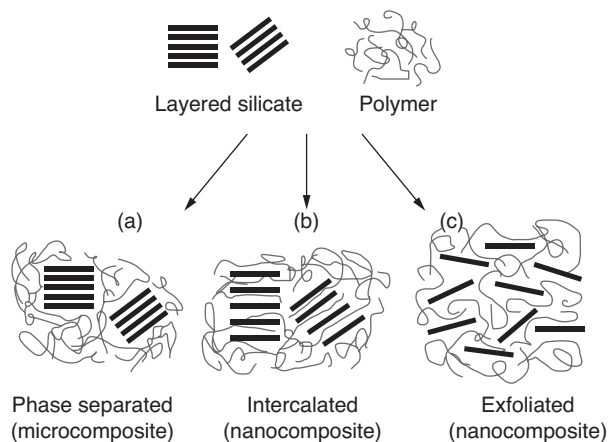
Figure 9.8 *Nanoclay filler structures. (Reproduced from Hussain, F., Jojjati, M., Okamoto, M. et al. (2006) Review article: polymer-matrix nanocomposites, processing, manufacturing, and application: an overview. J. Compos. Mater.,* **40***, 1511–1575. Copyright (2006) Sahe Publications.)*

Other mechanical properties such as strength and fracture toughness are also affected by the addition of nanofiller, though the picture is generally more complex than with stiffness. Increased stiffness may be accompanied by an increase in yield stress, which as a result of smaller plastic zones is associated with brittleness and lower toughness. Another possibility is that the progress of cracks can be influenced by the microstructure beneficially if it forces an increase in crack surface area. These factors may be the reason why both negative and positive effects have been observed in different contexts. Thus, in the polyamide/clay system, clay loading has been shown to produce an entirely negative effect on fracture toughness and fracture energy [39, 40], while other workers have shown increases in toughness up to small clay loadings in epoxy/clay systems [41, 42].

Carbon nanotubes (CNTs) have very high aspect ratios, typically with diameters in the range 1–30 nm and lengths of several μm. While nanoclays possess an elastic modulus of around 180 GPa, the modulus of carbon CNTs can be in excess of 1 TPa. On this basis, we would expect, for the same filler loading, much higher composite stiffnesses using CNTs than with nanoclay, and this has been achieved for a number of systems. As with clays, Nylon 6 proved to be an effective matrix material without the need for surface modification of the filler, with Zhang, Shen and Phang [43], using simple melt-compounding, reporting a doubling of both stiffness and strength at a 1 wt% filler loading.

To make effective composites using polyolefins, problems must be solved that are similar to those associated with nanoclays. CNTs tend to agglomerate, leading to problems in dispersion, which have been addressed in the review by Szleifer and Yerushalmi-Rozen [44]. As with clays, poor bonding and unexceptional mechanical properties are obtained with non-polar polymers such as polyethylene [45] when there is no surface treatment. However, Gong *et al*. [46] showed the benefit of the use of surfactants in this regard. Following work by Khabashesku, Billups and Margreave [47], Shofner, Khabashesku and Barrera [48] and McIntosh, Khabashesku and Barrera [49] established the effectiveness of the chemical modification of the CNT sidewalls by fluorination for both polyethylene and polypropylene nanocomposites. In the latter case, the benefit of surface functionalisation was demonstrated directly by comparing the mechanical properties of both functionalised and pristine CNT. There is no discernible increase in modulus for the pristine filler, but for functionalised sidewalls there is a doubling of modulus at a 5 wt% filler loading. Strength is also increased significantly. There is no sign of the effect observed with nanoclays, where the modulus increase can result in the penalty of poor fracture properties.

9.5 Takayanagi Models for Semi-Crystalline Polymers

It was realised by Takayanagi [50] that oriented highly crystalline polymers with a clear lamellar texture might be modelled in terms of a two-component composite in which the alternating layers corresponded to the crystalline and amorphous phases [51]. The model was later extended to include a parallel component in addition to that in series, and was applied first to describe the relaxation behaviour of amorphous polymers with two distinct phases, and later to crystalline polymers in which the parallel component represented either interlamellar crystalline bridges or amorphous tie molecules threading through the amorphous phase.
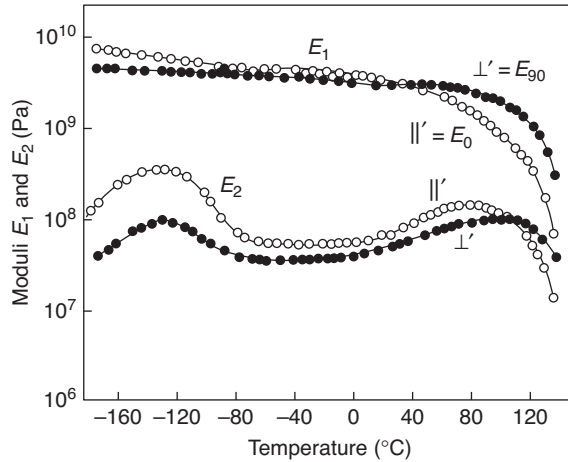
Figure 9.9   *Temperature dependence of E_1 and E_2, the components of the dynamic modulus, in directions parallel ($\parallel$) and perpendicular ($\perp'$) to the initial draw direction for annealed samples of high-density polyethylene. (Reproduced from Takayanagi, M., Imada, I. and Kajiyama, T. (1966) Mechanical properties and fine structure of drawn polymers. J. Polym. Sci. Pol. Sym., **15**, 263. Copyright (1966) John Wiley & Sons, Ltd.)*

9.5.1   The Simple Takayanagi Model

High-density polyethylene that has been drawn uniaxially (i.e. with fibre symmetry) and then annealed has a distinct lamellar texture, and we will show that the orientation of the lamellae, as distinct from the molecular orientation, plays the dominant role in determining the mechanical anisotropy. The temperature variation in the in-phase (E_1) and out-of-phase (E_2) components of the dynamic modulus, both parallel with ($\parallel$) and perpendicular to ($\perp$) the draw direction, is shown in Figure 9.9, with the parallel modulus ($E_0 = \parallel$) crossing the perpendicular modulus ($E_{90} = \perp$) at high temperatures; at low temperatures $E_0 > E_{90}$, but at high temperatures $E_{90} > E_0$. The principal features can be explained in terms of a simple model of amorphous (A) and crystalline (C) components, which are in series in the draw direction but in parallel in the transverse direction (Figure 9.10). In the orientation direction, each component is subject to the same stress, so that compliances are added as in the Reuss averaging scheme. The stiffness above the relaxation transition is primarily determined by the compliant amorphous regions (Equation 9.6), so giving a large fall in modulus as the temperature is increased. In the perpendicular direction, the parallel components are each subject to the same strain, and stiffnesses are added as in the Voigt scheme. The crystalline regions support the applied stress at temperatures above the relaxation transition, and so a comparatively high stiffness is maintained. Takayanagi and colleagues considered that appropriate values of the modulus might be $E^c(\parallel) = 100$ GPa, $E^c(\perp) = 1$ GPa, E_A (low T) = 1 GPa, E_A (high T) = 0.01 GPa.

9.5.2   Takayanagi Models for Dispersed Phases

Takayanagi [50] devised series-parallel and parallel-series models as an aid to understanding the viscoelastic behaviour of a blend of two isotropic amorphous polymers in terms of the
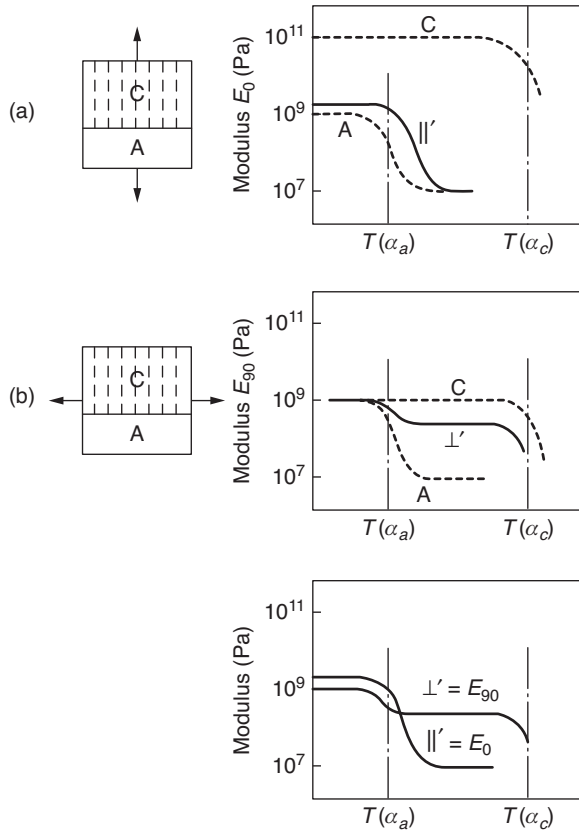
Figure 9.10 *Schematic representations of change in modulus E with temperature on the Takayanagi model for (a) the ∥′ and (b) the ⊥′ situations corresponding to E_0 and E_{90} respectively. Calculations assume amorphous relaxation at temperature $T(\alpha_a)$ and crystalline relaxation at temperature $T(\alpha_c)$ and (c) shows combined results. C, crystalline phase; A, amorphous phase. (Reproduced from Takayanagi, M., Imada, I. and Kajiyama, T. (1966) Mechanical properties and fine structure of drawn polymers. J. Polym. Sci. Pol. Sym., **15**, 263. Copyright (1966) John Wiley & Sons, Ltd.)*

properties of the individual components. For an A phase dispersed in a B phase, there are two extreme possibilities for the stress transfer. For efficient stress transfer perpendicular to the direction of tensile stress, we have the series-parallel model (Figure 9.11(a)) in which the overall modulus is given by the contribution for the two lower components in parallel (as in Equation (9.3)) in series with the contribution for the upper component (as in Equation (9.5)):

$$\frac{1}{E^*} = \frac{\phi}{\lambda E_A^* + (1 - \lambda)E_B^*} + \frac{1 - \phi}{E_B^*}, \tag{9.17}$$

where E^*, etc., represent the complex moduli associated with dynamic experiments. If the stress transfer across planes containing the tensile stress is weak, a parallel-series model
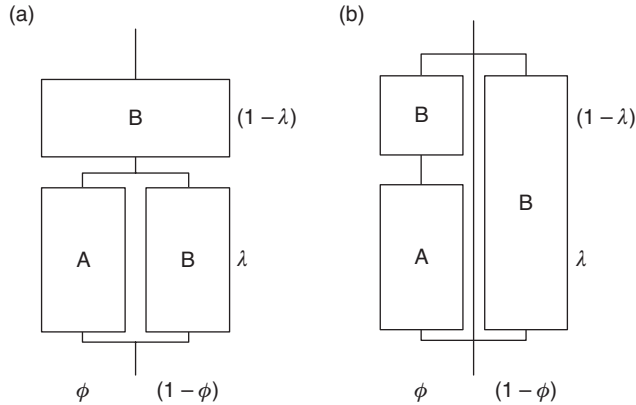
Figure 9.11 *Takayanagi models for polymer blends: (a) the series-parallel model and (b) the parallel-series model.*

(Figure 9.11(b)) is appropriate, for which the two left-hand components combine in series (as in Equation (9.5)) before combining in parallel with the right-hand component (Equation (9.3)), giving a modulus

$$E^* = \lambda \left(\frac{\phi}{E_A^*} + \frac{1 - \phi}{E_B^*} \right)^{-1} + (1 - \lambda)E_B^*. \tag{9.18}$$

Note that λ and ϕ correspond to volume fractions as indicated in Figure 9.11.

The predictions of both models were then compared with measurements of the temperature variation in storage and loss moduli for a film made from a blend of polyvinyl chloride and nitrile butadiene rubber (Figure 9.12). It is seen that the series-parallel model (a) gives the better fit. The performance of polymer blends was well represented by a series-parallel model in which the relative values of λ and ϕ were related to the shape of the dispersed phase: $\lambda = \phi$ for homogeneous dispersions, and $\lambda > \phi$ for dispersions in the form of elongated aggregates. For semi-crystalline polymers in general, however, with A and B representing the crystalline and amorphous components, experimental dispersions were usually broader than the predictions, suggesting that at least some of the unordered material was not identical to that in a completely amorphous state.

Gray and McCrum [52] have criticised the Takayanagi model as applied to partially crystalline polymers, and refute the assertion that if mechanical relaxation occurs in the amorphous phase the peak value of the out-of-phase modulus is proportional to the volume fraction of the amorphous phase. They assert that as the model represents a Voigt average solution, it can give only upper bounds to moduli. Stress and strain fields must differ between the crystalline and amorphous components, so a Reuss-type average is equally inadmissible, and a correct solution must lie between the two limits. An empirical logarithmic mixing hypothesis is advanced as an acceptable law of mixing

$$\log G^* = V_A \log G_A^* + V_C \log G_C^*, \tag{9.19}$$
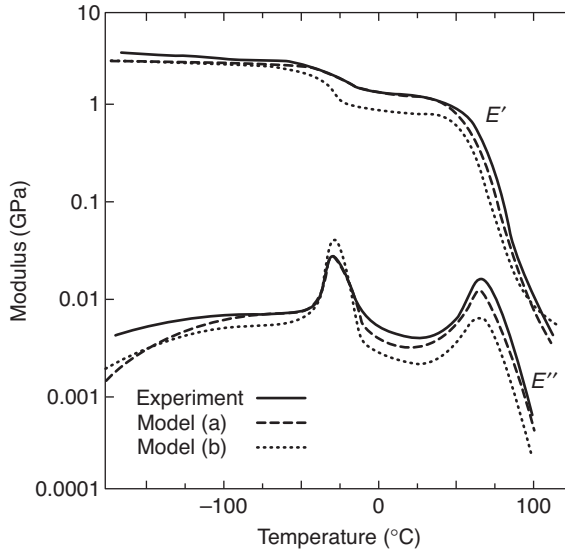
Figure 9.12 *Temperature dependence of storage and loss moduli for a polyvinyl chloride–nitrile bidadiere rubber film bonded in parallel to a polyvinyl chloride film. Takayanagi model type (a) gives better fit to experiment. (Reproduced from Takayanagi, M. (1963) Viscoelastic properties of crystalline polymers. Memoirs of the Faculty of Engineering Kyushu Univ., 23, 41. Copyright (1963) Kyushu University.)*

where G^* represents the complex shear modulus and V represents a volume fraction. The logarithmic decrement of the polymer (Λ) is then given as a weighted combination of the logarithmic decrement of the two phases:

$$\Lambda = V_A \Lambda_A + V_C \Lambda_C, \tag{9.20}$$

which is a mathematical statement of the assumptions of some earlier workers.

9.5.3   Modelling Polymers with a Single-Crystal Texture

The Takayanagi models were remarkably successful in providing a simple interpretation of the dynamic mechanical behaviour of crystalline polymers and polymer blends. The theoretical basis is contained in Equations (9.1) to (9.6) of Section 9.2, and is deficient in two respects. First, only tensile deformations are considered and shear deformations are ignored. Secondly, as emphasised in Chapter 8, Voigt and Reuss schemes (i.e. parallel and series) only provide bounds to the true behaviour.

These deficiencies became very apparent when Ward and co-workers [53] studied the mechanical behaviour of well-defined lamellar textures. Rolling and annealing processes established by Hay and Keller [54] enable sheets of low-density polyethylene to be produced with well-defined crystallographic and lamellar orientations (Figure 9.13), and it was possible to study the behaviour of three types of special structure sheet illustrated in Figure 9.14: 'bc sheet', in which the *c* axes of the crystallites lie along the initial draw direction, the *b* axes lie in the plane of the sheet and the *a* axes are normal to the plane of
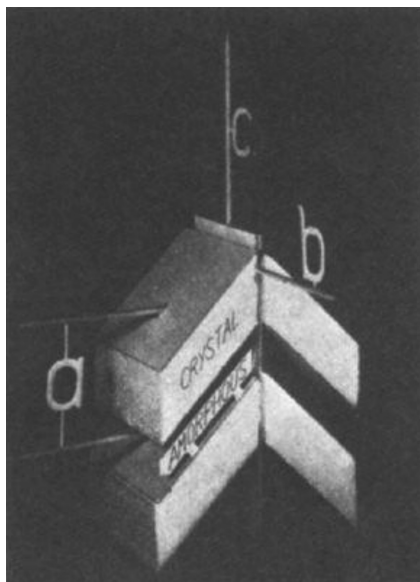
Figure 9.13   *Model of morphology of oriented and annealed sheets of low-density polyethylene. This photograph shows the structure of the bc sheet; a, b and c axes indicate the crystallographic directions in the crystalline regions. (Reproduced from Stachurski, Z.H. and Ward, I.M. (1968) Anisotropy of viscoelastic transitions in oriented polyethylenes. J. Polym. Sci. A2, **6**, 1817. Copyright (1968) John Wiley & Sons, Ltd.)*

the sheet; 'ab sheet', in which the *a* axes lie along the draw direction, the *b* axes again lie in the plane of the sheet and the *c* axes are normal to the sheet; and 'parallel lamellae sheet', where the lamellar plane normals lie along the initial draw direction and the *c* axes make an angle of about 45° with this direction. For specimens of bc and ab sheet a four-point small-angle X-ray diffraction pattern is shown, which is interpreted as indicating the presence of lamellae inclined at about 45° to the direction of the *c* axes. This type of morphology is represented schematically for the bc sheet by the model shown in Figure 9.13, in which the solid blocks represent crystalline lamellae, and the intermediate spaces are occupied by disordered material and interlamellar tie molecules, which are relaxed as a result of the annealing treatment. In contrast, the parallel lamellae sheet has a twinned structure with regard to the crystallographic orientation but a single-texture structure (only a two-point, low-angle diffraction pattern) as far as lamellar orientation is concerned.

In contrast with the Takayanagi model, which considers only extensional strains, a major deformation process involves shear in the amorphous regions. Rigid lamellae move relative to each other by a shear process in a deformable matrix. The process is activated by the resolved shear stress $\sigma \sin \gamma \cos \gamma$ on the lamellar surfaces, where γ is the angle between the applied tensile stress σ and the lamellar plane normals, which reaches a maximum value for $\gamma = 45°$ (see Chapter 12 for discussion of resolved shear stress in plastic deformation processes).

Gupta and Ward found crossover points in the extensional moduli for bc and ac sheets similar to those found by Takayanagi in high-density polyethylene, but at lower temperatures
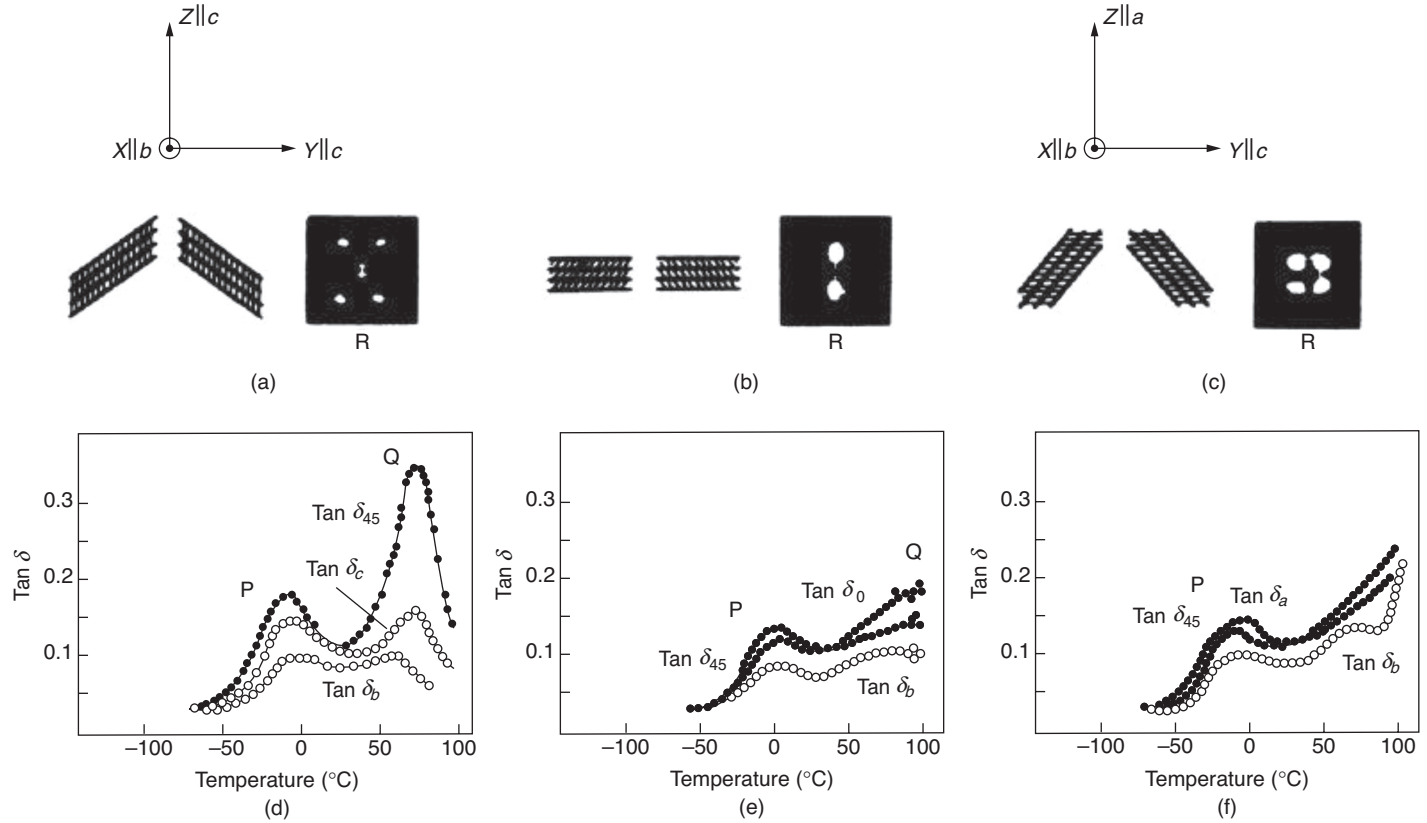
Figure 9.14 Schematic structure diagrams of mechanical loss spectra and 10 s isochronal creep moduli: (a), (d) and (g) for bc sheet; (b), (e) and (h) for parallel lamellae sheet; (c), (f) and (i) for ab sheet. P, interlamellar shear process; Q, c-shear process (note absence of c-shear process in (f)); R, small-angle X-ray diagram, beam along X.
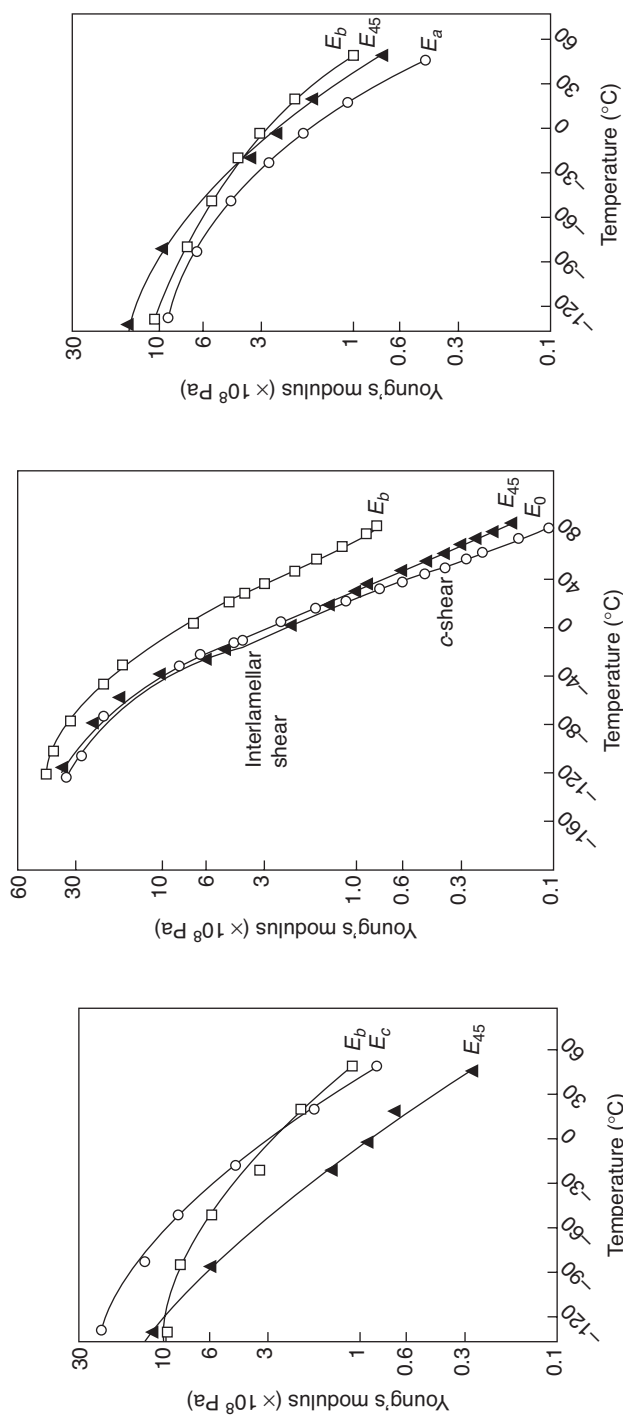
Figure 9.14 (Continued)

corresponding to the β relaxation (see Chapter 10 for a discussion of relaxation processes). The fall in modulus in the c-direction in bc sheet and the a-direction in ab sheet can be attributed to an interlamellar shear process. As the lamellar planes are approximately parallel to the b-axis, a tensile stress in this direction will not favour interlamellar shear, so that at temperatures above the relaxation transition $E_b > E_a \sim E_c$ (Figure 9.14). Dynamic mechanical loss spectra show significant anisotropy, both for the lower temperature β relaxation, which corresponds to the crossover in tensile moduli previously discussed, and for the higher temperature α relaxation, where the results are consistent with the proposal that the α process involves shear in the c-axis direction on planes containing the c-axis of the crystallites (the c-shear process). In the bc sheet, $\tan\delta_{45}$ is larger than $\tan\delta_0$ and $\tan\delta_{90}$ (angles being measured from the original draw direction) because it represents the situation in which there is maximum resolved shear stress parallel to the c-axis directions. Similarly, for the parallel lamellae sheets, the greatest losses for the α process occur when the stress is applied parallel to the initial draw direction. Finally, in ab sheet the α relaxation is very small, as there are no planes containing the c-axis that will shear in the c direction when a tensile stress is applied in the plane of the sheet.

Other applications of the Takayanagi model to oriented polymers have included linear polyethylene that was cross-linked and then crystallised by slow cooling from the melt under a high tensile strain [55], and sheets of nylon with orthorhombic elastic symmetry [56]. A fuller discussion is given in the previous edition of this text by Ward [57].

The studies of the viscoelastic behaviour of the specially oriented sheets are valuable in emphasising the composite nature of these materials and defining where the lamellar texture determines the mechanical anisotropy, thus carrying our understanding one stage further than the simple series/parallel Takayanagi models. It is, however, also possible to use the composite laminate model to gain a more quantitative understanding of the mechanical anisotropy, and carry the discussion further than the evaluation of Reuss and Voigt bounds for the Young's moduli.

In recent research, Al-Hussein, Davies and Ward [58] prepared an oriented low-density polyethylene with a parallel lamellar stack morphology where the c axes of the crystalline lamellae were parallel to the lamellar plane normals. For this structure, explicit equations can be obtained for the elastic constants in terms of the crystalline volume fraction and the elastic constants of the crystalline lamellae (c_{11}^c, c_{33}^c, c_{44}^c, etc.) and the amorphous layer (c_{11}^a, c_{33}^a, c_{44}^a, etc.).

For example, on the assumption that the lateral dimensions are very large, the elastic constants of the composite (c_{11}^u, c_{33}^u, c_{44}^u, etc.) are given by

$$c_{11}^u = Xc_{11}^c + (1-X)c_{11}^a - \frac{\left(c_{13}^c - c_{12}^a\right)^2}{\left[c_{33}^c/X + c_{33}^a/(1-X)\right]} \tag{9.21a}$$

$$\frac{1}{c_{33}^u} = \frac{X}{c_{33}^c} + \frac{1-X}{c_{33}^a} \tag{9.21b}$$

$$\frac{1}{c_{44}^u} = \frac{X}{c_{44}^c} + \frac{1-X}{c_{44}^a}, \tag{9.21c}$$

where X is the crystalline volume fraction.

The composite model leading to the rather simple Equations (9.21) assumes that there is uniform strain in the lateral direction. The amorphous phase is soft and therefore extends

more than the crystalline phase in response to an axial stress. The lateral contraction necessary to maintain constant volume for the rubbery elastic phase would therefore be considerably greater than that of the stiffer crystalline phase. But it is assumed that the amorphous layers and the crystalline lamellar layers are tightly bonded together. This means that the lateral contraction of the crystalline phase will be much greater in the composite than that predicted theoretically for an isolated crystal. Al-Hussein, Davies and Ward [58] used wide-angle X-ray diffraction to measure the crystalline compliances s_{13}^c and s_{23}^c for their parallel lamellar structure and showed that the values were indeed much greater than those for the theoretical perfect crystal.

9.6   Ultra-High-Modulus Polyethylene

Conventional drawing processes, which usually involve the polymer being uniaxially extended between two sets of rollers rotating at different speeds, rarely permit a draw ratio greater than 10× (see Chapter 12). Such materials show an extensional modulus that is only a comparatively small fraction (∼10%) of the chain modulus, due to the dominant effect of the relatively compliant unordered component. In the case of polyethylene, however, it is possible to produce an oriented polymer whose Young's modulus at low temperatures approaches the theoretical value of the crystal chain modulus of about 300 GPa (by comparison, the Young's modulus of ordinary steel is about 210 GPa). Several production methods have been used, including solution spinning techniques [59] and a two-stage draw process [60], in which an initial stage of drawing (draw ratio 8.3) is followed by a continuing stage of extension so that the already drawn material thins down to achieve a final draw ratio of 30× or more. These production processes are somewhat slower to operate than conventional methods, but nevertheless high-stiffness polyethylene is produced commercially for specific end uses. Young's modulus as a function of draw ratio is shown in Figure 9.15 for a range of initially isotropic polyethylenes drawn at 75°C. It is seen that the modulus, which even at room temperature can reach an appreciable fraction of the crystal modulus, depends only on the final draw ratio and is independent of the relative molecular mass and the initial morphology, so that an appropriate model appears to be one that depends on the structure produced during deformation rather than on the starting material.

We shall outline two different models used to interpret the elastic behaviour of highly oriented linear polyethylene. Both models take macroscopic composite theory as their starting point but diverge in the way in which they account for the evidence from morphological studies for crystalline regions that can extend for more than 100 nm in the draw direction.

9.6.1   The Crystalline Fibril Model

This model, proposed by a group working at Bristol University [61], is a development of a larger scale model that was used to account for the high mechanical anisotropy of certain copolymers [62]. Electron microscopy demonstrated that, when a three-block polystyrene–polybutadiene–polystyrene copolymer was extruded into a mould, long and completely aligned filaments of glassy polystyrene with a diameter about 15 nm were arranged with hexagonal symmetry in a rubber matrix. Despite the macroscopic anisotropy, for which the ratio of the longitudinal to the transverse Young's modulus was almost 100:1, both phases were comprised of randomly oriented molecular chains.
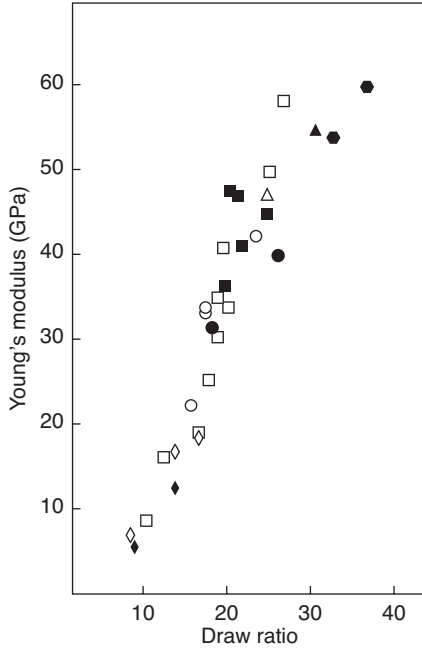
Figure 9.15   *A 10 s isochronal creep modulus, measured at room temperature, as a function of draw ratio for a range of quenched (open symbols) and slowly cooled (closed symbols) samples of linear polyethylene drawn at 75°C. (●), Rigidex 140–60; (△, ▲), Rigidex 25; (□, ■), Rigidex 50; (○, ●), P40; (◇,◆), H020–54P. (Reproduced from Capaccio, Crompton and Ward (1976) Drawing Behavior of Linear Polyethylene .1. Rate of Drawing As a Function of Polymer Molecular-weight and Initial Thermal-treatment J. Polym. Sci., Polym. Phys. Ed., **14**, 1641. Copyright (1976).)*

   The model for highly oriented polyethylene similarly assumed that fibrils of high aspect ratio were arranged with hexagonal symmetry in a compliant matrix, but the discontinuous nature of the fibrils was now the determining factor for the extensional modulus. Fibrils observed in thin sections of the oriented polymer after staining with chlorosulfonic acid and uranyl acetate were considered to represent a needle-like crystal phase with the theoretical stiffness of the polyethylene chain ($E^c \sim 300$ GPa). These crystals, whose concentration (V_f) was estimated to be 0.75, were embedded in a partially oriented matrix containing both amorphous and crystalline components, with a shear modulus $G^m \sim 1$ GPa (Figure 9.16).

   Using the Cox model for a fibre composite, already discussed [12], and neglecting the very small contribution $E^m V^m$ arising from the tensile modulus of the compliant matrix, the extensional modulus E of the highly oriented polymer becomes

$$E = V_f E^c \left(1 - \frac{\tan hax}{ax} \right), \tag{9.22}$$

where a is the fibre aspect ratio

$$\left(\frac{\ell_c}{2r_c} \right)$$
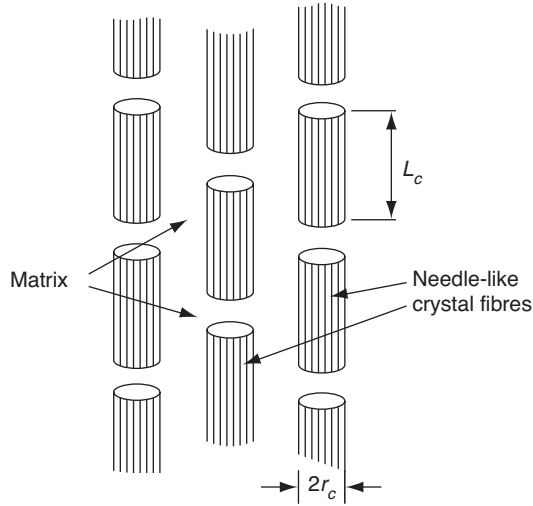
Figure 9.16 *Schematic diagram of the Barham and Arridge model for ultra-high-modulus polyethylene.*

and

$$x = 2 \left(\frac{G^m}{E^c \ln 2\pi / \sqrt{3V_f}} \right),$$

which is a restatement of Equation (9.15).

The increased stiffness that results from post-neck drawing is postulated to be a direct consequence of the increased aspect ratio of the crystalline fibrils (from slightly less than 2 to greater than 12 in extreme cases), which thus become more effective reinforcing elements. On the assumption that post-neck drawing is homogeneous on a structural level, so that the fibrils deform affinely, the initial aspect ratio $(\ell_0/2r_0)$ transforms to $\ell_c/2r_c = (\ell_0/2r_0) \, t^{3/2}$, where t is the draw ratio in the post-neck region. Barham and Arridge [61] show that the observed change in modulus with draw ratio implies that x in Equation (9.22) should depend on $t^{3/2}$. The good agreement (Figure 9.17) is advanced as a strong argument in favour of the model.

9.6.2   The Crystalline Bridge Model

An alternative approach, due to Gibson, Davies and Ward [63], is based on a Takayanagi model, which is then modified to include an efficiency ('shear-lag') factor that takes into account the discontinuous nature of the crystalline reinforcing component. The model was derived by comparing microstructural studies of conventionally drawn polyethylene and ultra-high-modulus material. At a draw ratio $\sim 10\times$, wide-angle X-ray diffraction indicates that the crystalline component is highly oriented and, together with a clear two-point small-angle X-ray diffraction pattern, suggests a regular stacking of crystal blocks whose length,
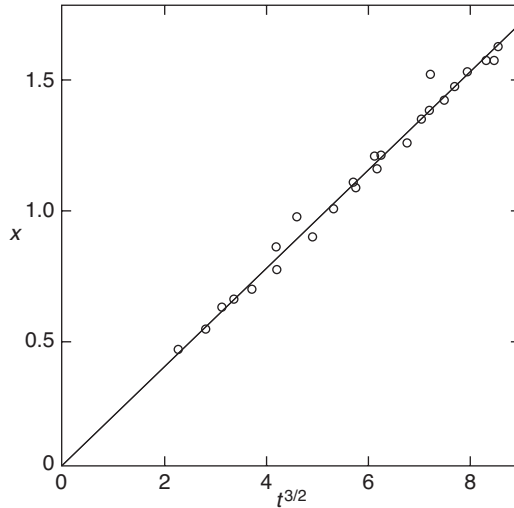
Figure 9.17   *Parameter x in Equation (9.22) as a function of the taper draw ratio t to the 3/2 power. (Reproduced from Barham, P.J. and Arridge, R.G.C. (1977) A fiber composite model of highly oriented polyethylene. J. Polym. Sci. Polym. Phys., 15, 1177. Copyright (1977).)*

to accommodate the non-crystalline regions, is less than the long period *L*, as shown in Figure 9.18. At increasing draw ratio, the small-angle pattern retains the same periodicity but diminishes in intensity, and a variety of techniques indicate an increase in the orientation of non-crystalline material. The average crystal length increases to about 50 nm, compared with the constant long period of about 20 nm. The concentration of crystals > 100 nm is low, in contrast with the implied lengths of 100–1000 nm for the crystalline fibrils in the model previously discussed (Section 9.6.1). Reasons for this discrepancy have not been examined in detail and the differences may be a consequence of the specific method used to produce the material, despite the inference from Figure 9.15 that the final drawing process dominates over differences in the initial morphology.

The large increase in stiffness is considered to be a consequence of the linking of adjacent crystal sequences by crystalline bridges (Figure 9.18). In this model, the crystalline bridges play a similar role to the taut tie molecules suggested earlier by Peterlin [64], and are equivalent to the continuous phase of a Takayanagi model. The increase in modulus with increasing draw ratio is considered here to arise primarily from an increase in the proportion of fibre phase material, and not from the changing aspect ratio of a constant proportion of the fibre phase.

In the absence of information regarding the arrangement of the crystalline bridges, it is assumed that they are randomly placed so that the probability of a crystalline sequence traversing the disordered regions to link adjacent crystalline blocks is given in terms of a single parameter *p*, defined as

$$p = \frac{\bar{L} - L}{\bar{L} + L},$$
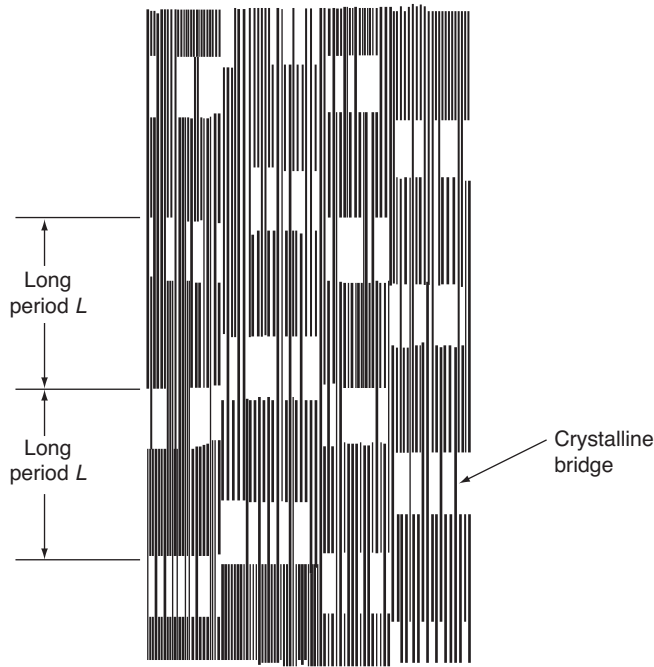
Figure 9.18   *Schematic representation of the structure of the crystalline phase in ultra-high-modulus polyethylene (constructed for p = 0.4). (Reproduced from Gibson, A.G., Davies, G.R. and Ward, I.M. (1978) Dynamic mechanical-behavior and longitudinal crystal thickness measurements on ultrahigh modulus linear polyethylene – quantitative model for elastic-modulus. Polymer, 19, 683. Copyright (1978) IPC Business Press Ltd.)*

where $\bar{L}$ is the average crystal length determined from wide-angle X-ray diffraction and L is the long period obtained from small-angle X-ray scattering. It can be shown that the volume fraction of continuous phase V_f is given by

$$V_f = Xp(2 - p),$$

where X is the crystallinity expressed as a fraction.

   As a first stage, the contribution of the crystalline bridges can be considered as one element of a Takayanagi model (in Figure 9.9(b) this is the continuous phase) that is in parallel with the series combination of the remaining lamellar material and the amorphous component. Young's modulus would then be

$$E = E^c Xp(2 - p) + E^a \frac{\{1 - X + X(1 - p)\}^2}{1 - X + X(1 - p)^2 E^a / E^c}. \tag{9.23}$$

The first term in this expression, which corresponds to the crystalline bridge sequences, is next treated as an array of short fibres, so introducing the shear lag (efficiency) factor

Φ, which is a function of the finite aspect ratio of the crystalline bridges. The analogous equation to Equation (9.22) is

$$E = E^c X p(2 - p)\Phi' + E^a \frac{\left\{1 - X + X(1 - p)^2\right\}^2}{1 - X + X(1 - p)^2 E^a / E^c}, \tag{9.24}$$

where Φ' is an average shear lag factor for all materials in the fibre phase. The advantage gained by converting from the one-dimensional Takayanagi model to the Cox short fibre model is that measurable tensile properties are able to yield information about the shear stress development in the matrix (see Section 9.3.1). In particular, it can be shown for the case of sinusoidally varying strain that the out-of-phase component of the tensile modulus $E^{c'}$ is related to the out-of-phase component of the shear modulus of the matrix $G^{m'}$ by an expression that involves the volume fraction of fibres (i.e. crystalline bridges) and the fibre aspect ratio, together with the ratio $G^{m'}/E^{f'}$, where $G^{m'}$ is the in-phase component of the shear modulus of the matrix. The geometric factors are constant for a given structure, but the modulus ratio varies with temperature because of the temperature dependence of $G^{m'}$.

The aspect ratio of the fibre component, which is a measure of the width of the crystalline bridges, is not directly accessible but can be deduced from the value of the shear lag factor Φ' required to give the best match between the predicted and observed patterns of mechanical behaviour as a function of temperature. This exercise yields a radius of 1.5 nm for the crystalline bridge sequences, which suggests that each bridge is comprised of several extended polymer chains. Detailed considerations of the way in which the modulus increases at temperatures below $-50°C$ suggest that the modulus of the matrix increases with increasing draw ratio due to an increase in E^a in Equation (9.24), which corresponds to an increase in the modulus of the non-crystalline material.

9.7 Conclusions

Models of increasing sophistication have been developed to predict the elastic properties of composite materials from the properties of their constituent parts. These range from the simple rule-of-mixtures approach to the Halpin–Tsai and Mori–Tanaka analyses, where the geometry – essentially, the aspect ratio – of the reinforcing particles can be taken into account. This has the potential to model the effects of extreme aspect ratios that are seen in nanocomposites. Direct finite element simulation of the microstructure is an option that is becoming increasingly feasible at both the micro and nano levels.

A major application of ultra-high-modulus polymers such as those discussed above is as an inert reinforcing fibre in composite materials [65]. A detailed analysis of the overall anisotropy will thus require appropriate theories on both microscopic and macroscopic scales. There are, however, important and highly significant differences between the two scales. In the macroscopic composite, the fibre and the matrix are distinct entities, bonded only by weak secondary forces, whereas the crystalline and amorphous phases of an oriented semi-crystalline homopolymer must blend gradually into one another: chain folds and chain ends are associated with crystallites, some of the less regular material is significantly oriented and bridging molecules (either crystalline bridges or tie molecules) that link crystallites traverse amorphous material in the process.

Even for block copolymers, in which the phase separation can be distinguished in electron micrographs, there are problems in matching parameters such as Poisson's ratios of the two components: nevertheless the simple Takayanagi models, particularly when extended by a treatment to account for the finite length of the reinforcing component, can describe numerous features of static and dynamic elastic behaviour.

References

1. Wilczynski, A.P. (1990) A basic theory of reinforcement for unidirectional fibrous composites. *Comp Sci. Tech.*, **38**, 327.
2. Ward, I.M. and Wilczynski, A.P. (1993) Bounds for the elastic constants of a unidirectional fibre composite: a new approach. *J. Mater. Sci.*, **28**, 1973.
3. Wilczynski, A.P. and Lewinski, J. (1995) Predicting the properties of unidirectional fibrous composites with monotropic reinforcement. *Comp. Sci. Tech.*, **55**, 139.
4. Hine, P.J., Duckett, R.A. and Ward, I.M. (1993) Modelling the elastic properties of fibre-reinforced composites: II theoretical predictions. *Comp. Sci. Tech.*, **49**, 13.
5. Hine, P.J., Lusti, H.R. and Gusev, A.A. (2002) Numerical simulation of the effects of volume fraction, aspect ratio and fibre length distribution on the elastic and thermoelastic properties of short fibre composites. *Comp. Sci. Tech.*, **62**, 1445.
6. Halpin, J.C. and Kardos, J.L. (1976) The Halpin-Tsai equations: A review. *Polym. Eng. Sci.*, **16**, 344.
7. Hermans, J.J. (1967) The elastic properties of fiber reinforced materials when the fibers are aligned. *Proc. Kon. Ned. Akad. Wetensch. B.*, **65**, 1.
8. Eshelby, J.D. (1957) The determination of the elastic field of an ellipsoidal inclusion, and related problems. *Proc. Roy. Soc. A*, **241**, 376.
9. Mori, T. and Tanaka, K. (1973) Average stress in matrix and average elastic energy of materials with misfitting inclusions. *Acta. Metall.*, **21**, 571.
10. Tandon, G.P. and Weng, G.J. (1984) Effect of aspect ratio of inclusions on the elastic properties of unidirectionally aligned composites. *Polym. Comp. Sci.*, **5**, 327.
11. Tucker, C.L. and Liang, E. (1999) Stiffness predictions for unidirectional short-fiber composites: review and evaluation. *Comp. Sci. Tech.*, **59**, 655.
12. Cox, H.L. (1952) The elasticity and strength of paper and other fibrous materials. *Br. J. Appl. Phys.*, **3**, 72.
13. Kelly, A. (1966) *Strong Solids*, Clarendon Press, Oxford.
14. Hull, D. and Clyne, T.W. (1996) *An Introduction to Composite Materials*, 2nd edn, Cambridge University Press, Cambridge.
15. Brody, H. and Ward, I.M. (1971) Modulus of short carbon and glass fiber reinforced composites. *Polym. Eng. Sci.*, **11**, 139.
16. Advani, S.G. and Tucker, C.L. (1987) The use of tensors to describe and predict fiber orientation in short fiber composites. *J. Rheol.*, **31**, 751.
17. Hine, P.J., Duckett, R.A., Ward, I.M. *et al.* (1996) A comparison of short glass fiber reinforced polypropylene plates made by conventional injection molding and using shear controlled injection molding. *Polym. Composite.*, **17**, 400.
18. Lusti, H.R., Hine, P.J. and Gusev, A.A. (2002) Direct numerical predictions for the elastic and thermoelastic properties of short fibre composites. *Comp. Sci. Tech.*, **62**, 1927.

19. Gusev, A.A. (1997) Representative volume element size for elastic composites: a numerical study. *J. Mech. Phy. Solids,* **45**, 1449.

20. Gusev, A.A., Hine, P.J. and Ward, I.M. (2000) Fiber packing and elastic properties of a transversely random unidirectional glass/epoxy composite. *Comp. Sci. Tech.*, **60**, 535.

21. Price, C.D., Hine, P.J., Whiteside, B. *et al.* (2006) Modelling the elastic and thermoelastic properties of short fibre composites with anisotropic phases. *Comp. Sci. Tech.*, **66**, 69.

22. Qui, Y.P. and WengG.J. (1990) On the application of Mori–Tanaka's theory involving transversely isotropic spheroidal inclusions. *Int. J. Eng. Sci.*, **28**, 1121.

23. Okada, A. and Usuki, A. (2006) Twenty years of polymer-clay nanocomposites. *Macromol. Mater. Eng.*, **291**, 1449–1476.

24. Gopakumar, T.G., Lee, J.A., Kontopoulou, M. *et al.* (2002) Influence of clay exfoliation on the physical properties of montmorillonite/polyethylene composites. *Polymer*, **43**, 5483.

25. Kornmann, X., Thomann, R., Műlhaupt, R. *et al.* (2002) High performance epoxy-layered silicate nanocomposites. *Polym. Eng. Sci.*, **42**, 1815–1826.

26. Ke, Y.C., Yang, Z.B. and Zhu, C.F. (2002) Investigation of properties, nanostructure, and distribution in controlled polyester polymerization with layered silicate. *J. Appl. Polym. Sci.*, **85**, 2677–2691.

27. Hussain, F., Jojjati, M., Okamoto, M. *et al.* (2006) Review article: polymer-matrix nanocomposites, processing, manufacturing, and application: an overview. *J. Compos. Mater.*, **40**, 1511–1575.

28. Crosby, A.J. and Lee, Y.-J. (2007) Polymer nanocomposites: the "nano" effect on mechanical properties. *Polym. Rev.*, **47**, 217–229.

29. Rittigstein, P. and Torkelson, J.M. (2006) Polymer–nanoparticle interfacial interactions in polymer nanocomposites: confinement effects on glass transition temperature and suppression of physical aging. *J. Polym. Sci. Pol. Phys.*, **44**, 2935–2943.

30. Sargsyan, A., Tonoyan, A., Davtyan, S. *et al.* (2007) The amount of immobilized polymer in PMMA SiO2 nanocomposites determined from calorimetric data. *Eur. Polym. J.*, **43**, 3113–3127.

31. Fertig, R.S. and Garnich, M.R. (2004) Influence of constituent properties and microstructural parameters on the tensile modulus of a polymer/clay nanocomposite. *Compos. Sci. Technol.*, **64**, 2577.

32. Sheng, N., Boyce, M.C., Parks, D.M. *et al.* (2004) Multiscale micromechanical modeling of polymer/clay nanocomposites and the effective clay particle. *Polymer*, **45**, 487–506.

33. Fornes, T.D. and Paul, D.R. (2003) Modeling properties of nylon 6/clay nanocomposites using composite theories. *Polymer*, **44**, 4993.

34. Hbaieb, K., Wang, Q.X., Chia, Y.H.J. *et al.* (2007) Modelling stiffness of polymer/clay nanocomposites. *Polymer*, **48**, 901–909.

35. Spencer, P.E. and Sweeney, J. (2009) Modelling polymer clay nanocomposites for a multiscale approach in *Nano- and Micro-Mechanics of Polymer Blends and Composites*, (eds J. Karger-Kocsis and F. Fakirov), Carl Hanser Verlag, Munich, Chap. 15.

36. Kato, M., Usuki, A. and Okada, A. (1997) Synthesis of polypropylene oligomer—clay intercalation compounds. *J. Appl. Polym. Sci.*, **66**, 1781–1785.

37. Chiu, F.-C., Lai, S.-M., Chen, J.-W. *et al.* (2004) Combined effects of clay modifications and compatibilizers on the formation and physical properties of melt-mixed polypropylene/clay nanocomposites. *J. Polym. Sci. Polym. Phys.*, **42**, 4139.

38. Liu, X. and Wu, Q. (2001) PP/clay nanocomposites prepared by grafting-melt intercalation. *Polymer*, **42**, 10013.

39. Chen, L., Phang, I.Y., Wong, S.C. *et al.* (2006) Embrittlement mechanisms of nylon 66/organoclay nanocomposites prepared by melt-compounding process. *Mater. Manuf. Process.*, **21**, 153.

40. He, C., Liu, T., Tjiu, W.C. *et al.* (2008) Microdeformation and fracture mechanisms in polyamide-6/organoclay nanocomposites. *Macromolecules*, **41**, 193.

41. Wang, K., Chen, L., Wu, J.S. *et al.* (2005) Epoxy nanocomposites with highly exfoliated clay: mechanical properties and fracture mechanisms. *Macromolecules*, **38**, 788.

42. Zerda, A.S. and Lesser, A.J. (2001) Intercalated clay nanocomposites: morphology, mechanics, and fracture behavior. *J. Polym. Sci. Polym. Phys.*, **39**, 1137.

43. Zhang, W.D., Shen, L., Phang, I.Y. *et al.* (2004) Carbon nanotubes reinforced nylon-6 composite prepared by simple melt-compounding. *Macromolecules*, **37**, 256.

44. Szleifer, I. and Yerushalmi-Rozen, R. (2005) Polymers and carbon nanotubes—dimensionality, interactions and nanotechnology. *Polymer*, **46**, 7803.

45. McNally Pötschke, P., Halley, P., Murphy, M. *et al.* (2005) Polyethylene multiwalled carbon nanotube composites. *Polymer*, **46**, 8222.

46. Gong, X.Y., Liu, J., Baskaran, S. *et al.* (2000) Surfactant-assisted processing of carbon nanotube/polymer composites. *Chem. Mater.*, **12**, 1049.

47. Khabasheku, V.N., Billups, W.E. and Margreave, J.L. (2002) Fluorination of single-wall carbon nanotubes and subsequent derivatization reactions. *Acc. Chem. Res.*, **35**, 1087.

48. Shofner, M.L., Khabashesku, V.N. and Barrera, E.V. (2006) Processing and mechanical properties of fluorinated single-wall carbon nanotube−polyethylene composites. *Chem. Mater.*, **18**, 906.

49. McIntosh, D., Khabashesku, V.N. and Barrera, E.V. (2006) Nanocomposite fiber systems processed from fluorinated single-walled carbon nanotubes and a polypropylene matrix. *Chem. Mater.*, **18**, 4561.

50. Takayanagi, M. (1963) Viscoelastic properties of crystalline polymers. *Mem. Fac. Eng. Kyushu Univ.*, **23**, 41; Takayanagi, M., Imada, I. and Kajiyama, T. (1966) Mechanical properties and fine structure of drawn polymers. *J. Polym. Sci. Pol. Sym.*, **15**, 263.

51. Wu, C.T.D. and McCullough, R.C. (1977) Constitutive relationships for heterogeneous materials in *Developments in Composite Materials*, (ed G.S. Holister), Applied Science Publishers, London, pp. 119–187.

52. Gray, R.W. and McCrum, N.G. (1969) Origin of the γ relaxations in polyethylene and polytetrafluoroethylene. *J. Polym. Sci. A2*, **7**, 1329.

53. Gupta, V.B. and Ward, I.M. (1968) The temperature dependence of tensile modulus in anisotropic polyethylene sheets. *J. Macromol. Sci. B*, **2**, 89; Stachurski, Z.H. and Ward, I.M. (1968) Anisotropy of viscoelastic transitions in oriented polyethylenes. *J. Polym. Sci. A2*, **6**, 1083; Stachurski, Z.H. and Ward, I.M. (1969) Anisotropy of viscoelastic relaxation in low-density polyethylene in terms of an aggregate model. *J. Macromol. Sci. B*, **3**, 427, 445; Stachurski, Z.H. and Ward, I.M. (1969) Mechanical relaxations in polyethylene. *J. Macromol. Sci. B*, **3**, 445; Davies, G.R., Owen, A.J., Ward, I.M. *et al.*

(1972) Interlamellar shear in anisotropic polyethylene sheets. *J. Macromol. Sci. B*, **6**, 215; Davies, G.R. and Ward, I.M. (1972) Anisotropy of mechanical and dielectric-relaxation in oriented poly(ethylene terephthalate). *J. Polym. Sci. B*, **6**, 215.

54. Hay, I.L. and Keller, A. (1966) A study on orientation effects in polyethylene in the light of crystalline texture. *J. Mater. Sci.*, **1**, 41.

55. Kapuscinski, M., Ward, I.M. and Scanlan, J. (1975) Mechanical anisotropy of strain-crystallized linear polyethylenes. *J. Macromol. Sci. B*, **11**, 475.

56. Lewis, E.L.V. and Ward, I.M. (1980) Anisotropic mechanical-properties of Drawn Nylon-6 .2. The Gamma-phase. *J. Macromol. Sci. B*, **18**, 1; (1981) 19, 75.

57. Ward, I.M. (1983) *Mechanical Properties of Solid Polymers*, John Wiley & Sons, Chichester, Chap. 10.

58. Al-Hussein, M., Davies, G.R. and Ward, I.M. (2000) Mechanical properties of oriented low-density polyethylene with an oriented lamellar-stack morphology. *J. Polym. Sci. Polym. Phys.*, **38**, 755.

59. Zwijnenburg, A. and Pennings, A.J. (1976) Longitudinal growth of polymer crystals from flowing solutions. IV. The mechanical properties of fibrillar polyethylene crystals. *J. Polym. Sci. Polym. Lett.*, **14**, 339; Smith, P. and Lemstra, P.J. (1980) Ultra-high-strength polyethylene filaments by solution spinning/drawing. *J. Mater. Sci.*, **15**, 505.

60. Capaccio, G. and Ward, I.M. (1973) Properties of ultra-high modulus linear polyethylenes. *Nature Phys. Sci.*, **243**, 143; (1974) Preparation of Ultrahigh Modulus Linear Polyethylenes - Effect of Molecular-weight and Molecular-weight Distribution on Drawing Behavior and Mechanical-properties. *Polymer*, **15**, 223.

61. Arridge, R.G.C., Barham, P.J. and Keller, A. (1977) Self-hardening of highly oriented polyethylene. *J. Polym. Sci. Polym. Phys.*, **15**, 389; Barham, P.J. and Arridge, R.G.C. (1977) A fiber composite model of highly oriented polyethylene. *J. Polym. Sci. Polym. Phys.*, **15**, 1177.

62. Arridge, R.G.C. and Folkes, M.J. (1972) The mechanical properties of a 'single crystal' of SBS copolymer – a novel composite material. *J. Phys. D.*, **5**, 344.

63. Gibson, A.G., Davies, G.R. and Ward, I.M. (1978) Dynamic mechanical-behavior and longitudinal crystal thickness measurements on ultrahigh modulus linear polyethylene – quantitative model for elastic-modulus. *Polymer*, **19**, 683.

64. Peterlin, A. (1979) Mechanical properties of fibrous structure in *Ultra-High Modulus Polymers*, (eds A. Ciferri and I.M. Ward), Applied Science Publishers, London, Chap. 10.

65. Ladizesky, N.H. and Ward, I.M. (1985) Ultra high modulus polyethylene composites. *Pure Appl. Chem.*, **57**, 1641.

Further Reading

Bucknall, C.P. (1977) *Toughened Plastics*, Applied Science Publishers, London.

10

Relaxation Transitions: Experimental Behaviour and Molecular Interpretation

We shall discuss the assignment of viscoelastic relaxations in a molecular sense to different chemical groups in the molecule, and in a physical sense to features such as the motion of molecules in crystalline or amorphous regions. Because amorphous polymers exhibit fewer structure-dependent features than those that are semi-crystalline, we shall use these simpler materials to illustrate some general characteristics of relaxation behaviour.

10.1   Amorphous Polymers: An Introduction

It is customary to label relaxation transitions in polymers as α, β, γ, δ and so on in alphabetical order with decreasing temperature. Three of the four transitions in polymethyl methacrylate (PMMA)

$$\left[\begin{array}{c} H_3C\!-\!O\!-\!C\!=\!O \\ | \\ -\!C\!-\!CH_2\!- \\ | \\ CH_3 \end{array} \right]_n$$
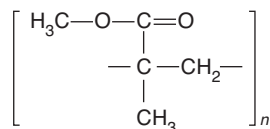
are shown in Figure 10.1, which summarises data obtained using a low-frequency torsion pendulum. The highest temperature relaxation, the α relaxation, is the glass transition and is associated with a large change in modulus. Comparative studies on similar polymers, together with nuclear magnetic resonance (NMR) and dielectric measurements [1–6], have shown the β relaxation to be associated with side-chain motions of the ester group. The γ and δ relaxations involve motion of the methyl groups attached to the main chain and the side chain, respectively.
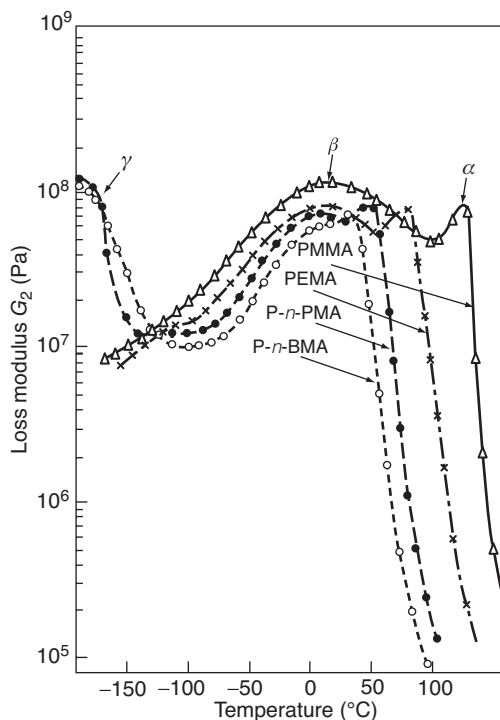
Figure 10.1 *Temperature dependence of loss modulus G_2 for polymethyl methacrylate (PMMA), polyethyl methacrylate (PEMA), poly-n-propyl methacrylate (P-n-PMA) and poly-n-butyl methacrylate (P-n-BMA). (Reproduced from Heijboer, J. (1965) Physics of Non-Crystalline Solids, North-Holland, Amsterdam, p. 231. Copyright (1965) Elsevier Ltd.)*

More extensive recent researches on the β relaxation have been undertaken by Monnerie, Lauprêtre and Halary [7]. It was concluded that for polymers with side chains such as PMMA the β relaxation involved π flips of the ester group around the bond with the main chain. These were isolated in the low temperature part of the relaxation but intramolecular cooperativity was involved in the high temperature part. These ring flips are accompanied by a change in the rotation angles of the main chain. The β transition was also studied in maleimide and glutarimide PMMA copolymers. In all cases, the cooperativity of the molecular motions is intramolecular and in the maleimide copolymers their rigidity hinders the propagation of main-chain adjustment.

The case of amorphous poly(ethylene terephthalate) (PET), where there are no side groups, is considered in Section 10.3.2 in conjunction with semi-crystalline forms of this polymer. Worthy of mention is the use of antiplasticisers to show that the β relaxation is composite [8, 9]. In studies of bisphenol A (and tetramethyl bisphenol A), polycarbonate intramolecular cooperativity associated with the carbonate residue was shown by the introduction of the methyl groups on the phenyl rings [10], and intermolecular cooperativity was shown by the dielectric behaviour of blends [11]. Further evidence for intermolecular contributions to the ring motions was obtained from the observed pressure dependence of the proton NMR transverse relaxation time [12]. There is a key conclusion for polymers

without side chains containing phenyl rings such as PET and bisphenol A polycarbonate. For the linear polymer PET, phenyl ring π flips occurring in the high temperature parts of the β transition are associated with intramolecular cooperativity only, whereas for polycarbonate there is intermolecular cooperativity.

10.2 Factors Affecting the Glass Transition in Amorphous Polymers

Two distinct models have been used for interpreting the influence of features such as chemical structure, molecular mass, cross-linking and plasticisers on the glass transition in amorphous polymers. The first approach considers changes in molecular flexibility, which modify the ease with which conformational changes can take place. The alternative approach relates all these effects to the amount of free volume, which is assumed to attain a critical value at the glass transition.

10.2.1 Effect of Chemical Structure

Although these factors have been intensively studied because of their importance in selecting polymers for commercial exploitation, much of our knowledge is empirical in nature, due primarily to the difficulty in distinguishing between intra- and intermolecular effects. Some general features are, however, evident.

10.2.1.1 Main-Chain Structure

Flexible groups such as an ether link will enhance main-chain flexibility and reduce the glass transition temperature, with the opposite effect being shown by the introduction of an inflexible group, such as a terephthalate residue.

10.2.1.2 Side Groups [13]

Bulky, inflexible side groups increase the temperature of the glass transition, as is illustrated in Table 10.1 for a series of substituted poly-α-olefins:

$$\left[-CH_2-\underset{\underset{R}{|}}{CH}- \right]_n$$
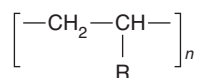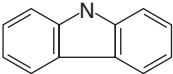
Table 10.1 *Glass transition of some vinyl polymers.*

Polymer	R	Transition temperature in °C at ~1 Hz
Polypropylene	CH_3	0
Polystyrene	C_6H_5	116
PolyN-vinylcarbazole		211

Table 10.2   *Glass transition of some isomeric polyvinyl butyl ethers.*

Polymer	R_1	Transition temperature in °C at ~1 Hz
Polyvinyl *n*-butyl ether	$CH_2CH_2CH_2CH_3$	−32
Polyvinyl isobutyl ether	$CH_2CH(CH_3)_2$	−1
Polyvinyl *t*-butyl ether	$C(CH_3)_3$	+83

Source: Reproduced with permission from Vincent, P.I. (1965) *The Physics of Plastics* (ed. P.D. Ritchie), Iliffe, London.

A difference between the effect of rigid and flexible side groups is shown in Table 10.2 for a series of polyvinyl butyl ethers:

$$\left[-CH_2-CH-\right]_n$$
$$\qquad\qquad OR_1$$
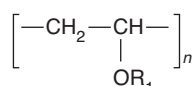
All these polymers contain the same atoms in the side group OR_1 (where R_1 represents the butyl isomeric form), but more compact arrangements reduce the flexibility of the molecule and give a marked increase in the transition temperature.

Increasing the length of flexible side groups reduces the temperature of the glass transition, as is evident from Table 10.3 for a series of polyvinyl ethers:

$$\left[-CH_2-CH-\right]_n$$
$$\qquad\qquad OR_2$$
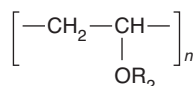
where R_2 represents the *n*-alkyl group. Here, the increase in length is associated with an increase in free volume at a given temperature.

Table 10.3   *Glass transition of some polyvinyl n-alkyl ethers.*

Polymer	R_2	Transition temperature in °C at ~1 Hz
Polyvinyl methyl ether	CH_3	−10
Polyvinyl ethyl ether	CH_2CH_3	−17
Polyvinyl *n*-propyl ether	$CH_2CH_2CH_3$	−27
Polyvinyl *n*-butyl ether	$CH_2CH_2CH_2CH_3$	−32

Source: Reproduced with permission from Vincent, P.I. (1965) *The Physics of Plastics* (ed. P.D. Ritchie), Iliffe, London.
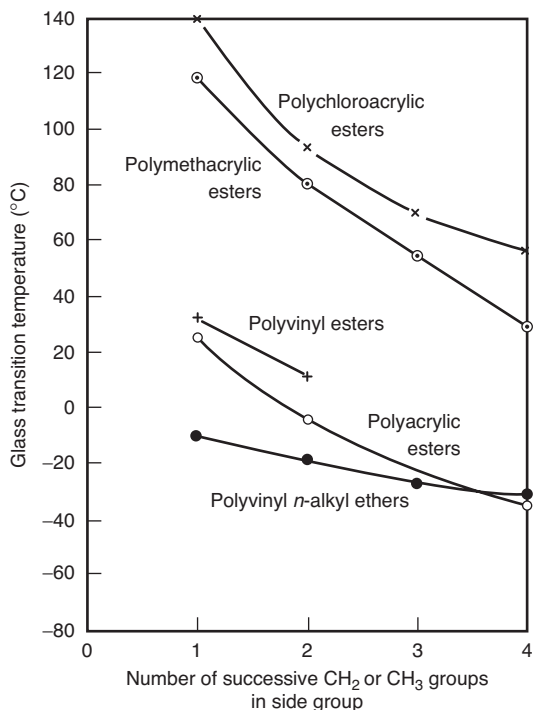
Figure 10.2 *The effect of polarity on the position of the glass transition temperature for five polymer series. (Reproduced from Vincent, P.I. (1965) The Physics of Plastics (ed. P.D. Ritchie), Iliffe, London. Copyright (1965) Plastics Institute.)*

10.2.1.3 Main-Chain Polarity

In a series of polymers of similar main-chain composition, the temperature of the glass transition may be significantly depressed as the number of successive —CH_2 or —CH_3 groups in the side groups is increased (Figure 10.2). It is evident that the temperature of the glass transition increases with main-chain polarity and it is assumed that the associated reduction in main-chain mobility is due to the increase in intermolecular forces. In particular, it is suggested that the higher values for the polychloracrylic esters arise from the increased valence forces associated with the chlorine molecules.

10.2.2 Effect of Molecular Mass and Cross-Linking

The length of the main chain does not affect the dynamic mechanical properties of polymers in the glassy state, where molecular motions are of restricted extent, but the glass transition temperature is depressed at very low relative molecular masses as a consequence of the additional free volume introduced by the increased proportion of chain ends [14].

As already discussed (see Section 7.1.1), molecular mass has a large effect in the glass transition range, where viscous flow transforms to a plateau range of rubber-like behaviour due to entanglements between the longer molecular chains.
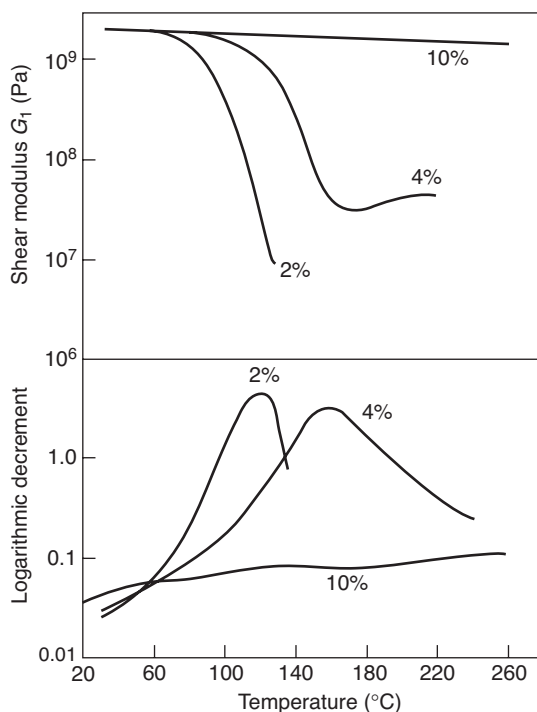
Figure 10.3 *Shear modulus G_1 and logarithmic decrement of a phenol–formaldehyde resin cross-linked with hexamethylene tetramine at stated concentrations. (Reproduced from Drumm, M.F., Dodge, W.H. and Nielsen, L.E. (1956) Cross linking of a phenol-formaldehyde novolac – determination by dynamic mechanical measurements. Ind. Eng. Chem.,* **48**, *76. Copyright (1956) American Chemical Society.)*

Chemical cross-links reduce the free volume by bringing adjacent chains close together and so raise the temperature of the glass transition, as is shown in Figure 10.3 for phenol–formaldehyde resin cross-linked with hexamethylene tetramine to different extents. The transition region is greatly broadened [15], so that in very highly cross-linked materials, where motions of extensive segments of the main chain are not possible, there is no glass transition.

10.2.3   Blends, Grafts and Copolymers

The mechanical properties of blends and graft polymers are determined primarily by the mutual solubility of the two homopolymers. For complete solubility, the properties of the mixture are close to those of a random copolymer of the same composition, as is shown in Figure 10.4, which compares a 50:50 mixture of polyvinyl acetate and polymethyl acrylate with the equivalent copolymer [15]. Note that the damping peak occurs at 30°C, compared with 15°C for the polymethyl acrylate and 45°C for polyvinyl acetate.

A theoretical interpretation of the glass transition temperature of a copolymer is based on the assumption that the transition occurs at a constant fraction of free volume. Gordon and Taylor [16] assume that in an ideal copolymer the partial specific volumes of the two components are constant and equal to the specific volumes of the two homopolymers. The
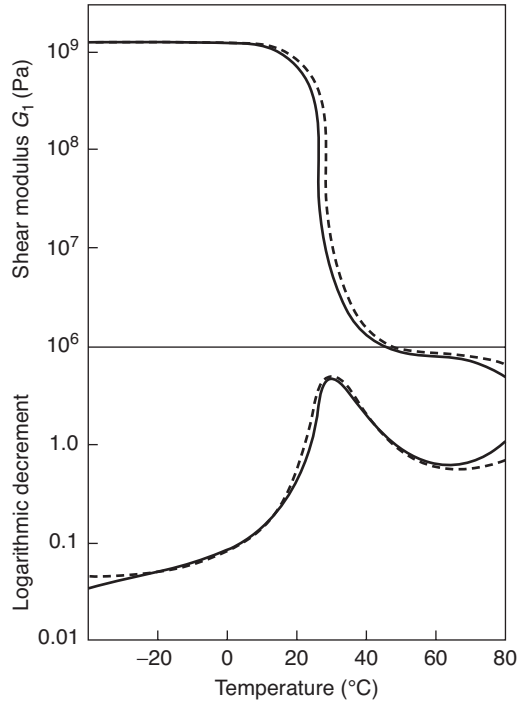
Figure 10.4   *Shear modulus G_1 and logarithmic decrement for a miscible blend of polyvinyl acetate and polymethyl acrylate (- - -) and a copolymer of vinyl acetate and methyl acrylate (_ _ _ _). (Reproduced from Nielsen, L.E. (1962) Mechanical Properties of Polymers, Van Nostrand-Reinhold, New York. Copyright (1962) Taylor and Francis.)*

specific volume–temperature coefficients for the two components in the rubbery and glassy states are assumed to remain the same in the copolymer as in the homopolymers, and to be independent of temperature. The glass transition temperature T_g for the copolymer is then given by [17]

$$\frac{1}{T_g} = \frac{1}{(w_1 + Bw_2)} \left[\frac{w_1}{T_{g1}} + \frac{Bw_2}{T_{g2}} \right],$$

where w_1 and w_2 are the mass fractions of the two monomers whose homopolymers have transition temperatures T_{g1} and T_{g2}, respectively, and B is a constant close to unity.

Where the two polymers in a mixture are insoluble they exist as separate phases, so that two glass transitions are observed as shown in Figure 10.5 for a polyblend of polystyrene and styrene–butadiene rubber [15]. The two loss peaks are very close to those for pure polystyrene and pure styrene–butadiene rubber.

10.2.4   Effects of Plasticisers

Plasticisers, which are relatively low molecular mass organic materials added to soften rigid polymers, must be soluble in the polymer and usually they dissolve it completely at high temperature. Figure 10.6 shows the change in the loss peak associated with the glass transition of polyvinyl chloride (PVC) when plasticised with varying concentrations
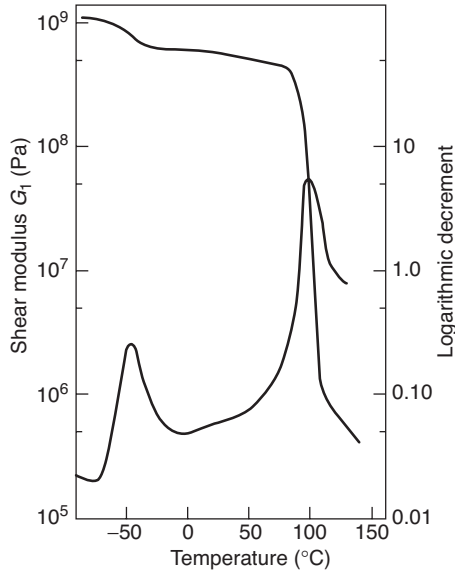
Figure 10.5   *Shear modulus G₁ and logarithmic decrement for an immiscible polyblend of polystyrene and a styrene–butadiene copolymer. (Reproduced from Nielsen, L.E. (1962) Mechanical Properties of Polymers, Van Nostrand-Reinhold, New York. Copyright (1962) Taylor and Francis.)*
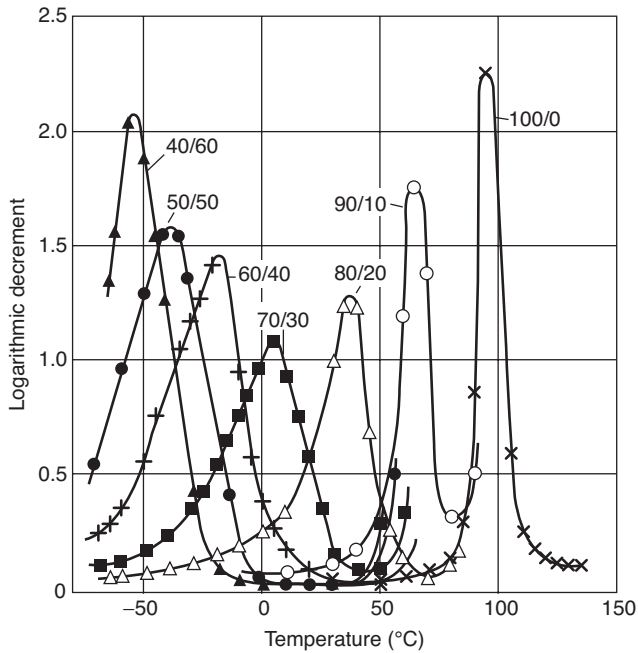
Figure 10.6   *The logarithmic decrement of PVC plasticised with various amounts of di(ethylhexyl) phthalate. (Reproduced from Wolf, K. (1951) Beziehungen zwischen mechanischem und elektrischem Verhalten von Hochpolymeren. Kunststoffe, **41**, 89. Copyright (1951).)*
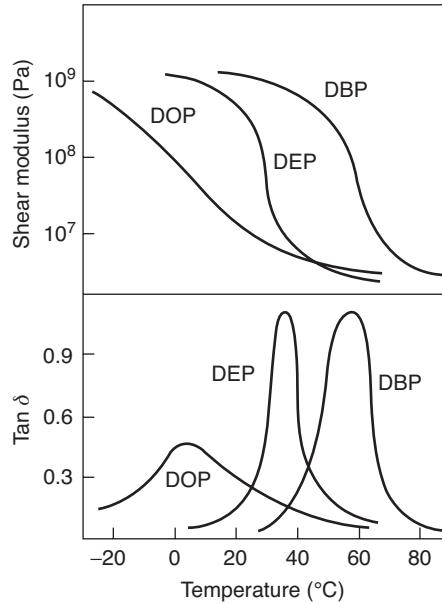
Figure 10.7 *Shear modulus and loss factor tan δ for PVC plasticised with diethyl phthalate (DEP), dibutyl phthalate (DBP) and n-dioctyl phthalate (DOP). (Reproduced from Neilsen, L.E. Buchdahl, R. and Levreault, R., (1950) Mechanical and electrical properties of plasticised vinyl chloride compositions. J. Appl. Phys., **21**, 607. Copyright (1950) American Institute of Physics.)*

of di(ethylhexyl)phthalate [18]. In this polymer, plasticisation is of major commercial importance: rigid PVC is used in applications such as replacement window frames, and the plasticised material supplies flexible sheeting and inexpensive footwear.

Plasticisers make it easier for changes in molecular conformation to occur, and so lower the temperature of the glass transition. They also broaden the loss peak, with the extent of broadening depending on the nature of the interactions between the polymer and the plasticiser. A broad damping peak is found where the plasticiser has a limited solubility in the polymer or tends to associate in its presence. The increased width of the damping peak as the plasticiser becomes a poorer solvent is shown in Figure 10.7 for plasticised PVC [15]. Diethyl phthalate is a relatively good solvent, dibutyl phthalate is intermediate and *n*-dioctyl phthalate is a very poor solvent.

10.3   Relaxation Transitions in Crystalline Polymers

10.3.1   General Introduction

Semi-crystalline polymers are less sensitive to wide variations of stiffness with temperature than those that are totally amorphous, but even so stiffnesses may vary by an order of magnitude over the useful working range of a given material. Oriented crystalline polymers may additionally show contrasts between extensional and shear deformations, and also angular-dependent changes in relaxation strength.

Some polymers, notably low-density polyethylene (LDPE), show clearly resolved α, β and γ processes. The high-temperature α relaxation is frequently related to the proportion of crystalline material present, the β process is related to a greatly broadened glass–rubber relaxation and the γ relaxation has been associated, at least in part, with the amorphous phase. Other materials – an example to be discussed shortly being that of PET – show only two relaxation processes. In these cases, the α relaxation is akin to the β process in polymers where all three relaxations are evident.

In earlier editions of this work, it was noted that the interpretation of viscoelastic relaxations in crystalline polymers was at a very speculative stage but, as a working hypothesis, it was assumed that the tangent of the phase lag angle (tan δ), or its equivalent the logarithmic decrement (Λ), was an appropriate measure of the relaxation strength. Boyd in two important review articles [19, 20] has demonstrated that the situation is more complex: for instance, the apparent trend of relaxation strength with changing crystallinity can depend on whether tan δ or the real (in-phase) or imaginary (out-of-phase) components of modulus (G_1 and G_2, respectively) or compliance (J_1, J_2) are used to record the relaxations, and the interpretation of the data depends on the composite model used to determine the interaction between crystalline and amorphous phases. However, it is still the case that tan δ_{max} (but not necessarily G''_{max} or J''_{max}) usually may be expected to correlate directly with phase origin, although a plot versus crystallinity may not be linear.

We shall begin with a brief and simplified discussion of the main features of experimental observations and proceed to consider the interpretation of these features. Three polymers are selected as paradigms: PET, which can exist in the wholly amorphous state but also as a partially crystalline polymer; polyethylene, which is a high crystalline polymer and a liquid crystalline polymer, the thermotropic copolyester whose mechanical anisotropy was discussed in Section 7.5.4 above.

10.3.2 Relaxation in Low-Crystallinity Polymers

The temperature variation of the complex modulus of PET as a function of crystallinity has been studied by Takayanagi [21] in extension at 138 Hz (Figure 10.8) and by Illers and Breuer [22] in shear at $\sim$1 Hz. At the lowest levels of crystallinity, there is a sudden and severe drop in stiffness associated with the α process that is characteristic of amorphous polymers. With increasing crystallinity, the α peak broadens as the change in stiffness is greatly reduced. This behaviour is consistent with that of a composite for which only one phase softens, with the broadening of the peak resulting from restriction of long-range segmented motions in the amorphous phase by the remaining crystals. Illers and Breuer noted also that the temperature at which the loss peak (G_2) was a maximum increased up to 30% crystallinity and then decreased slightly at high crystallinities. Studies involving small-angle X-ray scattering indicate that high-crystallinity specimens have both thicker crystal layers and thicker amorphous layers than those of low crystallinity [23]. This latter feature will reduce the constraints imposed by crystal surfaces.

In contrast to the α relaxation, both the shape and location of the subglass β process are insensitive to the degree of crystallisation. Dielectric studies [24] yield the same conclusion. The process is therefore consistent with localised molecular motions, in contrast with the restrained long-range segmental motions involved in the glass–rubber α relaxation.
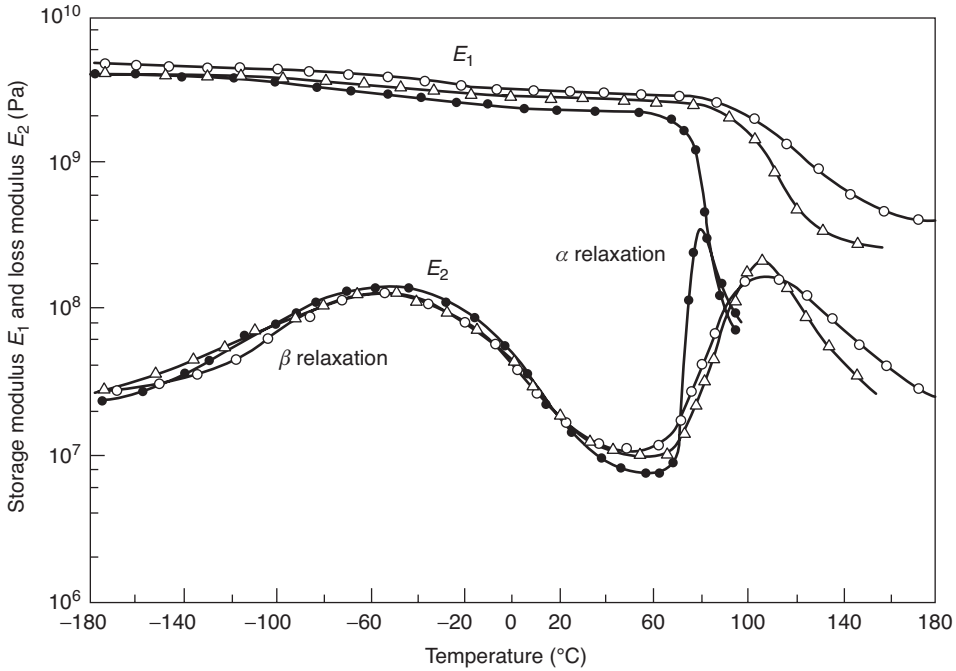
Figure 10.8 *Storage modulus E_1 and loss modulus E_2 as a function of temperature at 138 Hz for PET samples of differing degrees of crystallinity (●, 5%; Δ, 34%; ○, 50%). (Reproduced from Takayanagi, M. (1964) Viscoelastic properties of crystalline polymers. Memoirs of the Faculty of Engineering Kyushu Univ., **23**, 1. Copyright (1964).)*

Boyd [20] has analysed the dynamic mechanical behaviour of PET in terms of a composite model of crystalline and amorphous phases. The relaxation strengths for the α and β processes, determined from the shear modulus results of Illers and Breuer, were shown to be related to the crystallinity, indicating that both relaxation processes related to the amorphous regions. For the β processes, the shear modulus for the amorphous phase lies between the upper (Voigt) and lower (Reuss) bounds in both the relaxed and unrelaxed states. The α process, however, appeared to fit best near the lower bound behaviour.

Although the phenomenological approach of Boyd gives some insight into the dynamic mechanical behaviour, it does not provide any significant understanding of the molecular origins of the relaxation processes. In recent publications, Ward and co-workers [8,9] have shown how it is necessary to bring together dynamic mechanical, NMR and dielectric measurements to achieve such an understanding, and NMR spectroscopy is probably the most powerful tool in this respect. The main advantage of NMR is that it allows the mobility in different parts of the molecule to be examined. There are several investigations of the molecular relaxations in PET using NMR. Using selectively deuterated samples to distinguish between molecular motions in the aliphatic and aromatic parts of the PET molecule, English [25] identified significant motion of the ethylene glycol units at the glass transition temperature, which have been assumed to be due to a unique *trans-gauche* movement of these units (see Figure 1.7). It is important to note that the ethylene glycol

units do not contribute to the relaxation processes present in the β peak. This result is consistent with much earlier NMR studies on selectively deuterated PET samples by Ward [26], which showed that the α relaxation in PET involved significant motions of both the aliphatic and aromatic moieties.

Dielectric and dynamic measurements by Maxwell *et al*. [9] showed that the β peak consists of two different relaxation processes, one on the high temperature side and the other on the low temperature side. High-resolution carbon-13 chemical shift and deuterium NMR experiments showed that both the phenyl rings and the carbonyl groups undergo small-angle oscillations at temperatures below the glass transition, and that the phenyl groups also undergo rapid 180° flips. It was confirmed that the ethylene glycol group does not contribute to the β relaxation and it was concluded that the high temperature side of the relaxation is due to the 180° flips and the low temperature side to motion of the carbonyl groups, which has a significantly lower activation energy and activation enthalpy (see Section 7.3).

10.3.3   Relaxation Processes in Polyethylene

Polyethylene is the obvious choice for investigating relaxations in the more highly crystalline polymers. Its structure has been studied in great detail, and the material is readily obtainable in two forms. LDPE typically contains about three short side branches per 100 carbon atoms, together with about one longer branch per molecule. High-density polyethylene (HDPE) is much closer to the pure $(CH_2)_n$ polymer, and the proportion of side branches is often less than 5 per 1000 carbon atoms. The main features of the temperature dependence of tan δ for each material are indicated schematically in Figure 10.9. The LDPE shows clearly resolved α, β and γ loss peaks. In HDPE, the low-temperature γ peak is very
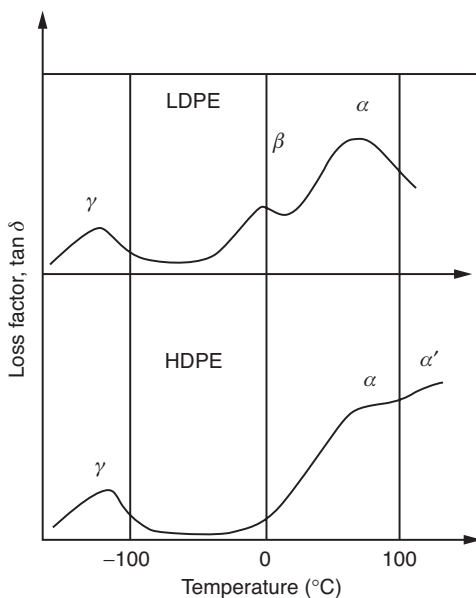
Figure 10.9   *Schematic diagram showing α, α', β and γ relaxation processes in LDPE and HDPE.*

similar to that in LDPE, but the β relaxation is hardly resolved and the α relaxation is often considerably modified appearing to consist of at least two processes (α and α') with different activation energies. The high-temperature behaviour is also dependent on whether loss angle or loss modulus is the quantity being measured. At one time, some investigators questioned the existence of the β relaxation in HDPE, but further work involving a range of polymers intermediate between the extremes indicated in Figure 10.9 has established its presence.

We must conclude that α, β and γ relaxations occur in all forms of polyethylene. The first stage in the process of analysis is to determine whether a given relaxation is related to the crystalline or the amorphous component, or to an interaction involving both phases. Next, one deduces a process that is able to account for each relaxation. Finally, an attempt must be made to model a molecular mechanism that can cause the process to occur.

In two review articles, Boyd [19, 20] presents evidence for two major conclusions regarding the origins of the α, β and γ relaxations in polyethylene. First, the mechanical strengths of all three relaxations relate to the amorphous fraction. Secondly, both mechanical and dielectric measurements show that the location of the α relaxation depends on the crystal lamellar thickness. These conclusions might appear to be in conflict regarding the α relaxation, but we will see that recent research by Ward and co-workers [27, 28] resolves this issue and also the relationship between the relaxations and LDPE and HDPE, as to whether they are of similar molecular origin. Two extra ingredients were required to answer this question: dynamic mechanical measurements on specially produced oriented samples and measurements over a wide range of frequencies to determine the activation energies for the processes, as discussed in Section 7.3.

Key results for the mechanical anisotropy of LDPE sheets have already been discussed in Section 9.5.3. Oriented and annealed sheets can be considered as composite solids, where the β relaxation is an interlamellar shear process, consistent with its assignment by Boyd to an amorphous process. Figure 10.10 shows results for cold-drawn and annealed
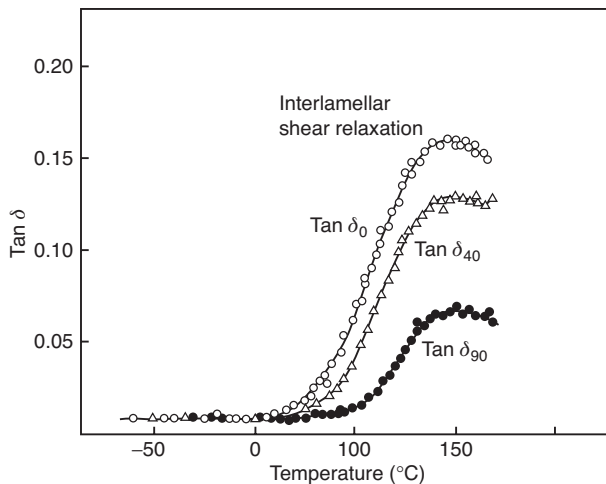
Figure 10.10 *Temperature dependence of tan δ in a cold-drawn and annealed HDPE sheet in different directions at 50 Hz. (Reproduced from Stachurski, Z.H. and Ward, I.M. (1969) Mechanical relaxations in polyethylene. J. Macromol. Sci. Phys. B, **3**, 445. Copyright (1969) Taylor and Francis.)*
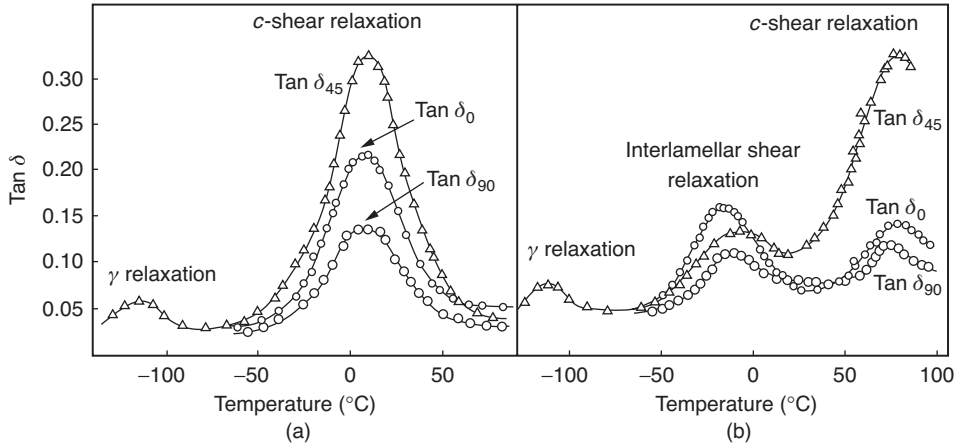
Figure 10.11 *Temperature dependence of tan δ in three directions in cold-drawn (a) and cold-drawn and annealed (b) LDPE sheets at approximately 500 Hz. (Reproduced from Stachurski, Z.H. and Ward, I.M. (1968) β relaxations in polyethylenes and their anisotropy. J. Polym. Sci. A2, **6**, 1817. Copyright (1968) Taylor and Francis.)*

HDPE, where no β relaxation is observed [29]. In these sheets, the crystal lamellae make an acute angle of about $40°$ with the initial draw direction [30]. Applying the stress along the initial draw direction then gives the maximum resolved shear stress parallel to lamellar planes. We see from Figure 10.10 that the maximum loss is tan δ_0, confirming that the α relaxation in HDPE is primarily an interlamellar shear process from a macroscopic mechanical viewpoint.

The situation is apparently made more confusing by comparison of the results of Stachurski and Ward [31] for cold-drawn (a) and annealed (b) sheets of LDPE illustrated in Figure 10.11. For the cold-drawn sheet, the maximum loss in the $0°C$ region occurs at $45°$ to the draw direction. Only one loss process is observed and this shows the anisotropy appropriate for a relaxation that involves shear parallel to the draw direction in a plane containing the draw direction. This material does not show a clear lamellar texture, so it is reasonable to associate this process with the α relaxation. In the cold-drawn and annealed sheet, the process has moved to about $70°C$. These results, taken together with the measurements on specially oriented sheets, suggest that the draw or c-axis orientation of the crystalline regions is the governing factor. Because the relaxation involves shear in the c-axis direction in planes containing the c axis it has been termed the 'c-shear relaxation'. The annealed LDPE sheet also shows a β relaxation below $0°C$ with an anisotropy consistent with interlamellar shear, as discussed in Section 8.4.3.

The identification of the α process as a c-shear relaxation and the β process as interlamellar shear in a drawn and annealed LDPE sheet was nicely confirmed by measurements of the anisotropy of dielectric relaxation [32]. Pure polyethylene shows no dielectric response, so experiments were made on specimens that had been lightly decorated with dipoles by means of oxidation, to such a small extent that the overall relaxation behaviour was not significantly affected. The dielectric relaxation data showed marked anisotropy for the relaxation, consistent with its assignment to the c-shear relaxation, but the β relaxation

Table 10.4 *Activation energies for α and β relaxations in HDPE and LDPE.*

Sample	β relaxation activation energy (kJ/mol)	α relaxation activation energy (kJ/mol)
Isotropic LDPE	430	120
Oriented LDPE	500	110
Isotropic HDPE	Not present	120
Oriented HDPE	Not present	80–90

showed no anisotropy, confirming that the mechanical anisotropy observed related to the lamellar texture and not to anisotropy at a molecular level.

We are still left with an apparent paradox that the α relaxation in HDPE relates to interlamellar shear whereas in LDPE, it is the c-shear relaxation. Recent measurements of the activation energies for these materials by Matthews *et al*. (Table 10.4) [28] show, however, that the α relaxation in both polymers has a comparatively low activation energy consistent with the relaxation being the c-shear mechanism at a molecular level, that is the α relaxation in both HDPE and LDPE is associated with identical molecular mechanisms. It appears that interlamellar shear in the mechanical α process in HDPE requires coupled motions of the chains that run through the lamellae (c-shear) together with chains on the lamellar surface. In contrast, c-shear and interlamellar shear in LDPE are two distinct mechanical relaxations, and interlamellar shear has a much higher activation energy, akin to a glass transition.

Mansfield and Boyd [33] have proposed that the dielectric α process can be represented by the torsional movement of a segment of chain about 12CH_2 units in length. This motion, which will cause the short-twisted mismatch region to move through the crystal one carbon atom at a time, is consistent with the dependence of activation energy on crystal thickness (Figure 10.12).

In the mechanical situation, the translational component of the crystal process can lead to reorganisation of the crystal surface and hence modify the connections of amorphous
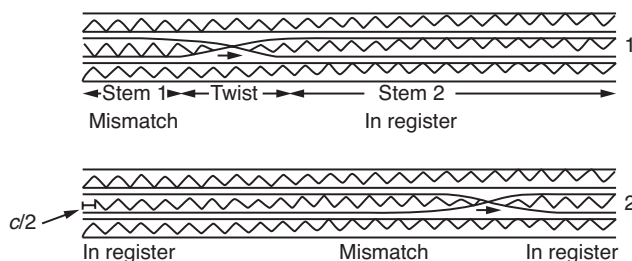
Figure 10.12 *Propagation of a localised smooth twist along the chain. As the twist starts (1) it leaves behind it a translational mismatch. As the twist proceeds (2) the mismatch becomes attenuated at large distances from the twist by elastic distortion of the stem valence angles and bond length. (Reproduced with Mansfield, M. and Boyd, R.H. (1978) Molecular motions, the alpha-relaxation and chain transport in polyethylene crystals, J. Polymer Sci., Phys Ed.,* **16***, 1227. Copyright (1978) John Wiley & Sons, Ltd.)*
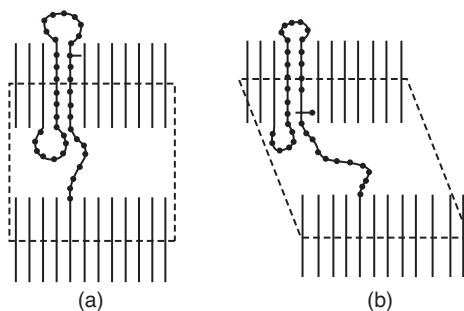
Figure 10.13   *Further relaxation of the amorphous fraction resulting from translational mobility in the crystal (the latter acquired in the α process). Illustrated in this case is reorganisation of the interface in (a) through shortening of two loops that in (b) permits lengthening of a tight tie chain, which in turn permits more deformation of the amorphous fraction. Also shown is a decorating dipole in the crystal that moves through a number of translational, rotational steps. One such step suffices for dielectric activity. (Reproduced from Boyd, R.H. (1985) Relaxation processes in crystalline polymers – molecular interpretation – a review. Polymer, **26**, 1123. Copyright (1985) Elsevier Ltd.)*

chains to the crystal surface. An example is shown in Figure 10.13, where translational motion of a decorated dipole (indicated by a horizontal arrow) permits lengthening of the tight tie chain in (a), and so enables further deformation of the amorphous fraction.

The β relaxation is very broad compared with that in completely amorphous polymers due to the immobilising effect of the crystals on the amorphous fraction. Boyd speculates that the shortest relaxation times may be associated with motions of very loose folds and relatively non-extended tie chains; conversely tight folds are unable to relax. The relative prominence of the β relaxation in LDPE compared with HDPE is enhanced by the lower value of the relaxed β process modulus in LDPE, which will increase the relative intensity of the β and decrease that of the α. On a molecular basis, the branching of LDPE gives a more loosely organised amorphous component, capable of relaxing to a lower limiting rubbery modulus.

As it occurs below the glass transition temperature the γ relaxation will involve simple conformational motions that are relatively short range in character. Such motions must leave the molecular stems adjacent to the bonds undergoing transition relatively undisturbed; they must require only a modest activation energy, and the swept-out volume during the relaxation should be small. Following Willbourn's [34] suggestion that the γ relaxation in many amorphous and semi-crystalline polymers can be attributed to a restricted motion of the main chain that involves at least four successive —CH_2 groups, both Shatzki [35] and Boyer [36] have proposed that subglass relaxations can be modelled in terms of a so-called crankshaft mechanism (Figure 10.14). Shatzki's five-bond mechanism involves the simultaneous rotation about bonds one and seven such that the intervening carbon bonds move as a crankshaft. Boyer's proposal involves only three intermediate carbon bonds. The mechanisms are, as Boyd [19] has pointed out, the simplest allowed moves of a tetrahedrally bonded chain on a diamond lattice that leave the adjacent stem bonds in place. The internal energetics of the five-bond model are modest, but the swept-out volume is large in the context of a motion in a glassy matrix. For the three-bond transition, a double
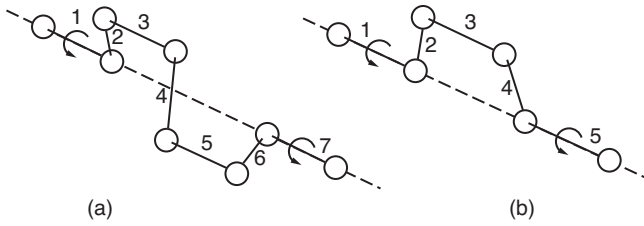
Figure 10.14   *The crankshaft mechanisms of Shatzki (a) and Boyer (b). (Reproduced from McCrum, N.G., Read, B.E. and Williams, G. (1967) Anelastic and Dielectric Effects in Polymeric Solids, John Wiley & Sons, London. Copyright (1991) Dover Publications.)*

energy barrier system with an intermediate energy minimum is implied, and the motion associated with one of these barriers requires a significant free volume, and so is inhibited by the matrix. Despite these drawbacks, a crankshaft mechanism has been proposed as being relevant to the γ relaxation in polyethylene.

Boyd [19] discusses a motion related to the three-bond mechanism that can accomplish the appropriate shape change without encountering problems associated with free volume. It involves the conformational sequence GTG′ occurring in an otherwise all-*trans* chain (*G* and *G*′ represent alternative *gauche* transformations). From Figure 10.15 it can be seen
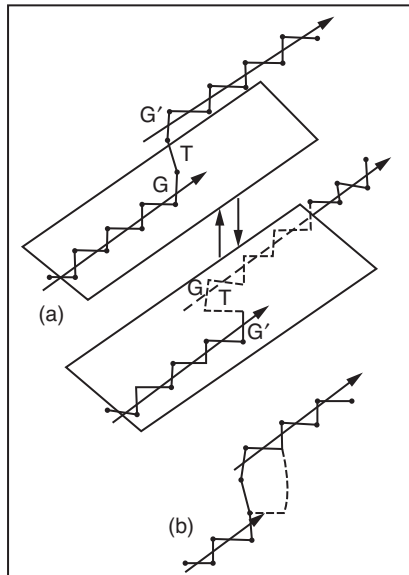
Figure 10.15   *Kinks and kink inversion. (a) The conformational sequence . . . TTTGTG′TTT . . . has parallel offset planar zigzag stems (indicated by arrows) on either side of the GTG′ portion. The transition TGTG′ → TG′TGT (called here kink inversion) creates a mirror image of the kink about the displaced stems. (b) A three-bond crankshaft move is shown at a kink site (as dashed line). This move advances the kink along the chain by 2CH$_2$ units. (Reproduced from Boyd, R.H. (1985) Relaxation processes in crystalline polymers – molecular interpretation – a review. Polymer, **26**, 1123. Copyright (1985) Elsevier Ltd.)*
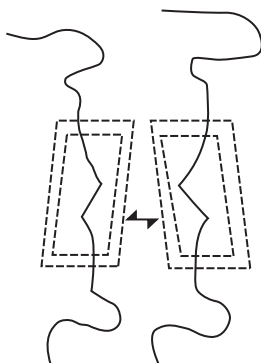
Figure 10.16 *Strain fields set up by stem displacement accompanying kink inversion. (Reproduced from Boyd, R.H. (1985) Relaxation processes in crystalline polymers – molecular interpretation – a review. Polymer,* **26**, *1123. Copyright (1985) Elsevier Ltd.)*

that this sequence, known as a kink [37], has the effect of displacing the separated *trans* components of a planar zigzag yet leaving them parallel to one another. Interchanging the senses of the *gauche* bonds

$$\ldots \mathrm{TTGTG'TT} \ldots \rightarrow \ldots \mathrm{TTG'TGTT} \ldots$$
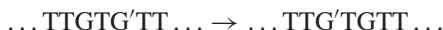
converts the kink into a mirror image of itself. The kink inversion process, shown in Figure 10.16, involves only a small swept-out volume and requires a modest activation energy. The stem displacement causes a localised shape change that can propagate through the specimen as a shear strain. The kink inversion process is therefore a possible candidate on which to base a molecular model of the γ relaxation, but it must be emphasised that there is no direct evidence to demonstrate that it is appropriate for modelling the behaviour of polyethylene.

10.3.4 Relaxation Processes in Liquid Crystalline Polymers

Liquid crystalline polymers form another class of polymers from a structural viewpoint and can be produced either from a liquid crystalline solution (termed lyotropic) or a liquid crystalline melt (thermotropic). In this section, we will consider thermotropic liquid crystalline polymers, of which the simplest chemically are those invented by Calundann [38], which are random copolymers of hydroxybenzoic acid (HBA) and hydroxynaphthoic acid (HNA) (Figure 10.17). The random arrangement of HBA and HNA units along the chain prevents normal crystallisation into three-dimensional order (although there is debate about the extent to which there may be some regions of three-dimensional order [39]). Molecular alignment of the chains can be achieved readily by melt spinning. This produces an oriented liquid crystalline structure (termed a mesophase) in which there is axial alignment of the chains, which are close packed on hexagonal or orthorhombic lattices without any regularity within the chains along the axial direction.

   The dynamic mechanical properties of these oriented HBA/HNA copolymers have been studied by Yoon and Jaffe [40], Blundell and Buckingham [41] and Ward and co-workers [42]. It is of particular interest to compare different compositions based on HBA and HNA
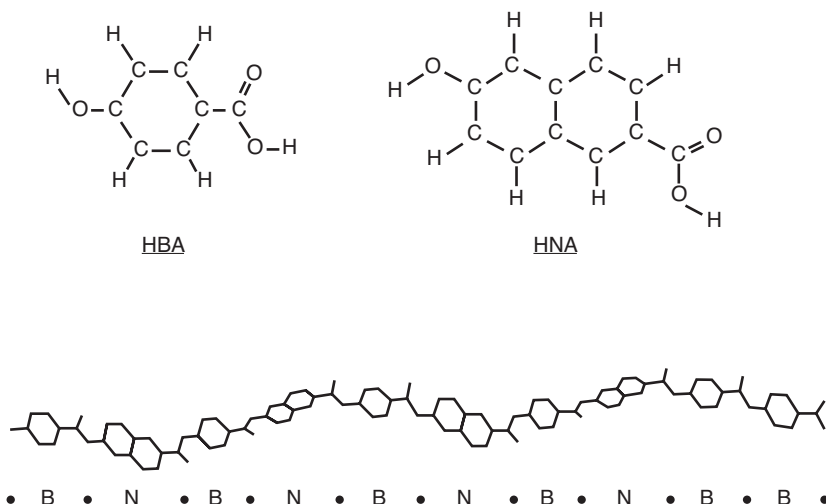
Figure 10.17 *Monomers of HBA and HNA and a projection of the random chain. (Reproduced from Davies, G.R. and Ward, I.M. (1988) High Modulus Polymers (eds A.E. Zachariades and R.S. Porter), Marcel Dekker, New York, pp. 37–69. Copyright (1988) Taylor and Francis.)*

only, with two other copolymers that incorporate terephthalic acid (TA) dihydroxynaphthalene (DNA) and biphenol (BP) [43]. The compositions of the four copolymers to be discussed are shown in Table 10.5. The most instructive comparisons come from consideration of the dynamic mechanical loss factors in shear (Figure 10.18) and the dielectric loss data (Figure 10.19). It can be seen that there are three relaxation processes, labelled α, β and γ. Because these polymers are essentially single phase, it is possible to seek an understanding entirely in terms of molecular relaxation processes. The relatively high intensity of the β relaxation in CO 30/70 identifies this relaxation with the naphthalene residue because this has the highest concentration in all these polymers. It is clear from comparison with CO 2,6 (where the naphthalene residue is linked by oxygen) that the relaxation does not depend on whether it is linked to carbonyl or ether oxygen. This is not

Table 10.5   *Chemical compositions of thermotropic liquid crystalline polymers.*

Polymer	Composition (mole fraction in %)				
	HBA	HNA	TA	DHN	BP
CO 73/27	73	27			
CO 30/70	30	70			
CO 2,6	60		20	20	
COTBP	60	5	17.5		17.5

HBA, 4-hydroxybenzoic acid; HNA, 2-hydroxy 6-naphthoic acid; TA, terephthalic acid; DHN, 2,6 dihydroxynaphthalene; BP, 4,4′ biphenyldiol.
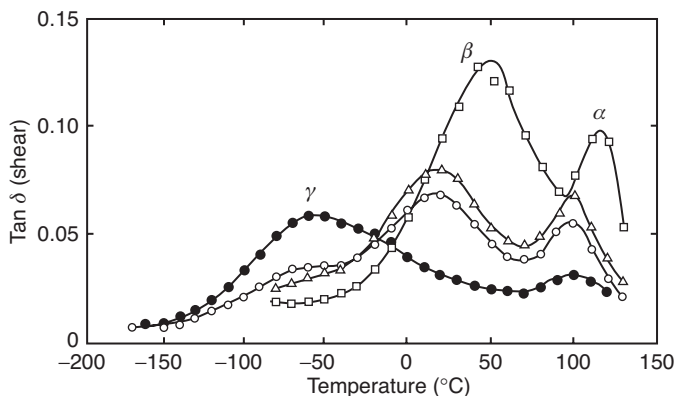
Figure 10.18   *Dynamic mechanical loss factor (shear) for CO 30/70 (□), CO 73/27 (△), CO 2,6 (○) and COTBP (●). (Reproduced from Green, D.I., Ahaj-Mohammed, M.H., Abdul Jawad, S., Davies, G.R. and Ward, I.M. (1990) Mechanical and dielectric relaxations in liquid crystalline copolyesters. Polym. Adv. Tech., 1, 41. Copyright (1990) John Wiley & Sons, Ltd.)*

true for the dielectric relaxation; the results in Figure 10.19 show that the β relaxation is not observed in CO 2,6, where the carbonyl groups are not attached to the benzene rings.

The γ relaxation is associated with the motion of phenylene groups, and this is shown most clearly by comparison of the dielectric relaxations for the CO 73/27 and CO 30/70 copolymers. These results suggest that the carbonyl group is strongly coupled to the aromatic ring to which it is attached so that in this case there is a direct correlation between the mechanical and dielectric relaxations.
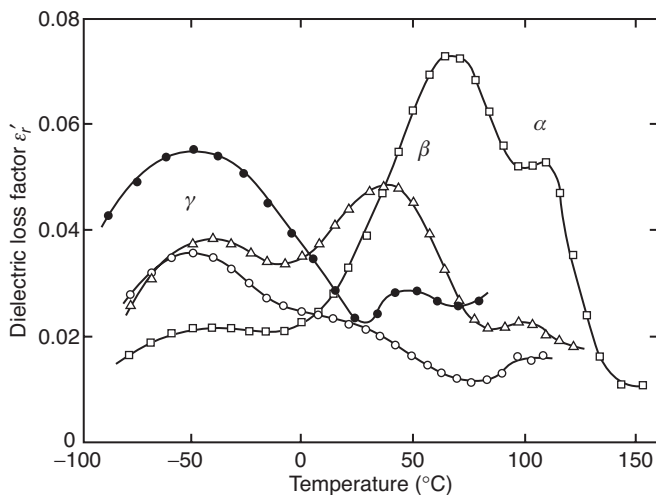
Figure 10.19   *Dielectric loss data for CO 73/27(△), CO 30/70 (□), CO 2,6 (○) and COTBP (●). (Reproduced from Ward, I.M. (1993) Relaxation processes in oriented liquid crystalline polymers. Macromol. Chem. Macromol. Symp., 69, 75. Copyright (1993) Hüthig & Wepf Verlag.)*
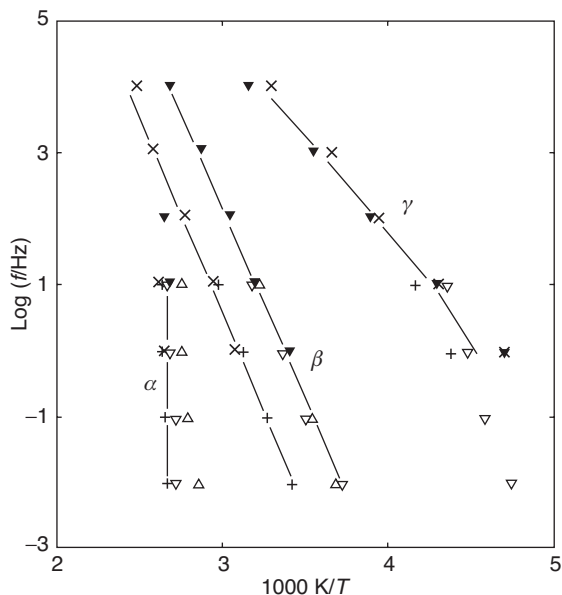
Figure 10.20 *Loci of loss maxima. Mechanical tan δ for oriented specimens: (△) CO 73/27; (□) CO 30/70: Dielectric ε'' for isotropic specimens: (▼) CO 73/27; (×) CO 30/70. (Reproduced from Troughton, M.J., Davies, G.R. and Ward, I.M. (1989) Dynamic mechanical properties of random copolyesters of 4-hydroxybenzoic acid and 2-hydroxy-6-naphthoic acid. Polymer, **30**, 58. Copyright (1989) Elsevier Ltd.)*

Further information is obtained by measurements at different frequencies to determine the activation energies of these relaxations. As shown in Figure 10.20 and Table 10.6, measurements at frequencies from 10^{-2} to 10^4 Hz, combining dynamic mechanical and dielectric measurements, yield activation energies of ≈ 120 kJ/mol for the β relaxation, similar energies for the γ relaxation but a very high activation energy for the α process. These results are consistent with assigning the α relaxation to the glass transition and the other relaxations to local processes. These conclusions have been confirmed by NMR studies, including measurements on deuterated polymers by Ward and co-workers [44].

There are several conclusions to be made regarding the relaxation behaviour of these thermotropic liquid crystalline polymers that have broad implications. First, there is a very

Table 10.6 *Activation energies for mechanical and dielectric data.*

Sample	Activation energy (kJ/mol)			
(U, unannealed; A, annealed)	Method	α	β	γ
CO 73/27 U	Tensile tan δ	460	130	
CO 73/27 A	Tensile tan δ	880	110	160
CO 30/70 A	Tensile tan δ	1600	130	
Isotropic CO 73/27 and CO 30/70	Dielectric ε''	~700	100	50

clear identification of the relaxations with the molecular structure. Secondly, the tensile and shear modulus fall very greatly with increasing temperature. This is the downside of incorporating sufficient mobility within the chains to permit melt processing, rather than the solution processing of the stiff chain lyotropic liquid crystalline polymers. Finally, it is to be noted that the shear moduli are low ($\approx$1 GPa), which leads to low compressive strengths [45].

10.4   Conclusions

We have seen that there is a general understanding of the main factors that can modify the relaxation behaviour of non-crystalline polymers. With semi-crystalline polymers, it is frequently possible to attribute each relaxation to either the crystalline component or the amorphous component or to an interaction whereby the crystalline component constrains motions in the less well-ordered material. For polyethylene, considerable progress has been made in unravelling the complex relaxation processes, although it is far from clear whether measurements indicate that two or more mechanisms can operate simultaneously, with the dominant mechanism being dependent on structural features such as the density of branch points. Progress has also been made towards understanding relaxation mechanisms in other polymers, which we have no space to discuss. For these materials, a smaller amount of structural information is available than is the case for polyethylene, so we cannot hope for a complete picture of relaxation behaviour. Nevertheless, the methods used for elucidation of the relaxations in polyethylene can provide guidelines for future advancement.

References

1. Deutsch, K., Hoff, E.A. and Reddish, W. (1954) Relation between the structure of polymers and their dynamic mechanical and electrical properties. 1. Some alpha-substituted acrylic. *J. Polym. Sci.*, **13**, 565.
2. Powles, J.G., Hunt, B.I. and Sandiford, D.J.H. (1964) Proton spin lattice relaxation and mechanical loss in a series of acrylic polymers. *Polymer*, **5**, 505.
3. Sinnott, K.M. (1960) Nuclear magnetic resonance and molecular motion in polymethyl acrylate, polymethyl methacrylate and polyethyl methacrylate. *J. Polym. Sci.*, **42**, 3.
4. Heijboer, J. (1965) *Physics of Non-Crystalline Solids*, North-Holland, Amsterdam, p. 231.
5. McCrum, N.G., Read, B.E. and Williams, G. (1967) *Anelastic and Dielectric Effects in Polymeric Solids*, John Wiley & Sons, London.
6. Roberts, G.E. and White, E.F.T. (1973) *The Physics of Glassy Polymers*, Applied Science Publishers Ltd, London, p. 212.
7. Monnerie, L., Lauprêtre, F.O. and Halary, J.L. (2005) Investigation of solid-state transitions in linear and crosslinked amorphous polymers. *Adv. Polym. Sci.*, **187**, 35–213; (2011) *Polymer Materials: Macroscopic Properties and Molecular Interpretations*, John Wiley & Sons, Hoboken, New Jersey.

8. Maxwell, A.S., Ward, I.M., Lauprêtre, F. *et al.* (1998) Secondary relaxation processes in polyethylene terephthalate-additive blends: 1. N.m.r. investigation. *Polymer*, **39**, 6835–6849.

9. Maxwell, A.S., Monnerie, L. and Ward, I.M. (1998) Secondary relaxation processes in polyethylene terephthalate-additive blends: 2. Dynamic mechanical and dielectric investigations. *Polymer*, **39**, 6851.

10. Aoki, Y. and Brittain, J.O. (1977) Isothermal and nonisothermal dielectric relaxation studies on polycarbonate. *J. Polym. Sci. Polym. Phys.*, **14**, 1297.

11. Katana, G., Kremer, F., Fischer, E.W. *et al.* (1993) Broad-band dielectric study on binary blends of bisphenol-a and tetramethylbisphenol-a polycarbonate. *Macromolecules*, **26**, 3075–3080.

12. Walton, J.H., Lizak, M.J., Conradi, M.S. *et al.* (1990) Hydrostatic pressure dependence of molecular motions in polycarbonates. *Macromolecules*, **23**, 416–422.

13. Vincent, P.I. (1965) *The Physics of Plastics* (ed. P.D. Ritchie), Iliffe, London.

14. Fox, T.G. and Flory, P.J. (1950) 2nd- order transition temperatures and related properties of polystyrene. 1. Influence of molecular weight. *J. Appl. Phys.*, **21**, 581; (1954) The glass temperature and related properties of polystyrene-influence of molecular weight. *J. Polym. Sci.*, **14**, 315.

15. Nielsen, L.E. (1962) *Mechanical Properties of Polymers*, Van Nostrand-Reinhold, New York.

16. Gordon, M. and Taylor, J.S. (1952) Ideal copolymers and the 2nd-order transitions of synthetic rubbers. 1. Non-crystalline copolymers. *J. Appl. Chem.*, **2**, 493.

17. Mandelkern, L., Martin, G.M. and Quinn, F.A. (1957) Glassy state transitions of poly-(chlorotrifluoroethylene), poly-(vinylidene fluoride), and their copolymers. *J. Res. Natl. Bur. Stand.*, **58**, 137; Fox, T.G. and Loshaek, S. (1955) Influence of molecular weight and degree of crosslinking on the specific volume and glass temperature of polymers. *J. Polym. Sci.*, **15**, 371.

18. Wolf, K. (1951) Beziehungen zwischen mechanischem und elektrischem Verhalten von Hochpolymeren. *Kunststoffe*, **41**, 89.

19. Boyd, R.H. (1985) Relaxation processes in crystalline polymers – molecular interpretation – a review. *Polymer*, **26**, 1123.

20. Boyd, R.H. (1985) Relaxation processes in crystalline polymers – experimental behavior – a review. *Polymer*, **26**, 323.

21. Takayanagi, M. (1963) Viscoelastic properties of crystalline polymers. *Mem. Fac. Eng, Kyushu Univ.*, **23**, 1.

22. Illers, K.H. and Breuer, H. (1963) Molecular motions in polyethylene terephthalate. *J. Colloid. Sci.*, **18**, 1.

23. Kilian, H.G., Halboth, H. and Jenckel, E. (1960) X-ray photographic examination of the melting and crystallization behavior of poly(ethylene terephthalate) (PET). *Kolloid Z.*, **176**, 166.

24. Coburn, J.C. (1984) PhD Dissertation. University of Utah.

25. English, A.D. (1984) Macromolecular dynamics in solid poly(ethylene-terephthalate)–H-1 and C-13 solid-state NMR. *Macromolecules*, **17**, 2182.

26. Ward, I.M. (1960) Nuclear magnetic resonance studies of polyethylene terephthalate and related polyesters. *Trans. Faraday Soc.*, **56**, 648.

27. Matthews, R.G., Ward, I.M. and Capaccio, G. (1999) Structural heterogeneity and dynamic mechanical relaxations of ethylene α-olefin copolymers. *J. Macromol. Sci. Phys.*, **37**, 51.

28. Matthews, R.G, Unwin, A.P., Ward, I.M. *et al.* (1999) A comparison of the mechanical relaxation behavior of linear low and high density polyethylenes. *J. Macromol. Sci. Phys. B*, **38**, 123.

29. Stachurski, Z.H. and Ward, I.M. (1969) Mechanical relaxations in polyethylene. *J. Macromol. Sci. Phys. B*, **3**, 445.

30. Hay, I.L. and Keller, A. (1967) A study on orientation effects in polyethylene in the light of crystalline texture. *J. Mater. Sci.*, **2**, 538; Seto, T. and Hara, T. (1967) *Rep. Prog. Polym. Phys. (Japan)*, **7**, 63.

31. Stachurski, Z.H. and Ward, I.M. (1968) β relaxations in polyethylenes and their anisotropy. *J. Polym. Sci. A2*, **6**, 1817.

32. Davies, G.R. and Ward, I.M. (1969) The anisotropy of dielectric relaxation in oxidised low density polyethylene. *J. Polym. Sci.*, **B7**, 353.

33. Mansfield, M. and Boyd, R.H. (1978) Molecular motions, alpha-relaxation and chain transport in polyethylene crystals. *J. Polym. Sci. Phys. Ed.*, **16**, 1227.

34. Willbourn, A.H. (1958) The glass transition in polymers with the $(CH_2)_n$ group. *Trans. Faraday Soc.*, **54**, 717.

35. Schatzki, T.F. (1962) Statistical computation of distribution functions of dimensions of macromolecules. *J. Polym. Sci.*, **57**, 337.

36. Boyer, R.F. (1963) The relation of transition temperatures to chemical structure in high polymers. *Rubber Rev.*, **36**, 1303.

37. Pechhold, W., Blasenbrey, S. and Woerner, S. (1963) Eine Niedermolekulare Modell-substanz fur Lineares Polyathylen – Vorschlag des Kinkenmodells zur Deutung des Gamma- und Alpha- Relaxationsprozesses. *Kolloid-Z, Z. Polym.*, **189**, 14.

38. Calundann, G.W., British Patent 1,585,511 (priority 13 May 1976, USA) (US Patent 4067 852).

39. Donald, A.M. and Windle, A.H. (1992) *Liquid Crystalline Polymers*, Cambridge University Press, Cambridge, p. 162.

40. Yoon, H.N. and Jaffe, M. Abstract Paper, 185th Am. Chem. Soc. Natl. Meet., Seattle, WA, ANYL-72.

41. Blundell, D.J. and Buckingham, K.A. (1985) The b-loss process in liquid-crystal polyesters containing 2,6-naphthyl groups. *Polymer*, **26**, 1623.

42. Davies, G.R. and Ward, I.M. (1988) *High Modulus Polymers* (eds A.E. Zachariades and R.S. Porter), Marcel Dekker, New York, pp. 37–69.

43. Ward, I.M. (1993) Relaxation processes in oriented liquid crystalline polymers. *Makromol. Chem. Macromol. Symp.*, **69**, 75.

44. Allen, R.A. and Ward, I.M. (1991) Nuclear magnetic resonance studies of highly oriented liquid crystalline co-polyesters. *Polymer*, **32**, 202.

45. Ward, I.M. and Coates, P.D. (2001) in *Solid Phase Processing of Polymers* (eds I.M. Ward, P.D. Coates and M.M. Dumoulin), Hanser, Munich, pp. 1–10.

11

Non-linear Viscoelastic Behaviour

In Chapter 5, we introduced linear viscoelasticity. In this scheme, the observed creep or stress relaxation behaviour can be viewed as the defining characteristic of the material. The creep compliance function – the ratio of creep strain $e(t)$ to the constant stress σ – is a function of time only and is denoted as $J(t)$. Similarly and necessarily, the stress relaxation modulus, the ratio of stress to the constant strain, is the function $G(t)$. Any system in which these two conditions do not apply is *non-linear*. Then, the many useful and elegant properties associated with the linear theory, notably the Boltzmann superposition principle, no longer apply and theories to predict stress or strain are approximations that must be supported by experiment.

The non-linearity may arise for a variety of reasons. First, the linear theory has been developed for small strains,[1] and to generalise it to large strain requires decisions on the appropriate definitions of both strain and stress, in effect making it necessary to create a new theory. Typical polymer applications may require the material to operate at strains in excess of 10%, and for elastomers the strains may be up to several hundred percent. Secondly, even at small strains linear behaviour may not be obtained. The behaviour may be quite rich, with the possibility of the polymer being initially linear but becoming non-linear at large times.

There is not at present a representation of non-linear viscoelasticity that gives an adequate description of the behaviour and provides some physical insight into the origins of this behaviour. This is a subject where the divergence of the experimentalist and the theoretician is most marked. Faced with non-linear viscoelastic behaviour, the experimentalist makes a number of measurements, necessarily finite, and then reduces his data empirically to a series of equations relating stress, strain and time. Although these equations can be extremely valuable in reducing the experimental data to manageable proportions, they often do not reveal anything of the essential nature of the non-linearity, and may even be misleading in this respect.

---

[1] By 'small strains', we mean that only linear terms in the strain–displacement equations are required (Section 3.1.5).

The theoretician, on the other hand, will attempt to form a constitutive relation of a most general nature and examine how the form of this relation is determined by such features as 'short-term' memory, material symmetry and invariance under rigid body rotation. The disadvantage of this approach is that in many cases it is too general. The experimentalist may well conclude that it is of no relevance to his particular problem, particularly if it does not appear to provide any physical insight into the situation.

As the subject of non-linear viscoelastic behaviour cannot be provided with an approach that satisfies all these requirements, the various attempts to deal with the situation will be considered under three headings:

1. *The engineering approach*. The design engineer requires the ability to predict behaviour exactly for a proposed situation in terms of as few initial experiments as possible. Empirical relations that describe the performance are adequate, and these need not have any physical significance.
2. *The rheological approach*. There has been a rich variety of attempts to create formal descriptions of non-linear behaviour beginning in the early 1950s. Some have taken the form of generalisations of linear theory, such as those that resemble the Boltzmann integral – the so-called single-integral theories. More complex approaches have involved the use of multiple integrals. A limited number of theoretical descriptions remain in active use at present. To retain the context, we shall give a generally inclusive historical introduction, and then proceed to develop further the more successful attempts.
3. *The molecular approach*. The starting point in this case is the incorporation of a thermally activated rate process as the viscous element in a model representation. This approach has the attraction of possible identification of molecular mechanisms and hence links with structural understanding. Although there may be disadvantages in respect of the formal mathematical development, these are to some extent balanced by the advantages of built-in non-linearity and temperature dependence.

There is a limited coverage of this field by textbooks. A theoretical survey, using sophisticated mathematical methods, is given in the text by Lockett [1], and the contrasting approach of the practical engineer is typified in the work of Turner [2]. Ferry's textbook [3] covers both theoretical and practical aspects of polymer viscoelasticity. The more recent work of Lakes [4] covers some aspects of non-linearity.

11.1 The Engineering Approach

11.1.1 Isochronous Stress–Strain Curves

The aim here is to predict the behaviour for a proposed application, using the minimum of experimental data. A general picture of non-linear viscoelastic polymer is shown in Figure 11.1. Empirical relations between stress, strain and time can be obtained that will approximately reproduce that part of the surface of Figure 11.1 that is of practical interest. These relations may have no physical significance, and their use may be restricted to very specific stress or strain programmes. In the general case, creep curves need to cover the complete range of stresses over as long a period of time as feasible. However, Turner [2] has shown that when stress and time dependence are approximately separable, it may be
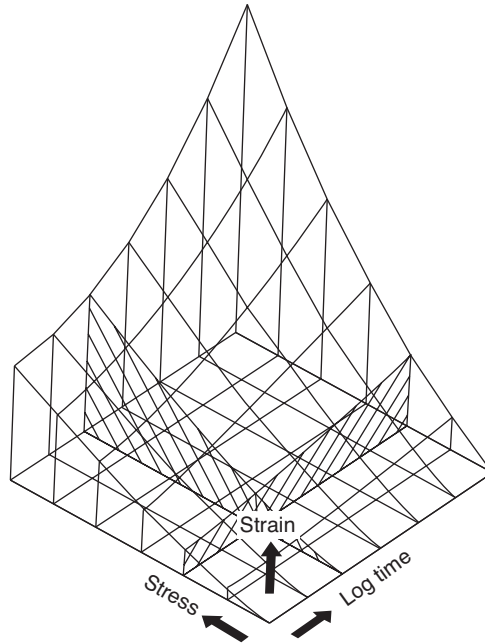
Figure 11.1 *The stress–strain time relation obtained from creep. (Reproduced from Turner, S. (1966) The strain response of plastics to complex stress histories. Polym. Eng. Sci., **6**, 306. Copyright (1966) Society of Plastics Engineers.)*

possible to interpolate creep curves at intermediate stresses from a knowledge of two creep curves, combined with a knowledge of the stress–strain curve for a fixed time (say 100 s): so-called isochronal stress–strain curves represented by the vertical lines in Figure 11.2. However, these data cannot give a generally accurate prediction of the non-linear response. When, for instance, the rate of strain applied to a polymer specimen is changed abruptly, a transient 'bump' in stress will be produced in the stress–strain curve; this will not be reproduced in the corresponding path across the smooth surface of Figure 11.1.

11.1.2 Power Laws

To describe the creep behaviour of glassy or tough polymers where the creep strains involved are small (~5% say), as distinct from elastomers where the deformations are large (~100% say), separable stress and time functions have been proposed.

Pao and Marin [5, 6] followed the approach originally suggested by Marin and others for metals [7], where the total creep strain e is considered to consist of three independent components, an elastic strain e_1, a transient recoverable viscoelastic strain e_2 and a permanent non-recoverable plastic strain e_3. At constant stress, the elastic strain is given by $e_1 = \sigma/E$, where E is Young's modulus. The viscoelastic strain is defined by integrating the condition that the transient creep is a function of the stress σ and the transient creep strain, that is $de_2/dt = f(e_2, \sigma)$. The plastic strain is found by integrating the condition that the plastic strain rate is a function of stress only. For simplicity, the functions of stress for
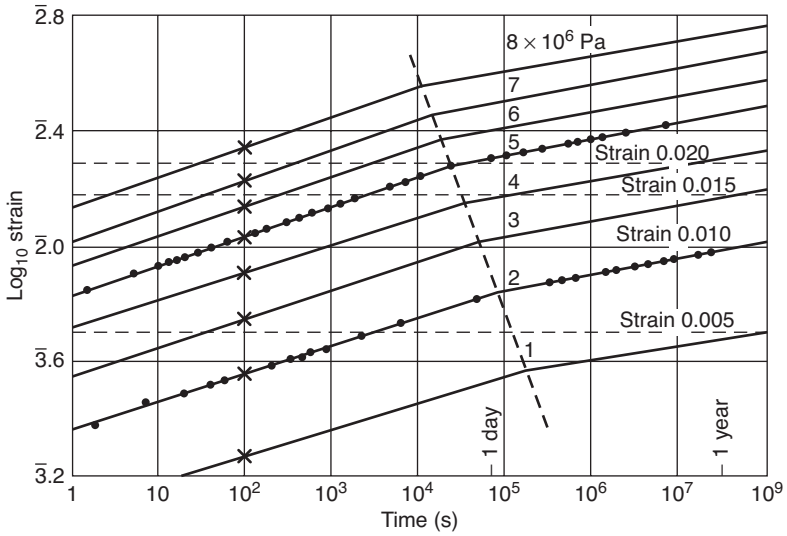
Figure 11.2 *Tensile creep of polypropylene at 60°C. The stress and time dependence are approximately separable and therefore creep curves at intermediate stresses can be interpolated from a knowledge of two creep curves (•) and the isochronous stress–strain relationship (×). (Reproduced from Turner, S. (1966) The strain response of plastics to complex stress histories. Polym. Eng. Sci.,* **6**, *306. Copyright (1966) Society of Plastics Engineers.)*

both the viscoelastic and the plastic strains are assumed to be simple power laws of stress, and most usually the same power law is adopted.

The total creep strain for loading under a constant stress σ is then proposed to be

$$e = \frac{\sigma}{E} + K\sigma^n(1 - e^{-qt}) + B\sigma^n t, \tag{11.1}$$

where K, n, q and B are material constants.

Findley and his collaborators [8] have attempted to fit the creep of many plastics and plastic laminates to analytical relationships similar to those suggested for metals [9]. It was found that the creep strain e_c at time t could be related by an equation of the form

$$e_c(t) = e_0 + mt^n,$$

where e_0 and m are functions of stress for a given material and n is a material constant. Further work revealed possible forms for these functions of stress:

$$e_c(\sigma, t) = e_0' \sin h\frac{\sigma}{\sigma_e} + m't^n \sin h\frac{\sigma}{\sigma_m},$$

where m', σ_e and σ_m are material constants. This equation was a good fit to single-step creep data, and so represents Turner's stress–strain time surface of Figure 11.1. It has also been shown to fit accurately the creep data of graphite–epoxy composites [10].

A similar relationship was found for the creep of nitrocellulose by Van Holde [11]. He proposed that

$$e_c(t) = e_0 + m't^{1/3} \sin \alpha\sigma,$$

where α is a constant. Since both m' and $\sin \alpha \sigma$ are constant for constant stress, under creep conditions this relationship reduces to the Andrade creep law for metals [12]

$$e_c(t) = e_0 + \beta' t^{1/3},$$

where β' is a constant. If e_0 and β' are proportional to stress, this equation is consistent with *linear* viscoelastic behaviour. Plazek and his collaborators [13] have suggested that the Andrade creep law holds for several polymers and gels, although there is a divergence from linear behaviour at long times.

Findley's empirical equations are very useful to design engineers for constant stress loading conditions as they can predict the creep of a given material once the required material parameters are known.

The empirical approaches suggested so far have two principal limitations:

1. They do not provide a general representation for creep, recovery and behaviour under complicated loading conditions.
2. Creep data in these formulations cannot be simply related to stress relaxation and dynamic mechanical data.

11.2   The Rheological Approach

11.2.1   Historical Introduction to Non-linear Viscoelasticity Theory

The history of non-linear viscoelasticity is complex. On the one hand, it has become apparent that there are no exact mathematical approaches that give rise to tractable results. On the other hand, there is a clear technological motivation to develop methods that can give predictions of practical value. The tension between complexity and practicality has given rise to some interesting approaches that vary between the highly formal and the pragmatic. Over the decades, a process of selection has taken place, in which some initially promising theories have fallen out of use and essentially become extinct while others have maintained their presence. This has been influenced by the extent of the experimental programmes that the theories demand, and by the growth in the application of numerical methods, for which some approaches are better adapted. Thus we have seen the relative neglect of complex multiple-integral models and the progress in the practical application of rate-dependent plasticity approaches.

Wineman [14] has recently reviewed the field of non-linear viscoelasticity, noting its 40-year history, and the limited number of engineering applications hitherto. Drapaca, Sivaloganathan and Tenti [15] have also produced a review, in which they note the large variety of different and seemingly unconnected theories.

11.2.1.1   *Adaptations of Linear Theory*

The differential approach to linear viscoelasticity can be modified to accommodate non-linearity. There have been two principal attempts using this approach that have had significant impact. In the first, Smith [16] generalised linear theory to large strain, using an analysis that can be viewed as a generalisation of the Maxwell model. In the contrasting approach of Kitagawa, Mori and Matsutani [17], the differential equation of the standard linear solid

formed the starting point. Both approaches continue to make significant contributions, and will be discussed further below.

Non-linear viscoelastic theories can also be created by generalising the Boltzmann superposition principle (see Chapter 5). Leaderman [18], working on polymer fibres, was the first to do this and Findley and Lai [19] have adopted a similar approach. Non-linearity is introduced into the Boltzmann integral by including strain or stress dependence into the integrand. Leaderman's integral takes the form

$$e(t) = \int\limits_{-\infty}^{t} J(t - \tau) \frac{\mathrm{d}}{\mathrm{d}\tau} f\{\sigma(\tau)\} \, \mathrm{d}\tau \tag{11.2}$$

for the strain in terms of the stress history. Here, f is a function that is to be determined experimentally for each polymer. The form of the integrand indicates that it has been assumed that the creep compliance is separable into functions of time and of stress. Particular forms of separability of the creep compliance (or equivalently, of the separability of the stress relaxation modulus into functions of strain and time) define different single-integral models. The most general form, in which there is no assumption of separability, is that due to Pipkin and Rogers [20] and is the first term of the multiple-integral series discussed below. These single-integral forms are still being developed and applied, and will be discussed further in the chapter. They can be viewed as forms of the principle of *non-linear* superposition, in contrast with the linear superposition of Boltzmann.

11.2.1.2   Multiple-Integral Theories – Green and Rivlin, Pipkin and Rogers

Green and Rivlin [21] made minimal physical assumptions, to the effect that

1. Stresses are 'objective', such that different observers will derive consistent results; and
2. The stress depends only on the history of the strain, or equivalently that the strain depends only on the stress history.

Taking a purely mathematical approach to the concept embodied in (2), they made use of the Fréchet series of multiple integrals to express it. In the one-dimensional case, for the strain e at time t in terms of the history of stress σ this takes the form

$$e(t) = \int\limits_{-\infty}^{t} J_1(t - \tau_1)\dot{\sigma}(\tau_1)\mathrm{d}\tau_1 + \int\limits_{-\infty}^{t}\!\!\int J_2(t - \tau_1, t - \tau_2)\dot{\sigma}(\tau_1)\dot{\sigma}(\tau_2)\mathrm{d}\tau_1\mathrm{d}\tau_2$$

$$+ \int\!\!\int\!\!\int\limits_{-\infty}^{t} J_3(t - \tau_1, t - \tau_2, t - \tau_3)\dot{\sigma}(\tau_1)\dot{\sigma}(\tau_2)\dot{\sigma}(\tau_3)\mathrm{d}\tau_1\mathrm{d}\tau_2\mathrm{d}\tau_3 + \cdots. \tag{11.3}$$

There is an identical form of this infinite series for the stress in terms of the strain history. In both cases, the first term is recognisable as the Boltzmann integral (see Chapter 5).

To use this theory, it is necessary to evaluate a sufficient number of the functions J_i, the 'kernel functions' that are essentially the material parameters, so that the series can be calculated to give an acceptable level of accuracy of the stress or strain prediction. In the years following the proposal of the theory, there were a number of specific applications to polymers. A broader discussion centred around several issues, principally: the size

of the experimental programme needed to derive the J_i; their physical significance; the practicality of determining them with sufficient accuracy and the convergence of the series (11.3). Haddad [22] has given a brief account of this discussion.

Early applications were to relatively simple stress or strain histories. Ward and Onat [23], working on the creep of oriented polypropylene, noted the inadequacy of Leaderman's approach in representing their results. One critical aspect was that the initial linear elastic response predicted by Leaderman was not mirrored in the polypropylene results. Furthermore, Leaderman's restrictive assumption for the form of the integral kernel function – its separability into functions of stress and of time – led to the prediction of identical creep and recovery curves at the same stress, another qualitative difference from the polypropylene observations. This was their motivation for exploring the Green–Rivlin theory. They concluded that for their study, only the first and third terms of Equation (11.3) were required for an adequate representation. Later, however, Hadley and Ward [24] also working on polypropylene, concluded that in general more terms were needed, depending on load level and step duration.

On the subject of practicality of the multiple-integral representation, Turner [2] has remarked that there are in general 'great difficulties' in defining a suitable experimental programme to determine the kernel functions. Lockett [1, 25] has quantified the size of an adequate experimental programme and concluded that it is in general impractically large, even for the one-dimensional case. In three dimensions, having made the simplification of incompressible material, he estimated that a programme of 287 experiments would be required for a satisfactory representation. He remarked that this 'demonstrates the futility of mathematical theories which do not consider the consequent experimental requirements' (Reference [1], p. 95).

Another aspect that relates to practicality is the degree of accuracy required for the experiments. Gradowczyk [26] has shown that the kernel functions are very sensitive to experimental error, and that as the number of terms in the representation is increased, so do the errors in the higher order terms. Thus, a point is reached at which the benefit in accuracy of adding a higher order term is outweighed by the accompanying uncertainty in its value.

11.2.1.3   *The Implicit Equation Approach*

Brereton *et al*. [27] proposed a radical approach to multiple-integral theories by recognising that formulations were possible other than the explicit expressions like Equation (11.3) for stress or their analogues for strain. They considered an implicit equation, which after truncation took the symbolic form

$$a\sigma + be + c\sigma e = 0, \tag{11.4}$$

where the first, second and third terms are, respectively, integral expressions in stress, strain and the product stress $\times$ strain. With the series truncation having been applied to the implicit form, explicit forms for the stress in terms of the strain history or for the strain in terms of the stress history could be generated for particular strain or stress inputs, and series expansions of Equation (11.3) are avoided. After some modelling of the kernel functions, predictions were generated for three diverse polymers in stress relaxation, creep and for a range of constant strain rates. Strikingly accurate predictions were made of the linearity

with stress of the creep compliance at short and long times, and correspondingly of the linearity with strain of the stress relaxation modulus at short and long times.

11.2.1.4   Pipkin and Rogers

Some discussion has taken place on the physical significance of the terms in the Green–Rivlin expansion. The first term corresponds to linear viscoelasticity, and so can be viewed as having physical significance without being related to specific mechanisms. Otherwise, since there are no physical mechanisms implicit in the theory, there would seem to be no reason to expect any direct physical interpretation. The situation seems to be analogous to the use of a polynomial function to fit to a non-linear elastic stress–strain curve. The linear term (if fitted with care) would correspond to the linear elastic regime, and any correlation of the higher order terms with physical mechanisms would be entirely coincidental. This is essentially the conclusion reached for the Green–Rivlin theory by Yannas and Haskell [28] who concluded that, apart from for the first term, the kernels have a correspondence to observable quantities that was 'either nil or else cannot be ascertained conveniently'.

To address some of the objections and difficulties of the Green–Rivlin theory outlined above, Pipkin and Rogers [20] introduced an alternative multiple-integral expansion. This takes the form

$$\sigma(t) = \int_{-\infty}^{t} \mathrm{d}_{e(\tau_1)} R_1\left[e(\tau_1), t - \tau_1\right] + \frac{1}{2!} \int \int_{-\infty}^{t} \mathrm{d}_{e(\tau_1)} \mathrm{d}_{e(\tau_2)} R_2\left[e(\tau_1), t - \tau_1; e(\tau_2), t - \tau_2\right]$$

$$+ \frac{1}{3!} \int \int \int_{-\infty}^{t} \mathrm{d}_{e(\tau_1)} \mathrm{d}_{e(\tau_2)} \mathrm{d}_{e(\tau_3)} R_3\left[e(\tau_1), t - \tau_1; e(\tau_2), t - \tau_2; e(\tau_3), t - \tau_3\right] + \cdots$$

$$(11.5)$$

for the stress in terms of the strain history. The kernel functions can be related to experimental stress relaxation results. In the first term, the quantity $R_1(e, t)$ is the stress in stress relaxation at strain e. This term includes non-linear behaviour, and is an extension of the Leaderman integral mentioned above; it is a generalisation, in that the kernel function is no longer assumed to be separable into functions of strain and time. The first term represents non-linear superposition and reproduces exactly the experimental response to single-step stress relaxation tests. It will also give approximate predictions for two-step stress relaxation tests. The second term provides the correction needed to produce the exact result for two-step tests. Thus, as the series is built up each term added suggests the experimental programme required for its evaluation. In this way, a physical interpretation is built into the theory and, since each term is non-linear, it is to be expected that fewer terms are necessary than with the Green–Rivlin approach. Most applications of the Pipkin–Rogers theory have involved the evaluation of the first term only, but Mittal and Singh [29] have applied the theory up to second order for nylon-6.

There have, however, been criticisms of the practicality of this approach. Stafford [30] has pointed out that the second term requires the evaluation of a function of four variables. He argued that this would make it less experimentally tractable than the two-variable kernel in Green and Rivlin's second term. Nevertheless Pipkin and Rogers demonstrated that the first term of their expansion was more effective than a three-term Green–Rivlin model.

The Pipkin–Rogers model was and remains a significant theoretical development since, as noted by Drapaca, Sivaloganathan and Tenti [31], many of the alternative approaches can be shown to be special cases of it.

11.2.1.5   Interpretation of Multiple-Integral Models

Further insight into multiple-integral models has been provided by Kinder and Sternstein [32]. They introduced the concept of interaction between different load or strain steps. Suppose a constant stress is applied to a specimen for a time, and then the stress level abruptly changed – a two-step creep test. For a linear material, the strain during the second step is equal to the sum of the strains that would arise from the two stress steps applied separately. The same would apply for a material obeying the principle of non-linear superposition. That the strain in a real non-linear viscoelastic material is not exactly equal to the sum of the component strains is attributed to the interaction between the two steps; the imposition of the second step changes the rate at which the strain arising from the first step is changing. They showed that each multiple-integral term in the Green–Rivlin series could be separated into a term representing non-linear superposition and other terms representing interactions. For example, the second term can be rewritten as

$$\int_0^t J_2(t-\tau, t-\tau)\mathrm{d}\sigma^2\mathrm{d}\tau$$

$$-\int_0^t \int_0^\tau [J_2(t-\tau, t-\tau) - J_2(t-\tau, t-\xi)]\mathrm{d}\sigma(\xi)\mathrm{d}\sigma(\tau) \qquad (11.6)$$

$$-\int_0^t \int_0^\tau [J_2(t-\tau, t-\tau) - J_2(t-\xi, t-\tau)]\mathrm{d}\sigma(\xi)\mathrm{d}\sigma(\tau).$$

Here, the first integral corresponds to non-linear superposition and the other terms are interaction terms. Each term in the Green–Rivlin series can be rewritten in the same way, with a single-integral term added to multiple-integral terms. When summing the whole Green–Rivlin series of expressions like Equation (11.6), the sum of all the single integrals becomes one non-linear single-integral term, representing non-linear superposition, and there remains a series of multiple integrals representing interactions. The single-integral term now suggests itself as the first term of the Pipkin–Rogers expansion for the strain in terms of the stress history, and by equating the two series, the higher order terms like those in Equation (11.6) can be similarly equated to Pipkin–Rogers terms. Kinder and Sternstein concluded that all the higher order terms in the Pipkin–Rogers expansion are interaction terms, which are transient terms with zero asymptotic value. This seems to be the closest that we can approach a physical interpretation of the multiple-integral representation.

11.2.1.6   Current Usage

It is now possible to include quite complex non-linear theories into finite element analysis schemes for engineering applications. Multiple-integral theories have made no impact in this area, most probably because of the experimental difficulties that they impose and also

the complexity of the numerical schemes required in their implementation. The other forms of constitutive equation discussed in this introduction have provided more fruitful areas for numerical exploitation. The numerical implementation of integral models is a somewhat more challenging computing problem than that for differential or rate theories. For a rate model, the strain rate at any time is calculated using the current strain and the strain at the end of the previous time step, so that only the immediately previous strains need be stored in memory. For the single-integral model, the strains at all previous time steps need to be stored, so that there is a greater memory requirement. Rate theories are thus more efficient, though, with the ongoing progress in computer technology, this consideration continues to diminish in importance. This is evidenced by recent developments [33] in which a single-integral model is being applied to the long-term deformation behaviour of poly(oxymethylene), with a view to its application within a finite element scheme.

11.2.2   Adaptations of Linear Theory – Differential Models

11.2.2.1   *Large-Strain Behaviour of Elastomers*

It is possible to take the equations of linear spring and dashpot models and adapt them to non-linear conditions. Thus, Smith [16] has described the large-strain behaviour of elastomers by taking as his starting-point the (linear) Maxwell element. Rewriting Equation (5.15), we have

$$\frac{\mathrm{d}e}{\mathrm{d}t} = \frac{\sigma}{\eta} + \frac{1}{E}\frac{\mathrm{d}\sigma}{\mathrm{d}t}.$$

Imposing a constant strain rate $\mathrm{d}e/\mathrm{d}t = R$, it can be readily shown (see Section 5.25 above) that

$$\sigma = R\tau(1 - e^{-t/\tau}),$$

where $\tau = \eta/E$, and equivalently

$$\sigma = R\tau E(1 - e^{-t/\tau}).$$

For a continuous distribution of relaxation times $H(\tau)$, equivalent to an infinite parallel array of Maxwell elements, the total stress is summed by the integral to give

$$\sigma = R \int_{-\infty}^{\infty} \tau H(\tau)(1 - e^{-t/\tau})\mathrm{d}\ln\tau.$$

With $R = e/t$, this becomes

$$\frac{\sigma}{e} = \frac{1}{t} \int_{-\infty}^{\infty} \tau H(\tau)(1 - e^{-t/\tau})\mathrm{d}\ln\tau + E_e,$$

where the term E_e, equivalent to an additional parallel elastic element, denotes the equilibrium modulus. The quantity

$$\frac{\sigma}{e} = \frac{\sigma(e, t)}{e}$$

is clearly a function of time only and is known as the *constant strain-rate modulus F(t)*. When generalised to large strain, the theory will become non-linear and *F* will be a function of both strain and time. Smith assumes that *F* is separable into a function of strain and a function of time, such that

$$F(t) = \frac{g(e)\sigma(e, t)}{e}.$$

This is also expressible as

$$\log F(t) = \log \left(\frac{g(e)}{e} \right) + \log \sigma(e, t). \tag{11.7}$$

To return linear viscoelasticity, it is required that $g(e)$ approaches unity for small strain. The stress–strain data for Smith's SBR vulcanisate rubber material are plotted in Figure 11.3(a). Log stress against log time plots were obtained for fixed strains and, as shown in Figure 11.3(b), form parallel linear relationships. This suggests via Equation (11.7) that the quantity $g(e)/e$ is independent of time. It was found that for extension ratios up to 2, $g(e) \cong 1$ provided that σ is understood to denote the true stress. At higher strains, the empirical function

$$g(e) = \lambda \exp \left(\frac{1}{\lambda} - \lambda \right)$$

was used, equivalent to that proposed by Martin, Roth and Stiehler [34].

In this approach, the non-linearity is introduced as a consequence of large deformation. We would not expect it to be generally successful for polymers as non-linearity is sometimes observed at small strains. However, similar approaches have been successful for rubbers by Guth, Wak and Anthony [35] and Tobolsky and Andrews [36].

11.2.2.2   *Creep and Recovery of Plasticised Polyvinyl Chloride*

Leaderman [37] carried the type of analysis used by Smith one stage further in analysing the creep and recovery of a sample of plasticised polyvinyl chloride (PVC). The apparently remarkable result was obtained here that the initial rate of recovery from a given load was larger than the initial creep under that load (see also Section 11.4). The situation is illustrated in Figure 11.4.

Leaderman showed that if $\frac{1}{3}(\lambda - 1/\lambda^2)$ is used as a measure of the deformation, both creep and recovery, and creep curves at different load levels, can be described by a single time-dependent function. This is shown in Figures 11.5(a) and (b). The quantity $\frac{1}{3}(\lambda - 1/\lambda^2)$ is the equivalent quantity to the Lagrangian strain measure in the theory of finite elasticity.

Let us consider why using $\frac{1}{3}(\lambda - 1/\lambda^2)$ as a measure of the deformation brings the creep and recovery curves into coincidence. As Leaderman defines, recovery (this is *not* how we have defined recovery previously in this textbook) measures the quantity

$$\frac{1}{3} \left(\lambda_1 - \frac{1}{\lambda_1^2} \right) - \frac{1}{3} \left(\lambda_2 - \frac{1}{\lambda_2^2} \right),$$
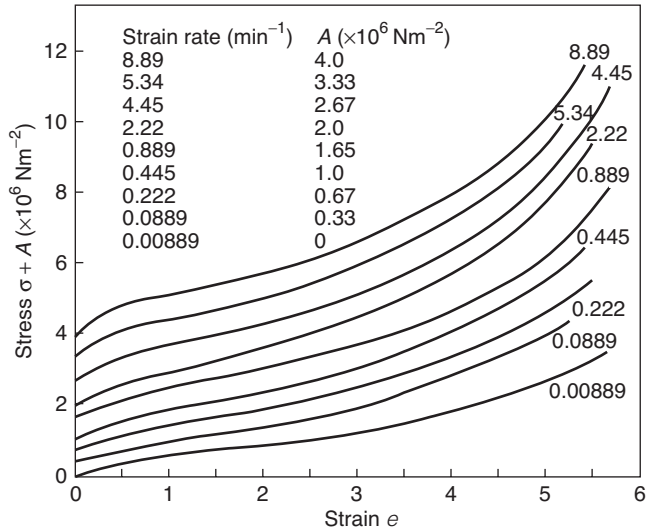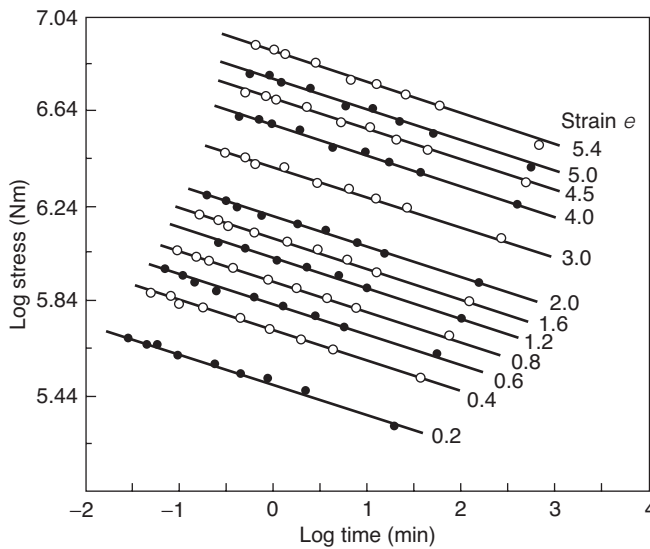
Figure 11.3   *(a) Tensile stress–strain curves of SBR vulcanised rubber at −34.4°C and strain rates between 8.89 × 10⁻³ and 8.89 min⁻¹. The stress ordinates are displaced upwards for clarity. (b) Variation of log stress with log time at different strain values, obtained from (a). The strain values are indicated for each line. (Reproduced from Smith, T.L. (1962) Nonlinear viscoelastic response of amorphous elastomers to constant strain rates. Trans. Soc. Rheol., **6**, 61. Copyright (1962) Society of Rheology.)*
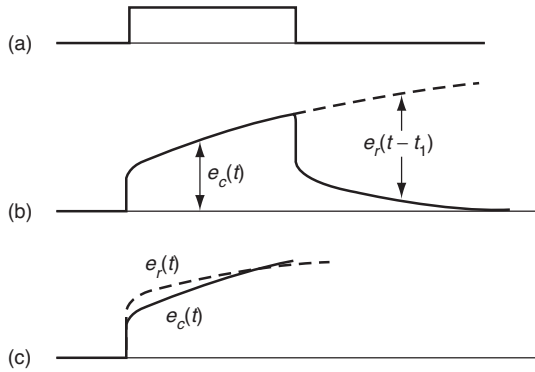
Figure 11.4   *(a) Loading programme, (b) deformation and (c) direct comparison of creep $e_c(t)$ and recovery $e_r(t)$ for a non-linear viscoelastic solid.*
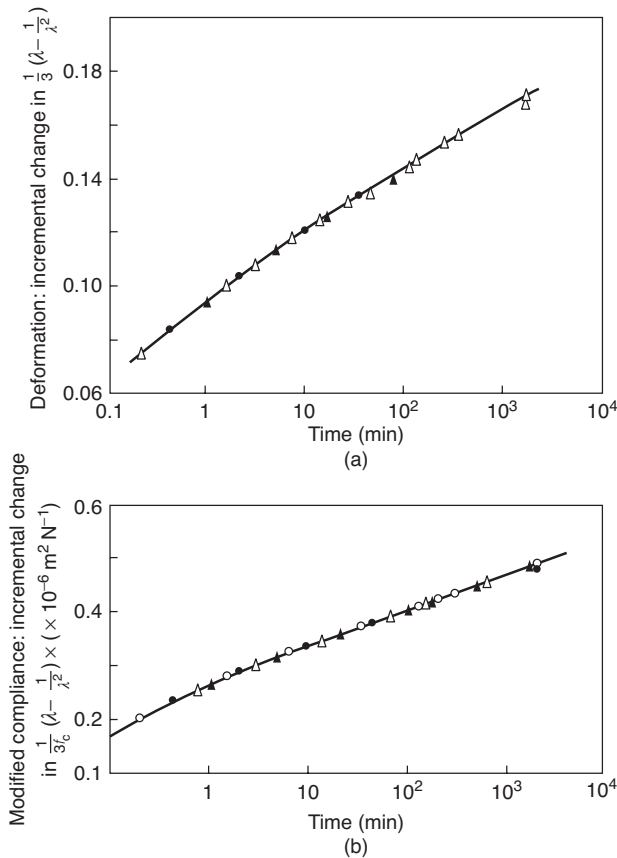
Figure 11.5   *(a) Comparison of creep ($\triangle$) and recovery ($\blacktriangle$) of plasticised polyvinyl chloride under a constant nominal stress of 0.355 MPa. (b) Creep of plasticised polyvinyl chloride under constant nominal stress: $\circ$, $f_0 = 0.444$ MPa; $\bullet$, $f_0 = 0.355$ MPa; $\triangle$, $f_0 = 0.267$ MPa; $\blacktriangle$, $f_0 = 0.178$ MPa. (Redrawn from Leaderman (1962) Trans. Soc. Rheol., **6**, 361. Copyright (1962) Society of Rheology.)*

where λ_1 is the extension at the time of unloading and λ_2 is the extension at a chosen time after unloading. If e_1 is the conventional strain at the time of unloading and e_2 is the conventional strain at a chosen time after unloading, $\lambda_1 = 1 + e_1$, $\lambda_2 = 1 + e_2$ and the recovery at small strain as defined by Leaderman in terms of conventional strain is $e_1 - e_2$.

Now, a given change in the quantity $\frac{1}{3}(\lambda - 1/\lambda^2)$ at large λ (e.g. in the recovery situation, where we change from λ_1 to λ_2), will involve a greater change in conventional strain $e_1 - e_2$ than it will at small strain (e.g. from $\lambda \approx 1$ in creep). Thus recovery curves, which coincide with creep curves using $\frac{1}{3}(\lambda - 1/\lambda^2)$ as a strain measure will have higher values than creep curves in the conventional strain representation.

11.2.2.3   Overstress Theories

While Smith's analysis above took the Maxwell model as its starting point, a useful alternative is to take the standard linear solid as the basis. This is the case in the study of polypropylene by Kitagawa, Mori and Matsutani [17] and of polyethylene by Kitagawa and Takagi [38]. The differential equation of the standard linear solid is given by Equation (5.18):

$$\sigma + \tau \frac{d\sigma}{dt} = E_a e + (E_m + E_a)\tau \frac{de}{dt}. \tag{5.18}$$

Recall that the first term on the right is equal to the stress after a long time, or equivalently the stress produced by loading at an infinitely slow rate. The equation can be generalised to

$$\sigma + K \frac{d\sigma}{dt} = f(e) + M \frac{de}{dt}, \tag{11.8}$$

where $f(e)$ is simply the stress response of the material at infinitely slow strain rate, which we no longer require to be linear. M and K are in general functions of stress, strain and their time derivatives, so that Equation (11.8) defines a non-linear material. It can be rearranged as

$$\sigma - f(e) = M \frac{de}{dt} - K \frac{d\sigma}{dt}. \tag{11.9}$$

The quantity $\sigma - f(e)$ on the left, the excess of stress over that obtaining at very slow strain rate, is termed the *overstress*; theories formulated in this way are termed *overstress theories*. This approach has been applied to metals by Lui and Krempl [39], who used the term *viscoplastic* to categorise their model. From the form of Equation (11.8), it is clear that the function K could be measured experimentally using stress relaxation tests ($\frac{de}{dt} = 0$), or that M could be measured using creep tests ($\frac{d\sigma}{dt} = 0$). Additional information can be gained from small strain, high strain rate experiments, where the response of the model can be assumed linear elastic. In these conditions, we may revert to Equation (5.18) and notice that, for fast loading, the time derivative terms become dominant, so that the elastic response of the standard linear solid is characterised by the elastic modulus $E_a + E_m$. Then, inspection of Equation (11.8) reveals that the instantaneous modulus E is given by

$$E = \frac{M}{K} \tag{11.10}$$

for small strains and fast loading. The model is simplified if Equation (11.10) is assumed to apply under all conditions, so that K and M have the same functional form; this approach was adopted by Lui and Krempl [39], Kitagawa *et al.* [17] and Kitagawa and Takagi [38].

Kitagawa *et al.* in their work on polypropylene, and Kitagawa and Takagi, working on polyethylene, used torsion testing. Their equivalent of Equation (11.9) in terms of shear stress and shear strain takes the form

$$\tau - f(\gamma) = M\frac{d\gamma}{dt} - K\frac{d\tau}{dt} \tag{11.11}$$

and Equation (11.10) becomes

$$G = \frac{M}{K}, \tag{11.12}$$

where G is the shear modulus. In both cases, K was found to depend on the overstress and on the strain, and took the form

$$K = K_0 \exp(-K_1(\gamma)(\tau - f(\gamma))), \tag{11.13}$$

where K_0 was found to be constant and

$$K_1(\gamma) = p_0 + \frac{p_1}{p_2 + \gamma} \tag{11.14}$$

with p_0, p_1 and p_2 material constants.

Stress relaxation tests were used to evaluate K. According to Equation (11.13),

$$\ln K = \ln K_0 - K_1(\gamma)(\tau - f(\gamma)) \tag{11.15}$$

suggesting the form required for graphs to show linear relationships at constant shear strain. Such a plot is shown for the polypropylene data [17] in Figure 11.6, taken at a series of strain levels. There is a good approximation to linearity, with the common intercept corresponding to the constancy of the parameter K_0. The efficacy of the model in predicting torsional stress–strain curves is shown in Figure 11.7. Here, strain rates are initially constant, but are changed abruptly to different constant rates so that transient stresses are generated. This provides a severe test for the model, which performs well.

Similar work with polyethylene [38] revealed a comparable level of accuracy. The differential approach has also been applied to high-density polyethylene by Zhang and Moore [40,41]. Brusselle-Dupend *et al.* [42] have extended the approach to a more complex model that encompasses unloading as well as loading behaviour in polypropylene.

11.2.3   Adaptations of Linear Theory – Integral Models

In the course of the extensive studies of the creep and recovery behaviour of textile fibres already referred to, Leaderman [18] became one of the first to appreciate that the simple assumptions of linear viscoelasticity might not hold even at small strains. For nylon and cellulosic fibres, he discovered that although the creep and recovery curves may be coincident at a given level of stress – a phenomenon associated with linear viscoelasticity (p. 54) – the creep compliance plots indicated a softening of the material as stress increased, except at
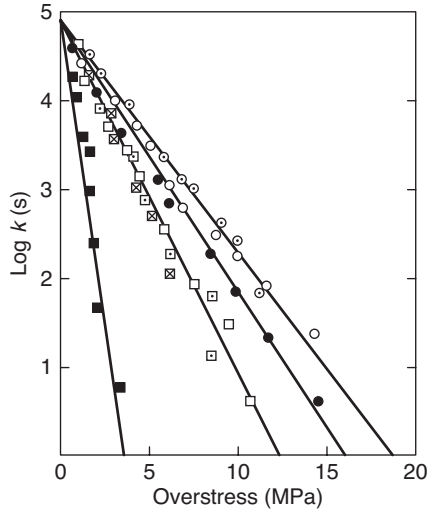
Figure 11.6   *The function K of Equations (11.11) and (11.13) for polypropylene obtained from stress relaxation at various strains, with strain applied at varying rates. Symbols correspond to ■ strain 0.01, strain rate 1.4 × 10⁻³ s⁻¹; ⊡ 0.045, 1.4 × 10⁻³; ⊠ 0.055, 1.4 × 10⁻³; □ 0.053, 1.4 × 10⁻²; ● 0.108, 1.4 × 10⁻³; ⊙ 0.253, 1.4 × 10⁻⁴; ○ 0.267, 1.4 × 10⁻³. (Reproduced from Kitagawa, M., Mori, T. and Matsutani, T. (1989) Rate-dependent nonlinear constitutive equation of polypropylene. J. Polym. Sci. B, **27**, 85. Copyright (1989) John Wiley & Sons, Ltd.)*
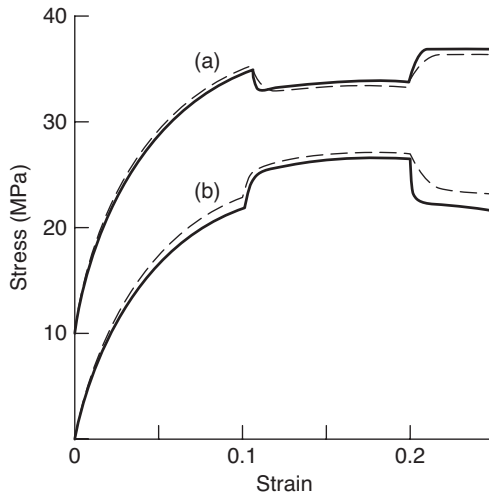
Figure 11.7   *Modelling of stress–strain curves with step changes in strain rate. (a) 1.1 × 10⁻² → 1.4 × 10⁻³ → 1.4 × 10⁻² s⁻¹. (b) 1.0 × 10⁻³ → 1.4 × 10⁻² → 6 × 10⁻⁴ s⁻¹. Curve (b) is shifted by 10 MPa along the vertical axis. (Reproduced from Kitagawa, M., Mori, T. and Matsutani, T. (1989) Rate-dependent nonlinear constitutive equation of polypropylene. J. Polym. Sci. B, **27**, 85. Copyright (1989) John Wiley & Sons, Ltd.)*
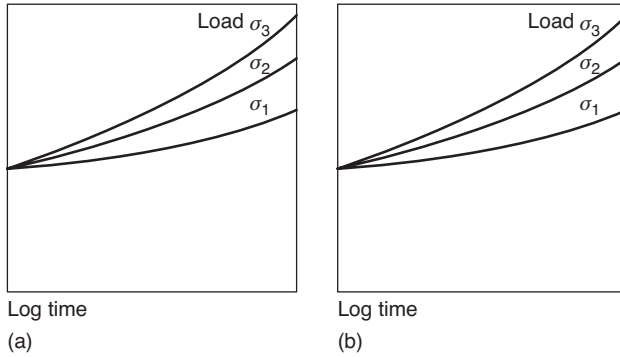
Figure 11.8 *Comparison of creep compliance (a) and recovery compliance (b) at three load levels a₁, a₂, a₃ for a non-linear viscoelastic material obeying Leaderman's modified Boltzmann superposition principle. Note that the creep and recovery curves for a given load level are identical.*

the shortest times (Figure 11.8). Thus, the creep compliance function is a function of both time and stress. For materials such as the polypropylene filament illustrated in Figure 11.9, the non-linearity is even more pronounced; at a given stress, the instantaneous recovery is greater than the instantaneous elastic deformation, although the delayed recovery proceeds at a slower rate than the preceding creep.
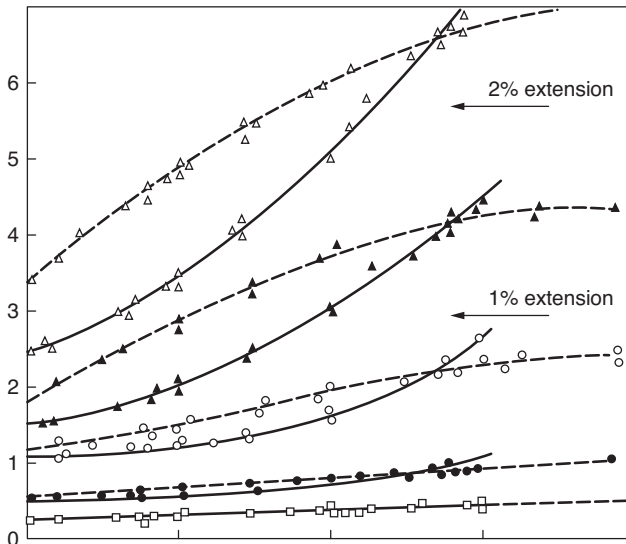
Figure 11.9 *Successive creep (———) and recovery (– – – –) for an oriented mono-filament of polypropylene of total length 302 mm. The load levels are 587 g (△), 401.8 g (▲), 281 g (●) and 67.7 g (□). (Reproduced with permission from Ward, I.M. and Onat, E.T. (1963) Non-linear mechanical behaviour of oriented polypropylene. J. Mech. Phys. Solids, **11**, 217–219. Copyright (1963).)*

Leaderman's approach, as described above in Section 11.2.1, was to modify the basic Boltzmann superposition principle of linear viscoelasticity, so that the strain was given by Equation (11.2), restated here

$$e(t) = \int\limits_{-\infty}^{t} J(t - \tau)\frac{\mathrm{d}}{\mathrm{d}\tau} f\{\sigma(\tau)\}\,\mathrm{d}\tau, \tag{11.2}$$

where $f(\sigma)$ is an empirical function of stress that depends arbitrarily on the test fibres. This form of empiricism is inadequate to describe the behaviour in loading programmes of greater complexity than creep and recovery, and emphasises that no general treatment is known to cope with the problems of non-linear viscoelasticity.

Another simple adaptation of the Boltzmann superposition principle is that of Findley and Lai [19], who worked with step stress histories applied to specimens of poly(vinyl chloride). Their theory was reformulated by Pipkin and Rogers [20] for general stress and strain histories. Pipkin and Rogers took a non-linear stress relaxation modulus $R(t,e)$ defined in differential form:

$$R(t, e) = \frac{\partial \sigma(t, e)}{\partial e}. \tag{11.16}$$

The Pipkin and Rogers integral is, for the stress in terms of the strain history,

$$\sigma(t) = \int\limits_{-\infty}^{t} \frac{\mathrm{d}e}{\mathrm{d}\tau}(\tau)R(t - \tau, e(\tau))\mathrm{d}\tau. \tag{11.17}$$

Similarly, for the strain in terms of the stress history, a creep function C was defined as

$$C(t, \sigma) = \frac{\partial e(t, \sigma)}{\partial \sigma} \tag{11.18}$$

with a corresponding integral law:

$$e(t) = \int\limits_{-\infty}^{t} \frac{\mathrm{d}\sigma}{\mathrm{d}\tau}(\tau)C(t - \tau, \sigma(\tau))\mathrm{d}\tau. \tag{11.19}$$

Pipkin and Rogers tested their model (11.19) using published data on poly(vinyl chloride) under multi-step creep conditions. This kind of testing programme consists of a constant stress being applied for pre-determined period, and then abruptly changed to a different value for a second time interval, and so on (see Figure 5.6); this testing regime gives a more severe test of the theory than, for instance, constant strain rates. As an illustration, we show their results for the five-step stress history in Figures 11.10(a) and (b).

The most significant difference between the Leaderman and the Pipkin and Rogers approach is that, in the former, the material response is separable into time and stress dependence. Thus, in Equation (11.2), there is a function f of stress multiplied by a function J of time. By contrast, in Equation (11.19), C is explicitly a function of two variables that may or may not be separable in this sense. The Pipkin and Rogers approach is thus more general and we would expect it to be capable of modelling a greater range of material behaviour.
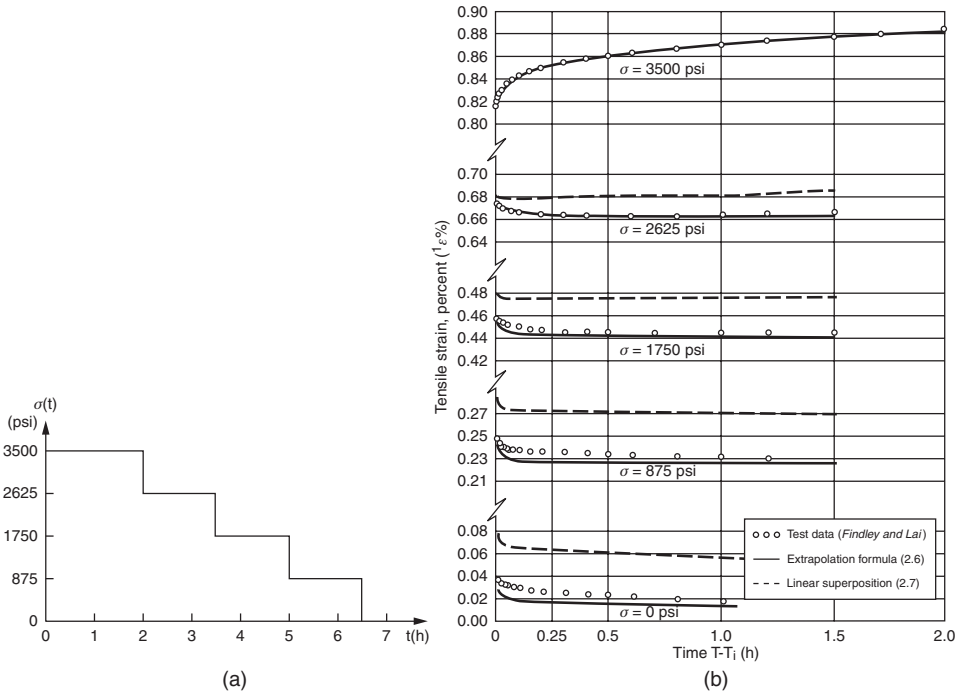
Figure 11.10   *(a) Step stress history. (b) Strain resulting from stress history in (a). Successive steps are shown from the top down. (Reproduced from Pipkin, A.C. and Rogers, T.G. (1968) A non-linear integral representation for viscoelastic behaviour. J. Mech. Phys. Solids, **16**, 59–72. Copyright (1968).)*

11.2.4   More Complicated Single-Integral Representations

11.2.4.1   The Schapery Theory

Schapery [43, 44] has used the theory of the thermodynamics of irreversible processes to produce a model that may be viewed as a further extension of Leaderman's. Schapery continued Leaderman's technique of replacing the stress by a function of stress $f(\sigma)$ in the superposition integral and also replaced time by a function of time, the *reduced time ψ*. The material is assumed to be linear viscoelastic at small strains, with a creep compliance function of the form [44]

$$J(t) = \frac{e(t)}{\sigma} = D_0 + \Delta D(t). \tag{11.20}$$

The constant term D_0 corresponds to the instantaneous elastic response (the unrelaxed compliance J_u of Equation (5.22)). In general, the strain in terms of the stress history is given by

$$e(t) = g_0 D_0 \sigma + g_1 \int_0^t \Delta D(\psi - \psi') \frac{\mathrm{d}g_2 \sigma}{\mathrm{d}\tau} \mathrm{d}\tau, \tag{11.21}$$

where the stress history is assumed to start at zero time. g_0, g_1 and g_2 are stress-dependent parameters for which $g_0 = g_1 = g_2 = 1$ at sufficiently small stresses. The reduced times are defined by

$$\Psi = \Psi(t) = \int_0^t \frac{dt'}{a_\sigma(\sigma(t'))},$$

$$\Psi' = \Psi'(\tau) = \int_0^\tau \frac{dt'}{a_\sigma(\sigma(t'))},$$

(11.22)

where the stress-dependent factor $a_\sigma = 1$ at sufficiently small stresses. The small-stress values of unity ensure that the linear Boltzmann integral is returned under these conditions. When $g_0 = g_1 = a_\sigma = 1$, and g_2 is allowed to depend on stress, Leaderman's theory results. An entirely analogous system of equations involving the stress relaxation behaviour gives the stress in terms of the strain history [44].

In the theory of Equation (11.21), four functions of stress g_0, g_1, g_2 and a_σ characterise the non-linearity and must be evaluated over the required stress range. Experimental regimes that involve periods of constant stress, during which the functions are constants, have proved useful for this purpose. For a single-step creep test at stress σ applied at time $t = 0$, the Equation (11.21) can be evaluated, noting that it contains a Duhamel integral like Equation (5.3), to give the result

$$e(t) = g_0 D_0 \sigma + g_1 g_2 \Delta D \left(\frac{t}{a_\sigma} \right) \sigma,$$

(11.23)

where Equations (11.22) have been used. Clearly, even if the low-stress linear behaviour defined by D_0 and ΔD is known, the creep test does not allow for the separation of the functions g_1, g_2 and a_σ. Schapery [44] showed how the addition of two-step creep experiments, including creep and recovery tests (in which the second step is at zero stress), could be used to generate distinct values for the parameters. This was aided by the use of a power-law approximation for the creep compliance function, such that

$$\Delta D(\psi) = D_1 \psi^n.$$

(11.24)

He showed how the use of double logarithmic plots of the recovery strain against time, obtained for different stress levels, could be related to one another by shift factors; the shift factors could then be simply related to g_1 and a_σ. The technique of step loading combined with Equation (11.23) has also been used by Crook [45] and Lai and Bakker [46]. Schapery's model has been applied to nitrocellulose, fibre-reinforced phenolic resin and polyisobutylene [44]; polycarbonate [45]; high-density polyethylene [46] and graphite–epoxy composites [10].

11.2.4.2   BKZ Theories

The theory of Bernstein, Kearsley and Zapas [47] and developments of it (e.g. Zapas and Craft [48]) – so-called BKZ theories – are aimed in particular at large-deformation

behaviour. The Gaussian model of rubber elasticity tells us that, in uniaxial stretching, the true stress σ is in the form

$$\sigma = C(\lambda^2 - 1/\lambda), \tag{11.25}$$

where C is a constant and λ is the extension ratio. This follows from Equations (3.41) or (4.31), which give the nominal or engineering stress; when nominal stress is replaced by true stress via the use of the incompressibility condition, Equation (11.25) results. The form of Equation (11.25) suggests that a theory in which the quantity $\sigma/(\lambda^2 - 1/\lambda)$ plays a central role might be particularly appropriate for large strains.

Perhaps the most important feature of the BKZ model, which distinguishes it from all the models discussed so far, is the choice of strain measure. Hitherto, all the materials have been assumed to be solids, in that they have an initial undeformed, stress-free state, which acts as a reference relative to which all strained states are measured. In BKZ theories, there is no such special state, and the material may therefore be classed as a fluid. At any 'present' time t, the state of strain is measured relative to the state at previous times τ. This is done by adopting as the strain measure the quantity $\lambda(t)/\lambda(\tau)$. Reflecting on the remarks in the paragraph above now suggests the importance of the quantity $\dfrac{\lambda^2(t)}{\lambda^2(\tau)} - \dfrac{\lambda(\tau)}{\lambda(t)}$ in a theory in which the stress depends on the strain history. The BKZ form given by Zapas and Craft [48] is, in uniaxial stretching,

$$\sigma(t) = \int\limits_{-\infty}^{t} \left(\frac{\lambda^2(t)}{\lambda^2(\tau)} - \frac{\lambda(\tau)}{\lambda(t)} \right) h\left(\frac{\lambda(t)}{\lambda(\tau)}, t - \tau \right) \mathrm{d}\tau. \tag{11.26}$$

Since τ runs through all values previous to t, the stress depends on the strain at time t as measured relative to all previous strain states. For a specimen that is unstrained prior to time $t = 0$, there are contributions to the stress at positive times from the part of the strain history occurring at times less than zero. In this respect, the theory differs from those mentioned so far. Splitting the integral in Equation (11.26) into parts before and after zero time, and setting $\lambda(\tau) = 1$ for $\tau < 0$, we obtain

$$\sigma(t) = \left(\lambda^2(t) - 1/\lambda(t) \right) \int\limits_{-\infty}^{0} h(\lambda(t), t - \tau) \mathrm{d}\tau + \int\limits_{0}^{t} \left(\frac{\lambda^2(t)}{\lambda^2(\tau)} - \frac{\lambda(\tau)}{\lambda(t)} \right) h\left(\frac{\lambda(t)}{\lambda(\tau)}, t - \tau \right) \mathrm{d}\tau. \tag{11.27}$$

In particular, for stress relaxation starting at zero time the second term is zero. We may then write

$$\sigma(t) = \left(\lambda^2 - 1/\lambda \right) H(\lambda, t), \tag{11.28}$$

where

$$h(\lambda, t) = -\frac{\partial H}{\partial t}(\lambda, t). \tag{11.29}$$

Here, the assumption has been made that the function h is zero at large times. This is appropriate for a fluid and in any case causes no significant loss of generality. It is clear from Equations (11.28) and (11.29) that the function h is entirely determined by single-step
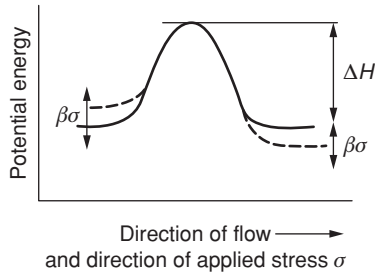
Figure 11.11   *The Eyring model for creep.*

stress relaxation measurements. Therefore, the stress for a general strain history can be calculated once stress relaxation data have been gathered over the appropriate range of strain. There is no parallel formulation for the strain in terms of the stress history.

In the original paper [47], the authors reported work on the uniaxial tension of plasticised poly(vinyl chloride), sulfur vulcanisates of butyl rubber, and polyisobutylene. Very successful predictions were made at extension ratios up to approximately five. Zapas and Craft [48] applied their formulation to multi-step stress relaxation and creep and recovery of both plasticised poly(vinyl chloride) and polyisobutylene. McKenna and Zapas applied a modified form of the model to the torsional deformation of PMMA [49]. McKenna and Zapas [50] have used the model in the analysis of the tensile behaviour of carbon-black-filled butyl rubbers.

11.2.5   Comparison of Single-Integral Models

The three principal single-integral theories are that of Pipkin and Rogers, Schapery's thermodynamic theory and the BKZ model. The first two concern solid material, with the Pipkin and Rogers approach being the simpler of the two. The Schapery approach is more complex as a result of its basis in thermodynamics, whereas Pipkin and Rogers' theory is purely a continuum model and is essentially devoid of physics. The BKZ fluid theory is of interest at large strains. Smart and Williams [51] compared the performance of the three models when applied to tensile stretching of polypropylene and poly(vinyl chloride) fibres, but only up to moderate strains ($\sim$4%). The BKZ model appeared to be of little interest at these strains. The Pipkin and Rogers approach, while having the advantage of simplicity over the Schapery theory, gave a somewhat worse performance.

11.3   Creep and Stress Relaxation as Thermally Activated Processes

We have shown (Section 5.2.7) that the standard linear solid, a three-component spring and dashpot model, provides to a first approximation a description of linear viscoelastic behaviour. Eyring and his colleagues [52] assumed that the deformation of a polymer was a thermally activated rate process involving the motion of segments of chain molecules over potential barriers, and modified the standard linear solid so that the movement of the dashpot was governed by the activated process. The model, which now represents non-linear viscoelastic behaviour, is useful because its parameters include an activation energy and

an activation volume that may give an indication of the underlying molecular mechanisms. The activated rate process may also provide a common basis for the discussion of creep and yield behaviour.

11.3.1   The Eyring Equation

In the following account, we outline the application of the Eyring process to mechanical behaviour and show how it reproduces the basic phenomena of viscoelasticity, with inherent non-linearity. We leave more specific physical interpretations, and more applications to elastic–plastic modelling, until Chapter 12. Macroscopic deformation is assumed to be the result of basic processes that are either intermolecular (e.g. chain-sliding) or intramolecular (e.g. a change in the conformation of the chain), whose frequency v depends on the ease with which a chain segment can surmount a potential energy barrier of height ΔH. In the absence of stress, dynamic equilibrium exists, so that an equal number of chain segments move in each direction over the potential barrier at a frequency given by

$$v = v_0 \exp\left(-\frac{\Delta H}{kT}\right). \tag{11.30}$$

The equation above is equivalent to Equation (7.5) describing the frequency of a molecular event, but here we use Boltzmann's constant k rather than the gas constant R as we are interested in the absolute number of molecular events rather than the overall effect of a mole of material.

An applied stress σ is assumed to produce linear shifts $\beta\sigma$ of the energy barriers in a symmetrical way (Figure 11.11), where β has the dimensions of volume. The flow in the direction of the applied stress is then given by

$$v_1 = v_0 \exp\left[-\frac{(\Delta H - \beta\sigma)}{kT}\right]$$

compared with a smaller flow in the backward direction of

$$v_2 = v_0 \exp\left[-\frac{(\Delta H + \beta\sigma)}{kT}\right].$$

The net flow in the forward direction is then

$$v' = v_1 - v_2 = v_0 \exp\left(-\frac{\Delta H}{kT}\right)\left[\exp\left(\frac{\beta\sigma}{kT}\right) - \exp\left(-\frac{\beta\sigma}{kT}\right)\right]. \tag{11.31}$$

The resemblance of the large bracket to the sinh function should be noted.

Assuming that the net flow in the forward direction is directly related to the rate of change of strain, we have

$$\frac{de}{dt} = \dot{e} = \dot{e}_0 \exp\left(-\frac{\Delta H}{kT}\right) \sinh\left(\frac{V\sigma}{kT}\right), \tag{11.32}$$

where $\dot{e}_0$ is a constant pre-exponential factor and V, which replaces β, is termed the activation volume for the molecular event.

The rate of strain Equation (11.32) defines an 'activated' viscosity, which is then incorporated in the dashpot of the standard linear solid model, and leads to a more complicated relationship between stress and strain than that for the linear model. The activated dashpot

model was tested against Leaderman's data for several fibres [14], and, by a suitable choice of model parameters, gave a good fit, at a given level of stress, over the four decades of time observed.

Subsequently the limitations of simple viscoelastic models have been recognised, and it is accepted that exact fitting of data requires a retardation or relaxation time spectrum, so we must consider why the activated dashpot model was so successful. Although creep curves are sigmoidal when plotted on a logarithmic time-scale, over a long intermediate time region they are, to good approximation, linear. The model predicts creep of the form $e = a' + b' \log t$, which is appropriate to this central region.

11.3.2   Applications of the Eyring Equation to Creep

Sherby and Dorn [53] investigated the creep under constant stress of glassy PMMA at different temperatures by applying step temperature changes, and constructed plots of creep rate versus total creep strain at a given stress level (Figure 11.12). The data were then superposed by assuming that the temperature dependence at each stress level followed an activated process, to give a relation between strain rate and strain (Figure 11.13). The temperature shifts were interpreted in terms of an activated process where the activation energy fell in a linear manner with increasing stress, to give a creep rate of the form

$$\dot{e} \exp\left[(\Delta H - V)/kT\right] = F(e), \tag{11.33}$$

which is the high stress approximation of the Eyring equation, where $\sin hx \approx \frac{1}{2} \exp x$ and V is the activation volume.
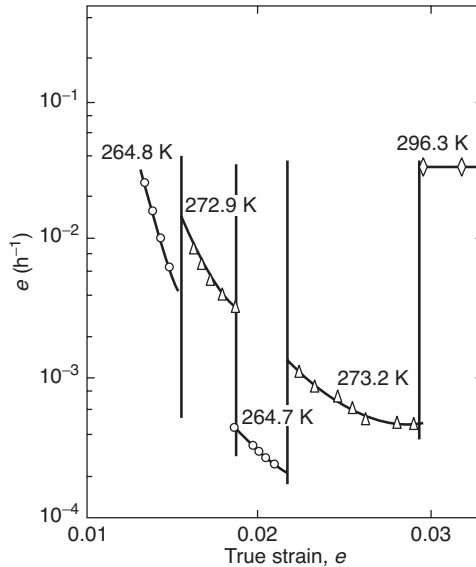
Figure 11.12 *Creep rates as a function of total creep strain for polymethyl methacrylate at indicated temperatures for a stress level of 56 MPa. (Reproduced from Sherby, O.D. and Dorn, J.B. (1958) Anelastic creep of polymethyl methacrylate. J. Mech. Phys. Solids, **6**, 145. Copyright (1958) Elsevier Ltd.)*
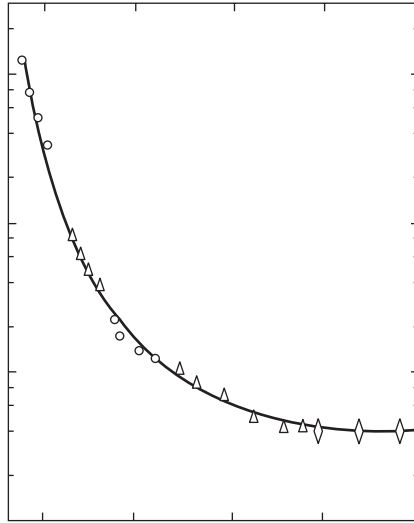
Figure 11.13 *Superposition of creep data for polymethyl methacrylate at different temperatures at a stress level of 56 MPa. (Reproduced from Sherby, O.D. and Dorn, J.B. (1958) Anelastic creep of polymethyl methacrylate. J. Mech. Phys. Solids, **6**, 145. Copyright (1958) Elsevier Ltd.)*

Mindel and Brown [54] performed a Sherby–Dorn type analysis on data for the compressive creep of polycarbonate. Superposition was achieved using an equation of the form of Equation (11.33) with an activation volume of 5.7 nm^3, which was very close to the values of the activation volume obtained from measurements of the strain rate dependence of the yield stress (Section 12.5.1).

The results suggest that creep rate can be represented by a general equation of the form

$$\dot{e} = f_1(T) f_2(\sigma/T) f_3(e), \tag{11.34}$$

where $f_1(T)$, $f_2(\sigma/T)$ and $f_3(e)$ are separate functions of the variables T, σ and e. Although $f_1(T)$ has the exponential form expected for a thermally activated process, the exponential form $f_2(\sigma/T)$ is modified to take into account the hydrostatic component of stress, giving different activation volumes for tensile, shear and pressure measurements. Mindel and Brown also proposed that in the region where the creep rate is falling rapidly with increasing strain $f_3(e)$ has the form

$$f_3(e) = \text{constant} \times \exp(-ce_R),$$

where e_R is the recoverable component of the creep strain and c is a constant. We then have

$$\dot{e} = \dot{e}_0 \exp\left[-(\Delta H - \tau V + p\Omega)/kT\right] \exp(-ce_R), \tag{11.35}$$

where τ and p are the shear and hydrostatic components of stress and V and Ω are the shear and pressure activation volumes. See Chapter 12 for an account of these two distinct activation volumes. The equation may be rewritten as

$$\dot{e} = \dot{e}_0 \exp\left[-(\Delta H - \{\tau - \tau_i\} V + p\Omega)/kT\right], \tag{11.36}$$
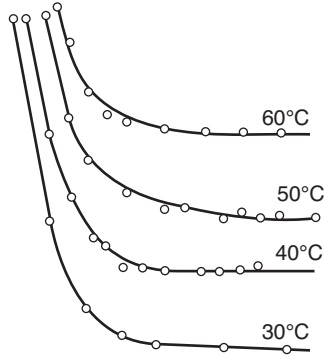
Figure 11.14 *Sherby–Dorn plots of creep of ultrahigh modulus polyethylene at different temperatures. (Reproduced from Wilding M.A. and Ward I.M. (1981) Routes to improved creep behaviour in drawn linear polyethylene. Plast. Rubber Proc. Appl., **1**, 167. Copyright (1981).)*

where $ce_R = \tau_i V/kT$; τ_i, which has the character of an internal stress, increases with strain and is proportional to absolute temperature as would be expected for the stress in a rubber-like network.

Wilding and Ward [55] have used the Eyring rate process to model the creep of ultrahigh modulus polyethylene, and show that at high strains, which correspond to long creep times, the creep rate reaches a constant value called the plateau (or equilibrium) creep rate (Figure 11.14). For polymers of low relative molecular mass, the stress and temperature dependence of the final creep rate can be modelled by a single-activated process with an activation volume of 0.08 nm^3. In molecular terms, this volume is then swept out by a single molecular chain moving through the lattice by a discrete distance.

For polymers of a higher molecular mass, and for copolymers, the permanent flow process was activated only at high stress levels, which suggested that there are two Eyring processes coupled in parallel (Figure 11.15). This suggestion is akin to the representation proposed to describe the strain rate dependence of the yield stress in polymers [56–58]. Process A has the smaller tensile activation volume ($\sim$0.05 nm^3) and larger pre-exponential factor, and is activated only at high stress levels. Process B has the larger tensile activation volume ($\sim$1 nm^3) and a smaller pre-exponential factor, and is operative at low stress levels. At low stresses, there will be little permanent flow because B carries almost the whole load. Although the overall creep and recovery behaviour can be represented by a model containing two activated dashpots, a spectrum of relaxation times would be required to give an accurate fit to experimental data over the complete time and strain scales.

11.3.3   Applications of the Eyring Equation to Stress Relaxation

Guiu and Pratt [59] have shown how a model consisting of an Eyring dashpot in series with an elastic element leads to a simple equation to describe stress relaxation curves in tension. Suppose that there is a total strain e on the system of Figure 11.16, consisting of an elastic component e_E and an Eyring or viscous component e_V, such that

$$e = e_E + e_V. \tag{11.37}$$
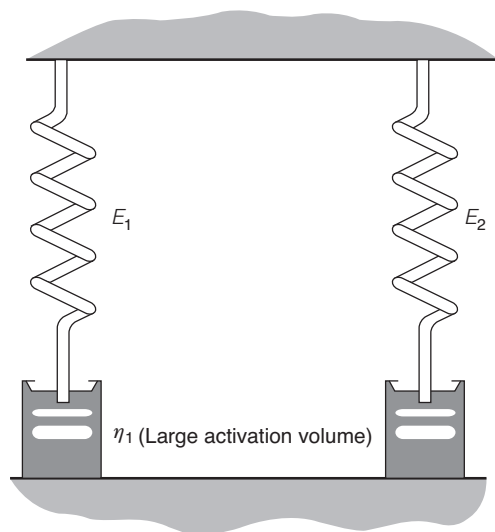
Figure 11.15   *The two-process model for permanent flow creep. (Reproduced from Wilding, M.A. and Ward, I.M. (1981) Routes to improved creep behaviour in drawn linear polyethylene. Plast. Rubber Proc. Appl.,* **1**, *167. Copyright (1981).)*

Differentiating with respect to time gives

$$\dot{e} = \dot{e}_E + \dot{e}_V. \tag{11.38}$$

We now replace the viscous strain rate $\dot{e}_V$ with the high stress adaptation of Equation (11.32), which is

$$\dot{e}_V = \dot{e}_0 \exp\left(-\frac{\Delta H}{kT}\right) \frac{1}{2} \exp\left(\frac{V\sigma}{kT}\right) = A \exp(B\sigma), \tag{11.39}$$
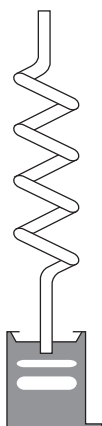
Figure 11.16   *Series model spring plus Eyring dashpot.*

where the constants A and B have been introduced for brevity. Assuming a linear relation for the elastic component, with modulus E, Equation (11.38) can now be rewritten so that only stresses appear on the right-hand side:

$$\dot{e} = \frac{\dot{\sigma}}{E} + A\exp(B\sigma).$$

Under conditions of stress relaxation, the total strain rate is zero, and the stress decays in a manner governed by the relation

$$0 = \frac{\dot{\sigma}}{E} + A\exp(B\sigma). \tag{11.40}$$

This can be solved by separation of variables to give the stress as

$$\sigma_0 - \sigma = \frac{1}{B}\ln\left(1 + \frac{t}{c}\right), \tag{11.41}$$

where σ_0 is the stress at time $t = 0$ and c is a constant.

Equation (11.41), the Guiu and Pratt expression, has been shown to be remarkably effective in representing stress relaxation curves for polymers. Escaig [60] has discussed its general utility. Sweeney and Ward [61] applied the expression successfully to the stress relaxation behaviour of highly oriented polyethylene fibres at small strains. They also showed that the two-process model, which in some circumstances will generate stress relaxation predictions approximating to Guiu–Pratt curves, gave a more satisfactory model of the overall behaviour.

11.3.4 Applications of the Eyring Equation to Yield

Suppose the system of Figure 11.16 is subjected to a constant total strain rate $\dot{e}$, starting at zero load. Initially, the stress is low and causes only a small rate of strain in the Eyring dashpot, and the elastic spring is stretched. Continued stretching of the spring increases the stress and thus the rate of strain $\dot{e}_V$ in the Eyring dashpot, until eventually it becomes equal to the total applied strain rate $\dot{e}$. At this point, the spring ceases to extend, and so the stress in it, which is equal to the total stress on the system, becomes constant. Thus, behaviour resembling yield is predicted. It is easily shown that this yield stress depends on strain rate. Adopting the notation of the previous section, once the spring reaches its state of constant strain, $\dot{e}_E = 0$. Then, using Equation (11.38)

$$\dot{e} = \dot{e}_V$$

and from Equation (11.39)

$$\dot{e} = A\exp(B\sigma_Y) \tag{11.42}$$

where σ_Y denotes the yield stress. Rearranging gives the relation

$$\sigma_Y = \frac{1}{B}\ln\left(\frac{\dot{e}}{A}\right)$$

or, regaining the expressions for A and B implicit in Equation (11.39),

$$\sigma_Y = \frac{RT}{\nu}\ln\left[\frac{2\dot{e}}{\dot{e}_0}\exp\left(\frac{\Delta H}{kT}\right)\right]. \tag{11.43}$$
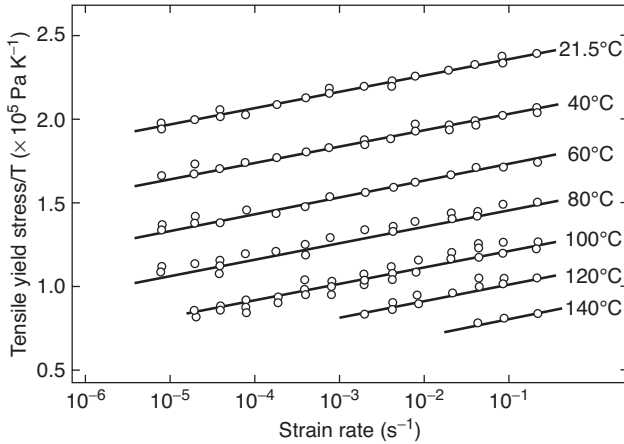
Figure 11.17 *Measured ratio of yield stress to temperature as a function of the logarithm of strain rate for polycarbonate. The set of parallel straight lines is calculated from Equation (11.43). (Reproduced from Bauwens-Crowet, C., Bauwens, J.C. and Homès, G. (1969) Tensile yield-stress behavior of poly(vinyl chloride) and polycarbonate in the glass transition region. J. Polymer Sci. A2, **7**, 735. Copyright (1969) John Wiley & Sons, Ltd.)*

These equations imply a linear relationship between $\dfrac{\sigma_Y}{T}$ and $\ln(\dot{e})$. This has been demonstrated for a number of polymers. For example, the work of Bauwens-Crowet *et al.* [57] on polycarbonate is illustrated in Figure 11.17.

The stress–strain behaviour of models such as that of Figure 11.16 can be explored by solving the associated equations using numerical techniques. In the work of Sweeney *et al.* on PET fibres [62], a model similar to that of Figure 11.16 but with the Eyring dashpot restrained by a Gaussian network, was solved in this way. The strain at which yield occurs, the general shape of the stress–strain curve, and the stability of the deformation were predicted and found to compare well with experiment.

11.4 Multi-axial Deformation: Three-Dimensional Non-linear Viscoelasticity

The discussion so far has been dominated by one-dimensional behaviour, reflecting the most convenient and customary materials testing methods. However, any engineering application will be for a three-dimensional body, subject to multi-axial stresses. It is now feasible to implement non-linear viscoelastic models in numerical schemes to perform analyses of structures, and this is often the motivation for generalising a viscoelastic theory to two or three dimensions.

A very valuable technique, well known in plasticity theory, is to split the stress into its hydrostatic and deviatoric components, associated respectively with volumetric and shear strain. On the basis that creep is caused by shearing of molecules past one another, we would expect creep to be only associated with deviatoric stress. This is constructed by subtracting the hydrostatic component from the stress tensor Σ to give the deviatoric stress Σ':

$$\Sigma' = \Sigma - \bar{\sigma},$$

where $\bar{\sigma}$ is the mean stress:

$$\bar{\sigma} = \frac{1}{3}(\sigma_{11} + \sigma_{22} + \sigma_{33})$$

and the terms on the right are the diagonal components of the stress tensor. Thus, in principal directions I, II and III the diagonal components of the stress deviator are terms such as

$$\frac{1}{3}(2\sigma_{I} - \sigma_{II} - \sigma_{III}).$$

In an early attempt by Pao and Marin [6] at a three-dimensional extension of their uniaxial creep law Equation (11.1), strains in the principal directions are given by terms such as

$$e_{I} = \frac{1}{E}(\sigma_{I} - \nu(\sigma_{II} + \sigma_{III})) + \frac{1}{2}(2\sigma_{I} - \sigma_{II} - \sigma_{III})J_{2}^{(n-1)/2}\left(K(1 - e^{-qt}) + Bt\right).$$

The first term represents elasticity, and the second term represents the viscoelastic component. In the latter term, the deviatoric stress component is apparent. J_2 is a scalar invariant closely associated with the deviatoric stress tensor

$$J_2 = \frac{1}{2}\left((\sigma_{I} - \sigma_{II})^2 + (\sigma_{II} - \sigma_{III})^2 + (\sigma_{III} - \sigma_{I})^2\right),$$

which is itself associated with the equivalent stress $\sqrt{J_2}$.
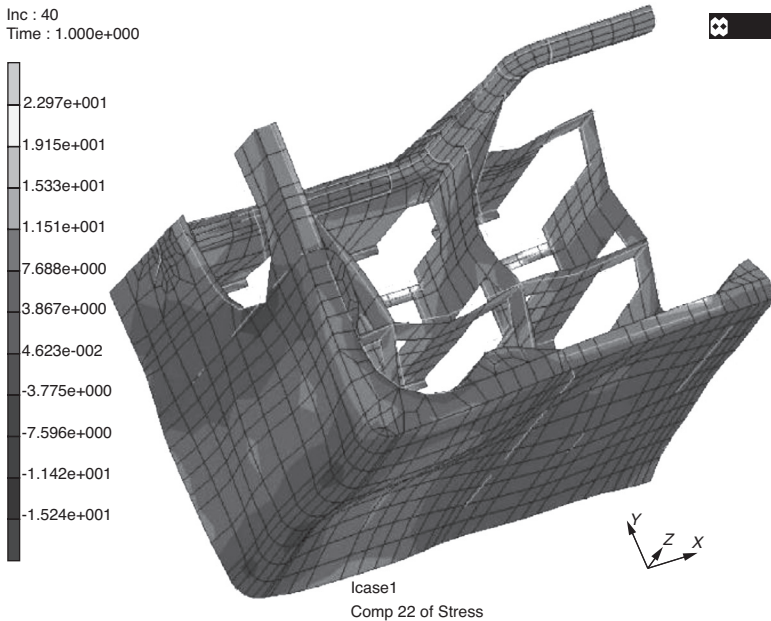
Figure 11.18 *Quarter model of a bottle crate subject to compressive loading along the z axis. The contours represent normal stresses along z in MPa. (Reproduced from Beijer, J.G.J. and Spoormakerb, J.L. (2002) Solution strategies for FEM analysis with nonlinear viscoelastic polymers. Computers & Structures, **80**, 1213–1229. Copyright (2002) Elsevier Ltd.)*

This essential technique has been used in more sophisticated analyses. The Schapery model has been implemented in a three-dimensional form in a commercial finite element scheme (MARC) by Lai and Bakker [63] and also by Beijer and Spoormakerb [64]. In these formulations, the volumetric response was assumed to be linear elastic and the deviatoric terms defined by Schapery integrals involving the effective stress. Lai and Bakker applied their finite element solution is to high-density polyethylene structures. One such example is of a bottle crate subject to vertical loading to simulate stacking, the results of which are illustrated in Figure 11.18 in terms of stress along the loading direction. Realistic predictions of buckling were obtained.

Karamanou *et al*. [65] have performed finite element analyses to large strains to simulate the thermoforming process, in which thin sheets of polymer are inflated using gas pressure. They adopted a model comprising hyperelastic components and a linear viscous element. Applying a thin shell analysis enabled them to produce realistic predictions of the inflating membrane.

Models involving non-linear rate-dependent plastic elements such as the Eyring process – so-called viscoplastic models – have also been implemented in finite element schemes. Some of these will be discussed in Chapter 12.

References

1. Lockett, F.J. (1972) *Non-Linear Viscoelastic Solids*, Academic Press, London.
2. Turner, S. (1966) The strain response of plastics to complex stress histories. *Polym. Eng. Sci*., **6**, 306.
3. Ferry, J.D. (1980) *Viscoelastic Properties of Solids*, John Wiley & Sons, New York, ISBN 0-471-04894-1.
4. Lakes, R.S. (1999) *Viscoelastic Solids*, CRC Press, Boca Raton, Florida USA, ISBN 0-8493-9658-1.
5. Pao, Y.H. and Marin, J. (1952) Deflection and stresses in beams subjected to bending and creep. *J. Appl. Mech*., **19**, 478.
6. Pao, Y.H. and Marin, J. (1953) An analytical theory of the creep deformation of materials. *J. Appl. Mech*., **20**, 245.
7. Marin, J. (1937) Design of members subjected to creep at high temperatures. *J. Appl. Mech. Trans. ASME*, **59**, A21.
8. Findley, W.N. and Khosla, G. (1955) Application of the superposition principle and theories of mechanical equation of state, strain, and time hardening to creep of plastics under changing loads. *J. Appl. Phys*., **26**, 821.
9. Nutting P.G. (1943) A general stress-strain-time formula, *J. Franklin Inst*., 235, 513.
10. Dillard, D.A., Straight, M.R. and Brinson, H.F. (1987) The nonlinear viscoelastic characterization of graphite/epoxy composites. *Polymer Engineering and Science*, **27**, 116–123.
11. Van Holde, K. (1957) A study of the creep of nitrocellulose. *J. Polym. Sci*., **24**, 417.
12. Andrade, E.N.da C. (1910) On the viscous flow in metals, and allied phenomena. *Proc. Roy. Soc. A*, **84**, 1.
13. Plazek, D.J. (1960) Dynamic mechanical and creep properties of a 23% cellulose nitrate solution; Andrade creep in polymeric systems. *J. Colloid. Sci*., **15**, 50.

14. Wineman, A. (2009) Nonlinear viscoelastic solids – a review. *Mathematics and Mechanics of Solids*, **14**, 300–366.
15. Drapaca, C.S., Sivaloganathan, S. and Tenti, G. (2007) Nonlinear Constitutive Laws in Viscoelasticity. *Mathematics and Mechanics of Solids*, **12**, 475–501.
16. Smith, T.L. (1962) Nonlinear viscoelastic response of amorphous elastomers to constant strain rates. *Trans. Soc. Rheol.*, **6**, 61.
17. Kitagawa, M., Mori, T. and Matsutani, T. (1989) Rate-dependent nonlinear constitutive equation of polypropylene. *J. Polym. Sci. B*, **27**, 85.
18. Leaderman, H. (1943) *Elastic and Creep Properties of Filamentous Materials and Other High Polymers*, Textile Foundation, Washington, DC.
19. Findley, W.N. and Lai, J.S.Y. (1967) A modified superposition principle applied to creep of nonlinear viscoelastic material under abrupt changes in state of combined stress. *Trans. Soc. Rheol.*, **11**, 361–381.
20. Pipkin, A.C. and Rogers, T.G. (1968) A non-linear integral representation for viscoelastic behaviour. *J. Mech. Phys. Solids*, **16**, 59–72.
21. Green, A.E. and Rivlin, R.S. (1957) The mechanics of non-linear materials with memory – Part I. *Arch. Ration Mech. Anal.*, **1**, 1–21.
22. Haddad, Y.M. (1995) *Viscoelasticity of Engineering Materials*, Chapter 6, Chapman and Hall, London.
23. Ward, I.M. and Onat, E.T. (1963) Non-linear mechanical behaviour of oriented polypropylene. *J. Mech. Phys. Solids*, **11**, 217–219.
24. Hadley, D.W. and Ward, I.M. (1965) Non-linear creep and recovery behaviour of polypropylene fibres. *J. Mech. Phys. Solids*, **13**, 397–411.
25. Lockett, F.J. (1965) Creep and stress-relaxation experiments for non-linear materials. *Int. J. Eng. Sci.*, **3**, 59–75.
26. Gradowczyk, M.H. (1969) On the accuracy of the Green–Rivlin representation for viscoelastic materials. *Int. J. Solids Structures*, **5**, 873–877.
27. Brereton, M.G., Croll, S.G., Duckett, R.A. and Ward, I.M. (1974) Non-linear viscoelastic behaviour of polymers: an implicit equation approach. *J. Mech. Phys. Solids*, **22**, 97–125.
28. Yannas, I.V. and Haskell, V.C. (1971) Utility of the Green–Rivlin theory in polymer mechanics. *J. Appl. Phys.*, **42**(2), 610–613.
29. Mittal, R.K. and Singh, I.P. (1986) Time-dependent behavior of Nylon-6 under uniaxial and biaxial loadings at constant rate. *Polym. Eng. Sci.*, **26**, 318–325.
30. Stafford, R.O. (1969) On mathematical forms for the material functions in nonlinear viscoelasticity. *J. Mech. Phys. Solids*, **17**, 339–358.
31. Drapaca, C.S., Sivaloganathan, S. and Tenti, G. (2007) Nonlinear constitutive laws in viscoelasticity. *Mathematics and Mechanics of Solids*, **12**, 475–501.
32. Kinder, D.F. and Sternstein, S.S. (1976) A path-dependent variable approach to nonlinear viscoelastic behavior. *Trans. Soc. Rheol.*, **20**, 119–140.
33. Dean, G., McCartney, L.N., Crocker, L. and Mera, R. (2009) Modelling long term deformation behaviour of polymers for finite element analysis. *Plastics, Rubber and Composites*, **38**, 433–443.
34. Martin, G.M., Roth, F.L. and Stiehler, R.D. (1956) Behavior of "pure gum" rubber vulcanizates in tension. *Trans. Inst. Rubber Ind.*, **32**, 189.

35. Guth, E., Wak, P.E. and Anthony, R.L. (1946) Significance of the equation of state for rubber. *J. Appl. Phys.*, **17**, 347.
36. Tobolsky, A.V. and Andrews, R.D. (1945) Systems manifesting superposed elastic and viscous behavior. *J. Chem. Phys.*, **13**, 3.
37. Leaderman, H. (1962) Large longitudinal retarded elastic deformation of rubberlike network polymers. *Trans. Soc. Rheol.*, **6**, 361.
38. Kitagawa, M. and Takagi, H. (1990) Nonlinear constitutive equation for polyethylene under combined tension and torsion. *J. Polym. Sci. B*, **28**, 1943.
39. Lui, M.C.M. and Krempl, E. (1979) A uniaxial viscoplastic model based on total strain and overstres. *J. Mech. Phys. Solids*, **27**, 377.
40. Zhang, C. and Moore, I.D. (1997) Nonlinear mechanical response of high density polyethylene. Part I: Experimental investigation and model evaluation. *Polym. Eng. Sci.*, **37**, 404.
41. Zhang, C. and Moore, I.D. (1997) Nonlinear mechanical response of high density polyethylene. Part II: Uniaxial constitutive modeling. *Polym. Eng. Sci.*, **37**, 414.
42. Brusselle-Dupend, N., Lai, D., Feaugas, X. *et al.* (2003) Mechanical behavior of a semicrystalline polymer before necking. Part II: Modeling of uniaxial behavior. *Polym. Eng. Sci.*, **43**, 501–518.
43. Schapery, R.A. (1966) A engineering theory of nonlinear viscoelasticity with applications. *Int. J. Solids. Structures*, **2**, 407.
44. Schapery, R.A. (1969) On the characterization of nonlinear viscoelastic materials. *Polym. Eng. Sci.*, **9**, 295.
45. Crook, R.A. (1993) Damage and the nonlinear viscoelastic response of glassy polycarbonate and LaRC-TPI. *Polym. Eng. Sci.*, **33**, 56.
46. Lai, J. and Bakker, A. (1995) An integral constitutive equation for nonlinear plasto-viscoelastic behavior of high-density polyethylene. *Polym. Eng. Sci.*, **35**, 1339.
47. Bernstein, B., Kearsley, B.A. and Zapas, L.J. (1963) A study of stress relaxation with finite strain. *Trans. Soc. Rheol.*, **7**, 391.
48. Zapas, L.J. and Craft, T. (1965) Correlation of large longitudinal deformations with different strain histories. *J. Res. Nat. Bur. Stand A.*, **69**, 541.
49. McKenna, G.B. and Zapas, L.J. (1979) Nonlinear viscoelastic behavior of poly(methyl methacrylate) in torsion. *J. Rheol.*, **23**, 151.
50. McKenna, G.B. and Zapas, L.J. (1981) Response of carbon black filled butyl rubber to cyclic loading. *Rubber Chemistry and Technology*, **54**, 718.
51. Smart, J. and Williams, J.G. (1972) A comparison of single-integral non-linear viscoelasticity theories. *J. Mech. Phys. Solids*, **20**, 313.
52. Halsey, G., White, H.J. and Eyring, H. (1945) Mechanical properties of textiles, I. *Text Res. J.*, **15**, 295.
53. Sherby, O.D. and Dorn, J.B. (1958) Anelastic creep of polymethyl methacrylate. *J. Mech. Phys. Solids*, **6**, 145.
54. Mindel, M.J. and Brown, N. (1973) Creep and recovery of polycarbonate. *J. Mater. Sci.*, **8**, 863.
55. Wilding, M.A. and Ward, I.M. (1978) Tensile creep and recovery in ultrahigh modulus linear polyethylenes. *Polymer*, **19**, 969; Creep and recovery of ultrahigh modulus polyethylene. *Polymer*, **22**, 870 (1981).

56. Roetling, J.A. (1965) Yield stress behaviour of polymethylmethacrylate. *Polymer*, **6**, 311.
57. Bauwens-Crowet, C., Bauwens, J.C. and Homès, G. (1969) Tensile yield-stress behavior of poly(vinyl chloride) and polycarbonate in the glass transition region. *J. Polymer Sci. A2*, **7**, 735.
58. Robertson, R.E. (1963) On the cold-drawing of plastics. *J. Appl. Polymer Sci.*, **7**, 443.
59. Guiu, F. and Pratt, P.L. (1964) Stress relaxation and the plastic deformation of solids. *Phys. Status Solidi*, **6**, 111.
60. Escaig, B. (1982) Kinetics and thermodynamics of plastic flow in polymeric glasses, in *Plastic Deformation of Amorphous and Semi-Crystalline Materials*, (eds B. Escaig and C. G'Sell), Les Éditions de Physique, Les Ulis, France, pp. 187–225.
61. Sweeney, J. and Ward, I.M. (1990) A unified model of stress relaxation and creep applied to oriented polyethylene. *J. Mater. Sci.*, **25**, 697–705.
62. Sweeney, J., Shirataki, H., Unwin, A.P. and Ward, I.M. (1999) Application of a necking criterion to PET fibers in tension. *J. Appl. Polym. Sci.*, **74**, 3331–3341.
63. Lai, J. and Bakker, A. (1996) 3-D schapery representation for non-linear viscoelasticity and finite element implementation. *Computational Mechanics*, **18**, 182–191.
64. Beijer, J.G.J. and Spoormakerb, J.L. (2002) Solution strategies for FEM analysis with nonlinear viscoelastic polymers. *Computers & Structures*, **80**, 1213–1229.
65. Karamanou, M., Warby, M.K. and Whiteman, J.R. (2006) Computational modelling of thermoforming processes in the case of finite viscoelastic materials. *Computer Methods in Applied Mechanics and Engineering*, **195**, 5220.

Further Reading

Brinson, H.F. and Brinson, L.C. (2008) *Polymer Engineering Science and Viscoelasticity: An Introduction*, Springer, New York.
Shaw, M.T. and MacKnight, W.J. (2005) *Introduction to Polymer Viscoelasticity*, 3rd edn, John Wiley and Sons, Ltd, Hoboken, New Jersey.

12

Yielding and Instability in Polymers

As we observed at the end of the Chapter 11, the non-linear behaviour of polymers, as represented by the Eyring model, gives rise to a phenomenon resembling yield. The observed maximum stress can be treated as a yield stress, though Equation (11.41) shows that this yield stress depends on the rate of strain. Wineman and Waldron [1] have pointed out that there appear to be two approaches to the modelling of yield in polymers: the use of non-linear viscoelasticity and the direct application of metal plasticity. The use of the Eyring model is one example of the former approach. Relatively simple theories of plasticity, where there is no rate dependence, are available from the metals field. These theories, that embody the classical concepts of plasticity, may still be applied usefully to polymers, for instance in cases where changes in strain rate are small.

Allied to the subject of yielding is that of instability. Necking in a tensile test specimen is an example of instability, and is caused by the underlying yield properties of the material. Yielding may lead to a maximum in the applied force, which may then allow the strain in the specimen to increase with no increase in force – the unstable condition. We should note that yielding and instability are qualitatively different phenomena, in that yielding is an intrinsic material characteristic, whereas instability is a function of the geometry and loading conditions of the loaded body.

A number of different factors contribute to the present interest in the yield behaviour. First, it has been recognised that the classical concepts of plasticity are relevant to forming, rolling and drawing processes in polymers. Secondly, there has been a number of striking experimental studies of 'slip bands' and 'kink bands' in polymers, which suggest that deformation processes in polymers might be similar to those in crystalline materials such as metals and ceramics. Finally, it is evident that distinct yield points are observed and there is much interest in understanding these in the context of other ideas in polymer science.

Our first task in this chapter is to discuss the relevance of classical ideas of plasticity to the yielding of polymers. Although the yield behaviour is temperature and strain rate dependent, it will be shown that provided that the test conditions are chosen suitably, yield stresses can be measured which satisfy conventional yield criteria. The temperature and time

dependence often obscure some generalities of the yield behaviour. For example, it might be concluded that some polymers show necking and cold-drawing, whereas others are brittle and fail catastrophically. Yet another type of polymer (a rubber) extends homogeneously to rupture. A salient point to recognise is that polymers in general can show all these types of behaviour depending on the exact conditions of test (Figure 13.1), quite irrespective of their chemical nature and physical structure. Thus explanations of yield behaviour, which involve, for example cleavage of crystallites or lamellar slip or amorphous mobility are only relevant to specific cases. As in the case of linear viscoelastic behaviour or rubber elasticity, we must first seek an understanding of the relevant phenomenological features, decide on suitable measurable quantities and then provide a molecular interpretation of the subsequent constitutive relations.

12.1   Discussion of the Load–Elongation Curves in Tensile Testing

The most dramatic consequence of yield is seen in a tensile test when a neck or deformation band occurs, as in Figure 12.1, with the plastic deformation concentrated either entirely or primarily in a small region of the specimen. The precise nature of the plastic deformation depends both on the geometry of the specimen and on the form of the applied stresses, and will be discussed more fully later.

The characteristic necking and cold-drawing behaviour is as follows. On the initial elongation of the specimen, homogeneous deformation occurs and the conventional load–extension curve shows a steady increase in load with increasing elongation (AB in Figure 12.2). At the point B, the specimen thins to a smaller cross section at some point, i.e. a neck is formed. Further elongation brings a fall in load. Continuing extension is achieved by causing the shoulders of the neck to travel along the specimen as it thins from the initial cross section to the drawn cross section. The existence of a finite or *natural draw ratio* is an important aspect of polymer deformation and is discussed in Section 12.6 below. Ductile behaviour in polymers does not always give a stabilised neck, so that the requirements for necking and cold-drawing must now be considered in some detail.

(a)

(b)
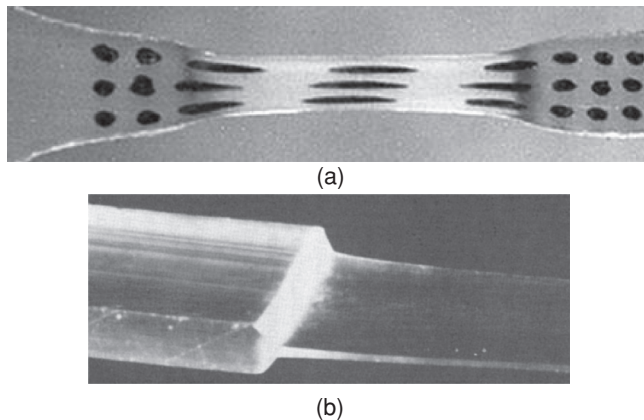
Figure 12.1   *Photograph of necks formed in the drawing of (a) isotropic polypropylene and (b) oriented polyethylene.*
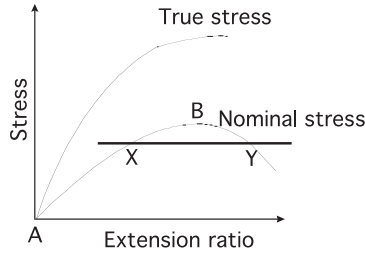
Figure 12.2   *Comparison of nominal stress–elongation curve (load–elongation curve) and true stress–elongation curve.*

12.1.1   Necking and the Ultimate Stress

It is important to distinguish between the nominal stress, which is the load at any time during deformation divided by the initial cross-sectional area, and the true stress, which is the load divided by the actual cross section at any time. The cross section of the sample decreases with increasing extension, so that the true stress may be increasing when the apparent or conventional stress or load may be remaining constant or even decreasing. This has been very well discussed by Nadai [2] and Orowan [3].

Consider the conventional stress–strain curve or the load–elongation curve for a ductile material (Figure 12.2). The ordinate is equal to the nominal stress obtained by dividing the load P by the original cross-sectional area A_0:

$$\sigma_a = P/A_0.$$

This gives a stress–strain curve of the form shown. The load reaches its maximum value at the instant the extension of the sample ceases to be uniform. At this elongation, the specimen begins to neck and consequently the load falls as shown by the last part of the stress–strain curve. Finally, the sample fractures at the narrowest point of the neck.

It is instructive to plot the true tensile stress at any elongation rather than the nominal stress σ_a. This is given by $\sigma = P/A$, where A is the actual cross section at any time. We now assume, as is usual for plastic deformation, that the deformation takes place at constant volume. Then $Al = A_0 l_0$, and if we put $l/l_0 = \lambda$ where λ is the extension ratio,

$$A = \frac{A_0 l_0}{l} = \frac{A_0}{\lambda}.$$

The true stress is given by

$$\sigma = \frac{P}{A} = \frac{\lambda P}{A_0} = \lambda \sigma_a. \tag{12.1}$$

Thus if we know σ_a, the true stress as a function of λ, i.e. the true stress–strain curve, can be computed. The nominal and true stress–strain curves are compared in Figure 12.2.

Consideration of the nominal stress can lead to insight into the mechanical instability associated with necking. For a tensile specimen of initially uniform cross section, equilibrium of forces ensures that the nominal stress σ_a is the same all along its length. Therefore, when the curve of σ_a against λ possesses a maximum such as that in Figure 12.2, a small strain (point X) can coexist with a large strain (point Y). Point X corresponds to the unnecked region of the specimen, and point Y to a region that is beginning to neck. If the specimen

were stretched to the same elongation without necking, the strain would be uniform at a level somewhere between that of X and that of Y. It is clear that such a state of strain corresponds to a nominal stress higher than the line XY, and therefore to a strain energy higher than that in the necked specimen. On this basis, we would expect the necked state, corresponding to the lower strain energy, to be preferred.

The argument above is based on the assumption that the stress–strain curve completely defines the material behaviour. In reality, with polymers stress depends on strain rate, and since necking is associated with a local increase in strain rate, the issue is more complex. A strong dependence of stress on strain rate can inhibit necking even when the nominal stress reaches a maximum; the existence of the maximum is a necessary condition for necking, but not a sufficient one. Necking in rate-dependent materials has been discussed by Sweeney *et al.* [4].

Another aspect of the energy/equilibrium argument, that at first seems problematic, is the question of how the material moves from the unnecked state at X to the necked state at Y without violating equilibrium. Intermediate strain states are clearly (Figure 12.2) at a higher nominal stress than that pertaining at X and Y. However, as the neck develops and material moves from one state to the other, the cross-sectional area is non-uniform, and so the true stress varies along the neck. Equilibrium equations then ensure that shear stresses are acting, and so the material is not in a state of uniaxial stress or strain. Therefore, the stress–strain state of the transitional material cannot be plotted on the curve of Figure 12.2. Its combined state of normal and shear stress is such as to maintain equilibrium. This has been explained by Vincent [5], and corresponding work on metals has revealed the complexity of the stress field in the neck [6].

In mathematical terms, the existence of a stress maximum as the condition necessary for necking is

$$\frac{d\sigma_a}{d\lambda} = 0. \tag{12.2}$$

This can be re-expressed in terms of the true stress σ. From Equation (12.1), Equation (12.2) is equivalent to

$$\frac{d}{d\lambda}\left(\frac{\sigma}{\lambda}\right) = 0,$$

which becomes

$$\frac{1}{\lambda}\frac{d\sigma}{d\lambda} - \frac{\sigma}{\lambda^2} = 0,$$

i.e.

$$\frac{d\sigma}{d\lambda} = \frac{\sigma}{\lambda}. \tag{12.3}$$

Equation (12.3) defines a geometric condition for the true stress–strain curve, corresponding to the simple construction due to Considère shown in Figure 12.3. The ultimate stress is obtained when the tangent to the true stress–strain curve $d\sigma/d\lambda$ is given by the line from the point $\lambda = 0$ on the extension axis. The angle α in Figure 12.3 is defined by

$$\tan\alpha = \frac{d\sigma}{d\lambda}.$$

The ultimate stress has a much greater significance than is the case for metals as it is a determining factor in deciding whether a polymer will neck and cold-draw.
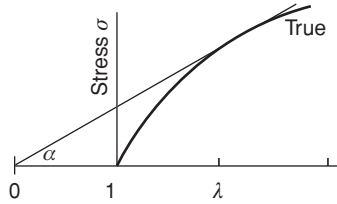
Figure 12.3 *The Considère construction.*

The significance of the argument at this stage relates to the failure of plastics in the ductile state. Orowan [3] first pointed out that for ductile materials the ultimate stress is entirely determined by the stress–strain curve, i.e., by the plastic behaviour of the material, without any reference to its fracture properties, provided that fracture does not occur before the load maximum corresponding to $d\sigma/d\lambda = \sigma/\lambda$ is reached. Yield stress is thus an important property in many plastics, and defines the practical limit of behaviour much more than the ultimate fracture, unless the plastic fails by brittle fracture.

12.1.2 Necking and Cold-Drawing: A Phenomenological Discussion

Figure 12.4 shows that there are four distinct regions on the nominal stress–strain curve of a typical cold-drawing polymer:

1. Initially the stress rises in an approximately linear manner as the applied strain increases.
2. The nominal stress reaches a maximum. During the subsequent fall in stress, the neck shape develops. From this point on, the strain in Figure 12.4 should be understood to be that at the centre of the neck.
3. The nominal stress reaches a minimum. The strain at this point corresponds to the natural draw ratio. In tensile stretching, the strain stays at this approximately constant level for some considerable time as the neck propagates through the specimen and the specimen continues to be elongated – the phenomenon termed 'stable necking'.
4. The specimen is of finite dimensions, so that at some stage the propagating neck occupies the whole of its length – it reaches the grips at both end of the tensile specimen. Now, further elongation causes an increase in strain and a corresponding increase in nominal stress as molecular chains are stretched – phenomenologically, this process may be termed 'strain-hardening'.
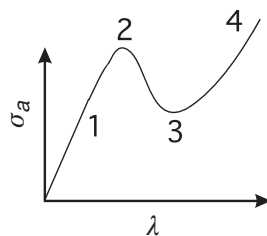
Figure 12.4 *Nominal stress–strain behaviour of a necking tensile specimen.*

In some materials, notably metals, there is no minimum region 3 and the stress continues to decrease. Then, there is no stable necking and the neck continues to stretch, becoming continuously thinner until fracture.

The maximum mentioned above as occurring in region 2 corresponds to the condition (12.2). This condition involves the nominal stress only, and the existence or otherwise of a maximum in the true stress is unspecified by the physical arguments employed so far. Observations show that a maximum in true stress may arise or may not, depending on the polymer and test conditions. This is well illustrated in the work of Amoedo and Lee [7]. In Figure 12.5, two sets of tensile true stress–strain curves are shown, one set for
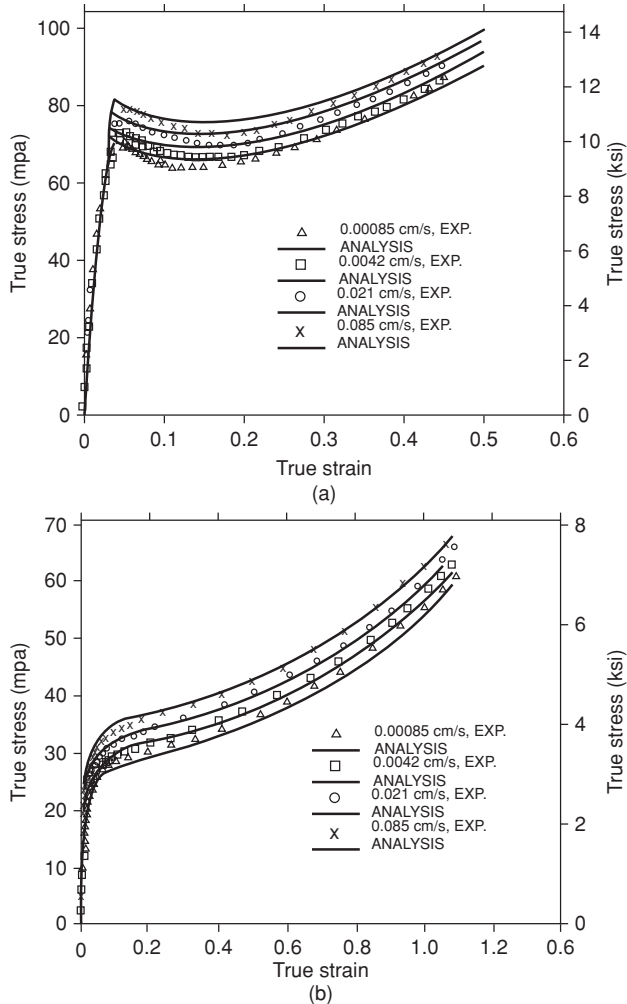
Figure 12.5 *True stress–strain curves at room temperature for (a) polycarbonate (b) polypropylene. (Reproduced from Amoedo, J. and Lee, D. (1992) Modeling the uniaxial rate and temperature dependent behavior of amorphous and semi-crystalline polymers. Polym. Eng. Sci., **32**, 1055–1065. Copyright (1992) John Wiley & Sons, Ltd.)*

polycarbonate and the other for polypropylene. The stress maximum is clearly present in the case of polycarbonate and, equally clearly, absent in the case of polypropylene. It is of significance here that the comparison is between an amorphous polymer (polycarbonate) and a semi-crystalline one (polypropylene).

There are two ways in which a neck may be initiated. First, if the cross section of the sample is not uniform, perhaps as a result of a flaw, the element with the smallest effective cross section will be subjected to the highest true stress, and so will reach the yield point before any other element in the sample. Secondly, a fluctuation in material properties may cause a localised reduction of the yield stress in a given element so that this element reaches the yield point at a lower applied load. When a particular element has reached its yield point, it is easier to continue deformation entirely within this element because it has a lower flow stress stiffness than the surrounding material. Hence, further deformation of the sample is accompanied by straining in only one region and a neck is formed.

12.1.3   Use of the Considère Construction

Corresponding with the above description of the four regions of the nominal stress–strain curve, a parallel description is possible using true stress. The maximum and minimum in regions 2 and 3 are replaced by tangents to the stress–strain curve corresponding to Equation (12.3). In Figure 12.6, two such tangent lines have been drawn to the true stress–strain curve from the point $\lambda = 0$. Inspection of the figure reveals that the slopes of the tangents $\dfrac{d\sigma}{d\lambda}$ are as given by Equation (12.3). The regions 1–4 correspond to the same physical stages as those in Figure 12.4. When the curve is such that it is possible to construct the tangent to region 2, the polymer has the potential to neck; the existence of the tangent at region 3 implies a potential for stable necking and cold-drawing. Similar deductions can be made from the presence or otherwise of maxima and minima in the nominal stress–strain relations of Figure 12.4.

An example of a stress–strain relation for which a Considère tangent is not possible is the upwardly curving line shown in Figure 12.7(a). In Figure 12.7(b), one tangent is possible that corresponds to necking, but the second one associated with stable necking is not. The typical polymer behaviour of necking followed by strain hardening and stable necking is only possible for curves resembling those of Figure 12.6.
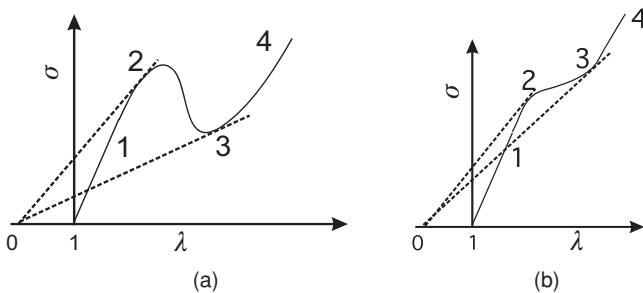
Figure 12.6   *Considère tangents. In (a), the true stress has reached a maximum, whereas in (b) there is no maximum.*
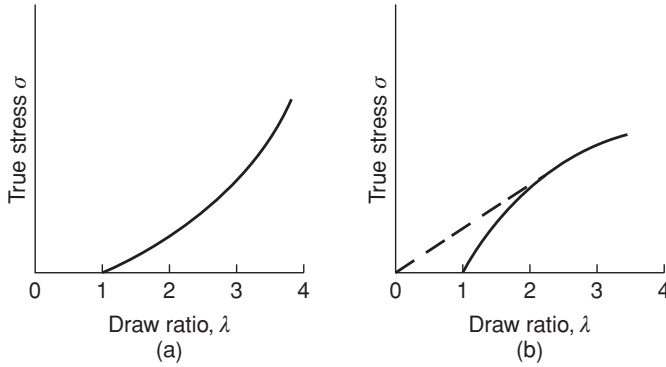
Figure 12.7 *Stress–strain curves for which (a) no Considère tangent is possible and (b) only one tangent, corresponding to the onset of necking, has been drawn.*

12.1.4   Definition of Yield Stress

Yield stress may most simply be regarded as the minimum stress at which permanent strain is produced when the stress is subsequently removed. Although this definition is satisfactory for metals, where there is a clear distinction between elastic recoverable deformation and plastic irrecoverable deformation, in polymers the distinction is not so straightforward. In many cases, such as the tensile tests discussed above, yield coincides with the observation of a maximum load in the load–elongation curve. The yield stress can then be defined as the true stress at the maximum observed load (Figure 12.8(a)). Because this stress is achieved at a comparatively low elongation of the sample, it is often adequate to use the engineering definition of the yield stress as the maximum observed load divided by the initial cross-sectional area.

In some cases, there is no observed load drop and another definition of yield stress is required. One approach is to determine the stress where the two tangents to the initial and final parts of the load–elongation curve intersect (Figure 12.8(b)).
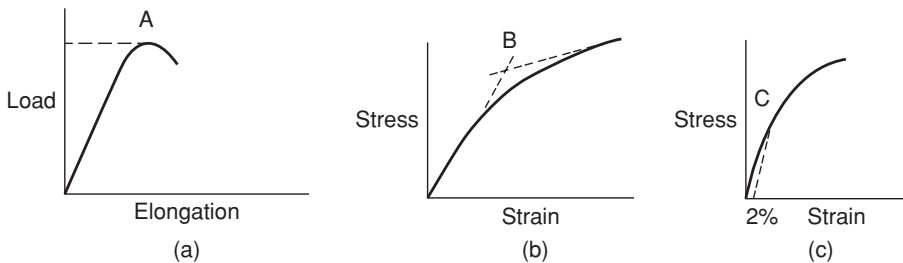
Figure 12.8   *(a) The yield stress is defined as the load divided by the cross-sectional area at the point A. (b) The yield stress is defined as the stress at the point B. (c) The yield stress is defined as the stress at the point C.*

An alternative is to attempt to define an initial linear slope on the stress–strain curve and then to draw a line parallel to this, which is offset by a specified strain, say 2%. The interception of this line with the stress–strain curve then defines the offset or proof stress, which is considered to be the yield stress (Figure 12.8(c)).

12.2   Ideal Plastic Behaviour

12.2.1   The Yield Criterion: General Considerations

The simplest theories of plasticity exclude time as a variable and ignore any feature of the behaviour, which takes place below the yield point. In other words, we assume a rigid-plastic material whose stress–strain relationship in tension is shown in Figure 12.9. For stresses below the yield stress there is no deformation. Yield can be produced by a wide range of stress states, not just simple tension. In general, it must therefore be assumed that the yield condition depends on a function of the three-dimensional stress field. In a Cartesian axis set, this is defined by the six components of stress, σ_{11}, σ_{22}, σ_{33}, σ_{12}, σ_{23} and σ_{31}. However, the numerical values of these components depend on the orientation of the axis set, and it is crucial that the yield criterion be independent of the observer's chosen viewpoint; the yield criterion must be invariant with respect to changes in the axis set. It is often convenient to make use of the principal stresses. If the material itself is such that its tendency to yield is independent of the direction of the stresses – that is if it is isotropic – then the yield criterion is a function of the principal stresses only

$$f(\sigma_{\mathrm{I}}, \sigma_{\mathrm{II}}, \sigma_{\mathrm{III}}) = \text{constant}.$$

12.2.2   The Tresca Yield Criterion

The earliest yield criterion to be suggested for metals was Tresca's proposal that yield occurs when the maximum shear stress reaches a critical value [8],

$$\sigma_{\mathrm{I}} - \sigma_{\mathrm{III}} = \text{constant}$$

with $\sigma_{\mathrm{I}} > \sigma_{\mathrm{II}} > \sigma_{\mathrm{III}}$.

Of a similar nature is the Schmid critical resolved shear-stress law for the yield of metal single crystals [9].
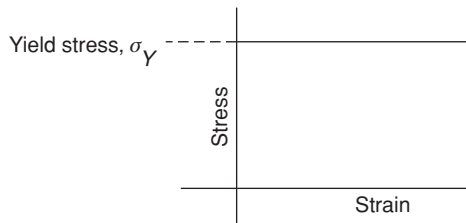
Figure 12.9   *Stress–strain relationship for an ideal rigid-plastic material.*

12.2.3   The Coulomb Yield Criterion

The Tresca yield criterion assumes that the critical shear stress is independent of the normal pressure on the plane on which yield is occurring. Although this assumption is valid for metals, it is more appropriate in polymers to consider the possible applicability of the Coulomb yield criterion [10] which states that the critical shear stress τ for yielding to occur in any plane varies linearly with the stress normal to this plane, that is

$$\tau = \tau_c - \mu \sigma_N. \tag{12.4}$$

The Coulomb criterion was originally conceived for the failure of soils and τ_c was termed the 'cohesion' and μ the coefficient of internal friction. For a compressive stress, σ_N has a negative sign so that the critical shear stress τ for yielding to occur on any plane increases linearly with the pressure applied normal to this plane.

The Coulomb criterion is often written as

$$\tau = \tau_c - \tan \phi \sigma_N, \tag{12.5}$$

where μ has been written as $\tan \phi$, for reasons which will now become apparent.

Consider uniaxial compression under a compressive stress σ_1 where yield occurs on a plane whose normal makes an angle θ with the direction of σ_1 (Figure 12.10).

The shear stress is $\tau_1 = \sigma \sin \theta \cos \theta$ and the normal stress $\sigma_N = -\sigma_1 \cos^2 \theta$. Yield occurs when

$$\sigma_1 \sin \theta \cos \theta = \tau_c + \sigma_1 \tan \phi \cos^2 \theta,$$

i.e. when

$$\sigma_1 (\cos \theta \sin \theta - \tan \phi \cos^2 \theta) = \tau_c.$$

For yield to occur at the lowest possible value of σ_1, ($\cos\theta \sin\theta - \tan \phi \cos^2\theta$) must be a maximum, which gives

$$\tan \phi \tan 2\theta = -1 \ or \ \theta = \frac{\pi}{4} + \frac{\phi}{2}. \tag{12.6}$$
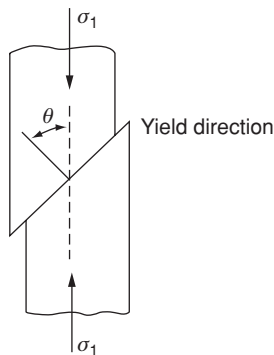
Figure 12.10   *The yield direction under a compressive stress σ_1 for a material obeying the Coulomb criterion.*

Thus, $\tan\phi$ determines the direction of yield and conversely the direction of yielding can be used to define ϕ, where $\tan\phi$ is the coefficient of friction. If the stress σ_1 is tensile the angle θ is given by

$$\theta = \frac{\pi}{4} - \frac{\phi}{2}.$$

We see that the Coulomb yield criterion therefore defines both the stress condition required for yielding to occur and the directions in which the material will deform. Where a deformation band forms, its direction is that which is neither rotated nor distorted by the plastic deformation, because its orientation marks that direction which establishes material continuity between the deformed material in the deformation band and the undistorted material in the rest of the specimen. If volume is conserved, the band direction therefore denotes the direction of shear in a simple shear (by the definition of a shear strain). Thus for a Coulomb yield criterion, the band direction is defined by Equation (12.6).

12.2.4   The von Mises Yield Criterion

The von Mises yield criterion [11] assumes that the yield behaviour is independent of hydrostatic pressure and that the yield stresses in simple tension and compression are equal. It is expressed most simply in terms of the principal components of stress so that

$$(\sigma_\mathrm{I} - \sigma_\mathrm{II})^2 + (\sigma_\mathrm{II} - \sigma_\mathrm{III})^2 + (\sigma_\mathrm{III} - \sigma_\mathrm{I})^2 = \text{constant.} \tag{12.7}$$

The constant term in Equation (12.7) can be easily expressed in terms of the yield stress σ_Y in uniaxial testing. Then we can assign the values $\sigma_\mathrm{I} = \sigma_Y$, $\sigma_\mathrm{II} = \sigma_\mathrm{III} = 0$ and the constant on the right is found to be $2\sigma_Y^2$.

In rather more sophisticated terms, the von Mises yield criterion assumes that the yield criterion depends only on the components of the deviatoric stress tensor obtained by subtracting the hydrostatic components of stress from the total stress tensor. In terms of principal components of stress, the deviatoric stress tensor is

$$\begin{bmatrix} \sigma_\mathrm{I}' & 0 & 0 \\ 0 & \sigma_\mathrm{II}' & 0 \\ 0 & 0 & \sigma_\mathrm{III}' \end{bmatrix} = \begin{bmatrix} \sigma_I + p & 0 & 0 \\ 0 & \sigma_\mathrm{II} + p & 0 \\ 0 & 0 & \sigma_\mathrm{III} + p \end{bmatrix},$$

where $p = -\frac{1}{3}(\sigma_\mathrm{I} + \sigma_\mathrm{II} + \sigma_\mathrm{III})$ is the hydrostatic pressure. The von Mises yield criterion can then be written as

$$\sigma_\mathrm{I}'^2 + \sigma_\mathrm{II}'^2 + \sigma_\mathrm{III}'^2 = \text{constant.} \tag{12.8}$$

The von Mises yield criterion is often written in terms of the so-called octahedral shear stress τ_oct, where

$$\tau_\mathrm{oct} = \frac{1}{3}\left\{(\sigma_\mathrm{I} - \sigma_\mathrm{II})^2 + (\sigma_\mathrm{II} - \sigma_\mathrm{III})^2 + (\sigma_\mathrm{III} - \sigma_\mathrm{I})^2\right\}^{\frac{1}{2}}$$

giving the yield criterion as $\tau_\mathrm{oct} = \text{constant}$.

In an arbitrary 1-2-3 axis set, the criterion is in the form of the invariant expression

$$(\sigma_{11} - \sigma_{22})^2 + (\sigma_{22} - \sigma_{33})^2 + (\sigma_{33} - \sigma_{11})^2 + 2\left(\sigma_{12}^2 + \sigma_{23}^2 + \sigma_{31}^2\right) = \text{constant.} \tag{12.9}$$

We have seen that the Coulomb yield criterion defines both the stresses required for yield and also the directions in which the material deforms. In the case of the von Mises yield criterion, we require a further development of the theory to predict the directions in which plastic deformation starts.

It is important to appreciate that plasticity is different in kind from elasticity, where there is a unique relationship between stress and strain defined by a modulus or stiffness constant. Once we achieve the combination of stresses required to produce yield in an idealised rigid-plastic material, deformation can proceed without altering stresses, and is determined by the movements of the external constraints, for example the displacement of the jaws of the tensometer in a tensile test. This means that there is no unique relationship between the stresses and the total plastic deformation. Instead, the relationships that do exist relate the stresses and the incremental plastic deformation, as was first recognised by St Venant, who proposed that for an isotropic material the principal axes of the strain increment are parallel to the principal axes of stress.

If the material is assumed to remain isotropic after yield there is no dependence on the deformation or stress history. Furthermore, if we assume that the yield behaviour is independent of the hydrostatic component of stress then the principal axes of the strain increment are parallel to the principal axes of the deviatoric stress tensor.

Levy [12] and von Mises [11] independently proposed that the principal components of the strain-increment tensor

$$\begin{bmatrix} de_I & 0 & 0 \\ 0 & de_{II} & 0 \\ 0 & 0 & de_{III} \end{bmatrix}$$

and the deviatoric stress tensor

$$\begin{bmatrix} \sigma_I' & 0 & 0 \\ 0 & \sigma_{II}' & 0 \\ 0 & 0 & \sigma_{III}' \end{bmatrix}$$

are proportional, that is

$$\frac{de_I}{\sigma_I'} = \frac{de_{II}}{\sigma_{II}'} = \frac{de_{III}}{\sigma_{III}'} = d\lambda, \tag{12.10}$$

where $d\lambda$ is not a material constant but is determined by our choice of the extent of deformation of the material, for example by the displacement of the jaws of the tensometer.

Rewriting the individual deviatoric stresses

$$\sigma_I' = \sigma_I + p$$
$$\sigma_{II}' = \sigma_{II} + p$$
$$\sigma_{III}' = \sigma_{III} + p$$

and adding them gives

$$\sigma_I' + \sigma_{II}' + \sigma_{III}' = \sigma_I + \sigma_{II} + \sigma_{III} - 3 \times \frac{1}{3}(\sigma_I + \sigma_{II} + \sigma_{III}) = 0.$$

From Equation (12.10), we have three relations

$$\sigma'_I = \frac{de_I}{d\lambda}, \sigma'_{II} = \frac{de_{II}}{d\lambda}, \sigma'_{III} = \frac{de_{III}}{d\lambda}$$

that when added give

$$\sigma'_I + \sigma'_{II} + \sigma'_{III} = \frac{de_I + de_{II} + de_{III}}{d\lambda}.$$

It follows that $de_I + de_{II} + de_{III} = 0$, that is that deformation takes place at constant volume.

If the stress–strain relations are referred to other than principal axes we have

$$de_{ij} = \sigma'_{ij}d\lambda \ (i,j = 1, 2, 3),$$

that is

$$\frac{de_{11}}{d\sigma'_{11}} = \frac{de_{22}}{d\sigma'_{22}} = \frac{de_{33}}{d\sigma'_{33}} = \frac{de_{23}}{d\sigma'_{23}} = \frac{de_{31}}{d\sigma'_{31}} = \frac{de_{12}}{d\sigma'_{12}} = d\lambda.$$

These equations are called the Levy–Mises equations.

12.2.5 Geometrical Representations of the Tresca, von Mises and Coulomb Yield Criteria

The assumption of material isotropy which implies that σ_I, σ_{II} and σ_{III} are interchangeable, means that the Tresca and von Mises yield criteria take very simple analytical forms when expressed in terms of the principal stresses. Thus the yield criteria form surfaces in principal stress space, that is that space where the three rectangular Cartesian axes are parallel to the principal stress directions. Points lying closer to the origin than the yield surface represent combinations of stress where yield does not occur; points on or outside the surface represent combinations of stress where yield does occur.

Because the yield criterion is independent of the hydrostatic component of stress, we can replace σ_I, σ_{II} and σ_{III} by $\sigma_I + p$, $\sigma_{II} + p$ and $\sigma_{III} + p$, respectively, without affecting the material's state with regard to yield. Thus, if the point in principal stress space $(\sigma_I, \sigma_{II}, \sigma_{III})$ lies on the yield surface, so does the point $(\sigma_I + p, \sigma_{II} + p, \sigma_{III} + p)$. This shows that the yield surface must be parallel to the $\{111\}$ direction, and has the appearance as sketched in Figure 12.11. The material isotropy implies equivalence between σ_I, σ_{II} and σ_{III} and hence that the section has a threefold symmetry about the $\{111\}$ axis. The assumption that the behaviour is the same in tension and compression implies an equivalence between σ_1 and $-\sigma_1$ and so on and hence we have finally sixfold symmetry about the $\{111\}$ direction. This is most clearly shown by the Tresca yield surface in Figure 12.11.

12.2.6 Combined Stress States

For the analysis of combined stress in the two-dimensional situation the Mohr circle diagram (see standard texts [13]) is of value. Normal stresses are represented along the 1 axis and shear stresses along the 2 axis, so that the Mohr circle thus represents a state of stress, with each point representing the stresses on a particular plane. The direction of the plane normal is given relative to the directions of the principal stresses by the rule that a rotation in real space of θ in a clockwise direction, corresponds to a rotation in Mohr circle space of 2θ
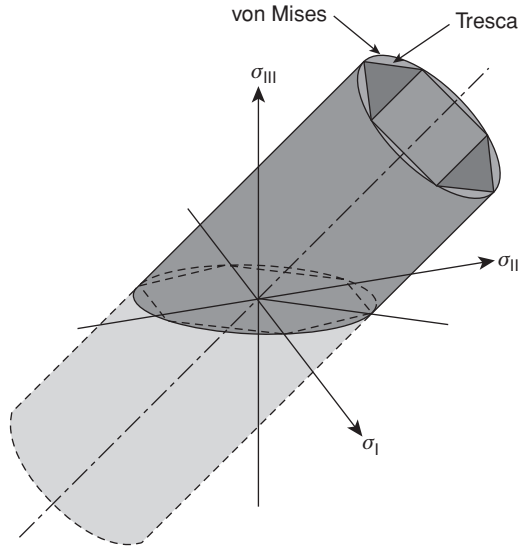
Figure 12.11   *Tresca and von Mises yield surfaces in principal stress space.*

in an anticlockwise direction. In Figure 12.12(a), two states of stress which produce yield with principal stresses σ_1 and σ_2, σ_3 and σ_4, respectively, are represented by two circles of identical radius, tangential to the yield surface. The yield criterion in this case is assumed to be that of Tresca and the yield surface degenerates for the two-dimensional case to two lines parallel to the normal stress axis.

In Figure 12.12(b), two states of stress causing yield for a material which satisfies the Coulomb criterion are shown as σ_5 and σ_6, σ_7 and σ_8, respectively. In this case, the yield
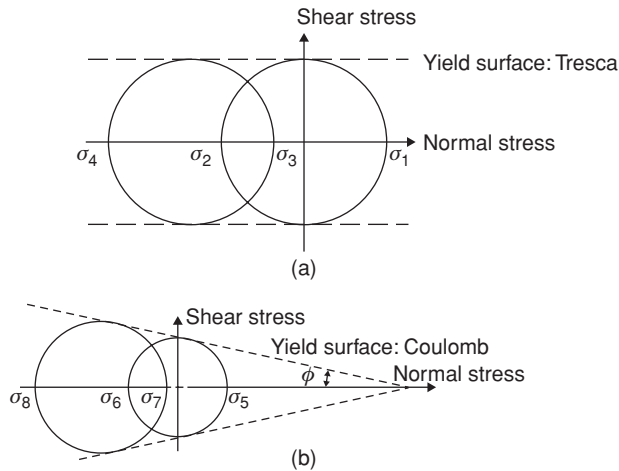
Figure 12.12   *Mohr circle diagram for two states of stress which produce yield in a material satisfying (a) the Tresca yield criterion, and (b) the Coulomb yield criterion.*

stress depends on the magnitude of the (negative) normal stress, and so the diameters of the Mohr circles will vary with applied stress, increasing as we move to a more compressive stress field. The tangents to the Mohr circles represent the Coulomb yield surface, the critical shear yield stress for yield decreasing as the normal stress becomes more tensile. It can be shown that these tangents make an angle ϕ with the normal stress axis, where $\tan \phi$ is the coefficient of friction as defined in Section 12.2.3.

12.2.7 Yield Criteria for Anisotropic Materials

A very simple yield criterion for anisotropic materials is the critical resolved shear stress of Schmid [14]. This is concerned with crystal slip. The law states that yield occurs when the resolved shear stress in the slip direction in the slip plane reaches a critical value. Although this law is extensively used in metal plasticity, it is of restricted application in polymers.

Hill [15] has developed a generalisation of the von Mises criterion for anisotropic materials. Anisotropy is defined with respect to specific axes fixed within the material which, in the case of orthotropic materials, are mutually perpendicular. Then, a 1–2–3 axes set can be chosen to align with the directions of orthotropy and the yield criterion defined with respect to the stresses in this axis set. This precludes the use of principal stresses as the principal directions do not in general coincide with the directions of orthotropy. Therefore, Hill's criterion is a generalisation of Equation (12.9)

$$F(\sigma_{22} - \sigma_{33})^2 + G(\sigma_{33} - \sigma_{11})^2 + H(\sigma_{11} - \sigma_{22})^2 + 2(L\sigma_{23}^2 + M\sigma_{31}^2 + N\sigma_{12}^2) = 1.$$

$$(12.11)$$

Here F, G, H, L, M and N are material parameters that define the anisotropy. When they are all equal to unity, the criterion reduces to that of von Mises. Clearly the observed tensile yield stress will depend on the direction of stress according to this criterion. This criterion has recently been applied to particle-filled polymers by Van Dommelen and Meijer [16], who made use of the direction-dependent yield stress to fit their model.

12.2.7.1 Back Stress and Bauschinger Effect

When a polymer is oriented predominantly in one direction, it is observed that the tensile yield stress along the direction of drawing is greater than in other directions, and also greater than the compressive yield stress. This latter phenomenon is known as the *Bauschinger effect* and has been observed for both glassy and semi-crystalline-oriented polymers for many years, as studied by Brown *et al*. [17] and Duckett *et al*. [18]. In order to represent this effect and to improve the treatment of the anisotropy of yielding, Brown *et al*. [17] introduced an *internal stress* or *back stress* σ_i. This can be thought of as the compressive stress in the material that is required to balance the tension resulting from chains extended in the draw direction, which must be overcome before tensile yield processes can begin to act. The internal stress was introduced as a modification to the Hill criterion, which for a material oriented in the 1 direction becomes

$$F(\sigma_{22} - \sigma_{33})^2 + G(\sigma_{33} - \sigma_{11} + \sigma_i)^2 + H(\sigma_{11} - \sigma_i - \sigma_{22})^2$$
$$+ 2(L\sigma_{23}^2 + M\sigma_{31}^2 + N\sigma_{12}^2) = 1.$$
$$(12.12)$$

Brown *et al*. showed that this modified version gave a better fit to the yield in simple shear of oriented polycarbonate than Equation (12.11). For experiments in which the direction of
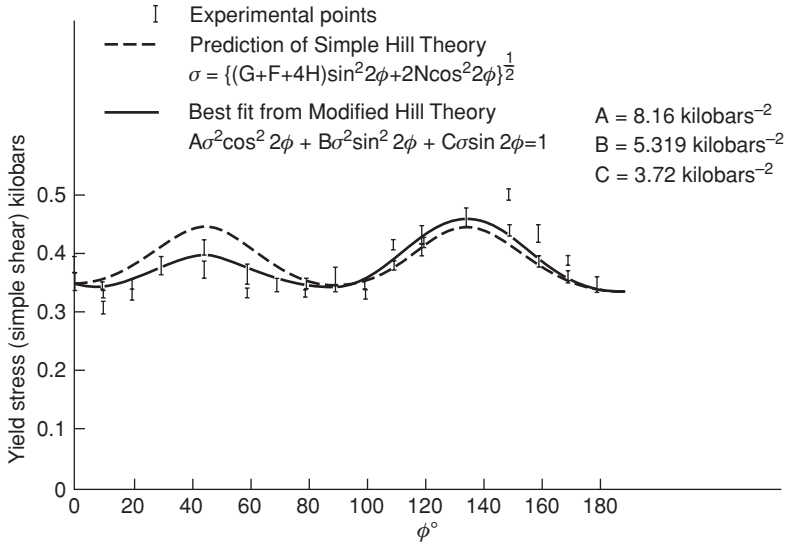
Figure 12.13   *Comparison of the effectiveness of the Hill criterion and its modified form with internal stress. (Redrawn with permission from Brown, N., Duckett, R.A. and Ward, I.M. (1968) The yield behaviour of oriented polyethylene terephthalate. Phil. Mag.,* **18**, 483. Copyright (1968).)

shearing was varied with respect to the orientation axis, the results in terms of shear yield stress are plotted in Figure 12.13. The presence of the back stress enables the theoretical fit to show maxima of different heights, in line with the experimental findings.

We have so far not addressed the physical origin of the internal stress. The modified Hill criterion is not a complete constitutive material model. It would ideally arise as a consequence of such a model, in which case it would be possible to explore its other implications and its evolution during the drawing process. The question of, for instance, whether it is entropic or energetic is not addressed. These issues will be discussed further below in Section 12.8.

12.2.8   The Plastic Potential

The Levy–Mises equations define one of a number of possible flow rules that can be derived via an argument that depends upon a concept known as the plastic potential. This idea has been discussed by Hill [15]. It is assumed that the components of the plastic strain increment tensor are proportional to the partial derivatives of the plastic potential, which is a scalar function of stress. The flow rule can thus be generated by this differentiation process. We may choose to assume, for a particular form of yield criterion, that the plastic potential has the same functional form as the yield criterion; then, the derived flow rule is described as being *associated* with the yield criterion (or as an *associative* flow rule). However, this assumption is not obligatory and when it is not true we will be applying a yield criterion together with a *non-associated* flow rule. This is discussed further by de Souza Neto *et al*. [19].

As an example, suppose that we have a plastic potential f of the same functional form as the von Mises criterion. Then, in principal directions we assume that

$$f = \frac{d\lambda}{6} \left((\sigma_I - \sigma_{II})^2 + (\sigma_{II} - \sigma_{III})^2 + (\sigma_{III} - \sigma_I)^2 \right),$$

where $d\lambda$ is a constant. For each principal direction, we may obtain an expression for the plastic strain increment. Taking the 1 direction as an example,

$$de_I = \frac{\partial f}{\partial \sigma_I} = \frac{d\lambda}{6} \left(2(\sigma_I - \sigma_{II}) - 2(\sigma_{III} - \sigma_I) \right)$$

$$= d\lambda \left(\sigma_I - \frac{1}{3}(\sigma_I + \sigma_{II} + \sigma_{III}) \right) = d\lambda(\sigma_I - \bar{\sigma}) = d\lambda \sigma_I'.$$

This reproduces the first of the Levy–Mises Equation (12.10). The Levy–Mises flow rule is thus associated with the von Mises criterion.

Similarly, let us on the basis of Equation (12.11) construct the plastic potential for the Hill criterion

$$f = \frac{d\lambda}{2} \left[F(\sigma_{22} - \sigma_{33})^2 + G(\sigma_{33} - \sigma_{11})^2 + H(\sigma_{11} - \sigma_{22})^2 + 2(L\sigma_{23}^2 + M\sigma_{31}^2 + N\sigma_{12}^2) \right].$$

Then, we can construct Hill's flow rule [15] from the expressions given by

$$de_{ij} = \frac{\partial f}{\partial \sigma_{ij}} \quad (i, j = 1, 2, 3),$$

which results in

$$
\begin{aligned}
de_{11} &= d\lambda \left[H(\sigma_{11} - \sigma_{22}) + G(\sigma_{11} - \sigma_{33}) \right] \\
de_{22} &= d\lambda \left[F(\sigma_{22} - \sigma_{33}) + H(\sigma_{22} - \sigma_{11}) \right] \\
de_{33} &= d\lambda \left[G(\sigma_{33} - \sigma_{11}) + F(\sigma_{33} - \sigma_{22}) \right] \\
de_{23} &= d\lambda L \sigma_{23} \\
de_{13} &= d\lambda M \sigma_{13} \\
de_{12} &= d\lambda N \sigma_{12}.
\end{aligned}
\tag{12.13}
$$

12.3　Historical Development of Understanding of the Yield Process

We have seen that yield is often associated with a load drop on the load–extension curve, and always involves a change in slope on the true stress–strain curve. This load drop has sometimes been attributed either to adiabatic heating of the specimen or to the geometrical reduction in cross-sectional area on the formation of a neck. Present knowledge leads to the conclusion that yielding is an intrinsic property of the material, and that temperature rises and necking are secondary consequences. This is supported by the observations in the previous chapter (see Section 11.3.4), to the effect that the Eyring process gives a consistent model of yield in polymers. Localised or geometrical effects can have no relevance to this molecular-based model. However, temperature and geometrical effects are present during yielding, and must be understood if the phenomenon is to be interpreted correctly.

12.3.1   Adiabatic Heating

Under conventional conditions of cold-drawing, where the specimen is extended at strain rates of the order of 10^{-2} s^{-1} or higher, a considerable rise of temperature occurs in the region of the neck. Marshall and Thompson [20], following Müller [21], proposed that cold-drawing involves a local temperature rise and that necking occurs because of strain softening produced by the consequent fall in flow stress with rising temperature. The stability of the drawing process was then attributed to the stability of a localised process of heat transfer through the shoulders of the neck, with extension taking place at constant tension throughout the neck.

Hookway [22] later attempted to explain the cold-drawing of nylon 6.6 on somewhat similar grounds, suggesting that there is a possibility of local melting in the neck due to a combination of hydrostatic tension and temperature.

There is no doubt that an appreciable rise in temperature does occur at conventional drawing speeds, and the ideas of Marshall and Thompson are very relevant to an understanding of the complex situation of fibre drawing. Calorimetric measurements by Brauer and Müller [23] have, however, shown that at slow rates of extension the increase in temperature is quite small ($\sim$10°C) and not sufficient to give an explanation for necking and cold-drawing and cold-drawing in terms of adiabatic heating. In addition, Lazurkin [24] demonstrated that necking could still take place under quasi-static conditions, for elastomers below their glass transition temperature, cold-drawn at very low speeds. A comparable result was shown by Vincent [5] for (semi-crystalline) polyethylene which cold-draws at very slow extension rates at room temperature.

The adiabatic heating explanation arose at least in part because the initial yield process was not regarded as distinct from the drawing process. It is now recognised that up to the yield point the deformation of the sample is homogeneous and generally quite small strains are involved, whereas once a neck forms, the deformation is inhomogeneous and large strains are involved in the neck. The work of plastic deformation can then lead to a large rise in temperature in the neck. For example, Figure 12.14 shows results for the cold-drawing of PET [25] where both the yield stress and the drawing stress were measured as a function of strain rate. It can be seen that the yield stress continues to rise with increasing strain rate, beyond the strain rate at which the drawing stress falls quite distinctly. It is argued that provided the drawing is carried out at a low strain rate, any heat which is generated will be conducted away from the neck sufficiently rapidly for no significant temperature rise to occur. As the strain rate is increased and the process becomes more nearly adiabatic, the effective temperature at which the drawing is taking place is increased. In particular, heat is conducted into the unyielded portion of the sample, and so lowers the yield stress of the undeformed material and reduces the force necessary to propagate the neck.

The observed temperature rise in the neck has been found to be in approximate agreement with that calculated from the work done in drawing, assuming that no heat is generated due to crystallisation. In PET, X-ray diffraction diagrams of cold-drawn fibres show that very little crystallisation has occurred.

The work done per unit volume is given by $W = \sigma_D (\lambda_N - 1)$, where σ_D is the drawing stress and λ_N the natural draw ratio (see Sections 12.1 and 12.6). From the results obtained $\sigma_D = 23$ MPa when $\lambda_N = 3.6$, giving $W = 4.7$ MJ/m^3. For PET where the specific heat is
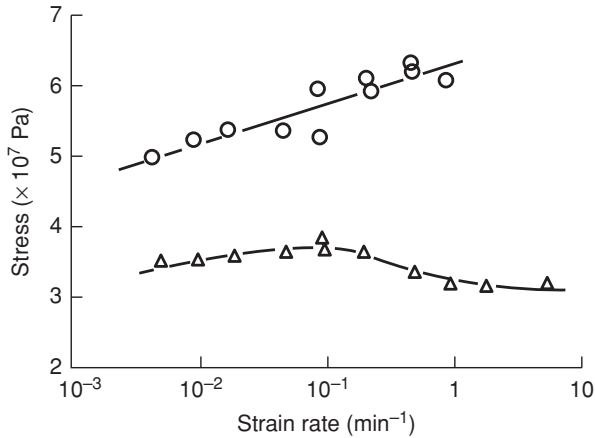
Figure 12.14 *Comparison of yield stress (○) and drawing stress (△) as a function of strain rate for PET.*

67 J/kg/K and the density is 1.38 Mg/m^3, the calculated temperature rise is 57°C, compared with the measured value of 42°C.

12.3.2 The Isothermal Yield Process: The Nature of the Load Drop

There is no doubt that a temperature rise does occur in cold-drawing under many conditions of test. We have shown, however, that there is very good evidence to support the view that necking can still take place under quasi-static conditions where there is no appreciable temperature rise. Vincent [5] therefore proposed that the observed fall in load is a geometrical effect because the fall in cross-sectional area during stretching is not compensated for by an adequate degree of strain hardening. This effect, called strain softening, was attributed to the reduction in the slope of the stress–strain curve with increasing strain.

Contrary to this latter explanation of the load drop in terms of geometric softening, results reported by Whitney and Andrews [26] showed a yield drop in compression for polystyrene and PMMA where there are no geometrical complications. Brown and Ward [27] then made a detailed investigation of yield drops in PET, studying isotropic and oriented specimens, in tension, shear and compression. They concluded that in most cases there is clear evidence for the existence of an intrinsic yield drop, that is that a fall in true stress can occur in polymers, as in metals. This is reflected in the work of Amoedo and Lee [7], shown above in Figure 12.5(a). We have seen from the energetic argument in Section 12.1.1 that an intrinsic stress drop can be physically associated with necking.

There is, however, a significant difference between polymers and many metals with regard to yield behaviour. For a polymer, as shown in Figure 12.2, only one maximum is observed on the load–extension curve, in contrast with metals (illustrated by mild steel in Figure 12.15), where often two maxima are observed on a typical load–extension curve. The first maximum (point A in Figure 12.14) called the upper yield point, represents a fall in true stress, an intrinsic load drop, and corresponds to a sudden increase in the amount of
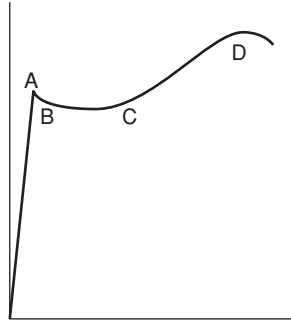
Figure 12.15   *Load–extension curve in tension of mild steel.*

plastic strain which relaxes the stress. From B to C, Lüders bands propagate throughout the specimen. Lüders bands have also been observed in polymers [25]. At C, the specimen is homogeneously strained and the stress begins to rise as the material work hardens uniformly. A second maximum is observed at point D, and is always associated with the beginning of necking in the specimen. Necking occurs when the effects of strain hardening of the metal are overwhelmed by the geometrical softening due to the reduction in the cross-sectional area of the specimen as it is strained, that is the Orowan–Vincent explanation, discussed in Section 12.1.1.

The second maximum, as we have seen previously, is not observed if the true stress–strain curve is plotted instead of the load–extension curve. The first maximum, on the other hand, would exist on the true stress–strain curve. It is called an intrinsic yield point, because it relates to the intrinsic behaviour of the material.

In polymers, as we have emphasised, only one maximum is observed in the load–extension curve. The investigations of Whitney and Andrews [26] and Brown and Ward [27] show that this maximum combines the effect of the geometrical changes and an intrinsic load drop, and cannot be attributed to the geometrical changes alone. In particular, the cold-drawing results are not accounted for by a decrease in the slope of the true stress–strain curve, as suggested in the explanation of Vincent. It is important to note that not every element of the material follows the same true stress–strain curve, since the stress for initiation is greater than for propagation of yielding, so confirming (as has already been noted in Section 11.1.3) that it will not be possible to give a complete explanation of necking and cold-drawing in terms of the Considère construction on a true stress–strain curve.

12.4   Experimental Evidence for Yield Criteria in Polymers

Many studies of the yield behaviour of polymers have bypassed the question of strain rate and temperature and sought to establish a yield criterion as discussed in Section 12.2. In very general terms, such studies divide into two categories: (1) those which attempt to define a yield criterion on the basis of determining yield for different stress states and (2) those which confine the experimental studies to an examination of the influence of hydrostatic pressure on the yield behaviour.
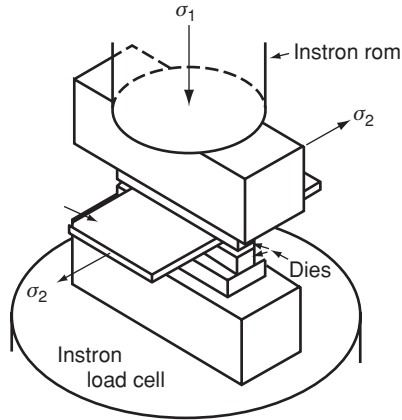
Figure 12.16 *The plane-strain compression test. (Reproduced from Bowden, P.B. and Jukes, J.A. (1968) The plastic yield behaviour of polymethylmethacrylate. J. Mater. Sci., **3**, 183. Copyright (1968) Springer Science and Business Media.)*

12.4.1 Application of Coulomb Yield Criterion to Yield Behaviour

From the early studies of yield behaviour of polymers, one example has been selected; the plane-strain compression tests on PMMA, carried out by Bowden and Jukes [28].

The experimental set-up is shown in Figure 12.16. A particular advantage of this technique is that yield behaviour can be observed in compression for materials, which normally fracture in a tensile test. In this case, PMMA was studied at room temperature, i.e. below its brittle–ductile transition temperature in tension.

The yield point in compression σ_1 was measured for various values of applied tensile stress σ_2. The results, shown in Figure 12.17, give $\sigma_1 = -110.0 + 13.65\sigma_2$, where both σ_1 and σ_2 are expressed as true stresses in units of MPa. The results therefore clearly do not fit the Tresca criterion, where $\sigma_1 - \sigma_2 = $ constant at yield; neither do they fit a von Mises yield criterion. They are, however, consistent with a Coulomb yield criterion with $\tau = 47.4 - 1.58\sigma_N$.

12.4.2 Direct Evidence for the Influence of Hydrostatic Pressure on Yield Behaviour

There have been a number of detailed investigations of the influence of hydrostatic pressure on the yield behaviour of polymers [29–35]. Because it illustrates clearly the relationship between a yield criterion which depends on hydrostatic pressure and the Coulomb yield criterion, an experiment will be discussed where Rabinowitz, Ward and Parry [29] determined the torsional stress–strain behaviour of isotropic PMMA under hydrostatic pressures up to 700 MPa. The results are shown in Figure 12.18.

There is a substantial increase in the shear yield stress up to a hydrostatic pressure of about 300 MPa. After this pressure brittle failure occurs, unless prevented by protecting the specimens from the hydraulic fluid [36] (e.g. by coating with a layer of solidified rubber solution). A study of polyethylene under conditions of combined pressure and tension has
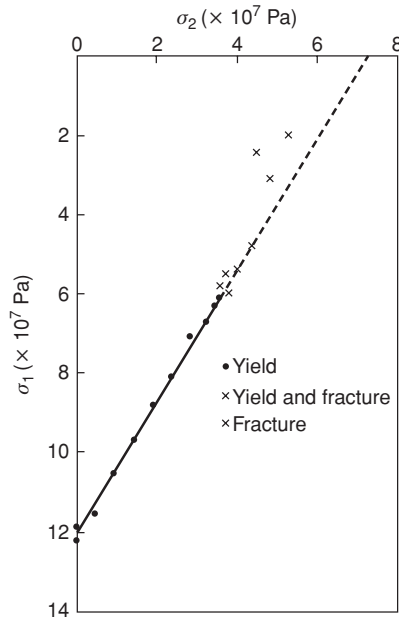
Figure 12.17 *Measured values of the compressive yield stress σ₁ (true stress) plotted against applied tensile stress σ₂ (nominal stress). The full circles denote ductile yield, the crosses, brittle fracture, and the combined points, tests where ductile yielding occurred, followed immediately by brittle fracture. (Reproduced from Bowden, P.B. and Jukes, J.A. (1968) The plastic yield behaviour of polymethylmethacrylate. J. Mater. Sci., **3**, 183. Copyright (1968) Springer Science and Business Media.)*
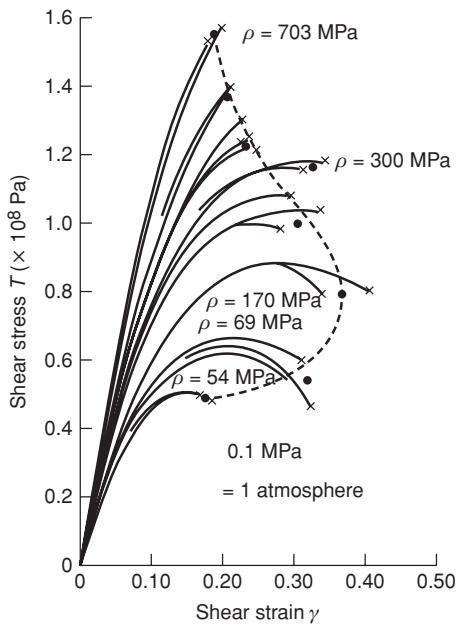
Figure 12.18 *Shear stress–strain curves for PMMA showing fracture envelope. (Reproduced with permission from Rabinowitz, S., Ward, I.M. and Parry, J.S.C. (1970) The effect of hydrostatic pressure on the shear yield behaviour of polymers. J. Mater. Sci., **5**, 29 Copyright (1970) Springer Science and Business Media.)*
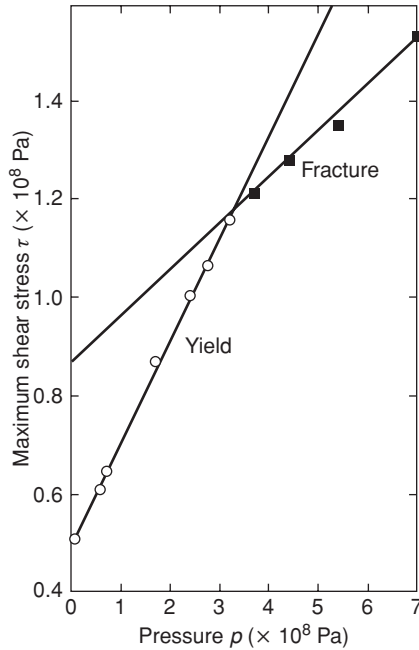
Figure 12.19 *Maximum shear stress τ as a function of hydrostatic pressure p for PMMA. (○) Yield; (■) fracture. (Reproduced with permission from Rabinowitz, S., Ward, I.M. and Parry, J.S.C. (1970) The effect of hydrostatic pressure on the shear yield behaviour of polymers. J. Mater. Sci., 5, 29. Copyright (1970) Springer Science and Business Media.)*

shown that the yield stress of polyethylene increases approximately linearly up to pressures of 850 MPa [37]. The strain at which yield occurs also increases with increasing pressure, similar to the results of other workers for tensile tests under pressure. The shear yield stress increases linearly with pressure to an excellent approximation (Figure 12.19).

There are two other ways in which these results can be presented. First, recalling Section 12.2.6 and Figure 12.12, the Mohr circle diagram can be constructed from the data, as shown in Figure 12.20 where Bowden and Jukes's results appear as crossed points. This diagram leads naturally to a Coulomb yield criterion.

However, it is equally reasonable to interpret Figure 12.19 directly in terms of the equation

$$\tau = \tau_0 + \alpha p, \tag{12.14}$$

where τ is the shear yield stress at pressure p, τ_0 is the shear yield stress at atmospheric pressure and α is the coefficient of increase of shear yield stress with hydrostatic pressure.

We will see that this simple form of pressure-dependent yield criterion is more satisfactory than the Coulomb criterion when a representation is developed which includes the effects of temperature and strain rate on the yield behaviour. In physical terms, the hydrostatic pressure can be seen as changing the state of the polymer by compressing the polymer significantly, unlike the situation in metals where the bulk moduli are much larger (~100 GPa compared
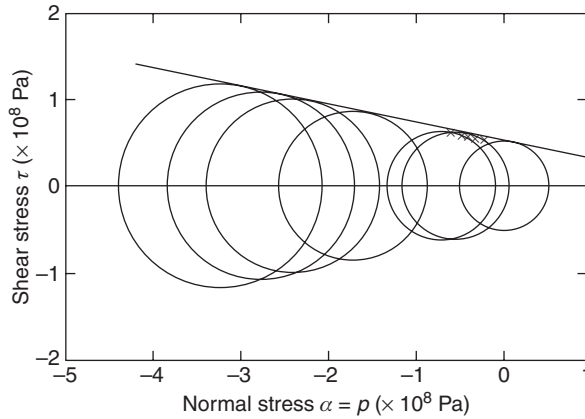
Figure 12.20 *Mohr circles for yield behaviour of polymethyl methacrylate obtained from results of Rabinowitz, Ward and Parry. The crosses are the results of Bowden and Jukes. (Reproduced with permission from Rabinowitz, S., Ward, I.M. and Parry, J.S.C. (1970) The effect of hydrostatic pressure on the shear yield behaviour of polymers. J. Mater. Sci., **5**, 29. Copyright (1970) Springer Science and Business Media.)*

with ~5 GPa). Although such experimental evidence as exists is not unequivocal in this respect, it seems likely that the yield criterion for the polymer subjected to hydrostatic pressure is still given by Equation (12.9), i.e. pressure has the sole effect of increasing the magnitude of the yield stresses.

Recent studies of yield behaviour, using a variety of multi-axial stressing experiments, can all be adequately described by a generalisation of Equation (12.14), i.e. a generalised von Mises equation where τ is replaced by the octahedral shear stress (see Section 12.5.1 for a fuller development).

Finally, it can be noted that the coefficient α in Equation (12.14) depends on the temperature of measurement and increases markedly near a viscoelastic transition. Briscoe and Tabor [38] have pointed out that α is equivalent to the coefficient of friction μ in sliding friction, and show that there is good numerical agreement between values of μ and the values of α obtained from yield stress/pressure measurements.

12.5   The Molecular Interpretations of Yield

Two principal approaches have been used to model the yield behaviour of polymers. The first approach addresses the temperature and strain-rate dependence of the yield stress in terms of the Eyring equation for thermally activated processes [39]. This approach has been applied to many amorphous and crystalline polymers (see Section 12.5.1) and links have been established with molecular relaxation processes determined by dynamic mechanical and dielectric measurements and with non-linear viscoelastic behaviour determined by creep and stress relaxation. The Eyring approach assumes that the yield process is velocity controlled, i.e. the yield process relates to existing thermally activated processes that are accelerated by the application of the yield stress to the point where the rate of plastic deformation reaches the applied macroscopic strain rate. This approach has

been very successful in modelling the yield behaviour of polymers at comparatively high temperatures [40, 41].

The second approach is based on classical ideas of crystal plasticity. It is considered that yield involves applying a critical stress to cause the movement of dislocations or disclinations. For this reason, yield is considered to be nucleation controlled. This approach was originally proposed by Bowden and Raha [42] and Argon [43] and has been applied by Young [44], Argon [43] and others to the yield behaviour of both amorphous and crystalline polymers. Young developed this crystal plasticity approach by assuming that the yield stress relates to the energy required to nucleate screw dislocations within the crystalline lamellae of a crystalline polymer. Research by Ward and co-workers [45] and Crist *et al.* [46] have confirmed that the Young approach appears to be valid for yield at low strain rates in polyethylene at $-60°C$ and temperatures below this. Detailed structural studies do suggest that at higher temperatures interlamellar shear occurs, although Young and co-workers [44, 47] and Darras and Seguela [48] have successfully used the crystal plasticity approach to model the yield behaviour of bulk crystalline and annealed semi-crystalline polymers at much higher temperatures.

12.5.1   Yield as an Activated Rate Process

We have already seen in Section 11.3.4 that yield can be modelled using the Eyring process. Many workers [19, 49–56] have considered that the applied stress induces molecular flow much along the lines of the Eyring viscosity theory where internal viscosity decreases with increasing stress. The basic equation for the plastic strain rate has been given as Equation (11.31) as

$$\dot{e} = \dot{e}_0 \exp\left(-\frac{\Delta H}{kT}\right) \sinh\left(\frac{V\sigma}{kT}\right)$$

(12.15)

for a tensile stress σ. On this view, the yield stress denotes the point at which the internal viscosity falls to a value such that the applied strain rate is identical to the plastic strain rate $\dot{e}_p$ predicted by the Eyring equation. We may make use of the exponential approximation to the hyperbolic sine function to give

$$\dot{e} = \frac{\dot{e}_0}{2} \exp\left[-\left(\frac{\Delta H - V\sigma}{kT}\right)\right].$$

(12.16)

Then, the analysis of Section 11.3.4 reveals the linear relationship between yield stress and log strain rate, corresponding to the observations of Bauwens and co-workers [52].

In an earlier paper, Lazurkin [24] rejected a previous proposal by Hookway [22] and Horsley and Nancarrow [57] that the molecular flow occurs because the applied stress reduced the melting point of the crystals. He remarked that similar behaviour is observed for both crystalline and non-crystalline polymers, the dependence of the yield stress on strain rate following the logarithmic form in both cases.

Haward and Thackray [55] have compared the Eyring activation volumes obtained from yield stress data with the volume of the 'statistical random link'. The latter was obtained from solution studies, by assuming that the real chain can be represented by an equivalent chain with freely jointed links of a particular length. Table 12.1 is based on data collated by Haward and Thackray and shows that the activation volumes are very large in molecular terms and range from about two to 10 times that of the statistical random link. The result

Table 12.1   *A comparison of the statistical segment volume for a polymer measured in solution with the flow volumes derived from the Eyring theory (after Haward and Thackray [55]).*

Polymer	Volume of statistical link in solution (nm³)	Eyring flow volume V (nm³)
Polyvinyl chloride	0.38	8.6
Polycarbonate	0.48	6.4
Polymethyl methacrylate	0.91	4.6
Polystyrene	1.22	9.6
Cellulose acetate	2.06	8.8
Cellulose trinitrate	2.62	6.1
Cellulose acetate	2.05	17.4

suggests that yield involves the cooperative movement of a larger number of chain segments than would be required for a conformational change in dilute solution.

12.5.1.1   Pressure Dependence

We have seen that the effect of pressure on the shear yield stress of a polymer can be very well represented by the Equation (12.14)

$$\tau = \tau_0 + \alpha p.$$

This suggests that the Eyring equation in its approximate form (12.16) may be very simply modified [58] to include the effect of the hydrostatic component of stress p to give

$$\dot{e} = \frac{\dot{e}_0}{2} \exp\left[-\left(\frac{\Delta H - \tau V + p\Omega}{kT} \right) \right], \tag{12.17}$$

where V and Ω are known as the shear and pressure activation volumes, respectively and τ is a suitably defined shear stress. This will be successful in an operational sense in representing tensile behaviour. To retrieve the non-approximate form resembling Equation (12.15), we need to consider the physical role of the pressure p. As discussed in Section 11.3.1, the tensile stress affects the motion of chain segments such as to produce a bias in favour of greater plastic strain in the direction of the stress. The hyperbolic sine function operates on strain events both in and opposed to the applied stress. A positive hydrostatic pressure, however, has the effect of decreasing the available free volume, so will slow down the event rates relating to both directions. The hyperbolic sine function is therefore inappropriate for the hydrostatic pressure, and so we retain an exponential function for this term. To generalise the form (12.17) to one that resembles (12.15), we then write [59]

$$\dot{e} = \dot{e}_0 \exp\left[-\left(\frac{\Delta H + p\Omega}{kT} \right) \right] \sinh\left(\frac{\tau V}{kT} \right). \tag{12.18}$$

Bauwens [60] arrived at an identical form by considering separately the action of deviatoric stress to produce strain, and that of hydrostatic stress to contribute to the formation of a hole to accommodate the chain segment motion.

Equations (12.17) and (12.18) can be used in three-dimensional stress analyses on the basis that they give scalar rates of plastic strain, which can be converted to tensor strain rate components via the use of a flow rule. The shear stress τ is defined as the octahedral shear stress in terms of the principal stresses

$$\tau_{oct} = \frac{1}{3} \left[(\sigma_I - \sigma_{II})^2 + (\sigma_{II} - \sigma_{III})^2 + (\sigma_{III} - \sigma_I)^2 \right]^{1/2}. \tag{12.19}$$

The scalar strain rate is defined as the octahedral strain rate, which for small strains is given by

$$\dot{\gamma}_{oct} = \frac{2}{3} \left[(\dot{e}_I - \dot{e}_{II})^2 + (\dot{e}_{II} - \dot{e}_{III})^2 + (\dot{e}_{III} - \dot{e}_I)^2 \right]^{1/2}. \tag{12.20}$$

The form of Equation (12.18) applicable for all stress fields is then

$$\dot{\gamma}_{oct} = \dot{\gamma}_0 \exp\left[-\left(\frac{\Delta H + p\Omega}{kT} \right) \right] \sinh\left(\frac{\tau_{oct} V}{kT} \right). \tag{12.21}$$

We can again use the exponential approximation, and see that for a constant strain rate test we have

$$\Delta H - \tau_{oct} + p\Omega = \text{constant}$$

from which an expression similar to Equation (12.14) is obtained with

$$\tau_{oct} = (\tau_{oct})_0 + \alpha p,$$

where $\alpha = \Omega/V$. Figure 12.21 shows results for polycarbonate at atmospheric pressure [61] using data from torsion, tension and compression. It can be seen that on average the values of τ_{oct} lie in the order compression > torsion > tension. The differences are therefore consistent with the observed linear dependence of τ_{oct} on pressure shown by
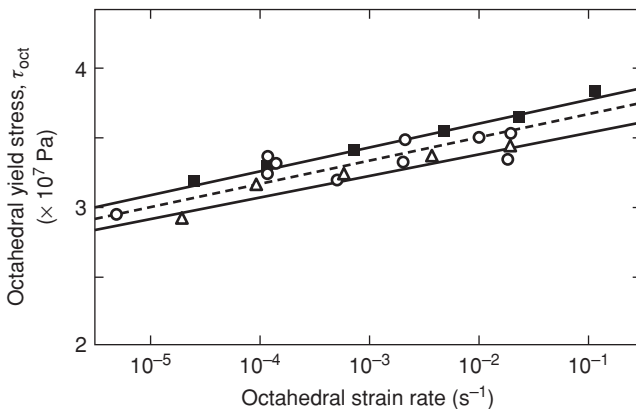
Figure 12.21 *The strain rate dependence of the octahedral shear stress r at atmospheric pressure using data from torsion ($\circ$), tension (Δ), and compression. (Reproduced with permission from Duckett, R.A., Goswami, B.C., Smith, L.S.A. et al. (1978) Yielding and crazing behavior of polycarbonate in torsion under superposed hydrostatic-pressure. Brit. Polym. J., **10**, 11. Copyright (1978) Society of Chemical Industry.)*

direct measurement of the yield stress in torsion over a range of hydrostatic pressures (see Section 12.4.2), and there is good numerical agreement between the two sets of measurements.

12.5.1.2   The Two-Stage Eyring Process Representation

Extensive studies of the yield behaviour of polymethyl methacrylate and polycarbonate over very wide ranges of strain rate and temperature by Roetling and by Bauwens have shown that the yield stresses increase more rapidly with increasing strain rate and decreasing temperature at low temperatures and high strain rates than at high temperature and low strain rates. Following Ree and Eyring [39, 62], it has therefore been proposed that the activated rate process approach should be extended by assuming that there is more than one activated rate process with all species of flow units moving at the same rate, the stresses being additive. For polymethyl methacrylate, polyvinyl chloride and polycarbonate, it has been shown that the yield behaviour can be represented very satisfactorily by the introduction of two activated processes. By re-arranging Equations (12.15) and (12.16) to give the stress as a function of the strain rate, the sum of the two processes is given by

$$\sigma = \frac{kT}{v_1}\left[\frac{\Delta H_1}{kT} + \ln\frac{\dot{e}}{\dot{e}_{01}}\right] + \frac{kT}{v_2}\sinh^{-1}\left[\frac{\dot{e}}{\dot{e}_{02}}\exp\frac{\Delta H_2}{kT}\right], \qquad (12.22)$$

where it has been assumed that the same strain rate is applied to each process, which are denoted by the subscripts 1 and 2. At high temperatures and low strain rates, process 1 predominates and this has a comparatively low strain rate dependence (v_1 is large). Therefore, we can use the approximation $\sinh x = \frac{1}{2}\exp(x)$. Process 2 also becomes important at low temperatures and high strain rates and shows a much higher strain rate dependence (v_2 is small compared to v_1) The sinh form is retained to cover the intermediate range where process 2 is giving a smaller contribution to the magnitude of the total yield stress. Figure 12.22 shows the fit obtained using Equation (12.22) to experimental data for polyvinyl chloride [52]. Similar results were also obtained for polycarbonate, although in a later paper on polymethyl methacrylate [63] it was shown that the Ree–Eyring equation only fitted the data well in the region where the approximation $\sinh x = \frac{1}{2}\exp(x)$ is valid. It was proposed that a modification of the theory taking into account a distribution of relaxation times not only gave a much better fit to the theory but established a quantitative link between process 2 and the dynamic mechanical β-relaxation.

12.5.1.3   Double Yield in Polyethylenes

As we have seen, the strain rate dependence does suggest that yield behaviour often indicates the presence of two thermally activated processes, as discussed above. In some cases, notably polyethylene, a double yield point is observed. Ward and co-workers [64], Seguala and Darras [65] and Gupta and Rose [66] concur that these two deformation processes are essentially interlamellar shear and intra lamellar shear (or *c*-slip). They are akin to the dynamic mechanical relaxation processes identified in Chapter 10.7.1 for the specially oriented PE sheets, and Seguala and Darras have related them to the α_1 and α_2 transitions reported by Takayanagi [67]. This establishes a direct link between yield and viscoelastic behaviour.
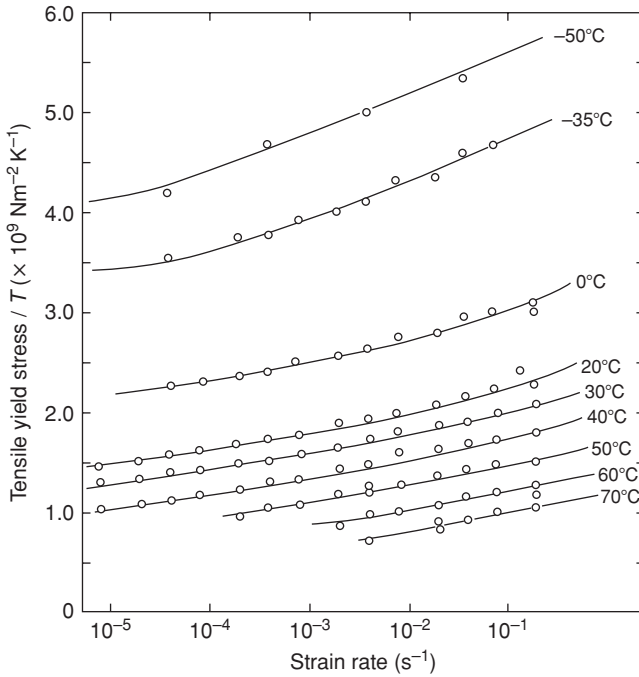
Figure 12.22 *Measured ratio of yield stress to temperature as a function of logarithm of strain rate for polyvinyl chloride. The set of parallel curves is calculated from Equation (12.22). (Redrawn from Bauwens-Crowet, C., Bauwens, J.A. and Homès, G. (1969) Tensile yield-stress behavior of glassy polymers. J. Polym. Sci. A2, 7, 735. Copyright (1969) John Wiley & Sons, Inc.)*

12.5.1.4 Relationship of Yield to Creep

As discussed in Section 11.3.1, Eyring and collaborators had already considered the application of activated rate theory to the creep of polymers. For polymethyl methacrylate, Sherby and Dorn [68] showed that the creep rate could be fitted to an equation of the form

$$\dot{e} = A(e) \exp\left[-\frac{\Delta H - B\sigma}{kT}\right], \tag{12.23}$$

where B is a constant (equivalent to the activation volume v of Equation (12.15)) and $A(e)$ is a function of creep strain.

Mindel and Brown [69], in a later study, proposed that for the initial part of the creep curve it could be considered that the logarithmic creep rate diminishes linearly with strain. Then

$$\dot{e} = \dot{e}_0 \exp\left[-\left(\frac{\Delta H - B\sigma}{kT}\right)\right] \exp(-ce_R),$$
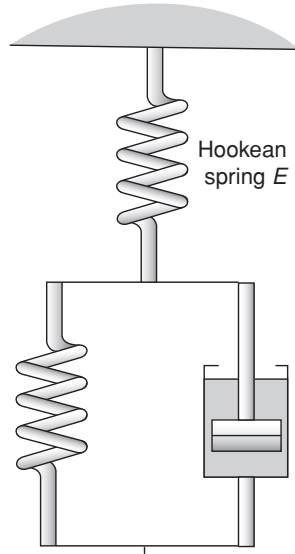
Figure 12.23   *Schematic diagram of the Haward–Thackray model.*

where we denote the strain in this initial region as e_R, recoverable strain and c is a constant. We can also write

$$\dot{e} = \dot{e}_0 \exp\left(-\frac{\Delta H}{kT}\right) \exp\left[\frac{(\sigma - \sigma_{\text{int}})V}{kT}\right],$$

where $\sigma_{\text{int}} V / kT = ce_R$ defines a rubber-like internal stress σ_{int} which is proportional to absolute temperature T. (For a further discussion, see Section 11.3.2).

In an earlier development, Haward and Thackray [55] had proposed a very similar representation to describe the yield behaviour of polymers. Their model is shown schematically in Figure 12.23. The initial part of the stress–strain curve is modelled by the Hookean spring E and the yield point and subsequent strain hardening by the Eyring dashpot and the Langevin spring. Haward and Thackray relate the total strain e and the plastic strain e_A from the activated dashpot to the nominal stress σ_n (load applied divided by initial cross-sectional area). We have

$$e = \frac{\sigma_n(1+e)}{E} + e_A \tag{12.24}$$

and

$$\frac{d\left[\ln(1+e_A)\right]}{dt} = \dot{e}_A \exp\left(-\frac{\Delta H}{kT}\right) \sinh\frac{V(\sigma_n - \sigma_R)}{kT}, \tag{12.25}$$

where σ_R is the internal rubber-like stress, which is proposed can be determined from rubber elasticity theory (see Equation (4.41)), so that

$$\sigma_R = \frac{1}{3} NkTn^{1/2}\left[\mathscr{L}^{-1}\left(\frac{1+e_A}{n^{1/2}}\right) - (1+e_A)^{-3/2}\mathscr{L}^{-1}\left(\frac{1}{(1+e_A)^{1/2}n^{1/2}}\right)\right], \tag{12.26}$$
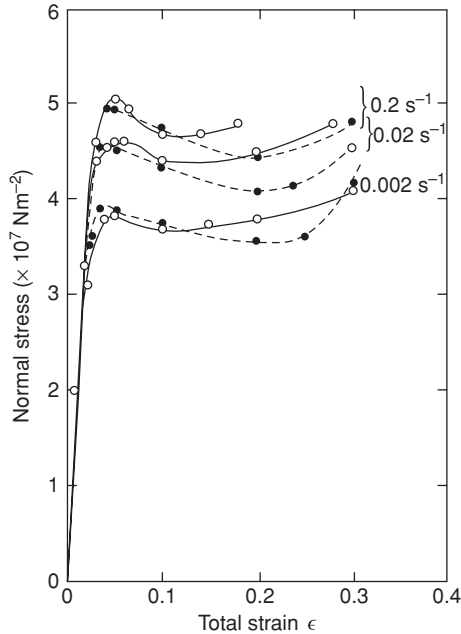
Figure 12.24 *Stress–strain curves for cellulose nitrate at 23°C. Experimental curves (0) and calculated curves, Langevin model (e). n 1/2 = 0.30, N = 1.57 × 10²⁶ chain m⁻³●. (Redrawn from Haward, R.N. and Thackray, G. (1968) The use of a mathematical model to describe isothermal stress-strain curves in glassy thermoplastics. Proc. Roy. Soc. A, **302**, 453. Copyright (1968).)*

where $\mathscr{L}^{-1}$ is the inverse Langevin function, N is the number of chains between cross-link points per unit volume and n is the average number of random links per chain.

Equation (12.25) was then integrated numerically, using Equations (12.24) and (12.26), to give results like those shown in Figure 12.24. It can be seen that the Haward and Thackray model is able to reproduce the main features of the stress–strain curve and provide a semi-quantitative fit to the experimental data. However, it may be recalled that the size of the activation volumes are very large compared with the size of an individual molecular segment.

Fotheringham and Cherry [70] adopted a similar representation to Haward and Thackray and used the stress-transient dip test to determine the internal stress σ_R and hence the effective stress $\sigma_n - \sigma_R$ acting on the Eyring dashpot. Fotheringham and Cherry proposed a model based on cooperative Eyring processes with the probability of a successful cooperative event involving the simultaneous occurrence of n transitions. Then

$$\dot{e} = \dot{e}_0 \exp\left[-\frac{n\Delta H}{kT}\right] \sinh^n\left(\frac{V\tau}{2kT}\right).$$

Results for linear polyethylene were fitted to give a value of about three for n and an activation volume of 0.5 nm³, which is in the same range as the volume swept out by an elementary displacement of a defect moving through the crystal lattice.

Recent research on the recovery behaviour of oriented polymers (so-called shape memory polymers) where the initial plastic deformation can be reversed, either fully or partially, by heating to temperatures higher than that of the initial deformation, has thrown more light on the nature of the internal stress. It is clear that this stress cannot be simply regarded as directly akin to a rubber-like stress because its behaviour with regard to temperature and strain rate does not correspond quantitatively with that expected for a rubber.

12.5.1.5   The Robertson Theory

Robertson [71] has developed a slightly more elaborate version of the Eyring viscosity theory. For simplicity, it is considered that there are only two rotational conformations, the *trans* low-energy state and the *cis* high-energy state, which Robertson terms the 'flexed state'. Applying a shear stress τ causes the energy difference between the two stable conformational states of each bond to change from ΔU to $(\Delta U - \tau V \cos \theta)$. $\tau V \cos \theta$ represents the work done by the shear stress in the transition between the two states and θ is the angle defining the orientation of a particular element of the structure with respect to the shear stress.

Prior to application of stress the fraction of elements in the high-energy state is

$$\chi_i = \frac{\exp\left\{-\Delta U / k\theta_g\right\}}{1 + \exp\left\{-\Delta U / k\theta_g\right\}},$$

where $\theta_g = T_g$ if the test temperature $T < T_g$ and $\theta_g = T$ if $T > T_g$, i.e. below T_g the configurational state 'freezes' at that which exists at T_g. For application of a shear stress τ at a temperature T, the fraction of elements in the upper state with orientation θ is given by

$$\chi_f(\theta) = \frac{\exp\left\{-(\Delta U - \tau V \cos \theta)/kT\right\}}{1 + \exp\left\{-(\Delta U - \tau V \cos \theta)/kT\right\}}.$$

Clearly the fraction of flexed elements increases for orientations such that

$$\frac{\Delta U - \tau V \cos \theta}{kT} \leq \frac{\Delta U}{k\theta_g}.$$

For one part of the distribution of structural elements, applying the stress tends to make for an equilibrium situation where there are more flexed bonds and this can be regarded as corresponding to a rise in temperature. For the other part of the distribution, the effect of stress can be regarded as tending to lower the temperature. Robertson now argues that the *rate* at which conformational changes occur is very dependent on temperature (cf. WLF equation). Hence, the rate of approach to equilibrium is much faster for these elements that flex under the applied stress, so that changes in the others can be ignored in calculating the maximum flexed-bond fraction which can occur under a given applied stress. This maximum corresponds to a rise in temperature to a temperature θ_1. The strain rate $\dot{e}$ at θ_1 is calculated from the WLF equation

$$\dot{e} = \frac{\tau}{\eta_g} \exp\left\{-2.303\left[\left(\frac{C_1^g C_2^g}{\theta_1 - T_g + C_2^g}\right)\frac{\theta_1}{T} - C_1^g\right]\right\},$$

where C_1^g, C_2^g are the universal WLF parameters (see Section 7.4.1) and η_g is the 'universal' viscosity of a glass at T_g.
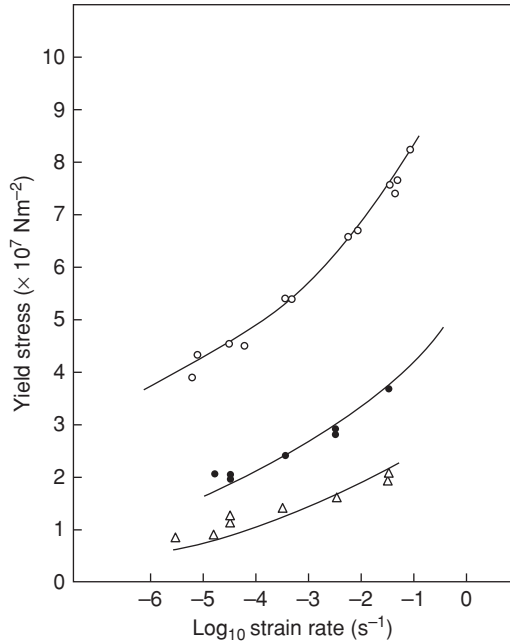
Figure 12.25   *Yield stress of polymethyl methacrylate as a function of strain rate. ○, compression at 23°C; △, tension at 90°C; ●, tension at 60°C. Curves represent the best theoretical fit (see the text).*

Duckett, Rabinowitz and Ward [72] have modified the Robertson model to include the effect of the hydrostatic component of stress p. It was proposed that p also does work during the activation event and that the energy difference between the two states should therefore be

$$\Delta U - \tau V \cos\theta + p\Omega,$$

where Ω is the pressure activation volume. Figure 12.25 shows that in this modified form the Robertson model can bring consistency to yield data in tension and compression for polymethyl methacrylate, together with the measured effect of hydrostatic pressure.

12.5.2   Yield Considered to Relate to the Movement of Dislocations or Disclinations

It is well known [73] that plastic deformation in crystals can occur when the applied shear stress can cause one plane of atoms to slip over another plane because there is an imperfect match between these adjacent planes at a particular point in the crystal lattice. These points of imperfection are called dislocations [74] and were identified by electron diffraction techniques to relate to specific crystal defects. Dislocations are observed in polyethylene single crystals by Peterman and Gleiter [75] and give credence to the idea that yield in crystalline polymers can be understood in similar terms to those used by metallurgists for crystalline solids.

A starting point for the discussion is the Frenkel argument for predicting the maximum theoretical shear strength of a crystal [73,76]. For a simple lattice of identical atoms with a repeat distance b in the direction of shear on planes separated by a distance h it can most simply be considered that the shear stress τ follows a sine curve with shear displacement x to give

$$\tau = k \sin 2\pi \frac{x}{b}. \tag{12.27}$$

The shear stress is zero when each atom is situated half way between one equilibrium position and the next, that is $x = \dfrac{b}{2}$ and the shear strain is 0.5. In the simplest case, the slip of one plane will involve a movement where $x = b$. This characteristic slip distance b is called the Burgers vector.

For small strains

$$\tau = 2\pi k \frac{x}{b} \tag{12.28}$$

and the shear strain is given by

$$\gamma = \frac{x}{h}.$$

The shear modulus G is then

$$\frac{\tau}{\gamma} = 2\pi k \frac{h}{b} \tag{12.29}$$

and the maximum shear stress

$$\tau_{\text{max}} = \frac{\tau}{\gamma} = k = \frac{Gb}{2\pi h}. \tag{12.30}$$

Since $b \sim h$ it follows that the maximum shear stress is

$$\tau_{\text{max}} \sim \frac{G}{2\pi}$$

and occurs when $x = \dfrac{b}{4}$, where the shear strain $\dfrac{x}{h} = \dfrac{x}{b} = 0.25$.

On this approach, yield can be considered to be nucleation controlled as distinct from the viscoelastic approach that can be considered to be velocity controlled. It implies a direct link between the shear modulus and the shear yield stress. Brown [77] proposed that there is good empirical evidence for this supposition, which had been suggested by other workers previously [25,78,79], and it is an essential ingredient of nucleation controlled yield behaviour as developed formally by Bowden and Raha [42], Argon [43] and others.

The discussion so far has considered a regular lattice, but Bowden and Argon have proposed that in an amorphous polymer in the glassy state similar ideas can be developed. Following Li and Gilman [80], the analogy in amorphous polymers to dislocations in crystalline polymers has been called *disclinations*.

12.5.2.1   The Young Theory

Following treatments given by Kelly [76], Bowden and Raha [42], Young [44] and others, the increase in energy U associated with forming a dislocation loop of Burgers vector b

and radius R in a solid with a shear modulus G under an applied shear stress τ is given approximately by

$$U = 2\pi R \frac{Gb^2}{4\pi} \ln \frac{2R}{r_0} - \pi R^2 \tau b, \qquad (12.31)$$

where r_0 is the core radius of the dislocation.

The energy of the loop increases as R increases until it reaches a maximum value U_c at R_c. This is found by differentiating Equation (12.31) and is given by

$$U_c = \frac{Gb^2 R_c}{4} \left[\ln \frac{2R_c}{r_0} - 1 \right] \qquad (12.32)$$

at

$$R_c = \frac{Gb}{4\pi\tau} \left[\ln \frac{2R_c}{r_0} + 1 \right]. \qquad (12.33)$$

The core radius r_0 can be calculated by the argument developed in Equations (12.27)–(12.30) above where $\tau \sim \dfrac{G}{2\pi}$ and leads to a value for $r_0 \sim b$.

The discussion so far considers the theoretical shear stress of a crystal in the absence of thermal fluctuations. Frank [81] considered that there are always local thermal fluctuations, which must be taken into account. At any temperature T, there is a significant chance of thermal fluctuations in the timescale of the experiments supplying an energy up to 50 kT. Furthermore, this discussion only relates the yield stress to the elastic energy whereas U is strictly the activation enthalpy. Analogous to the site model theory (see Section 7.3), we should discuss the Gibbs free energy ΔG, where $\Delta G = T\Delta S$ and the shear strain rate is

$$\dot{\gamma} = \exp\left(-\frac{\Delta G}{kT}\right) = \exp\left(-\frac{U}{kT}\right) \exp\left(\frac{\Delta S}{k}\right). \qquad (12.34)$$

Frank's assumption is equivalent to putting $\dfrac{\Delta S}{k} = 1$ and $U = 50$ kT at the applied strain rate, which for typical experiments is 10^{-3} s^{-1}.

Young has followed these ideas to relate the yield behaviour in crystalline polymers to the lamellar thickness. Following Shadrake and Guiu [82], Young showed that the change in the Gibbs free energy ΔG_a associated with the nucleation of a screw dislocation in a lamella of thickness d, having a Burgers vector of magnitude b in the chain direction gives a shear yield stress

$$\tau_y = \frac{K}{4\pi} \exp\left[-\left(\frac{2\pi\Delta G_a}{dKb^2} + 1 \right) \right], \qquad (12.35)$$

where $K = (c_{44}c_{55})^{1/2}$ with c_{44}, c_{55} the shear moduli.

d should more correctly be interpreted as the stem length (i.e. the length traversed by the polymer chains within the crystalline lamella) and not the lamellar thickness. The yield stress then depends on the stem length, and on temperature and strain rate through the shear modulus term K. ΔG_a is assumed to be 50 kT in accordance with Frank's assumption.

12.5.2.2   The Argon Theory

Argon [43] has proposed a theory of yielding for glassy polymers based on the concept that deformation at a molecular level consists in the formation of a pair of molecular kinks.
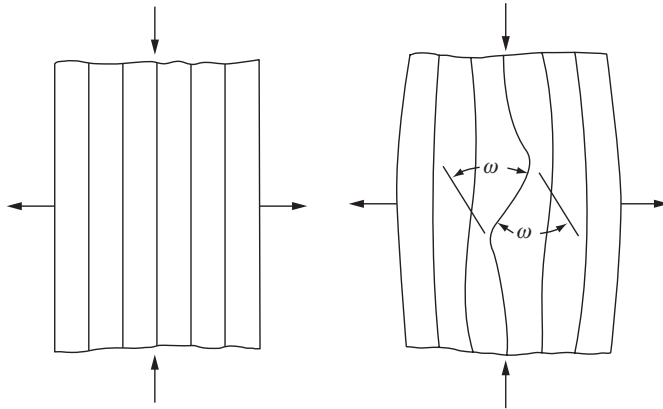
Figure 12.26 *Schematic representation of the unit process of deformation consisting of un-bending and bending a molecular segment.*

The unit process of deformation is shown in Figure 12.26. The resistance to double kink formation is considered to arise from the elastic interactions between a chain molecule and its neighbour, i.e. from intermolecular forces in contrast to the Robertson theory where intramolecular forces are the primary consideration. The intermolecular energy change associated with a double kink is then calculated by modelling these as two wedge disclination loops as proposed by Li and Gilman [80] (Figure 12.27).
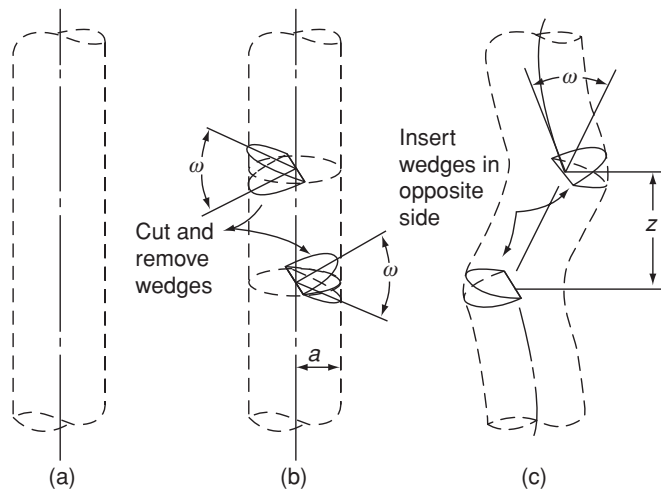
Figure 12.27 *Modelling of a molecular kink pair by a pair of wedge disclination loops: (a) outline of polymer molecule in an elastic surrounding made up of other neighbouring molecules, (b) make the circular cuts of radius a at distance 2a apart and cut and remove wedges of angle ω and (c) insert cut wedges into opposite side and join all parts together. (Redrawn from Argon, A.S. (1973) A theory for the low-temperature plastic deformation of glassy polymers. Phil. Mag., 28, 839 Copyright (1973) Taylor and Francis.)*
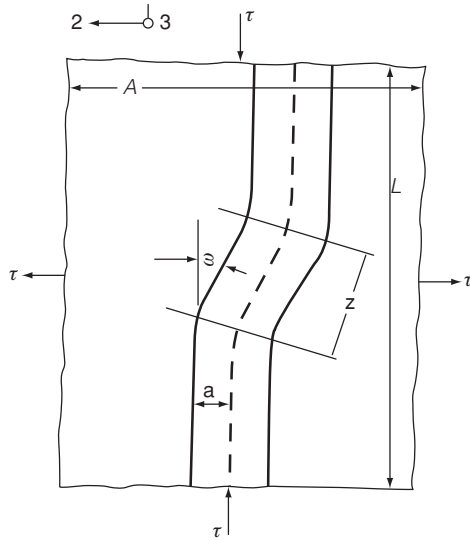
Figure 12.28 *Plastic strain increment by formation of a pair of kinks in a polymer molecule. (Redrawn from Argon, A.S. (1973) A theory for the low-temperature plastic deformation of glassy polymers. Phil. Mag., **28**, 839. Copyright (1973) Taylor and Francis.)*

The activation energy (strictly enthalpy) for the formation of a pair of molecular links under an applied shear stress τ is given by

$$\Delta H^* = \frac{3\pi G \omega^2 a^3}{16(1-\nu)} \left[1 - 6.75(1-\nu)^{5/6} \left(\frac{\tau}{G} \right)^{5/6} \right], \qquad (12.36)$$

where G, ν are the shear modulus and Poisson's ratio, respectively, a is the molecular radius and ω the angle of rotation of the molecular segment (Figure 12.28). The shear strain rate is then

$$\dot{\gamma} = \gamma_0 \Omega C \nu_a \exp\left[-\frac{\Delta H^*}{kT} \right], \qquad (12.37)$$

where γ_0 is the shear strain in the local volume $\Omega = \pi a^2 z_{eq}$ (z_{eq} is the equilibrium molecular segment length), C is the total volume density of potentially rotatable segments in the polymer, and ν_a is a frequency factor of the order of (but somewhat smaller than) the atomic frequency.

It can be noted that when Equation (12.36) is substituted into Equation (12.37) the resultant equation is quite similar in form to the Eyring equation

$$\dot{\gamma} = \dot{\gamma}_0 \exp\left[-\left(\frac{\Delta H - \tau v}{kT} \right) \right].$$

The shear yield stress τ is given from Equation (12.37) as

$$\tau = \frac{0.102G}{1-\nu} \left[1 - \frac{16(1-\nu)}{3\pi G \omega^2 a^3} kT \ln \frac{\dot{\gamma}_0}{\dot{\gamma}} \right]^{6/5}, \qquad (12.38)$$

where $\dot{\gamma}_0 = \gamma_0 \nu_a \Omega C$.

12.5.2.3   Experimental Studies Based on the Nucleation Approach

The first experimental studies based on the nucleation approach were for glassy polymers. Bowden and Raha [42] assumed that the dislocation loop theory set out above for crystalline solids could be regarded as modelling the behaviour of a small volume of amorphous solid. The two key variables in Equation (12.38) are the shear modulus and the Burgers vector b. Bowden and Raha used literature values for the shear modulus and assumed values of b, which gave reasonable fits to the temperature dependence of the shear stress. Argon [43] developed Li and Gilman's ideas to explain the concept of disclinations and fitted results of Ward and co-workers on glassy polyethylene terephthalate.

Figure 12.29 shows Argon's fit to very extensive data for polyethylene terephthalate. The fit is good, but it may be noted that if we replace the factor 6/5 in Equation (12.36) by unity, which makes a comparatively small difference numerically, then this equation reduces to

$$\tau = \frac{0.102G}{1 - \nu} - \frac{16 \times 0.102kT}{3\pi\omega^2 a^3} \ln \frac{\dot{\gamma}_0}{\dot{\gamma}}, \tag{12.39}$$

which is of similar form to the Eyring equation where

$$\tau = \frac{\Delta H}{V} - \frac{kT}{V} \ln \frac{\dot{\gamma}_0}{\dot{\gamma}}. \tag{12.40}$$
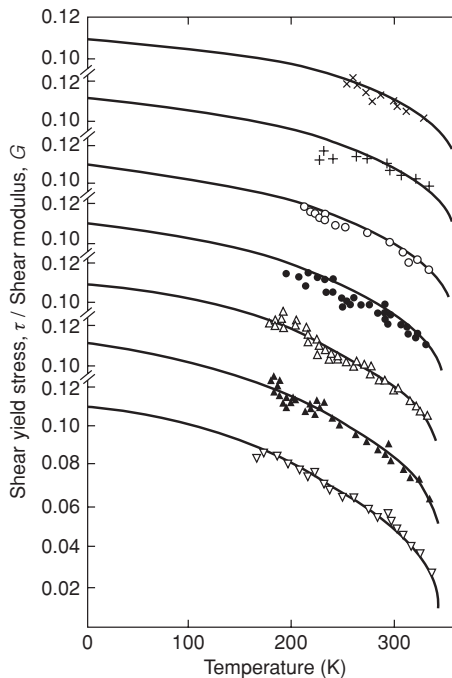
Figure 12.29   *Ratio of shear yield stress to shear modulus as a function of temperature at different strain rates, for amorphous polyethylene terephthalate. Points from unpublished data of Foot and Ward, curves from Argon theory. Strain rates: x, $1.02 \times 10^2 \ s^{-1}$; $+$, $21.4 \ s^{-1}$; ∇, $1.96 \ s^{-1}$; 0, $9 \times 10^{-2} \ s^{-1}$; $\square$, $9 \times 10^{-3} \ s^{-1}$; $\triangle$, $9 \times 10^{-4} \ s^{-1}$; $\lozenge$, $9 \times 10^{-3} \ s^{-1}$.*

The two approaches of Argon and Eyring therefore cannot be clearly distinguished at a curve-fitting level. On the Argon theory, the shear-yield stress at 0 K is simply a function of the shear modulus and Poisson's ratio. This is consistent with the observation, first made by Vincent [79] and supported by later workers [25,77] that the yield stress of a polymer is proportional to the modulus. Argon also calculates the shear activation volume from his theory as $5.3\omega^2 a^3$. Comparing the simplified Equation (12.40) with Equation (12.39), we have

$$\nu = \frac{3\pi\omega^2 a^3}{16 \times 0.102} = 5.77\omega^2 a^3 \approx 10a^3$$

(since $\omega \sim 1$). It is therefore not surprising that Argon's shear activation volumes are comparable in magnitude to those obtained from fits to Eyring theory, and are generally in the range of 1 nm^3 or greater. The yield process cannot merely involve the formation of double kinks or single molecules as envisaged in Figure 12.26, but must require the cooperative change of several adjacent molecular segments This conclusion is, of course, identical to that reached in Section 12.5.1.

Parallel studies on crystalline polymers were initiated by Young and co-workers [44,47,83] on polyethylene and polypropylene. Young proposed that the critical parameter was the thickness of the crystals in the crystalline lamellae, and more precisely the stem length of the molecular chains in the lamellae. This follows clearly the ideas of Shadrake and Guiu [82]. Figure 12.30 shows the effect of stem length on the yield stress of polyethylene at $-60°$C, showing very reasonable fit to Equation (12.35). Results by Ward and co-workers [84] on a wide range of polyethylenes confirm the validity of the approach. However, as mentioned above it does appear from the research by Ward and co-workers [85–87], Nikolov and Raabe [88], and Brooks and Mukhtar [89], that there is a transition in behaviour from elasto/plastic to viscoelastic at a temperature below the onset of interlamellar shear. These results cannot therefore be considered to invalidate the concept of applying velocity controlled Eyring process approach at higher temperatures.

A point of some interest is that on the Argon theory changes in modulus are automatically incorporated. At a phenomenological level, this explains the success of fitting data to a single activated process, whereas the Eyring equation approach generally requires two processes acting in parallel dealing with data covering a wide range of temperatures and strain rates. It
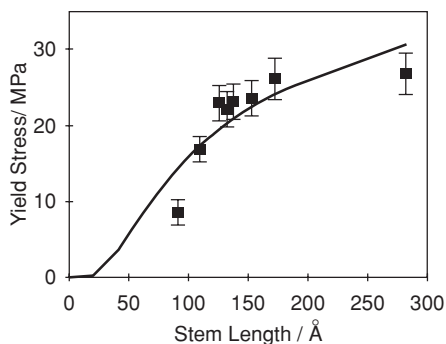
Figure 12.30   *Yield stress against stem length for polyethylenes at $-20°$C. (Reproduced from Brooks, N.W.J. and Mukhtar, M. Temperature and stem length dependence of the yield stress of polyethylene. (2000) Polymer, **41**, 1475 Copyright (2000) Elsevier Ltd.)*

could also be claimed that this aspect of Argon's theory and other similar theories [42,90], where the modulus is inextricably linked to the yield stress, is an essential ingredient of any satisfactory molecular theory of yield behaviour.

A final consideration is that the Argon theory essentially regards yield as nucleation controlled, analogous to the stress-activated movement of dislocations in a crystal produced by the applied stress, aided by thermal fluctuations. The application of the Eyring theory, on the other hand, implies that yield is not concerned with the initiation of the deformation process, but only that the application of stress changes the rate of deformation until it equals imposed rate of change of strain. The Eyring approach is consistent with view that the deformation mechanisms are essentially present at zero stress, and are identical to those observed in linear viscoelastic measurements (site model analyses in Section 7.3.1). Here, a very low stress is applied merely to enable detection of the thermally activated process, without modification of the polymer structure.

At present, these two approaches appear to be alternative ways of dealing with the yield behaviour of polymers. It could be argued that the Eyring equation is likely to be appropriate at high temperatures, whereas the Argon theory and similar theories are most relevant to the behaviour at very low temperatures. In this respect, it is interesting to recall that as we approach absolute zero the ratio of yield stress to modulus approaches a limiting value, which is consistent with classical theoretical shear strength arguments.

As clearly discussed, the mechanical behaviour of polymers changes rapidly as the temperature is reduced or the strain rate increased. Brooks *et al*. have shown that for polyethylene there is a sudden transition in the yield strain at temperatures below ambient, the exact temperature depending on the sample morphology. Figure 12.31 shows results for linear PE. It was also found that this temperature marks the change from classical elastic–plastic behaviour to time-dependent viscoelastic behaviour where the yielded samples show
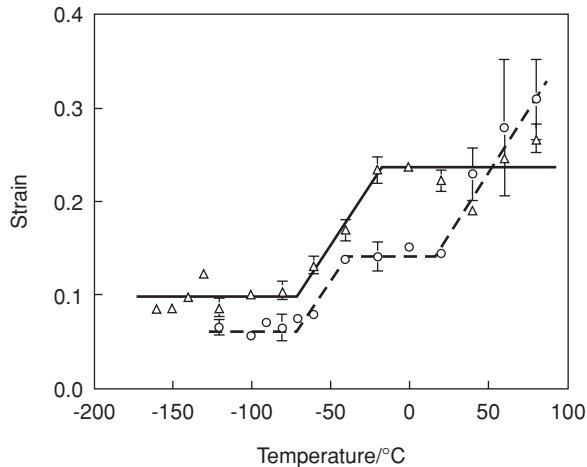
Figure 12.31   *Yield strain for polyethylene at strain rates Δ 2.08 × 10^{-3} s^{-1} and $\circ$ 8.3 s^{-1}. (Reproduced with permission from Brooks, N.W., Unwin, A.P., Duckett, R.A. et al. (1997) Temperature and strain rate dependence of yield strain and deformation behavior in polyethylene. J. Polym. Sci. B: Phys. Edn., **35**, 545. Copyright (1997) John Wiley & Sons, Inc.)*

evidence of interlamellar shear. Below the transition temperature, the yield behaviour is consistent with nucleation-controlled yield as proposed by Bowden, Young and others and an excellent correlation is obtained between the yield stress and the lamellar stem thickness.

12.6   Cold-Drawing, Strain Hardening and the True Stress–Strain Curve

12.6.1   General Considerations

We have seen that strain hardening is a necessary prerequisite for cold-drawing (see Section 12.1.2). There are two possible sources of strain hardening:

1. Drawing causes molecular alignment so that the drawing stress (often called the flow stress) is increased. This is a general phenomenon, true for both crystalline and amorphous polymers. (Note that the theories of mechanical anisotropy developed in Sections 8.6 and 8.7 apply to the final drawn material and do not relate directly to the strain-hardening effect.)
2. Strain-induced crystallisation may occur at the high degree of extension occurring in cold-drawing. This may be similar to the crystallisation occurring in rubber at high degrees of stretching (see Section 4.4.6). It may involve at a morphological level extended chain crystallisation or the formation of shish–kebab structures.

12.6.2   Cold-Drawing and the Natural Draw Ratio

We have seen in Section 12.1 above that cold-drawing through a neck leads to the movement of the neck to accommodate the stretching of more material to what is termed the natural draw ratio. Cold-drawing occurs at temperatures below the glass transition, sometimes as much as ~150°C below. It has been concluded by Andrews and others that the yield process and subsequent cold-drawing do not involve long-range molecular flow but are associated with molecular re arrangements between points of entanglement and/or cross-linkage. This view is consistent with the observation of yield, necking and cold-drawing, in highly cross-linked rubbers at temperatures below their glass transition. It is evident that cross-linking does not prevent the required molecular rearrangements.

The natural draw ratio for amorphous polymers is very sensitive to the degree of pre-orientation, i.e. the molecular orientation in the polymer before cold-drawing. This was reported for polyethylene terephthalate by Marshall and Thompson [20] and for PMMA and polystyrene by Whitney and Andrews [26].

It has been proposed [78] that the sensitivity of natural draw ratio to pre-orientation arises as follows. The extension of an amorphous polymer to its natural draw ratio is regarded as equivalent to the extension of a network to a limiting extensibility. This limiting extensibility is then a function of the original geometry of the network and the nature of the links of which it is comprised.

During fibre spinning, the network forms immediately below the point of extrusion from the small holes, and the fibre is subsequently stretched in the rubber-like state before cooling further and being collected as a frozen stretched rubber. Quantitative stress-optical measurements have confirmed this part of the hypothesis [91]. Cold-drawing then extends the network to its limiting extensibility. The ratio of the extended to unextended lengths of the network is a constant independent of the division of the extension between the spinning,
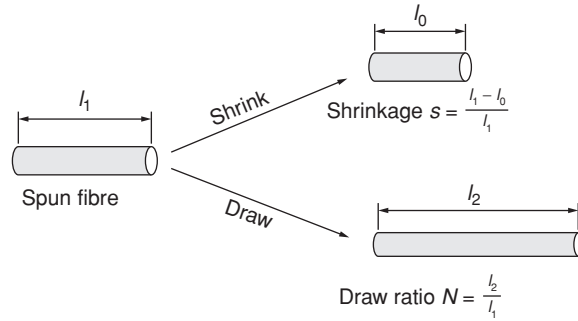
Figure 12.32   *A representation of the shrinkage and drawing processes.*

hot-drawing and cold-drawing processes, providing that the junction points holding the network together are not ruptured nor the links in the chain broken.

The dimensions of the unstrained network can be measured by shrinking the pre-oriented fibres back to the state of zero strain, that is isotropy [78]. These results can then be combined with measurements of the natural draw ratio to give the maximum extensibility for the network.

Consider the cold-drawing of a sample of length l_1 (Figure 12.32). If the fibre were allowed to shrink back to its isotropic state, length l_0, the shrinkage s would be defined by

$$s = \frac{l_1 - l_0}{l_1}. \tag{12.41}$$

Drawing to a length l_2 gives a natural draw ratio

$$N = \frac{l_2}{l_1}. \tag{12.42}$$

Combining Equations (11.41) and (11.42), we have

$$\frac{l_2}{l_0} = \frac{N}{1 - s}. \tag{12.43}$$

Table 12.2 shows collected results for a series of PET filaments. It can be seen that N varied from 4.25 to 2.58 and s from 0.042 to 0.378, but the ratio l_2/l_0 calculated from Equation (11.42) remained constant at a value of about 4.0.

Table 12.2   *Value of $l_2/l_0 = N/(1 - s)$ for samples of differing amounts of pre-orientation (polymer: polyethylene terephthalate, see Reference [79]).*

Initial birefringence ($\times 10^3$)	Natural draw ratio, N	Shrinkage, s	$1 - s$	$N/(1 - s)$
0.65	4.25	0.042	0.958	4.44
1.6	3.70	0.094	0.906	4.08
2.85	3.32	0.160	0.840	3.96
4.2	3.05	0.202	0.798	3.83
7.2	2.72	0.320	0.680	4.01
9.2	2.58	0.378	0.622	4.14

It is, of course, possible that the natural draw ratio is determined directly by the strain-hardening requirements. This does not invalidate the hypothesis that cold-drawing involves the extension of a molecular network, but suggests that strain hardening increases very rapidly as the network reaches its limiting extensibility.

12.6.3 The Concept of the True Stress–True Strain Curve and the Network Draw Ratio

In 1960, Vincent [5] proposed the concept of a true stress–true strain curve for the plastic deformation of a ductile polymer, based on the following experiment. First, the polymer is subjected to extension beyond the yield point less than that required to produce failure. The polymer sample is then allowed to relax by removing the load, after which the loading regime is repeated, again stopping the extension before ultimate failure. This procedure is repeated, each successive loading taking the sample closer to failure. As shown in Figure 12.33, it is found that on each reloading the new true stress–true strain curve could be made to coincide with the curve obtained by taking the sample to failure in a single experiment. It is vital to plot true stress (load divided by current cross-sectional area) versus true strain (natural logarithm of length divided by initial length).

Another very important idea is that drawing involves the stretching of a polymer network in which the junction points of the network are formed by physical entanglements. Even if crystallisation occurs, the deformation of the polymer network determines the overall constraints on the macroscopic deformation, which can occur during the fibre or film extrusion process and in subsequent tensile drawing or die drawing processes. The development of molecular orientation is a major factor in the development of physical properties such as tensile modulus and tensile strength and hence relates to the deformation of the molecular network.

From the viewpoint of practical polymer processing, it is well known that fibre and film properties can be empirically correlated with draw ratio, but it is important to recognise
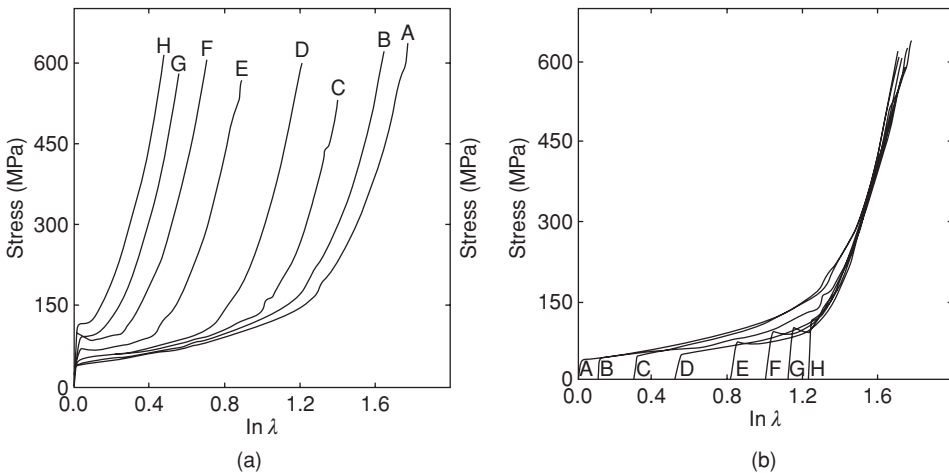
Figure 12.33 *Curve matching procedure to obtain the network draw ratios for polyester fibres. (Reproduced with permission from Long, S.D. and Ward, I.M. (1991) Shrinkage force studies of oriented polyethylene terephthalate. J. Appl. Polym. Sci., **42**, 1921. Copyright (1991) John Wiley & Sons, Inc.)*

that the true correlation is with the total network draw ratio which occurs from the point where the first network forms, that is it is important to relate the structure and properties of the drawn material to the network draw ratio.

Long and Ward [92] showed how the concept of a true stress–true strain curve could be combined with the concept of a molecular network to provide a better understanding of the relationship of the properties of oriented polymers to the processing route. It is assumed that these properties will relate to the network draw ratio for multi-stage processing even if there are dramatic changes in morphology. The additional ingredient is to determine the network draw ratio at each stage by superimposing true stress–true strain curves. This procedure of curve matching was first proposed by Brody [93] and has been used by fibre technologists [94]. Long and Ward studied the conventional two stage process for producing oriented polyester fibres where melt spinning is followed by stretching above the glass transition temperature (not by cold-drawing as described in Section 12.1). The network draw ratio in the melt spinning stage was determined by curve matching (Figure 12.33) and the total network draw ratio λ_{net} calculated as $\lambda_{net} = \lambda_s \, \lambda_{ha}$ where λ_{ha} is the draw ratio imposed by stretching the spun yarn in the solid phase at a temperature above T_g. As shown in Figures 12.34 and 12.35 [92], the birefringence and modulus of the oriented fibres relate very well to the network draw ratio.

The assumption that plastic deformation of polymers involves a network draw ratio has been developed further to predict the properties of the oriented polymer. It was recognised that for fibres and films the magnitude of the birefringence could be related to the draw ratio. For cold-drawing, as discussed in Section 8.6.3, the molecular orientation follows the pseudo-affine deformation scheme and it is possible to calculate the birefringence quantitatively. Assuming an aggregate model the anisotropic mechanical behaviour can also be predicted. For drawing above T_g, which is more usual in commercial processes, it can be assumed that this is akin to stretching a rubber network. It has been customary to follow the Kuhn and Grün [95] model where the actual network is replaced by an equivalent network of identical chains each containing freely jointed links. This is called the affine
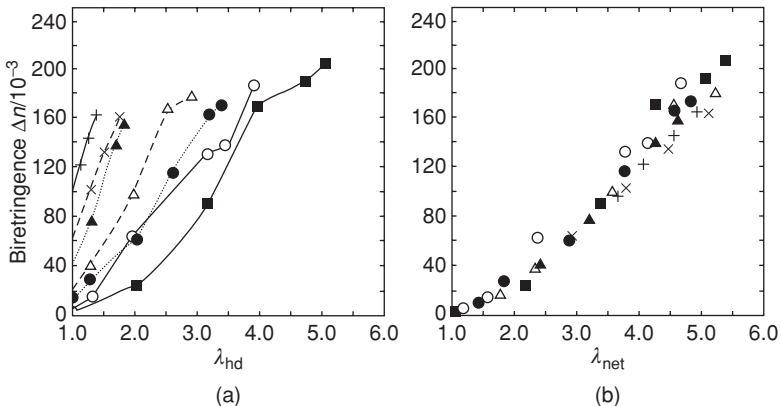
Figure 12.34 *Birefringence versus total (λ_{hd}) and network (λ_{net}) draw ratio for polyester fibres. (Reproduced with permission from Long, S.D. and Ward, I.M. (1991) Shrinkage force studies of oriented polyethylene terephthalate. J. Appl. Polym. Sci., **42**, 1921. Copyright (1991) John Wiley & Sons, Inc.)*
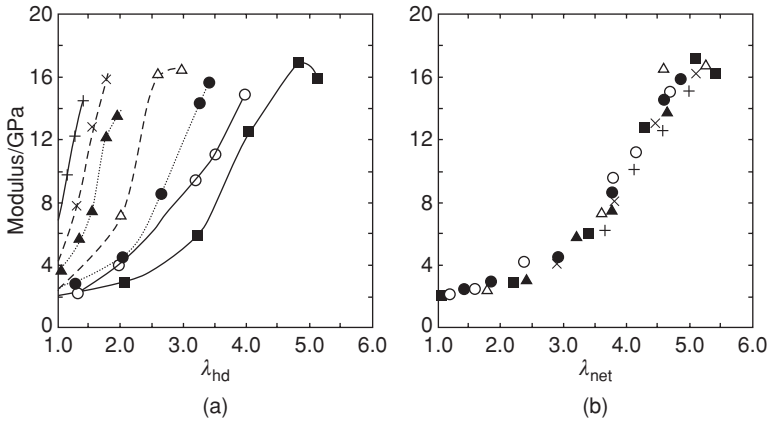
Figure 12.35 *Modulus versus total (λ_{hd}) and network (λ_{net}) draw ratio for polyester fibres. (Reproduced with permission from Long, S.D. and Ward, I.M. (1991) Shrinkage force studies of oriented polyethylene terephthalate. J. Appl. Polym. Sci., **42**, 1921. Copyright (1991) John Wiley & Sons, Inc.)*

deformation scheme, because the network junction points undergo identical displacements to points marked on the macroscopic body (see Section 8.6.3). Recent research has refined this semi-phenomenological approach by more appropriate molecular modelling procedures involving rotational isomeric state calculations [96].

Recent research has also addressed two issues. First, to what extent does the macroscopic measured draw ratio reflect the network draw ratio, and whether slippage occurs at a molecular level. Although curve matching attempts to resolve this problem it has also been instructive to invite more sophisticated molecular studies, for example by scanning near-field optical microscopy [97].

Secondly, there is the question of any relaxation of the molecular network, which can occur, during any further heating of the oriented polymer. Early work by Pinnock and Ward [91] showed excellent correlation between shrinkage force and birefringence for spun PET fibres, with the rate of recovery to isotropy correlating well with time temperature equivalence according to the WLF equation. Recent work by Hine and co-workers [98] suggests that in oriented polystyrene it is possible to identify relaxation processes relating to the different stress relaxation modes described for entangled networks (see Section 7.6). The concept of a true stress/true strain/strain rate surface can also be used to predict the creep to failure of oriented polyethylene, as discussed in Section 13.6.3.

12.6.4   Strain Hardening and Strain Rate Sensitivity

The discussions of the true stress–true strain curve and the network draw ratio are clearly consistent with the concept of a molecular network, which provides a physical understanding of what is known to engineers as strain hardening and has also been shown to be relevant to slow crack propagation (see Section 13.6.3).

However, it is also relevant to consider that plastic flow in polymers is determined by a thermally activated process following Eyring (see Section 12.5.1).

Therefore, the flow stress can be represented by a viscosity stress acting in parallel with a network stress, akin to the Voigt or Kelvin model of Section 5.2.5. The effect of strain (total network deformation) and strain rate on the flow stress σ can thus be represented mathematically by

$$d\sigma = \left(\frac{\partial \sigma}{\partial e}\right)_{\dot{e}} de + \left(\frac{\partial \sigma}{\partial \dot{e}}\right)_{e} d\dot{e}, \tag{12.44}$$

where $\left(\frac{\partial \sigma}{\partial e}\right)_{\dot{e}}$ represents the strain-hardening spring E_v and $\left(\frac{\partial \sigma}{\partial \dot{e}}\right)_{e}$ represents the strain rate sensitivity dashpot η_v.

In terms of the strain-hardening modulus, this has been developed by the use of Kuhn and Grün models and Kratky models to relate the development of molecular orientation and mechanical anisotropy (see Section 8.6.3). With regard to the strain rate sensitivity the strain rate-dependent viscosity has been developed by studies of creep and yield behaviour (see Sections 11.3 and 12.5.1).

12.6.5   Process Flow Stress Paths

The concept of a true stress–true strain curve has been extended to include the effect of strain rate to provide a baseline for quantitative modelling of polymer processing, including tensile drawing, hydrostatic extrusion and die drawing. It is necessary to take into account the effect of the rate of deformation that was explicitly neglected in the analyses described above. The key assumption is that the current flow stress depends only on the total plastic strain (the strain hardening relating to the deformation of the molecular network) and the current strain rate (the relevant strain rate sensitivity). As before, properties relate to the network draw ratio, sometimes called the effective draw ratio. It is therefore possible to consider that any engineering process involves taking the polymer on a chosen route across a flow stress/strain/strain rate surface. Figure 12.36 shows Ward and Coates' illustration of such a surface for a polyethylene polymer at 100°C, from which the major increases in flow stress with strain and strain rate can be seen [99]. Figure 12.37 shows their image of
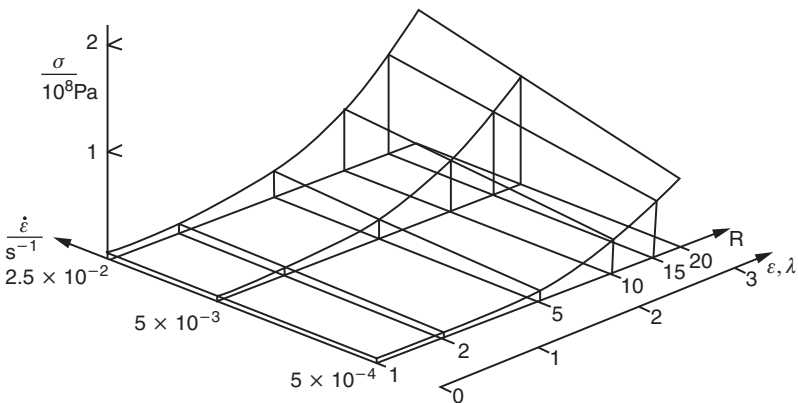
Figure 12.36   *True stress–true strain–strain rate surface for high-density polyethylene stretched at 100°C. (Reproduced with permission from Hope, P.S. and Ward, I.M. (1981) An activated rate theory approach to the hydrostatic extrusion of polymers. J. Mater. Sci., 16, 1511. Copyright (2000) Hanser Publications.)*
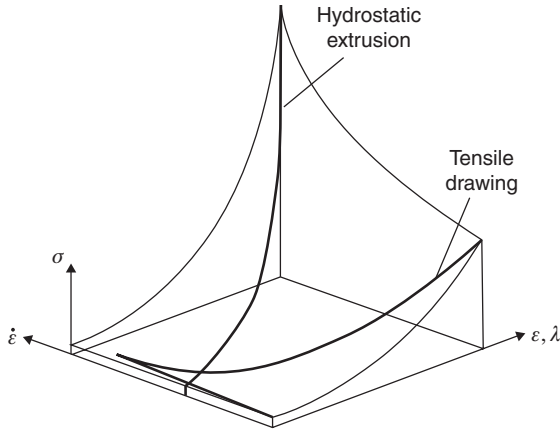
Figure 12.37   *Process flow stress paths for hydrostatic extrusion and die drawing. (Reproduced with permission from Hope, P.S. and Ward, I.M. (1981) An activated rate theory approach to the hydrostatic extrusion of polymers. J. Mater. Sci., **16**, 1511. Copyright (2000) Hanser Publications.)*

two typical flow process paths for tensile drawing and hydrostatic extrusion. It can be seen that in tensile drawing where a neck is formed (see Section 12.1.2) there is a peak in flow stress at the high strain rates in the neck, whereas in hydrostatic extrusion both strain and strain rate increase monotonically to a maximum value at the exit of the conical die.

These ideas have been developed extensively by Ward and co-workers to provide quantitative analyses of the mechanics of hydrostatic extrusion and die drawing for a range of polymers [100–103].

12.6.6   Neck Profiles

Coates and Ward showed that neck profiles in tensile drawing which are determined by the strain rate field in the neck can be related to the strain hardening and strain rate sensitivity by Equation (12.44). This equation can be rewritten as

$$\frac{\partial \dot{e}}{\partial \lambda} = \frac{\dfrac{\mathrm{d}\sigma}{\mathrm{d}\lambda} - \left(\dfrac{\partial \sigma}{\partial \lambda}\right)_{\dot{e}}}{\left(\dfrac{\partial \sigma}{\partial \dot{e}}\right)_{\lambda}},$$

where we have chosen to represent strain by the draw ratio λ to emphasise the relationship with the tensile drawing process.

A sharp neck implies a high value of $\left(\dfrac{\partial \dot{e}}{\partial \lambda}\right)$, and $\left(\dfrac{\partial \dot{e}}{\partial \lambda}\right)$ represents a specific path across the true stress, strain (λ) and strain rate surface.

There will be a very large positive change in the strain rate in an element of material crossing the process surface if both the strain hardening is small compared with $\dfrac{\mathrm{d}\sigma}{\mathrm{d}\lambda}$ (which is essentially the Considère line) and the strain rate sensitivity $\left(\dfrac{\partial \sigma}{\partial \dot{e}}\right)_{\lambda}$ is low. This will give a sharp neck.

These ideas were developed further in several publications [101–103].

12.6.7   Crystalline Polymers

The plastic deformation of crystalline polymers, in particular polyethylene has been studied intensively from the viewpoint of changes in morphology. Notable contributions to this area have been made by Keller and co-workers and Peterlin, Geil and others [104–106]. It is now evident that very drastic reorganisation occurs at the morphological level, with the structure changing from a spherulitic to a fibrillar type as the degree of plastic deformation increases. The molecular reorientation processes are very far from being affine or pseudo-affine and can also involve mechanical twinning in the crystallites. It is surprising that some of the continuum ideas for mechanical anisotropy are nevertheless still relevant, although they must be appropriately modified.

In a few highly crystalline polymers, notably high-density polyethylene, extremely large draw ratios, ~30 or more, have been achieved by optimising the chemical composition of the polymers and the drawing conditions [107, 108]. These high draw ratios lead to oriented polymers with very high Young's moduli as discussed in Section 9.6. In spite of the much more complex deformation processes in a crystalline polymer, it has been concluded [109] that the molecular topology and the deformation of a molecular network are still the overriding considerations in determining the strain-hardening behaviour and the ultimate draw ratio achievable. For high-molecular-weight, high-density polyethylene, the key network junction points are physical entanglements, as in amorphous polymers. For low-molecular-weight, high-density polyethylene, both physical entanglements and crystallites where more than one molecular chain is incorporated, can provide the network junction points. Junction points associated with the crystallites will be of a temporary nature. Very high draw ratios involve the breakdown of the crystalline structure and the unfolding of molecules, so that the simple ideas of a molecular network suggested for amorphous polymers have to be extended and modified.

12.7   Shear Bands

As we have seen above in Section 12.1, sometimes the tensile stretching of a polymer results in strain localisation. So far it has been assumed that the localisation takes the form of a neck, but an alternative geometric form is possible – the shear band. In uniaxial straining, localisation of strain occurs in a narrow band at an oblique angle to the straining direction, as illustrated in Figure 12.38. Shear bands have been observed in many ductile materials. Nadai [2], for instance, gives an account of their occurrence in mild steel. Bowden [110] has described the phenomenon for polymers.

Given that a shear band has formed in isotropic material under uniaxial conditions, a simple analysis is available to predict the angle at which it occurs with respect to the
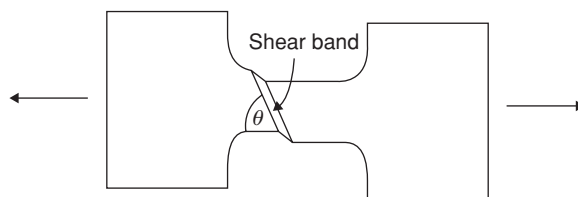
Figure 12.38   *Schematic diagram of shear band in tensile specimen.*

direction of straining. It is assumed [2] that the material in the shear band is plastic and that the material outside it remains elastic. For an incompressible and isotropic material, an axial strain e is accompanied by a transverse strain $-e/2$; this is consistent with the Levy–Mises flow rule. At some oblique angle to the axis, the normal strain must be zero. It is argued that the shear band forms at this angle, since this corresponds to there being no additional constraint on the band material and therefore the least stress. The strains within the band are generally much larger than those in the surrounding elastic material, but at this angle the zero plastic strain in the band is essentially compatible with the small elastic strain in the adjacent unyielded material. For the angle θ shown, the normal strain e_n is given by

$$e_n(\theta) = e \cos^2 \theta - (e/2) \sin^2 \theta SD$$

so that when $e_n = 0$, $\tan \theta = \sqrt{2}$, giving an angle of 54.7°. This was shown to be consistent with experiments on steel [2]. Early work on polyvinyl chloride by Bauwens [60] confirmed the result.

Given an appropriate constitutive equation that includes a flow rule, numerical methods should provide a means of modelling shear banding. The finite element method has been used in this way by Lu and Ravi-Chandar [111], who devised a simplified constitutive model with no strain rate dependence. A more realistic constitutive model, combining the plasticity model of Argon and an entropic network, was used by Wu and van der Giessen [112, 113] in finite element modelling of shear bands in polycarbonate and polystyrene. Sweeney *et al.* [114] found that a Maxwell type series model, incorporating a Gaussian elastic element and an Eyring process operating with a Levy–Mises flow rule, was sufficient to capture shear banding behaviour in polycarbonate. Results for a tensile specimen are shown in Figure 12.39. The angle of the band is consistent with the simple analysis outlined above.
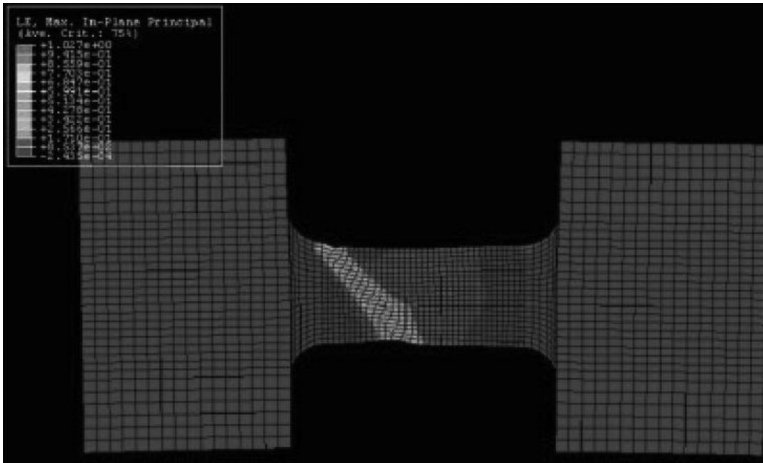
Figure 12.39   *Finite element model of tensile specimen of polycarbonate showing shear banding. Analysis is using ABAQUS 6.8, with contours of maximum principal true strain. (Reproduced with permission from Sweeney, J., Caton-Rose, P., Spares, R. et al. (2007) A unified model of necking and shearbanding in amorphous and semicrystalline polymers. J. Appl. Polym. Sci., **106**, 1095. Copyright (2007) John Wiley & Sons, Inc.)*

   When discussing the issue of instabilities, the question arises as to why in some instances they take the form of a neck and in other cases that of a band. The solution appears to lie in the nature of the deformation mechanism that is dominant. We generally have a combination of elastic and plastic mechanisms, with the latter governed by a flow rule that will tend to favour shear banding. On this basis our expectation would be that, if most of the total strain was due to plasticity, a shear band would be observed, whereas otherwise the instability would take the form of a neck. This question was explored by Sweeney *et al.* [114] by changing the relative strengths of the Eyring and Gaussian mechanisms. With material parameters appropriate for polycarbonate and the Eyring process producing most of the strain, a shear band was predicted as shown. With parameters appropriate for polypropylene and most of the deformation due to the elastic mechanism, a neck was predicted. This contrasting behaviour was in line with experimental observation.

   The above observations apply to initially isotropic material. Shear bands have also been observed in oriented polymers. Brown *et al.* [17] performed experiments on oriented polyethylene terephthalate in both tension and simple shear and measured the angles of the observed shear bands. To predict the band angle, they were able to apply the same physical condition – that the normal strain be zero along the band – as with that discussed for isotropic material above. However, with anisotropic material the Levy–Mises flow rule no longer applies. Brown *et al.* used the Hill criterion (see Section 12.2.7) as modified to include an internal stress according to Equation (12.12), in order to accommodate the observed Bauschinger effect. The shear band angles were modelled successfully in this way, with the Hill coefficients having been derived from yield stress data taken at various angles to the draw direction. The predictions are compared with observations in Figure 12.40.
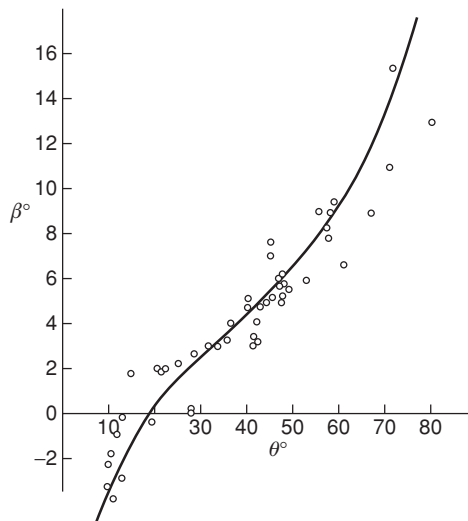
Figure 12.40   *Graph of angle β of band with draw direction for various angles θ of the tensile direction. (Reproduced from Brown, N., Duckett, R.A. and Ward, I.M. (1968) The yield behaviour of oriented polyethylene terephthalate. Phil. Mag.,* **18***, 483. Copyright (1968) Taylor and Francis.)*

12.8   Physical Considerations behind Viscoplastic Modelling

The combinations of elastic and viscous element such as that of Figure 12.23 presuppose some aspects of the underlying physics. In particular, the use of an entropic element, such as the Gaussian spring in Haward and Thackray's pioneering work [55] and entropic networks in many successive investigations ([114–118]), relies implicitly on there being sufficient free volume around an individual chain so that it is free to explore configurations and oscillate about that which corresponds to maximum entropy. This implies that the material should, by definition, be above its glass transition temperature. However, these models have been consistently used for materials in the glassy state since their inception. This is because they are effective at a macroscopic scale. This effectiveness – for example the observation of the $(\lambda^2 - 1/\lambda)$ dependence of stress in uniaxial stretching – may have been taken by some as evidence of the entropic nature of the stress. This is false logic; in particular, the factor $(\lambda^2 - 1/\lambda)$ is associated with maximum shear strain for large deformation in general and is not confined to rubber elasticity (see Section 3.3).

There are other objections to the use of entropic models in modelling of glassy polymer deformation. First, for a given strain and strain rate, the stress in a polymer tends to decrease with temperature; as a result, an elastic network fitted to experimental data as a component of a model has a strength that tends to decrease with temperature also. This is the opposite of what we would expect for an entropic mechanism, in which the magnitude of the stress is governed by the pre-multiplying factor NkT, N being the number of cross-links per unit volume, k Boltzmann's constant and T the absolute temperature. While it may be argued that, as temperature decreases, less available free volume may result in more chain–chain interactions that resemble cross-links so that N effectively increases, we again come to the objection that the structure is now resembling a glass. Secondly, in many models, the entropic mechanism is responsible for the post-yield strain-hardening response (the strain-hardening modulus). N can be estimated independently, and comparisons over a range of polymer systems [119–121] strongly suggest that it is not the controlling factor in the magnitude of the strain-hardening modulus. Furthermore, the observed strain-hardening moduli are too high in that they greatly exceed NkT [119].

There is no doubt that entropic forces can be directly observed in oriented polymer systems, in the form of retractive or shrinkage forces (a phenomenon discussed in detail in Chapter 4). Then, the observed stresses are consistent with entropic theory [92]. The experimental and theoretical considerations point to there being different mechanisms for strain hardening and shrinkage forces. This has been explored by molecular dynamics modelling. Hoy and Robbins [122] simulated a polymer glass using a coarse-grained bead-spring polymer model that included important features such as covalent backbone bonds, excluded volume and adhesive interactions, and chain stiffness. They simulated uniaxial and plane strain compression and were able to produce stress–strain curves with the upward curvature that would routinely be associated with entropy, but showed that the entropic contribution to the stress was small, with the energetic contribution dominant. They also simulated shrinkage, confirming that it was driven by entropic stresses that were at a low level in comparison with those associated with strain hardening.

Recent work involving the detailed analysis of macroscopic stress–strain–strain rate behaviour of polymers has led to re-examination of the physical origin of strain harden-ing. Sweeney *et al.* [123], working with initially isotropic ultra-high molecular weight
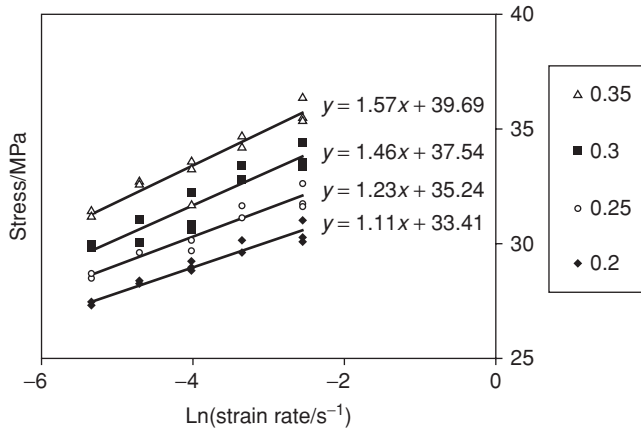
Figure 12.41 *Plots of tensile stress at a range of levels of true strain against log strain rate. (Reproduced with permission from Sweeney, J., Naz, S. and Coates, P.D. (2011) Modeling the tensile behavior of ultra-high-molecular-weight polyethylene with a novel flow rule. J. Appl. Polym. Sci.,* **121**, *2936. Copyright (2011) John Wiley & Sons, Inc.)*

polyethylene, made observations of the dependence of strain rate sensitivity on strain. As shown in Figure 12.41, Eyring-style plots of stress against strain rate show increasing slopes with increasing strain. This can be interpreted in terms of an activation volume that decreases with strain, as proposed previously [102,124,125], though such a quantity would be associated only with stretching in the direction of orientation. An Eyring process, however, operating via an anisotropic flow rule, exhibits strain hardening in itself, and Sweeney *et al.* [123] found that they could develop an adequate constitutive model of the material without the incorporation of an entropic network.

A similar experimental finding, using pre-oriented polypropylene tapes, is that the strain rate dependence of stress is a function of the level of pre-orientation [121,126]. In this case, it was concluded that strain hardening could be viewed as originating entirely from a strain-dependent Eyring process.

12.8.1 The Bauschinger Effect

The Bauschinger effect is the term for asymmetry in the yield response of a material between tension in compression. For isotropic polymers the effect is small (the yield stress in compression being slightly higher than that in tension) and can be seen as a consequence of the differing levels of hydrostatic pressure. It can thus be adequately modelled by the inclusion of the pressure activation volume in the Eyring process. For oriented polymer, however, the asymmetry is much greater (see the early results for oriented polypropylene of Duckett *et al.* [18], where a draw ratio of 5 increased the yield stress by a factor of 8).

As shown by Senden *et al.* [121], conventional material models that incorporate entropic strain hardening give a qualitatively incorrect prediction of the Bauschinger effect. This can be illustrated by investigating the effects of cyclic loading. For a two-arm model such as that of Haward and Thackray, when loaded in tension and then unloaded, during unloading the
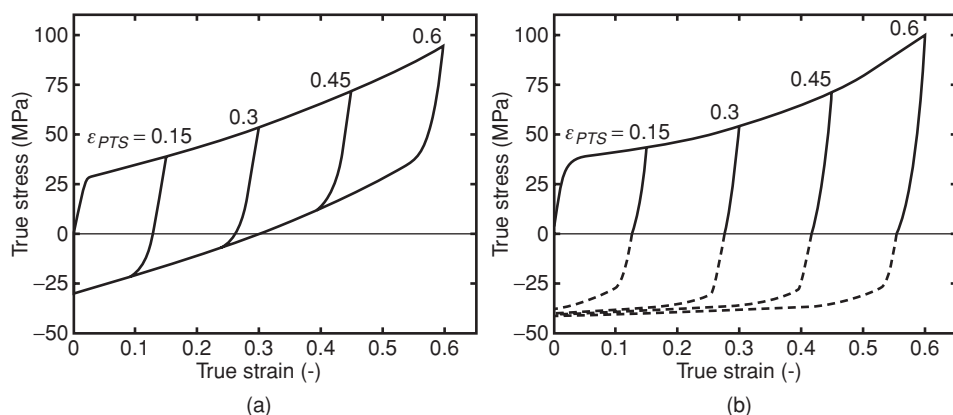
Figure 12.42 *(a) Predictions of the response of polycarbonate to cyclic loading, based on a constitutive model incorporating entropic strain hardening. (b) Realistic unloading behaviour. (Reproduced from Senden, D.J.A., van Dommelen, J.A.W. and Govaert, L.E. (2010) Strain hardening and its relation to Bauschinger effects in oriented polymers. J. Polym. Sci. Part B: Polym. Phys., **48**, 1483. Copyright (2010) John Wiley & Sons, Ltd.)*

stress in the arm containing the Eyring process becomes negative while the total stress is still positive. The Eyring process then yields, so that the total stress shows yield behaviour while still tensile. This is shown in Figure 12.42(a), and is clearly unrealistic when compared with the observed pattern of 12.42(b).

The discussion above has introduced an alternative model of strain hardening, the strain-dependent Eyring process. With a model incorporating a strain-hardening arm of this nature, a reversal of the direction of straining would rapidly change the sign of the stress in this arm. This is in contrast to the behaviour of the entropic mechanism where large strains need to be removed to reverse the stress. The revised ideas of strain hardening thus provide a probable means of gaining a realistic prediction of the Bauschinger effect. The work in this area is, however still incomplete. According to Senden *et al*. [121], for polycarbonate the strain hardening would be best modelled by a combination of entropic and strain-dependent Eyring processes.

12.9   Shape Memory Polymers

The recovery of oriented polymers has long been recognised as having significant applications, and more recently in medical applications [127–130]. The term shape memory polymers has been coined for such materials.

The stress relaxation behaviour has been addressed in terms of complex constitutive equations and simpler models based on Maxwell and Kelvin–Voigt elements [131–134].

Recently Bonner *et al*. [135] have shown that the recovery behaviour of a lactide based copolymer can be predicted by a Kelvin–Voigt model (see Chapter 5, Section 5.2.5) where the recovery stress in the spring and the dashpot viscosity can be determined using the transient stress dip test of Fotheringham and Cherry [70]. The recovery stress σ_R is

determined by the draw temperature and the draw ratio λ for the stretching of an internal network so that

$$\sigma_R = E\left(\lambda^2 - 1/\lambda\right),$$

where E is an effective modulus.

The viscosity stress σ_V is determined by the recovery temperature and the strain rate $\dot{e}$. The viscosity is then given by

$$\eta = \frac{\sigma_V}{\dot{e}}$$

and the recovery half-life τ is then given by

$$\tau = \frac{\eta}{E}.$$

The validity of this simple model was confirmed by Heuchel *et al.* [136].

References

1. Wineman, A.S. and Waldron, W.K. (1993) Interaction of nonhomogeneous shear, nonlinear viscoelasticity, and yield of a solid polymer. *Polym. Eng. Sci.*, **33**, 1217–1228.
2. Nadai, A. (1963) *Theory of Flow and Fracture of Solids*, McGraw-Hill, New York.
3. Orowan, B. (1949) Fracture and strength of solids. *Rept. Prog. Phys.*, **12**, 185.
4. Sweeney, J., Shirataki, H., Unwin, A.P. *et al.* (1999) Application of a necking criterion to PET fibers in tension. *J. Appl. Polym. Sci.*, **74**, 3331–3341.
5. Vincent, P.I. (1960) The necking and cold-drawing of rigid plastics. *Polymer*, **1**, 7.
6. Bridgeman, P.W. (1952) *Studies in Large Plastic Flow and Fracture*, McGraw-Hill, New York.
7. Amoedo, J. and Lee, D. (1992) Modeling the uniaxial rate and temperature dependent behavior of amorphous and semi-crystalline polymers. *Polym. Eng. Sci.*, **32**, 1055–1065.
8. Tresca, H. (1864) Mémoire sur l'ecoulement des corps solides soumis a de fortes pressions. *C. R. Acad. Sci. (Paris)*, **59**, 754; **64**, 809 (1867).
9. Smith, W.F. (1996) *Principles of Materials Science and Engineering*, 3rd edn, McGraw-Hill, New York.
10. Coulomb, C.A. (1776) Essai sur une application des règles des maximis et minimis à quelques problèmes de statique relatifs à l'architecture. *Mem. Math. Phys.*, **7**, 343.
11. von Mises, R. (1913) Mechanik der festen Korper im plastisch deformablen Zustand. *Gottinger Nach. Math. -Phys. Kl.*, 582.
12. Levy, M. (1870) Mémoire sur les équations générales des mouvements intérieurs des corps ductiles au delà des limites en élasticité pourrait les ramener à leur premier état. *C. R. Acad. Sci. (Paris)*, **70**, 1323.
13. Timoshenko, S.P. and Goodier, J.N. (1970) *Theory of Elasticity*, 3rd edn, McGraw-Hill International Editions, New York.
14. Gottstein, G. (2004) *Physical Foundations of Materials Science*, Springer, Berlin.

15. Hill, R. (1985) *The Mathematical Theory of Plasticity*, Oxford University Press, New York.

16. Van Dommelen, J.A.W. and Meijer, H.E.H. (2005) Micromechanics of particle-modified semi-crystalline polymers: influence of anisotropy due to transcrystallinity and/or flow, in *Mechanical Properties of Polymers Based on Nanostructure and Morphology*, (eds G.H. Michler and F.J. Baltá-Calleja), Taylor and Francis, Florida.

17. Brown, N., Duckett, R.A. and Ward, I.M. (1968) The yield behaviour of oriented polyethylene terephthalate. *Phil. Mag.*, **18**, 483.

18. Duckett, R.A., Ward, I.M. and Zihlif, A.M. (1972) Direct measurements of the reverse stress asymmetry in the yielding of anisotropic polypropylene. *J. Mater. Sci.*, **7**(Letters), 480–482.

19. De Souza Neto, E.A., Peric, D. and Owen, D.R.J. (2008) *Computational Methods for Plasticity*, John Wiley & Sons, Chichester.

20. Marshall, I. and Thompson, A.B. (1954) The cold drawing of high polymers. *Proc. Roy. Soc.*, **A221**, 541.

21. Müller, F.H. (1949) Zum Problem der Kaltverstreckung hochpolymerer Substanzen. *Kolloidzeitschrift*, **114**, 59; **115**, 118 (1949); **126**, 65 (1952).

22. Hookway, D.C. (1958) The cold-drawing of nylon 6.6. *J. Text. Inst.*, **49**, 292.

23. Brauer, P. and Müller, F.H. (1954) Über die Temperaturüberhöhung in der Fließzone während der Kaltverstreckung Anwendung von Leuchtstoffen zur Temperaturmessung. *Kolloidzeitschrift*, **135**, 65.

24. Lazurkin, Y.S. (1958) Cold-drawing of glass-like and crystalline polymers. *J. Polym. Sci.*, **30**, 595.

25. Allison, S.W. and Ward, I.M. (1967) The cold drawing of polyethylene terephthalate. *Brit. J. Appl. Phys.*, **18**, 1151.

26. Whitney, W. and Andrews, R.D. (1967) Yielding of glassy polymers: volume effects. *J. Polym. Sci. C*, **16**, 2981.

27. Brown, N. and Ward, I.M. (1968) Load drop at upper yield point of a polymer. *J. Polym. Sci. A2*, **6**, 607.

28. Bowden, P.B. and Jukes, J.A. (1968) The plastic yield behaviour of polymethyl-methacrylate. *J. Mater. Sci.*, **3**, 183.

29. Rabinowitz, S., Ward, I.M. and Parry, J.S.C. (1970) The effect of hydrostatic pressure on the shear yield behaviour of polymers. *J. Mater. Sci.*, **5**, 29.

30. Ainbinder, S.B., Laka, M.G. and Maiors, I.Y. (1965) Effect of hydrostatic pressure on mechanical properties of plastics. *Mech. Comp. Mater.*, **1**, 50.

31. Biglione, G., Baer, E. and Radcliffe, S.V. (1969) *Fracture 1969* (ed. P.L. Pratt), Chapman and Hall, London, p. 520.

32. Christiansen, A.W., Baer, E. and Radcliffe, S.V. (1971) The mechanical behaviour of polymers under high pressure. *Phil. Mag.*, **24**, 451.

33. Matsushigi, K., Radcliffe, S.V. and Baer, E. (1975) The mechanical behaviour of polystyrene under pressure. *J. Mater. Sci*, **10**, 833.

34. Pae, K.D., Maers, D.R. and Sauer, J.A. (1968) Stress–strain behavior of polypropylene under high pressure. *J. Polym. Sci. Part B: Polymer Letters*, **6**, 773.

35. Maers, D.R., Pae, K.D. and Sauer, J.A. (1969) Effects of hydrostatic pressure on the mechanical behavior of polyethylene and polypropylene. *J. Appl. Phys.*, **40**, 4229.

36. Harris, J.S., Ward, I.M. and Parry, J.S.C. (1971) Shear strength of polymers under hydrostatic pressure: surface coatings prevent premature fracture. *J. Mater. Sci.*, **6**, 110.

37. Sweeney, J., Duckett, R.A. and Ward, I.M. (1986) The fracture toughness of a tough polyethylene using tension testing in a high-pressure environment. *J. Mater. Sci. Letters*, **5**, 1109.

38. Briscoe, B.J. and Tabor, D. (1978) in *Polymer Surfaces* (eds D.T. Clark and W.J. Feast), John Wiley & Sons, New York, Chap. 1.

39. Halsey, G., White, H.J. and Eyring, H. (1945) Mechanical properties of textiles, I. *Text. Res. J.*, **15**, 295.

40. Truss, R.W., Clarke, P.L., Duckett, R.A. *et al.* (1984) The dependence of yield behavior on temperature, pressure, and strain rate for linear polyethylenes of different molecular weight and morphology. *Polym. Sci. B: Polym. Phys.*, **22**, 191.

41. Brereton, M.S., Croll, S.G., Duckett, R.A. *et al.* (1974) Nonlinear viscoelastic behavior of polymers – an implicit equation approach. *J. Mech. Phys. Solids*, **22**, 97.

42. Bowden, P.B. and Raha, S. (1974) A molecular model for yield and flow in amorphous glassy polymers making use of a dislocation analogue. *Phil. Mag.*, **29**, 149.

43. Argon, A.S. (1973) A theory for the low-temperature plastic deformation of glassy polymers. *Phil. Mag.*, **28**, 839.

44. Young, R.J. (1974) A dislocation model for yield in polyethylene. *Phil. Mag.*, **30**, 85.

45. Brooks, N.W., Unwin, A.P., Duckett, R.A. *et al.* (1997) *Deformation, Yield and Fracture of Polymers*. Conference Papers. Cambridge, UK, pp. 53–56.

46. Crist, B., Fisher, C.J. and Howard, P.R. (1989) Mechanical properties of model polyethylenes: tensile elastic modulus and yield stress. *Macromolecules*, **22**, 1709.

47. O'Kane, W.J. and Young, R.J. (1995) The role of dislocations in the yield of polypropylene. *J. Mater. Sci. Letters*, **14**, 433.

48. Darras, O. and Seguala, R. (1993) Tensile yield of polyethylene in relation to crystal thickness. *J. Polym. Sci. Part B: Polym. Phys.*, **31**, 759.

49. Lazurkin, Y.S. and Fogelson, R.L. (1951) Nature of the large deformations of high-molecular compounds in the vitreous state. *Zhur. Tech. Fiz.*, **21**, 267.

50. Robertson, R.E. (1963) On the cold-drawing of plastics. *J. Appl. Polym. Sci.*, **7**, 443.

51. Crowet, C. and Homès, G.A. (1964) Interpretation of the load-elongation curve of polymethyl methacrylate. *Appl. Mater. Res.*, **3**, 1.

52. Bauwens-Crowet, C., Bauwens, J.A. and Homès, G. (1969) Tensile yield-stress behavior of glassy polymers. *J. Polym. Sci. A2*, **7**, 735.

53. Bauwens-Crowet, C., Bauwens, J.A. and Homès, G. (1969) Tensile yield-stress behavior of poly(vinyl chloride) and polycarbonate in the glass transition region. *J. Polym. Sci. A2*, **7**, 1745.

54. Roetling, J.A. (1965) Yield stress behaviour of polymethylmethacrylate. *Polymer*, **6**, 311.

55. Haward, R.N. and Thackray, G. (1968) The use of a mathematical model to describe isothermal stress-strain curves in glassy thermoplastics. *Proc. Roy. Soc. A*, **302**, 453.

56. Holt, D.L. (1968) The modulus and yield stress of glassy poly(methyl methacrylate) at strain rates up to 103 inch/inch/second. *J. Appl. Polym. Sci.*, **12**, 1653.

57. Horsley, R.A. and Nancarrow, H.A. (1951) The stretching and relaxing of polyethylene. *Brit. J. Appl. Phys.*, **2**, 345.

58. Ward, I.M. (1971) The yield behaviour of polymers: review. *J. Mater. Sci.*, **6**, 1397.

59. Buckley, C.P. and Jones, D.C. (1995) Glass-rubber constitutive model for amorphous polymers near the glass transition. *Polymer*, **36**, 3301.

60. Bauwens, J.C. (1967) Déformation plastique des hauts polymères vitreux soumis á un système de contraintes quelconque. *J. Polym. Sci. A2*, **5**, 1145.

61. Duckett, R.A., Goswami, B.C., Smith, L.S.A. *et al.* (1978) Yielding and crazing behavior of polycarbonate in torsion under superposed hydrostatic-pressure. *Brit. Polym. J.*, **10**, 11.

62. Eyring, H. and Ree, T. (1955) A generalized theory of plasticity involving the virial theorem. *Proc. Natl. Acad. Sci. U S A*, **41**(3), 118.

63. Bauwens, J.C. (1972) Relation between the compression yield stress and the mechanical loss peak of bisphenol-A-polycarbonate in the β transition range. *J. Mater. Sci.*, **7**, 577.

64. Brooks, N.W., Duckett, R.A. and Ward, I.M. (1992) Investigation into double yield points in polyethylene. *Polymer*, **33**, 1872.

65. Seguela, R. and Darras, D. (1994) Phenomenological aspects of the double yield of polyethylene and related copolymers under tensile loading. *J. Mater. Sci.*, **29**, 5342.

66. Gupta, V.B. and Rana, S.K. (1998) Double yield in tensile deformation of high-density polyethylene fiber. *J. Macromolecular Sci. Phys.*, **B37**, 783.

67. Takayanagi, M. (1974) Some morphological factors in thermomechanical analysis of crystalline polymers. *J. Macromolecular Sci. Phys.*, **B9**, 391.

68. Sherby, O.D. and Dorn, J.E. (1958) Anelastic creep of polymethyl methacrylate. *J. Mech. Phys. Solids*, **6**, 145.

69. Mindel, M.J. and Brown, N. (1973) Creep and recovery of polycarbonate. *J. Mater. Sci.*, **8**, 863.

70. Fotheringham, D.G. and Cherry, B.W. (1978) The role of recovery forces in the deformation of linear polyethylene. *J. Mater. Sci.*, **13**, 951.

71. Robertson, R.E. (1966) Theory for the plasticity of glassy polymers. *J. Chem. Phys.*, **44**, 3950.

72. Duckett, R.A., Rabinowitz, S. and Ward, I.M. (1970) The strain-rate, temperature and pressure dependence of yield of isotropic poly(methylmethacrylate) and poly(ethylene terephthalate). *J. Mater. Sci.*, **5**, 909.

73. Cottrell, A.H. (1953) *Dislocations and Plastic Flow in Crystals*, Clarendon Press, Oxford.

74. Taylor, G.I. (1934) The mechanism of plastic deformation of crystals. Part I. Theoretical. *Proc. Roy. Soc.*, **A145**, 362.

75. Petermann, J. and Gleiter, H. (1972) Direct observation of dislocations in polyethylene crystals. *Phil. Mag.*, **25**, 813.

76. Kelly, A. and Macmillan, N.H. (1987) *Strong Solids*, 3rd edn, Clarendon Press, Oxford.

77. Brown, N. (1971) The relationship between yield point and modulus for glassy polymers. *Mater. Sci. Eng.*, **8**, 69.

78. Allison, S.W., Pinnock, P.R. and Ward, I.M. (1966) The cold drawing of polyethylene terephthalate. *Polymer*, **7**, 66.

79. Vincent, P.I. (1967) in *Encyclopedia of Polymer Science & Technology*, John Wiley & Sons, New York.

80. Li, J.C.M. and Gilman, J.J. (1970) Disclination loops in polymers. *J. Appl. Phys.*, **41**, 4248.

81. Frank, F.C. (1950) Symposium on Plastic Deformation of Crystalline Solids. Carnegie Institute of Technology, Pittsburgh.

82. Shadrake, L.G. and Guiu, F. (1976) Dislocations in polyethylene crystals: line energies and deformation modes. *Phil. Mag.*, **34**, 565.

83. Young, R.J. (1988) A dislocation model for yield in polyethylene. *Materials Forum*, **11**, 210.

84. Brooks, N.W., Ghazali, M., Duckett, R.A. *et al.* (1999) Effects of morphology on the yield stress of polyethylene. *Polymer*, **40**, 821.

85. Brooks, N.W., Unwin, A.P., Duckett, R.A. *et al.* (1997) Temperature and strain rate dependence of yield strain and deformation behavior in polyethylene. *J. Polym. Sci. B: Phys. Edn.*, **35**, 545.

86. Brooks, N.W.J., Duckett, R.A. and Ward, I.M. (1999) Effects of crystallinity and stress state on the yield strain of polyethylene. *Polymer*, **40**, 7367.

87. Brooks, N.W.J., Duckett, R.A. and Ward, I.M. (1998) Temperature and strain-rate dependence of yield stress of polyethylene. *J. Polym. Sci. B*, **36**, 2177

88. Nikolov, S. and Raabe, D. (2006) Yielding of polyethylene through propagation of chain twist defects: Temperature, stem length and strain-rate dependence. *Polymer*, **47**, 1696.

89. Brooks, N.W.J. and Mukhtar, M. Temperature and stem length dependence of the yield stress of polyethylene. (2000) *Polymer*, **41**, 1475.

90. Brown, N. (1971) Fundamental tensile stress-strain relationship for yielding of linear polymers. *Bull. Amer. Phys. Soc.*, **16**, 428.

91. Pinnock, P.R. and Ward, I.M. (1966) Stress-optical properties of amorphous polyethylene terephthalate fibres. *Trans. Faraday Soc.*, **62**, 1308.

92. Long, S.D. and Ward, I.M. (1991) Shrinkage force studies of oriented polyethylene terephthalate. *J. Appl. Polym. Sci.*, **42**, 1921.

93. Brody, H. (1983) The extensibility of polyethylene terephthalate fibers spun at high wind-up speeds. *J. Macromol. Sci. Phys.*, **B22**, 19.

94. Bessey, W. and Jaffe, M. (2000) in *Solid Phase Processing of Polymers*, (eds I.M. Ward, P.D. Coates and M.M. Dumoulin), Hanser, Munich, Chap. 4.

95. Kuhn, W. and Grun, F. (1942) Relationships between elastic constants and stretching double refraction of highly elastic substances. *Kolloid. Z*, **101**, 248.

96. Cail, J.J., Stepto, R.F.T. and Ward, I.M. (2007) Experimental studies and molecular modelling of the stress–optical and stress–strain behaviour of poly(ethylene terephthalate). Part III: Measurement and quantitative modelling of birefringence–strain, stress–strain and stress–optical properties. *Polymer*, **48**, 1379.

97. Ube, T., Aoki, H., Ito, S. *et al.* (2007) Conformation of single PMMA chain in uniaxially stretched film studied by scanning near-field optical microscopy. *Polymer*, **48**, 6221.

98. Hine, P.J., Duckett, R.A. and Read, D.J. (2007) Influence of molecular orientation and melt relaxation processes on glassy stress−strain behavior in polystyrene. *Macromolecules*, **40**, 2782.

99. Ward, I.M. and Coates, P.D. (2000) in *Solid Phase Processing of Polymers*, (eds I.M. Ward, P.D. Coates and M.M. Dumoulin), Hanser, Munich, Chap. 1.

100. Coates, P.D. and Ward, I.M. (1980) Neck profiles in drawn linear polyethylene. *J. Mater. Sci.*, **15**, 2597.

101. Coates, P.D., Gibson, A.G. and Ward, I.M. (1980) An analysis of the mechanics of solid phase extrusion of polymers. *J. Mater. Sci.*, **15**, 359.

102. Hope, P.S. and Ward, I.M. (1981) An activated rate theory approach to the hydrostatic extrusion of polymers. *J. Mater. Sci.*, **16**, 1511.

103. Mohanraj, J., Bonner, M.J., Barton, D.C. *et al.* (2007) Analysis and design of profiled dies for the polymer wire die-drawing process. *Proc. I. Mech. E, Part E: J. Process Mechanical Engineering*, **221**, 47.

104. Hay, I.L. and Keller, A. (1965) Polymer deformation in terms of spherulites. *Kolloidzeitschrzft*, **204**, 43.

105. Peterlin, A. (1965) Crystalline character in polymers. *J. Polym. Sci.*, **C9**, 61.

106. Geil, P.H. (1964) Polymer deformation. III. Annealing of drawn polyethylene single crystals and fibers. *J. Polym. Sci. A*, **2**, 3835.

107. Capaccio, G. and Ward, I.M. (1973) Properties of ultra-high modulus linear polyethylenes. *Nature Phys. Sci.*, **243**, 43.

108. Capaccio, G. and Ward, I.M. (1974) Preparation of ultra-high modulus linear polyethylenes; effect of molecular weight and molecular weight distribution on drawing behaviour and mechanical properties. *Polymer*, **15**, 233.

109. Capaccio, G., Crompton, T.A. and Ward, I.M. (1976) Drawing behavior of linear polyethylene. Part 1. Rate of drawing as a function of polymer molecular-weight and initial thermal-treatment. *J. Polym. Sci. Polym. Phys. Edn.*, **14**, 1641.

110. Bowden, P.B. (1973) in *The Physics of Glassy Polymers* (ed. R.N. Haward), Applied Science, London.

111. Lu, J. and Ravi-Chandar, K. (1999) Inelastic deformation and localization in polycarbonate under tension. *Int. J. Solids Struct.*, **36**, 391.

112. Wu, P.D. and van der Giessen, E. (1994) Analysis of shear band propagation in amorphous glassy polymers. *Int. J. Solids Struct.*, **31**, 1493.

113. Wu, P.D. and van der Giessen, E. (1996) Computational aspects of localized deformations in amorphous glassy polymers. *Eur. J. Mech. A/Solids*, **15**, 799.

114. Sweeney, J., Caton-Rose, P., Spares, R. *et al.* (2007) A unified model of necking and shearbanding in amorphous and semicrystalline polymers. *J. Appl. Polym. Sci.*, **106**, 1095.

115. Boyce, M.C., Parks, D.M. and Argon, A.S. (1988) Large inelastic deformation of glassy polymers. part I: rate dependent constitutive model. *Mech. Mater.*, **7**, 15.

116. Boyce, M.C., Parks, D.M. and Argon, A.S. (1989) Plastic flow in oriented glassy polymers. *Int. J. Plasticity*, **5**, 593.

117. Arruda, E.M. and Boyce, M.C. (1993) Evolution of plastic anisotropy in amorphous polymers during finite straining. *Int. J. Plasticity*, **9**, 697.

118. Boyce, M.C., Socrate, M. and Llana, P.G. (2000) Constitutive model for the finite deformation stress–strain behavior of poly(ethylene terephthalate) above the glass transition. *Polymer*, **41**, 2183.

119. Haward, R.N. (1993) Strain hardening of thermoplastics. *Macromolecules*, **26**, 5860.

120. van Melick, H.G.H., Govaert, L.E. and Meijer, H.E.H. (2003) On the origin of strain hardening in glassy polymers. *Polymer*, **44**, 2493.

121. Senden, D.J.A., van Dommelen, J.A.W. and Govaert, L.E. (2010) Strain hardening and its relation to Bauschinger effects in oriented polymers. *J. Polym. Sci. Part B: Polym. Phys.*, **48**, 1483.

122. Hoy, R.S. and Robbins, M.O. (2008) Strain hardening of polymer glasses: Entanglements, energetics, and plasticity. *Physical Review E*, **77**, 031801.

123. Sweeney, J., Naz, S. and Coates, P.D. (2011) Modeling the tensile behavior of ultra-high-molecular-weight polyethylene with a novel flow rule. *J. Appl. Polym. Sci.*, **121**, 2936.

124. Hope, P.S., Ward, I.M. and Gibson, A.G. (1980) The hydrostatic extrusion of polymethylmethacrylate. *J. Mater. Sci.*, **15**, 2207.

125. Ward, I.M. (1984) The role of molecular networks and thermally activated processes in the deformation-behavior of polymers. *Polym. Eng. Sci.*, **24**, 724.

126. Van Erp, T.B., Reynolds, C.T., Peijs, T. *et al.* (2009) Prediction of yield and long-term failure of oriented polypropylene: kinetics and anisotropy. *J. Polym. Sci. Part B: Polym. Phys.*, **47**, 2026–2035.

127. Mather, P.T., Luo, X.F. and Rousseau, I.A. (2009) Shape memory polymer research. *Annu. Rev. Mater. Res.*, **39**, 445–471.

128. Behl, M., Zotzmann, J. and Lendlein, A. (2010) Shape-memory polymers and shape-changing polymers. *Adv. Polym. Sci.*, **226**, 1–40.

129. Ratna, D. and Karger-Kocsis, J. (2008) Recent advances in shape memory polymers and composites: a review. *J. Mater. Sci.*, **43**, 254–269.

130. Xie, T. (2011) Recent advances in polymer shape memory. *Polymer*, **52**, 4985–5000.

131. Nguyen, T.D., Qi, H.J., Castro, F. and Long, K.N. (2008) A thermoviscoelastic model for amorphous shape memory polymers: incorporating structural and stress relaxation. *J. Mech. Phys. Solids*, **56**, 2792–2814.

132. Chen, Y.C. and Lagondas, D.C. (2008) A constitutive theory for shape memory polymers. Part II: A linearized model for small deformations. *J. Mech. Phys. Solids*, **56**, 1766–1778.

133. Lin, T.R. and Chen, L.W. (1999) Shape-memorized crosslinked ester-type polyurethane and its mechanical viscoelastic model. *J. Appl. Polymer Sci.*, **73**, 1305–1319.

134. Li, F. and Larock, R.C. (2002) New soybean oil–styrene–divinylbenzene thermosetting copolymers. V. shape memory effect. *J. Appl. Polymer Sci.*, **84**, 1533–1543.

135. Bonner, M., Montes de Oca, H., Brown, M. *et al.* (2010) A novel approach to predict the recovery time of shape memory polymers. *Polymer*, **51**, 1432–1436.

136. Heuchel, M., Cui, J., Kratzk, K. *et al.* (2010) Relaxation based modeling of tunable shape recovery kinetics observed under isothermal conditions for amorphous shape-memory polymers. *Polymer*, **51**, 6216–6218.

Further Reading

Halary, J.L., Lauprêtre, F. and Monnerie, L. (2011) *Polymer Materials: Macroscopic Properties and Molecular Interpretations*, John Wiley & Sons, Ltd, Hoboken, New Jersey.

McCrum, N.G., Read, B.E. and Williams, G. (1991) *Anelastic and Dielectric Effects in Polymeric Solids*, Dover Publications, New York.

13

Breaking Phenomena

13.1 Definition of Tough and Brittle Behaviour in Polymers

The mechanical properties of polymers are greatly affected by temperature and strain rate, and the load–elongation curve at a constant strain rate changes with increasing temperature as shown schematically (not necessarily to scale) in Figure 13.1. At low temperatures, the load rises approximately linearly with increasing elongation up to the breaking point, when the polymer fractures in a brittle manner. At higher temperatures, a yield point is observed and the load falls before failure, sometimes with the appearance of a neck, that is ductile failure, but still at quite low strains (typically 10–20%). At still higher temperatures, under certain conditions, strain hardening occurs, the neck stabilises and cold-drawing ensues. The extensions in this case are generally very large, up to 1000%. Finally, at even higher temperatures, homogeneous deformation is observed, with a very large extension at break. In an amorphous polymer, this rubber-like behaviour occurs above the glass transition temperature so the stress levels are very low.

For polymers, the situation is clearly more complicated than that for the brittle–ductile transition in metals, as there are in general four regions of behaviour and not two. It is of considerable value to discuss the factors that influence the brittle–ductile transition, and then to consider further factors that are involved in the observation of necking and cold-drawing.

Ductile and brittle behaviour are most simply defined from the stress–strain curve. Brittle behaviour is designated when the specimen fails at its maximum load, at comparatively low strains (say <10%), whereas ductile behaviour shows a peak load followed by failure at a lower stress (Figures 13.1(a) and (b)).

The distinction between brittle and ductile failure is also manifested in two other ways: (1) the energy dissipated in fracture and (2) the nature of the fracture surface. The energy dissipated is an important consideration for practical applications and forms the basis of the Charpy and Izod impact tests (discussed in Section 13.8). At the testing speeds under which the practical impact tests are conducted it is difficult to determine the stress–strain curve,
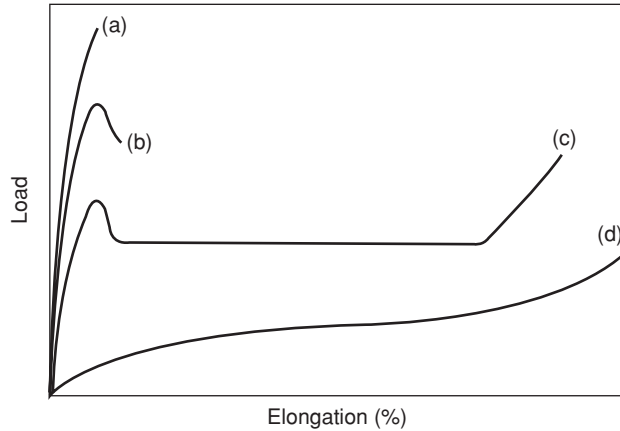
Figure 13.1 *Load–extension curves for a typical polymer tested at four temperatures showing different regions of mechanical behaviour: (a) brittle fracture; (b) ductile failure; (c) necking and cold-drawing; (d) homogeneous deformation (quasi-rubber-like behaviour).*

so impact strengths are customarily quoted in terms of the fracture energy for a standard specimen.

The appearance of the fracture surface also can be an indication of the distinction between brittle and ductile failure, although the present state of knowledge concerning the crack propagation is not sufficiently extensive to make this distinction more than empirical.

13.2   Principles of Brittle Fracture of Polymers

Modern understanding of the fracture behaviour of brittle materials stems from the seminal research of Griffith [1] on the brittle fracture of glass. The Griffith theory of fracture, which is the earliest statement of linear elastic fracture mechanics, has been applied extensively to the fracture of glass and metals, and more recently to polymers. Although it was conceived initially to describe the propagation of a crack in a perfectly elastic material at small elastic strains (hence linear elastic), subsequent work has shown that it is still applicable for situations including localised plastic deformation at the crack tip, which does not lead to general yielding in the specimen.

13.2.1   Griffith Fracture Theory

First, Griffith considered that fracture produces a new surface area and postulated that for fracture to occur the increase in energy required to produce the new surface must be balanced by a decrease in elastically stored energy.

Secondly, to explain the large discrepancy between the measured strength of materials and those based on theoretical considerations, he proposed that the elastically stored energy is not distributed uniformly throughout the specimen but is concentrated in the neighbourhood of small cracks. Fracture thus occurs due to the spreading of cracks that originate in pre-existing flaws.

In general, the growth of a crack will be associated with an amount of work dW being done on the system by external forces and a change dU in the elastically stored energy U. The difference between these quantities, dW − dU, is the energy available for the formation of the new surface. The condition for growth of a crack by a length dc is then

$$\frac{\mathrm{d}W}{\mathrm{d}c} - \frac{\mathrm{d}U}{\mathrm{d}c} \geq \gamma \frac{\mathrm{d}A}{\mathrm{d}c}, \qquad (13.1)$$

where γ is the surface free energy per unit area of surface and dA is the associated increment of surface. If there is no change in the overall extension Δ when the crack propagates, d$W = 0$ and

$$\left(\frac{\mathrm{d}U}{\mathrm{d}c}\right)_{\Delta} \geq \gamma \frac{\mathrm{d}A}{\mathrm{d}c}. \qquad (13.1\mathrm{a})$$

The elastically stored energy decreases and so $-(\mathrm{d}U/\mathrm{d}c)_{\Delta}$ is essentially a positive quantity.

Griffith calculated the change in elastically stored energy using a solution obtained by Inglis [2] for the problem of a plate, pierced by a small elliptical crack that is stressed at right angles to the major axis of the crack. Equation (13.1) then allows the fracture stress σ_B of the material to be defined in terms of the crack length $2c$ by the relationship

$$\sigma_B = (2\gamma E^*/\pi c)^{1/2}, \qquad (13.2)$$

where E^* is the 'reduced modulus', equal to Young's modulus E for a thin sheet in plane stress and equal to $E/(1 - \nu^2)$, where ν is Poisson's ratio for a thick sheet in plane strain.

13.2.2   The Irwin Model

An alternative formulation of the problem due to Irwin [3] considers the stress field near an idealised crack length $2c$ (Figure 13.2). In two-dimensional polar coordinates with the
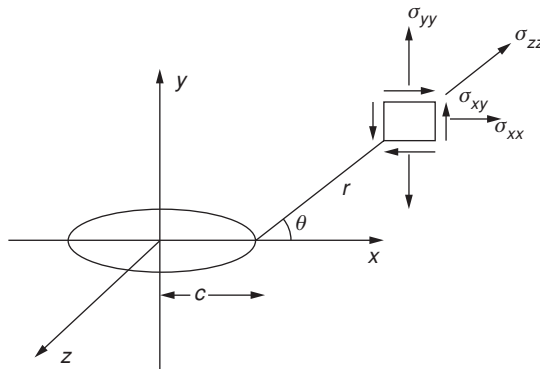
Figure 13.2   *The stress field near an idealised crack of length 2c.*

x axis as the crack axis and $r \ll c$,

$$\sigma_{xx} = \frac{K_\mathrm{I}}{(2\pi r)^{1/2}} \cos(\theta/2)[1 - \sin(\theta/2)\sin(3\theta/2)]$$

$$\sigma_{yy} = \frac{K_\mathrm{I}}{(2\pi r)^{1/2}} \cos(\theta/2)[1 + \sin(\theta/2)\sin(3\theta/2)]$$

$$\sigma_{zz} = v(\sigma_{xx} + \sigma_{yy}) \quad \text{for plane strain}$$

$$\sigma_{zz} = 0 \quad \text{for plane stress}$$

$$\sigma_{xy} = \frac{K_\mathrm{I}}{(2\pi r)^{1/2}} \cos(\theta/2)\sin(\theta/2)\sin(3\theta/2)$$

$$\sigma_{yz} = \sigma_{zx} = 0.$$

(13.3)

In these equations, θ is the angle between the axis of the crack and the radius vector.

The value of Irwin's approach is that the stress field around the crack is identical in form for all types of loading situation normal to the crack, with the magnitude of the stresses (i.e. their intensity) determined by K_I, which is constant for given loads and geometry; K_I is called the stress intensity factor, the subscript I indicating loading normal to the crack. This crack opening mode I is distinct from a sliding mode II, which is not considered here. As we approach the crack tip, σ_{xx} and σ_{yy} clearly become infinite in magnitude as r tends to zero, but the products $\sigma_{xx}\sqrt{r}$ and $\sigma_{yy}\sqrt{r}$ and hence K_I remain finite.

For an infinite sheet with a central crack of length $2c$ subjected to a uniform stress σ, it was shown by Irwin that

$$K_\mathrm{I} = \sigma(\pi c)^{1/2}.$$

(13.4)

He postulated that, when σ reaches the fracture stress σ_B, K_I has a critical value given by

$$K_\mathrm{IC} = \sigma_B(\pi c)^{1/2}.$$

(13.5)

The fracture toughness of the material then can be defined by the value of K_IC, termed the critical stress intensity factor, which defines the stress field at fracture.

There is clearly a link with the earlier Griffith formulation in that Equation (13.5) can be written as

$$\sigma_B = (K_\mathrm{IC}^2/\pi c)^{1/2},$$

(13.6)

which is identical in form to Equation (13.2).

13.2.3   The Strain Energy Release Rate

In linear elastic fracture mechanics, it is useful also to consider the energy G available for unit increase in crack length, which is called the 'strain energy release rate'. Following Equation (13.1) above, G is

$$G = \frac{\mathrm{d}W}{\mathrm{d}A} - \frac{\mathrm{d}U}{\mathrm{d}A} = \frac{1}{B}\left[\frac{\mathrm{d}W}{\mathrm{d}c} - \frac{\mathrm{d}U}{\mathrm{d}c}\right],$$

(13.7)
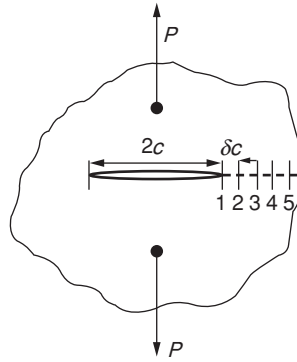
Figure 13.3 *Schematic diagram of a specimen with a centre crack of length 2c.*

where B is the thickness of the specimen. It is assumed that fracture occurs when G reaches a critical value of G_c. The equivalent Equation to (13.1) is then

$$G \geq G_c \tag{13.8}$$

and G_c is equal to 2γ in the Griffith formulation but is generalised to include all work of fracture, not just the surface energy.

Comparison of Equations (13.2) and (13.6) shows

$$G_{\text{IC}} = K_{\text{IC}}^2 / E^*. \tag{13.9}$$

Although the Griffith and Irwin formulations of the fracture problems are equivalent, most recent studies of polymers have followed Irwin. Before discussing results for polymers, it is useful to show how G_c can be calculated.

Consider a sheet of polymer with a crack of length $2c$ (Figure 13.3). We now define a quantity termed the compliance of the cracked sheet, C, which is the reciprocal of the slope of the linear load–extension curve from zero load up to the point at which crack propagation begins. At the latter point, the load is P and the extension is Δ, so $C = \Delta/P$.

This quantity C is not to be confused with an elastic stiffness constant as defined in Section 8.1. The work done in an elemental step of crack propagation is illustrated by Figure 13.4. As the crack moves from 4 to 5, for example, the energy available for the formation of a new crack surface is the difference between the work done (45XY) and the increase in elastic-stored energy (triangle 05Y – triangle 04X). This energy corresponds to the area of the shaded triangle in Figure 13.4, and for an increase of crack length dc is given by $\frac{1}{2}P^2 \, \mathrm{d}C$. Hence

$$G_c = \frac{P^2}{2B} \frac{\mathrm{d}C}{\mathrm{d}c}, \tag{13.10}$$

which is generally known as the Irwin–Kies relationship [4].

Here G_c can be determined directly by combining a load–extension plot from a tensile testing machine with determination of the movement of the crack across the specimen, noting the load P for given crack lengths (points 1, 2, 3, 4, 5 in Figure 13.4). Alternatively, test pieces of standard geometry can be used, for which the compliance is known as a
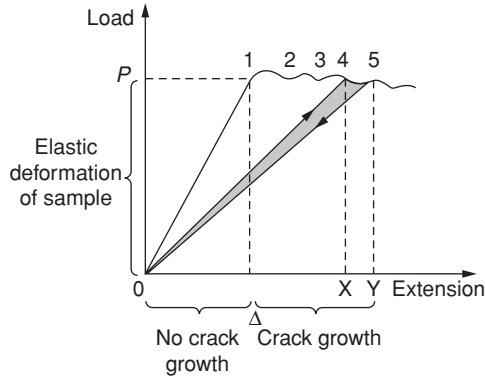
Figure 13.4 *The load–extension curve for the specimen shown in Figure 13.3.*

function of crack length. For example, the relationship between the extension Δ (usually termed the deflection in this case) and the load P for a double cantilever beam specimen of thickness B (see Figure 13.5) is given by

$$\Delta = \frac{64c^3}{EBb^3} P.$$

Hence

$$C = \frac{\Delta}{P} = \frac{64c^3}{EBb^3} \text{ and } \frac{dC}{dc} = \frac{192c^2}{EBb^3} \tag{13.11}$$

giving

$$G_c = \frac{P^2}{2B} \frac{dC}{dc} = \frac{P^2}{2B} \frac{192c^2}{EBb^3} \tag{13.12a}$$

or

$$G_c = \frac{3\Delta^2 b^3}{128c^4} E. \tag{13.12b}$$

The critical strain-energy release rate (or, in the original Griffith terminology, the fracture surface energy γ) therefore can be obtained by measurements of either the load P or the deflection Δ for given crack lengths c.
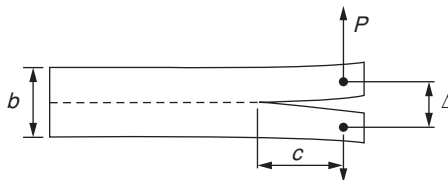
Figure 13.5 *The double cantilever beam specimen.*

The exact equivalent formulation in terms of the critical stress intensity factor can be obtained from Equation (13.9), giving

$$K_{IC} = 4\sqrt{6}\frac{P^2}{Bb^{3/2}}. \tag{13.13}$$

We have discussed only the calculation for a geometrically simple specimen, so that the principles involved are not obscured by complex stress analysis. For a comprehensive discussion of the calculation of the fracture toughness parameters G_c and K_c for specimens with different geometries, see standard texts [5–7].

13.3   Controlled Fracture in Brittle Polymers

In its simplest form the Griffith theory, and the linear elastic fracture mechanics (LEFM) that developed from it, ignore any contribution to the energy balance arising from the kinetic energy associated with movement of the crack. A basic study of the brittle fracture of polymers is therefore likely to be most rewarding if the fracture takes place slowly so that a negligible amount of energy is dissipated in this way.

With these ideas in mind the seminal experimental studies of brittle fracture in polymers were undertaken by Benbow and Roesler at ICI in the United Kingdom [8] and by Berry at GE in the United States [9]. Benbow and Roesler devised a method of fracture in which flat strips of poly(methyl methacrylate) (PMMA) were cleaved by gradually propagating a crack down the middle, as in a cantilever double beam. Essentially, their experiments involved determining the deflection Δ for a given length c (symbols as in Figure 13.5). The results were expressed in terms of the surface energy γ. Following Equation (13.12b)

$$\frac{G_c}{E} = \frac{2\gamma}{E} = \frac{3\Delta^2 b^3}{128c^4}. \tag{13.14}$$

Knowing a value for the Young's modulus, E, the surface energy γ can be found.

Berry adopted a slightly different approach to evaluate γ, and also confirmed the validity of Equation (13.2) for the fracture of PMMA and polystyrene by measuring the tensile strength of small samples containing deliberately introduced cracks of known magnitude.

Berry's summary of his own results and those of other workers is shown in Table 13.1. The very important conclusion to be drawn from these values for fracture surface energy is that they are very much greater than values estimated from the assumption that the energy

Table 13.1   *Fracture surface energies (in J m^2 × 10^2).*

Method	Polymers	
	Poly(methyl methacrylate)	Polystyrene
Cleavage (Benbow [10])	4.9 ± 0.5	25.5 ± 3
Cleavage (Svensson [11])	4.5	9.0
Cleavage (Berry [9])	1.4 ± 0.07	7.13 ± 0.36
Tensile (Berry [12])	2.1 ± 0.5	17 ± 6

required to form a new surface originates in the simultaneous breaking of chemical bonds, which might appear to provide an upper theoretical estimate. Take the bond dissociation energy as 400 kJ and the concentration of molecular chains as 1 chain per 0.2 nm^2, giving 5×10^{18} molecular chains m^{-2}. To form 1 m^2 of new surface requires about 1.5 J, which is two orders of magnitude less than that obtained from cleavage and tensile measurements.

13.4   Crazing in Glassy Polymers

The large discrepancy between experimental and theoretical values for the surface energy is comparable to that found for metals, where it was proposed by Orowan and others that the surface free energy may include a large term that arises from plastic work done in deforming the metal near the fracture surface as the crack propagates. Andrews [13] suggested that the quantity measured in the fracture of polymers should be described by J, the 'surface work parameter', to distinguish it from a true surface energy, and proposed a generalised theory of fracture that embraces viscoelastic as well as plastic deformation, both of which may be important in polymers.

   On the basis of the results shown in Table 13.1, Berry concluded that the largest contribution to the surface energy of a glassy polymer comes from a viscous flow process that in PMMA, he suggested [14], was related to the interference bands observed on the fracture surfaces, as seen in Figure 13.6. He proposed that work was expended in the

Figure 13.6   *Matching fracture surfaces of a cleavage sample of poly(methyl methacrylate) showing colour alternation (green filter). (Reproduced from Berry, J.P. (1959) in Fracture (eds B.L. Auerbach et al.), John Wiley & Sons, New York, p. 263. Copyright (1959) John Wiley & Sons, Inc.)*
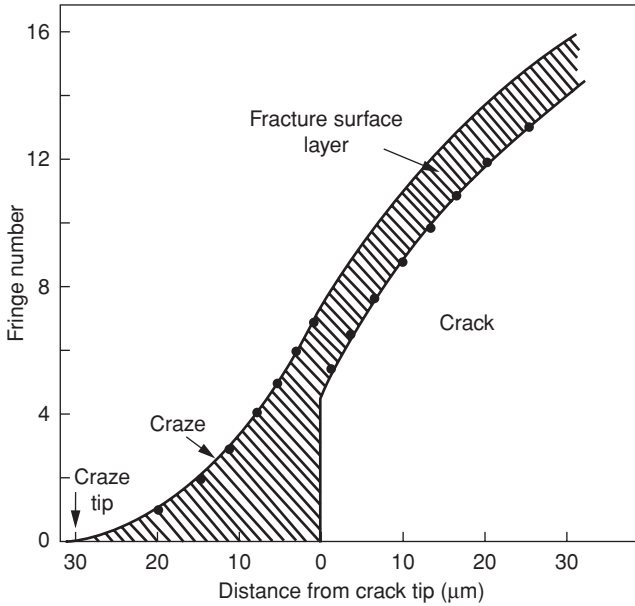
Figure 13.7 *Schematic diagram of a craze. (Reproduced from Brown, H.R. and Ward, I.M. (1973) Craze shape and fracture in poly(methyl methacrylate). Polymer, **14**, 469. Copyright (1973) IPC Business Press.)*

alignment of polymer chains ahead of the crack, the subsequent crack growth leaving a thin, highly oriented layer of polymeric material on the fracture surface. Following on from these ideas, Kambour [15–17] showed that a thin wedge of porous material termed a craze forms at a crack tip in a glassy polymer, as shown schematically in Figure 13.7. The craze forms under plane strain conditions, so that the polymer is not free to contract laterally and there is a consequent reduction in density. Several workers [18, 19] have attempted to determine the craze profile by examining the crack tip region in PMMA in an optical microscope. In reflected light, two sets of interference fringes were observed, which correspond to the crack and the craze, respectively. It was found that the craze profile was very similar to the plastic zone model proposed by Dugdale [20] for metals, which will now be described.

Equation (13.3) implies that there is an infinite stress at the crack tip. In practice this clearly cannot be so, and there are two possibilities. First, there can be a zone where shear yielding of the polymer occurs. In principle, this can occur in both thin sheets where conditions of plane stress pertain and in thick sheets where there is a plane strain. Secondly, for thick specimens under conditions of plane strain, the stress singularity at the crack tip can be released by the formation of a craze, which is a line zone, in contrast to the approximately oval (plane stress) or kidney-shaped (plane strain) shear yield zones. As indicated, its shape approximates very well to the idealised Dugdale plastic zone where the stress singularity at the crack tip is cancelled by the superposition of a second stress field in which the stresses are compressive along the length of the crack (Figure 13.8). A constant compressive stress is assumed and is identified with the craze stress. It is not the
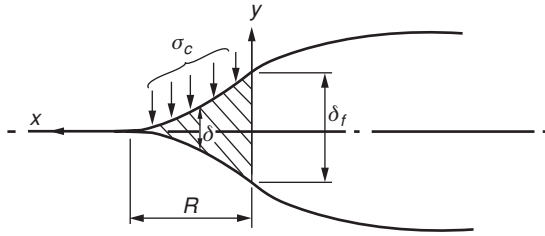
Figure 13.8   *The Dugdale plastic zone model for a craze.*

yield stress, and crazing and shear yielding are different in nature and respond differently to changes in the structure of the polymer.

Rice [21] has shown that the length of the craze for a loaded crack on the point of propagation is

$$R = \frac{\pi}{8} \frac{K_{\text{IC}}^2}{\sigma_c^2} \qquad (13.15)$$

and the corresponding separation distance δ between the upper and lower surface of the craze is

$$\delta = \frac{8}{\pi E^*} \sigma_c R \left[\zeta - \frac{x}{2R} \log\left(\frac{1+\zeta}{1-\zeta} \right) \right], \qquad (13.16)$$

where $\zeta = (1 - x/R)^{1/2}$ and E^* is the reduced modulus as defined in 13.2.1.

The crack opening displacement (COD) δ_t is the value of the separation distance δ at the crack tip, where $x = 0$, and is therefore

$$\delta_t = 8\sigma_c R / \pi E^* = K_{\text{IC}}^2 / \sigma_C E^*. \qquad (13.17)$$

The fracture toughness of the polymer then relates to two parameters δ_t and σ_c (the craze stress), the product of which is equal to G_{IC}, the critical strain energy release rate. Direct measurements of craze shapes for several glassy polymers, including polystyrene, poly(vinyl chloride) and polycarbonate [19, 22], have confirmed the similarity to a Dugdale plastic zone. A result of some physical significance is that the COD is often insensitive to temperature and strain rate for a given polymer, although it has been shown to depend on molecular mass. For constant COD, the true dependence of G_{IC} on strain rate and temperature is determined only by the sensitivity of the craze stress to these parameters. Because $G_{\text{IC}} = K_{\text{IC}}^2 / E^*$, the fracture toughness K_{IC} will in addition be affected by E^*, which is also dependent on strain rate and temperature.

This approach offers a deeper understanding of the brittle–ductile transition in glassy polymers in terms of competition between crazing and yielding. Both are activated processes, in general with different temperature and strain rate sensitivities, and one will be favoured over the other for some conditions and vice versa for other conditions. An additional complexity can arise from the nature of the stress field that may favour one process rather than the other, but the latter consideration does not enter into our discussion of the
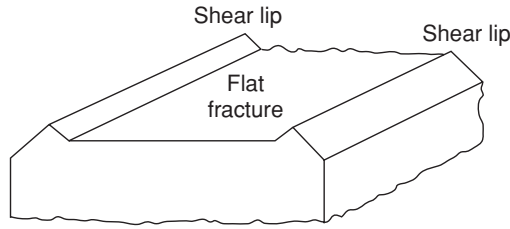
Figure 13.9 *The shear lips in polycarbonate. (Reproduced with pemission from Fraser R.A.W and Ward I.M. (1978) Temperature-dependence of Craze Shape and Fracture in Polycarbonate. Polymer, **19**, 220. Copyright (1978) Elsevier Ltd.)*

craze at the crack tip. The line of travel of the crack is a line of zero shear stress within the plane but maximum triaxial stress. In later discussion, we will see that such a stress field favours crazing and that for long cracks where the stress field of the crack is the dominant factor, the craze length is determined solely by the requirement that the craze grows to cancel the stress singularity at the crack tip.

In several glassy polymers [22, 23], such as the polycarbonate shown in Figure 13.9, a complication occurs in that a thin line of material called a shear lip forms on the fracture surface where the polymer has yielded. Analogous to the behaviour of metals, it has been proposed that the overall strain energy release rate G_C^0 is the sum of the contribution from the craze and that from the shear lips. To a first approximation, we would expect the latter to be proportional to the volume of yielded material. If the total width of the shear lip on the fracture surface is w, B is the specimen thickness and the shear lip is triangular in cross section, then

$$G_C^0 = G_{IC} \left(\frac{B - w}{B} \right) + \frac{\phi w^2}{2B},\qquad(13.18)$$

where ϕ is the energy to fracture a unit volume of shear lip. It has been shown that this relationship describes results for polycarbonate and poly(ether sulfone) very well [22, 23] and that ϕ corresponds quite closely to the energy to fracture in a simple tensile extension experiment.

An alternative approach [24] assumes an additivity rule based on a plane strain K_{IC}, which pertains to fracture in the central part of the specimen and is designated K'_{IC}, and a plane stress K_{IC}, which is effective for the two surface skins of depth $w/2$ and is designated K''_{IC}. For the overall specimen, it is then proposed that

$$K_{IC} = \left(\frac{B - w}{B} \right) K'_{IC} + \left(\frac{w}{B} \right) K''_{IC}.\qquad(13.18a)$$

Although Equation (13.18a) is more empirically based than Equation (13.18) and is not formally equivalent, it has been shown to model fracture results very well. Moreover, in this formulation w relates to the size of the so-called Irwin plastic zone r_y, which can be defined simply on the basis of Equation (13.3) by assuming that a point r_y the stress reaches
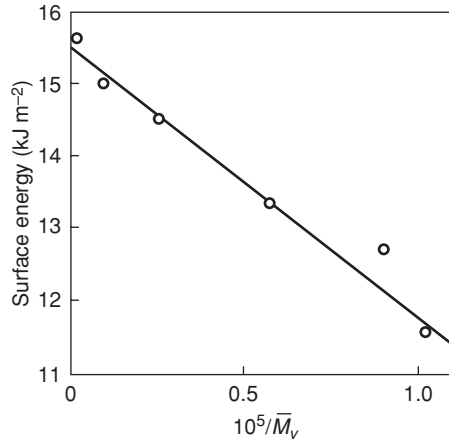
Figure 13.10   *Dependence of fracture surface energy on reciprocal molecular mass) M_v is viscosity average molecular mass). (Reproduced from Berry, J.P. (1964) Fracture Processes in polymeric materials. V. Dependence of ultimate properties of poly(methyl methacrylate) on molecular weight. J. Polym. Sci. A2, **2**, 4069. Copyright (1964) John Wiley & Sons, Ltd.)*

the yield stress σ_y. Hence

$$r_y = \frac{1}{2\pi} \left(\frac{K_{IC}}{\sigma_y} \right)^2$$

for plane stress and $w/2 = r_y$ in Equation (13.18a).

For PMMA, Berry showed that the surface energy was strongly dependent on polymer molecular mass [25]. His results (Figure 13.10) fitted an approximately linear dependence of the fracture surface energy on reciprocal molecular mass, such that $\gamma = A' - B'/\bar{M}_V$, where $\bar{M}_V$ is the viscosity average molecular mass. Many years previously, Flory [26] had proposed that the brittle strength is related to the number average molecular mass.

More recently, Weidmann and Döll [27] have shown that the craze dimensions decrease markedly in PMMA at low molecular masses. In a study of the molecular mass dependence of fracture surfaces in the same polymer, Kusy and Turner [28] could observe no interference colours for a viscosity average molecular mass of less than 90 000 daltons, concluding that there was a dramatic decrease in the size of the craze. Based on craze shape studies of polycarbonate, Pitman and Ward [22] reported a very high dependence of both craze stress and COD on molecular mass and observed that both would be expected to become negligibly small for $\bar{M}_w < 10^4$. Berry speculated that the smallest molecule that could contribute to the surface energy would have its end on the boundaries of the craze region, on opposite sides of the fracture plane, and be fully extended between these points. Kusy and Turner [29] presented a fracture model for PMMA in which the surface energy measured was determined by the number of chains above a critical length. Their data fitted well with their predictions, showing a limit to the surface energy at high molecular weight, but the model appeared inappropriate for the polycarbonate data of Pitman and Ward. Moreover, the extended molecular lengths, based on the extension of a random coil, would be much less than the COD (as discussed by Haward, Daniels and Treloar [30]) so that there is no

direct correlation between the two quantities. The craze structure relates to the stretching of fibrils and the key molecular factors are the presence of random entanglements and the distance between these entanglements, not the extension of an isolated molecular chain.

13.5   The Structure and Formation of Crazes

We have seen how the craze at the crack tip in a glassy polymer plays a vital role in determining its fracture toughness. Crazing in polymers also manifests itself in another way. When certain polymers, notably PMMA and polystyrene, are subjected to a tensile test in the glassy state, above a certain tensile stress opaque striations appear in planes whose normals are the direction of tensile stress, as shown in Figure 13.11.

The interference bands on the fracture surfaces, which relate to the craze at the crack tip, were first observed by Berry [31] and by Higuchi [32]. Kambour confirmed that the PMMA fracture-surface layers were qualitatively similar to the internal crazes of this polymer, by showing that the refractive indices were the same [15]. Both surface layer and bulk crazes appear to be oriented polymer structures of low density, which are produced by orienting the polymer under conditions of abnormal constraint: it is not allowed to contract in the lateral direction, while being extended locally to strains of the order of unity, and so has undergone inhomogeneous cold-drawing.
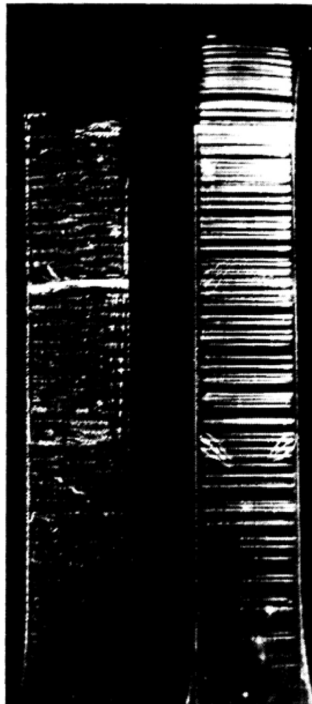
Figure 13.11   *Craze formation in polystyrene.*

Detailed studies have been made of the structure of crazes, the stress or strain criteria for their formation and environmental effects. These subjects now will be discussed in turn.

13.5.1   The Structure of Crazes

The structure of crazes in bulk specimens was studied by Kambour [15], who used the critical angle for total reflection at the craze/polymer interface to determine the refractive index of the craze, and showed that the craze was roughly 50% polymer and 50% void. Another investigation involved transmission electron microscopy of polystyrene crazes impregnated with an iodine–sulfur eutectic to maintain the craze in its extended state [33, 34]. The structure of the craze was clearly revealed as fibrils separated by the voids that are responsible for the overall low density.

Our understanding of the structure of crazes in glassy polymers developed in two stages, the first of which followed from a combination of techniques, starting with refractive index measurements and transmission electron microscopy, followed by small-angle X-ray scattering (SAXS) and small-angle electron scattering (SAEX). The SAXS measurements, initiated by Parades and Fischer [35] with further contributions by Brown, Kramer and their collaborators [36], together with the SAEX measurements by Berger, Brown and Kramer [37, 38] confirmed the craze structure of a forest of cylindrical fibrils oriented normal to the craze surface. Figure 13.12 shows bright-field transmission electron microscopy and SAEX measurements by Berger [39], which were also most important in showing the presence of cross-tie fibrils between the main fibrils, suggesting the structure postulated in Figure 13.13.

Porod analysis of the SAXS and SAEX measurements provided a quantitative estimate of the mean craze fibril spacing. Brown [40] subsequently made the key observation that the presence of the cross-tie fibrils has a profound effect on the failure mechanism of a craze because they enable stress transfer between broken and unbroken fibrils. Brown [40], and then Kramer [41], followed this idea through to produce a quantitative theory of craze failure of the molecular chains at the mid-rib of the craze. Brown's theory is a very ingenious mixture of the macroscopic and the microscopic. Starting at the macroscopic level, the craze can be modelled as a continuous anisotropic elastic sheet. The stress on the craze plane in front of the crack is then

$$\sigma = \frac{K_{\text{tip}}}{(2\pi r)^{1/2}},$$

where r is the distance from the crack tip and K_{tip} is the crack tip stress intensity factor. This is classical LEFM following Irwin (Equation (13.6)). A more sophisticated analysis [41] makes use of the model of the craze as an anisotropic solid characterised by stiffness constants c_{pq} (see Chapter 7). The dimensionless quantity α is introduced defined as $\alpha^2 = c_{66}/c_{22}$ in a two-dimensional axis set with the 1 axis along the crack. The craze is opened by a drawing stress σ_d acting along the 2 direction normal to rigid boundaries either side of the craze. For a craze half-width h, the stress intensity at the tip is given by

$$K_{\text{tip}} = \sigma_d (2\alpha h)^{1/2}. \tag{13.19}$$
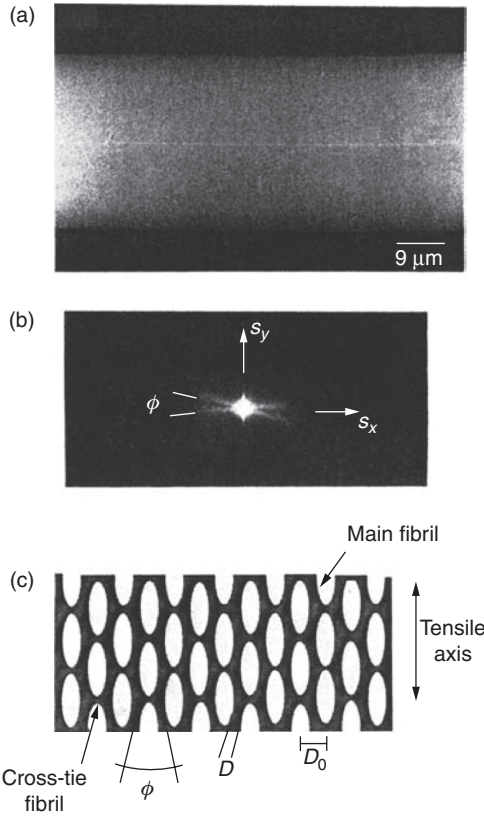
*Figure 13.12   Bright-field TEM image of craze (a) formed in PMMA and its corresponding low-angle electron diffraction pattern (b); an idealised representation of the craze microstructure is shown in c. (Reproduced from Berger, L.L. (1989) Relationship between craze microstructure and molecular entanglements in glassy-polymers. Macromolecules, **22**, 3162. Copyright (1989) American Chemical Society.)*
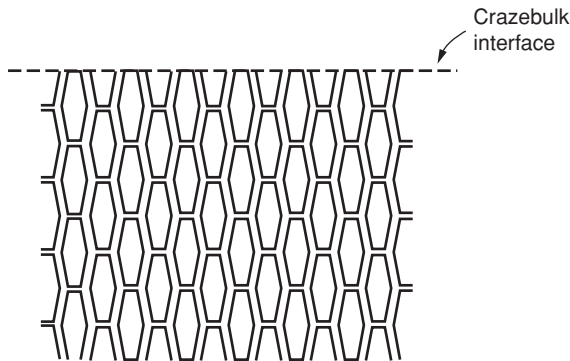
*Figure 13.13   Schematic illustration of the fibril structure of a craze showing a regular arrangement of cross-tie fibrils. (Reproduced from Brown H.R. (1987) Polymer degradation by crazing and its study by small angle scattering techniques. Mater. Sci. Rep., **2**, 315. Copyright (1987) Elsevier Ltd.)*

The highest stress in the craze is assumed to be in the fibril closest to the crack tip, and can be approximated by putting $r = d/2$, where d is the fibril spacing, to calculate

$$\sigma_{\text{tip}} = \frac{K_{\text{tip}}}{(\pi d)^{1/2}}. \tag{13.20}$$

Putting together Equations (13.19) and (13.20) shows the stress concentration

$$\sigma_{\text{tip}} = \sigma_d \left(\frac{2\alpha h}{\pi d} \right)^{1/2}. \tag{13.21}$$

The next key idea, proposed by Brown and by Kramer, follows from the recognition that the craze is not continuous material, and that the stress is concentrated into the fibrils, which have a smaller cross-sectional area than the model continuum. This has the effect of concentrating the stress by the draw ratio λ in the fibril, to give a stress σ_f given by

$$\sigma_f = \frac{\lambda K_{\text{tip}}}{(\pi d)^{1/2}}.$$

Values for the extension ratios, estimated by Kramer and colleagues [36,42] and also by Ward and co-workers [18,22] from analysis of optical interference patterns, compare reasonably well with estimates of the network extensibility from small-angle neutron scattering data [36] or stress-optical measurements [43]. It was therefore proposed that the criterion for craze failure, and hence crack propagation via a craze, is to assume that the entangled strands crossing the section of the craze at the crack tip break due to the development of the critical stress at the crack tip σ_{fail}.

Quantitatively, $\sigma_{\text{fail}} = \Sigma_{\text{eff}} f_b$, where f_b, is the force required to break a single polymer molecule and Σ_{eff} is the effective crossing density of chains at the craze tip. If no chains are broken by forming the forest of fibrils when the craze is produced, the cross density of strands is given by

$$\Sigma_{\text{eff}} = \upsilon d_e/2,$$

where υ is the number of chains per unit volume and d_e is the root-mean-square end-to-end distance of a random coil strand. This can be seen to follow from the number of entanglements in a rectangular box of cross section υ and thickness d_e:

$$\upsilon = k_B T / G_N^0 = \rho N / M_e,$$

where G_N^0 is the rubbery plateau shear modulus, M_e is the entanglement molecular weight, N is Avogadro's number and ρ is the density (see Section 4.3.4).

If a fraction q of strands survives fibrillation, it can be shown that

$$\Sigma_{\text{eff}} = (q\upsilon d_e/2)[1 - (M_e/q M_n)].$$

To calculate the fracture energy, the Dugdale model analysis is followed. Adapting Equation (13.17) using the relation $G_c = K_{IC}^2/E^*$ gives

$$G_c = \sigma_d \delta = 2h(1 - v_f)\sigma_d, \tag{13.22}$$

where $v_e = 1/\lambda$ is the volume fraction of the craze. Putting $\sigma_{tip} = \sigma_{fail} = \Sigma_{eff} f_b$ using Equation (13.21) yields an expression for h

$$h = \frac{\pi d}{2\alpha} \left(\frac{\Sigma_{eff} f_b}{\sigma d} \right)^2,$$

which when substituted into Equation (13.22) gives

$$G_c = \frac{\pi d(1 - v_f) f_b^2 \Sigma_{eff}^2}{\alpha \sigma_d}. \tag{13.23}$$

As stated above, this calculation crosses between the macroscopic and the microscopic. It is therefore of interest to examine the numerical estimates that follow to obtain some assessment of the validity of the assumptions.

One example is the stress concentration equation (Equation (13.21)). Experimental results for PMMA suggest typical values of $h = 2$ μm and $d = 20$ nm. If α lies in the range 0.01–0.05, σ_{tip} will be in the range $0.96\sigma_d$–$2.1\sigma_d$, which gives some credence to the theory in that it is remarkably consistent with values of the craze stress obtained from Dugdale zone measurements, and will account for failure in the mid-rib of the craze.

Secondly, we can follow Brown [40] in estimating a value for f_b from the fracture toughness G_c on the basis of Equation (13.23) above. Brown takes $\Sigma_{eff} = 2.8 \times 10^{17}$ m^{-2} and a modulus ratio of 0.025 for the elastic tensile moduli of the craze normal and parallel to the fibril direction to obtain a value of 1.4×10^{-9} N for f_b. This value is within the range of 3×10^{-9} N estimated by Kausch [44] for the chain-breaking force and between 2.5 and 12×10^{-9} N estimated by Odell and Keller [45] from elongational flow experiments.

13.5.2 Craze Initiation and Growth

The studies of craze formation and structure described above indicate that there are clear differences between crazing and yield. Yield is essentially a shear process where the deformation occurs at constant volume (ignoring structural changes such as crystallisation), but crazing occurs at a crack tip or in a solid section with a very appreciable increase in volume. It therefore appears that tensile stresses and in particular, the hydrostatic tensile stress will be important in craze initiation and growth.

It would be desirable to obtain a stress criterion for craze initiation analogous to that for yield behaviour described in Chapter 12. Although all proposals made so far have not achieved general acceptance, it is of value to review the most important findings. Sternstein, Ongchin and Silverman [46] examined the formation of crazes in the vicinity of a small circular hole (1.59 mm diameter) punched in the centre of PMMA strips (13.7 mm × 50.8 mm × 0.79 mm) when the latter are pulled in tension. A typical pattern is shown in Figure 13.14(a). When the solutions for the elastic stress field in the vicinity of the hole were compared with the craze pattern, it was found that the crazes grew parallel to the minor principal stress vector. Because the contours of the minor principal stress vector are

(a)

(b)
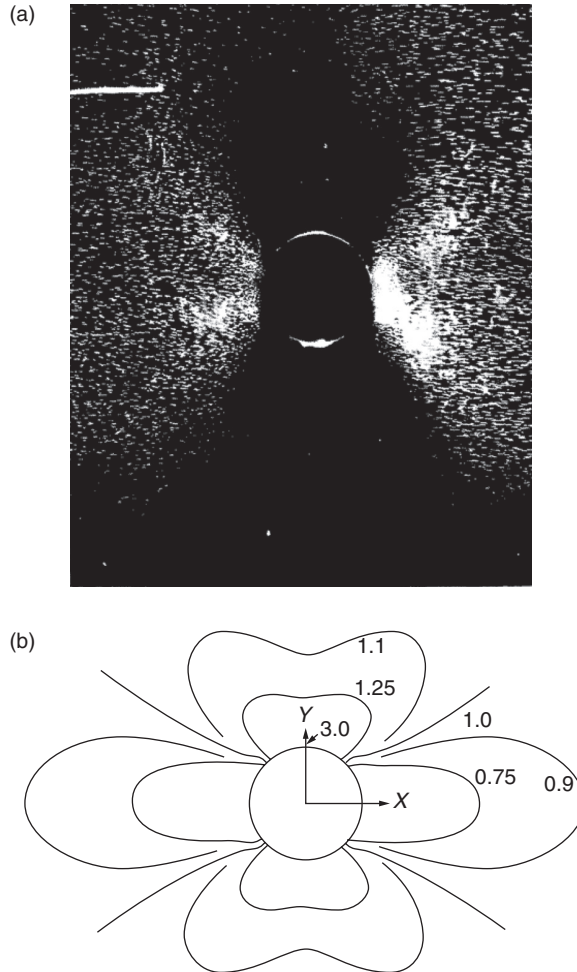
Figure 13.14   *(a) Craze formation in the vicinity of a hole in a strip of PMMA loaded in tension. (Result obtained by L.S.A. Smith.) (b) Major principal stress contours (σ_1) for an elastic solid containing a hole. The specimen is loaded in tension in the x direction. Contour numbers are per unit of applied tensile stress. (Reproduced from Sternstein, S.S., Ongchin, L. and Silverman, A. (1968) Yield criteria for plastic deformation of glassy high polymers in general stress fields. Appl. Polym. Symp., 7, 175. Copyright (1968) John Wiley & Sons, Inc.)*

orthogonal to those of the major principal stress vector, this result shows that the major principal stress acts along the craze plane normal and therefore parallels to the molecular orientation axis of the crazed material.

The boundary of the crazed region coincided to a good approximation with contour plots showing lines of constant major principal stress σ_1, as shown in Figure 13.14(b) where the contour numbers are per unit of applied stress. At low applied stresses, it is not possible to discriminate between the contours of constant σ_1 and contours showing constant values of

the first stress invariant $I_1 = \sigma_1 + \sigma_2$. However, the consensus of the results is in accord with a craze-stress criterion based on the former rather than on the latter and, as we have seen, the direction of the crazes is consistent with the former.

Sternstein and Ongchin [47] extended this investigation by examining the formation of crazes under biaxial stress conditions, and found that the stress conditions for crazing involved both the principal stresses σ_1 and σ_2. The most physically acceptable explanation of these results was proposed by Bowden and Oxborough [48], who suggested that crazing occurs when the extensional strain in any direction reaches a critical value e_1, which depends on the hydrostatic component of stress.

For small strains, for the two-dimensional stress field e_1 is given by

$$e_1 = \frac{1}{E}(\sigma_1 - v\sigma_2),$$

where E is Young's modulus and v is Poisson's ratio.

It was proposed that the crazing criterion was

$$Ee_1 = \sigma_1 - v\sigma_2 = A + B/I_1, \tag{13.24}$$

where $I_1 = \sigma_1 + \sigma_2$. Equation (13.24) predicts that the stress required to initiate a craze becomes infinite when $I_1 = 0$, that is crazing requires a dilational stress field. Unfortunately there are several pieces of experimental evidence [49–51] that contradict this assumption, so there is still no completely satisfactory stress criterion for craze initiation.

There is, however, a theory for the growth of crazes that is consistent with all the experimental evidence. Argon, Hannoosh and Salama [52] have proposed that the craze front advances by a meniscus instability mechanism in which craze tufts are produced by the repeated break-up of the concave air/polymer interface at the crack tip, as illustrated in Figure 13.15. A theoretical treatment of this model predicted that the steady-state craze velocity would relate to the five-sixths power of the maximum principal tensile stress, and support for this result was obtained from experimental results on polystyrene and PMMA [52].

13.5.3 Crazing in the Presence of Fluids and Gases: Environmental Crazing

The crazing of polymers by environmental agents is of considerable practical importance and has been studied extensively with notable contributions from Kambour [16,53–55], Andrews and Bevan [56], Williams and co-workers [57, 58] and Brown [59–61]. The subject has been reviewed by Kambour [62] and by Brown [63]. In general environmental agents, which can be fluids or solids, reduce the stress or strain required to initiate crazing.

Kambour and co-workers [16,53–55] showed that the critical strain for crazing decreased as the solubility of the environmental agent was increased. It was also found that the critical strain decreased as the glass transition temperature of the solvated polymer decreased. Andrews and Bevan [56], adopting a more formal approach and applying the ideas of fracture mechanics, performed fracture tests on single-edge-notched tensile specimens, where a central edge crack of length c is introduced into a large sheet of polymer that is then loaded in tension. The fracture stress is related to the surface work parameter $\mathscr{I}$ of Andrews (or the strain energy release rate $G_c = 2\gamma$) by an equation identical in
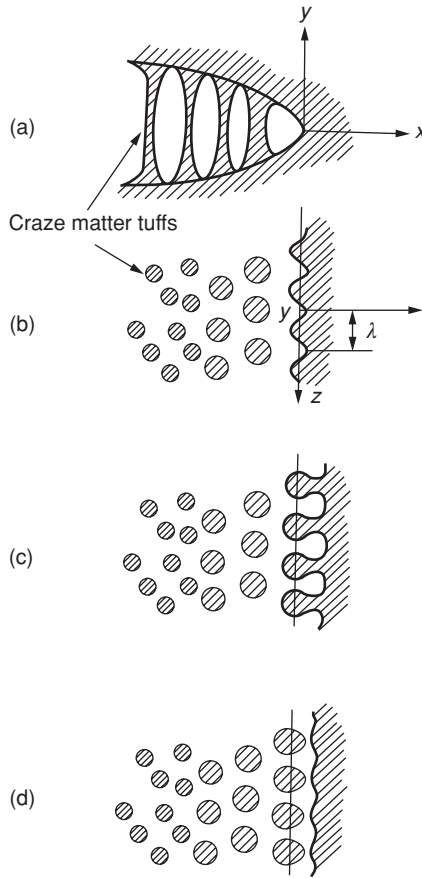
Figure 13.15 *Schematic diagram showing craze matter production by the mechanism of meniscus instability: (a) outline of a craze tip; (b) cross section in the craze plane across craze matter tufts; (c, d) advance of the craze front by a completed period of interface convolution. (Reproduced from Argon, A.S., Hannoosh, J.C. and Salama, M.M. (1977) in Fracture 1977, Vol. 1, Waterloo, Canada, p. 445. Copyright (1977) John Wiley & Sons, Ltd.)*

form to Equation (13.2) above. The critical stress for crack and craze propagation σ_c was indeed proportional to $c^{-1/2}$, so the $\mathscr{I}$ values could be determined. For constant experimental conditions, a range of values of $\mathscr{I}$ was obtained from which a minimum value $\mathscr{I}_0$ was estimated. From tests in a given solvent over a range of temperatures, it was found that values of $\mathscr{I}_0$ decreased with increasing temperatures up to a characteristic temperature, above which $\mathscr{I}_0$ remained constant at value $\mathscr{I}_0^*$. The values of $\mathscr{I}_0^*$ for the different solvents were shown to be a smooth function of the difference between the solubility parameters of the solvent and the polymer, reaching a minimum when this difference was zero (Figure 13.16).

These findings were explained on the basis that the work done in producing the craze can be modelled by the expansion of a spherical cavity of radius r under a negative hydrostatic
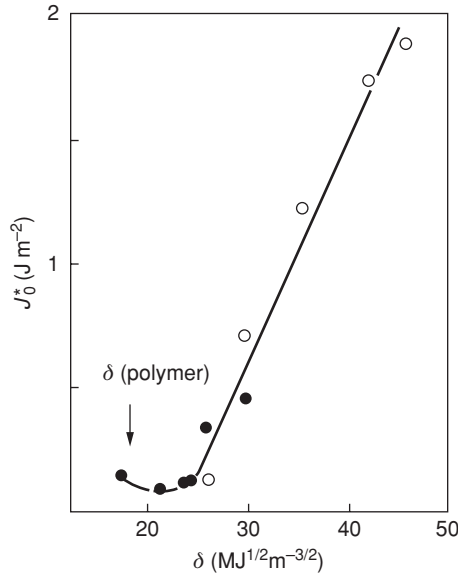
Figure 13.16 *Variation of J_0^* for PMMA with the solubility parameter of the solvent: (●) pure solvents; (○) water isopropanol mixtures. (Reproduced from Andrews, E.H. and Bevan, L. (1972) Mechanics and mechanism of environmental crazing in a polymeric glass. Polymer,* **13***, 337. Copyright (1972) IPC Business Press Ltd.)*

pressure p, which has two terms so that

$$p = \frac{2\gamma_\tau}{r} + \frac{2\sigma_Y}{3}\psi, \tag{13.25}$$

where γ_τ is the surface tension between the solvent in the void and the surrounding polymer, σ_Y is the yield stress and ψ is a factor close to unity. The effect of temperature is to change the yield stress, so that with increasing temperature σ_Y falls eventually to zero at T_c, which is the glass transition temperature of the plasticised polymer. Above T_c, the fracture surface energy $\mathscr{J}_0^*$ relates solely to the intermolecular forces represented by the surface tension γ_τ.

Brown has pointed out that gases at sufficiently low temperatures make almost all linear polymers craze [59–61,63]. Parameters such as the density of the crazes and the craze velocity increase with the pressure of the gas and decrease with increasing temperature. It was concluded that the surface concentration of the absorbed gas was a key factor in determining its effectiveness as a crazing agent.

In a related but somewhat different development, Williams and co-workers [57,58] studied the rate of craze growth in PMMA in methanol. In all cases, the craze growth depended on the initial stress intensity factor K_0, calculated from the load and the initial notch length. Below a specific value of K_0 termed K_0^*, the craze would decelerate and finally arrest. For $K_0 > K_0^*$, the craze would decelerate initially and finally propagate at constant speed.

It was argued that the controlling factor determining craze growth was the diffusion of methanol into the craze. Where $K_0 < K_0^*$, the methanol is considered to diffuse along the
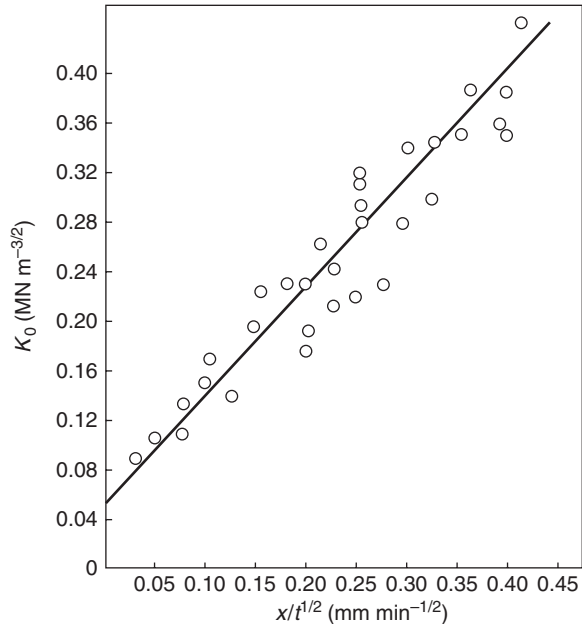
Figure 13.17   *Craze growth behaviour for poly(methyl methacrylate) in methanol at 20°C. (Reproduced from Williams, J.G. and Marshall, G.P. (1975) Environmental crack and craze growth phenomena in polymers. Proc. Roy. Soc. A,* ***342****, 55. Copyright (1975) Royal Society of Chemistry.)*

length of the craze, and it may be shown that the length of the craze x is proportional to the square root of the time of growth (Figure 13.17). In the second type of growth, where $K_0 > K_0^*$, it is considered that the methanol diffuses through the surface of the specimens, maintaining the pressure gradient in the craze and producing craze growth at constant velocity.

13.6   Controlled Fracture in Tough Polymers

The development of brittle fracture, as outlined in Sections 13.2.1–13.2.3, is directly applicable to the failure of many glassy polymers, including PMMA and polystyrene, which have been studied intensively by LEFM. A key criterion for quantitative analysis is that extensive yielding should not occur, either at the crack tip or in the body of the specimen, for which explicit rules have been proposed. In essence, the load–extension curves should be of the form shown in Figure 13.4, i.e. elastic deformation up to the point of initiation of crack growth. In practice, this means that fracture occurs under conditions of plane strain for specimens of minimum thickness, whereas for thin specimens plane stress conditions apply and the stress–strain curve will show a yield point as shown in Figure 13.1, curves (a) and (c).

   The fracture of most semi-crystalline polymers, notably polyethylene, polypropylene and nylon, cannot be described by LEFM based on the theory of Griffith and Irwin because large-scale yielding occurs at the crack tip prior to failure. For these materials and for

toughened polymers and polymer blends other approaches have been developed, three of which will be discussed in detail:

1. The *J*-integral.
2. Essential work of fracture.
3. Crack opening displacement (COD).

13.6.1 The *J*-Integral

The *J*-integral approach was initiated by Rice [64] and developed by Begley and Landes [65]. It is most instructive to follow the exposition adopted by Landes and Begley [66] and later by Chan and Williams [67].

Rice defined a quantity termed the *J*-integral, which describes the flow of energy into the crack tip region. It is defined for the two-dimensional problem of a straight crack in the *x* direction (Figure 13.18), and Γ is any contour surrounding the crack tip. Formally

$$J = \int W \, \mathrm{d}y - T_i \frac{\mathrm{d}u_i}{\mathrm{d}x} \mathrm{d}s,$$

where $W = \int \sigma_{ij} \mathrm{d}\varepsilon_{ij}$ is the strain energy density relating to the stress and strain components σ_{ij} and ε_{ij} in the crack tip region and $T_i \, \mathrm{d}u_i$ are the work terms when components of the surface tractions T_i on the contour path move through displacements $\mathrm{d}u_i$. Rice showed that *J* is independent of the path chosen for integration of the total energy. In the case of linear elasticity, *J* equates the strain energy release rate *G*.

When the displacements are prescribed the *J*-integral is more simply defined as the rate of decrease of potential energy *U* with crack length. As shown in Figure 13.19, the *J*-integral is then given by the shaded area and

$$J = -\frac{1}{B}\frac{\mathrm{d}U}{\mathrm{d}a}, \tag{13.26}$$
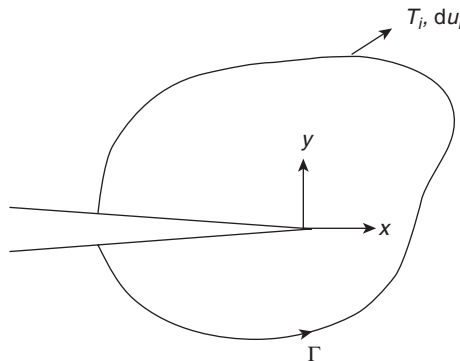
Figure 13.18 *Line integral contour.*
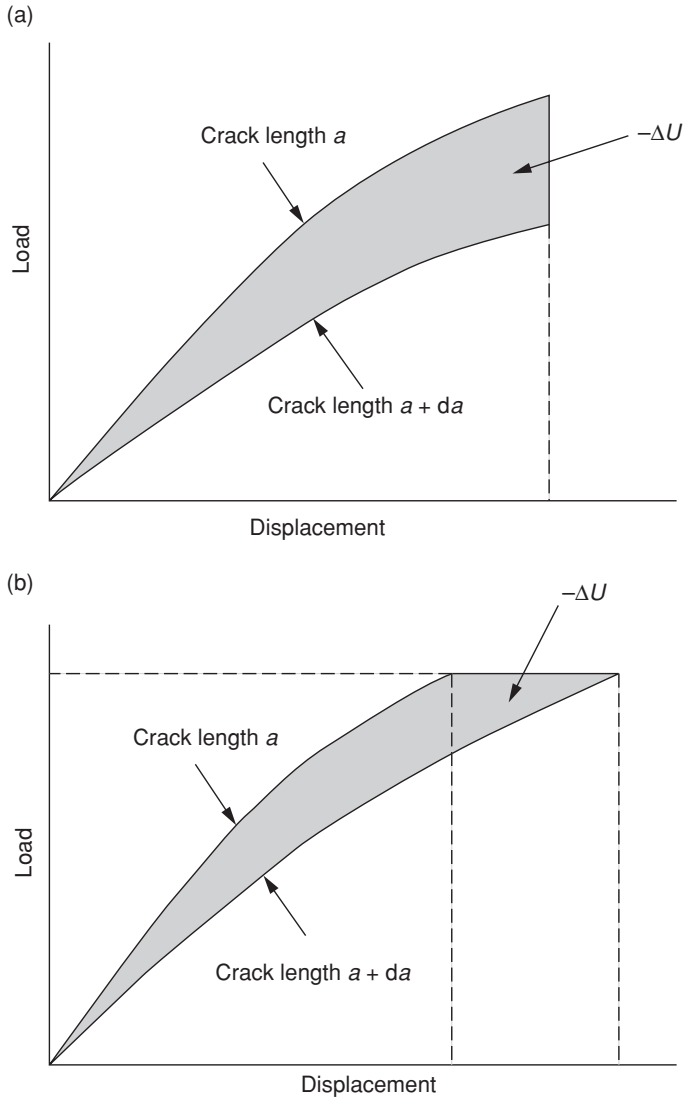
Figure 13.19 *Load–displacement curves for crack growth: (a) constant displacement; (b) constant load.*

where B is the specimen thickness and a is the crack length. It can be seen that the difference between constant load and constant displacement is second order and can be neglected.

Sumpter and Turner [68] have expressed J as the sum of elastic and plastic components J_e and J_p, respectively

$$J = J_e + J_p,$$

where

$$J_e = \frac{\eta_e U_e}{B(W-a)} \quad \text{and} \quad J_p = \frac{\eta_p U_p}{B(W-a)},$$

and η_e and η_p are elastic and plastic work factors dependent on the specimen geometry.

For single-edge-notch blend specimens, when

$$0.4 < \frac{a}{w} < 0.6 \quad \text{and} \quad \eta_e = \eta_p = 2,$$

then

$$J = \frac{2U}{B(W-a)}. \tag{13.27}$$

The accepted procedure is to introduce a sharp crack into a single-edge-notch sample. This is usually done by machining a notch, which is then sharpened by insertion of a razor blade, either by tapping (for brittle polymers) or by slicing (for ductile polymers). After each loading, the specimens (either in tension or bending) are broken up so that the amount of crack extension Δa can be measured. This can be done by cooling the specimen to low temperatures and then breaking it to observe the difference in the fracture surface that occurs at the point of initial crack extension.

The value of J is calculated from Equation (13.27) and plotted against Δa as shown in Figure 13.20(b). Initially the crack extends by blunting the initial sharp crack. If it is assumed that the blunted crack has a semi-circular profile (this is not precisely the case for polymers) so that $\Delta a = \delta/2$, where δ is the COD, the crack blunting line is given by

$$J = \sigma_y \delta = 2\sigma_y \Delta a, \tag{13.28}$$

where σ_y is the yield stress or craze stress.

The J resistance curve shows a point of inflection where true crack growth starts, and this defines an equivalent quantity to the G_{IC} of LEFM for plane strain brittle fracture, which is termed J_{IC}. The sample size requirements for a valid J_{IC} are given by

$$a, W - a \quad \text{and} \quad B \geq 25 \left(\frac{J_{IC}}{\sigma_y} \right).$$

In very tough polymers, an idealised plot like that of Figure 13.20 is not obtained and a more arbitrary procedure has been proposed [69]. The J resistance curve is represented by a power law

$$J = C_1 \Delta a^{C_2}, \tag{13.29}$$

where C_1 and C_2 are fitting parameters, and a crack initiation value $J_{0.2}$ is defined that is determined from the J value for a crack extension of 0.2 mm.

(a)

(b)
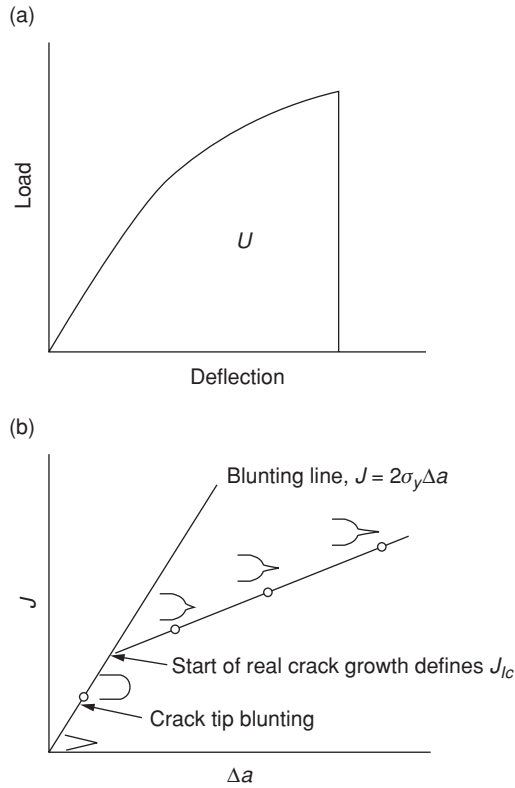
Figure 13.20   *Procedure for J$_{IC}$ measurement: (a) load identical specimens to a range of deflections; (b) plot of J against Δa, showing crack tip blunting and crack growth. (Reproduced from Chan, M.K.V. and Williams, J.G. (1983) J-integral studies of crack initiation of a tough high-density polyethylene. Int. J. Fracture, **23**, 145. Copyright (1983) Springer Science and Business Media.)*

13.6.2   Essential Work of Fracture

Another approach to the fracture of ductile polymers stems from the recognition that for such materials the crack tip deformation zone has two components, as shown in Figure 13.21. There is an inner zone where the fracture process occurs – which could involve a combination of shear yielding and crazing – and an outer zone where extensive yielding and plastic deformation occur. This approach was originally proposed by Broberg [70], and has been developed by Mai and Cottrell [71], Hashemi and Williams [72], Mai [73] and others.

The measurements are carried out on deeply notched specimens, either single-edge-notched tension (SENT) or double-edge-notched tension (DENT) (see Figure 13.22). The total work of fracture W_f consists of two components. First, there is the work expended in the inner zone W_e, which is called the essential work of fracture. This relates directly to the energy required to fracture the sample and is therefore proportional to the ligament
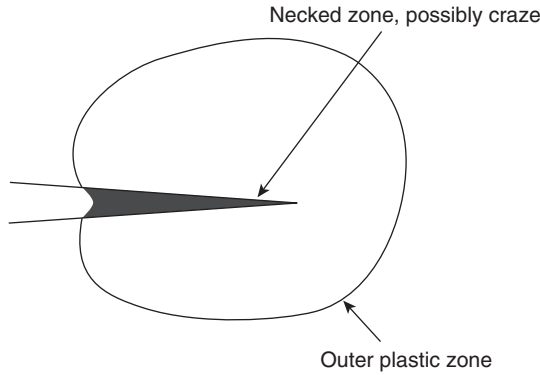
Figure 13.21   *Schematic diagram of process zone in ductile fracture specimen. (Reproduced with permission from Wu, J. and Mai, Y.-W. (1996) The essential fracture work concept for toughness measurement of ductile polymers. Polym. Eng. Sci., **36**, 2275. Copyright (1996) John Wiley & Sons, Ltd.)*

length *l*. Secondly, there is what is termed the non-essential work of fracture W_p, the energy dissipated in the outer plastic zone, where shear yielding and other forms of plastic deformation can occur. This component is proportional to the second power of the ligament length.

We have

$$W_e + W_p, \tag{13.30}$$
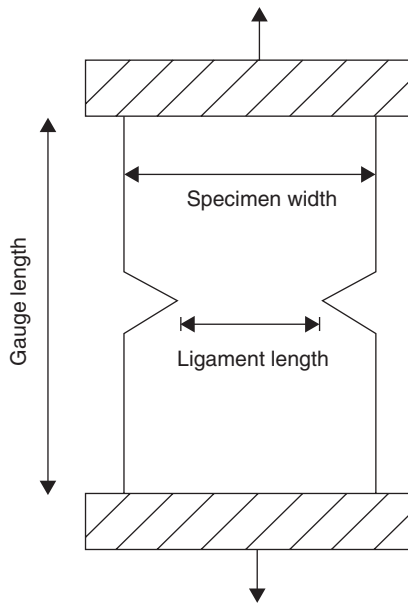
Figure 13.22   *Schematic diagram of test specimen for essential work of fracture test.*
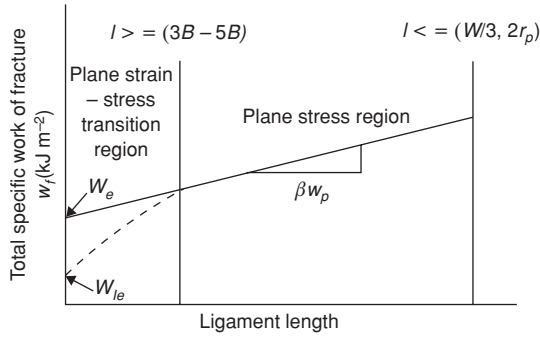
Figure 13.23 *Schematic diagram showing specific total work of fracture against ligament length.*

which can be written as

$$W_f = w_e Bl + \beta w_p Bl^2, \tag{13.31}$$

where w_e is the specific essential work of fracture, w_p is the specific non-essential work of fracture, B is the specimen thickness and β is a shape factor for the plastic zone. More conveniently, the specific total work of fracture W_f is given by

$$W_f = \frac{W_f}{lB} = w_e + \beta w_p l. \tag{13.32}$$

It is necessary to consider whether the fracture occurs under conditions of plane stress or of plane strain. Figure 13.23 shows schematically how the total specific work of fracture varies with ligament length. At high ligament length, conditions of plane stress pertain and Equation (13.32) applies to give an extrapolated value of W_e, the essential work of fracture for plane stress fracture; βw_p is the work dissipation in the outer plastic zone. At low ligament length, there is a transition from plane stress to plane strain and extrapolation to zero ligament length gives W_{le}, the plane strain essential work of fracture.

Wu and Mai [73] have examined the relationship between the essential work of fracture method and the J-integral method. Figure 13.24 shows w_f as function of ligament length for a DENT specimen of thickness 0.285 mm. At large ligament lengths, failure occurs under conditions of plane stress; at low ligament lengths, failure occurs under plane strain. The corresponding values for w_e are 46.93 and 16.70 kJ/m². Wu and Mai concluded that the plane stress w_e obtained by linear extrapolation is equivalent to the plane strain J_{IC}, as proposed earlier by Mai and Cotterell [71].

The validity of results obtained using this method depends on the specimen dimensions being within specified ranges. Most importantly, the specimen dimensions control whether plane strain or plane stress conditions apply. Williams and Rink [74], gathering experimental data from a number of laboratories, have produced guidelines for the standardisation of the test and the interpretation of results.

The very simple analysis that is enabled by the use of Equation (13.32) requires the assumption that the shape factor β is a constant. This is equivalent to the shape of the plastic zone ahead of the crack tip remaining the same for all the crack lengths studied. Naz *et al*.
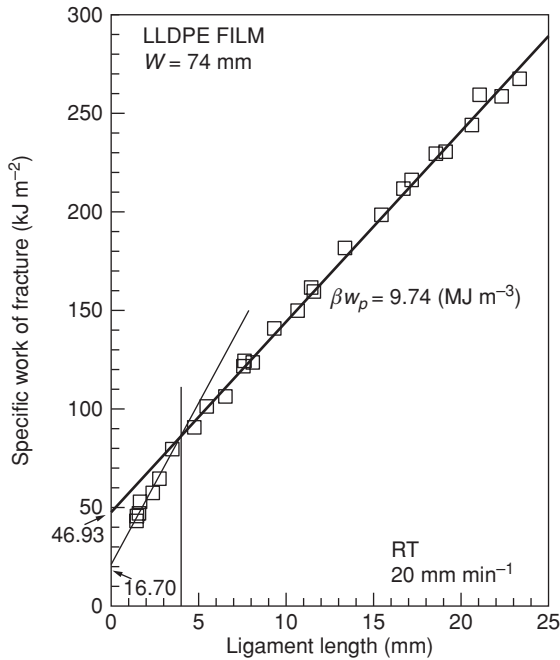
Figure 13.24 *Specific work of fracture versus ligament length for linear low-density polyethylene films. (Reproduced from Wu, J. and Mai, Y.-W. (1996) The essential fracture work concept for toughness measurement of ductile polymers. Polym. Eng. Sci., 36, 2275. Copyright (1996) John Wiley & Sons, Ltd.)*

[75], working with ultra high molecular weight polyethylene, used finite element modelling to predict the plastic zone shape in double-edge-notched specimens, and concluded that the shape was highly dependent on the notch depth. However, a re-analysis of their fracture results using the model plastic zone shapes did not result in significant changes in the result for w_e. This suggests that the method is robust.

13.6.3 Crack Opening Displacement

For LEFM, there is an explicit relationship between K_{IC} and the COD, which is exemplified by the Dugdale plastic zone model (Equation (13.17)). For tough polymers, it cannot be assumed that this is still the case. Nevertheless, the measurement of COD can still be a valuable tool and it has been used extensively for assessing the toughness of polyethylene gas pipes, especially by Brown and co-workers [76,77]. The COD is measured under plane strain conditions or nearly plane strain conditions (which cannot always be assumed for very tough samples), where a damage zone forms at the root of the notch, a craze similar to that observed in a glassy polymer (see Section 13.4). These tests are conducted under conditions of slow crack growth, and usually under constant stress, at elevated temperatures to accelerate the crack growth. Figure 13.25 shows a typical experimental set-up.

For tough polyethylenes, the craze angle remains approximately constant as the damage zone grows so the growth of the craze in the crack direction is linearly related to the COD.
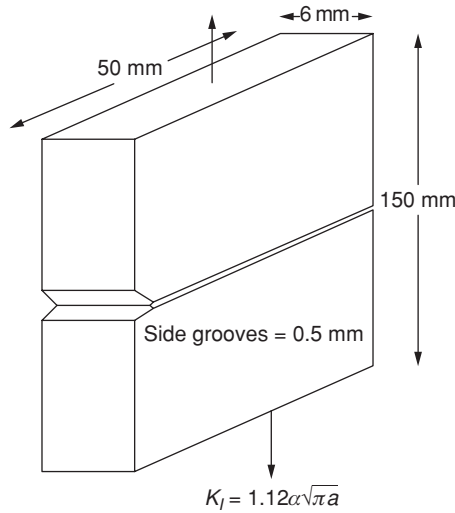
Figure 13.25 *Single-edge-notched fracture specimen. (Reproduced from O'Connell, P.A., Bonner, M.J., Duckett, R.A. et al. (1995) The relationship between slow crack-propagation and tensile creep – behavior in polyethylene. Polymer, 36, 2355. Copyright (1995) Elsevier Ltd.)*

Figure 13.26 shows the COD versus time for a polyethylene copolymer. There is an initial linear portion followed by an accelerating rate. Experimental observations show that the point at which the COD rate starts to accelerate T_p, is associated with the first signs of fracture at the base of the craze, with failure occurring in the mid-rib of the fibrils of the craze, and this gives the failure time for slow crack growth. The situation as envisaged is shown schematically in Figure 13.27.
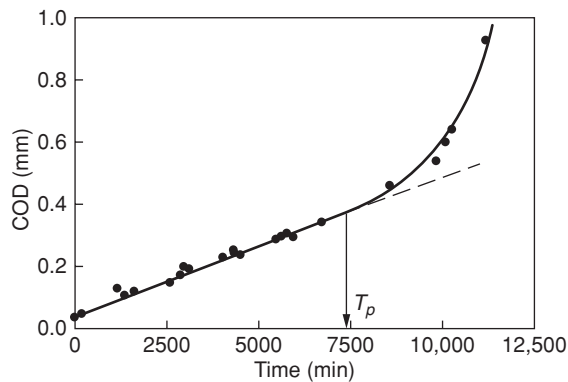
Figure 13.26 *Crack opening displacement (COD) for polyethylene copolymer at a bulk stress of 3 MPa. (Reproduced from O'Connell, P.A., Bonner, M.J., Duckett, R.A. et al. (1995) The relationship between slow crack-propagation and tensile creep – behavior in polyethylene. Polymer, 36, 2355. Copyright (1995) Elsevier Ltd.)*
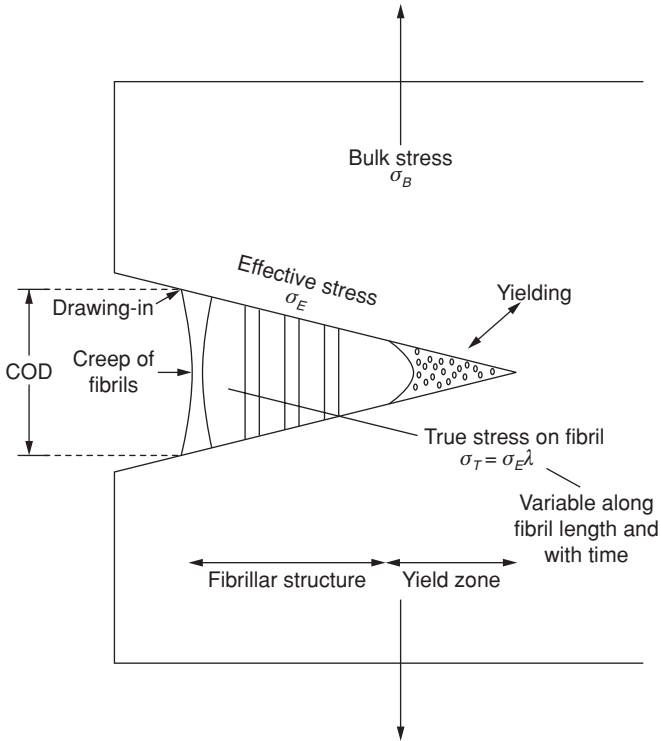
Figure 13.27 *Schematic diagram showing model for craze growth and processes involved. (Reproduced from O'Connell, P.A., Bonner, M.J., Duckett, R.A. et al. (1995) The relationship between slow crack-propagation and tensile creep – behavior in polyethylene. Polymer, **36**, 2355. Copyright (1995) Elsevier Ltd.)*

Ward and co-workers [78] showed that slow crack growth data obtained from measurements of COD can be related to creep of the fibrils in the craze. The COD rate and hence the fracture time are dominated by creep to failure of the fibrils. This result gives support to the previous observations by Capaccio and co-workers [79] who showed that there was a good correlation between the creep rate of oriented polyethylene samples and bottle stress crack resistance. Because slow crack growth is a very slow process, it is customary to use an accelerated test where notched compression moulded samples are immersed in a non-ionic surfactant environment at an elevated temperature (typically 75°C). Capaccio and co-workers devised a novel test, by determining the creep behaviour of a dumbbell cut from compression-moulded sheet, which was drawn to its natural draw ratio. Following the ideas discussed in Section 11.3.2, Sherby–Dorn plots were produced for creep rate versus total strain (or draw ratio). Typically, the log creep rate versus draw ratio plots were linear (Figure 13.28) and the gradient of the plots was called the creep rate deceleration factor (CRDF). Good correlations were obtained between CRDF values and notched pipe test failure times T_p [80] (Figure 13.29). The larger the value of CRDF, that is the greater the reduction in creep rate with strain, the more resistance a polymer has to stress crack
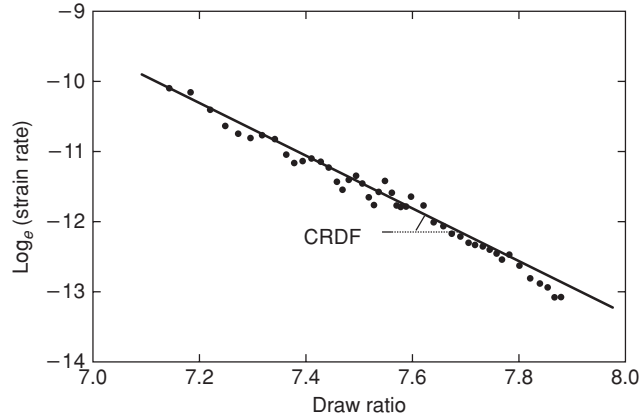
Figure 13.28   *Plot to give creep rate deceleration factor (CRDF). (Reproduced from Cawood, M.J., Channell, A.D. and Capaccio, G. (1993) Crack initiation and fiber creep in polyethylene. Polymer, **34**, 423. Copyright (1993) Elsevier Ltd.)*

resistance, and to slow crack growth. The creep rates were reduced in polyethylene by copolymerisation (introducing side groups into the polyethylene chains) and increasing molecular weight, as previously shown by Wilding and Ward [81]. Short chain branches were most effective when placed in the high molecular weight chains. These results are consistent with the conclusions of Brown and co-workers [82] on the basis of their very extensive COD measurements of slow crack growth in a range of polyethylenes.

The use of CRDF measurements was shown by Ward and co-workers [78] to be understood in terms of the relationship of creep behaviour to plastic strain following the concept of the true stress–true strain – strain rate surface (see Section 12.6). Ward and co-workers
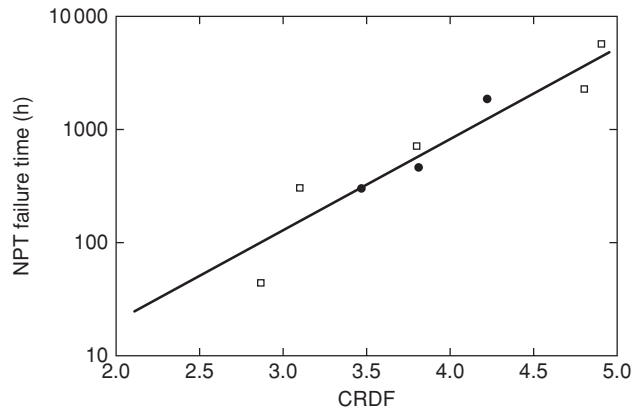
Figure 13.29   *Correlation between creep rate deceleration factor (CRDF) and notched pipe test (NPT) failure times. (Reproduced from Clutton, E.Q., Rose, L.J. and Capaccio, G. (1998) Slow crack growth and impact mechanisms in polyethylene. Plast. Rubber Comp. Proc. Appl., **27**, 478. Copyright (1998) Maney Publishing.)*
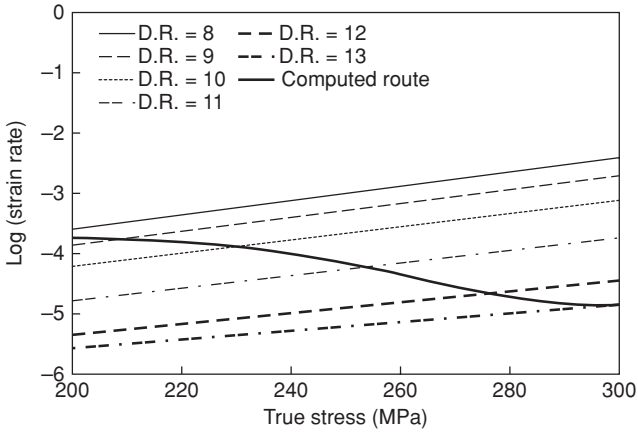
Figure 13.30 *Log₁₀ (strain rate) versus true stress at constant draw ratio for polyethylene copolymer at indicated draw ratios (D.R.). (Reproduced from O'Connell, P.A., Bonner, M.J., Duckett, R.A. et al. (1995) The relationship between slow crack-propagation and tensile creep – behavior in polyethylene. Polymer, **36**, 2355. Copyright (1995) Elsevier Ltd.)*

used extensive creep data to construct master plots of log strain rate versus true stress at constant plastic strain (draw ratio). One such plot for a polyethylene copolymer is shown in Figure 13.30. It was shown by computation that slow crack propagation data for this material were consistent with the proposition that this related to creep to failure of oriented fibrils in the craze. These fibrils followed the computed route to failure shown in Figure 13.30.

In several publications, Brown and co-workers [82] developed the idea that the reduction in growth rate in polyethylene due to incorporation of branches relates to a difference in the tie molecules in the initial structure. The extensive studies of Capaccio and co-workers [80] confirmed by the computer model of Ward *et al*. suggest that the critical factor is the creep failure of the fibrils in the craze and is not related directly to the initial morphology [83].

An alternative approach was adopted by Kurelec *et al*. [84] who determined true stress–true strain curves at 80°C for a range of polyethylenes. It was shown that the slope of the tensile curve above the natural draw ratio (called the strain-hardening modulus) correlated well with the measured stress crack resistance (Figure 13.31). These results are entirely consistent with those obtained by Capaccio and co-workers and Ward and co-workers described above. Kurelec *et al*. found similar effects on the environmental stress cracking resistance (ESCR) performance with regard to short chain branches, and elaborated these in terms of the exact nature of the branches, particularly with regard to bimodal molecular weight distribution polymers.

More recently, Cazenave *et al*. [85] have reviewed these findings and added another ingredient, pointing out that ESCR can perhaps be correlated with the natural draw ratio (Figure 13.32). Although the molecular factors that determine natural draw ratio may be similar to those determining CRDF or the strain-hardening modulus, it seems safer to assume that slow crack growth relates to the true stress–true strain – strain rate surface, whilst seeking satisfactory short cuts to define the situation.
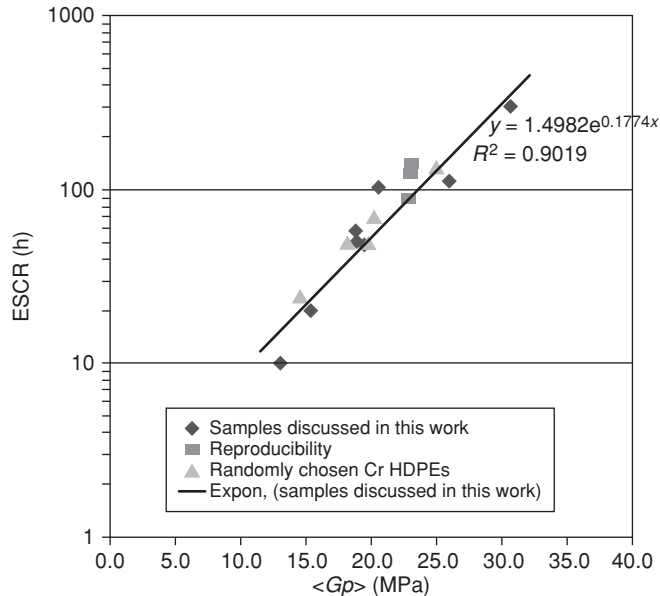
Figure 13.31   *Environmental stress cracking resistance (ESCR) plotted against strain-hardening modulus <Gp> for a range of HDPEs, both catalyst based with broad molecular weight distribution, and bimodal. Points labelled 'reproducibility' are repeated tests on the same sample. (Reproduced from Kurelec, L., Teeuwen, M., Schoffeleers, H. et al. (2005) Strain hardening modulus as a measure of environmental stress crack resistance of high density polyethylene. Polymer, **46**, 6369. Copyright (2005) Elsevier Ltd.)*
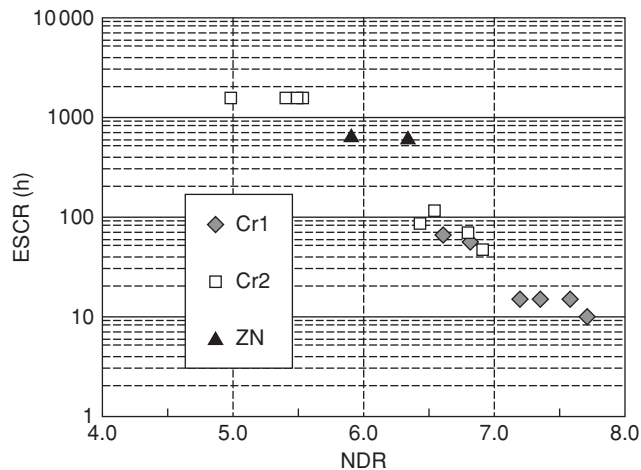
Figure 13.32   *Environmental stress cracking resistance (ESCR) against natural draw ratio (NDR). Cr1 and Cr2 are high density polyethylenes with different catalysation regimes, and ZN is an ethylene–hexene copolymer. (Reproduced from Cazenave, J., Seguela, R., Sixou, B. et al. (2006) Short-term mechanical and structural approaches for the evaluation of polyethylene stress crack resistance. Polymer, **47**, 3904. Copyright (2006) Elsevier Ltd.)*

13.7 The Molecular Approach

It has long been recognised that oriented polymers (i.e. fibres) are much less strong than would be predicted on the basis of elementary assumptions that fracture involves simultaneously breaking the bonds in the molecular chains across the section perpendicular to the applied stress. Calculations of this nature were originally undertaken by Mark [86] and rather more recently by Vincent [87] on polyethylene. It was found that in both cases the measured tensile strength was at least an order of magnitude less than that calculated.

We have seen one possible explanation of this discrepancy – the Griffith flaw theory of fracture. It has been considered also that there may be a general analogy between this difference between measured and calculated strengths and the difference between measured and calculated stiffnesses for oriented polymers. A general argument for both discrepancies could be that only a small fraction of the molecular chains are supporting the applied load. In Chapter 9, we discussed how the tie molecules or crystalline bridges that connect adjacent crystalline blocks play a key role in determining the axial stiffness of an oriented semi-crystalline polymer. There has therefore been considerable interest in examining chain fracture in oriented polymers, using electron paramagnetic resonance to observe the free radicals produced or infrared spectroscopy to identify such entities as aldehyde-end groups, which suggest chain scission. A very comprehensive survey of the results of such studies has been given by Kausch [88]. Kausch and Becht [89] have emphasised that the total number of broken chains is much too small for their load-carrying capacity to account for the measured reductions in macroscopic stress. We must therefore conclude that the tie molecules that eventually break are not the main source of strength of highly oriented polymers, a conclusion confirmed by the lack of any positive correlations between the strength of fibres and the radical concentration at break.

Although these strong reservations have to be borne in mind, studies using molecular methods are relevant to the deformation of polymers. Examination of the infrared and Raman spectra of oriented polymers under stress show that there are distinct shifts in frequency from the unstressed state [90,91] indicative of a distortion of bonds in the chain due to stress. Furthermore, changes in the shape of the spectrum lines are observed, which is interpreted as implying that certain bonds are much more highly stressed than the average.

Recent Raman spectroscopy studies, notably by Young and co-workers [92,93] have shown that the shifts in the Raman frequency per unit strain for a range of oriented fibres are proportional to the fibre tensile moduli. This is consistent with a series aggregate model for the fibre structure (see Section 8.6). For this model, strain and stress σ are related by

$$\varepsilon = \sigma / E_3.$$

The Raman shift $\Delta \upsilon$ with stress is a constant so that

$$\frac{\mathrm{d}\Delta\upsilon}{\mathrm{d}\sigma} = \alpha$$

and the Raman shift with strain is given by

$$\frac{\mathrm{d}\Delta\upsilon}{\mathrm{d}\varepsilon} = \frac{\mathrm{d}\Delta\upsilon}{\mathrm{d}\sigma} \cdot \frac{\mathrm{d}\sigma}{\mathrm{d}\varepsilon} = \alpha E_3.$$

A positive attempt to obtain a molecular understanding of fracture took as its starting point the time and temperature dependence of the fracture process. This approach dates back to the early work of Bueche [94] and Zhurkov and co-workers [95]. It is assumed that the fracture process relates to the rate of bond breakage υ_B at high stress, via an Eyring-type thermally activated process, so that

$$\upsilon_B = \upsilon_{B0} \exp[-(U_0 - \upsilon\sigma_B)/kT],$$

where U_0 is the activation energy and υ is an activation volume. The time to failure τ under an applied stress σ_B is then given by

$$\tau = \tau_0 \exp[(U_0 - \upsilon\sigma_B)/kT].$$

This equation was shown to hold for a wide range of polymers, and moreover, the values obtained for U_0 correlated very well with values obtained for the activation energy for thermal degradation.

The existence of submicrocracks in polymers has already been mentioned in connection with the Argon theory of craze initiation. Zhurkov, Kuksenko and Slutsker [96] have used small-angle X-ray scattering to establish the presence of such submicroscopic cracks. Although it has been proposed by Zakrevskii [97] that the formation of these submicrocracks is associated with a cluster of free radicals and the associated ends of molecular chains, Peterlin [98] has argued that the cracks occur at the ends of microfibrils, and Kausch [88] has concluded that the submicrocrack formation is essentially independent of chain scission.

13.8   Factors Influencing Brittle–Ductile Behaviour: Brittle–Ductile Transitions

13.8.1   The Ludwig–Davidenkov–Orowan Hypothesis

Many aspects of the brittle–ductile transition in metals, including the effect of notching, which we will discuss separately, have been discussed in terms of the Ludwig–Davidenkov–Orowan hypothesis that brittle fracture occurs when the yield stress exceeds a critical value [99], as illustrated in Figure 13.33(a). It is assumed that brittle fracture and plastic flow are independent processes, giving separate characteristic curves for the brittle fracture stress σ_B and the yield stress σ_Y as a function of temperature at constant strain rate (as shown in Figure 13.33(b)). Changing strain rate will produce a shift in these curves. It is then argued that whichever process, either fracture or yield can occur at the lower stress will be the operative one. Thus, the intersection of the σ_B/σ_Y curves defines the brittle–ductile transition and the material is ductile at all temperatures above this point.

The influence of chemical and physical structure on the brittle–ductile transition can be analysed by considering how these factors affect the brittle stress curve and the yield stress curve, respectively. As will be appreciated, this approach bypasses the relevance of fracture mechanics to brittle failure. If, however, we consider fracture initiation (as distinct from propagation of a crack) as governed by a fracture stress σ_B, the concept of regarding yield and fracture as competitive processes provides a useful starting point.

Vincent and others [100–102] have shown that the brittle stress is not much affected by strain and temperature (e.g. by a factor of 2 in the temperature range $-180°$C to $+20°$C).
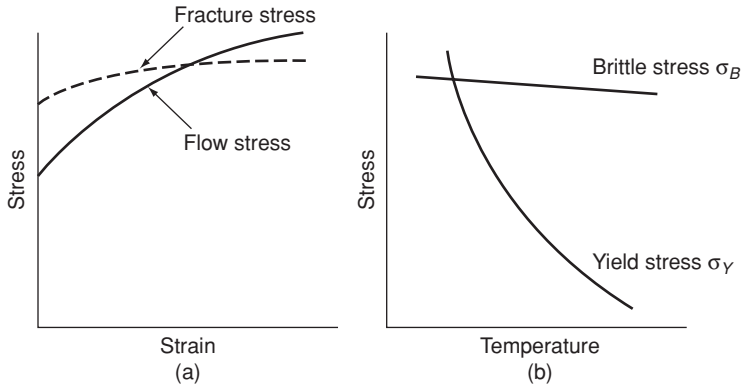
Figure 13.33 *Diagrams illustrating the Ludwig–Davidenkov–Orowan theories of brittle–ductile transitions.*

The yield stress, on the other hand is greatly affected by strain rate and temperature, increasing with increasing strain rate and decreasing with increasing temperature. (A typical figure would be a factor of 10 over the temperature range $-180°C$ to $+20°C$.) These ideas are clearly illustrated by results for PMMA shown in Figure 13.34(a). The brittle–ductile transition will therefore be expected to move to higher temperatures with increasing strain rate (Figure 13.34(b)). The effect can be illustrated by varying the strain rate in a tensile test on a sample of nylon at room temperature: at low strain rates the sample is ductile and cold-draws, whereas at high strain rates it fractures in a brittle manner.

A further complication in varying strain rate occurs at low speeds, where within a certain temperature range cold-drawing occurs. It is possible that at high speeds the heat is not conducted away rapidly enough, so that strain hardening is prevented and the specimen fails in a ductile manner. Such an isothermal–adiabatic transition does not affect the yield stress and therefore does not affect the brittle–ductile transition; but it does cause a considerable reduction in the energy to break and may be operative in impact tests, even if brittle fracture does not intervene. It has been proposed therefore that there are two critical velocities at which the fracture energy drops sharply as the strain rate is increased: the isothermal–adiabatic transition and at higher strain rates, the brittle–ductile transition. Changes in ambient temperature have very little effect on the position of the isothermal–adiabatic transition but have a large effect on the brittle–ductile transition.

It was thought at first that the brittle–ductile transition was related to mechanical relaxation and in particular to the glass transition, which is true for natural rubber, polyisobutylene and polystyrene but is not the case for most thermoplastics. It was then proposed [103] that where there is more than one mechanical relaxation the brittle–ductile transition may be associated with a lower temperature relaxation. Although again it appeared that there might be cases where this is correct, it was soon shown that this hypothesis has no general validity. Because the brittle–ductile transition occurs at fairly high strains, whereas the dynamic mechanical behaviour is measured in the linear, low-strain region, it is unreasonable to expect that the two can be linked directly. It is certain that fracture, for example, depends on several other factors such as the presence of flaws, which will not affect the low-strain
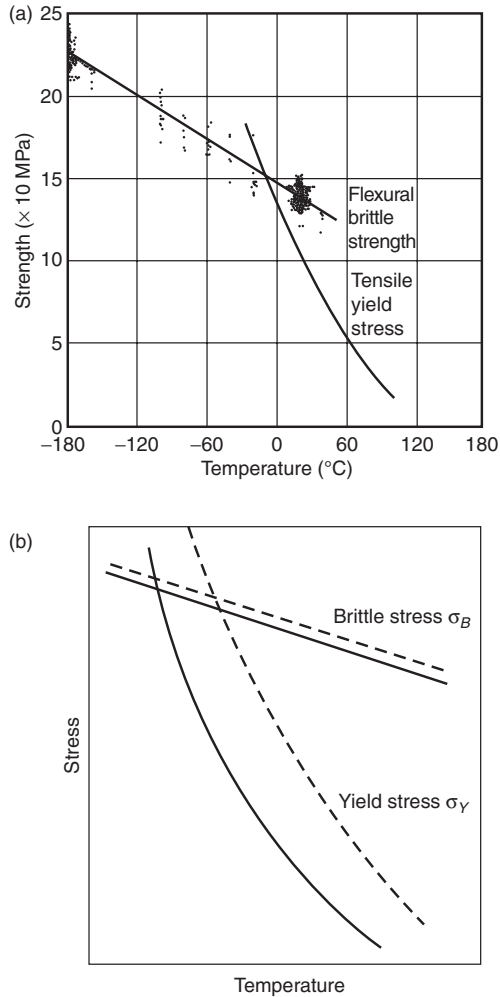
Figure 13.34 *(a) Effect of temperature on brittle strength and tensile yield stress of PMMA. (Reproduced from Vincent P.I. (1961) The effect of temperature. Plastics, **26**, 141. Copyright (1961) John Wiley & Sons, Ltd.) (b) Diagram illustrating the effect of strain rate on the brittle–ductile transition: (—) low strain rate; (- - -) high strain rate.*

dynamic mechanical behaviour. The subject has been discussed extensively by Boyer [104] and by Heijboer [105].

13.8.2   Notch Sensitivity and Vincent's σ_B–σ_Y Diagram

As for metals, the presence of a sharp notch can change the fracture of a polymer from ductile to brittle. For this reason, a standard impact test for a polymer is the Charpy or Izod test, where a notched bar of polymer is struck by a pendulum and the energy dissipated in fracture is calculated.

(a)

(b)
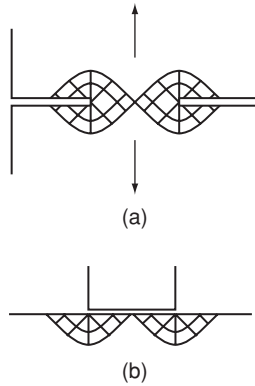
Figure 13.35 *The slip-line field for a deep symmetrical notch (a) is identical to that for the frictionless punch indenting a plate under conditions of plane strain (b). (Reproduced from Cottrell, A.H. (1964) The Mechanical Properties of Matter, John Wiley & Sons, New York, p. 327. Copyright (1964) John Wiley & Sons, Ltd.)*

A very simple explanation of the effect of notching has been given by Orowan [99]. For a deep, symmetrical tensile notch, the distribution of stress is identical to that for a flat frictionless punch indenting a plate under conditions of plane strain [106] (Figure 13.35). The compressive stress on the punch required to produce plastic deformation can be shown to be $(2 + \pi)K$, where K is the shear yield stress. For the Tresca yield criterion, the value is $2.57\sigma_Y$ and for the von Mises yield criterion the value is $2.82\sigma_Y$, where σ_Y is the tensile yield stress. Hence, for an ideally deep and sharp notch in an infinite solid, the plastic constraint raises the yield stress to a value of approximately $3\sigma_Y$ which leads to the following classification for brittle–ductile behaviour first proposed by Orowan [99]:

1. If $\sigma_B < \sigma_Y$, the material is brittle.
2. If $\sigma_Y < \sigma_B < 3\sigma_Y$, the material is ductile in an unnotched tensile test but brittle when a sharp notch is introduced.
3. If $\sigma_B < 3\sigma_Y$, the material is fully ductile, that is ductile in all tests, including those in notched specimens.

13.8.2.1   Vincent's σ_B–σ_Y Diagram

We may ask how relevant the above ideas are to the known behaviour of polymers. Vincent [107] has constructed a σ_B–σ_Y diagram that is very instructive in this regard (Figure 13.36).

Where possible, the value of σ_Y was taken as the yield stress in a tensile test at a strain rate of about 50% per minute; for polymers that were brittle in tension, σ_Y was the yield stress in uniaxial compression and σ_B was the fracture strength measured in flexure at a strain rate of 18 min^{-1} at $-180°C$.

The yield stresses were measured at $+20°C$ and $-20°C$, the idea being that the $-20°C$ values would give a rough indication of the behaviour in impact at $+20°C$, that is lowering the temperature by $40°C$ is assumed to be equivalent to increasing the strain rate by a factor of about 10^5.
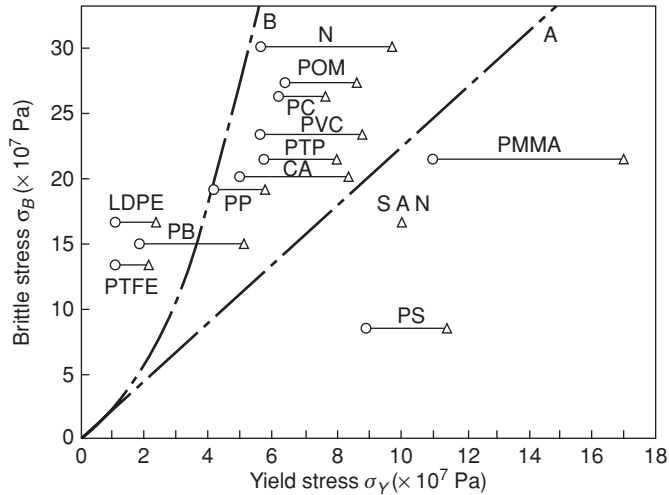
Figure 13.36 *Plot of brittle stress at about −180°C against a line joining yield-stress values at −20°C (○), respectively, for various polymers. Line A divides polymers that are brittle unnotched from those that are ductile unnotched but brittle notched, and line B divides polymers that are brittle notched but ductile unnotched from those that are ductile even when notched. PMMA, poly(methyl methacrylate); PVC, poly(vinyl chloride); PS, polystyrene; PET, poly(ethylene terephthalate); SAN, copolymer of styrene and acrylonitrile; CA, cellulose acetate; PP, polypropylene; N, nylon 6:6; LDPE, low-density polyethylene; POM, polyoxymethylene; PB, polybutene-1; PC, polycarbonate; PTFE, polytetrafluoroethylene. (Reproduced from Vincent P.E. (1961) The effect of temperature. Plastics, **26**, 141. Copyright (1961) John Wiley & Sons, Ltd.)*

In the diagram, the circles represent σ_B and σ_Y at $+20°C$; the triangles represent σ_B and σ_Y at $-20°C$. Both σ_Y and σ_B are affected by subsidiary factors such as molecular mass and the degree of crystallinity so that each point can be regarded only as of first-order significance.

From the known behaviour of the 13 polymers shown in this diagram, two characteristic lines can be drawn. Line A divides the brittle materials on the right, which are brittle when notched from those on the left, which are ductile even when notched. Both of these lines are approximations, but they do summarise the existing knowledge.

For line A, the ratio $\sigma_B/\sigma_Y \sim 2$ rather than unity, but the difference may be accounted for by the measurement of σ_B at very low temperatures and possibly by the measurement of σ_B in flexure rather than in tension. (The latter may reduce the possibility of fracture at serious flaws in the surface.) It is encouraging that even an approximate relationship holds along the lines of the Ludwig–Davidenkov–Orowan hypothesis. Even more encouraging is the fact that line B has a slope $\sigma_B/\sigma_Y \sim 6$, which is three times that of A, as expected on the basis of the plastic constraint theory.

The principal value of the σ_B–σ_Y diagram is that it may guide the development of modified polymers or new polymers. Together with the ideas of the previous section on the influence of material variables on the brittle strength and yield stress, it can lead to a systematic search for improvements in toughness.

13.8.3   A Theory of Brittle–Ductile Transitions Consistent with Fracture Mechanics: Fracture Transitions

The discussion of brittle–ductile transitions in the previous section assumes that brittle failure can be defined by a critical tensile stress. Although the results are very instructive, this assumption takes no account of the fact that there are what are termed size effects in the brittle behaviour of materials. In practice, this means that there is a characteristic length associated with each fracture test that will determine the severity of the test, where high severity means a greater propensity for brittle failure.

The arguments that lead to an understanding of size effects in brittle fracture stem from the basic ideas of energy scaling and similarity. These ideas were first appreciated by Roesler [108] and used by Benbow and Roesler [8] in their pioneering research described in Section 13.2. Their significance with regard to brittle–ductile transitions has been recognised by Puttick [109–111], who developed a theory of fracture transitions, which embraces the ideas of fracture mechanics.

To fix our ideas, consider a crack propagating in a brittle material under conditions of constant grip displacement, as in the plate with a centre crack $2c$ (Figure 12.3). According to the Griffith theory of fracture, the surface energy of the crack is supplied by the volume strain energy density stored in the material. The strain energy release rate G is therefore proportional to a length times, the strain energy density U per unit volume. For this case of a homogeneous stress field, the characteristic length is the crack length and we have

$$G = \beta c U,\tag{13.33}$$

where β is a non-dimensional constant and $U = \sigma^2/2E$.

As previously discussed the fracture stress σ_B is given by

$$\sigma_B = \left(\frac{G_c E}{\pi c}\right)^{1/2},\tag{13.34}$$

i.e. the fracture stress is determined by the material parameters G_c and E and a characteristic length, which is the length of the crack.

In most real situations, the stress field is inhomogeneous (i.e. finite with respect to the length of the crack) and the characteristic length is then to be identified with a characteristic length x_0 associated with the stress field, e.g. the size of a plastic zone or the length of a craze. We then have

$$G = \beta' \left(\frac{x_0}{c}\right) x_0 U,\tag{13.35}$$

where the concept of geometric similarity is invoked to enable us to conclude that the function β' depends only on (x_0/c).

In this case, the fracture stress σ_B is given by

$$\sigma_B = \left(\frac{G_c E}{x_0 \beta'(x_0/c)}\right),\tag{13.36}$$

i.e. the fracture stress is a function of the scale of the stress field, which enters directly through x_0. The non-dimensional function β' is evaluated by the methods of fracture mechanics.

Now consider the implications of these ideas for brittle–ductile transitions. This transition is marked by the change from brittle to ductile failure because the stress reaches the yield stress in a part of the specimen.

Equation (13.36) can equally well be written as defining the critical size of the stress field in terms of the characteristic length x_0. Thus, we have

$$x_0 = \frac{G_c E}{\sigma_B^2 \beta'(x_0/c)}. \tag{13.37}$$

Now consider decreasing the characteristic length (by changing the test and hence changing the stress field) so that σ_B rises until it eventually reaches the value of the yield stress σ_y. This causes a brittle–ductile transition, which can be defined by a critical length x_0^Y, where

$$x_0^Y = \frac{G_c E}{\sigma_Y^2 \beta'(x_0/c)}. \tag{13.38}$$

Fracture then occurs in an elastic–plastic rather than a purely elastic strain field. For example, in the double cantilever beam test (Figure 12.4) the maximum bending stress is $\sigma = (3G_c E/b)^{1/2}$, where b is the width of the beam. Hence, the critical width for the transition from yielding to brittle failure is

$$b_c = 3G_c E/\sigma_Y^2. \tag{13.39}$$

Puttick terms these transitions *lower* transitions, because they just mark the point where plastic flow commences.

A second type of transition, termed an *upper* transition, corresponds to the size of the plastic zone reaching a maximum dimension characteristic of the test. An example here is the critical size of the plastic zone at the tip of a crack in plane strain, which gives

$$x_{0c} = G_c E/\sigma_Y^2. \tag{13.40}$$

Another example is a notched bar test where, as we have seen, $\sigma_{max} \sim 2.5\sigma_Y$, and it can be shown that the critical zone size is

$$x_{0c} = G_c E/25\sigma_Y^2. \tag{13.41}$$

We therefore see that the most acceptable approach to brittle–ductile transitions or plane strain–plane stress transitions, i.e. all types of fracture transition, is to regard each test as relating to a characteristic length in a particular test. The transition is then characterised by a critical length x_{0c}, where $x_{0c} = \alpha G_c E/\sigma_Y^2$ and α is a numerical constant whose value is determined by the stress field in the test.

In terms of material behaviour, it is the quantity $G_c E/\sigma_Y^2$, which determines brittle–ductile behaviour. In Table 13.2, the situation is summarised for some typical tests and the implications of each test are indicated.

To summarise, the choice of the particular fracture test determines α, and defines a critical length, for example the width of the beam in the double cantilever beam test piece or the plastic zone size at general yield of a notched bar. The fracture transition then occurs

Table 13.2   *Fracture transitions.*

Test	α	Nature of transitions	
Notched bar (Charpy bend)	~0.04	Upper (below to above gross yield)	Griffith and Oates [112] Puttick [111]
Plane strain fracture	~0.5	Upper (plane strain to plane stress)	Irwin [113]
Double cantilever	3	Lower (elastic to elastic–plastic)	Gurney and Hunt [114]
Indentation by spherical metal ball	~25	Upper (radial fracture to no fracture)	Puttick [111]

at the temperature at which the quantity $\alpha G_c E / \sigma_Y^2$ is equal to the critical length in the chosen test. For a given test, σ_Y decreases with increasing temperature until this equality is satisfied and the transition from brittle to ductile behaviour occurs. We can now see the link between this rigorous treatment and the more simplistic approach of Vincent, described in Section 13.8.2, which is of considerable practical value. As pointed out by Puttick, it would be more accurate to replace the simplistic Figures 13.33 and 13.34 by curves which relate the critical characteristic length as the dependent variable plotted against temperature as shown in Figure 13.37. If we fix the specimen dimension at the value given by the horizontal dotted line, say 5 mm, then the transition temperatures are given by the temperatures T_1 and T_4.
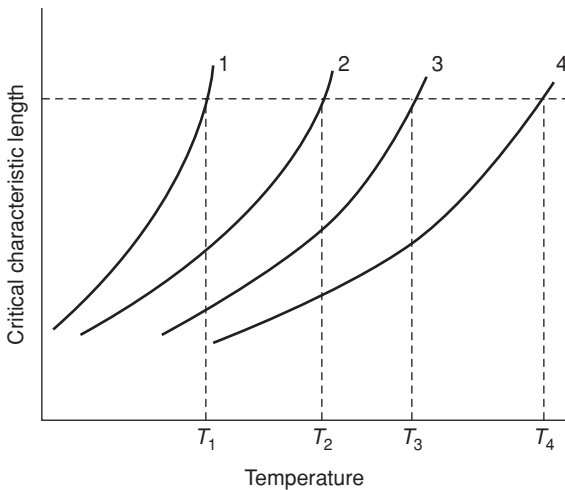
Figure 13.37   *Schematic comparison of the brittle–ductile temperature transition in four different tests: (1) Hertzian indentation (lower transition), (2) plastic–elastic indentation (upper transition), (3) Double cantilever beam (lower transition) and (4) notched bar (upper transition). (Reproduced from Puttick, K.E. (1980) The correlation of fracture transitions. J. Phys. D, 13, 2249. Copyright (1980) Institute of Physics.)*

13.9   The Impact Strength of Polymers

The ability of a structural part to maintain its integrity and to absorb a sudden impact is often a relevant issue when selecting a suitable material. Impact testing of polymers is thus a subject of some importance and is extensively employed although many of the results obtained are of an empirical and hence comparative nature.

The two major types of impact test are categorised as flexed beam and falling weight.

13.9.1   Flexed-Beam Impact

Examples of flexed-beam impact are the Izod and Charpy impact test, in which a small bar of polymer is struck with a heavy pendulum. In the Izod test, the bar is held vertically by gripping one end in a vice and the other free end is struck by the pendulum. In the Charpy test, the bar is supported near its ends in a horizontal plane and struck either by a single-pronged or two-pronged hammer so as to simulate a rapid three-point or four-point bend test, respectively (Figure 13.38(a)). It is customary to introduce a centre notch into the specimen so as to add to the severity of the test, as discussed in Section 13.5.1. The standard Charpy impact specimen has a 90° V-notch with a tip radius of 0.25 mm. For polymers, a very much sharper notch is often adopted by tapping a razor blade into a machined crack tip, which has important consequences for interpretation of the subsequent impact test.

The interpretation of impact tests is not straightforward and it is necessary to consider several alternatives, as follows:

1. It was proposed independently by Brown [115], and by Marshall, Williams and Turner [116], that Charpy impact tests on sharply notched specimens can be analysed quantitatively in terms of linear elastic fracture mechanics. It is assumed that the polymer deforms in a linear elastic fashion up to the point of failure, which occurs when the change in stored elastic energy due to crack growth satisfies the Irwin–Kies relationship (Equation (13.10) above). So that

$$G_c = \frac{K_c^2}{E^*} = \frac{P_0^2}{2B} \frac{dC}{dc},$$

   where E^* is the reduced modulus as defined in 13.2.1, P_0 is the load immediately prior to fracture, C and B are the specimen compliance and thickness, respectively, and c is the crack length as in Equation (13.12a) in Section 13.2.3. Because the elastically stored energy in the specimens immediately prior to failure is $U_0 = P_0^2 C / 2$,

$$G_c = \frac{U_0}{B} \frac{1}{C} \frac{dC}{dc}, \tag{13.42}$$

   where U_0 is determined in a commercial impact tester from the potential energy lost due to impact. The total measured impact energy U_I must be reduced by the kinetic energy of the sample U_k to give $U_0 = U_I - U_k$.

   It is conventional to follow Williams and co-workers [117] and express Equation (13.42) as

$$G_c = \frac{U_0}{BW} \frac{1}{C} \frac{dC}{d(c/W)}. \tag{13.43}$$
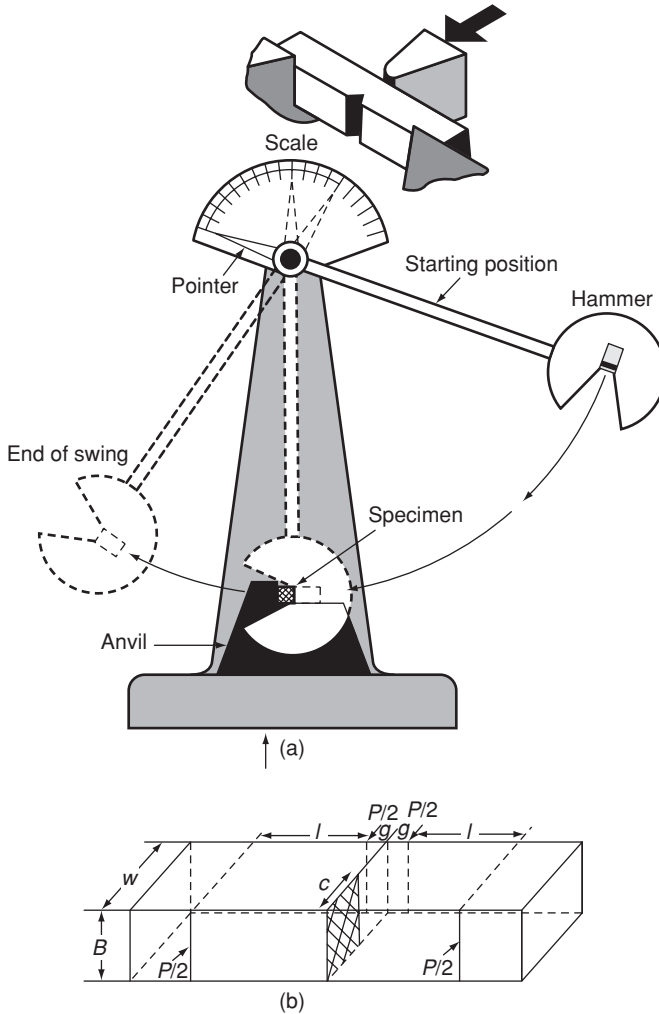
Figure 13.38   *(a) Schematic drawing of a Charpy impact tester. (b) The notched Charpy impact specimen. (Reproduced with permission from Fasce, L., Bernal, C., Frontini, P. et al. (2001) On the impact essential work of fracture of ductile polymers. Polym. Eng. Sci., **41**, 1. Copyright (2001) John Wiley & Sons, Ltd.)*

We then have

$$U_1 = BW\phi(c/W)G_c + U_k, \tag{13.44}$$

where $\phi(c/W) = \dfrac{c}{\mathrm{d}C/\mathrm{d}(c/W)}$ can be calculated (see [7], Chapter 4), and a plot of U_I versus $BW\phi$ produces a straight line with G_0 as slope and U_k as the intercept. This approach has been shown to give values for G_c that are independent of specimen geometry for impact tests on razor-notched samples of several glassy polymers, including PMMA, polycarbonate [118] and poly(ether sulfone) [119]. Similar results have been obtained also for razor-notched samples of polyethylene [120].

2. Vincent [121] and others have recognised that the impact strength depends on the geometry of the notch, which led Fraser and Ward [122] to propose that for comparatively blunt notches (i.e. those not introduced by a razor blade or a sharp cutting tool) failure occurs when the stress at the root of the notch reaches a critical value. This stress, which in a glassy polymer marks the stress required to initiate a craze, can be calculated by assuming that the deformation is elastic. On this hypothesis, the Charpy test, as undertaken in the impact tester, can be regarded as a four-point bend test with the bending moment $M = Pl/2$, where P is the applied load and l is a sample dimension (Figure 13.38)). Immediately prior to fracture, $M = M_0, P = P_0$ and the elastically stored energy is $U_0 = \frac{1}{2}(2M_0/l)^2 C$, where C is the sample compliance. Hence

$$M_0 = \frac{l}{2}\sqrt{\frac{2U_0}{C}},$$

where C is calculable from specimen geometry.

For pure bending, the nominal stress at the root of the notch σ_n is given by $\sigma_n = (M/I)y$, where I is the second moment of area ($= Bt^3/12$ for a rectangular beam) and y is the distance to the neutral axis.

Using the linear stress assumption, the maximum stress at the root of the notch is the product of the nominal stress and the stress concentration factor α_k. Calculations of α_k for general shapes of notch are available in the literature, but when the crack length c is much greater than the notch tip radius ρ, α_k reduces to the simple expression $\alpha_k = 2\sqrt{c/\rho}$.

It has been shown that the impact behaviour of blunt-notched specimens of PMMA is consistent with a critical stress at the root of the notch [122], and similar considerations apply to polycarbonate [118] and poly(ether sulfone) [119] in the absence of shear lips. In these instances, it appears therefore that the maximum local stress is the fracture criterion, independent of specimen geometry.

3. The most unsophisticated interpretation of the flexed bend impact test is that it is a measure of the energy required to propagate the crack across the specimen, irrespective of whether the specimen is notched or unnotched. Notch sensitivity is ignored and only the energy of propagation is involved. In this case

$$G_c = \frac{U_0}{A} = \frac{U_0}{BW(1 - c/W)}, \tag{13.45}$$

where the area of the uncracked cross section is $A = B(W - c)$.

Justification for this approach has been given by Plati and Williams [110], where

$$J_c = \sigma_y u. \tag{13.46}$$

If full yielding is assumed in bending impact

$$U_0 = \frac{u}{2}\sigma_y B(W - c) = \frac{J_c B(W - c)}{2}.$$

Because the ligament area $A = B(W - c)$, then

$$J_c = \frac{2U_0}{A}.$$

This differs only by a factor of 2 from Equation (13.45), which arises because the average displacement in bending is $u/2$, compared with u in tension. Plati and Williams showed results from high-impact polystyrene (HIPS) and acrylonitrile–butadiene–styrene (ABS) polymers that agreed with values of J_c from impact tests.

More recent work has extended the J-integral and essential work of fracture methods described in Section 13.6 to impact tests.

Bramuzzo [123] used high-speed photography to monitor the crack propagation in a three-point bend test in parallel with determining the force–time curve. In this way, resistance curves were obtained for polypropylene copolymers by plotting the J-integral as fraction of crack length. Martinatti and Riccio [124] used the multi-specimen technique to determine the J_R curves for rubber-toughened polypropylenes using an instrumented Charpy test where the hammer of the pendulum could be stopped at different displacements of the specimen. The crack advancement of each loading was measured after successive fractures at low temperatures using an optical microscope. Crouch and Huang [125] produced multi-specimen resistance curves for toughened nylon by impacting SENT three-point bend specimens to different levels of crack growth using a falling-weight impact tower. Force–time curves were determined to obtain the total energy up to maximum deflection.

In further recent work, Ramsteiner [126] determined $J_{0.2}$ values by constructing the J values as a function of crack length, impacting specimens of HDPE with different masses from the same height to give a constant impact velocity of 2 m/s. Finally, Fasce and co-workers [127] have attempted to apply the essential work of fracture methodology to impact testing of two PP copolymers and ABS using pre-cracked specimens of different notch deeply double-edge-notched tension (DENT) and single-edged-notched bend (SENB) depth. In both cases, the specific total work of fracture was plotted against ligament length (Figure 13.39).
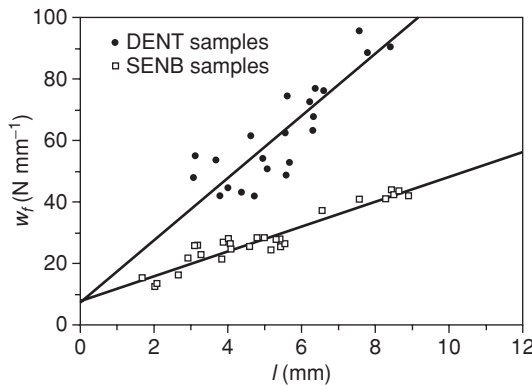
Figure 13.39 *Specific total work of fracture w_f versus ligament length l for deeply double-edge-notched tension (DENT) (●) and single-edge-notched bend (SENB) (□) 3 mm thick polypropylene random copolymer samples. (Reproduced from Fasce, L., Bernal, C., Frontini, P. et al. (2001) On the impact essential work of fracture of ductile polymers. Polym. Eng. Sci., 41, 1. Copyright (2001) John Wiley & Sons, Ltd.)*

13.9.2   Falling-Weight Impact

In the falling-weight impact test, a circular disc of material (typically 6 cm diameter and 2 mm thickness, freely supported on an annulus of 4 cm diameter) is impacted by a metal dart with a hemispherical tip (typically of radius 1 cm). The tests are carried out either under conditions where the impact energy is far in excess of that required to break the specimen or at low levels of impact energy so that damage tolerance and the possible initiation of a crack can be observed.

Moore and his colleagues have described the application of such tests to polymers and to polymer composites [128–130]. It is emphasised that for any reasonable attempt at interpretation the following must be carried out:

1. Measurement of the force–time curve so that the input energy to maximum force can be determined as well as the total impact energy.
2. Photography of the tension surface during the impact event.

For fibre composites, Moore and colleagues showed that the peak on the force–time curve corresponds well with the energy required to initiate a crack. It was shown also that for both composites and polymers the total fracture energy corresponded quite well with that determined from notched Charpy tests.

Only for the Charpy test, and to a rather lesser extent the Izod test, has a satisfactory theoretical analysis been achieved. Even for these tests, however, there is still a gap between the engineering analysis and any accepted interpretation in physical terms. For example, although it seems likely that the brittle failure of razor-notched impact specimens is associated with the craze at the crack tip, there is no convincing numerical link between craze parameters and the fracture toughness K_{IC}, as exists for the cleavage fracture of compact tension specimens (see Section 13.2). Again, although the mechanics point to a critical stress criterion for some blunt-notched specimens and there is an empirical correlation with the craze stress determined in other ways, the magnitude of the critical stress is very great and suggests that a more sophisticated explanation may be required. For the brittle epoxy resins, which do not show a craze at the crack tip, Kinloch and Williams [131] have suggested that the fracture of both razor-notched and blunt-notched specimens can be described by a critical stress at a critical distance ($\sim$10 μm) below the root of the notch.

As the temperature and strain rate in a polymer change, the nature of the stress–strain curve can alter remarkably. It is therefore natural to seek correlations between the area beneath the stress–strain curve and the impact strength, and between dynamic mechanical behaviour and the impact strength. Attempts to make such correlations directly have met with mixed success [132], which is not surprising in view of the complex quantitative interpretations of impact strength suggested above.

Vincent [133] has examined the statistical significance of a possible inverse correlation between impact strength and dynamic modulus and concluded that, at best, this correlation only accounts for about two-thirds of the variance in impact strength. Factors such as the influence of molecular mass, and details of molecular structure such as the presence of bulky side groups, are not accounted for. He also reported impact tests over a wide temperature range on some polymers, notably polytetrafluoroethylene and polysulfone, where peaks in brittle impact strength were observed at temperatures close to dynamic loss peaks, suggesting that in some instances it may be necessary to consider the relevance of a more

generalised form of fracture mechanics [134], where the viscoelastic losses occurring during loading and unloading must be taken into account.

13.9.3 Toughened Polymers: High-Impact Polyblends

The comparatively low impact strength of many well-known polymers, such as PMMA, polystyrene and PVC, led to the production of rubber-modified thermoplastics with high impact strength. The best-known examples are high-impact polystyrene (HIPS) and ABS copolymer, where the rubbery phase is dispersed throughout the polymer in the form of small aggregates or balls. Other polymers that have been toughened in this way include PMMA, PVC, polypropylene, polycarbonate, nylons and thermosets such as epoxies, polyesters and polyimides.

In an excellent review, Bucknall [135] explains that rubber toughening involves three principal deformation mechanisms: shear yielding, crazing and rubber particle cavitation. The rubber particles, with a much lower stiffness than the matrix polymer, give rise to stress concentrations for the initiation of shear yielding and crazing.

Nielson [136] lists three conditions that are required for an effective polyblend:

1. The glass temperature of the rubber must be well below the test temperature.
2. The rubber must form a second phase and not be soluble in the rigid polymer.
3. The two polymers should be similar enough in solubility behaviour for good adhesion between the phases.

In rubber-toughened ABS, shear yielding is dominant. Optical microscopy examination by Newman and Strella [137] showed that plastic deformation had occurred in the matrix around the rubber particles. Later studies, notably by Kramer and co-workers, suggested that the rubber particles initiate microshear bands. Donald and Kramer [138] showed that cavitation in the rubber particles initiates shear yielding of the matrix and that shear deformation occurs when the particles are small, and crazing when the particles are large.

In rubber-toughened HIPS, Bucknall and Smith [139] showed that the improved toughness was related to crazing and stress whitening. The crazes are initiated at points of maximum triaxial stress concentration produced by incorporation of the rubber particles. The rubber particles also act as craze terminators so that a large number of small crazes are produced to give high-energy absorption and extensive stress whitening. Work by Yang and Bucknall [140] suggests that cavitation in the rubber particles precedes crazing.

Bucknall [141] and Bucknall and Smith compared the force–time curves for impact specimens over a range of temperatures, with both the notched Izod impact strength and the falling-weight impact strength and the nature of the fracture surface. The force–time curves, such as in Figure 13.40(a), show regions similar to those observed for a homopolymer as discussed in the introduction above. Both impact strength tests also showed three regions (Figures 13.40(b) and (c)). The fracture surfaces at the lowest temperature were quite clear, whereas at high temperatures stress whitening or craze formation occurred. Three temperature regions were considered:

1. *Low temperature*. The rubber is unable to relax at any stage of fracture. There is no craze formation and brittle fracture occurs.
2. *Intermediate temperature*. The rubber is able to relax during the relatively slow build-up of stress at the base of the notch, but not during the fast crack propagation stage. Stress

Fracture direction

1

2

3

(a)

Time (ms)

(b)

Izod impact strength (arbitrary units)

Temperature (°C)

I   II   III

(c)

Drop weight impact strength (arbitrary units)

Temperature (°C)
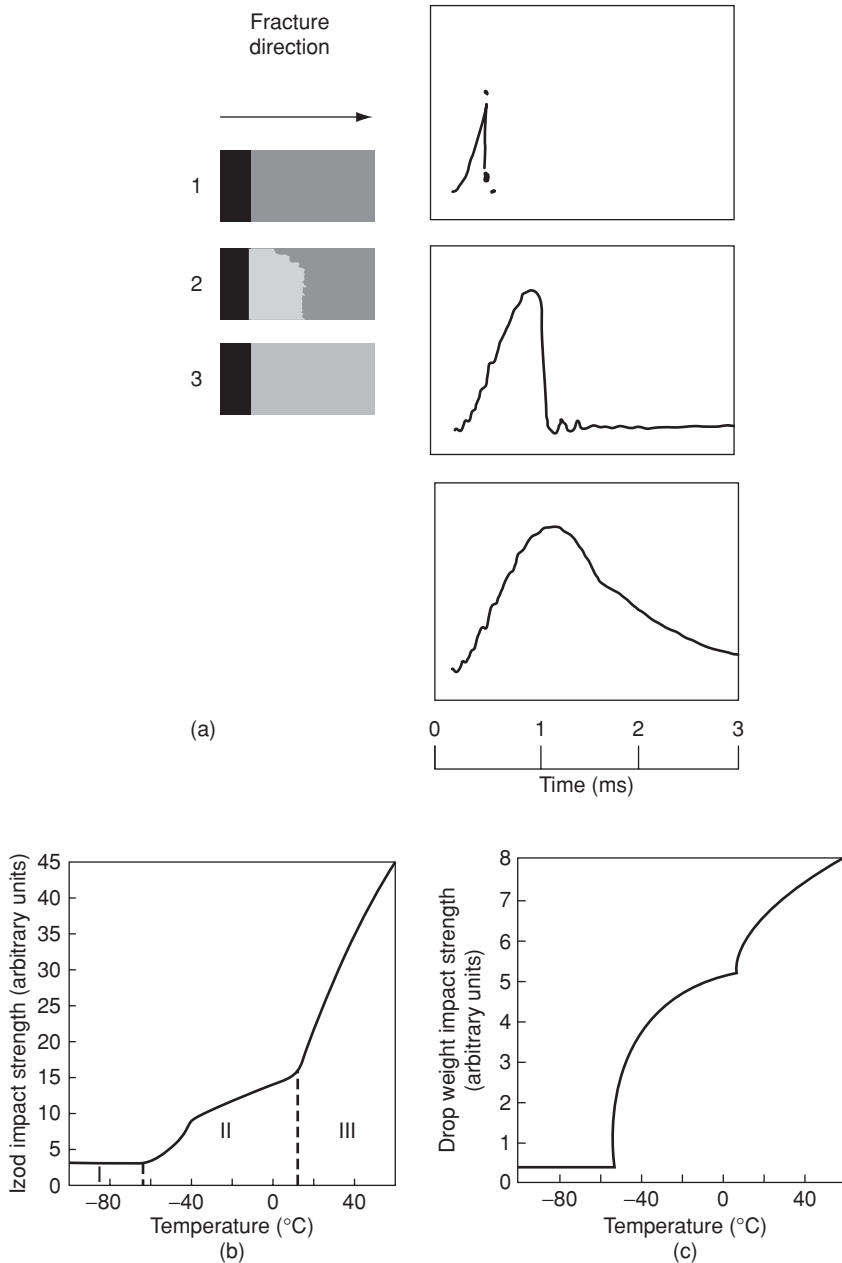
Figure 13.40 *(a) Fracture surfaces of modified polystyrene-notched Izod impact specimens: top, broken at −70°C, type I fracture; centre, broken at 40°C, type II fracture; bottom, broken at 150°C, type III fracture. (b) Notched Izod impact strength of modified polystyrene as a function of temperature, showing the limits of the three types of fracture behaviour. (c) Falling-weight impact strength of 2.03 mm high-impact polystyrene sheet as a function of temperature. (Reproduced from Bucknall, C.B. (1967) Relationship between structure and mechanical properties of rubber-modified thermoplastics. Br. Plast., **40**, 84. Copyright (1967) Crain Communications Ltd.)*

whitening occurs only in the first (pre-crack) stage of fracture and is therefore confined to the region near the notch.

3. *High temperature*. The rubber is able to relax even in the rapidly forming stress field ahead of the travelling crack. Stress whitening occurs over the whole of the fracture surface. Bucknall and Smith [139] report similar results for other rubber-modified impact polymers.

13.9.4 Crazing and Stress Whitening

Bucknall and Smith [139] remarked on the connection between crazing and stress whitening. It was observed that the fracture of high-impact polystyrene, which incorporates rubber particles into the polystyrene, is usually preceded by opaque whitening of the stress area. Figure 13.11 shows a stress-whitened bar of high-impact polystyrene that failed at an elongation of 35%. A combination of different types of optical measurements (polarised light to measure molecular orientation and phase contrast microscopy to determine refractive index) showed that these stress-whitened regions are similar to the crazes formed in unmodified polystyrene. They are birefringent, of low refractive index, capable of bearing load and are healed by annealing treatments. The difference between stress whitening and crazing exists merely in the size and concentration of the craze bands, which are of much smaller size and greater quantity in stress whitening. Thus, the higher conversion of the polymer into crazes accounts for the high breaking elongation of toughened polystyrene. It is suggested that the effect of the rubber particles is to lower the craze initiation stress relative to the fracture stress, thereby prolonging the crazing stage of deformation. The crazing stage appears to require the relaxation of the rubber phase, so that it behaves like a rubber and not a glass. The function of the rubber particles is not, however, merely to provide points of stress concentration, and there must be a good bond between the rubber and polystyrene, which is achieved by chemical grafting. The rubber must bear part of the load at the stage when the polymer has crazed but not fractured. Bucknall and Smith suggested that the rubber particles may be constrained by the surrounding polystyrene matrix so that their stiffness remains high. These ideas lead directly to an explanation of the three regimes for impact testing, as discussed above. At low temperatures, there is no stress whitening because the rubber does not relax during, the fracture process, giving low impact strengths. At intermediate temperatures, stress whitening occurs near the notch, where the crack initiates and is travelling sufficiently slowly compared with the relaxation of the rubber. Here the impact strength increases. Finally, at high temperatures, stress whitening is observed along the whole of the crack and the impact strength is high.

13.9.5 Dilatation Bands

Lazzeri and Bucknall [142] have proposed that the pressure dependence of yield behaviour caused by the presence of microvoids can explain the observation of dilatation bands in rubber-toughened epoxy resins [143], rubber-toughened polycarbonate [144] and styrene–butadiene diblock copolymers [145]. These dilatation bands combine in-plane shear with dilatation normal to the shear plane. Whereas true crazes contain interconnecting strands, as described in Section 13.5.1, dilatation bands contain discrete voids that, for rubber-toughened polymers, are confined to the rubber phase.

13.10   The Tensile Strength and Tearing of Polymers in the Rubbery State

13.10.1   The Tearing of Rubbers: Extension of Griffith Theory

The Griffith theory of fracture implies that the quasi-static propagation of a crack is a reversible process. Rivlin and Thomas [146, 147] recognised, however, that this may be unnecessarily restrictive, and also that the reduction in elastically stored energy due to the crack propagation may be balanced by changes in energy other than that due to an increase in surface energy. Their approach was to define a quantity termed the 'tearing energy', which is the energy expended per unit thickness per unit increase in crack length. The tearing energy includes surface energy, energy dissipated in plastic flow processes and energy dissipated irreversibly in viscoelastic processes. Provided that all these changes in energy are proportional to the increase in crack length and are primarily determined by the state of deformation in the neighbourhood of the tip of the crack, then the total energy will still be independent of the shape of the test piece and the manner in which the deforming forces are applied.

In formal mathematical terms, if the crack increases in length by an amount dc, an amount of work $TB\,dc$ must be done, where T is the tearing energy per unit area and B is the thickness of the sheet. Assuming that no external work is due, this can be equated to the change in elastically stored energy, giving

$$-\left[\frac{\partial U}{\partial c}\right]_{l} = TB. \tag{13.47}$$

The suffix l indicates that differentiation is carried out under conditions of constant displacement of the parts of the boundary that are not force-free. Equation (13.47) is similar in form to Equation (13.1) above but T is defined for unit thickness of specimen and is therefore equivalent to 2γ in Equation (13.1). As in the case of glassy polymers, T is not to be interpreted as a surface free energy, but involves the total deformation in the crack tip region as the crack propagates.

The so-called trouser tear experiment shown in Figure 13.41 is a particularly simple case where the equation can be evaluated immediately. After making a uniform cut in a rubber sheet, the sample is subjected to tear under the applied forces P. The stress distribution at the tip of the tear is complex, but provided that the legs are long it is independent of the depth of the tear.
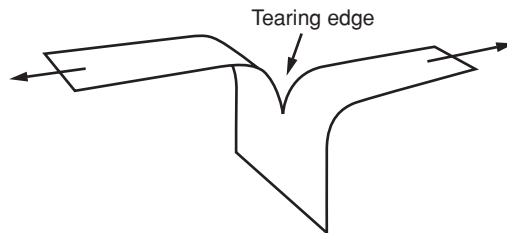
Figure 13.41   *The standard 'trouser tear' experiment.*

If the sample tears a distance Δc under the force F, and changes in extension of the material between the tip of the tear and the legs are ignored the work done is given by $\Delta W = 2F\Delta c$.

Because the tearing energy $T = \Delta W/B\Delta c$, $T = 2F/B$ and can be measured easily.

Rivlin and Thomas [135] found that two characteristic tearing energies could be defined, one for very slow rates of tearing ($T = 37$ kJ/m^2) and one for catastrophic growth ($T = 130$ kJ/m^2), and that both of these quantities were independent of the shape of the test piece.

The tearing energy is the energy required to extend the rubber to its maximum elongation and does not relate directly to tensile strength but depends on the shape of the stress–strain curve together with the viscoelastic nature of the rubber. For example, we may contrast two different rubbers, the first possessing a high tensile strength but a very low elongation to fracture and very low viscoelastic losses, and the second possessing a low tensile strength but a high elongation to fracture and high viscoelastic losses. In spite of its comparatively low tensile strength, the second rubber may still possess a high tearing energy.

13.10.2   Molecular Theories of the Tensile Strength of Rubbers

Most molecular theories of the strength of rubber treat rupture as a critical stress phenomenon. It is accepted that the strength of the rubber is reduced from its theoretical strength in a perfect sample by the presence of flaws. Moreover, it is assumed that the strength is reduced from that of a flawless sample by approximately the same factor for different rubbers of the same basic chemical composition. It is then possible to consider the influence on the strength of such factors as the degree of cross-linking and the primary molecular mass.

Bueche [148] has considered the tensile strength of a model network consisting of a three-dimensional net of cross-linked chains. Figure 13.42 illustrates a unit cube whose edges are parallel to the three chain directions in the idealised network. Assume that there are N chains in this unit cube and that the number of chains in each strand of the network is n. There are then n^2 strands passing through each face of the cube. To relate the number n to the number of chains per unit volume of the network (and so form a link with rubber elasticity theory), we note that the product of the number of strands passing through each
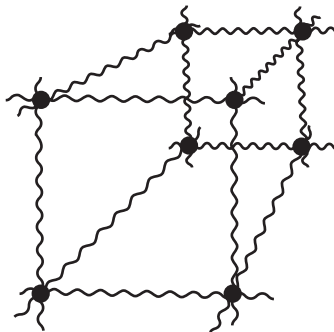
Figure 13.42   *Model network of cross-linked chains.*

cube face and the number of chains in each strand will be $\frac{1}{3}N$ because there are three strand directions. Thus

$$n^3 = \frac{1}{3}N, \quad n = (N/3)^{1/3}. \tag{13.48}$$

Apply a stress σ parallel to one of the three strand directions and assume that the strands break simultaneously at an individual fracture stress σ_c. Then

$$\sigma_B = n^2\sigma_c,$$

which from Equation (13.48) can be written as

$$\sigma_B = (N/3)^{2/3}\sigma_c.$$

For a real network, N is the number of effective chains per unit volume and is given in terms of the actual number of chains per unit volume N_a by the Flory relationship

$$N = N_a[1 - 2\bar{M}_c/M_n],$$

where $\bar{M}_c$ and $\bar{M}_n$ are the average molecular mass between cross-links and the number average molecular mass of the polymer, respectively. (Note that for a network there must be at least two cross-links per chain, i.e. $\bar{M}_n > 3\bar{M}_c$.)

This substitution gives

$$\sigma_B \alpha [1 - 2\bar{M}_c/\bar{M}_n]^{2/3}\sigma_c.$$

Flory [149] found that the variation of tensile strength with the polymer molecular mass $\bar{M}_n$, for butyl rubber, follows the predicted $[1-2\bar{M}_c/\bar{M}_n]^{2/3}$ relationship, but for natural rubber [150] an initial increase in tensile strength with increasing degree of cross-linking was followed by a decrease at very high degrees of cross-linking. Flory attributed this decrease to the influence of cross-links in the crystallisation of the rubber. However, a similar effect was observed for the non-crystallising styrene–butadiene rubber by Taylor and Darin [151], which led Bueche [152] to propose that the simple model described above fails because of the assumption that each chain holds the load at fracture, which may be a good approximation at low degrees of cross-linking but is less probable at high degrees of cross-linking.

It is of considerable technological importance that the tensile strength of rubbers can be much increased by the inclusion of reinforcing fillers such as carbon black and silicone, which increase the tensile strength by allowing the applied load to be shared among a group of chains, thus decreasing the chance that a break will propagate [153].

13.11   Effect of Strain Rate and Temperature

The influence of strain rate and temperature on the tensile properties of elastomers and amorphous polymers has been studied extensively, particularly by Smith and co-workers [154–156], who measured the variation of tensile strength and ultimate stain as a function of strain rate for a number of elastomers. The results for different temperatures could be superimposed, by shifts along the strain rate axis, to give master curves for tensile strength and ultimate strain as a function of strain rate. Results of this nature are shown in
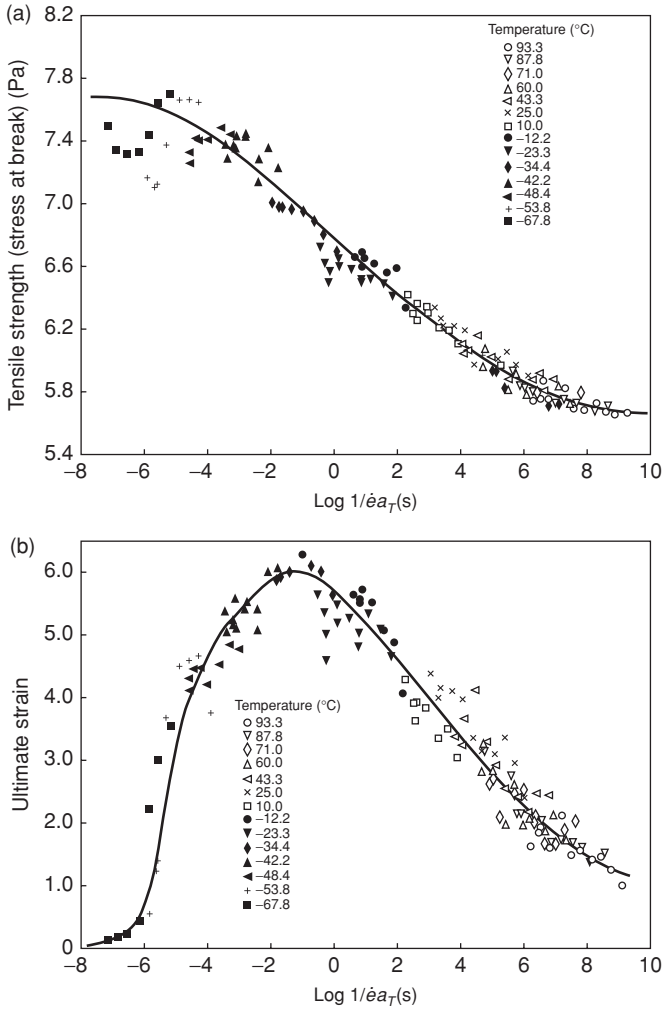
Figure 13.43 *Variation of tensile strength (a) and ultimate strain (b) of a rubber with reduced strain rate $\dot{e}a_T$. Values were measured at various temperatures and rates and reduced to a temperature of 263 K. (Reproduced from Smith, T.L. (1958) Dependence of the ultimate properties of a GR-S rubber on strain rate and temperature. J. Polym. Sci.,* **32***, 99. Copyright (1958) John Wiley & Sons, Inc.)*

Figure 13.43, which summarises Smith's data for an unfilled styrene–butadiene rubber. Remarkably, the shift factors obtained from superposition of both tensile strength and ultimate strain took the form predicted by the WLF equation (see Section 6.3.2) for the superposition of low-strain linear viscoelastic behaviour of amorphous polymers (Figure 13.44). The actual value for T_g agreed well with that obtained from dilatometric measurements.

    This result suggests that, except at very low strain rates and high temperatures where the molecular chains have complete mobility, the fracture process is dominated by viscoelastic
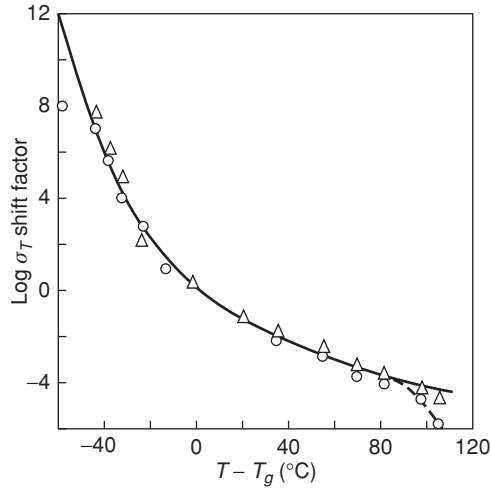
Figure 13.44   *Experimental values of log a_T shift factor obtained from measurement of ultimate properties compared with those predicted using the WLF equation: ($\triangle$) from tensile strength; ($\circ$) from ultimate strain; (----) WLF equations with $T_g = 263$ K. (Reproduced from Smith, T.L. (1958) Dependence of the ultimate properties of a GR-S rubber on strain rate and temperature. J. Polym. Sci., 32, 99. Copyright (1958) John Wiley & Sons, Inc.)*

effects. Bueche [157] has treated this problem theoretically and obtained the observed form of the dependence of tensile strength on strain rate and temperature. Later theories have attempted to obtain the time dependence for both tensile strength and ultimate strain, or the time to break at a constant strain rate [158,159].

Smith plotted log σ_B/T against log e for the above and similar data to obtain a unique curve for all strain rates and test temperatures, which he termed the 'failure envelope' for elastomers. It was also found [156] that the failure envelope can represent failure under more complex conditions such as creep and stress relaxation. In Figure 13.45, such failure can take place by starting from the initial stage G and progressing parallel to the abscissa (constant stress, i.e. creep) or parallel to the ordinate (constant strain, i.e. stress relaxation) until a point is reached on the failure envelope ABC, as indicated by the progress along the dotted lines.

13.12   Fatigue in Polymers

Materials frequently fail by fatigue due to the cyclic application of stress below that required to cause yield or fracture when a continuously rising stress is applied. The effect of such cyclic stresses is to initiate microscopic cracks at centres of stress concentration within the material or on the surface, and subsequently to enable these cracks to propagate, leading to eventual failure.

Early studies of fatigue in polymers concentrate on stress cycling of unnotched samples, to produce S versus N plots similar to those that have proved so useful for characterising fatigue in metals (S being the maximum loading stress and N the number of cycles to failure). An example of this type of plot for PVC [160] is shown in Figure 13.46. A major
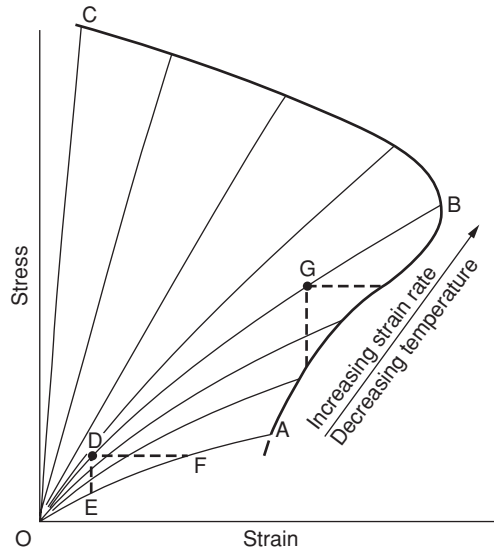
Figure 13.45 *Schematic representation of the variation of stress–strain curves with the strain rate and temperature. Envelope connects rupture point and the dotted lines illustrate stress relaxation and creep under different conditions. (Reproduced from Smith, T.L. and Stedry, P.J. (1960) Time and temperature dependence of the ultimate properties of an SBR rubber at constant elongations. J. Appl. Phys., **31**, 1892. Copyright (1960) American Institute of Physics.)*

aspect of such a test is the question of adiabatic heating, which can lead to failure by thermal melting. Clearly there will be a critical frequency above which thermal effects become important.

Stress cycling tests on unnotched samples do not readily distinguish between crack initiation and crack propagation. Further progress requires a similar approach to that adopted in fracture studies, namely the introduction of very sharp initial cracks in order to examine crack propagation utilising fracture mechanics concepts.
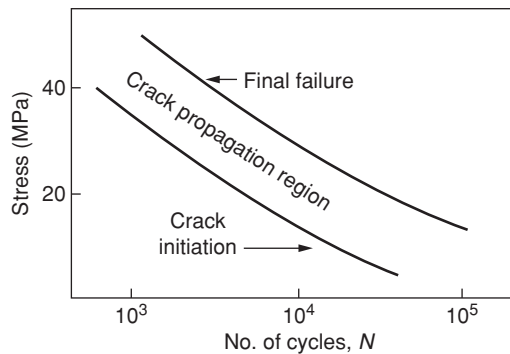
Figure 13.46 *Fatigue response of PVC: relationship between applied stress σ and number of cycles to failure N, for both initiation of fatigue cracks and final failure. (Reproduced from Manson, J.A. and Hertzberg, R.W. (1973) Fatigue Failure in Polymers. CRC Crit. Rev. Macromol. Sci., **1**, 433. Copyright (1973) Taylor and Francis.)*

The first quantitative studies of fatigue in polymers, which concentrated on rubbers [161–163], applied the tearing energy concept of fracture proposed by Rivlin and Thomas to fatigue crack propagation. Thomas [161] showed that the fatigue crack growth rate could be expressed in the form of an empirical relationship

$$\frac{\mathrm{d}c}{\mathrm{d}N} = A\mathscr{J}^{n}, \tag{13.49}$$

where c is the crack length, N is the number of cycles and $\mathscr{J}$ is the surface work parameter, which is analogous to the strain energy release rate G in linear elastic fracture mechanics. For a SENT specimen

$$\mathscr{J} = 2k_1 cU, \tag{13.50}$$

where $U = \sigma^2/2E$ is the stored energy density for a linear elastic material and k_1 is a constant that varies from π at small extensions (the linear elastic value) to approximately unity at large extensions [164]. Here A and n are constants that are dependent on the material and generally vary with test conditions such as temperature. The exponent n usually lies between 1 and 6 and for rubber is approximately 2 for anything other than very small $\mathrm{d}c/\mathrm{d}N$.

As expressed in Equation (13.49), $\mathscr{J}$ is essentially a positive quantity and can be considered to vary during the test cycle from zero ($\mathscr{J} = \mathscr{J}_{\min} = 0$) to a finite value ($\mathscr{J} = \mathscr{J}_{\max}$). It has been found that where $\mathscr{J}_{\min}$ is increased there is a corresponding decrease in A, which has been attributed to reduced crack propagation where strain-induced crystallisation occurs. Furthermore, it has been shown that there is a fatigue limit $\mathscr{J} = \mathscr{J}_0$ below which a fatigue crack will not be propagated. Lake and Thomas showed that $\mathscr{J}_0$ corresponds to the minimum energy required per unit area to extend the rubber at the crack tip to its breaking point. Andrews [165] pointed out that initiation requires either intrinsic flaws of magnitude c_0 or that flaws of this size are produced during the test itself, with c_0 defined by Equation (13.50), where $\mathscr{J}_0 = k_1 c_0 U$. Andrews and Walker [166] carried this approach one stage further, incorporating a generalised form of fracture mechanics to analyse the fatigue behaviour of low-density polyethylene, which was viscoelastic in the range of interest so the more generalised fracture mechanics was required to deal with unloading as well as loading during crack propagation. The fatigue characteristics were predicted from the crack growth data using a single fitting constant, the intrinsic flaw size c_0, which it was suggested corresponded to the spherulite dimensions so that inter-spherulite boundary cracks constituted the intrinsic flaws.

For glassy polymers, fracture mechanics has been the usual starting point [167–170], with the fatigue crack growth rate usually expressed as an empirical relationship

$$\frac{\mathrm{d}c}{\mathrm{d}N} = A'(\Delta K)^{m}, \tag{13.51}$$

where c is the crack length, N is the number of cycles, ΔK is the range of the stress intensity factor (i.e. $K_{\max} - K_{\min}$, where $K_{\min}$ is generally zero) and A' and m are constants depending on the material and test conditions.

For $K_{\min} = 0$, Equation (13.51) is clearly identical in form to Equation (13.49), which is generally adopted for rubbers. Recall from Section 13.2.3 that the strain energy release

rate $G = K^2/E$ for plane stress. Then

$$G = 2\mathscr{I} = K_{max}^2/2E = (\Delta K)^2/2E$$

and Equations (13.49) and (13.51) are formally equivalent if $m = 2n$.

Equation (13.51) is also the most general form of the law proposed by Paris [171,172] for predicting fatigue crack growth rates in metals. The general situation for glassy polymers is illustrated in Figure 13.47(a), with some typical results shown in Figure 13.47(b). The data differ in two respects from the Paris equation: first, analogous to the case of rubbers, there is a distinct threshold value of ΔK, denoted by ΔK_{th}, below which no crack growth
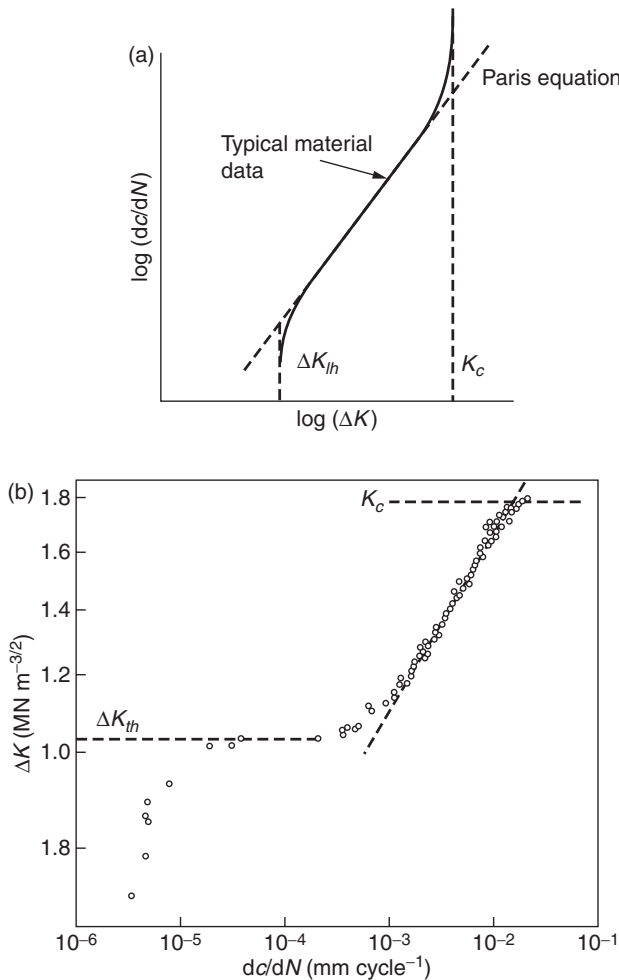
Figure 13.47 *(a) Schematic diagram of fatigue crack growth rate dc/dN as a function of the range of stress intensity factor ΔK. (b) Fatigue crack growth characteristics for a vinyl urethane polymer. (Reproduced from Harris, J.S. and Ward, I.M. (1973) Fatigue-crack propagation in vinyl urethane polymers. J. Mater. Sci.,* **8**, *1655. Copyright (1973).)*

is observed; secondly, as ΔK approaches the critical stress intensity factor K_c, the crack accelerates. A further criticism of Equation (13.51) is that it allows for the influence of the stress intensity factor but not for the mean stress, which usually has an important influence on the crack growth rate. The latter consideration led Arad, Radon and Culver [173] to suggest an equation of the form

$$\frac{dc}{dN} = \beta \lambda^n, \qquad (13.52)$$

where $\lambda = (K_{max}^2 - K_{min}^2)$. This relation is equivalent to Equation (13.51) because the cycle strain energy release rate ΔG is given by

$$\Delta G = \frac{1}{E}\left(K_{max}^2 - K_{min}^2\right).$$

A comprehensive review of the application of the Paris equation and its modified form (Equation (13.52)) to the fatigue behaviour of polymers has been given by Manson and Hertzberg [160], who considered the effect of physical variables such as crystallinity and molecular mass. They noted a strong sensitivity of fatigue crack growth to molecular mass: in polystyrene a fivefold increase in molecular mass resulted in a more than tenfold increase in fatigue life. A general correlation was observed between the fracture toughness K_c and the fatigue behaviour, expressed as the stress intensity range ΔK corresponding to an arbitrary value of dc/dN (chosen as 7.6×10^{-7} m/cycle), as is shown in Figure 13.48. A study of fatigue behaviour in polycarbonate by Pitman and Ward [174] also brought out the similarity between fatigue and fracture, so that the fatigue behaviour can be analysed in terms of
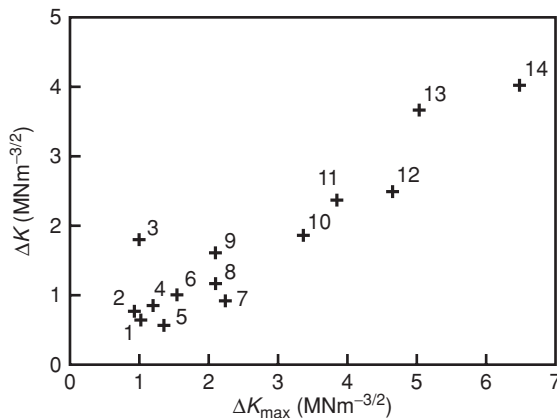
Figure 13.48   *Relationship between the stress intensity range ΔK, corresponding to an arbitrary value of dc/dN 7.6×10^{-7} m/cycle, and the maximum stress intensity factor range ΔK_{max} observed at failure for a group of polymers. The polymers are: (1) cross-linked polystyrene, (2) PMMA, (3) PVC, (4) LDPE, (5) polystyrene, (6) polysulfone, (7) high-impact polystyrene, (8) ABS resin, (9) chlorinated polyether, (10) poly(phenylene oxide), (11) nylon 6, (12) polycarbonate, (13) nylon 6:6 and (14) poly(vinylidene fluoride). (Reproduced from Manson, J.A. and Hertzberg, R.W. (1973) Fatigue Failure in Polymers. CRC Crit. Rev. Macromol. Sci., **1**, 433. Copyright (1973) Taylor and Francis.)*

mixed mode failure. Similar to the fracture behaviour described in Section 13.2, changing molecular mass again changed the balance between energy dissipated in propagating the craze and shear lips, respectively. A development by Williams [175, 176] attempts to model fatigue crack propagation behaviour in terms of the Dugdale plastic zone analysis of the crack tip. Each fatigue cycle is considered to reduce the craze stress in one part of craze, so that a two-stage plastic zone is established leading to an equation for crack growth of the form

$$\frac{\mathrm{d}c}{\mathrm{d}N} = \beta' \left(K^2 - \alpha K_c^2 \right), \tag{13.53}$$

which gives a good fit to experimental data for polystyrene over a substantial range of temperatures.

Both Williams and Pitman and Ward conclude that it is difficult to assign physical significance to the parameters in the Paris equation. Further developments in this area will require a more distinctly physical approach.

References

1. Griffith, A.A. (1921) The phenomena of rupture and flow in solids. *Philos. Trans. R. Soc.*, **221**, 163.
2. Inglis, G.E. (1913) Stresses in a plate due to the presence of cracks and sharp corners. *Trans. Inst. Nav. Architec.*, **55**, 219.
3. Irwin, G.R. (1957) Analysis of stresses and strains near the end of a crack traversing a plate. *J. Appl. Meek*, **24**, 361.
4. Irwin, G.R. and Kies, J.A. (1954) Critical energy analysis of fracture strength. *Welding J. Res. Suppl.*, **33**, 1935.
5. Brown, W.F. and Srawley, J.F. (1966) Plane strain crack toughness testing of high strength metallic materials. *ASTM STP 410*.
6. Srawley, J.E. and Gross, B. (1967) Stress Intensity Factors for Crackline-Loaded Edge-Crack Specimens, NASA Technical Note NASA-TN-D-3820, Washington D.C., NASA.
7. Williams, J.G. (1980) *Stress Analysis of Polymers*, 2nd edn, Ellis Horwood, Chichester.
8. Benbow, J.J. and Roesler, F.C. (1957) Experiments on controlled fractures. *Proc. Phys. Soc.*, **B70**, 201.
9. Berry, J.P. (1963) Determination of fracture surface energies by cleavage technique. *J. Appl. Phys.*, **34**, 62.
10. Benbow, J.J. (1961) Stable crack propagation in plastics. *Proc. Phys. Soc.*, **78**, 970.
11. Svensson, N.L. (1961) Variation of fracture energy of brittle plastics with temperature. *Proc. Phys. Soc.*, **77**, 876.
12. Berry, J.P. (1961) Fracture processes in polymeric materials. II. Tensile strength of polystyrene. *J. Polym. Sci.*, **50**, 313.
13. Andrews, E.H. (September 1966) Fracture mechanics approach to corrosion stress cracking in plastics in *Proceedings of the Conference on the Physical Basis of Yield and Fracture*, Oxford, (ed. A.C. Strickland), Institute of Physics & The Physical Society London, p. 127.

14. Berry, J.P. (1959) in *Fracture* (eds B.L. Auerbach *et al.*), John Wiley & Sons, Ltd, New York, p. 263.
15. Kambour, R.P. (1964) Structure and properties of crazes in polycarbonate and other glassy polymers. *Polymer*, **5**, 143.
16. Kambour, R.P. (1966) Mechanism of fracture in glassy polymers. 3. Direct observation of craze ahead of propagating crack in poly(methyl methacrylate) and polystyrene. *J. Polym. Sci. A2*, **4**, 349.
17. Kambour, R.P. (1973) A review of crazing and fracture in thermoplastics. *J. Pol. Sci.; Macromol. Rev.*, **7**, 1.
18. Brown, H.R. and Ward, I.M. (1973) Craze shape and fracture in poly(methyl methacrylate). *Polymer*, **14**, 469.
19. Doll, W. and Weidmann, G.W. (1976) Interferential optical measurement of craze zone before fracture process in PMMA with different molecular weights. *Colloid. Polym. Sci.*, **254**, 205.
20. Dugdale, D.S. (1960) Yielding of steel sheets containing slits. *J. Mech. Phys. Solids*, **8**, 100.
21. Rice, J.R. (1968) in *Fracture—An Advanced Treatise* (ed. H. Liebowitz), Academic Press, New York, Chap. 3.
22. Pitman, G.L. and Ward, I.M. (1979) Effect of molecular weight on craze shape and fracture toughness in polycarbonate. *Polymer*, **20**, 895.
23. Hine, P.J., Duckett, R.A. and Ward, I.M. (1981) A study of the fracture behaviour of polyethersulphone. *Polymer*, **22**, 1745.
24. Williams, J.G. and Parvin, M. (1975) Effect of temperature on fracture of polycarbonate. *J. Mater. Sci.*, **10**, 1883.
25. Berry, J.P. (1964) Fracture Processes in polymeric materials. V. Dependence of ultimate properties of poly(methyl methacrylate) on molecular weight. *J. Polym. Sci. A2*, **2**, 4069.
26. Flory, P.J. (1945) Tensile strength in relation to molecular weight of high polymers. *J. Am. Chem. Soc.*, **67**, 2048.
27. Doll, W. and Weidmann, G.W. (1979) Deformationsverhalten von PMMA-Crazes an Rißspitzen. *Prog. Colloid. Polym. Sci.*, **66**, 291.
28. Kusy, R.P. and Turner, D.T. (1977) Influence of molecular-weight of poly(methyl methacrylate) on fracture morphology in notched tension. *Polymer*, **18**, 391.
29. Kusy, R.P. and Turner, D.T. (1976) Influence of molecular-weight of poly(methyl methacrylate) on fracture surface-energy in notched tension. *Polymer*, **17**, 161.
30. Haward, R.N., Daniels, H.E. and Treloar, L.R.G. (1978) Molecular conformation and craze fracture. *J. Polym. Sci. Polym. Phys. Ed.*, **16**, 1169.
31. Berry, J.P. (1959) in *Fracture* (eds B.L. Averback *et al.*), John Wiley & Sons, Ltd, New York, p. 263.
32. Higuchi, M. (1959) On the Color of the Fracture Surface of Polymethyl Methacrylate Plate, Colorless and Transparent in Itself. *Rep. Res. Inst. Appl. Mech. Jpn.*, **6**, 173.
33. Kambour, R.P. and Holik, A.S. (1969) Electron microscopy of crazes in glassy polymers – use of reinforcing impregnants during microtomy. *J. Polym. Sci. A2*, **7**, 1393.
34. Kambour, R.P. and Russell, R.R. (1971) Electron microscopy of crazes in polystyrene and rubber modified polystyrene – use of iodine–sulphur eutectic as a craze reinforcing impregnant. *Polymer*, **12**, 237.

35. Parades, E. and Fischer, E.W. (1979) Small-angle X-ray investigations on the structure of crazes in polycarbonate and poly(methyl methacrylate). *Makromol. Chem.*, **180**, 2707.
36. Brown, H.R. and Kramer, E.J. (1981) Craze microstructure from small-angle X-ray-scattering (SAXS). *J. Macromol. Sci. Phys.*, **B19**, 487.
37. Yang, A.C.-M. and Kramer, E.J. (1986) Craze microstructure characterization by low-angle electron-diffraction and Fourier-transforms of craze images. *J. Mater. Sci.*, **21**, 3601.
38. Berger, L.L., Buckley, D.J., Kramer, E.J. *et al.* (1987) Low-angle electron-diffraction from high-temperature polystyrene crazes. *J. Polym. Sci. Polym. Phys. Ed.*, **25**, 1679.
39. Berger, L.L. (1989) Relationship between craze microstructure and molecular entanglements in glassy-polymers. *Macromolecules*, **22** 3162.
40. Brown, H.R. (1991) A molecular interpretation of the toughness of glassy-polymers. *Macromolecules*, **24**, 2752.
41. Sha, Y., Hui, C.Y., Ruina, A. *et al.* (1995) Continuum and discrete modeling of craze failure at a crack-tip in a glassy polymer. *Macromolecules*, **28**, 2450.
42. Donald, A.M. and Kramer, E.J. (1982) Effect of strain history on craze microstructure. *Polymer*, **23**, 457.
43. Rietsch, F., Duckett, R.A. and Ward, I.M. (1979) Tensile drawing behaviour of poly(ethylene terephthalate). *Polymer*, **20**, 1133.
44. Kausch, H.H. (1987) *Polymer Fracture*, 2nd edn, Springer Verlag, Berlin.
45. Odell, J.A. and Keller, A. (1986) Flow-induced chain fracture of isolated linear macromolecules in solution. *J. Polym. Sci. Polym. Phys. Ed.*, **24**, 1889.
46. Sternstein, S.S., Ongchin, L. and Silverman, A. (1968) Yield criteria for plastic deformation of glassy high polymers in general stress fields. *Appl. Polym. Symp.*, **7**, 175.
47. Sternstein, S.S. and Ongchin, L. (1969) Inhomogeneous deformation and yielding of glasslike high polymers. *Am. Chem. Soc. Polym. Prepr.*, **10**, 1117.
48. Bowden, P.B. and Oxborough, R.J. (1973) General critical strain criterion for crazing in amorphous glassy polymers. *Philos. Mag.*, **28**, 547.
49. Matsushige, K., Radcliffe, S.V. and Baer, E. (1975) The mechanical behaviour of polystyrene under pressure. *J. Mater. Sci.*, **10**, 833.
50. Duckett, R.A., Goswami, B.C., Smith, L.S.A. *et al.* (1978) The yielding and crazing behaviour of polycarbonate in torsion under superposed hydrostatic pressure. *Br. Polym. J.*, **10**, 11.
51. Kitagawa, M. (1976) Craze initiation of glassy polymers under action of crazing agent. *J. Polym. Sci. Polym. Phys. Ed.*, **14**, 2095.
52. Argon, A.S., Hannoosh, J.C. and Salama, M.M. (1977) in *Fracture 1977*, Vol. 1, Waterloo, Canada, p. 445.
53. Bernier, G.A. and Kambour, R.P. (1968) The role of organic agents in the stress crazing and cracking of poly(2,6-dimethyl-1,4-phenylene oxide). *Macromolecules*, **1**, 393.
54. Kambour, R.P., Gruner, C.L. and Romagosa, E.E. (1973) Solvent crazing of dry polystyrene and dry crazing of plasticized polystyrene. *J. Polym. Sci.*, **11**, 1879.

55. Kambour, R.P., Gruner, C.L. and Romagosa, E.E. (1974) Bisphenol-A polycarbonate immersed in organic media – swelling and response to stress. *Macromolecules*, **7**, 248.

56. Andrews, E.H. and Bevan, L. (1972) Mechanics and mechanism of environmental crazing in a polymeric glass. *Polymer*, **13**, 337.

57. Marshall, G.P., Culver, L.E. and Williams, J.G. (1970) Craze growth in polymethylmethacrylate – a fracture mechanics approach. *Proc. Roy. Soc.*, **A319**, 165.

58. Williams, J.G. and Marshall, G.P. (1975) Environmental crack and craze growth phenomena in polymers. *Proc. Roy. Soc. A*, **342**, 55.

59. Brown, N. and Imai, Y. (1975) Craze yielding of polycarbonate in N2, AR, and 02 at low pressures and temperatures. *J. Appl. Phys.*, **46**, 4130.

60. Imai, Y. and Brown, N. (1976) Environmental crazing and intrinsic tensile deformation in polymethylmethacrylate. 1. Mechanical behavior. *J. Mater. Sci.*, **11**, 417.

61. Brown, N., Metzger, B.D. and Imai, Y. (1978) Equation for creep in terms of craze parameters. *J. Polym. Sci. Polym. Phys. Ed.*, **16**, 1085.

62. Kambour, R.P. (April 1977) Mechanisms of environment sensitive cracking of glasslike high polymers in *Proceedings of the International Conference on the Mechanics of Environment Sensitive Cracking Materials*, University of Surrey, Guildford, UK, p. 213.

63. Brown, N. (1980) in *Methods of Experimental Physics*, Vol. 16, Part C (ed. R.A. Fava), Academic Press, New York, p. 233.

64. Rice, J.R. (1968) A path independent integral and approximate analysis of strain concentration by notches and cracks. *J. Appl. Mechan.*, **35**, 379.

65. Begley, J.A. and Landes, J.D. (1972) The J integral as a fracture criterion. *ASTM STP 514*.

66. Landes, J.D. and Begley, J.A. (1979) *Post Yield Fracture Mechanics* (ed. D.G.A. Latzko), Applied Science, London.

67. Chan, M.K.V. and Williams, J.G. (1983) J-integral studies of crack initiation of a tough high-density polyethylene. *Int. J. Fracture*, **23**, 145.

68. Sumpter, J.D. and Turner, C.E. (1973) Applicability of J to elastic–plastic materials. *Int. J. Fracture*, **9**, 320.

69. ESIS Technical Committee on Polymers and Composites, *A Testing Protocol for Conducting J Crack Growth Resistance Curve Tests on Plastics*, May 1995.

70. Broberg, K.B. (1968) Critical review of some theories in fracture mechanics. *Int. J. Fracture*, **4**, 11.

71. Mai, Y.W. and Cotterell, B. (1986) On the essential work of ductile fracture in polymers. *Int. J. Fracture*, **32**, 105.

72. Hashemi, S. and Williams, J.G. (2000) Temperature dependence of essential and non-essential work of fracture parameters for polycarbonate film. *Plast, Rubber Comp.*, **29**, 294.

73. Wu, J. and Mai, Y.-W. (1996) The essential fracture work concept for toughness measurement of ductile polymers. *Polym. Eng. Sci.*, **36**, 2275.

74. Williams, J.G. and Rink, M. (2007) The standardisation of the EWF test. *Engineering Fracture Mechanics*, **74**, 1009–1017.

75. Naz, S., Sweeney, J. and Coates, P.D. (2010) Analysis of the essential work of fracture method as applied to UHMWPE. *J. Mater. Sci.*, **45**, 448–459.

76. Lu, X. and Brown, N. (1986) The relationship of the initiation stage to the rate of slow crack growth in linear polyethylene. *J. Mater. Sci.*, **21**, 2423.

77. Huang, Y.-L. and Brown, N. (1990) The dependence of butyl branch density on slow crack-growth in polyethylene – kinetics. *J. Polym. Sci. Polym. Phys. Ed.*, **28**, 2007.

78. O'Connell, P.A., Bonner, M.J., Duckett, R.A. *et al.* (1995) The relationship between slow crack-propagation and tensile creep – behavior in polyethylene. *Polymer*, **36**, 2355.

79. Cawood, M.J., Channell, A.D. and Capaccio, G. (1993) Crack initiation and fiber creep in polyethylene. *Polymer*, **34**, 423.

80. Clutton, E.Q., Rose, L.J. and Capaccio, G. (1998) Slow crack growth and impact mechanisms in polyethylene. *Plast. Rubber Comp. Proc. Appl.*, **27**, 478.

81. Wilding, M.A. and Ward, I.M. (1978) Tensile creep and recovery in ultra-high modulus linear polyethylenes. *Polymer*, **19**, 969.

82. Huang, Y.-L. and Brown, N. (1991) Dependence of slow crack growth in polyethylene on butyl branch density – morphology and theory. *J. Polym. Sci. Polym. Phys. Ed.*, **29**, 129.

83. O'Connell, P.A., Bonner, M., Duckett, R.A. *et al.* (2003) Effect of molecular weight and branch content on the creep behaviour of oriented polyethylene. *J. Appl. Polym. Sci.*, **89**, 1663.

84. Kurelec, L., Teeuwen, M., Schoffeleers, H. *et al.* (2005) Strain hardening modulus as a measure of environmental stress crack resistance of high density polyethylene. *Polymer*, **46**, 6369.

85. Cazenave, J., Seguela, R., Sixou, B. *et al.* (2006) Short-term mechanical and structural approaches for the evaluation of polyethylene stress crack resistance. *Polymer*, **47**, 3904.

86. Mark, H. (1943) *Cellulose and its Derivatives*, Interscience, New York.

87. Vincent, P.I. (1964) True breaking stress of thermoplastics. *Proc. Roy. Soc. A*, **282**, 113.

88. Kausch, H.H. (1978) *Polymer Fracture*, Springer-Verlag, Berlin.

89. Kausch, H.H. and Becht, J. (1970) Uber Spannungsrelaxation und Zeitabhangige Elastische Bruchvorgange in Orientierten Fasern. *Rheol. Acta*, **9**, 137.

90. Zhurkov, S.N., Novak, I.I., Slutsker, A.I. *et al.* (March/April 1970) Connection between destruction of chain molecules and formation of sub micro cracks in stressed polymers in *Proceedings of the Conference on the Yield, Deformation and Fracture of Polymers*, Cambridge, Session 3, Talk 3, pp. 1–6.

91. Wool, R.P. (1975) Mechanisms of frequency shifting in infrared-spectrum of stressed polymer. *J. Polym. Sci.*, **13**, 1795.

92. Yeh, W.-Y. and Young, R.J. (1999) Molecular deformation processes in aromatic high modulus polymer fibres. *Polymer*, **40**, 857.

93. Ward, Y. and Young, R.J. (2001) Deformation studies of thermotropic aromatic copolyesters using NIR Raman spectroscopy. *Polymer*, **42**, 7857.

94. Bueche, F. (1955) Tensile strength of plastics above the glass temperature. *J. Appl. Phys.*, **26**, 1133.

95. Zhurkov, S.N. and Tomashevsky, E.E. (September 1966) An investigation of fracture process of polymers by the electron spin resonance method in *Proceedings of the Conference on the Physical Basis of Yield and Fracture*, Oxford, p. 200.

96. Zhurkov, S.N., Kuksenko, V.S. and Slutsker, A.I. (April 1969) Submicrocrack formation under stress in *Proceedings of the Second International Conference on Fracture*, Brighton, p. 531.

97. Zakrevskii, V.A. and Korsukov, V. Ye. (1972) Study of the chain mechanism of mechanical degradation of polyethylene. *Polym. Sci. USSR*, **14**, 1064.

98. Peterlin, A. (1975) Structural model of mechanical properties and failure of crystalline polymer solids with fibrous structure. *Int. J. Fracture*, **11**, 761.

99. Orowan, E. (1949) Fracture and strength of solids. *Rep. Prog. Phys.*, **12**, 185.

100. Vincent, P.I. (1960) The tough brittle transition in thermoplastics. *Polymer*, **1**, 425.

101. Stearne, J.M. and Ward, I.M. (1969) The tensile behaviour of polyethylene terephthalate. *J. Mater. Sci.*, **4**, 1088.

102. Clarke, P.L. (1982) Tensile yield and fracture of linear polyethylene. Ph.D. Thesis, Leeds University.

103. Hoff, E.A.W. and Turner, S. (1957) A Study of the Low-Temperature Brittleness Testing of Polyethylene. *Bull. Am. Soc. Test. Mater.*, **225**, TP208.

104. Boyer, R.F. (1968) Dependence of mechanical properties on molecular motion in polymers. *Polym. Eng. Sci.*, **8**, 161.

105. Heijboer, J. (1968) Dynamic mechanical properties and impact strength. *J. Polym. Sci. C*, **16**, 3755.

106. Cottrell, A.H. (1964) *The Mechanical Properties of Matter*, John Wiley & Sons, Ltd, New York, p. 327.

107. Vincent, P.I. (1964) Strength of Plastics -16. Conclusion - Yield stress and brittle strength. *Plastics*, **29**, 79.

108. Roesler, F.C. (1956) Brittle fractures near equilibrium. *Proc. Phys. Soc. B*, **69**, 981.

109. Puttick, K.E. (1978) Mechanics of indentation fracture in polymethylmethacrylate. *J. Phys. D*, **11**, 595.

110. Puttick, K.E. (August 1979) Size effects in brittle fracture in *Proceedings of the 3rd International Conference on Mechanical Behaviour of Materials*, Vol. 3, Pergamon Press, Oxford, p. 11.

111. Puttick, K.E. (1980) The correlation of fracture transitions. *J. Phys. D*, **13**, 2249.

112. Griffiths, J.R. and Oates, G. (April 1969) An experimental study of the critical tensile stress criterion for cleavage fracture in 3% silicon-iron in *Proceedings of the 2nd International Conference on Fracture*, Brighton, Paper 19.

113. Irwin, G.R. (1958) Fracture. *Handbuch Phys.*, **6**, 551.

114. Gurney, C. and Hunt, J. (1967) Quasi-static crack propagation. *Proc. Roy. Soc. A*, **229**, 508.

115. Brown, H.R. (1973) Critical examination of impact test for glassy polymers. *J. Mater. Sci.*, **8**, 941.

116. Marshall, G.P., Williams, J.G. and Turner, C.E. (1973) Fracture toughness and absorbed energy measurements in impact tests on brittle materials. *J. Mater. Sci.*, **8**, 949.

117. Plati, E. and Williams, J.G. (1975) Determination of fracture parameters for polymers in impact. *Polym. Eng. Sci.*, **15**, 470.

118. Fraser, R.A.W. and Ward, I.M. (1977) The impact fracture behaviour of notched specimens of polycarbonate. *J. Mater. Sci.*, **12**, 459.

119. Hine, P.J. (1981) The fracture behaviour of polyether-sulphone. Ph.D. Thesis, Leeds University.

120. Truss, R.W., Duckett, R.A. and Ward, I.M. (1983) A novel technique for measuring the impact properties of a tough polyethylene. *Polym. Eng. Sci.*, **23**, 708.

121. Vincent, P.I. (1971) *Impact Tests and Service Performance of Thermoplastics*, Plastics and Rubber Institute, London.

122. Fraser, R.A.W. and Ward, I.M. (1974) The fracture behaviour of notched specimens of polymethyl methacrylate. *J. Mater. Sci.*, **9**, 1624.

123. Bramuzzo, M. (1989) High speed fracture mechanics by photography of polypropylene copolymers. *Polym. Eng. Sci.*, **29**, 1077.

124. Martinatti, F. and Ricco, T. (1994) High rate testing of toughened polypropylene. *Polym. Testing*, **13**, 405.

125. Crouch, B.A. and Huang, D.P. (1994) The J-integral technique applied to toughened nylons under impact loading. *J. Mater. Sci.*, **29**, 861.

126. Ramsteiner, F. (1999) J(0.2)-values by impact testing. *Polym. Testing*, **18**, 641.

127. Fasce, L., Bernal, C., Frontini, P. *et al.* (2001) On the impact essential work of fracture of ductile polymers. *Polym. Eng. Sci.*, **41**, 1.

128. Johnson, A.E., Moore, D.R, Prediger, R.S. *et al.* (1986) The falling weight impact test applied to some glass-fiber reinforced nylons. 1. Appraisal of the method. *J. Mater. Sci.*, **21**, 3153; The falling weight impact test applied to some glass-fiber reinforced nylons. 2. Some results and interpretations. *J. Mater. Sci.*, **22**, 1724 (1987).

129. Moore, D.R. and Prediger, R.S. (1988) A study of low energy impact of continuous carbon-fiber- reinforced composites. *Polym. Compos.*, **9**, 330.

130. Jones, D.P., Leach, D.C. and Moore, D.R. (1986) The application of instrumented falling weight impact techniques to the study of toughness in thermoplastics. *Plast. Rubber, Proc. Appl.*, **6**, 67.

131. Kinlock, A.J. and Williams, J.G. (1980) Crack blunting mechanisms in polymers. *J. Mater. Sci.*, **15**, 987.

132. Evans, R.M., Nara, H.R. and Bobalek, R.G. (1960) Prediction of impact resistance from tensile data. *Soc. Plast. Eng. J.*, **16**, 76.

133. Vincent, P.I. (1974) Impact strength and mechanical losses in thermoplastics. *Polymer*, **15**, 111.

134. Andrews, E.H. (1974) Generalised theory of fracture mechanics. *J. Mater. Sci.*, **9**, 887.

135. Bucknall, C.B. (1977) in *Physics of Glassy Polymers*, 2nd edn (eds R.N. Haward and R.J. Young), Chapman & Hall, London, Chap. 8.

136. Nielsen, L.E. (1962) *Mechanical Properties of Polymers*, Reinhold, New York.

137. Newman, S. and Strella, S. (1965) Stress-strain behavior of rubber-reinforced glassy polymers. *J. Appl. Polym. Sci.*, **9**, 2297.

138. Donald, A.M. and Kramer, E.J. (1982) Plastic-deformation mechanisms in poly(acrylonitrile-butadiene styrene) [ABS]. *J. Mater. Sci.*, **17**, 1765.

139. Bucknall, C.B. and Smith, R.R. (1965) Stress-whitening in high-impact polystyrenes. *Polymer*, **6**, 437.

140. Yang, H.H. and Bucknall, C.B. (April 1997) Evidence for particle cavitation as the precursor to crazing in high impact polystyrene, *10th International Conference on Deformation, Yield & Fracture of Polymers, Churchill College, Cambridge*, Institute of Materials, London, p. 458.

141. Bucknall, C.B. (1967) Relationship between structure and mechanical properties of rubber-modified thermoplastics. *Br. Plast.*, **40**, 84.
142. Lazzeri, A. and Bucknall, C.B. (1995) Applications of a dilatational yielding model to rubber-toughened polymers. *Polymer*, **36**, 2895.
143. Yee, A.F. and Pearson, R.A. (1989) in *Fractography and Failure Mechanisms of Polymers and Composites* (ed. A.C. Roulin-Moloney), Elsevier, London, Chap. 8, pp. 291–350.
144. Cheng, J., Hiltner, A., Baer, E. *et al.* (1995) Deformation of rubber-toughened polycarbonate – microscale and nanoscale analysis of the damage zone. *J. Appl. Sci.*, **55**, 1691.
145. Argon, A.S. and Cohen, R.E. (1990) Crazing and toughness of block copolymers and blends. *Adv. Polym. Sci.*, **91/92**, 301.
146. Rivlin, R.S. and Thomas, A.G. (1953) Rupture of rubber. 1. Characteristic energy for tearing. *J. Polym. Sci.*, **10**, 291.
147. Thomas, A.G. (1955) Rupture of rubber. 2. The strain concentration at an incision. *J. Polym. Sci.*, **18**, 177.
148. Bueche, F. (1962) *Physical Properties of Polymers*, Interscience, New York, p. 237.
149. Flory, P.J. (1946) Effects of molecular structure on physical properties of butyl rubber. *Ind. Eng. Chem.*, **38**, 417.
150. Flory, P.J., Rabjohn, N. and Shaffer, M.C. (1949) Dependence of tensile strength of vulcanized rubber on degree of cross-linking. *J. Polym. Sci.*, **4**, 435.
151. Taylor, G.R. and Darin, S. (1955) The tensile strength of elastomers. *J. Polym. Sci.*, **17**, 511.
152. Bueche, F. (1957) Tensile strength of rubbers. *J. Polym. Sci.*, **24**, 189.
153. Bueche, F. (1958) Tensile strength of filled GR-S vulcanizates. *J. Polym. Sci.*, **33**, 259.
154. Smith, T.L. (1958) Dependence of the ultimate properties of a GR-S rubber on strain rate and temperature. *J. Polym. Sci.*, **32**, 99.
155. Smith, T.L. (1960) Ultimate Tensile Properties of Amorphous Polymers. *Soc. Plast. Eng. J.*, **16**, 1211.
156. Smith, T.L. and Stedry, P.J. (1960) Time and temperature dependence of the ultimate properties of an SBR rubber at constant elongations. *J. Appl. Phys.*, **31**, 1892.
157. Bueche, F. (1955) Tensile strength of plastics above the glass temperature. *J. Appl. Sci.*, **26**, 1133.
158. Bueche, F. and Halpin, J.C. (1964) Molecular theory for tensile strength of gum elastomers. *J. Appl. Phys.*, **35**, 36.
159. Halpin, J.C. (1964) Fracture of amorphous polymeric solids – time to break. *J. Appl. Phys.*, **35**, 3133.
160. Manson, J.A. and Hertzberg, R.W. (1973) Fatigue Failure in Polymers. *CRC Crit. Rev. Macromol. Sci.*, **1**, 433.
161. Thomas, A.G. (1958) Rupture of rubber. 5. Cut growth in natural rubber vulcanizates. *J. Polym. Sci.*, **31**, 467.
162. Lake, G.J. and Thomas, A.G. (1967) Strength of highly elastic materials. *Proc. Roy. Soc. A*, **300**, 108.
163. Lake, G.J. and Lindley, P.B. (September 1966) Fatigue of Rubber, in *Proceedings of the Conference on the Physical Basis of Yield and Fracture*, Oxford, p. 176.
164. Greensmith, H.W. (1963) The change in stored energy on making a small cut in a test piece held in simple extension. *J. Appl. Polym. Sci.*, **7**, 993.

165. Andrews, E.H. (1968) in *Testing of Polymers*, Vol. 4 (ed. W.E. Brown), John Wiley & Sons, Ltd, New York, p. 237.

166. Andrews, E.H. and Walker, B.J. (1971) Fatigue fracture in polyethylene. *Proc. Roy. Soc., A*, **325**, 57.

167. Borduas, H.F, Culver, L.E. and Burns, D.J. (1968) Fracture-mechanics analysis of fatigue-crack propagation in polymethylmethacrylate. *J. Strain Anal.*, **3**, 193.

168. Hertzberg, R.W., Nordberg, H. and Manson, J.A. (1970) Fatigue crack propagation in polymeric materials. *J. Mater. Sci.*, **5**, 521.

169. Arad, S., Radon, J.C. and Culver, L.E. (1971) Fatigue crack propagation in poly-methylmethacrylate – effect of mean value of stress intensity factor. *J. Mech. Eng. Sci.*, **13**, 75.

170. Harris, J.S. and Ward, I.M. (1973) Fatigue-crack propagation in vinyl urethane polymers. *J. Mater. Sci.*, **8**, 1655.

171. Paris, P.C. (1964) in *Fatigue, An Interdisciplinary Approach*, Syracuse University Press, New York, p. 107.

172. Paris, P.C. and Erdogan, F. (1963) A critical analysis of crack propagation laws. *J. Basic Eng. Trans. ASME*, **85**, 528.

173. Arad, S., Radon, J.C. and Culver, L.E. (1972) Growth of fatigue cracks in polycarbonate. *Polym. Eng. Sci.*, **12**, 193.

174. Pitman, G.L. and Ward, I.M. (1980) The molecular weight dependence of fatigue crack propagation in polycarbonate. *J. Mater. Sci.*, **15**, 635.

175. Williams, J.G. (1977) A model of fatigue crack growth in polymers. *J. Mater. Sci.*, **12**, 2525.

176. Mai, Y.W. and Williams, J.G. (1979) Temperature and environmental effects on the fatigue fracture in polystyrene. *J. Mater. Sci.*, **14**, 1933.

Further Reading

Kinloch, A.J. and Young, R.J. (1983) *Fracture Behaviour of Polymers*, Applied Science Publishers, London.

Index